Extended Abstracts of Presentations from the

16th International Symposium for the Advancement of Boundary-Layer Remote Sensing

5-8 June 2012
Boulder, Colorado

ISARS 2012

ISARS 2012

Extended Abstracts of Presentations from the

16th International Symposium for the Advancement of Boundary-Layer Remote Sensing

5-8 June 2012
Boulder, Colorado

Extended Abstracts of Presentations from the 16th International Symposium for the Advancement of Boundary-Layer Remote Sensing, 5-8 June 2012, Boulder, CO USA

Printed in the United States

Cover Photo: Mt. Audubon *(right)* at Brainard Lake, Colorado, © 2011 Paul Neiman

Foreward

The 16th International Symposium for the Advancement of Boundary-Layer Remote Sensing held June 5-8, 2012 in Boulder was hosted by the Cooperative Institute for Research in the Environmental Sciences (CIRES) on the campus of the University of Colorado in Boulder Colorado in cooperation with the Earth System Research Laboratory (ESRL) of the National Oceanic and Atmospheric Administration.

The International Symposium for the Advancement of Boundary-Layer Remote Sensing has been organized about every two years in various forms by the International Society for Acoustic Remote Sensing (ISARS) which held its first symposium in Calgary in 1981 following a number of small informal workshops held in Boulder and Norman in the 1970s. This was followed by subsequent symposia in Rome (1983), Paris (1985), Canberra (1988), New Delhi (1990), Athens (1992), Boulder (1994), Moscow (1996), Vienna (1998), Auckland (2000) and Rome (2002). In 2004 it was held in Cambridge where it was decided, based on the maturity of many remote sensing techniques and their application, to broaden the purpose of the symposia to advance boundary-layer remote sensing in general. Subsequent symposia were then held in Garmisch-Partenkirchen in 2006, Roskilde (2008) and Paris (2010).

The Conference included 124 presentations organized in oral and poster sessions with 107 first authors from nineteen countries. This Proceedings contains all extended abstracts received by 19 May 2012. Additional material and late arriving abstracts can be found on the conference website, currently at www.esrl.noaa.gov/psd/events/2012/isars/.

Boulder, Colorado, June 2012

William Neff, Chair ISARS 2012 Steering Committee
Christopher Fairall and Michael Hardesty Co-Chairs ISARS 2012 Steering Committee

Steering Committee

Philip Anderson	British Antarctic Survey, UK
Stefania Argentini	Istituto di Fisica dell'Atmosfera – CNR, Italy
Frank Beyrich	Meteorologisches Observatorium Lindenberg – DWD, Germany
Stuart Bradley	University of Auckland – New Zealand
Nico Cimini	IMAA-CNR Potenza and CETEMPS – University of L'Aquila, Italy
Steve Cohn	Earth Observing Laboratory – NCAR, USA
Stefan Emeis	Karlsruhe Institute of Technology (KIT), Germany
Chris Fairall *(Co-Chair)*	Earth System Research Laboratory – NOAA, USA
Martial Haeffelin	Institut Pierre Simon Laplace (IPSL) – CNRS/E. Polytechnique, France
Mike Hardesty *(Co-Chair)*	Earth System Research Laboratory – NOAA, USA
Margarita Kallistratova	Russian Academy of Science, Russia
Jakob Mann	Risø National Laboratory, Denmark
William Neff *(Chair)*	Earth System Research Laboratory – NOAA, USA
Dominique Ruffieux	MétéoSuisse, Switzerland
David Turner	National Severe Storms Laboratory – NOAA, USA
Sabine Von-Hünerbein	University of Salford, UK
Alain Weill	LATMOS/IPSL – CNRS/UVSQ, France

Local Organizing Committee

Barb DeLuisi	Earth System Research Laboratory – NOAA, USA
Chris Fairall	Earth System Research Laboratory – NOAA, USA
Lornay Hansen	CIRES – University of Colorado, USA
Mike Hardesty	Earth System Research Laboratory – NOAA, USA
Chris Kreutzer	Earth System Research Laboratory – NOAA, USA
William Neff	Earth System Research Laboratory – NOAA, USA
Linda Pendergrass	CIRES – University of Colorado, USA
Virginia Schultz	University of Colorado– USA

Extended Abstracts

Session 1 – Oral Presentations, Past ISARS Conveners, Chair: Neff

Session 2 – Oral Presentations, Chair: Mann

Session 3 – Oral Presentations, Chair: Ruffieux

Session 4 – Oral Presentations, Chair: Turner

Session 5 – Oral Presentations, Chair: Argentini

Session 6 – Oral Presentations, Chair: Kallistratova

Session 7 – Oral Presentations, Chair: Bradley

Poster Session 1

Session 8 – Oral Presentations, Chair: Emeis

Session 9 – Oral Presentations, Chair: Wilczak

Session 10 – Oral Presentations, Chair: Cohn

Poster Session 2

Session 11 – Oral Presentations, Chair: Hardesty

Session 12 – Oral Presentations, Chair: Banta

Session 13 – Oral Presentations, Chair: Neff

Session 1 – Oral Presentations

TURBULENCE WITHIN LOW-LEVEL JETS OBSERVED WITH A SODAR

Kallistratova M.A.[1], Kouznetsov R.D.[1,2], Kramar V.F.[1], Kuznetsov D.D.[1]

[1]*Obukhov Institute of Atmospheric Physics, 3 Pyzhevskii, 119017 Moscow, Russia, margo@ifaran.ru*
[2]*Finnish Meteorological Institute, 1 Erik Palménin, Helsinki, Finland, rostislav.kouznetsov@fmi.fi*

ABSTRACT

The continuous measurements of wind velocity profiles with a sodar were carried out at Zvenigorod scientific station of the Obukhov Institute of Atmospheric Physics since 2005. The station is located in a slightly inhomogeneous rural area about 45 km West of Moscow. These data were used to obtain the parameters of wind and turbulence within the low-level jets in a stably-stratified atmospheric boundary layer. Together with the mean velocity profiles, the variance of vertical wind velocity from the sodar, and the profiles of temperature from a microwave radiometer have been used to quantify turbulence and thermal stratification in the boundary layer. The data of sonic anemometers were used to get the near-surface parameters. No noticeable vertical variations of a turbulent mixing intensity were found within the jet streams. The typical standard deviation of the vertical speed fluctuations within the low level jet was found to be proportional to the maximum wind speed in the jet with a factor about 0.05. We did not reveal any noticeable impact of Kelvin-Helmholtz billows on the intensity of vertical mixing across the low level jets.

1. INTRODUCTION

The quantitative description of turbulent mixing in a statically-stable atmospheric boundary layer (SBL) is an extremely difficult problem. Hundreds of theoretical and experimental studies on this subject were published over the past half-century. However, the parameterizations and models which are successfully applied to the convective boundary layer, give a rather poor representation of the SBL [1, 13].

The low-level jet (LLJ) is a specific case of SBL in view of a particular shape of the profile of wind velocity. Figure 1 shows the profiles measured by sodar in the Moscow region, which are systematized in the shape and maximum speed. Profiles with a distinct peak within of LLJ (types a, e, i) were observed in approximately 50% of the events. In such cases, the gradient of the velocity and momentum flux are of opposite sign in the upper half of the SBL as compared to the lower half, so there might be some particularities of the vertical structure of the variance of wind velocity components, and the coefficient of turbulent mixing.

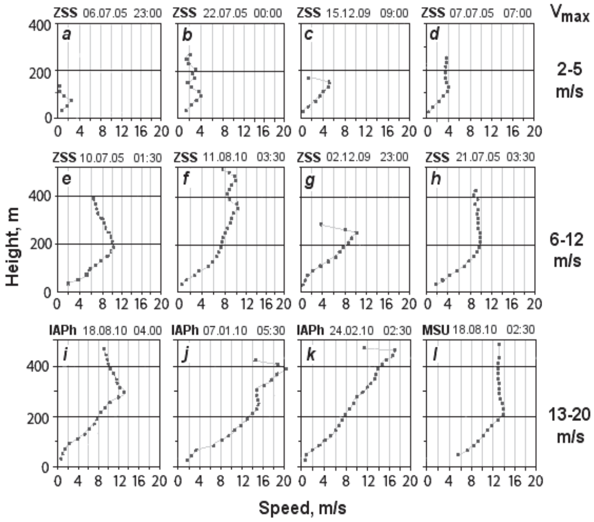

Figure 1. Samples of 30-minute-averaged wind speed profiles during LLJ observed by sodars at three sites in the Moscow region in 2005-2010.

Not many papers were published on the study of turbulence within LLJ, which had been carried out with the help of sodars [6, 8, 9, 12]. Only few episodes of LLJ where reported in these papers. Measurements [8] did not show any particularities in the vertical structure of the streamwise velocity standard deviation σ_U (see Fig.2), but in [12] the increase of σ_U at the LLJ core was found.

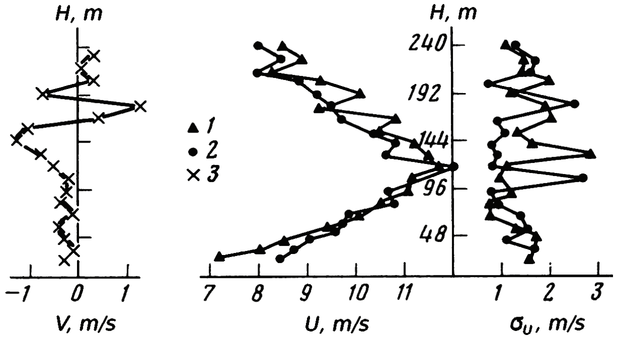

Figure 2. An example of U, V, and σ_U profiles measured by sodar in Tsimlyansk, 12 July 1981. 1 - 02:45-02:54, 2 – 02:55-03:04, 3 – 03:05-03:14 of Local Zonal Time. Adapted from [8].

In the last decade, turbulence parameters within the LLJ were intensively explored with the help of a unique high resolution Doppler lidar (HRDL) [2-4]. A minimum of σ_U^2 at the height of the LLJ core was revealed in studies [2, 3].

The aim of this work is to investigate characteristics of turbulent mixing within the LLJ using a sodar, and to evaluate the impact of Kelvin-Helmholtz billows (KHB) on these characteristics. To this end we used data of the three-axes Doppler sodar Latan-3 [10], the microwave radiometer Attex MTP-5 [7], and the sonics Metek USA-1 at 56-m mast, which were obtained in 2010-2011 at the Zvenigorod Scientific Station (ZSS) of Obukhov Institute of Atmospheric Physics (IAPh). ZSS is located in the weakly inhomogeneous rural area 45 km West of Moscow.

2. RESULTS

2.1 Turbulence within LLJ without wave activity

With the help of a visual analysis of the sodar echograms, a few dozens of episodes of durables LLJs with a pronounced maximum (as in panels a, e, and i in Fig. 1) were selected. These episodes have been traditionally divided into two classes: Class I - strong LLJ under a small temperature gradient, and Class II - weak LLJ under strong stability conditions.

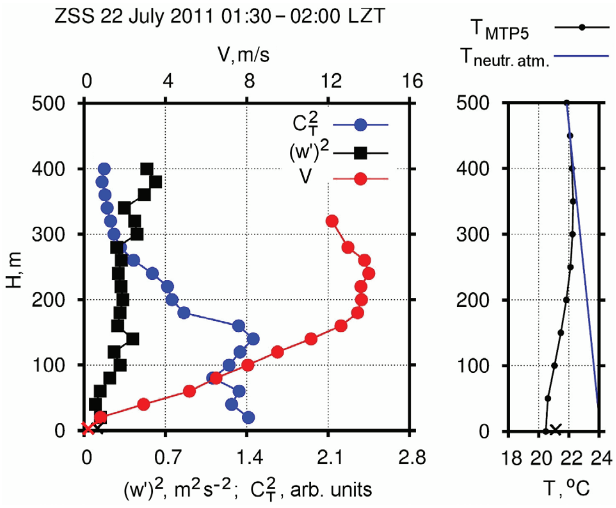

Figure 3. Moderately stable stratification of the ABL. Left: 30-minute-averaged vertical profiles of horizontal wind velocity modulus V, the level of the echo signal C_T^2, and the variance of the vertical wind velocity $(w')^2$, measured by sodar. Right: vertical profile of the air temperature T measured by radiometer; a straight line is the moist-adiabatic profile (γ = -0.0045 °C/m, relative humidity was 95%), coinciding with the upper part of the real temperature profile, which is close to the neutral stratification of the ABL. Crosses near abscissa axes are data of the sonic at mast.

Comparisons between simultaneously measured profiles of temperature, T (z), modulus of horizontal wind velocity V (z), variance of vertical velocity, σ_W^2, and the temperature structure parameter C_T^2 were made for each class.

Examples of such comparisons are shown in Fig. 3 (class I) and Fig. 4 (class II). The value of C_T^2, and the shape of its profile are quite different for the two classes, while the profiles of σ_W^2, characterizing the vertical mixing, are very similar. At the lowest levels of the sodar height range (at 30-50 m agl) σ_W^2 is close to zero. Farther its value remains approximately constant with increasing height within the LLJ, without any particularities at the height of maximum wind speed.

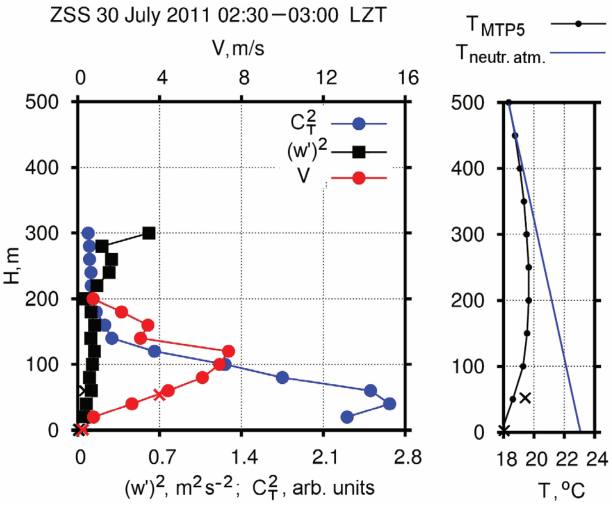

Figure 4. Same as in Fig. 3, but under strong stability conditions. A straight line on the right side is the dry-adiabatic profile (γ = -0.0095 °C/m, relative humidity was less than 80%).

The 30-min data were used to form composite vertical profiles. One example of composite profiles σ_W and V is shown in Fig. 5 for 8 nights in July-August 2011, in which clear jet streams were observed. No distinction between the classes of stability was made here.

The quantities σ_W and V were scaled by LLJ maximum wind speed, V_{max}. Heights were normalized by the height of the first LLJ maximum above the surface, H_{Vmax}. Note that an attempt to normalize V and σ_W by the surface-layer friction velocity u_* instead of V_{max} has led to a significant deterioration the scaled profiles as was indicated by too large error bars.

It follows from Fig. 5 that in average $\sigma_W \approx 0.05V_{max}$ for the both classes mentioned above. There was no obvious deviations from this ratio across the LLJs.

A small increase of the factor with the increase of the scaled height, H/H_{Vmax}, is within the statistical error.

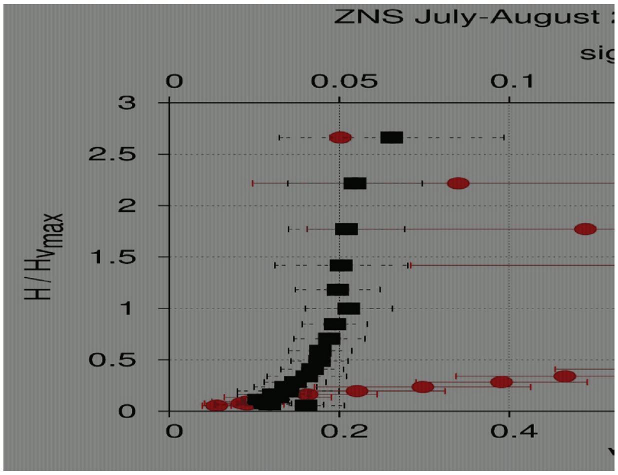

Figure 5. An example of composite profiles of wind speed, V, and standard deviation of vertical speed, σ_W, for 132 half-hour profiles with a clear jet stream, which were observed during 8 nights in July-August 2011. For the values of $H/H_{Vmax} > 1$, values of V/V_{max}, as well as values of σ_W/V_{max}, were united together in several adjacent height-gates to increase the statistical reliability. The horizontal error bars indicate the one-standard-deviation.

2.2 Turbulence within LLJ with Kelvin-Helmholtz billows

Kelvin-Helmholtz billows (KHB) were identified in the sodar echograms by a pattern of braid (or «herring bones») with varying clarity, amplitude, and time period. The KHBs were observed in about 30% of the total lifetime of the LLJ.

The effect of KHB on a turbulence intensity in the LLJ, to our knowledge, has been studied previously for only two short episodes of the wave activity, registered with a sodar [6], and a lidar [5, 11]. The conclusions of this two study are contradictory. According to [6], at episode October 1, 1985 that was observed during 4 hours in the gently rolling terrain near Chicago, the value of σ_W at the KHB period was approximately two times higher than the values measured in the previous quiet period of the same night. The author also showed that this increase was accompanied by a sharp increase in ground-level ozone concentrations. In an episode of October 6, 1999, persisted for about 30 min at south-central Kansas [5, 11], such an increase in the velocity variance was not observed.

We have considered several episodes with distinct KHB, observed at ZSS in 2010-2011. An example of sodar echogram and related wind profiles for one of these episodes is shown in Fig. 6.

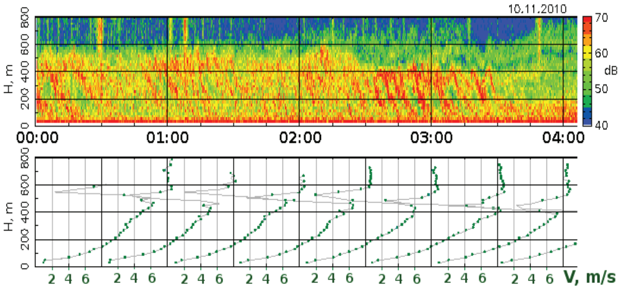

Figure 6. An example of KH billows in LLJ. Top: the sodar echogram; the Local Zonal Time (LZT) is indicated under the echogram. Bottom: the corresponding wind speed profiles. ZSS, Nov 10, 2010.

The profiles of T (z), V (z), σ_W^2, and C_T^2, averaged over half an hour 02:00 - 2:30 for the KHB episode of November 10, 2011, shown in Fig. 6, are presented in Fig. 7. The magnitude, and altitude variations of σ_W^2 in Figure 7 do not have noticeable differences from those in Fig. 3.

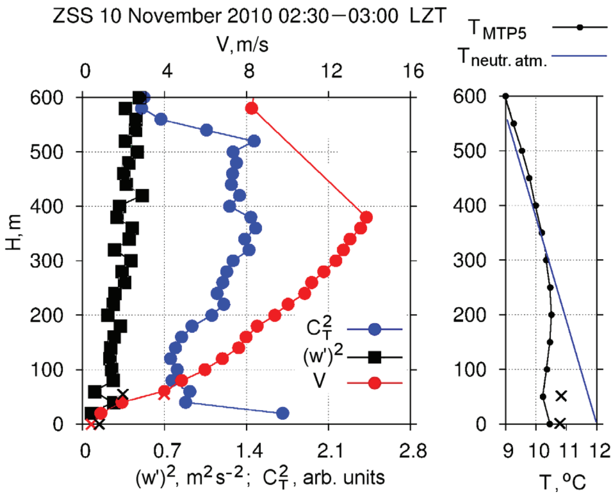

Figure 7. The same as in Fig. 3, but in the presence of the KH billows which are shown in Fig.6.

3. CONCLUSION

No dependence of W variance on the height within low level jet was found, while the lidar profiles [3] of the downstream velocity variance σ_U^2 had a minimum, and the sodar profiles [12] of σ_W^2 had a maximum in the vicinity of the jet core. Reasons for such discrepancies are unclear: whether it was the effect of differences in environmental conditions, or the effect of differences in the methods of data collection and processing.

Even near the surface, the scaling of velocity V and variance σ_W^2 with the LLJ speed V_{max} is better than with the surface layer friction velocity u_*. This inference confirms the findings of studies [2, 3].

The typical standard deviation of the vertical speed fluctuations σ_W within the low level jet was found to be proportional to the maximum wind speed in the jet V_{max} with a factor about 0.05:

$$\sigma_W/V_{max} \approx 0.05.$$

The same ratio was found in [3], but for the standard deviation of downstream velocity σ_U. These two results are inconsistent, since according to data summarized in [3], $\sigma_W/\sigma_U \approx 0.6$ in the SBL.

The study of several episodes of wave activity in the LLJ in Moscow region found no influence of KHB on the average profiles of the variance of vertical velocity.

The using of high-quality lidar, like HRDL, for investigation of the LLJ parameters (including a fine structure of Kelvin-Helmholtz billows) has some advantages over the using of sodar Latan-3. HRDL has a better spatial and temporal resolution, and can evaluate the spatial characteristics of the LLJ, as well as the KHB parameters, during several periods of oscillations, while sodar allows us to investigate only temporal characteristics. However, as it was suggested in [6], “The sodar is admirably suited to investigations of the nocturnal boundary layer”. Besides, sodars have the benefit of a possibility of long-term continuous measurements and a simplicity of data processing.

ACKNOWLEDGMENTS

This study is supported by the Russian Foundation for Basic Research (project No. 10-05-00802), by the EC FP7 project ERC PBL-PMES (No. 227915), and by Academy of Finland (projects ASTREX and IS4FIRES).

REFERENCES

1. Baas P., F.C. Bosveld, G. Lenderink, E. van Meijgaard, A.A.M. Holtslag, 2010: How to design single-column model experiments for comparison with observed nocturnal low-level jets, *Q. J. R. Meteor. Soc.*, **136**, pp. 671-684.

2. Banta R.M., 2008: Stable-boundary-layer regimes from the perspective of the low-level jet, *Acta Geoph.*, **56**, pp. 58-87.

3. Banta R.M., Y.L. Pichugina, W.A. Brewer, 2006: Turbulent velocity-variance profiles in the stable boundary layer generated by a nocturnal low-level jet. *J. Atmos. Sci.*, **63**, pp. 2700-2719.

4. Banta R.M., Y.L. Pichugina, R.K. Newsom, 2003: Relationship between low-level jet properties and turbulence kinetic energy in the nocturnal stable boundary layer, *J. Atmos. Sci.*, **60**, pp. 2549-2555.

5. Blumen W., R. Banta, S.P. Burns, D.C. Fritts, R.K. Newsom, G.S. Poulos, J. Sun 2001: Turbulence statistics of a KelvinHelmholtz billow event observed in the night-time boundary layer during the CASES99 field program. *Dynam. Atmos. Oceans,* **34**, pp. 189-204.

6. Coulter R.L., 1990: A case study of turbulence in the stable nocturnal boundary layer, *Bound.-Layer Meteor.*, **52**, pp. 75-91.

7. Kadygrov E.N., D.R. Pick, 1998: The potential for temperature retrieval from an angular–scanning single–channel microwave radiometer and some comparison with in situ observations, *Meteorol. Appl.*, **5**, pp. 393-404.

8. Kallistratova M.A., J. Keder, I.V. Petenko, N.S. Time, 1985: Averaged wind velocity profile measurements by Doppler sounder in the lower troposphere under inversion and convective conditions. *Izv. Acad. Sci. USSR, Atm. Ocean. Phys.*, **21**, pp. 492-497 (*Engl. Transl.*).

9. Karipot A., M.Y. Leclerc, G. Zhang, K.F. Lewin , et al., 2008: Influence of nocturnal low-level jet on turbulence structure and CO2 flux measurements over a forest canopy, *J. Geophys. Res*., **113**, D10102.

10. Kouznetsov R.D., 2007: LATAN-3 sodar for investigation of the atmospheric boundary layer, *Atmos. Ocean. Optics*, **20**, pp. 684-687 (*Engl. Transl.*).

11. Newsom R.K., R.M. Banta, **2003:** Shear-flow instability **i**n the stable nocturnal boundary layer as observed by Doppler lidar during CASES-99, *J. Atmos. Sci.,* **60**, pp. 16–33.

12. Prabha T.V., M.Y. Leclerc, A. Karipot, D.Y. Hollinger, E. Mursch-Radlgruber, 2008: Influence of nocturnal low-level jets on eddy-covariance fuxes over a tall forest canopy, *Bound.-Layer Meteor.*, **126**, pp. 219-236.

13. Steeneveld G.J., B.J.H. van de Wie, A.A.M. Holtslag, 2006: Modeling the evolution of the atmospheric boundary layer coupled to the land surface for three contrasting nights in CASES-99, J. Atmos. Sci., **63**, pp. 920-935.

RELATIONS BETWEEN MIXING-LAYER HEIGHT, LOW-LEVEL JETS AND CROSS-OVER HEIGHTS – EVALUATIONS OF SODAR AND RASS MEASUREMENTS

Stefan Emeis[1]

[1]*Institute for Meteorology and Climate Research, Karlsruhe Institute of Technology, Kreuzeckbahnstr. 19, 82467 Garmisch-Partenkirchen, Germany, stefan.emeis@kit.edu*

ABSTRACT

Wind profiles and dispersion conditions above the surface layer are influenced by the mixing-layer height and nocturnal or coastal effects such as low-level jets. This can lead to a cross-over of daytime and nocturnal vertical wind profiles (i.e., while the daytime wind speed is higher within the surface layer, the nocturnal wind speed is higher above the surface layer). Low-level jets are equally relevant for wind energy harvests as well as nocturnal regional-scale transport of pollutants in the residual layer.

Ground-based remote sensing techniques such as SODAR and RASS are well suited to observe mixing-layer height, low-level jets and cross-over height. This presentation shows a climatological analysis for the occurrence of low-level jets from several years of observations and identifies weather conditions which are most suited for the formation of low-level jets. Such identification can help to better forecast low-level jets. Subsequently, it is tried to relate mixing-layer height, height of low-level jet and cross-over height to each other. First evaluations show that the cross-over height is roughly one third of the height of the low-level jet core.

1. INTRODUCTION

Planning, installation and operation of wind turbines with hub heights considerably above 100 m require detailed information on the vertical structure of the boundary layer and the wind and turbulence profiles throughout this layer. This goes beyond the usual logarithmic or power laws for the surface layer.

Recently, several authors suggested profile laws for the whole boundary layer [1] [2] [3] [4] [5]. The mixing-layer height (MLH) enters into some of these profiles. Thus, climatological information on MLH should be part of wind site assessment.

The diurnal variation of atmospheric stratification during clear-sky weather conditions leads to different diurnal varitions of wind speed in the surface layer and the Ekman layer. While the wind speed maximum in the surface layer occurs at daytime, the maximum in the Ekman layer frequently occurs at night-time. Plotting averaged wind profiles for daytime hours and night-time hours for such days leads to profiles which often cross over in a certain height. Therefore, this height is also called "cross-over height". A discussion on the diurnal variation of wind profiles can, e.g., be found in [6].

The occurrence of low-level jets is an extreme feature coming with this diurnal variation. Low-level jets lead to night-time maxima in energy harvests and strong vertical wind shear across the rotor plane. Therefore, low-level jet climatologies should be a necessity for site assessment.

2. MIXING LAYER HEIGHT (MLH)

An example for the frequency distribution of MLH derived from half-hourly SODAR observations is given in Fig. 1 for Hannover, Germany for April 2002. Nocturnal MLH is usually around 100 to 200 m above ground, daytime MLH is most frequently around 400 to 500 m. The daytime distribution is much broader than the night-time distribution. No MLH could be derived for about 4% of nocturnal measurement intervals (30 min) and about 8% of daytime intervals. The method for deriving MLH from SODAR measurements is given in [7]. The monthly mean diurnal variation of MLH is shown in Fig. 2. Maximum MLH occurs around 12 and 3 pm, the minimum is found between 4 and 5 am (local time). More results of this kind are displayed in [7].

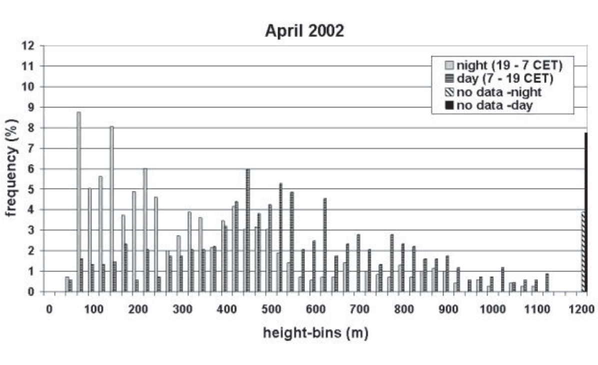

Figure 1. Frequency distribution of MLH from SODAR data for daytime (dark) and night-time (grey) half-hourly intervals in Hannover, Germany in April 2002.

The SODAR used in the Hannover study had a range of about 1000 m. The parallel operation of ta SODAR and a ceilometer in order to detect MLH is advisable due to the limited range of the SODAR. A review on MLH detection by ground-based remote sensing may be found in [8] and [9].

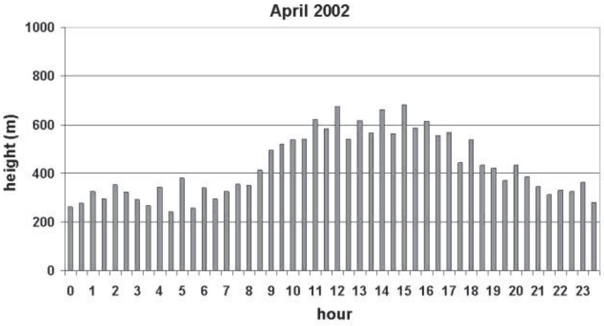

Figure 2. Monthly-averaged diurnal variation of MLH from SODAR data in Hannover, Germany in April 2002.

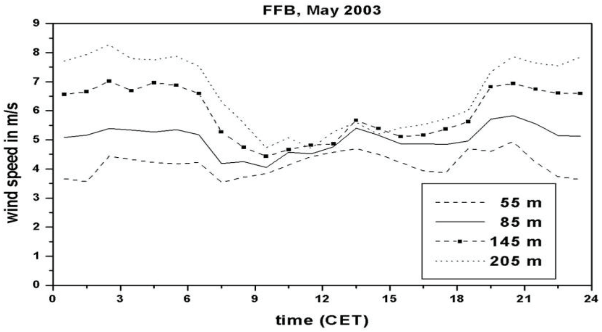

Figure 3. Monthly-averaged diurnal wind speed variations at different heights above ground in Fürstenfeldbruck west of Munich, Germany in May 2003.

3. CROSS-OVER HEIGHT (COH)

Fig. 3 displays diurnal wind speed variations in different heights above ground from SODAR observations in a flat area west of Munich, Germany in May 2003. Daytime wind speed maxima are observable near the surface at heights below about 80 m. Nocturnal wind speed maxima prevail above this height. May 2003 was characterized by clear skies in this area. These variations are usually absent with windy and unsettled weather.

Fig. 4 shows a typical example for wind profile cross-over. COH is at about 125 m above ground. Fig. 5 presents the relation between COH and the height of the core of the nocturnal low-level jet. Roughly speaking, COH is about one third of the height of the jet core.

4. LOW-LEVEL JETS (LLJ)

LLJs appear with certain weather conditions only (Fig. 6). Preferably they occur with clear skies and non-vanishing large-scale pressure gradients. Therefore, they are mostly found at the fringe of large anticyclones (Fig. 7).

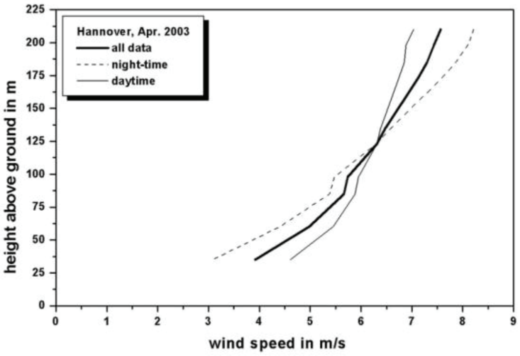

Figure 4. Monthly-averaged daytime and nocturnal wind profiles from SODAR data for Hannover, Germany in April 2003 showing a cross-over at about 125 m.

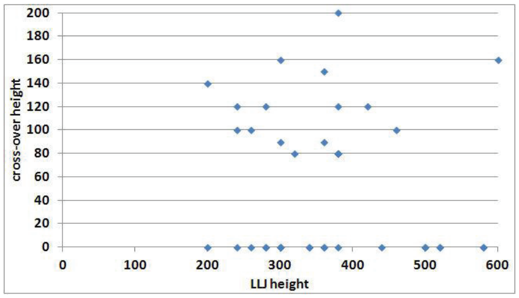

Figure 5. Correlation of COH and low-level jet core height from RASS data for Hamburg, Germany in spring 2011.

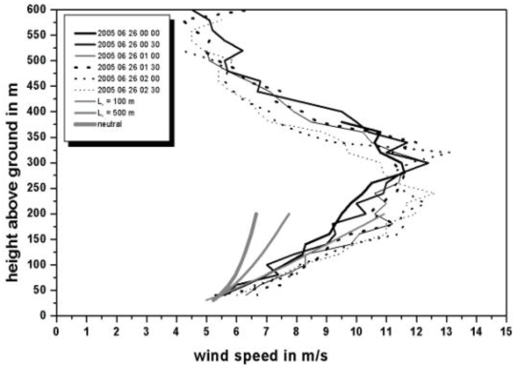

Figure 6. Sample SODAR measurement of low-level jet wind profiles at de Gaulle Airport, Paris in June 2005. Six consecutive half-hour means between midnight and 2.30 am are shown together with three theoretical wind profiles (full lines up to 200 m height).

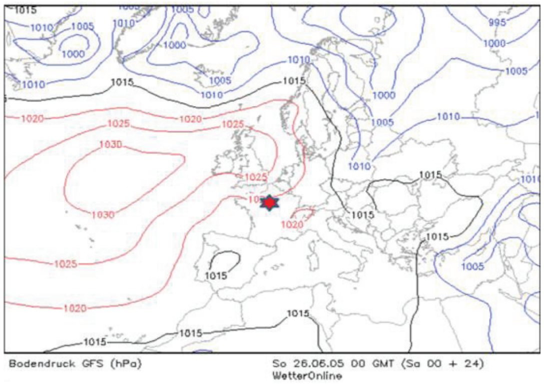

Figure 7. Surface weather map showing the surface pressure distribution prevailing during the measurements displayed in Fig. 6. The red asterisk denotes the measurement site.

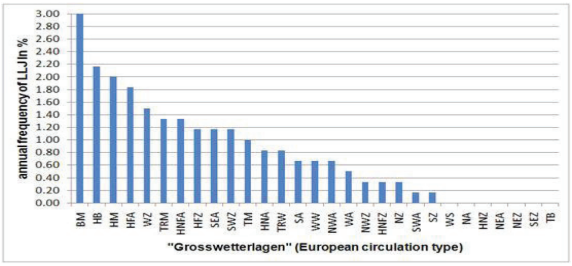

Figure 8. Frequency of the occurrence of LLJs over Hannover, Germany in the years 2002 to 2004 from SODAR data as function of large-scale circulation type (“Grosswetterlagen”).

Fig. 8 indicates that most LLJs over Northern Germany occur during the large-scale circulation types (“Grosswetterlagen”) ‘bridge over Central Europe (HM)’ and ‘high above British Isles (HB)’. Fig. 9 demonstrates that LLJs can be found in 40 to 60% of all occurrences of these two circulation types. The occurrence of LLJs is more or less guaranteed during the occurrence of the patterns ‘high over Fennoscandia (HFZ)’ and ‘high over the North Atlantic (HNFA)’. Thus, the forecast of these two circulation types would be a forecast of the occurrence of a LLJ.

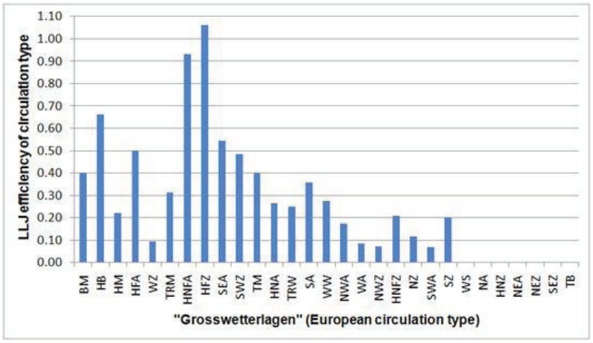

Figure 9. Frequency of the occurrence of LLJs over Hannover, Germany as function of large-scale circulation type normalized by the frequency of occurrence of these circulation types from SODAR observations.

5. OUTLOOK

The examples presented in this Extended Abstract demonstrate the ability of ground-based remote sensing for the assessment of sites for large wind turbines having hub heights larger than about 100 m. Mixing-layer height, cross-over height and the occurrence frequency of low-level jets is highly relevant for choosing the site, selecting the turbine for this site and for their operation.

The displayed cut-out from meteorological analyses is part of what is today called energy meteorology. With growing size of modern wind turbines this part of meteorology will become continuously more important in the near future.

REFERENCES

[1] Etling, D., 2002: *Theoretische Meteorologie - Eine Einführung*. 2. Auflage, Springer, Berlin, Heidelberg, New York.

[2] Emeis, S., K. Baumann-Stanzer, M. Piringer, M. Kallistratova, R. Kouznetsov, V. Yushkov, 2007: Wind and turbulence in the urban boundary layer – analysis from acoustic remote sensing data and fit to analytical relations. *Meteorol. Z.*, **16**, 393-406.

[3] Gryning S-E, Batchvarova E, Brümmer B, Jørgensen H, Larsen S., 2007: On the extension of the wind profile over homogeneous terrain beyond the surface layer. *Bound.-Lay. Meteorol.*, **124**, 251–268.

[4] Peña, A., S.-E. Gryning, J. Mann, C.B. Hasager, 2010a: Length Scales of the Neutral Wind Profile over Homogeneous Terrain. *J. Appl. Meteor. Climatol.*, **49**, 792-806.

[5] Peña, A., S.-E. Gryning, C. Hasager, 2010b: Comparing mixing-length models of the diabatic wind profile over homogeneous terrain. *Theor. Appl. Climatol.*, **100**, 325-335.

[6] Wieringa, J., 1989: Shapes of annual frequency distributions of wind speed observed on high meteorological masts. *Bound.-Lay.Meteorol.,* **47**, 85–110.

[7] Emeis, S., M. Türk, 2004: Frequency distributions of the mixing height over an urban area from SODAR data. *Meteorol. Z.*, **13**, 361-367.

[8] Emeis, S., K. Schäfer, C. Münkel, 2008: Surface-based remote sensing of the mixing-layer height – a review. *Meteorol. Z.*, **17**, 621-630.

[9] Emeis, S, 2011: *Surface-Based Remote Sensing of the Atmospheric Boundary Layer*. Series: Atmospheric and Oceanographic Sciences Library, Vol. 40. Springer Heidelberg etc., X+174 pp.

A REVIEW OF SODAR ACCURACY

Stuart Bradley[1], Torben Mikkelsen[2]

[1]*Physics Department, University of Auckland, Private Bag 92019, Auckland, New Zealand,*
s.bradley@auckland.ac.nz
[2]*Department of Wind Energy, Risø Campus Frederiksborgvej 399, 4000 Roskilde, Denmark, tomi@dtu.dk*

ABSTRACT

What accuracy and reliability can today be expected from SODAR wind measurements? Is there traceable evidence for performance? Environmental factors, turbulent fluctuations and non-uniform terrain all affect the wind speed uncertainty. So site-to-site variations for SODAR-mast comparisons can be large. On a uniform terrain site, differences between a SODAR and a mast-mounted cup anemometer will arise due to turbulent fluctuations and wind components being measured in different spaces, as well as to variable background noise. We develop theories for turbulence-related random fluctuations due to finite sampling rates and to sampling from spatially distributed volumes. Effects can be minimized by selecting the environment and selectively filtering the data for periods of low fluctuations. But there is still real difficulty in answering the question: How good is a SODAR? Most field use, away from an idealized test environment, appears to produce SODAR-mast rms differences greater than the 0.1 m s-1 or less typically quoted by SODAR manufacturers. However, in these real environments it is likely that much of the difference arises from the mast sensors and the SODAR actually measuring in different spaces. We show some field results which reinforce this view. Both the turbulence-related random fluctuations and systematic errors in complex terrain (where systematic wind shears arise) can potentially be removed by use of a vertical column geometry. Field results from a new bistatic receiver shed some light on the differences between such 'common volume' sampling and the usual monostatic sampling.

1. INTRODUCTION

A FP6 EU Program, WISE, reported in 2004 on the state of the art at that time for the use of SODARs in wind energy applications [1]. The conclusions were broadly that SODARs provided a number of advantages compared with mast installations but were not a direct replacement because of significant differences in estimated wind speeds. It was recommended that a small mast installation be used alongside a SODAR. A successor EU program, UpWind, researched improvements in remote sensing, particularly wind energy LIDARs which had emerged toward the end of WISE. Considerable effort in UpWind has gone into mast-LIDAR intercomparisons, with the result that, with careful field setup and data filtering, remarkable correlations can be consistently obtained between LIDAR winds and mast installation winds. Nevertheless, the final project report still recommends use of an accompanying small mast [2].

What do the reported R^2 values mean in terms of predicting differences in measured wind speed? What quality of wind measurements can be expected from SODARs in a typical installation? The first question arises since these differences between cup anemometers and remote sensing instruments are the essence of whether remote sensing gives 'bankable' data. The second question is relevant since the push during UpWind has been to perform intercomparisons under very restricted and controlled conditions, quite unlike those typically encountered at wind farm sites.

2. CORRELATION BETWEEN MAST AND REMOTE INSTRUMENTS

The quality of remote sensing instruments is generally judged by performing an intercomparison experiment such as PIE [3]. In an intercomparison wind speed and direction are measured at several heights by cup anemometers (and/or sonic anemometers) on a mast together with measurements by a remote sensing instrument where a number of sampling volumes are centered on the same heights as the mast measurements. For simplicity in the following we describe the geometry in (x, y, z) coordinates where the mean wind U is in the $+x$ direction, the remote instrument is co-located with the mast, and variations in wind vector components are (u, v, w). A scatter plot is obtained from N measurements of mast instrument wind speed $U_{m,n}$ and the corresponding remote instrument wind speed $U_{r,n}$ where $n = 1, 2, \ldots, N$. Similar pairs of measurements are made of wind direction, but for simplicity we will concentrate on wind speed. Neither of the measurement pairs, $U_{m,n}$ and $U_{r,n}$, necessarily is equal to the actual wind, U_n, which includes the turbulent fluctuations, because all instruments exhibit measurement errors. However, it has been conventional to consider the mast measurements as error-free and to attribute any error or differences as coming from the remote measurements. So we can write

$$U_{r,n} = U_n + \varepsilon_{r,n} . \tag{1}$$

Any systematic bias in differences between remote and mast measurements can be tested by fitting a model to the ($U_{r,n}$, $U_{m,n}$) data set. Since both mast and remote instruments have been proven to be highly linear, and both give an estimated zero wind when the actual wind speed is zero, the physically sensible model to use is a straight line through the origin, of the form

$$\hat{U}_{r,n} = aU_{m,n} \tag{2}$$

This describes the best estimate, $\hat{U}_{r,n}$, for what the remote measurement will be, if a measurement $U_{m,n}$ is made at the mast. A measure of the scatter around the best fit line is R^2, defined by

$$R^2 = 1 - \frac{\sum_{n=1}^{N}\left(U_{r,n} - aU_{m,n}\right)^2}{\sum_{n=1}^{N}\left(U_{r,n} - \overline{U}_{r,n}\right)^2} \approx 1 - \frac{\left(\frac{\Delta U_{rms}}{\overline{U}}\right)^2}{\left(\frac{\sigma_U}{\overline{U}}\right)^2} \tag{3}$$

since a is very close to 1. An R^2 value closer to 1 means that the differences between the two sensors are smaller. Here $\overline{U}$ and σ_U^2 are the mean and variance of the wind speed over the measurement intercomparison, and ΔU_{rms} is the rms difference between mast measured and remote measured wind speed

$$\Delta U_{rms} = \sqrt{\frac{1}{N}\sum_{n=1}^{N}\varepsilon_{r,n}^2}\,. \tag{4}$$

If $\overline{U}$ and σ_U^2 are expressed in terms of the Weibull distribution for the intercomparison site and period, then the ratio $\sigma_U/\overline{U}$ depends only on the shape parameter, k. The rms difference can arise from a number of causes, including

- The difference between scalar (cup-type) and vector (remote-type) measurements
- Remote sensing sampling over spatially distributed volumes
- Remote sensing sampling for each wind estimate spread over time
- Spatial separation between the remote sensing volumes and the mast sensor
- Remote sensing in the presence of background noise.

Except in the case of complex terrain, these differences are essentially random instead of systematic and, except for background noise, the differences are due to turbulent fluctuations in wind speed being sensed differently by the mast sensors and the remote sensors. We will treat the complex terrain case later, but concentrate for now on the random differences. Clearly, R^2 is *not* a property of the remote sensing instrument alone. It depends on the wind regime in which the intercomparisons were completed. For example, if the wind speeds were well spread, then R^2 will be closer to 1, meaning that an R^2 value achieved at a particular site during one measurement period will not necessarily be achieved at the same site in a different measurement period. Furthermore, a larger turbulent intensity will give a larger ΔU_{rms}.

Ultimately, if the site is uniform, turbulence intensity is very low, background noise is minimal, and wind speeds are widely distributed, then a very high R^2 should be achieved by any good quality SODAR or LIDAR remote sensing instrument, since the inherent limitations of the instrument are being reached. This essentially explains why it is possible to get very high R^2 values in some intercomparisons, while much lower values are obtained in others. One of the features of the efforts in UpWind to demonstrate the quality of remote sensing of LIDAR, has been filtering the wind data to remove occasions when there are background influences such as fog, or low ratios of signal to noise (SNR), and when there is not low shear and low turbulence. The outstanding results obtained for LIDARs in UpWind show that these remote sensing instruments can approach very closely to the wind speeds measured by high quality cup anemometers under these 'laboratory' conditions. Less attention has been paid to reducing the ΔU_{rms} for SODARs, and we need to consider where this technology is at, and what the sources of contributions to ΔU_{rms} are for SODARs.

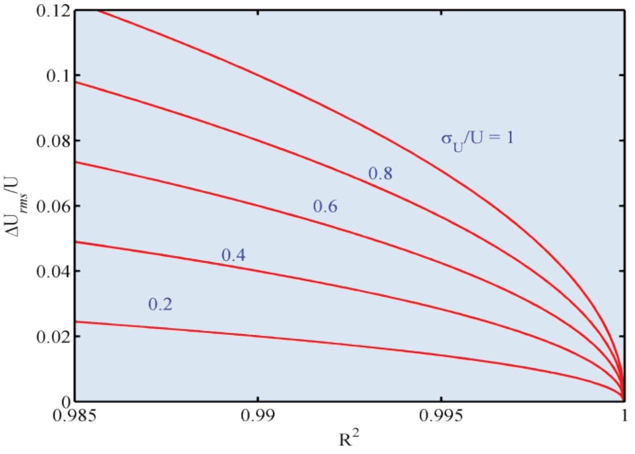

Figure 1. The relationship between fractional rms wind measurement difference and correlation R^2.

Fig. 1 shows the relationship between ΔU_{rms} and R^2 for a range of wind regimes. For $\sigma_U/\overline{U}$ = 0.52, or Weibull shape factor k = 2, the fractional rms wind difference is 6% for an intercomparison producing R^2 = 0.985, or 4% for an R^2 = 0.995. We have also checked this result via a simulation in which 1000 random mast winds are generated from a Weibull distribution, and for each mast wind a remote instrument wind is generated with an additional normally distributed variation.

3. CUP-SODAR DIFFERENCES DUE TO TURBULENCE

A cup anemometer measures the total wind run in a sampling period, whereas a remote sensing instrument averages the vector wind components measured during a sampling period. Kristensen [4] has described the bias arising from this different method of measuring wind, as follows.

The wind speed measured by a cup anemometer is

$$U_{m,n} = \sqrt{(U + u_n)^2 + v_n^2} \tag{5}$$

whereas a remote sensing instrument measures the vector

$$\underline{U}_{r,n} = \begin{pmatrix} U + u_n & v_n & w_n \end{pmatrix}. \tag{6}$$

The average measured by the mast-mounted cup anemometer is (to second order)

$$\begin{aligned} \overline{U_{m,n}} &= \frac{1}{N}\sum_{n=1}^{N} U_{m,n} \\ &= \frac{U}{N}\sum_{n=1}^{N}\left(1 + 2\frac{u_n}{U} + \frac{u_n^2}{U^2} + \frac{v_n^2}{U^2}\right)^{1/2} \\ &\approx U + \frac{\frac{1}{N}\sum_{n=1}^{N} v_n^2}{2U} \end{aligned} \tag{7}$$

whereas that measured by a remote instrument is

$$\overline{\underline{U}_{r,n}} = \frac{1}{N}\sum_{n=1}^{N} \underline{U}_{r,n} = \begin{pmatrix} U & 0 & 0 \end{pmatrix} \tag{8}$$

or speed $\overline{U_{r,n}} = U$. The normalized mean difference between mast and remote measured winds is

$$\frac{\overline{U_{m,n}} - \overline{U_{r,n}}}{U} = 1 + \frac{1}{2}\left(\frac{\sigma_v}{U}\right)^2. \tag{9}$$

The term in brackets is the transverse turbulent intensity and the difference in measured wind speeds will be typically in the range of 0 to 8%.

The work of [4] did not describe the random differences arising from scalar vs vector averaging. For a particular turbulence intensity these two different measures of wind speed will give rise to scatter in a plot of winds measured by mast instruments versus winds measured by remote instruments. This scatter derives from the *variance* in the difference $\overline{U_{m,n}} - \overline{U_{r,n}}$. For the cup measurements

$$\sigma_m^2 = \frac{1}{N}\sum_{n=1}^{N}\left(U_{m,n} - \overline{U_{m,n}}\right)^2 \approx \sigma_u^2 \tag{10}$$

and for the remote measurements

$$\sigma_r^2 = \frac{1}{N}\sum_{n=1}^{N}\left(U + u_n - U\right)^2 = \sigma_u^2 \tag{11}$$

so the variance of the difference is

$$\Delta U_{rms}^2 = \sigma_m^2 + \sigma_r^2 = 2\sigma_u^2 \tag{12}$$

However, wind measurements are typically averaged over 10 minutes. For a SODAR having a range of 300m, this is typically an average over around 70 wind estimates. The result is a reduction in the variance by about 60, giving

$$\frac{\Delta U_{rms}}{U} \approx \frac{1}{6}\frac{\sigma_u}{U}. \tag{13}$$

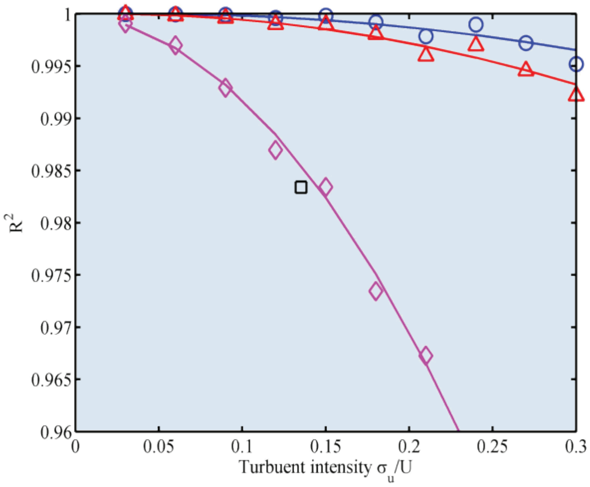

Figure 2. The effect on R^2 of scalar-vector averaging differences (circles), of a mast-SODAR separation of 80m (triangles) and of successively sampling from 3 volumes (diamonds). In all cases the Weibull scale parameter = 8 m s^{-1}, and shape factor = 2. Also shown is a data point from WISE (square).

The normalized standard deviation between mast and remote measured winds is therefore proportional to the turbulence intensity, and the scatter naturally affects R^2. We can simulate this by generating winds U from random Weibull deviates, and then generating random u_n, v_n, w_n values for a succession of samples at this U. These turbulent components are generated by filtering a white noise spectrum to obtain a Von Karman velocity spectrum. Fitting a straight line to the resulting scatter plot gives R^2 values for each chosen turbulence intensity, as shown in Fig. 2.

Remote sensing instruments measure the wind vector components in directions x, y, and z by solving (or fitting solutions to) equations which relate the wind components to the Doppler shift along each radial beam direction. As an example, a 3-beam system having two beams tilted at angle θ off-vertical and one vertical beam, would solve equations like

$$\begin{aligned} m_{n,1} &= (U + u_{n,1})\sin\theta + w_{n,1}\cos\theta \\ m_{n,2} &= v_{n,2}\sin\theta + w_{n,2}\cos\theta \\ m_{n,3} &= w_{n,3} \end{aligned} \tag{14}$$

with solution

$$\begin{aligned} U_{r,n} &= \frac{m_{n,1} - m_{n,3}\cos\theta}{\sin\theta} \\ &= U + u_{n,1} + (w_{n,1} - w_{n,3})/\tan\theta \end{aligned}. \tag{15}$$

In this case

$$\frac{\Delta U_{rms}}{U} = \sqrt{\left(\frac{\sigma_u}{U}\right)^2 + \frac{2}{\tan^2\theta}\left(\frac{\sigma_w}{U}\right)^2}. \tag{16}$$

The effect of this time delay in sampling distributed volumes is also simulated using the random Von Karman method, and is also shown in Fig. 2. One measured point from the WISE PIE campaign is also shown, as a square: this compares closely with the simulation.

Depending on the site, a SODAR can receive reflections from fixed non-atmospheric objects. This ‘fixed echo’ effect produces a second Doppler spectrum peak centered on zero Doppler shift. If the wind speed is relatively low, then the two spectral peaks can overlap and an incorrect lower estimate of the wind speed is obtained from the composite peak. In fact the same problem occurs with LIDAR systems and stray laser energy, but the effect only occurs for wind speeds below 3 m s^{-1}. In the case of SODARs, a comparable limit occurs, providing the spurious zero-Doppler peak and the required atmospheric reflection peak are of comparable magnitude. Unfortunately, this often is not the case if a SODAR is placed close to a mast. Consequently, SODAR-mast intercomparisons are inevitably conducted with the SODAR placed 80m or more from the mast. This introduces a further difference between the SODAR measured wind and the mast sensor winds, since the same volume of air is not being sensed. The fixed echo problem could be greatly reduced for SODARs if their design was with a greater off-vertical beam angle θ, such as 30° used by some LIDAR systems instead of the 15° typical of most SODARs. Fig. 2 also shows the effect on R^2 of a mast-SODAR separation of 80 m, using the same turbulence simulation method. In Fig. 2. the three turbulence-related effects are treated separately. It is clear that, even in uniform terrain, the sampling of three or more spatially separated volumes by a SODAR, over a time interval of something like 9 s, is the main cause for reduced R^2.

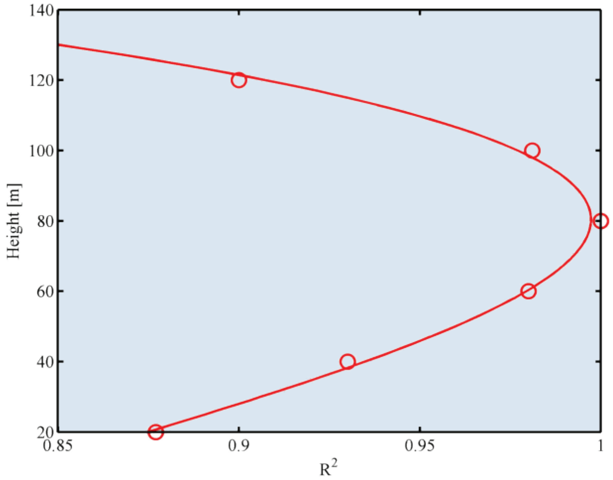

Figure 3. R^2 versus height for opposing beams aligned with the wind (adapted from Behrens et al. [5]). Measurements (circles), theory (solid line).

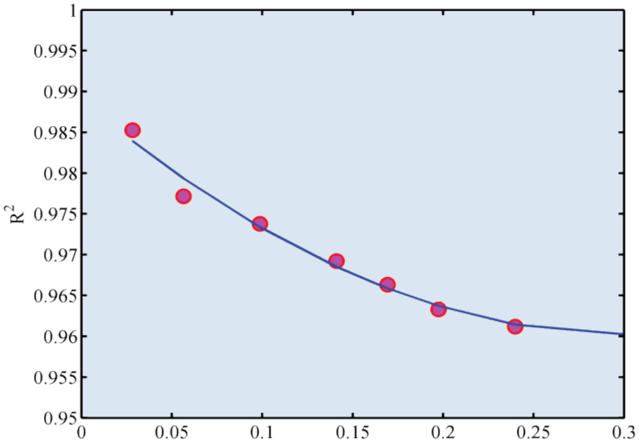

Figure 4. Measured R^2 and σ_u/U values inferred from [5]. The measurements were in complex terrain.

This effect has also been explored experimentally [5]. Fig. 3, adapted from this work, shows the correlation as a function of height between two opposing beams aligned with the wind for a five-beam Metek SODAR. A very high R^2 is measured at the height where turbulence from one sampled volume has moved to the second sampled volume in the time between sampling the two volumes. Measurements in complex terrain of

ΔU_{rms} vs mast measured σ_u are also given in [5]. In Fig. 4 we have assumed reasonable values of $\overline{U}$ and σ_U^2 so as to be able to plot these measurements as R^2 vs σ_u/U. The measured values follow roughly the predictions from Fig. 2.

The general conclusion from the above is that, in uniform terrain under low acoustic background noise conditions and retaining only those measurements during low turbulence, very high R^2 values can be anticipated for SODARs. This approach would match that taken over the past few years in showing that LIDARs can match closely the winds measured by cup anemometers. To date this type of careful intercomparison experiment has not been performed on SODARs. Note that such an intercomparison does not match what might be expected as typical field experience with these instruments. Indeed, it may be necessary to discard entire days of data in order to obtain optimal conditions, unlike with resource surveying or monitoring.

4. SODARS IN COMPLEX TERRAIN

It is now well-established that remote sensing instruments exhibit large errors in wind speed estimation in complex terrain [5][6][7]. There is only one theoretical model for the effect of complex terrain on spatially-separated sampling of wind by remote sensing instruments [7]. This theoretical model is based on potential flow over a bell-shaped hill of height-to-width *h*/*L*.

The speed-up of flow over the hill crest means that a mast placed at the top of the hill will measure higher winds than a remote sensing LIDAR or SODAR, since these instruments perform some of their measurements in volumes to the side of the hill peak where the wind speed is lower. In this case remote sensing produces an under-estimation in wind speed. Similarly, an instrument mounted half-way up the hill slope may do some of its measurements in a higher wind speed regime closer to the crest, thereby giving an over-estimation of wind speed. This model is very simple, but performs well when compared with field measurements in complex terrain [8][9]. The model in [7] gives estimates of errors for different hill geometries, different remote sensing configurations and orientations, but a simple approximation can be made. The fractional error in estimating the wind speed for a 3-beam sodar sited on the crest of the hill, with beam 1 facing downwind, is

$$\frac{\Delta U_{rms}}{U} \approx -5G_{\max}^2 \frac{z}{H} \qquad (17)$$

where z is the height of the sensing volume above the hill crest, H is the hill height, and $G_{\max}$ is the maximum gradient of the bell-shaped hill. The fractional error is negative because the maximum speed is directly above the instrument in this case, and the beam directed in the direction of the flow underestimates. So for a hill of maximum gradient 0.1, and with $z = H$, a 5% error in wind estimation is predicted. This is comparable to the error measured in practice in complex terrain, and is unacceptably high for wind energy applications. Note that this error is *generic* across all SODARs and LIDARs, and is insensitive to the beam zenith angle θ. Also, unlike the turbulence-related variations between remote instrument and mast sensor, the complex terrain difference is a systematic error.

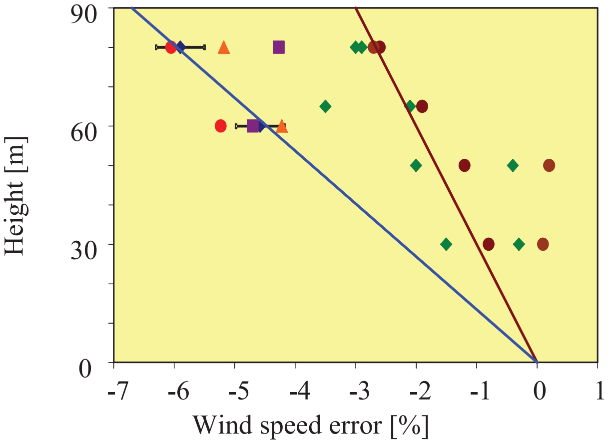

Figure 5. Measurements at a moderate hill site (ZephIR lidar measurements in green, AQ500 sodar measurements in brown), and at a complex site (Metek sodar measurements in blue). Model results are shown for a bell-shaped hill potential-flow model (orange), WindSim (purple) and OpenFOAM (red) for the complex site.

Fig. 5 shows complex terrain errors measured for both a ZephIR LIDAR and an AQ500 SODAR at Myres Hill in Scotland. These errors are characterized by their increasing with height. It can be seen there is no statistical difference between the LIDAR and SODAR errors. Measurements have also been made at Turitea in New Zealand [9], and compared with various flow models, alaso shown in Fig. 5. Again, similar errors are seen with increasing height. The simple bell hill model compares well with the industry-standard WindSim and the complex CFD OpenFoam model [9].

5. CONCLUSIONS

Given the above discussed differences between mast and SODAR, what is the best current estimate of the fundamental wind speed errors in a SODAR? We have distinguished *differences* and *errors*. Differences (between a SODAR and a mast-mounted cup anemometer) will arise due to turbulent fluctuations and wind components being measured in different spaces, as well as to variable background noise. Such differences can be minimized by selecting the environment and selectively filtering the data for periods of low fluctuations. The commonly quoted R^2 values for remote sensing instruments are *not* a property of the instrument.

There is real difficulty therefore in answering the question: How good is a SODAR? Most field use, away from the idealized 'lab' environment, seem to have an R^2 value of 0.975 to 0.985. From Eq. (3), this corresponds to a range of relative difference, compared to a cup anemometer, of 6% to 5%. For a 10 m s^{-1} mean wind speed, this corresponds to about 0.5 m s^{-1} rms difference. It is not known how this range compares with LIDARs under similar conditions, although there is some evidence that those institutions who have been operating both a LIDAR and a SODAR together or in similar environments are finding little difference.

We have examined, both analytically and via simulations, how the random differences between SODARs and cups could arise. It appears that the dominant effect is likely to be sampling from three spatially-separated volumes, each of which has different turbulent components. We have, in the current work, only evaluated this effect for one SODAR beam configuration, but the principle should apply for others. We have given supporting experimental evidence, but it would be good to test some of these predictions in a more rigorous field campaign. One approach to reducing this source of variation is to continuously transmit on all beams, instead of waiting for the return time of individual pulses.

All current remote sensing instruments produce winds with errors in complex terrain. The errors become larger for a steeper hill or for measuring further above the ground. These errors can be estimated from flow models, and actual field measurements suggest a relatively simple model (which can be run on a laptop in a few seconds) gives predictions comparable to much more complex models. There appears to still be more work required to demonstrate that the combination of in situ remote sensing measurements and flow models can robustly produce wind data of the required accuracy.

Both the turbulence-related random fluctuations and the complex terrain errors can potentially be removed by use of a vertical column geometry. As noted, this geometry also has other advantages, but it does have the disadvantage of having to distribute three sensors on the ground instead of one. However, a new design in progress has each of the two passive receivers as being quite small and mobile (can be carried in one hand).

Current experience being reported by virtually all SODAR users is very positive, with relatively little or no maintenance time. However, care does need to be taken with regard to nearby trees or other structures to ensure that the wind record is not contaminated by fixed echo returns.

REFERENCES

1. de Noord M, Curvers A, Eecen P, Antoniou I, Jørgensen HE, Pedersen TF, Bradley S, von Hünerbein S, Kindler D, Mellinghoff H, Emeis S. WISE Wind Energy SODAR Evaluation Final Report, EU project NNE5-2001-297, ECN-C--05-044, 2005, 1-95.

2. http://www.ewea.org/fileadmin/ewea_documents/documents/upwind/21895_UpWind_Report_low_web.pdf, 84-88, 2011

3. Antoniou I, Jørgensen HE, von Hünerbein S, Bradley SG, Kindler D, Warmbier G, de Noord, M. The profiler intercomparison experiment (PIE). EWEC European Wind Energy Conference, London, UK, November 2004.

4. Kristensen K. The perennial cup anemometer. *Wind Energy* 1999; 2 : 59-75.

5. Behrens P, Bradley S, Wiens T. A Multisodar Approach to Wind Profiling. *J. Atmos Ocean. Tech*. 2010; **27**: 1165-1174.

6. Bingol F, Mann J, Foussekis D. Conically scanning lidar error incomplex terrain. *Meteorologische Zeitschrift*, 2009; **18**: 189–195.

7. Bradley S. Wind speed errors for LIDARs and SODARs in complex terrain. *IOP Conf. Series: Earth and Environmental Science*, 2008; **1**; 1–7.

8. Bradley, S. G., Y. Perrott, and A. Oldroyd, 2012: Corrections for Wind-Speed Errors from Sodar and Lidar in Complex Terrain. *Bound. Layer Met,* **143**, 37-48.

9. Behrens, P., J. O'Sullivan, R. Archer, and S. Bradley, 2012: Underestimation of mono-static sodar measurements in complex terrain. *Bound. Layer Met*., **143**, 97-106.

Thermal Structure of the Boundary Layer Over the Snow: Results from an Under Way Experimental Field at Concordia Station, Dome C, Antarctica

S. Argentini[1], I. Petenko[1], A. Viola[1], G. Mastrantonio[1], I. Pietroni[1], G. Casasanta[1],
E. Aristidi[2], C. Ghenton[3], A. Conidi[1]

[1] *ISAC – CNR Area di Ricerca di Roma Tor Vergata,Via del Fosso del Cavaliere, 100 00133 Roma, Italy,*
s.argentini@isac.cnr.it
[2]*Laboratoire Lagrange, UNS/CNRS/OCA Parc Valrose - F 06108 Nice Cedex 2, France*
[3]*LGGE CNRS 54 Rue Moliere, DU BP 96 - F-38402 Saint Martin d'Heres Cedex, France*

ABSTRACT

A field experiment was launched at the French - Italian station of Concordia at Dome C, east Antarctic Plateau, on December 2011. The main objective of the experiment is to monitor the fine structure of the atmospheric surface layer in order to determine the space/time scales of the turbulent processes under very stable conditions. We also want to study the processes which lead to the formation of the warming events observed periodically during the winter. The experiment will last until January 2013. The measurements are made with a surface layer mini-sodar (SLM-sodar) and a sonic anemometer. The radiation budget and heat flux measurements into the snow are also provided. To ensure vertical extensions and resolutions suitable to the study of both processes, the SLM-sodar is set to operate in a configuration that allows to switch from high resolution surface layer observations (carrier frequency: 4850 Hz; pulse repetition time: 2 s; range: 2 - 300 m) to long range operation (carrier frequency: 2000 Hz; pulse repetition time: 6 s; range: 15 - 900 m). A few results of the first two months of measurements are presented together with the experimental strategy planned for the winter.

INTRODUCTION

At Dome C clear sky and light winds produce weak shear, turbulence, mixing and strong temperature gradients near the surface [1]. Though the winds are light and variable, the near surface structure of the boundary layer - depending on the relative importance of the mechanical generation of turbulence, and damping induced by stability - can change quite quickly, leading to different turbulent mixing depths. Above the surface layer a quiescent layer - often decoupled from the surface - may be observed.

To determine the time scales and the height evolution of the mixing turbulent processes is important to monitor the evolution of the boundary layer thermal structure starting from the surface layer for all the year.

During the summer, despite the low surface temperatures, a weak convection is observed which determines a mixed layer of a few hundred meters depth (300-400 m). The thickness of this layer strongly depends on solar elevation [1, 2, 3]. Several studies [1, 2, 4, 5] have shown the behaviour, and parameterised the evolution, of this convective layer during the summer using the measurements obtained with a mini-sodar system. Due to the low vertical resolution, and the inability to perform measurements below 30 meters (i.e. the surface layer), the turbulent activity in the near proximity of the snow surface couldn’t be studied either in summer or in winter [1]. A high resolution surface layer mini sodar (hereafter SLM-mini sodar), developed by the ISAC-CNR, was deployed at Concordia station after being tested at ISAC CNR research centre of Tor Vergata close to Rome [6]. The system, installed on December 2011, will be operational throughout January 2013. Parameters have been chosen in such a way to monitor - with the needed resolution - the stable layer depth , and the above quiescent layer where the trace of fronts responsible for the warming events are often observed at Dome C [11].

SITE AND INSTRUMENTATION

Concordia is a permanent station located at Dome C, Antarctica (74.1 °S, 123.3 °E, 3233 m a.s.l.), on the East Antarctic plateau approximately 1000 km from the nearest coastline. *In situ* turbulence and radiation measurements, as well as a SLM-sodar observations, are carried out. The SLM-sodar is an advanced version of the sodar described by [4] and [6] configured to study the atmospheric surface-layer. The system consists of 3 horn-type antennas - emitting simultaneously acoustic pulses at the same frequency - placed symmetrically around one parabolic receiving antenna. The receiving antenna is noise-protected by a structure of 1.50 L x 1.50 W x 2.00 m H. The transmission and receiving chains are kept separated to minimize the “cross-talk” between channels/antennas. Two sets of parameters are used alternately during the year to explore, with the appropriate height/time resolution, different parts of the boundary layer (Table 1).

Table 1: SLM-sodar running parameters

Carrier frequencies	2000 Hz, 4850 Hz
Pulse duration	200 m s, 10 m s
Pulse repetion rate	6 s, 2 s
Maximun Range	895 m, 94 m
Lowest observation height	31 m, 4 m
Vertical Resolution	27 m , 2 m

In this paper, unless told otherwise, the measurements are given in local standard time (LST). Measurements of turbulence are made with a Metek USA-1 sonic thermo-anemometer (sampling frequency 10 Hz) installed 3.5 m above the snow surface. The heat and momentum fluxes are estimated using the eddy covariance method [7]. The longwave and shortwave radiation components are measured using Kipp & Zonen pyrgeometers and pyranometers installed 1. 5 m above the snow surface.

RESULTS

In previous field experiments the processes occurring in the stable mixing layer and the mixing layer height (MH) evolution under stable conditions could not be studied because the electro-acoustic transducer ringing “obscured” the first 20-30 m [3, 1]. In addition the high frequencies, the low emitted acoustic power and the small receiver antenna diameter did not allow a good signal to noise ratio. Figure 2 shows the echogram obtained for the 28 December 2011 using 2 kHz frequency. This record presents the characteristic behavior of the atmospheric mixing layer during a summer day at Dome C. A stable boundary layer occurs between 0000 and 0900 LST. From 0900 LST to 1630 LST the ML depth increases due to surface buoyancy to decline immediately after to 50 m due to the radiative cooling of the surface. The ML height (red dots superimposed to the facsimile) was estimated using a simple method, originally proposed by [8], that can be applied using only the backscattered range corrected signal (RCS). In stable nocturnal conditions, the MH was determined either from the minimum of the first derivative or from the maximum curvature of the RCS, depending on the stage of the planetary boundary layer evolution, and on the shape of the sodar profile. In convective conditions, the MH was considered as the height at which an elevated secondary maximum occurs, i.e. in correspondence of the high turbulent zone that characterize the top of a well-mixed PBL.

The procedures suggested both in convective and stable conditions are summarized in Table 2.

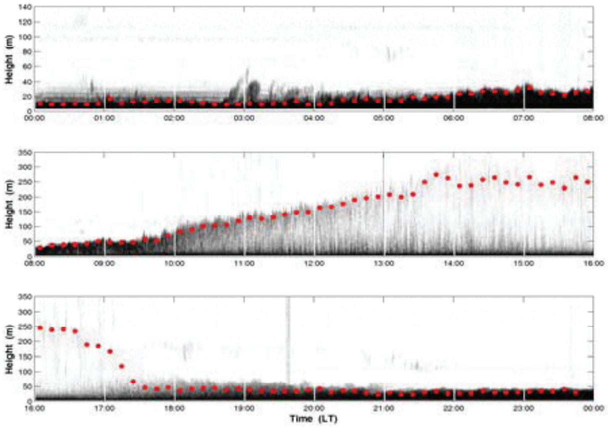

Figure 2. Facsimile recording for 28 December, 2011. From 0000 to 0600 LST the vertical scale between has been kept different from the other hours for a better resolution of the surface layer processes. The red dots represent the estimate of the mixing height under both stable and unstable conditions.

Table 2 - Suggested scheme for MH estimations based on sodar profiles [8]

PBL regime	Shape of the RCS	Applied method
Stable PBL	Continuous decrease with height	Maximum RCS curvature
	Elevated maximum in RCS	RCS first derivative minimum
Convective PBL	Elevated maximum in RCS	Height of the maximum

In the period 2-5 February 2012, the high frequency configuration was used. Persisting waves are observed in more than 35% of the time. When the thermal boundary layer develops vertical oscillations of increasing amplitude can be observed at the capping inversion. An example is shown in Figure 3. Vertical oscillations larger than 70 m are recorded in the interval 0930-1000 LST (see Figure 4a). All the wavy structures recorded during the analyzed days have a short apparent period that was estimated through the harmonic analysis of the sonic temperature and wind components of the sonic anemometers installed at different height (7m, 23m, and 39 m) on the Dome C 50 meter meteorological tower [9] located close to the SLM-sodar . In Figure 4b the first part of the spectral power densities (SPD) of the temperature and wind components measured at 39 m are shown. A high correlation is present in the wind component SPDs that can be associated with the horizontal variability of the flow (for example the vortices). A large peak is present contemporarily in the SPD’s temperature and wind component at 0.0098 Hz. This frequency and the corresponding period (102 s) are close to the one that may be estimated in the echogram. The analysis of sonic anemometers (at 7, 23, and 39 m) measurements in the interval 0800-1030 showed an apparent period ranging between 90 and 120 s as well. The relative constancy of the apparent wave periods even if the thermal stability is decreasing, suggests that these gravity waves are not generated locally.

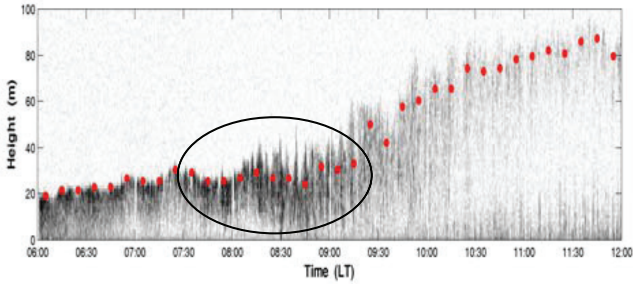

Figure 3. Facsimile recording of the backscattered echoes for 5 February 2012 (0600 to 1200 LST).

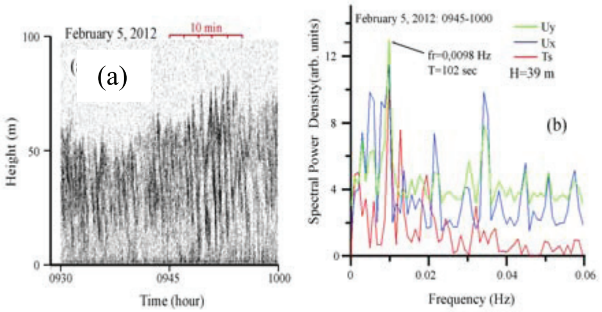

Figure 4. (a) Facsimile for 5 February, 2012 (0930 to 1000 LST). (b) Spectral analysis of the horizontal (Ux, Uy) and sonic temperature T_s.

A small amount of cloud cover is generally present above Dome C, since cloud cover and precipitation decrease when moving inland from the coast, and the level of the occurrence of active weather systems is low [10]. Argentini, et al. [11] have shown that warming events are periodically observed at Dome C during the winter, and the surface temperature sometimes reaches the values recorded in the summer. Figure 5 shows the arrival of a warm front between 0100 and 0300 LST. The wind direction varies and rotates from 135°-180° (180 ° is the most frequent wind direction) toward 245° due to the advection of warm air from the coast. . Studies at South Pole [12], [13], [14], [15], have found that these warming events generally occur in presence of clouds. Reference [16] analyzing the periods of cooling and warming at the South Pole, has correlated these phenomena to the variation in wind direction above the boundary layer. Carroll [12] has suggested two possible mechanisms: the advection of warm air, and/or the vertical mixing of air from different layers. Reference [17] analyzing the particle trajectories across Antarctica, has showed that the process of warming is mostly due to the intrusion of warm and moist air and to the condensation of nuclei which originate from the Weddell Sea, producing a wide variety of cloud types.

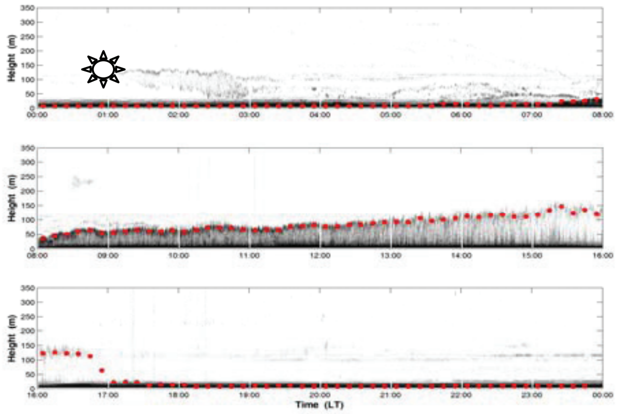

Figure 5. Facsimile recording of the backscattered echoes for 12 December, 2011. The sun on the picture indicate the arrival of the warm front at 0100 LST.

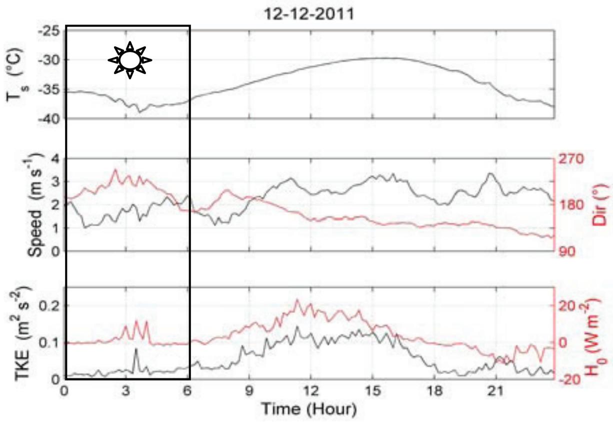

Figure 6. Time series of the sonic temperature, wind speed and direction, TKE for 12 December, 2011. The warming is observed up to 0600 LST.

Schwerdtfeger P., G. Weller [18] have related the surface warming to the variation of long-wave radiation emitted by the clouds associated with the moist air present in the upper part of the atmosphere. Using low frequencies we have the possibility to monitor the presence of fronts on the sodar facsimile recording up to 500 m while in the bottom of the boundary layer a regular daytime evolution is observed. Figure 7 shows the time behavior of the shortwave radiation (SW) down (orange) and up (pink), the longwave radiation (LW) down (blue) and up (black), the net radiation R_{net} and the net longwave radiation LW_{net} for the same figures as 5 and 6.

The arrival of the warming event is clearly shown by the increase of the longwave radiation between 0000 and 0600 LST.

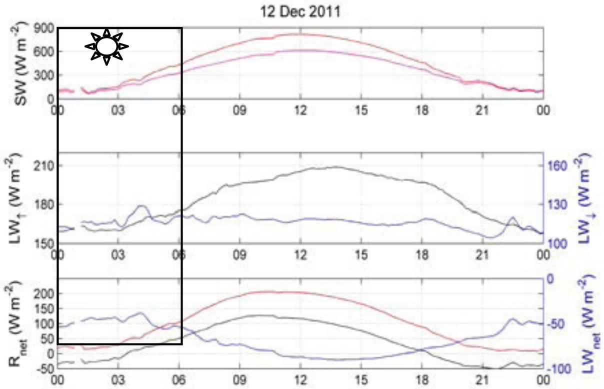

Figure 7. Time series of the sonic temperature, wind speed and direction, TKE for 12 December, 2011.

ACKNOWLEDGMENTS

This research is supported by the Piano Nazionale Ricerche in Antartide (PNRA) in the frame of French-Italian projects for Dome C. The authors thank Nicola Ferrara and Spartaco Ciampichetti for the technical support provided in the realization of the SLM-sodar antennas and the logistics staff at Concordia for their support during the field work

REFERENCES

1. Pietroni I., S. Argentini, I. Petenko, R. Sozzi, 2011: Measurements and parameterizations of the atmospheric boundary layer height at Dome C, Antarctica, *Boundary-Layer Meteorol*, **143**, pp. 189-206.

2. Argentini S., A. Viola, A. Sempreviva, I. Petenko, 2005: Summer boundary-layer height at the plateau site of Dome C, Antarctica, *Boundary-Layer Meteorol*, **115**, pp. 409-422.

3. Argentini S., I. Pietroni, 2010: An Integrated Observing System for BoundaryLayer Monitoring at Concordia Station, Antarctica. In *Integrated Ground-Based Observing Systems*, Springer, pp. 199-208.

4. Mastrantonio, G., V. Malvestuto, S. Argentini, T. Georgiadis, A. Viola, 1999: Evidence of a convective boundary layer developing on the Antarctic Plateau during the summer, *Meteorol. Atmos. Phys.*, **71**, pp. 127-132.

5. King J. C., S. A. Argentini, P. S. Anderson, 2006: Contrasts between the summertime surface energy balance and boundary layer structure at Dome C and Halley stations, Antarctica, *J. Geophys. Res.-Atmos.*, **111**, D02105 10.1029/2005jd006130.

6. Argentini S., I. Pietroni, G. Mastrantonio, I. Petenko, A. Viola, 2011: A Sodar to Study the Surface Layer Turbulent Structure, *Boundary-Layer Meteorol.*, **143**, pp.177-188.

7. Lee X., W. Massman, B. Law, 2004: Handbook of Micrometeorology, *Kluwer Academic Publishers*, Dordrecht.

8. Beyrich F., S. Weill, 1993: Some aspects of determining the stable boundary layer depth from sodar data, *Boundary-Layer Meteorol.*, **63**, pp. 97-116.

9. Genthon C. , D. Six, V. Favier, S. Argentini. A. Pellegrini, 2010: Meteorological Atmospheric Boundary Layer Meteorological Measurements and ECMWF analyses during summer at Dome C, Antarctica, *J. Geophys. Res.*, **115**, D05104, doi:10.1029/2009JD012741

10. King J. C., J. Turner, 1997: Antarctic Meteorology and Climatology, 409 pp., *Cambridge University Press*, Cambridge.

11. Argentini, S., I. Petenko, G. Mastrantonio, V. Bezverkhnii, A. Viola, 2001: Spectral characteristics of East Antarctica meteorological parameters during 1994, *J. Geophys. Res.*, **106**, pp. 12463-12476.

12. Carroll J. J., 1982: Long-term means and short-term variability of the surface energy balance components at the South Pole, *J. Geophys. Res.,* **87**, pp. 4277-4286.

13. Stone R. S., G. E. Dutton, J. J. DeLuisi, 1990: Surface radiation and temperature variations associated with Cloudiness at the South Pole, *Antarct. J. U. S*, **24**, pp. 230-232.

14. Stone R. S., J. D. Kahl, 1991: Variations in Boundary layer Properties associated with Clouds and Transient weather disturbance at the South Pole during winter, *J. Geophys. Res.,* **96**, D3, pp. 5137-5144.

15. Stone R. S., 1993: Properties of austral winter clouds derived from radiometric profiles at the South Pole, *J. Geophys. Res.,* **98**, D7, pp. 12961-12971.

16. Neff W. D., 1999: Decadal time scale trends and variability in the tropospheric circulation over the South Pole, *J. Geophys. Res.,* **104**, pp. 27 217-27 251.

17. Othake T., 1978: Atmospheric ice crystals at the South Pole in summer, *Antarct. J. U. S.*, **13**, pp. 174-175.

18. Schwerdtfeger P., G. Weller, 1977: Radiative heat transfer processes in snow and ice, Meteorological Studies at Plateau Station*, J. A. Businger*, Ed., Antarctic Research Series, Vol. 25, Amer. Geophys. Union, pp. 35-39.

Laser scanning of a recirculation zone on the Bolund escarpment

J. Mann, N. Angelou, M. Sjöholm, T. Mikkelsen

Technical University of Denmark, Department of Wind Energy
'Risø campus', Frederiksborgvej 399, 4000 Roskilde
Denmark

Abstract

Rapid variations in the height of the recirculation zone are measured with a scanning wind lidar over a small escarpment on the Bolund Peninsula. The lidar is essentially a continuous-wave laser Doppler anemometer with the capability of rapidly changing the focus distance and the beam direction. The instrument measures the line-of-sight velocity 390 times per second and scans ten wind profiles from the ground up to seven meters per second. The results will be used to test computational fluid dynamics models for flow over terrain, and has relevance for wind energy. The development of multiple lidar scanning systems is done primarily for that purpose.

1 Introduction

Flow over complex terrain is a challenge for wind energy, because it is often difficult to predict the turbulent flow implying uncertain estimates of power production and mechanical loading of the turbine. Scanning the wind flow with remote sensing devices offers great opportunities for wind energy and many lidar companies are starting to provide instruments to do that.

2 Experiment

Atmospheric flow over a small bluff with a 12-m tall vertical cliff have been studied experimentally at the Bolund peninsula in Roskilde Fjord, Denmark. The Bolund experiment was designed to provide a dataset for validation of numerical modeling of flow over complex terrain. The experiment undertaken during the winter 2007-2008 described in Berg et al. [1] engaged ten meteorological masts (see figure 1) and provided data for a blind comparison of fifty-seven models [2].

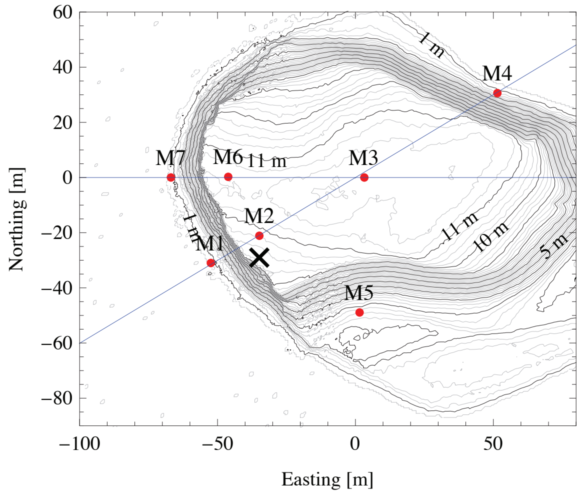

Figure 1: The position of seven of the ten meteorological masts in the Bolund Experiment. One mast is to the west in the fjord and the two last are to the east. The lidar is positioned between masts M6 and M3 twenty meters from the cliff pointing along the blue line (also called Line B in [1]) towards the cliff due west. The black cross is the position of a conically scanning standard ZephIR lidar.

The models displayed the largest errors in the calculated mean wind speed and turbulent kinetic energy close to the surface in regions where flow separation occurred. Every model, ranging from Reynolds-Averaged Navier-Stokes (RANS) over large eddy simulation (LES) to physical model scale tests in flumes or wind tunnels, underestimated the turbulent kinetic energy in the highly disturbed region right downstream of the vertical cliff. The purpose of the present experiment, undertaken in the fall of 2011 long after the meteorological masts were removed, was to study in detail this unsteady recirculation zone with a scanning laser anemometer.

3 Instrument

The laser anemometer, which is a part of the "windscanner.dk" project at DTU Wind Energy, steers the focused beam with two independently moving prisms in a patented configuration [3]. Simultaneously, the focus is changed so the point of measurement can be moved rapidly in space.

The two hundred thousand Doppler spectra acquired every second are averaged down to 390 spectra per second from which the line-of-sight velocities are derived through calculation of the median of the power spectral density after a suitably chosen background has been subtracted. The instrument under the prism scanner is an improved version of the ZephIR lidar described in [4, 5], with a larger effective aperture, more sensitive detector, and an incorporation of an acousto-optical modulator in order to distinguish the sign of the line-of-sight velocity. The lidar measuring on Bolund is shown in figure 2. Two of these instruments have been used simultaneously to study the unsteady downwash from a hovering helicopter, see Sjöholm et al. [6].

Figure 2: The scanning lidar measuring upwind towards the cliff of Bolund. See figure 1.

4 Results

The flow was scanned in seven vertical profiles at different distances from the escarpment extending from the surface and seven meters up, see figure 3. At every vertical position the wind profile was measured ten times per second allowing detailed unsteady characteristics to be derived. Between every seven vertical profiles the line-of-sight velocities were measured on a horizontal arc extending ±30° from the blue horizontal line in figure 1. The focus distance during that operation was 120 m, and it allow for a determination of the undisturbed upwind speed and wind direction. The vertical mean profiles shown in figure 4 were taken when the wind was due west, and they show speed-up over the escarpment at the higher heights while a turbulent inner layer is growing rapidly from the edge. The lowest part of the turbulent layer show reversed mean winds. Close to the edge the height of the inner layer seems constant, while it is oscillating violently further downstream from the edge as seen in figure 5.

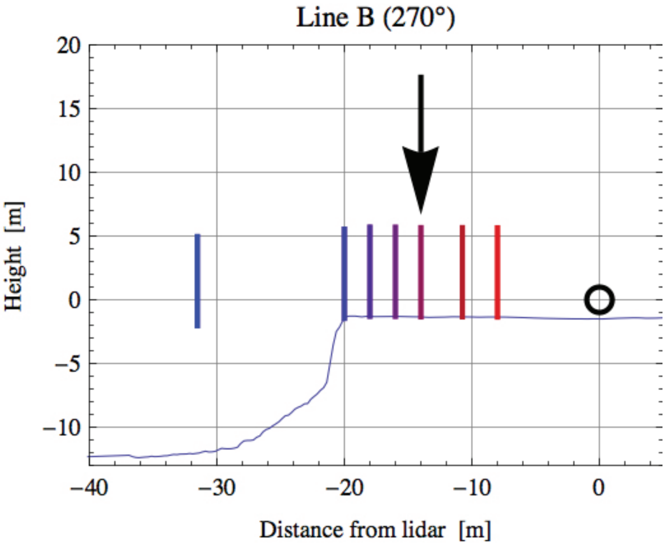

Figure 3: The position of the vertical scans relative to the Bolund escarpment. The position of the laser anemometer is indicated by a circle, and the position of the scan shown in figure 5 is indicated with an arrow.

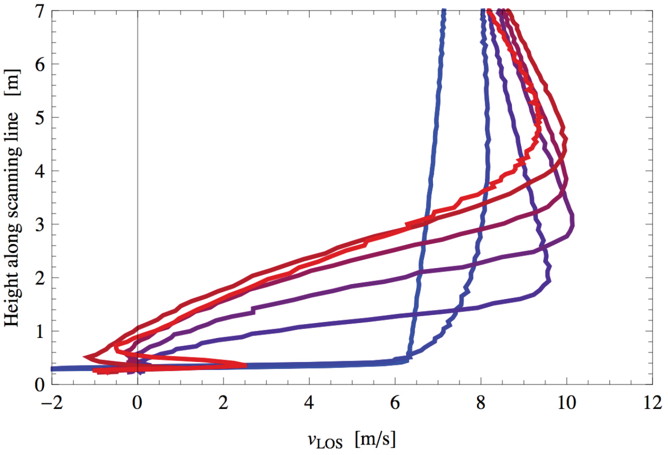

Figure 4: One hour average velocity profiles. The colors indicate the various positions as indicated in 3. Notice the reversed mean flow for some profiles in the lowest meter above the ground.

It is also possible to calculate the standard deviation of the velocity at every profile. The results are shown in figure 6. No compensation was done to account for consequences of the measurement volume on the turbulence, because the focus distance is quite short and consequently the measurement volume is limited. This issue is considered in [7]. With these reservations figure 6 shows that the strongest velocity fluctuations are elevated from the ground. We interpret that to be caused by the undulating sharp interface between slow and fast fluid, as also shown in figure 5.

The new remote sensing based wind profile measure-

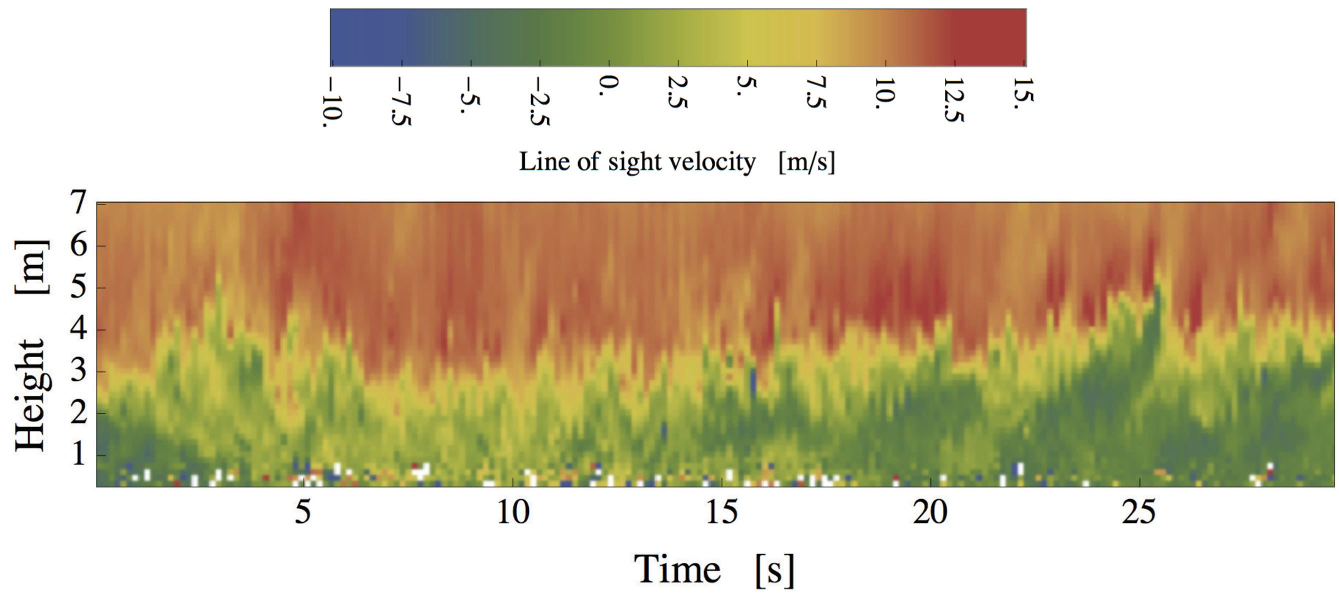

Figure 5: Example of a scan of the line-of-sight velocity lasting 30 seconds. The velocities of 300 consecutive profiles are plotted. Near the ground the instrument fails occasionally. A sharp and rapidly varying interface between fast and slowly moving air is observed. The distance from the cliff is approximately 6 m, while the height of the turbulent layer varies from 2 to 5 m.

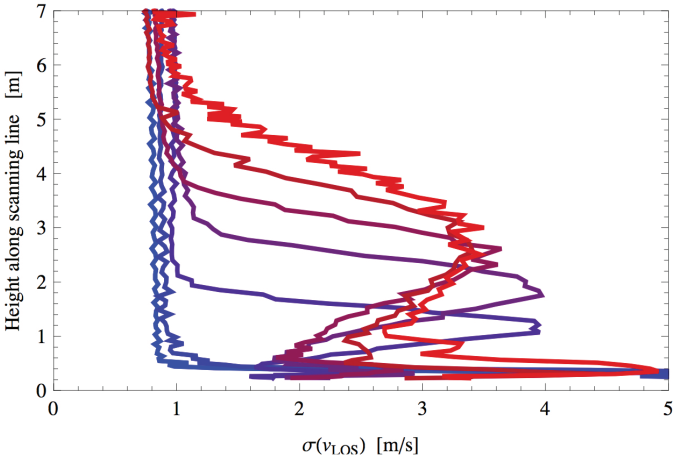

Figure 6: One hour profile of the standard deviation of the line-of-sight velocity. The colors are the same as in figure 4.

ments provide a unique dataset for validation of unsteady flow modeling over complex terrain for wind energy.

5 Future work

The analysis presented here is based on the first hour of data of the experiment, and the last twenty-five hours remains to be analyzed. Spectral analysis of the measured time series and detailed comparison with previous measurements on masts M6 and M7 is also outstanding.

Preliminary modeling of the flow with RANS and LES has limited success, probably due to inappropriate meshes. At DTU Wind Energy we are currently pursuing ways to improve the simulations, and we encourage others to compare their models with these new laser Doppler scans.

Acknowledgments

Kasper H. Hansen is highly acknowledged for writing the software acquiring the data and helping with the experimental campaign. The authors gratefully acknowledge the financial support from the Danish Agency for Science, Technology and Innovation through grant no. 2136-08-0022, the windscanner.dk project. The work was partially supported by the Center for Computational Wind Turbine Aerodynamics and Atmospheric Turbulence under the Danish council for strategic research, Grant No. 09-067216.

References

[1] J. Berg, J. Mann, A. Bechmann, M. S. Courtney, and H. E. Jørgensen. The Bolund experiment, Part I: Flow over a steep, three-dimensional hill. *Boundary-Layer Meteorol.*, 141(2):219–243, 2011. doi: 10.1007/s10546-011-9636-y.

[2] A. Bechmann, N. N. Sørensen, J. Berg, J. Mann, and P-E Réthoré. The Bolund experiment, Part II: Blind

comparison of microscale flow models. *Boundary-Layer Meteorol.*, 141(2):245–271, 2011. doi: 10.1007/s10546-011-9637.

[3] Torben Mikkelsen, Jakob Mann, and Morten Nielsen. Rotating prism scanning device and method for scanning. Patent no. WO 2009/155924 A1, 2009.

[4] David A. Smith, Michael Harris, Adrian S. Coffey, Torben Mikkelsen, Hans E. Jørgensen, Jakob Mann, and Régis Danielian. Wind lidar evaluation at the Danish wind test site Høvsøre. *Wind Energy*, 9(1–2): 87–93, 2006.

[5] Nikolas Angelou, Jakob Mann, Mikael Sjöholm, and Michael Courtney. Direct measurement of the spectral transfer function of a laser based anemometer. *Rev. Sci. Instrum.*, 83:033111, 2012.

[6] Mikael Sjöholm, Nikolas Angelou, Per Hansen, Kasper Hjorth Hansen, Torben Mikkelsen, Steinar Haga, Jon Arne Silgjerd, and Neil Starsmore. Helicopter downwash measured by continuous-wave doppler lidars with agile beam steering. In *ISARS 2012*, 2012.

[7] M. Sjöholm, T. Mikkelsen, J. Mann, K. Enevoldsen, and M. Courtney. Time series analysis of continuous-wave coherent Doppler lidar wind measurements. *Meteorol. Z*, 18(3):281–287, 2009.

Session 2 – Oral Presentations

ACOUSTIC TRAVEL-TIME TOMOGRAPHY OF THE ATMOSPHERE AT THE BOULDER ATMOSPHERIC OBSERVATORY

V. E. Ostashev[1,2], S. N. Vecherin[2], D. K. Wilson[2], A. J. Bedard[1], J. L. Leach[3], K. A. Clark[3], C. W. Fairall[3], and D. E. Wolfe[1]

[1]*CIRES/University of Colorado at Boulder and NOAA/Earth System Research Laboratory, 325 Broadway, Boulder, CO, 80305, USA, vladimir.ostashev@noaa.gov*
[2]*U.S. Army Engineer Research and Development Center, 72 Lyme Road, Hanover, NH, 03755, USA*
[3] *NOAA/Earth System Research Laboratory, 325 Broadway, Boulder, CO, 80305, USA*

ABSTRACT

Acoustic tomography of the atmospheric surface layer (ASL) is based on measurements of travel times of sound propagation between speakers and microphones, which constitute a tomography array. The temperature and wind velocity fields inside the tomographic region affect the travel times and can be reconstructed using different inverse algorithms. An array for acoustic tomography of the ASL has recently been built at the Boulder Atmospheric Observatory (BAO), CO, USA. The array consists of three speaker and five microphone towers located along the perimeter of a square with side length of 80 m. Speakers and microphones are connected via underground cables to the central command and data acquisition computer and other equipment located in a small modular building at the BAO. Using the BAO tomography array, the travel times of sound impulses between the speakers and microphones have been measured and analyzed. Subsequent reconstruction of the temperature and wind velocity fields is done with a recently developed time-dependent stochastic inversion. Examples of the reconstructed turbulence fields are presented and analyzed. Other developments in acoustic tomography are briefly discussed.

1. INTRODUCTION

Acoustic travel-time tomography of the atmospheric surface layer (ASL) is based on measurements of travel times of sound propagation between acoustic sources (usually, speakers) and microphones. Then, the temperature and wind velocity fields inside the tomographic region (area or volume) are reconstructed using different inverse algorithms. Improved knowledge about these fields is important for boundary layer meteorology, theories of turbulence, studies of sound and electromagnetic wave propagation in a turbulent atmosphere, etc. Acoustic tomography of the ASL has certain advantages [1] in comparison with point measurements of temperature and wind velocity using conventional meteorological devises.

The first experimental implementation of acoustic tomography of the ASL was done by Wilson and Thomson [2]. Since the mid 1990’s, many outdoor and indoor acoustic tomography experiments have been performed by scientists from the University of Leipzig, Germany, e.g., see [3,4]. At the end of the 2010’s, an array for acoustic tomography of the ASL was built [1,5] at the Boulder Atmospheric Observatory (BAO), near Boulder, CO, USA. The BAO is a premier meteorological site with many instrumentation for measurements of parameters of the atmospheric boundary layer.

In Sec. 2, the layout and principle of operation of the BAO acoustic tomography array are briefly discussed. A recently developed time-dependent stochastic inversion (TDSI) algorithm for reconstruction of the temperature and wind velocity fields from the travel times of sound propagation is outlined in Sec. 3. In Sec. 4, examples of the temperature and velocity fields reconstructed with the BAO array and TDSI algorithm are presented and discussed. In Sec. 5, other recent developments in acoustic tomography are outlined. In Sec. 6, the results obtained in the paper are summarized.

2. BAO ACOUSTIC TOMOGRAPHY ARRAY

The BAO acoustic tomography array consists of three speaker and five microphone towers located along the perimeter of a square with side length of 80 m. The towers are 9.1 m high; their (x, y) coordinates in a horizontal plane are shown in Fig. 1. Speakers and microphones are located on the towers at three adjustable levels ranging from about 3 to 9 m. Transducers at the upper level of the towers have been used so far for transmission and reception of acoustic signals, thus enabling 2D, horizontal slice tomography. Speakers and microphones are connected via underground cables to equipment inside a small modular building at the BAO: microphone filters, powers amplifiers, A/D interfaces, a central control and data acquisition computer, and an uninterruptible power supply.

Software was developed to run acoustic tomography experiments from the central computer and to store all data on the computer. The software allows choosing the form of a transmitted signal (with a length of about 30 ms) and the duration of an experiment (from 1 min to a few hours). In the current design, three speakers are activated in a sequence with 0.5 s delay. Five microphones record these signals. The travel times τ_i of sound propagation along different sound propagation paths are determined by the cross-correlation of the transmitted and received signals. Here, the subscript $i = 1,2,\ldots,15$ indicates a particular path shown in Fig.1. The temperature $T(x, y, t)$ and wind velocity $\vec{v}(x, y, t)$ fields inside the BAO tomography array are reconstructed from the measured travel times τ_i using the TDSI algorithm (explained in the next section). Here, t is time.

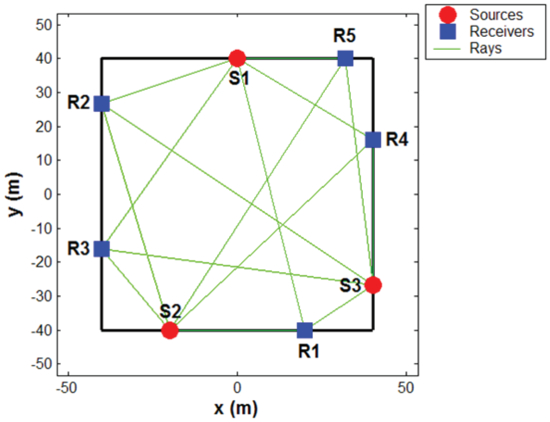

Figure 1. Location of eight towers of the BAO acoustic tomography array in a horizontal plane. Green lines indicate sound propagation paths from speakers (red circles) to microphones (blue squares).

To the best of our knowledge, the BAO tomography array is currently the only operational array for acoustic tomography of the ASL. The speakers and microphones are permanently installed on the towers. This allows continuous monitoring of the temperature and wind velocity fields. All previous tomography arrays were dismantled after a short time of operation.

Efforts are underway to upgrade capabilities of the BAO tomography array. Two new towers have been already mounted and connected via underground cables with the BAO modular building. All towers, except one in the middle of the array, will have both a speaker and microphone installed at the upper level of the array that will increase the number of sound propagation paths and allow reciprocal transmission. A sonic anemometer and thermometer probe will be installed on the tower, which is located in the middle of the array. A new PC and better A/D interfaces will be used to improve synchronization in transmitting and recording of acoustic signals, and to make more accurate measurements of the travel times.

3. TDSI ALGORITHM

In the TDSI algorithm, the temperature and wind velocity fields are expressed as sums of the mean fields and the fluctuations: $T(x, y, t) = T_0(t) + T_1(x, y, t)$, $\vec{v}(x, y, t) = \vec{v}_0(t) + \vec{v}_1(x, y, t)$. Here, the subscripts “0” and “1” correspond to the mean fields and the fluctuations, respectively. The mean fields are reconstructed with the least squares solution and the fluctuations with the TDSI algorithm.

The main idea of TDSI is to measure the travel times τ_i repeatedly at the time moments t_1, t_2, …, t_n, where n is the number of travel time measurements, and to assume that the temperature and velocity fluctuations are random fields with known spatial-temporal correlation functions. Using n sets of the travel times τ_i as input data, the $T_1(x, y, t)$ and $\vec{v}_1(x, y, t)$ fields are reconstructed with approaches developed in [6-9]. By repeated measurements of the travel times, TDSI increases the number of data used in the inversion without increasing the number of speakers and microphones, i.e., the number of sound propagation paths. Numerical results showed that TDSI allows better reconstruction of the temperature and velocity fields than other algorithms do, for example, stochastic inversion.

The developed TDSI was applied to numerical simulations of the BAO acoustic tomography array. In the simulations, the temperature and velocity fields were modeled with large eddy simulations (LES). The results obtained showed that the mean temperature and wind velocity and their fluctuations can be reliably reconstructed. The developed TDSI was also applied for reconstruction of the temperature and velocity fields in outdoor [3] and indoor [4] acoustic tomography experiments carried out by scientists from the University of Leipzig. The results obtained showed successful reconstruction of the temperature and wind velocity fields, which were in a good agreement with in situ measured data where those were available.

4. RECOSNTRUCTION OF TEMPERATURE AND VELOCITY FIELDS

After a thorough testing and refinement, the TDSI algorithm was applied for reconstruction of the temperature and wind velocity fields in acoustic tomography experiments with the BAO tomography array. The results presented below [9] correspond to the tomography experiment, carried out on 09 Jul 2008 at 21:31-21:33 UTC (15:31-15:33 of local time).

Figure 2 depicts the temporal evolution of the travel time $\tau_1(t)$ of signal propagation from speaker 1 to microphone 1 shown in Fig. 1. The travel time was calculated every 1.5 s during 180 s of the tomography experiment. The travel time gradually changes from one measurement to another due to changing temperature and wind velocity fields. A maximum deviation of the travel time from its mean value is of the order of 0.5 ms. Though not shown here for brevity, the travel times along other propagation paths depicted in Fig. 1 exhibit a similar temporal evolution.

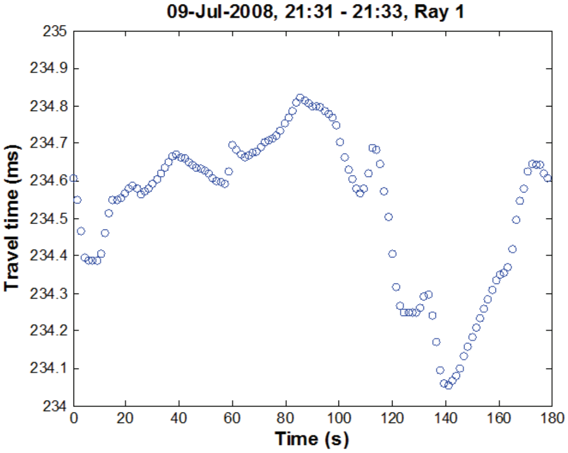

Figure 2. Temporal evolution of the travel time of sound propagation from speaker 1 to microphone 1 shown in Fig. 1 in the acoustic tomography experiment at the BAO on 09 Jul 2008.

The measured travel times τ_i were then used to reconstruct the temperature and wind velocity fields. Figure 3 shows the reconstructed temperature field $T(x,y)$, which corresponds to the time 21:32:30 of the experiment. The expected error in reconstruction is about 0.05°. Several "cold" and "warm" eddies are clearly seen in the figure. The eddies are reliably resolved since the temperature difference between them is larger than the error in reconstruction.

The magnitude of the wind velocity vector reconstructed for the same time 21:32:30 is depicted in Fig. 4. The expected error of reconstruction is 0.04 m/s. "Fast" and "slow" eddies are seen in the figure. Arrows indicate the direction of the wind velocity vector.

Similarly, the temperature $T(x,y)$ and wind velocity $\vec{v}(x,y)$ fields were reconstructed for other time moments of the tomography experiments. The resulting spatial fields were combined into two "movies", which show temporal evolutions of the temperature and velocity fields for 180 s of the experiment.

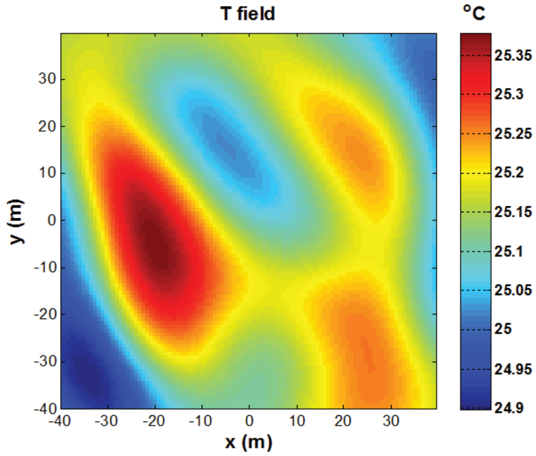

Figure 3. Temperature field reconstructed with TDSI in the acoustic tomography experiment at the BAO on 09 Jul 2008. (In color in the electronic version.)

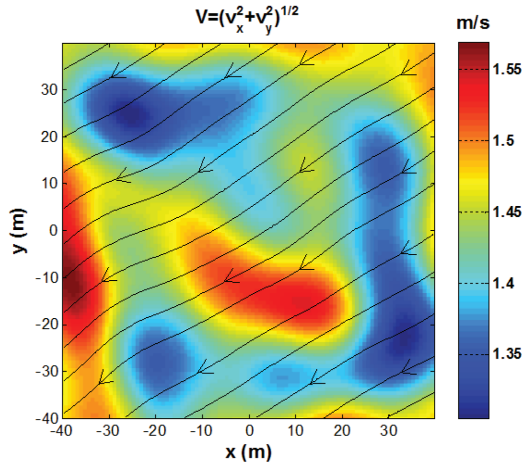

Figure 4. Magnitude of the wind velocity reconstructed with TDSI in the acoustic tomography experiment at the BAO on 09 Jul 2008. Arrows indicate the direction of the wind velocity vector. (In color in the electronic version.)

5. OTHER DEVELOPMENTS IN ACOUSTIC TOMOGARPHY

Though the BAO acoustic tomography array and the TDSI algorithm were built and developed to obtain results similar to those shown in Figs. 2-4, they can also be used for other research problems. In this section, we briefly outline some of these problems.

The BAO tomography array could be used a large sonic anemometer/thermometer for obtaining the area-averaged measurements of the temperature, wind velocity, and horizontal heat flux. Area-averaged measurements of these meteorological parameters are important since point measurements are often not representative due to spatial variations. An approach has been suggested to infer the vertical heat flux from the horizontal heat flux. Preliminary theoretical and experimental results obtained in this study are reported in [10,11].

The BAO tomography array can be used for testing theories of line-of-sight sound propagation through a turbulent atmosphere, including theories of broad-band propagation and temporal coherence, which are yet to be developed. In such experiments, the tomography array could provide information about both atmospheric turbulence and fluctuations in acoustic signals propagating through the turbulence.

Finally, to improve a spatial resolution of a sonic anemometer/thermometer, one might regard it as a small acoustic tomography array [10], and use the TDSI algorithm for fine reconstruction of the temperature and wind velocity fields. Numerical simulations have shown that if the number of transducers in a sonic is doubled, its spatial resolution would increase by a factor of ten.

6. CONCLUSIONS

In this paper, the layout and principle of operation of the BAO acoustic tomography array were presented. The array enables measurement of the travel times of sound signal propagation between different speakers and microphones, which constitute the tomography array. Efforts underway to upgrade capabilities of the BAO tomography array were outlined. The TDSI algorithm, which is used for reconstruction of the temperature and wind velocity fields from the measured travel times, was briefly explained and the results obtained with this algorithm were overviewed. The results in reconstruction of the temperature and wind velocity fields in the acoustic tomography experiment at the BAO on 09 Jul 2008 were presented and analyzed. The use of the BAO tomography array and the TDSI algorithm in other research problems was discussed.

ACKNOWLEDGMENTS

This material is based upon work supported in part by the U.S. Army Research Laboratory and Army Research Office under contract/grant number W911NF1010415.

REFERENCES

1. Ostashev, V. E., S. N. Vecherin, D. K. Wilson, A. Ziemann, G. H. Goedecke, 2009: Recent progress in acoustic travel-time tomography of the atmospheric surface layer, *Meteorol. Zeitschrift,* **18**, 125-133.

2. Wilson, D. K., D. W. Thomson, 1994: Acoustic tomographic monitoring of the atmospheric surface layer, *J. Atmos. Ocean. Tech.,* **11**, 751-769.

3. Raabe, A., K. Arnold, A. Ziemann, M. Schröter, S. Raasch, J. Bange, P. Zittel, Th. Spiess, Th. Foken, M. Göckede, F. Beyrich, J-P Leps, 2005: STINHO - STructure of turbulent transport under INHOmogeneous conditions - the micro-α scale field experiment and LES modeling, *Meteorol. Z.,* **14**, 315-327.

4. Seliger, M., M. Barth, A. Raabe, 2005: *Akustische Lauzeittomographie in Ilmenauer Fass* (Technical Report, Leipzig Institute of Meteorology, Leipzig).

5. Ostashev, V. E., A. Bedard, S. N. Vecherin, D. K. Wilson, 2009: Acoustic travel-time tomography of the atmospheric surface layer, *ASME Intern. Mech. Eng. Congress on Sound Propagation in the Atmosphere* (Lake Buena Vista, Florida).

6. Vecherin, S. N., V. E. Ostashev, G. H. Goedecke, D. K. Wilson, A. G. Voronovich, 2006: Time-dependent stochastic inversion in acoustic travel-time tomography of the atmosphere, *J. Acoust. Soc. Am.*, **119**, 2579-2588.

7. Vecherin, S. N., V. E. Ostashev, A. Ziemann, D. K. Wilson, K. Arnold, M. Barth, 2007: Tomographic reconstruction of atmospheric turbulence with the use of time-dependent stochastic inversion, *J. Acoust. Soc. Am.,* **122**, 1416-1425.

8. Vecherin, S. N., V. E. Ostashev, D. K. Wilson, A. Ziemann, 2008: Time-dependent stochastic inversion in acoustic tomography of the atmosphere with reciprocal transmission, *Meas. Sci. Technol.*, **19**.

9. Vecherin, S. N., V. E. Ostashev, D. K. Wilson: Assessment of the time delays in acoustic travel-time tomography of the atmosphere, *J. Acoust. Soc. Am.* (to be submitted).

10. Ostashev, V. E., S. N. Vecherin, D. K. Wilson, C. Fairall, 2011: Recent developments in acoustic tomography of the atmosphere, *14th Intern. Symp. on Long Range Sound Propagation* (Annapolis, MD).

11. Vecherin, S. N., V. E. Ostashev, D. K. Wilson, A. Grachev, 2012: Utilization of an acoustic tomography array as a large sonic anemometer/thermometer, *Proceedings of Meetings on Acoustics*, **14**, 045003.

ESTIMATION OF THE LIDAR OVERLAP FUNCTION BY NON-LINEAR REGRESSION

A. C. Povey[1], R. G. Grainger[1], D. M. Peters[1], J. L. Agnew[2], and D. Rees[3]

[1]*University of Oxford, Atmospheric, Oceanic, and Planetary Physics, Clarendon Laboratory, Parks Road, Oxford, OX1 3PU, United Kingdom, povey@atm.ox.ac.uk*
[2]*STFC Rutherford Appleton Laboratory, Harwell, Oxford, OX11 0QX, United Kingdom*
[3]*Hovemere Ltd., Tonbridge, TN9 1RF, United Kingdom, drees@hovemere.com*

ABSTRACT

The overlap function of a Raman channel for a lidar system is retrieved by non-linear regression using an analytic description of the optical system and a simple model for the extinction profile, constrained by aerosol optical thickness. Considering simulated data, the scheme is successful even where the aerosol profile deviates significantly from the simple model assumed. Application to real data is found to reduce by a factor of 1.4 – 2.0 the root-mean-square difference between the attenuated backscatter coefficient as measured by the calibrated instrument and a commercial instrument.

1. INTRODUCTION

A lidar's overlap function describes the efficiency with which light is coupled into its detectors as a function of height, dependent on overlap of the laser-illuminated volume with the system's field-of-view (FOV) and losses in the optical system. [1, 2] This limits the accuracy with which lidar can be used to investigate the planetary boundary layer (PBL), where aerosol is both most abundant and most variable. Further, many methods of lidar analysis are designed to only consider regions where the overlap function is constant and can incur significant errors if regions where it is not constant are considered.

The Robust And Compact Environmental Lidar (RACHEL) was developed by Hovemere Ltd. as a cost-effective and portable Raman lidar system for unattended monitoring of pollution by day and night. The prototype system was deployed at the NERC Chilbolton Facility for Atmospheric and Radio Research (CFARR) in southern England during Spring 2010. Due to a series of minor faults, the laser was operating at significantly less than its full power and had to be adjusted repeatedly in the field, such that the usually assumed analytic form could not be used. The low signal-to-noise ratio (SNR) of the data prevented iterative methods [3, 4] from converging to sufficiently smooth solutions to be useful. Further, the large, inhomogeneous aerosol loading ruled out integrating the signal over longer time periods to increase the SNR. A new method was sought to produce the best estimate of the overlap function possible under these challenging conditions.

Non-linear regression provides a framework to combine these noisy lidar profiles with other information about the system and atmosphere, such as an analytic model of the overlap function or aerosol optical thickness, to produce an estimate of the overlap function that makes optimal use of all the information available. The retrieved overlap function is then used to produce a simple lidar product, which is compared to independent observations as an initial validation. This extended abstract should serve as a brief outline for a paper of the same title currently under review for publication in *Applied Optics*.

2. METHOD

2.1 Optimal estimation

Optimal estimation is a non-linear regression scheme with rigorous incorporation of any prior information about the state of the system. [5] It solves for $\mathbf{x}$ the inverse problem,

$$\mathbf{y} = \mathbf{F}(\mathbf{x}, \mathbf{b}) + \varepsilon, \tag{1}$$

where $\mathbf{y}$ describes a set of measurements with noise ε; the state of the observing system and atmosphere are summarised by unknown parameters $\mathbf{x}$ and known parameters $\mathbf{b}$; and the forward model $\mathbf{F}$ translates this state into a simulated measurement.

If the uncertainty in the measurements is described by a covariance matrix $\mathbf{S}_\varepsilon$ and the probability density function for all variables is approximated as Gaussian, the probability that the system is in a state $\mathbf{x}$ given the measurement $\mathbf{y}$ can be expressed as,

$$\begin{aligned} -2\ln \mathrm{P}(\mathbf{x}|\mathbf{y}) &= [\mathbf{y} - \mathbf{F}(\mathbf{x}, \mathbf{b})]^T \mathbf{S}_\varepsilon^{-1} [\mathbf{y} - \mathbf{F}(\mathbf{x}, \mathbf{b})] \\ &\quad + [\mathbf{x} - \mathbf{x}_a]^T \mathbf{S}_a^{-1} [\mathbf{x} - \mathbf{x}_a] + c, \end{aligned} \tag{2}$$

where c is a constant. The second term above incorporates any information we may have about the system before making the measurement through an *a priori* state $\mathbf{x}_a$ with covariance matrix $\mathbf{S}_a$. These could, for example, describe a climatological mean state or expected correlations in some quantity with height due to vertical mixing.

It is then shown in [5] that the iteration,

$$\begin{aligned} \mathbf{x}_{i+1} &= \mathbf{x}_i + [(1+\Gamma_i)\mathbf{S}_a^{-1} + \mathbf{K}_i^T \mathbf{S}_\varepsilon^{-1} \mathbf{K}_i]^{-1} \\ &\quad \{\mathbf{K}_i^T \mathbf{S}_\varepsilon^{-1} [\mathbf{y} - \mathbf{F}(\mathbf{x}_i, \mathbf{b})] - \mathbf{S}_a^{-1}(\mathbf{x}_i - \mathbf{x}_a)\}, \end{aligned} \tag{3}$$

converges to the minimum of (2) — the most likely state. Here, $\mathbf{K}_i = \nabla_{\mathbf{x}} \mathbf{F}(\mathbf{x}_i, \mathbf{b})$ and the covariance of that state is,

$$\mathbf{S}_{\mathbf{x}} = (\mathbf{K}^T \mathbf{S}_\varepsilon^{-1} \mathbf{K} + \mathbf{S}_a^{-1})^{-1}. \tag{4}$$

General practice is that after an iteration, if the value of the cost function (2) has increased, the scaling factor Γ_i

Table 1. RACHEL system specification

Parameter	Value
Laser type	Nd-YAG
Emitted wavelength	354.7 nm
Pulse rate	20 Hz
Average pulse energy	45 mJ
Beam radius, R_L	17.5 mm
Beam divergence, ϕ_L	0.3 mrad
Telescope model	Meade LXD-75
Primary mirror radius, R_T	101.5 mm
Secondary mirror radius, R_o	37.5 mm
Fibre radius, R_p	0.2 mm
Focal length, f	2.0 m
Resolution	10.5 m

is increased by a factor of ten. Otherwise, it is reduced by a factor of two. Iteration ceases when either the cost function or all elements of the state vector change by less than some threshold after a step.

2.2 Application to lidar

The most common model for the response of a lidar to Raman scattering from particles is, [1, 2]

$$\begin{aligned} E_{\mathrm{ra}}(r) &= E_0 C_{\mathrm{ra}} r^{-2} A(r) N_{\mathrm{X}}(r) \\ &\quad \times \exp\left[-\int_0^r \alpha_m(\lambda_L, r') + \alpha_a(\lambda_L, r') \right. \\ &\quad \left. + \alpha_m(\lambda_{\mathrm{X}}, r') + \alpha_a(\lambda_{\mathrm{X}}, r')\, \mathrm{d}r' \right], \quad (5) \end{aligned}$$

where $E_{\mathrm{ra}}(r)$ is the energy observed from a range r; $\beta(\lambda, r)$ is the backscattering coefficient; $\alpha(\lambda, r)$ is the extinction coefficient; the subscripts m and a denote molecular and aerosol scattering; λ_L and λ_{X} are the wavelengths of the laser beam and Raman scattered radiation; E_0 is the energy of the laser pulse; $N_{\mathrm{X}}(r)$ is the number density of the scattering species; and C_{ra} is a constant.

For the purpose of estimating the overlap function, the measurement **y** will be the values of E_{ra} over some suitable range; the state **x** will be the values of C_{ra}, $A(r)$, and α_a over the same range; and the remaining variables are known from other measurements (such as a standard atmosphere) and so form **b**. To further constrain the problem, model analytic forms for $A(r)$ and α_a are introduced such that these profiles can be expressed in terms of a few unknown parameters.

Such a formulation for $A(r)$ was proposed in [6] (not outlined here for brevity). This presented the overlap function as an integral over the overlap of two circles — the assumed circular, continuous beam and the telescope's FOV. It neglects the effects of any components after the telescope and any variations in the beam profile. Some rearrangement of the form originally presented was made to improve accuracy and stability of the integration.

It is then hypothesised from observations [7, 8, 9] that stable PBLs can be approximated as having constant extinction up to some height z_0 (which is not necessarily the top of the PBL) and a rapid exponential decay above that over a scale height H. This profile can then be constrained by observations of the atmosphere, such as measurement of the aerosol optical thickness, χ, with a sun photometer. This profile can be written as (see fig. 1(a)),

$$\int_0^z \alpha_a(\lambda_L, r')\, \mathrm{d}r' = \begin{cases} \frac{\chi}{H+z_0} z, & z < z_0; \\ \frac{\chi}{H+z_0} \left[z_0 + H \left(1 - \exp \frac{z_0 - z}{H} \right) \right], & z \geq z_0. \end{cases} \quad (6)$$

3. SIMULATION

The behaviour of the retrieval scheme was investigated through the use of data simulated for the RACHEL platform (table 1). Such simulations are easily produced with the forward model, with four alignments of the system considered to highlight the expected range of states.

As shown in fig. 2, retrievals for all four cases demonstrate a high quality fit, with costs in the expected range. There is a slight tendency towards underestimation with height, most pronounced in curve ×. This is to be expected as this model has the lowest magnitude. That being directly proportional to the number of photons observed, the SNR will be lower for this profile, corresponding to a lower information content in the retrieval. When the integration time of this profile is increased, the fit is found to be equivalent to the others.

To investigate the suitability of the idealised extinction profile, a variety of perturbations were added, shown in fig. 1(b–c), and simulated using a well-aligned model.

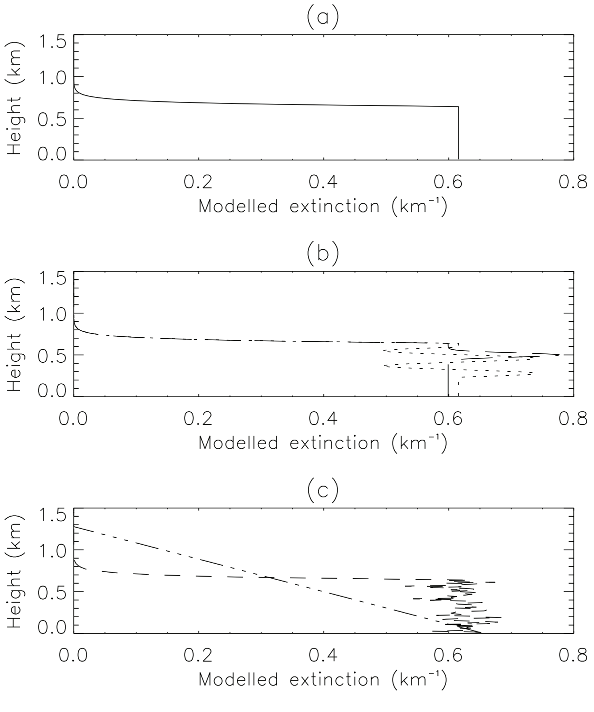

Figure 1. Aerosol extinction profiles used for simulating data. All have $\chi = 0.4$ at 355 nm. (a) Unperturbed model profile, where extinction is constant to 640 m and decreases exponentially above that; (b) Addition of a Gaussian peak (dash) or sinusoidal variations (dot); (c) Addition of normally-distributed multiplicative noise (short dashes) or a linear decrease in extinction (dot-dash).

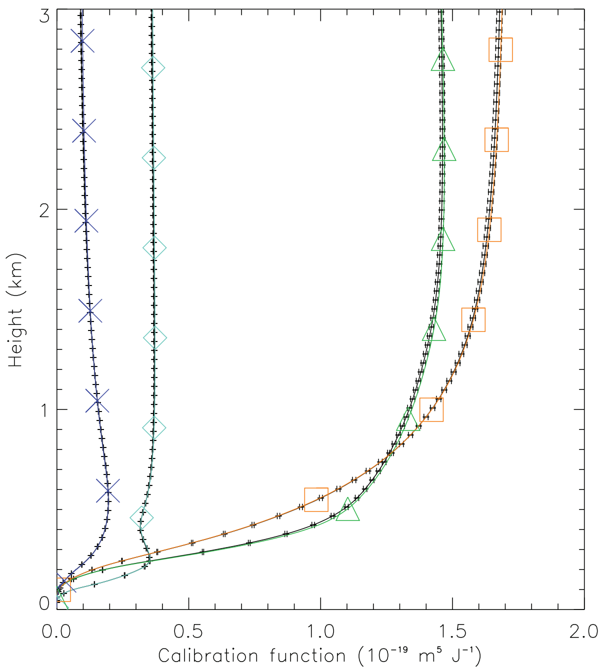

Figure 2. Retrieved calibration function, $C_{\mathrm{ra}}A(r)$, for four different model alignments (black) with errors derived from eqn. (4). The true profile is plotted in colour.

All are constructed to have an equal χ of 0.4 at 355 nm. In three cases, the retrieved profile was consistent with that used for simulation and in the case of a linear decrease in extinction with height, the retrieval is accurate to within 5 % despite the significant difference in extinction profile, though this difference is greater than the predicted error. These profiles also demonstrated a significant degeneracy in the model, with different sets of parameters producing practically identical overlap functions. As such, it is important to evaluate the success of any retrieval against the calibration function and its error and not the individual parameters, which may not be physically meaningful.

The impact of a different beam profile on the retrieval was also investigated. The overlap function was recalculated with a Gaussian beam profile for each of the four model states. The retrieval was then applied assuming a continuous profile. The results vary, with discrepancies of up to 10 % in the region 200 – 1000 m, where the overlap of the beam and FOV is most rapidly changing and the beam profile is most important. However, such cases are indicated by a large cost for the retrieval, and so can be identified and rejected.

4. APPLICATION

The retrieval was then applied to real data. Ideally, observations at night would be used as these have a higher SNR and, sufficiently long after sunset, the PBL will generally be stable. However, as it was not possible to measure χ at night, a balance was sought by considering early morning and dawn of days that showed minimal variation in χ within an hour of sunrise.

The retrieved calibration function from one morning's observations is plotted in fig. 3(a). For comparison, a simple arithmetic inversion of eqn. (5) is also shown (calculated by correcting the measurements for range, background, molecular scattering, and the *a priori* aerosol profile). Firstly, the overlap function tends smoothly to a constant value with height, indicating RACHEL was well aligned at this time. The retrieved profile is slightly

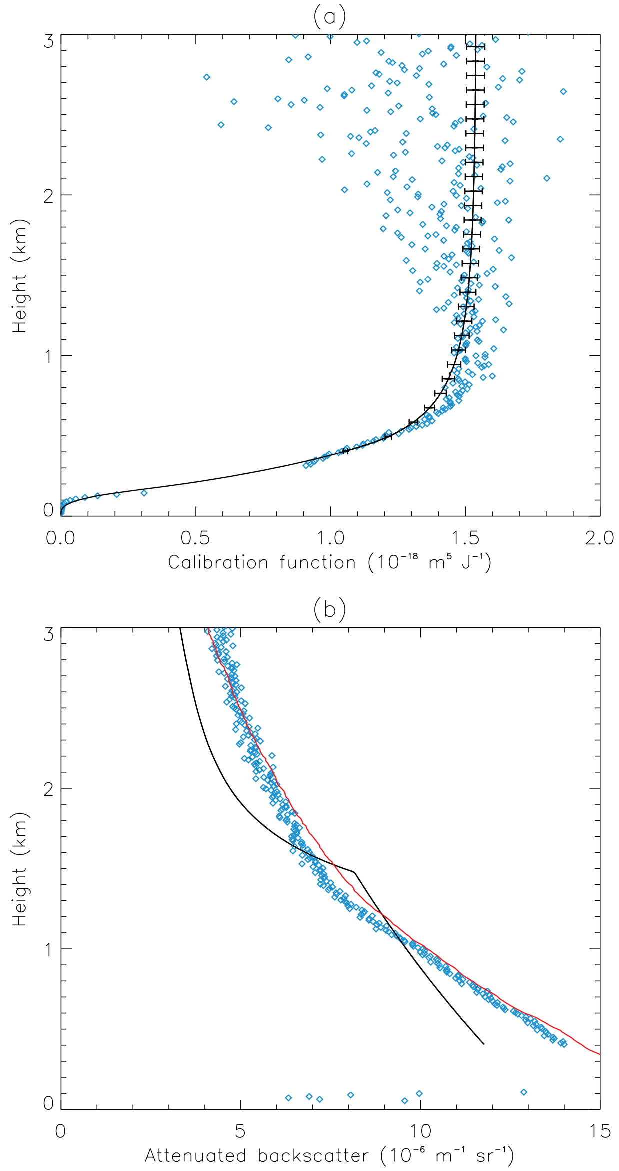

Figure 3. (a) The retrieved calibration function with errors. Plotted as points is an arithmetic inversion of the measurement, eqn. (5), with the *a priori* extinction profile. Measurements beyond the reasonably linear range of the detectors are not plotted and were not used in the retrieval. (b) The attenuated backscatter coefficient at 355 nm for the retrieved aerosol profile (black), the elastic profile corrected with the retrieved overlap function (blue), and as reported independently by an EZ lidar at the same site (red). A lidar ratio of 15 was chosen to give consistency between the three signals above 6 km.

smaller from 0.5 – 1 km than would be expected from the data without retrieval as the retrieved scale height is greater than initially guessed. It is further evident that the retrieval is returning larger errors than observed in the simulated data. The reason for this is clear from the broad scatter of data points above 1 km. The ability to fit a physically consistent function regardless is one of optimal estimation's strengths.

The validity of the retrieved extinction profile can be explored through use of the elastic channel. In particular, if a constant lidar ratio is assumed, the attenuated backscatter coefficient,

$$\begin{aligned} \beta^*(r) &= \frac{E_{\mathrm{el}}(r)\,r^2}{C_{\mathrm{el}}E_0A(r)}\exp\left[2\int_0^r \alpha_m(\lambda_L,r')\,\mathrm{d}r'\right] && (7)\\ &\equiv \frac{\beta_m(\lambda_L,r)+\beta_a(\lambda_L,r)}{\exp\left[2\int_0^r \alpha_a(\lambda_L,r')\,\mathrm{d}r'\right]}, && (8)\end{aligned}$$

can be calculated for the elastic channel and compared to that from direct substitution of the retrieved α_a into eqn. (8). This is presented in fig. 3(b), with the retrieved profile in black and the elastic data in blue . In addition, plotted in red is the β^* published by CFARR from a Leosphere EZ lidar operated continuously at the site, evaluated using Leosphere's commercial algorithm.

We can see that in this case, the retrieved α_a is reasonable up to 1.5 km, but then underestimates the scale height. However, the fairly good correspondence between the published β^* and that determined from RACHEL's elastic channel (the RMS deviation between them reduces from $2.4 \times 10^{-5}\,\mathrm{m}^{-1}\,\mathrm{sr}^{-1}$ without overlap correction to 1.4×10^{-5} with it) gives confidence that despite the extinction profile, the retrieved correction is useful. The difference in α_a may be due to a change in the lidar ratio between the PBL and free troposphere.

5. CONCLUSIONS

An optimal estimation scheme has been proposed for the retrieval of the overlap function of a Raman channel of a lidar system. The retrieval scheme was successful in retrieving overlap functions from simulated data, with various perturbations to the assumed aerosol profile found to not significantly affect the result. The use of a Gaussian beam profile was found to influence the retrieval in some circumstances, but these failures were indicated by high costs and so can be rejected.

The retrieval was then applied to measurements with the RACHEL system. This was found to be more consistent with independent observations than without the overlap correction by a factor of 1.4 – 2.0. The retrieved extinction profiles, though functional, were clearly only approximations to the truth. It is likely that a model of the extinction profile with more degrees of freedom could improve the technique in future.

Practically, the retrieved overlap function will be used within some algorithm to derive the extinction and backscatter. For a Klett-Fernald scheme, as the overlap function is effectively a multiplicative correction, it will simply add to the fractional error in the backscatter coefficient. For the conditions considered in Section 4, this varies from about 2 % when the system is well aligned, which is slightly better that that expected from existing techniques of determining the overlap function, to over 10 % when it isn't well aligned, which would be the dominant source of error in the retrieval, though this was in part due to the lower SNR of the data used in the retrieval (not presented here).

The impact of this error on a Raman lidar scheme is more subtle as there the correction is to the derivative of the overlap function. In its current form, the dominant error in this derivative is from numerical integration and can be over 100 % in certain cases. However, if an analytic form of the derivative is found, the errors should be equivalent to those introduced into the single-channel scheme. This is an aim for the near future.

ACKNOWLEDGEMENTS

Thanks to the staff of the NERC-funded CFARR for their assistance during the field work. Radiosonde data provided by the UK Meteorological Office. AERONET data available at `http://aeronet.gsfc.nasa.gov`.

REFERENCES

[1] Measures, R. M., 1992: *Lidar Remote Sensing: Fundamentals and Applications*. Krieger Publishing Company.

[2] Fujii, T., T. Fukuchi, 2005: *Laser remote sensing*. Taylor and Francis.

[3] Wandinger, U., A. Ansmann, 2002: Experimental determination of the lidar overlap profile with Raman lidar. *Applied Optics*, **41**, pp. 511–514.

[4] Guerrero-Rascado, J. L. *et al.*, 2010: Infrared lidar overlap function: an experimental determination. *Optics Express*, **18**, pp. 20350–20359.

[5] Rodgers, C. D., 2000: *Inverse methods for atmospheric sounding: Theory and practice*, World Scientific.

[6] Halldórsson, T., J. Langerholc, 1978: Geometrical form factors for the lidar function. *Applied Optics*, **17**, pp. 240–244.

[7] Steyn, D. G., M. Baldi, R. M. Hoff, 1999: The detection of mixed layer depth and entrainment zone thickness from lidar backscatter profiles. *Journal of Atmospheric and Oceanic Technology*, **16**, pp. 953–959.

[8] He, Q. S. *et al.*, 2008: Analysis of aerosol vertical distribution and variability in Hong Kong. *JGR — Atmospheres*, **113**, p. 13.

[9] Wiegner, M. *et al.*, 2006: Mixing layer height over Munich, Germany: Variability and comparisons of different methodologies. *JGR — Atmospheres*, **111**, p. 17.

OBTAINING CROSSWIND FROM A SINGLE APERTURE SCINTILLOMETER

Daniëlle van Dinther[1], Oscar Hartogensis[1], Arnold Moene[1]

[1]*Meteorology and Air quality group – Wageningen University, Droevendaalsesteeg 3 P.O. Box 6700 AA Wageningen*
The Netherlands, Danielle.vandinther@wur.nl

ABSTRACT

A scintillometer is a device that consist of a transmitter and receiver. The receiver records intensity fluctuations of the electromagnetic beam emitted by the transmitter. These fluctuations are caused by refraction of the beam upon its passage through the turbulent surface layer.

An increasingly popular application of scintillometry is to estimate the area-averaged surface fluxes following scintillometer theory [1]. A less known application of scintillometry is the estimation of the crosswind (i.e. the wind perpendicular on the scintillometer path). Past research focused on dual aperture scintillometers that use the time delay between the two signals to estimate the crosswind [2].

The goal of this study is to explore three algorithms to obtain the crosswind from single aperture scintillometers using spectral techniques. Clifford [3] described a theoretical model of the scintillation spectrum. From this model it is apparent that stronger crosswinds causes the spectrum to shift to higher frequency. Therefore, by using a salient point in the spectrum and its corresponding frequency the crosswind can be obtained.

The algorithms are examined with data, of a boundary layer scintillometer and sonic anemometer, collected at the Haarweg (The Netherlands). The scintillation spectra are obtained with Fast Fourier Transformations and wavelets. Wavelets are used to obtain a well-defined spectra for short time intervals (< 1 minute). From the results we conclude that it is possible to obtain the crosswind from a scintillometer by using spectral techniques for short time intervals it is preferable to use wavelets to determine the spectrum.

1. INTRODUCTION

In this study we are interested in obtaining the wind component perpendicular to a path, the so called crosswind ($U_\perp$), using scintillometer measurements. A scintillometer is a device that consist of a transmitter and receiver. The transmitter and receiver are placed over a path of 0.1 to 10 km. The transmitter emits a light beam which is refracted in the turbulent atmosphere, causing light intensity fluctuations that are measured by the receiver.

An application of line averaged crosswinds obtained from scintillometers is at airports. Strong crosswind along airport runways can introduce a serious safety risk to airplanes taking off or landing. Airports typically use cup anemometers and wind vanes to measure the crosswind. The disadvantage of these devices is that their measurements are representative for a small part of the runway, while the scintillometer averages the crosswind along a path.

The application of a scintillometer to measure crosswind is not new. Lawrence [4] constructed an optical wind sensor that consisted of a dual aperture scintillometer (DAS), which used the motion of the scintillation pattern to obtain the crosswind.

Wang [5] showed a technique where the frequency corresponding to the width of the auto-covariance function is used to obtain the crosswind. This frequency technique, as they called it, can also be applied to a single aperture scintillometer (SAS).

The techniques suggested by [4] and [5] rely on experimental calibration. This calibration is necessary to find the constant describing the relation between the crosswind and the covariance or frequency point used by the technique.

In this study we explore three algorithms to obtain the crosswind from power spectra of a SAS signal. A salient point in the scintillation spectra shifts linearly along the frequency axis as a function of $U_\perp$ The three algorithms are named after the salient points in different representation in the spectra, notably: the Corner Frequency (CF), Maximum Frequency (MF), and Cumulative Spectrum (CS) algorithm. We will use the theoretical model for scintillation spectra of Clifford [3] to establish the relation between the location of the different salient points and the crosswind.

This work is in more detail discussed in a paper entitled ‘Crosswind from a Single Aperture Scintillometer using Spectral Techniques’ in review at the *Journal of Atmospheric and Oceanic Technology* [6].

2. THEORY

A scintillometer sends a monochromatic light beam from a transmitter to a receiver, which are typically a few hundred meters to a few kilometers apart. This light is scattered by turbulent eddies, which are advected through the scintillometer path by the wind. Therefore, the amount of scattering varies in time, causing the measured light intensity to fluctuate. Assuming Taylor's frozen turbulence hypothesis, the wind advecting the eddies through the path is the only phenomena driving the light intensity fluctuations. If this assumption is not valid the decay of eddies also contributes to the intensity fluctuations.

Figure \ref{fig:spectrum} shows a typical measured spectrum of the scintillometer signal. The spectrum shows how much each frequency contributes to the variance of the log of the intensity signal (σ^2_{lnI})

Clifford [3] describes a theoretical model that represents the spectrum of intensity fluctuations measured by a scintillometer for spherical waves. Wang [7] added terms to include the spatially incoherent transmitting and receiving optics in the theoretical model, i.e. the step from a point source to a finite aperture. The theoretical power spectrum (S) is then defined by:

$$S(f) = 16\pi^2 k^2 \int_0^L \int_{\frac{2\pi f}{U_\perp}}^{\infty} K\, \phi_n(K)\, sin^2\left(\frac{K^2 x(L-x)}{2kL}\right) \left[(K\, U_\perp)^2 - 2\pi\, f{-12}\ 2J10.5\ K\, D\, x/L0.5\ K\, D\ (1{-}x/L2\ dK\ dx \right. \quad (1)$$

where f is the frequency, k is the turbulent spatial wave number, K the turbulent spatial wave number, x is the relative location on the path, J_1 is a first order Bessel function and $\phi_n(k)$ is the three dimensional spectrum of the refractive index in the inertial range given in [8].

For a given scintillometer set-up all variables except $U_\perp$ and the structure parameter of the refractive index (C_{n^2}) are constant in equation 1 (C_{n^2} determines the value of ϕ_n). Therefore, these two variables influence the location of the spectrum, but they do not alter the shape of the spectrum.

In Figure 1a the theoretical scintillation power spectrum is plotted with crosswinds of 0.1 and 10 m s^{-1}. From this figure it is apparent that a stronger crosswind causes the spectrum to shift to higher frequencies (to the right). This relation can be qualitatively explained as follows; the higher the crosswind the faster the eddies are advected through the scintillometer path. Therefore, the higher frequencies contribute more to the variance of the signal when the crosswind is higher. An important feature is that the frequency shift scales linearly with the crosswind. Therefore, a salient point in the spectrum moves linearly across the frequency domain due to the crosswind. We will use the theoretical model of Clifford to establish the factor describing the relation between $U_\perp$ and the salient frequency point.

3. METHOD

In this Section we will describe the three algorithms we used to obtain the crosswind from measured scintillation spectra. They are named the Corner Frequency (CF), the Maximum Frequency (MF), and the Cumulative Spectrum (CS). The algorithms indicate salient points in different representation of the spectra that can easily be traced by a computer algorithm. The salient points in the spectrum shift linearly along the frequency axis as a function of the crosswind, so:

$$U_\perp = C_{algorithm}\ D\ f_{algortihm} \qquad (2)$$

where $C_{algoritm}$ is a constant depending on the algorithm used, and $f_{algorithm}$ is the frequency corresponding to the salient points of the different algorithms. The values of $C_{algorithm}$ will be determined from the theoretical model for the scintillation spectrum of [3].

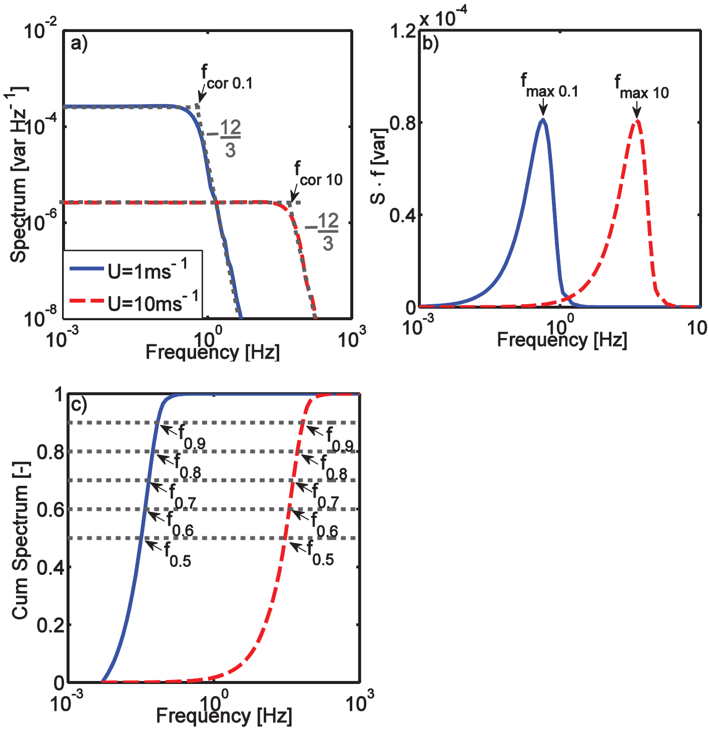

Figure 1. Theoretical scintillation spectra with a crosswind of 0.1 m s^{-1} (solid blue line) and 10 m s^{-1} (dashed red line) in loglog (a), semilog (b), and cumulative (c) representation.

The spectral representations we used are the loglog, semilog, and the cumulative spectrum for the CF, MF, and CS algorithm respectively.

The corner frequency is the inflection point in the loglog representation of the scintillation spectrum (Figure 1a). We will use the definition of the corner frequency given in [9], which states that it is the point of intersect between the zero-slope line and the power-law line.

The maximum frequency (f_{MF}) is the frequency where the maximum of the energy conserved representation of the scintillation spectrum is located (Figure 1b).

The cumulative spectrum, also known as Ogives, is obtained by integrating a spectrum from high to low frequencies. However, we integrate the spectrum from low to high frequency (left to right) and normalize the spectra with σ_{lnI}^2. The CS is a new algorithm we propose to obtain $U_\perp$ from a scintillation spectrum. Unlike the previously discussed algorithms, the CS algorithm takes into account the complete shape of the spectrum. We used five frequency points, which corresponded to the following points in the cumulative spectrum; 0.5, 0.6, 0.7, 0.8, and 0.9 (Figure 1c).

4. EXPERIMENTAL SET-UP

The data studied in this paper were collected at the meteorological site at the Haarweg, Wageningen, The Netherlands from 14 April till 20 May 2010. We deployed a Boundary Layer Scintillometer (BLS900, Manufacturer Scintec, Rottenburg, Germany). The BLS900 was installed at a height of 3.53 with a path length of 426 m. The scintillometer is fitted with a processing unit that has a measurement frequency of 500 Hz. We stored the raw 500 Hz intensity signal. We used Srun software version 1.07 of Scintec to operate the scintillometer. The BLS900 is a DAS, so with two transmitters and receivers with aperture diameters of 15 cm. Even though the BLS900 is a DAS, we will use it as a SAS, i.e. we will use only one of the two signals in our study.

The output of the BLS900 was validated against a CSAT3 sonic anemometer manufactured by Campbell scientific (Utah, United States of America), which was also located at the meteorological site at the Haarweg. The measurement height of the CSAT3 was 3.44 m. The measurement frequency of the sonic anemometer was 10 Hz. The wind component of the CSAT3 we used to calculate the crosswind were aligned with the flow using a planar fit correction [10]. To validate the BLS900 with the CSAT3, the wind component perpendicular to the scintillometer path was calculated from the horizontal wind components measured by the CSAT3.

5. RESULTS

5.1 Crosswinds from FFT spectra

In Figure \ref{fig:FFT}, scatter plots are given of the crosswind measured by the sonic anemometer ($U_{\perp Sonic}$) against crosswind determined with the BLS900 (used as a SAS – $U_{\perp SAS}$) for the three algorithms obtained from FFT spectra over 10 minutes time intervals. The points are color coded with the signal to noise ratio (S2N). The noise level was determined in the field as the standard deviation of the light intensity measured by the receiver when the light intensity emitted by the transmitter was not received, which was 15 arbitrary units.

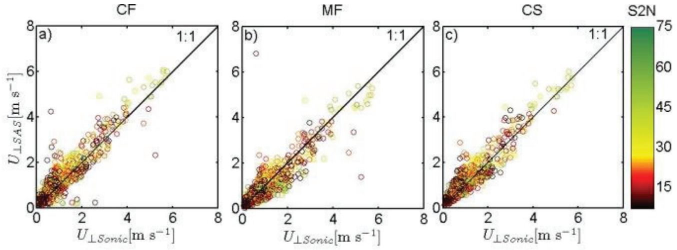

Figure 2. Scatter plots of 10 minute crosswinds averages with on the x-axis $U_{\perp Sonic}$ and on the y-axis $U_{\perp SAS}$ for CF (a), MF (b) and CS (c) algorithm with in colors S2N.

Figure 2 indicates that all spectral techniques obtained similar results as $U_{\perp Sonic}$. This similarity between the spectral techniques and the sonic anemometer is also visible in the regression statistics outlined in Table 1. In this Table the linear regression parameter and corresponding R^2, root mean square error (RMSE), and the percentage of data points left after filtering (N) are shown. A filter on the intensity signal (I) below 20 000 arbitrary units (2/3 of the clear sky conditions) was applied. Fog in the morning mainly resulted in the low intensity signal resulting in a loss of data of 17 %. An additional high–pass filter (HPF) of 0.1 Hz, a low-pass filter (LPF) of 90 Hz and a filter on the maximum frequency was applied and a filter on U_{CS} < 0.5 are also shown (see Table 1).

The fit of U_{CS} with $U_{\perp Sonic}$ is best, with a regression slope of 0.95 and a RMSE of 0.37 m s^{-1}. However, the amount of data points is smallest for this algorithm, with a N of only 75 %. For the CF algorithm the fit with the sonic anemometer is also very good (with a regression slope of 0.95). However, the scatter is somewhat higher than that of the CS algorithm (R^2 of 0.81 in comparison to 0.87, and a RMSE of 0.46 in comparison to 0.37). We assumed that the CS algorithm would not be valid for crosswinds below 0.5 m s^{-1}. However, using a filter on these low crosswinds did not improve the results, but did result in an extra loss of data of 11 %. The fit of the MF algorithm with the sonic anemometer is worst of the three spectral techniques (regression slope of 0.83 and RMSE of 0.53 m s^{-1}). On the other hand all the data points, where the signal is not below 20 000, result in a value for the crosswind. Therefore, the MF algorithm is most robust to determine the crosswind. From Figure 2b it is apparent that some outliers in U_{MF} occur when the S2N is low (< 10 m s^{-1}).

Table 1: Regression equations, R2 and RMSE for $U_{\perp SAS}$ with $U_{\perp Sonic}$ for CF, MF, and CS algorithm with different filters.

Algorithm	Filter	Regression eq	R^2	RMSE	N [%]
CF	HPF	y = 0.95x +0.23	0.81	0.46	80
MF	HPF & LPF	y = 0.83x +0.14	0.70	0.53	83
CS	$90 < f_{MF} < 0.1$	y = 0.95x +0.22	0.87	0.37	75
	$U_{CS} < 0.5$	y = 0.93x +0.26	0.85	0.39	64

6. CONCLUSIONS

We obtained the crosswind from a single aperture scintillometer (SAS) signal using three different algorithms, which are based on scintillation spectra without a calibration in the field. These algorithm are; the corner frequency (CF), maximum frequency (MF) and cumulative spectrum (CS). All three algorithms obtained similar results for the crosswind compared with a sonic anemometer, thereby proving that the three algorithms are able to obtain the crosswind from a scintillometer signal. However, some filters needed to be applied to obtain these results. A filter on the scintillometer intensity signal (*I*) was applied to all algorithms (*I*<20 000).

The CF algorithm has the disadvantage that it does not yield a result when the zero-slope and power-law line are not clearly present in the scintillometer spectrum. On the other hand this does serve as a quality check for how well the spectrum of the scintillometer signal is defined. This built in quality check is why this method achieves good results, also without additional filtering. Applying a high-pass filter did improve the results of the CF algorithm.

The MF algorithm was most robust in obtaining the crosswind, only an additional high-pass filter and low-pass filter were applied. These filters did not result in a loss of data. For the MF algorithm it was also possible to use a less strict filter on signal intensity (5 000 instead of 20 000) and still achieve similar results for the regression statistics as with the strict filter. In this study we also discussed a signal to noise filter, but in the end we did not apply this filter to our data.

The CS algorithm, a new algorithm we introduced in this paper, achieved the best result. The fit of this algorithm with the sonic anemometer was best, and the root mean square error was smallest. On the other hand, the amount of data points of the CS algorithm was smallest, since all the data points were the maximum frequency was below 0.1 Hz or above 90 Hz were filtered out.

ACKNOWLEDGMENTS

The authors would like to thank Frits Antonysen and Willy Hillen for their assistance with the BLS900 set-up. This study was funded by Knowledge for Climate project HSMS01.

REFERENCES

1. Tartarskii, V.I., 1961, Wave Propagation in a turbulent Medium, McGraw0Hill, New York, 285 pp.

2. Poggio, L.P., M. Furger, A.H. Prévôt, W.K. Garber, E.L. Andreas, 2000: Scintillometer Wind Measurements over Complex Terrain, *Journal of Atmospheric and Oceanic Technology*, **17 (1)**, pp. 17-26.

3. Clifford, S.F., 1971: Temporal-frequency spectra for a spherical wave propagating through atmospheric turbulence, *Journal of the Optical Society of America*, **61 (10)**, pp. 1285-1292

4. Lawrence, R. S., G. R. Ochs, S. F. Clifford, 1972: Use of scintillations to measure average wind across a light beam, *Applied optics*, **11 (2)**, pp. 239-243.

5. Wang, T. I., G. R. Ochs, R. S. Lawrence, 1981: Wind measurements by the temporal cross-correlation of the optical scintillations, *Applied optics*, **20 (23)**, pp. 4073 - 4081.

6. van Dinther, D., O.K. Hartogensis, A.F. Moene, in review, Crosswind from a Single Aperture Scintillometer using Spectral Techniques, *Journal of Atmospheric and Oceanic Technology*.

7. Wang, T. I., G. R. Ochs, S. F. Clifford, 1978, A saturation-resistant optical scintillometer to measure C_n^2, *Journal of the Optical Society of America*, **68 (3)**, pp. 334.

8. Kolmogorov, A. N., 1941, The local structure of turbulence in an incompressible viscous fluid for very large Reynolds numbers, *Dokl. Akad. Nauk.*, **30**, pp. 299-303.

9. Medeiros Filho, F. C., D. A. R. Jayasuriya, R. S. Cole, C. G. Helmis, 1983, Spectral density of millimeter wave amplitude scintillations in an absorption region, *IEEE Transactions on Antennas and Propagation*, **31 (4)**, 672-676.

10. Wilczak, J. M., S. P. Oncley, S. A. Stage, 2001, Sonic anemometer tilt correction algorithms, *Boundary-Layer Meteorology*, **99**, pp.127-150.

Session 3 – Oral Presentations

INNOVATIVE C-BAND LINEAR FM-CW RADAR TO STUDY PRECIPITATION FROM THE GROUND TO 300 METERS

Christopher R. Williams[1, 2]

[1]*Cooperative Institute for Research in Environmental Sciences (CIRES),*
University of Colorado Boulder, UCB 216, Boulder, CO 80305-0216, USA, Christopher.Williams@colorado.edu
[2]*NOAA Earth System Research Laboratory (ESRL), Physical Sciences Division (PSD), Boulder, CO, USA*

ABSTRACT

Using support from the University of Colorado at Boulder, Cooperative Institute for Research in Environmental Sciences (CIRES) Innovative Research Program, an inexpensive vertically pointing precipitation radar was developed to observe precipitation within 300 meters of the ground. The linear frequency modulated (FM) continuous wave (CW) technique was used to achieve a 5-m range resolution. The C-band radar operated in the point-to-point Internet service frequency band (5.8 GHz), transmitted low power, and all radar hardware costs were less than US$ 6 000.

The Doppler velocity power spectrum at each range gate was estimated using two fast Fourier transforms (FFTs). A range-FFT converted the sweep voltages into beat frequencies that correspond to discrete ranges. The real and imaginary components of each complex frequency were re-labeled as the in-phase and quadrature voltages (I and Q). Then, a Doppler-FFT converted the I and Q voltages from consecutive sweeps into Doppler velocity power spectra estimates. The Doppler-FFT is equivalent to the pulse-to-pulse processing use in standard wind profilers.

Another innovation of this project was that all Doppler-FFT calculations were performed using the Cell Broadband Engine parallel processor installed in a Sony PlayStation 3. Details not covered in this extended abstract are described in [1].

1. MOTIVATION

Vertically pointing radars are used to study the vertical structure of rain storms as they pass overhead [2]. Vertically pointing radars are also used to study the raindrop size distribution providing information on the dynamics and microphysical processes occurring in rain storms [3].

1.1 Technical Issues

Monostatic antenna pulse radars are ‘blind’ to close ranges because they cannot make observations during the transmit pulse and must wait for the switch from transmit to receive modes. This distance can be over 150 meters in some precipitation research radars [4]. The radar developed in this project is bistatic and uses the FM-CW technique to observe at close range.

1.2 Scientific Issues

At small spatial and temporal scales, raindrops are not uniformly distributed. Raindrops cluster and separate due to dynamics and turbulence. We see these clusters of raindrops as “cat paws” when rain falls on lakes. But typical precipitation radars do not observe raindrop clusters because their large radar sample volumes average out sub-resolution structures. By reducing the size of the radar resolution volume, we’ll have the opportunity to investigate the clustering of raindrops. Also, as numerical models resolve smaller cloud structures, we’ll need observations at comparable resolutions to verify their model simulations.

2. RADAR HARDWARE LAYOUT

The FM-CW radar followed a classical upward linear sawtooth frequency modulated homodyne radar design [5]. The radar was designed using commercial components purchased from major distributors via the Internet and hardware costs were less than US$ 6 000.

The hardware consists of electronics located either inside a shelter or outside under the antennas. Inside the shelter, a data acquisition system (DAS) is attached to a personal computer (PC) using a USB connection. The PC commands the DAS to start all logic signals and to acquire data. The DAS commands a direct digital synthesizer (DDS) to generate an upward linear sawtooth frequency sweep centered around 60 MHz. Using a 50 ft coax cable, the chirp signal is fed to the Tx & Rx Module located outside under the antennas and up-converts the signal to C-band (5.8 GHz). The receive antenna signal is mixed with the reference signal generating intermediate frequencies. Another 50 ft coax cable brings the intermediate frequency signals back inside the shelter where they are fed through a video filter to amplify the desired signals before being sampled by the DAS. Using DAS manufacture supplied device drivers, the sampled voltages are saved to the PC hard disk and all signal processing is done post-data collection on the Sony Playstation 3.

The C-band FM-CW radar 90-cm diameter offset parabolic antennas have ~4° beam widths and are shown in Figure 1. Also shown in Figure 1 are 60-cm diameter radome covered X-band antennas used for anther FM-CW precipitation radar. While a 4° beam width may not be suitable for long-distance viewing radars, a 4° beam width enables more raindrops to be observed with short range resolution. For example, a 4° by 5-m radar sample volume has the same sample volume as a 1° by 80-m radar volume.

Figure 1. Photograph of the outside hardware. Gray off-set parabolic dishes are the C-band antennas and white radome dishes are X-band antennas. Poles are 6 ft long and silver boxes contain the Tx and Rx Module circuitry. Hardware was installed in author's backyard.

3. FM-CW SIGNAL PROCESSING

The FM-CW radar signal processing consists of performing two Fourier transforms (FFTs) on the collected sweep voltages. The first FFT is the range-FFT [6] and converts the real valued voltage samples collected during each frequency sweep into complex valued intermediate frequencies (also called beat frequencies). The second FFT is called the Doppler-FFT and converts a time-series of complex frequencies at each height into a Doppler velocity power spectrum [7].

3.1 Range-FFT

Radars utilizing FM-CW techniques can observe targets at fine resolution and at close ranges [6]. This radar uses an upward sawtooth frequency modulated (FM) signal sweeping linearly from f_0 to $f_0 + B$ over the duration T_{sweep} followed by a waiting interval T_{wait} at f_0. For a linear sweeping FM signal, a target located at range R will generate an intermediate frequency f_{IF} that is dependent on the radar sweep rate B / T_{sweep} and the target two-way propagation time $2R/c$ such that

$$f_{\text{IF}} = \frac{B}{T_{\text{sweep}}} \frac{2R}{c} \tag{1}$$

where c is the electromagnetic wave propagation speed. During each linear FM sweep, the DAS collects n voltage samples each spaced Δt apart for a total dwell interval of $T_{\text{dwell}} = n\Delta t$. The intermediate frequency resolution is given by $\Delta f_{\text{IF}} = 1/(n\Delta t)$ and from equation (1) the range resolution is given by

$$\Delta R = \frac{cT_{\text{sweep}}}{2\text{B}} \Delta f_{\text{IF}} = \frac{cT_{sweep}}{2B} \frac{1}{n\Delta t}\,. \tag{2}$$

This C-band radar achieved a 5-m range resolution using a 500 kHz DAS sampling rate ($\Delta t = 2\ \mu\text{s}$) along with parameters: $T_{\text{sweep}} = 310\ \mu\text{s}$, $n = 128$, and $B = 36.3\ \text{MHz}$. Low cost is achieved because a 500 kHz sample rate DAS is much less expensive than a 120 MHz sample rate DAS needed for a pulse radar with a 5-m range resolution (without pulse compression, the pulse radar sample rate is given by $2c/\Delta R$). Another advantage of FM-CW radar is the reduced peak transmitted power because the transmitted duty cycle was about 80% when defined as $(n\Delta t)/(T_{\text{sweep}} + T_{\text{wait}})$.

3.2 Doppler-FFT

For this radar design, the range-FFT consisted of 128 samples yielding 64 ranges. The real and complex values from each frequency bin are renamed "*I*" and "*Q*" and are equivalent to in-phase (*I*) and quadrature (*Q*) voltages generated with heterodyne pulse radar processing [7]. The Doppler-FFT converts a time sequence of *I* and *Q* voltages at each frequency bin into Doppler velocity power spectra. Since the Doppler-FFT is performed on data from each frequency bin, or from each range gate, the Doppler-FFT is exactly the same as the Doppler processing used in pulse Doppler profiling radars.

4. EXAMPLE OBSERVATION

A rain event passed over Denver, Colorado, on 18 August 2009. Figure 2 shows a 21 second averaged uncalibrated Doppler velocity reflectivity spectra from 5 to 300 m with a 5-m range resolution. The decreased reflectivity in the lowest range gates is due to the two antennas being placed too far apart to observe close to the antennas. Moving the antennas closer will allow observations down to 5 m but will also increase the coupling between the Tx and Rx antennas leading to more ground clutter.

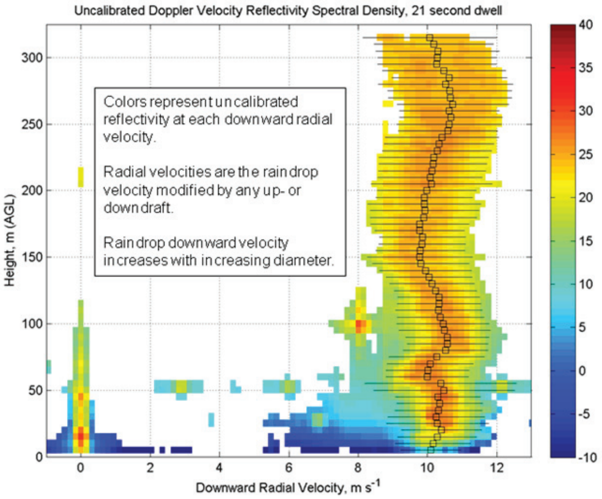

Figure 2. Profile of uncalibrated Doppler velocity reflectivity spectral density collected during a 21-s dwell.

Figure 3 illustrates the precipitation temporal and vertical structure during the 21 second dwell shown in Figure 2. The mean uncalibrated reflectivity and mean radial velocity profiles are shown on the left two panels of Figure 3 with the 0.5 second anomalies shown in the right two panels. Even though the reflectivity is not absolutely calibrated, the time-height anomaly diagrams show ~10 dBZ variation in reflectivity and ~4 m s^{-1} variation in mean radial velocity during this 21 second interval. These anomaly diagrams show high temporal and vertical precipitation structure not resolved in the 21-s dwell spectra profile shown in Figure 2. Interestingly, there appears to be an inverse correlation between reflectivity and radial velocities in this event that needs further investigation.

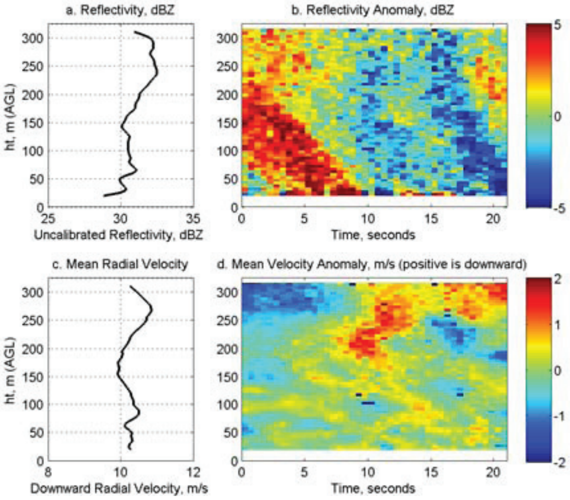

Figure 3. Mean profiles of uncalibrated reflectivity (a) and mean velocity (b) estimated during 21-s dwell shown in Figure 2. Reflectivity and velocity anomalies using 0.5 second dwells are shown in (c) and (d).

5. CONCLUDING REMARKS

An inexpensive C-band (5.8 GHz) vertically pointing Doppler radar utilizing FM-CW technology was developed to observe precipitation within 300 m of the surface and at a 5-m range resolution. Because the FM-CW radar technique does not require a fast data acquisition system, the hardware costs were less than US$ 6 000. The signal processing consisted of performing two sets of FFTs: one range-FFT was applied to each FM sweep to determine the I and Q voltages at each range and a Doppler-FFT was applied to each range over several FM sweeps to estimate the Doppler velocity power spectrum at each range. More information about this C-band FM-CW precipitation radar is available in [1].

ACKNOWLEDGMENTS

Support was provided by the University of Colorado Boulder, Cooperative Institute for Research in Environmental Sciences (CIRES) Innovative Research Program.

REFERENCES

1. Williams, C.R., 2011: Inexpensive FM-CW radar for boundary-layer precipitation studies. *IEEE Geoscience and Remote Sensing Letters*, **8**, 1031-1035, 10.1109/LGRS.2011.21507337.

2. Gage, K.S., C.R. Williams, W.L. Clark, P.E. Johnston, and D.A. Carter, 2002: Profiler contributions to Tropical Rainfall Measuring Mission (TRMM) ground validation field campaigns. *J. Atmos. Oceanic Technol.*, **19**, 843-863.

3. Cifelli, R., C.R. Williams, D.K. Rajopadhyaya, S.K. Avery, K.S. Gage, and P.T. May, 2000: Drop-size distribution characteristics in Tropical mesoscale convective systems. *J. Appl. Meteor.*, **39**, 760-777.

4. Tokay, A., P. Hartmann, A. Battaglia, K.S. Gage, W.L. Clark, and C.R. Williams, 2009: A field study of reflectivity and Z-R relations using vertically pointing radars and disdrometers. *J. Atmos. Oceanic Technol.*, **26**, 1120-1134.

5. M. Skolnik, 1990: *Radar Handbook*. McGraw-Hill, Boston, MA.

6. M. Jankiraman, 2007: *Design of Multi-Frequency CW Radars*. SciTech Publishing, Raleigh, NC.

7. R. Strauch, 1971: “Theory and application of the FM-CW Doppler radar.” Ph.D. dissertation, Dept. Electrical Eng., University of Colorado, Boulder, CO, 97 pp.

COMPARISON OF 482 MHZ RADAR WIND PROFILER AND DOPPLER LIDAR WIND MEASUREMENTS AT LINDENBERG

Bernd Stiller[1], Ronny Leinweber [1], Volker Lehmann [1]

[1] *Deutscher Wetterdienst, Richard-Aßmann-Observatorium, 15848 Lindenberg, Germany, Bernd.Stiller@dwd.de*

ABSTRACT

The wind field is one of the most important atmospheric parameters. Its accurate measurement with a high spatial and temporal resolution is crucial for the improvement of Numerical Weather Prediction (NWP) models as well as necessary to obtain reliable calculations of transport of air pollution and trace gases. Radar wind profilers (RWP) are the most thoroughly developed and widely used sensors for ground based remote sensing of the wind field. They provide vertical profiles of the horizontal wind at high temporal resolution under all weather conditions, that is in both the cloudy and clear atmosphere. Moreover, new portable IR Doppler Lidar systems have been recently developed mainly due to requirements from the renewable energy community.

We present the results of a comparison of three different Doppler Lidar systems, developed by Leosphere and Halo Photonics, respectively, with a 482 MHz Radar Wind Profiler. The measurements were performed at Lindenberg Observatory for a period of two months (November / December 2011). Radio Soundings and NWP model data was additionally used for the comparison.

1. RESULTS

Exemplarily the comparisons results for the StreamLine lidar are shown in Figure 1 and Figure 2. The differences in wind speed are shown in Figure 1, while the differences in wind direction are shown in Figure 2.

In summary all Doppler wind lidars are in good agreement with the radar wind profiler measurements. Differences in wind speed and wind direction of 0.2m/s or 2°, respectively, were found during the validation period. Large differences occur at the lowermost and uppermost altitude levels due to ground clutter in RWP measurements and weak CNR.

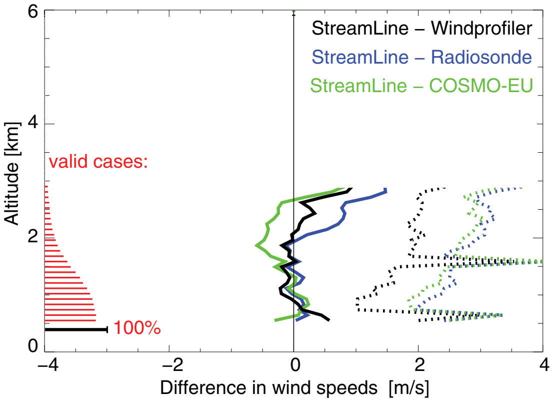

Figure 1. Differences in wind speed compared to the 482MHz wind profiler (black), radiosondes (blue) and NWP model COSMO-EU (green) for the period 29.11.2011 - 20.12.2011 (3 weeks). The solid lines indicate the differences in wind speed while the dashed lines indicate the RMS error. The red lines denote the wind lidar data availability for different altitude levels.

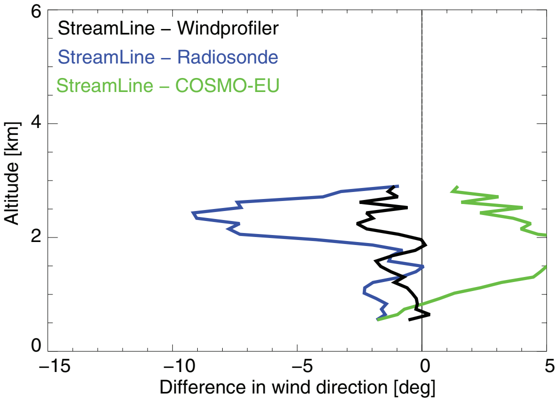

Figure 2. Differences in wind speed compared to the 482MHz wind profiler (black), radiosondes (blue) and NWP model COSMO-EU (green) for the period 29.11.2011 - 20.12.2011 (3 weeks).

SMALL-APERTURE SCINTILLOMETER MEASUREMENTS OF TURBULENT FLUXES AT A SUBURBAN SITE

Petra M. Klein[1], **Jose M. Galvez**[2]

[1]*School of Meteorology, Univ. of Oklahoma, 120 David L. Boren Blvd, Norman, OK 73072, USA,*
pkklein@ou.edu
[2]*Hydrometeorological Prediction Center, NCEP/NOAA, 5200 Auth Road Camp Springs, Maryland 20746, USA* jose.galvez@noaa.gov

ABSTRACT

Heat and Momentum fluxes measured with a Scintec SLS20 scintillometer during two field campaigns are presented. The studies were conducted in the summers of 2007 (06/22–09/13) and 2008 (05/22-09/05) at a site in flat terrain covered by prairie grasses. The site was located near the Norman MESONET site and for prevailing, southerly wind directions it is only 200 m downwind of the city of Norman. The scintillometer was operated over a 100-meter-long east-west oriented path and 2-m above the ground. Eddy-covariance measurements with several sonic anemometers were also conducted: in 2007 one RM-Young sonic anemometer was located at the center of the path and in 2008 one RM-Young and four CSAT-3 sonic anemometers were placed along the path. The scintillometer data were recorded at 1-minute intervals whereas sonic anemometer data were recorded at a frequency of 10 Hz. Scintillometer and eddy-covariance heat fluxes showed the same diurnal and seasonal trends, but the scintillometer data had a low bias with a tendency for larger differences as the heat fluxes increased. Clear differences can also be noted for stable conditions and the scintillometer momentum flux observations are generally not very good. A number of correction methods for improving the scintillometer skill are discussed. Initial tests that targeted various expressions for the Monin-Obukhov similarity functions for the dimensionless dissipation rate φ_ϵ and temperature structure function parameter $\varphi_{C_T^2}$ were not successful, while uncertainties in the integral length scale l_0 and form of the dissipation-range spectrum appear to play an important role.

1. INTRODUCTION

Scintillations are intensity fluctuations of electromagnetic radiation caused by turbulence in the atmosphere. Turbulent eddies result in variations in the refractive index, which alters the propagation of electromagnetic radiation. The intensity fluctuations can be measured with scintillometers, which consist of a transmitter and a receiver that are separated by path lengths that vary between tens of meters and about ten kilometers, which provides path-integrated turbulent heat and momentum fluxes. Path-averaged values are considered a major advantage compared to in-situ data. Scintillometer data are also unaltered by mast distortion and horizontal misalignment issues, and represent averages over short intervals while eddy-covariance measurements with sonic anemometers require much longer averaging times in the order of tens of minutes. The ability to measure fluxes over short averaging intervals has important applications such as measuring the often non-stationary stable boundary layer [1]. However, the computation of turbulent heat and momentum fluxes from the intensity fluctuations measured by the scintillometer relies on several assumptions about optical wave propagation and turbulent properties in the atmospheric surface layer (ASL), further discussed in the next section.

2. SCINTILLOMETER THEORY

The Scintec SLS20 is a displaced beam scintillometer, which means the laser light is split into two parallel beams. The intensity fluctuations of each beam are then recorded and by analyzing the log-amplitude variations of these fluctuations for each beam, B_1 and B_2, as well as their covariance B_{12} the inner-scale of turbulence l_0 and structure function parameter of the refraction index C_n^2 can be calculated. These three variables depend on wave propagation characteristics, the averaging of the intensity fluctuations over the detector, and averaging along the whole path as well as over the range of turbulent length scales in the refractive index spectrum. The shape of the refractive index spectrum becomes very important, and for accurate predictions of the inner scale of turbulence l_0 the decay of refractive index fluctuations in the dissipation range must be adequately described. The Scintec algorithm [2] uses a model for this part of the spectrum that is often referred to as the Hill bump [3]. However, Hill's expression is still limited in accuracy due to the difficulty of measuring refractive index spectra in the dissipation range, which requires accurate high frequency measurements, and inaccuracies in SLS fluxes can often be traced back to problems in the calculation of l_0 that are related to assumptions about the dissipation-range spectrum [1].

Once C_n^2 and l_0 become available from scintillations they can be used to calculate C_T^2 and ε. C_n^2 is affected by temperature, moisture and pressure, however the effects of pressure variations are so small that they can be neglected [1]. For scintillometers operating in the visible or near-infrared region, like the SCINTEC SLS20 model, the effects of moisture variations are also negligible and C_T^2 can be related to C_n^2 if pressure and temperature measurements are available. The dissipation rate ε is computed using the relationship

$$\varepsilon = \nu^3 \left(\frac{7.4}{l_0} \right)^4 , \tag{1}$$

whereby the kinematic viscosity of air ν can be calculated from temperature and pressure measurements.

Once C_T^2 and ε are available, Monin-Obukhov Similarity Theory (MOST) can be used to retrieve turbulent fluxes of heat and momentum, using expressions for the dimensionless dissipation rate $\phi_\varepsilon = \kappa z \varepsilon / u_*^3$, with $\kappa = 0.4$, and structure function parameter of temperature $\phi_{C_T^2} = z^{2/3} C_T^2 / \theta_*^2$, which according to MOST are only a function of the dimensionless height $\zeta = z/L$. The Monin-Obukhov length L also depends on the surface layer scales friction velocity u_* and friction temperature θ_*. The following expressions for ϕ_ε and $\phi_{C_T^2}$ are used in the algorithm for the SCINTEC SLS20 [2, 4]:

for $\zeta < 0$ (unstable):

$$\begin{aligned} \phi_\varepsilon &= \left[1 - 3\zeta\right]^{-1} - \zeta \\ \phi_{C_T^2} &= 4\beta_1 \left[1 - 7\zeta + 75\zeta^2\right]^{-1/3} , \end{aligned} \tag{2}$$

for $\zeta > 0$ (stable):

$$\begin{aligned} \phi_\varepsilon &= \left[1 + 4\zeta + 16\zeta^2\right]^{1/2} \\ \phi_{C_T^2} &= 4\beta_1 \left[1 + 7\zeta + 20\zeta^2\right]^{1/3} , \end{aligned} \tag{3}$$

where $\beta_1 \cong 0.86$ is the Obukhov-Corrsin constant. Solving equations 1 through 3 requires an iteration scheme and leads to the calculation of three surface layer scales: u_*, θ_* and L, which can then be used to determine turbulent fluxes of heat H_{SLS} and momentum M_{SLS} via:

$$H_{SLS} = -\rho c_p u_* \theta_* \tag{4}$$

and

$$M_{SLS} = -\rho u_*^2 . \tag{5}$$

One important limitation is that stability cannot be determined from the SLS data alone. It needs to be calculated using a complementary platform, which in the case of the current study were data collected with a sonic anemometer placed along the scintillometer path.

3. EXPERIMENTAL SETUP

Two field campaigns were made in a flat and homogeneous environment covered by ten to fifteen-centimeter tall prairie grasses. The selected site was located only 100 meters away from the Norman site (35°14’10’’ N, 97°27’47’’ W and 357 mASL) of the Oklahoma MESONET (http://www.mesonet.org). The placement was ideal for inter-comparisons with some of the MESONET data and for testing of MOST applicability. One limitation, however, was the closeness to the Norman, Oklahoma urban area, which justifies the use of the term 'sub-urban' instead of 'rural'. The closeness to an urban environment could lead to deviations of the MOST functions that are used in the scintillometer algorithm.

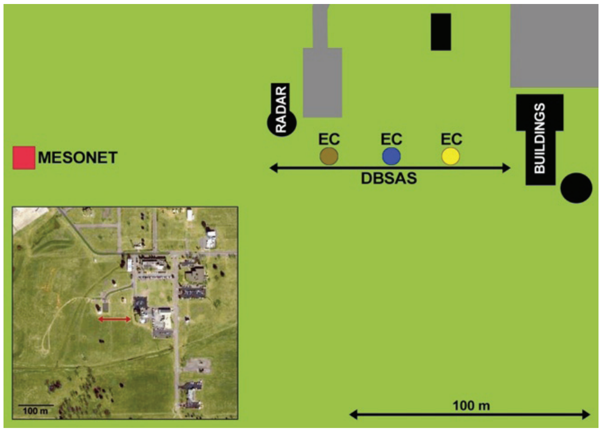

Figure 1. Map of the site were both ILREUM sub-urban campaigns were carried out. The Norman MESONET site is indicated by a red square, buildings are shown in black and paved surfaces in gray. The black arrow illustrates the scintillometer path and the colored circles highlight the position of the sonic anemometers (more details in the text).

The campaigns were conducted during the summers of 2007 (22 June - 13 September) and 2008 (22 May - 5 September). Relatively prolonged campaigns were planned to measure under a broad spectrum of flow and stability regimes. The Scintec SLS20 scintillometer was operated over a 100-meter-long east-west oriented path two meters above ground. Several sonic anemometers were operated along the path: In 2007, one RMYoung sonic was placed in the center of the path (blue circle in Fig. 1); while in 2008 two CSAT-3 and one RMYoung were located in the center of the path, with two additional CSAT-3 sonics placed along the path (brown and yellow circles in Fig. 1). Scintillometer data were recorded at 1-min intervals whereas sonic anemometer data were recorded at a frequency of 10 Hz. A map and aerial photo of the site are presented in Fig. 1; photographs of the instruments can be seen in Fig. 2. For the current analysis, both the scintillometer and sonic data were averaged to hourly values.

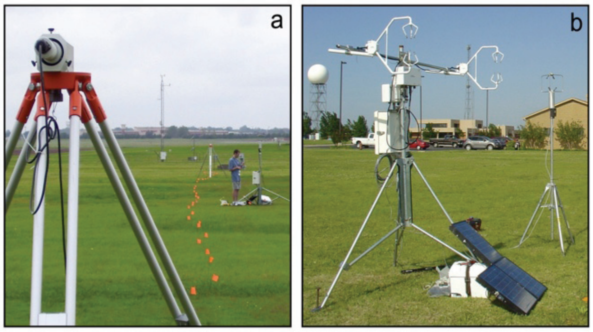

Figure 2. Photographs showing the scintillometer path (left) and sonic anemometers (right) deployed in the center of the path. The meteorological tower seen in the background on the left photo is the 10-m tower of the Norman Mesonet site

4. DISCUSSION OF RESULTS

Figure 3 shows a comparison of the heat and momentum fluxes measured in 2007 by the RM Young sonic with the corresponding values measured by the Scintec SLS 20 scintillometer. The SLS data plotted correspond to values computed using the original Scintec algorithm [2]. As can be seen in Fig. 3, the scintillometer tends to underestimate the turbulent fluxes, particularly for larger absolute values, whereby the disagreement is more pronounced for the momentum fluxes (Fig. 3a) than for the heat fluxes (Fig. 3b). Initial tests to modify the expressions (2) and (3) for the dimensionless MOST function ϕ_ε did not result in any significant improvement. This indicates that the errors largely stem from errors in the calculation of inner scale values l_0 from which the friction velocity u* is computed using:

$$u_* = \nu \left(\frac{7.4^4 \kappa z}{l_0^4 \cdot \phi_\varepsilon(\zeta)} \right)^{1/3} . \tag{6}$$

Eq. (6), which results from combining Eq. (1) with the definition of the dimensionless dissipation rate ϕ_ε, illustrates that small errors in l_0 will result in large u_*-errors, especially for small values of l_0 [1]. It should be noted, that the inner scale l_0 is directly proportional to the correlation coefficient $r_{12} = B_{12}/B_1$; the exact relationship depends however on the expressions for the refractive index spectrum in the dissipation range, the path length *D* used in the experiment and the displacement distance *d* between the two laser beams of the particular scintillometer used. Hartogensis [1] tested the impacts of various spectral relationships and of small inaccuracies in the value of *d* on the accuracy of the inner scale values measured with Scintec SLS 20 scintillometers. He found that the SLS results are very sensitive to both parameters. However, finding the optimal values for both these parameters is relatively difficult and not very practical.

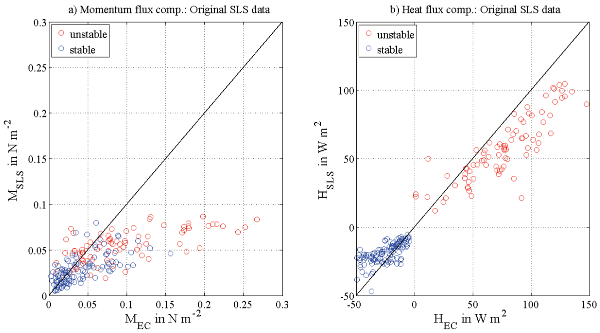

Figure 3. Comparison of momentum (a) and heat (b) fluxes for 2007 measured with an RM Young sonic using the eddy-covariance (EC, x-axis) method and the scintillometer (SLS, y-axis) using the original Scintec algorithm.

Thus, it was decided to use a more straightforward approach to evaluate the accuracy of the original l_0 data computed by the Scintec [2] algorithm and related improvements in the heat and momentum flux data. SLS inner-scale data were compared with l_0 values computed from the sonic data in two different ways. In the first method, l_0-values were computed using Eq. (1) whereby the dissipation rate ε was determined from the sonic spectra in the inertial sub-range. In the second method, the inner scale l_0 was computed from u_* values measured by the sonic by solving Eq. (6) for l_0, which results in:

$$l_0 = 7.4 \left(\frac{\nu^3 \kappa z}{u_*^3 \phi_\varepsilon(\zeta)} \right)^{1/4} . \tag{7}$$

Applying the second method is much simpler than the first method as it does not require analyzing spectra. It relies however on the accuracy of the expressions for the MOST function ϕ_ε. Values for l_0 computed from the sonic data using both methods, plotted as a function of r_{12}, are compared with the original SLS results in Fig. (4). For both methods, the Scintec algorithm overestimates the l_0-values derived from sonic data, whereby method 2 (Eq. 7) results in a larger scatter. For both sets of data, second-order polynomial fits (dashed lines in Fig. 4) were determined, which were then used to re-compute the SLS l_0-values from the correlation coefficients r_{12}. The expressions for these fits are not provided here, as they depend on the path length used during the experiment and are thus not applicable to other data sets.

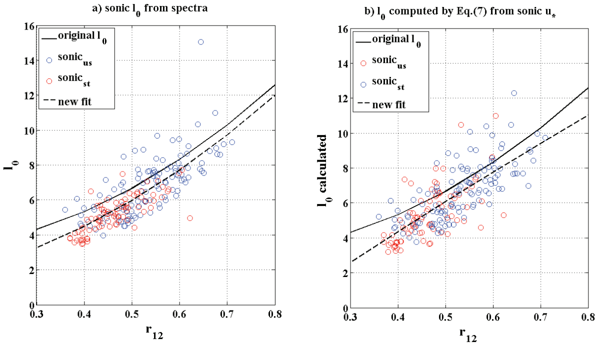

Figure 4. Dependence of l_0 values on correlation coefficients r_{12}. Shown are the original SLS values (solid line) together with l_0 values computed from the sonic spectra (a) and from sonic u_* values according to Eq. (7) (b). Polynomial fits (dashed lines) of the sonic data are also plotted.

The corrected turbulent fluxes that stem from applying the polynomial fits derived using methods 1 and 2 are shown in Fig. 5. In can be seen that both methods clearly improve the agreement between the turbulent fluxes measured by the Scintec SLS 20 and by a sonic anemometer. Larger values of the fluxes are still under-predicted, particularly in the case of the momentum flux. However, compared to the original Scintec algorithm, the slope of trend lines between SLS and sonic fluxes increased roughly by a factor of two for the momentum fluxes, and by ~35% for the negative heat fluxes after applying corrections to the l_0-values according to method 1 or 2 (Tab. 1 and 2). The skill of method 2, which uses the simpler approach to computes the sonic l_0-values using Eq. (7), is similar to the one of method 1, which relies on spectral analysis to determine the inner scale from sonic data. The analysis of the 2008 data gave very similar results, which could not be included here due to page limitations.

5. SUMMARY

The comparison of turbulent fluxes measured with a Scintec SLS 20 scintillometer and RM Young sonic anemometer confirmed previous findings that the SLS tends to under-predict turbulent fluxes, particularly the momentum fluxes. These errors are caused by inaccuracies in the calculation of inner scale values from the intensity fluctuations, and cannot be corrected by adjusting the expression for dimensionless MOST functions ϕ_ε. Using the sonic data, it was possible to correct the l_0-values, which overall improved the scintillometer skill. These expressions are however not universal and would need to be reevaluated for each new field campaign. Based on our findings, SLS data must be interpreted with caution, and, at this point a comparison against sonic data seems very important.

Table 1: Comparison of trend lines statistics for the SLS and sonic momentum fluxes.

Momentum flux	Intercept		Slope	
	unstable	Stable	Unstable	stable
Original SLS	0.04	0.02	0.18	0.32
Method 1	0.04	0.02	0.34	0.55
Method 2	0.04	0.01	0.40	0.62

Table 2: Same as Table 1 but for heat flux comparison.

Heat flux	Intercept		Slope	
	unstable	Stable	Unstable	stable
Original SLS	10.44	-8.88	0.61	0.40
Method 1	13.61	-9.66	0.66	0.54
Method 2	13.60	-8.56	0.66	0.66

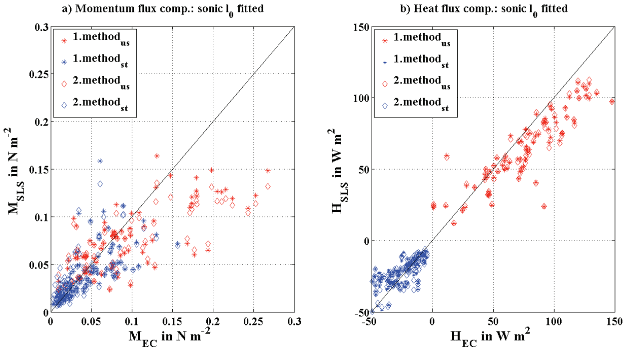

Figure 5. Same as Fig. 3 but with re-processed SLS data after correcting the l_0 –values based on sonic measurements using the 2 methods described in the text.

ACKNOWLEDGMENTS

This work was supported through the NSF Career award ILREUM (NSF ATM 0547882).

REFERENCES

1. Hartogensis, O. K., 2006: Exploring Scintillometry in the Stable Atmospheric Surface Layer. *Dissertation. Wageningen University*, 228 pp.
2. SCINTEC AG, 2006: Scintec Surface Layer Scintillometer, User Manual, 100 pp.
3. Hill, R.J. and Ochs G.R., 1978: Fine Calibration of Large-Aperture Optical Scintillometers and an Optical Estimate of the Inner Scale of Turbulence. *Appl. Optics,* **17**, 3608-3612.
4. Thiermann, V. and H. Grassl, 1992: The measurement of turbulent surface-layer fluxes by use of bichromatic scintillation. *Boundary-Layer Meteorology*, **28**, 367-389.

Session 4 – Oral Presentations

RETRIEVAL OF THE TURBULENT AND BACKSCATTERING PROPERTIES USING A NON-LINEAR FILTERING TECHNIQUE APPLIED TO DOPPLER LIDAR OBSERVATION

Christophe Baehr[1], **Claire Beigbeder**[2], **Fleur Couvreux**[2], **Alain Dabas**[2], **Bruno Piguet**[2]

[1]*Météo-France / CNRS and Institut de Mathématiques de Toulouse - Université de Toulouse III, Address : Météo-France CNRM-GAME URA1357 42 Avenue de Coriolis 31057 Toulouse France , E-mail: christophe.baehr@meteo.fr*
[2]*Météo-France / CNRS, Address : Météo-France CNRM-GAME URA1357 42 Avenue de Coriolis 31057 Toulouse France*

ABSTRACT

We present a new algorithm for the provision of real time estimations of turbulent parameters (TKE and EDR) as we filter the perturbed data of a Doppler lidar. The algorithm uses stochastic models for the atmospheric turbulence and for the remote sensor observation. The results show that we are able to catch fine and fast structures in the Boundary Layer. Here we applied our method to the experimental data of the BLLAST experiment which used a vertical lidar. We finish by comparing the structure of the estimated TKE profiles to the TKE profiles of a Meso-NH simulation.

1. INTRODUCTION

There is presently no proven ground-based instrumental technique able to measure automatically vertical profiles of turbulence properties (Turbulent Kinetic Energy, TKE or Eddy Dissipation Rate, EDR) in the boundary layer. The best approach consists in using aircraft or tethered balloons. The use of remote sensors has been considered for quite some time. Some works have also been done with Doppler lidars that confirms the great potential of this type of instrument for the observation of small-scale, fast evolving, atmospheric flows. They suggest that the Doppler lidar is a possible and interesting remote sensing technique for the characterization of turbulence ([1; 2]).

We have been working on the characterization of turbulent media (at the aerological scale) using non-linear filtering technique and stochastic modelling of the turbulence or/and the sensor measurements. These techniques are based on the particle approximation of the probability laws conditioned by the actual observation. These laws make it possible to denoise the observations and retrieve turbulence parameters. We will present the application of these works to Doppler lidars. This highlights the real possibility to retrieve wind, TKE or EDR in the Boundary Layer probed by this instrument.

We show the ability of our method to learn the vertical profiles of turbulence parameters from real data. We take examples during the experiment BLLAST held in June-July 2011 and we compare our results with slow estimations of EDR or TKE using tethered balloon. We also show how to compare our estimated profiles to numerical simulations using the Meso-NH model.

2. LEARNING THE RANDOM MEDIA PARAMETERS USING NON-LINEAR FILTERING

Before presenting the technological application, we outline the theoretical background with the acquisition process of a random field along a random path. A more precise presentation may be found in [3]

Here we consider a configuration space $E \subset \mathbb{R}^d$, $d \in \mathbb{N}^*$, a metric locally compact space and a phase space $E' \subset \mathbb{R}^{d'}$, $d' \in \mathbb{N}^*$, a vector space, both endowed with some $\sigma-$algebra, $\mathcal{E}$ and $\mathcal{E}'$. Then for any time $t \in [0, T]$ where $T < \infty$ we consider X_t a $(E, \mathcal{E})$-valued random variable called the acquisition path and for any point $x \in E$ we consider $X'_{t,x}$ a $(E', \mathcal{E}')$-valued random variable family (random vector field). Then we define the pair of applications $(X_t, X'_{t,x})$ as the Acquisition System of the random vector field and we define for any measurable function F the Acquisition Process by $A_t \overset{def}{=} F(X'_{t,X_t})$. As an easy example, the Lagrangian modelling could be seen as the Acquisition Process of an Eulerian field along the particle trajectories.

For a locally homogeneous medium, given a familly of balls $B_t^\varepsilon(x)$ along the random path X_t, we may compute the expectation $\mathbb{E}(f(X_t, A_t) \mid X_t \in B_t^\varepsilon)$. One may show [3] that there is a Feynman-Kac [4] structure to this conditional expectation. By this way, we can propose some algorithm to estimate the probability laws of this mean-field process with stochastic particle approximations. This is a two-step scheme. The first one is the Markovian prediction of the medium evolution. The second step is a Markovian state selection using a potential function given by the Acquisition Path. The selection kernel is composed of an acceptance/rejection part and a resampling for the rejected states. This update meets the conditioning of the medium to the Acquisition trajectory.

Using this background the filtering problem is then an overlay, the Markovian dynamics being driven by the Acquisition Process estimation (see [3]). The non-linear filtering consists in the computation of the probability laws of an hidden Markov process $\mathcal{X}_t$ conditionally to the observations $\mathcal{Y}_{[0,t]}$. Then the filtering learning retrieves the Markov components, including the non-observed ones. In this manner we realize the learning of the random medium as well as the filtering of the dynamical state.

What kind of prediction model should we use for the acquisition process estimation? If we have local observations of a random medium, it may be interesting to use a local model, such as Stochastic Lagrangian Model (SLM). The numerical domain is covered with a collection of local models. These models have local or global interactions. This is often the case when we have sparse observations. It is more powerfull to have adjusted local models instead of a global one with a mean adjustement. We use this type of dynamics in the case of lidar observations.

3. STOCHASTIC FILTERING FOR VERTICAL LIDAR OBSERVATIONS

The theoretical background being settled, the adaptation of the general problem to the lidar observation concerns mainly the management of a 1D medium observed by point measurements. In this study the lidar beam is vertical, therefore we use bounded column model splitted in several segments centered on the lidar measurement points. Therefore we have regular intervals driven by the observation with a minimum level and a maximum level. We use a stochastic particle approximation to feed a Stochastic Lagrangian Model, a conditionning to the finite size column and a filtering with respect to the observations. The SLM for the vertical velocity is derived from the SLM that we have developed for our pointwise filtering [3]:

$$\begin{aligned} X^i_{n+1} &= X^i_n + W^i_n \Delta t + \sigma^X \Delta B^{X,i}_n \\ W^i_{n+1} &= W^i_n + A_n - C_1 \frac{\varepsilon_n}{k^i_n}[W^i_n - < w >]\Delta t \\ &\qquad + C_2 \frac{\theta^i_n - < \theta >}{< \theta >}\Delta t + \sqrt{C_0 \varepsilon_n}\Delta B^{W,i}_n \end{aligned}$$

where (X^i_n, W^i_n) is the location and the vertical velocity of any particle $i \in [1, N]$, θ^i_n is its associated absolute temperature and $(\Delta B^{X,i}_n, \Delta B^{W,i}_n)$ its Brownian perturbation. The Eulerian average $< w >$ (resp. $< \theta >$) is the expectation $\mathbb{E}(W_n | X_n = x)$ (resp. $\mathbb{E}(\theta_n | X_n = x)$) approximated with the particle using a Gaussian interaction kernel. This local mean is also used for k^i_n is the local Turbulent Kinetic Energy. Δt is the time mesh and C_0, C_1 and C_2 are fixed constants. For the filtering step, for each segment the observations select the stochastic particles keeping alive the most adapted. For this selection phase, we have chosen to adopt a genetic kernel in order to minimize the variance errors [4]. At each step and for each segment, A_n and ε_n are learned as the mean and the quadratic mean of the velocity time increments. In this model ε_n is the Eddy Dissipation Rate. In order to not have to model the temperature θ_n, we drown out the whole term $\dfrac{\theta_n - < \theta >}{< \theta >}$ in a random variable and we have chosen a truncated normal distribution with a support $[-1, 1]$ and a standard deviation about 0.01.

In our method we use a stack of SLM and the stochastic particles are free to leave their segment. This may have (at least) two consequences. We have to deal with overloaded or underloaded segments. This is particularly true at the limits of the domain. The outgoing particles are randomized into the domain using an importance rule favouring the less loaded segments. The management of the particle number in the different segments is performed using min and max bounds around a mean profile determined at the beginning of the experiment using the atmospheric density. This profile is computed with a rough estimation of the temperature gradient. It is only used for the determination of the bound numbers for each segment. Using the max bounds if a segment overshoots the particle number, we withdraw particles and randomize them in other segments according to the importance rule. Using the same idea, if a segment is starved of particles, we withdraw some particle to the most filled segments using the importance rule. These different rules linked to the particle numbers ensure we have enough particles for the conditional expectation estimations. But whatever the precautions, the accuracy of the first and last level are affected by the algorithmic choices and suffer of the lack of physical sense. We will give some clues in the conclusion in order to improve this situation.

4. APPLICATION TO THE BLLAST EXPERIMENT LIDAR DATA

We present some results using the vertical lidar data recorded between 12h41 and 14h05 UTC the June 18th, 2011 at Lannemezan, France during the BLLAST experiment (`http://bllast.sedoo.fr/`). We have vertical profiles every 6 seconds with 10 stacked lidar observations (from 100m to 500m with 50m steps). They are used as a reference signal or truth for the mean vertical velocity. We add a numerical noise to get perturbed observations. Then the challenge to our filter consists in denoising the perturbed signal to retrieve the turbulent parameter and a realization of the original medium. Therefore we can compare the results with the signal considered as a reference. Obviously the main advantage of the method, besides the denoising, lies in the on-line estimation of the turbulence parameters with our SLM. For each time step, i-e every 6s, we have an estimation of Eulerian quantities like TKE or EDR.

First we examine time series (figure 1) of the vertical wind with the three kind of values (reference, perturbed and filtered) at the altitude of 250m. One can see that the general shape is well estimated, steep variations are also retrieved. The original signal and the filtered one are two realizations of the same random medium if the turbulent parameters are correctly assessed by the filter. This is the reason why they do not superimpose exactly. To extend the analyzes we can examine the Power Spectral

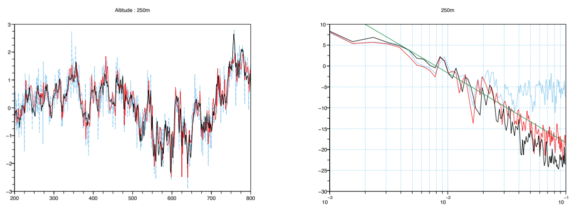

Figure 1: Detail of the vertical wind reference series at 250m (black), observations (cyan), filtered signal (red), with their PSD, sample number as x-axis. Data recorded the June 18th, 2011 every 6s between 12h41 and 14h05 UTC at Lannemezan, France.

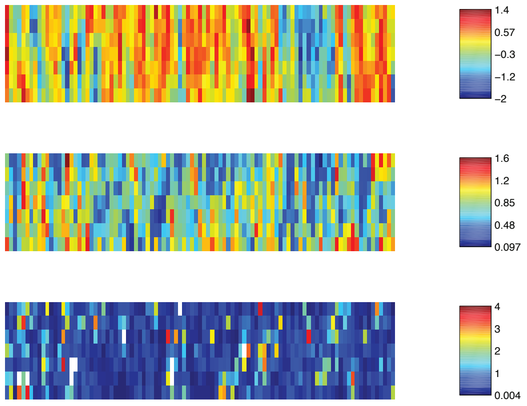

Figure 2: Time profiles averaged on 60s (10 time step) of filtered wind (above), estimated TKE (middle) and EDR (bottom). Data recorded the June 18th, 2011 between 12h41 and 14h05 UTC in Lannemezan, France.

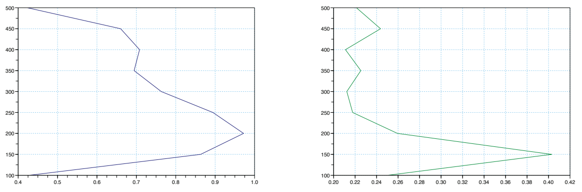

Figure 3: Mean profiles of wind variance (left) and TKE (right). Data recorded the June 19th, 2011 every 6s between 13h26 and 14h49 UTC at Lannemezan, France.

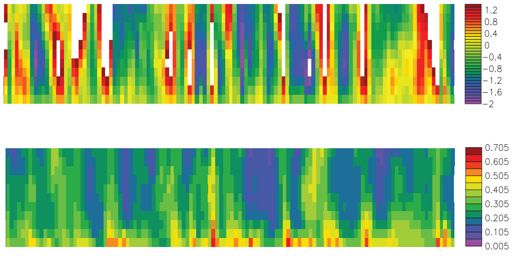

Figure 4: Time profiles produce by a Meso-NH simulation (time step 60s) of vertical wind (above), TKE (bottom).

Density (PSD) to have a look on the energy properties. The figure 1 presents the three PSD with the same colorcode. Clearly the spectrum of the filtered signal is better than the reference spectrum. The noise has been really switched off and we see that the lidar spectrum is perturbed by the spatial average of the instruments.

We may present (figure 2) the results as vertical profiles with a 1 minute (10 time steps) average, for the filtered velocities (upper part), the TKE (middle part) and the EDR (lower part). For the wind profiles, positive values are in red, negative are in blue. It is difficult to have an opinion on the behavior of the TKE or EDR with respect to the wind structures. We can notice that the TKE is more important at the transition between upward and downward stream.

5. COMPARISONS WITH CLASSICAL METHODS OR MESO-NH MODEL OUTPUTS

5.1. Balloon-borne in-situ measurements

For a first comparison we consider data taken from an aerodynamic ballon at Lannemezan on 19 June 2010 between 13h26 and 14h49 UTC in the vicinity of the lidar location. The sonic anemometer shipped by the balloon provides 10 Hz relative wind measurements. The ground speed estimated using the INS/GPS information is substracted from the relative wind to obtain an absolute wind. The ballon flew at 60m during the period. Then using the lidar observation, we compute the filtered wind and the TKE, the first level at 100m is representative of the 75-125m segment, and we compare.

The aerodynamical balloon measurements of the wind is at 0.1s. We subsample the wind at 6s and we compute a variance about 0.39 m^2s^{-2}. We can compute directly the variance of the filtered lidar signal at 100m and we obtain 0.42 m^2s^{-2}. The two values are very close. For the same period, the average TKE is assessed at 0.25 m^2s^{-2}. It is possible to produce a mean profile of wind variance with respect to the height and a mean profile of TKE. The figure 3 shows these profiles which are typical of a convective boundary layer.

5.2. Meso-NH profiles outputs

We have some difficulties to analyze the figure 2 because it is too early to assess the structures of the TKE or EDR in the boundary layer at this rate. In order to evaluate the realism of the TKE or EDR structures seen by lidar, we compared lidar profiles to a Meso-NH simulation. The code is not ready yet for the BLLAST experiment, therefore we use a numerical experiment of a well-know and published case [7].

The simulation is a Large-Eddy Simulation realised with Meso-NH over a domain of $10 \times 10 \times 5km^3$

with a horizontal resolution of 100m. This simulation represents a clear boundary layer observed over the Southern Great Plains during one day (June 14th, 2002) of the IHOP field campaign. It starts at 07h00 LT from an observed radiosounding profile and uses prescribed surface fluxes. It has been evaluated with observations up to 14h00 LT (see [7]). This simulation is run for 14 hours. Profiles have been extracted every 60s from this simulation and are compared to the observations.

In this comparison, we only examine the general shape of TKE and the order of the value both for the simulation and the 18th of June estimation. On the vertical wind, we have both for the filtered profiles and for the simulation, downward structures. It is consistent with advected ascending columns or descending areas seen by a vertical profile and the upper part of the advected structure is first observed. The simulation and the filtered signal have the same range of values. About the TKE, the structures are different with greater values in the bottom. While the simulation of the TKE is smoother, the filtered TKE reacts faster and gives profiles with more dynamical small scales. But is the reality smooth or coarse ? we have no answer at the moment. However we can remark that the structures are the same for the simulation and the filtering, with higher values of TKE at the transitions between upward and downward winds, with the same range of values.

6. OUTCOMES AND FURTHER DEVELOPMENTS

We have presented a new algorithm to estimate the turbulent parameters using lidar measurements. This algorithm is based on non-linear filtering, on a stochastic modeling of the medium and on a stochastic modeling of the sensor behavior. Applying our method to real data demonstrated the capability of the algorithm to estimate not only the vertical wind but also turbulent parameters such as the TKE or the EDR. The comparisons with pointwise balloon measurements and with a Meso-NH simulation are qualitatively and quantitatively good.

We have to improve the processing of the first level to avoid the algorithmic perturbations. A nice idea may be to use a ground anemometric measurement (for instance with sonic anemometer) with a particle approximation of the turbulent parameters. Therefore this ground system would be considered representative of the 0-75m layer and used to feed the first layer (75-125m) of the lidar particle system. It would be better than the current and purely algorithmic solution.

We intend to complete the measurement system with an X-band radiometer to provide some temperature vertical profiles. This slow observation would be helpful in order to include in the system an equation on temperature that will guide the vertical motions.

We have develop some mock-up for 3D estimations using lidars scanning the atmosphere within an hemisphere ([8]). In this work, the vertical interactions have not been taken into account. With the present studie about vertical lidar, we have developed the algorithmic solutions to finish the job and have full 3D estimations of wind, TKE and EDR.

At the same time we have to continue the work of comparison with other BLLAST cases and we are waiting for the Meso-NH simulations for the same experimental cases. It will end the qualification of our methodology.

ACKNOWLEDGMENTS

The authors thanks Dr. F. Gibert (LMD-IPSL/CNRS) and Y. Bezombes (LA-OMP/CNRS) for the lidar operations and data supply, LEOSPHERE company (in particular L. Thobois) for gratuitously putting the lidar at our disposal during BLLAST experiment, our colleagues of the ‘Moyens Mobiles de Mesures Météorologiques’ team for the deployment and operations of the tethered ballon and Dr. M. Lothon (LA-OMP/CNRS) for organizing BLLAST field campaign.

REFERENCES

1. Lothon M., Lenschow D. and Mayor S. 2009 : Doppler Lidar Measurements of Vertical Velocity Spectra in the Convective Planetary Boundary Layer. *Boundary-Layer Meteorology*, **132**, 205-226.
2. O’Connor E., Illingworth A., Brooks I., Westbrook C., Hogan R., Davies F. and Brooks B. 2010 : A method for estimating the turbulent kinetic energy dissipation rate from a vertically pointing doppler lidar, and independent evaluation from balloon-borne in situ measurements. *J. Atmos. Oceanic Technol.*, **27**, 16521664, doi: 10.1175/2010JTECHA1455.1.
3. Baehr, C. 2010 : Nonlinear Filtering for observations on a random vector field along a random path. *M2AN - ESAIM*, **44 (5)**, pp. 921-945, DOI No: 10.1051/m2an/2010047 .
4. Del Moral, P. *Feynman-Kac Formulae, Genealogical and Interacting Particle Systems with Applications*. Springer-Verlag, Berlin, 2004.
5. Pope, S.B. *Turbulent Flows*. Cambridge University Press, 2000).
6. Das S. and Durbin P. 2005 : A Lagrangian stochastic model for dispersion in stratified turbulence. *Phys. of Fluids*, **17**, 025109.
7. Couvreux F., Guichard F., Redelsperger J., Kiemle C., Masson V., Lafore J. and Flamant C. 2005 : Water-vapour variability within a convective boundary-layer assessed by large-eddy simulations and IHOP_2002 observations *Q. J. R. Meteorol. Soc.*, **131**, 2665-2693, DOI: 10.1256/qj.04.167.
8. Suzat F., Baehr C. and Dabas A. 2011 : A fast atmospheric turbulent parameters estimation using particle filtering. Application to lidar observations *J. Phys. Conf. Ser.*, **318-7**, doi:10.1088/1742-6596/318/7/072019

MONITORING WAKE VORTICES WITH A SCANNING DOPPLER LIDAR

Sophie Loaec[1], Ludovic Thobois[1], Jean-Pierre Cariou[1], Agnès Dolfi-Bouteyre[2], Didier Goular[2]
[1]*LEOSPHERE, 76 Rue Monceau, 75008 Paris, sloaec@leosphere.fr*
[2]*ONERA, DOTA/SLS, Palaiseau, agnes.dolfi-bouteyre@onera.fr*

ABSTRACT

Measuring and foreseeing wind conditions near airports are crucial issues for air traffic safety. Since aircraft manoeuvrability is the worst during takeoff and landing phases, strong air movements near airports such as wake vortices can have dramatic consequences on aircrafts. Wake vortices are created by all the aircrafts. Size and intensity of wake vortices are directly linked to the flight speed and also by plane characteristics, such as weight and wingspan. Even if strong efforts have been done to study and model wake vortices, on-site measurements remain the best way to detect them as they depend a lot on meteorological conditions near airports especially wind and turbulence.

Coherent laser radars or LIDARs can be very useful devices for measuring wake vortices on airports. A WINDCUBE 200S developed by LEOSPHERE has been deployed at Charles De Gaulle airport near Paris in the framework of the European project SESAR and the subpackage 12.2.2 dedicated to wake vortices detection in cooperation with THALES AIR SYSTEMS. With specific swept scenarios, the WINDCUBE 200S has been able to detect the wake vortices of heavy, medium and small aircrafts during takeoff and landing. Wake vortices have been monitored for a significant period. A dedicated post-treatment has been developed by the French Aerospace Lab ONERA for computing the cores position of wake vortices and for calculating theirs circulations. Thanks to that post-treatment the evolution of wake vortices trajectories and circulations can be determined. Several analyses have been achieved in order to determine the influence of the wind conditions on the trajectories of wake vortices. A variety of trajectories have been put in front.

1. INTRODUCTION

In the framework of the sub-package 12.2.2 of the SESAR European project (Single European Sky ATM Research) advanced researches are realized in order to determine the best sensors (or best set of sensors) to monitor in real time the wake vortices that are generated by aircrafts. Coordinated by THALES AIR SYSTEM, the aim of this subpackage is to be able to propose a solution based on remote sensors that can accurately provide the location and the intensity (circulation) of the wake vortices. Thanks to such a solution, the air traffic control can be improved in order to optimize the separation between two aircrafts while ensuring the air traffic safety. Today, the separation between two aircrafts is driven by the so called distance separation rule.

For this purpose, a scanning Doppler lidar WINDCUBE 200S developed by LEOSPHERE has been deployed at Charles de Gaulle airport in May 2011 for a first trial.

In this paper, the WINDCUBE 200S lidar is briefly described, as well as the campaign configuration. Then some wake vortices detection realized at different location are presented. Finally, wake vortices trajectories and circulation are computed and analysed.

2. INSTRUMENTAL SETUP

Developed in cooperation with the French Aerospace Lab (ONERA), the LEOSPHERE wind doppler technology is the results of 20 years of research and development in the domain of fiber lasers and lidar. A research Doppler lidar developed by ONERA has already been deployed at Frankfort airport during the CREDOS UE project. [1][4].

The WINDCUBE 200S is the industrialized lidar product that has been transferred from ONERA to LEOSPHERE [3]. This lidar has been first developed for airport applications like wind shears and wake vortices detection.

In the table below, there are the performances of the Windcube200S.

SPECIFICATIONS	PERFORMANCES
LIDAR	WINDCUBE 200S
Wavelength	1.54µm
Mini-Max range (aerosols detection)	100m to 6.5km
Avering time	1’’ to 2’’
Range resolution (range gate width)	50m to 200m
Number of programme gates	58
Radial Wind Speed accuracy	0.2m/s

Table 1 : Performances of the Windcube200S

For monitoring wake vortices with such a system, a dedicated software has been developed as well as a setting for the lidar in order to adapt the spatial resolution and the scanning speed. Wake vortices generated by every aircraft look like two counter-rotating vortices whose intensity and size depend on weight, wingspan and speed of the aircraft. They are induced by the air flow around the wing , due to the aircraft motion.

The schematic structure of wake vortices is a solid-body in rotation around a center called a core. The speed of a wake vortex can reach more than 20 m/s and the typical size of the cores is roughly of 5 m. Monitored by the WINDCUBE 200S, a wake vortex consists of two semicircles of positive and negative velocities. For instance on the Figure 1, the line of sight A will see a negative velocity since the flow is going away from the lidar. The line of sight B will see a positive velocity since the flow goes to the lidar.

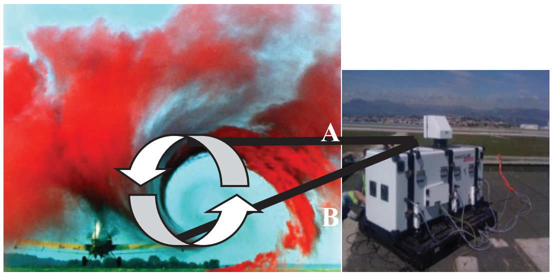

Figure 1: Scheme of a wake vortex detection by the WINDCUBE 200S

The Figure 2 represents an example of the signal measured by the WINDCUBE 200S, i.e. a map of radial velocity containing all the lines of sight. For this example, the aircraft is a B767 taking off.

This radial velocity contains both the wind velocity and the wake vortices velocity . When no airplane is present, the lidar measures directly the wind. In the example below, the wind field is almost homogeneous. Close to the runway, the lidar measures the velocity of the wake vortices with their particular structure.

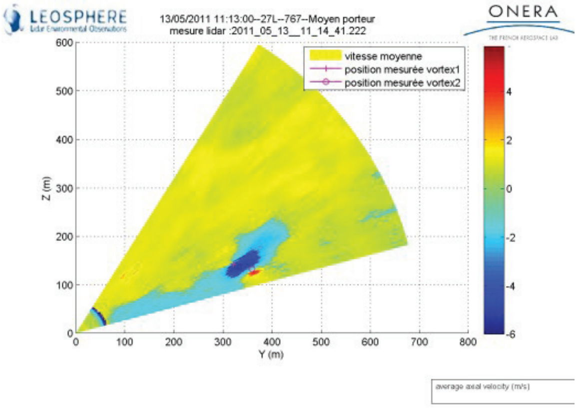

Figure 2: Radial velocity field obtained after processing

Note: A cross (x) is representing the left vortex core and the round (o) the right one measured by the Lidar.

Finally, the wake vortices are detected automatically on the velocity fields. An advanced algorithm has been developed by ONERA in order to implement this automatic process and to determine the cores positions and the circulation of the vortices. The positions and circulation computation is based on Smaliko algorithm [2]

3. MEASUREMENT PROTOCOL DURING THE SESAR CAMPAIGN

The WINDCUBE200S deployed for SESAR's campaign has been placed near the runways at Charles de Gaulle airport and below the glide at Villeneuve-sous Dammartin.

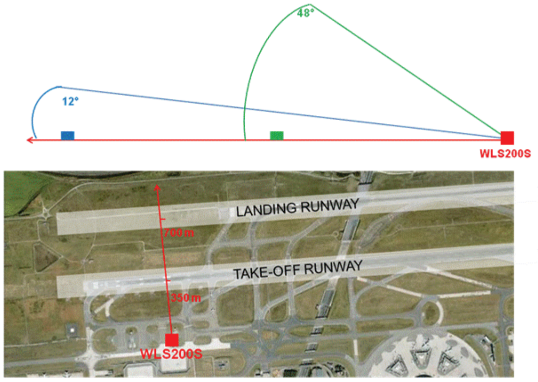

Figure 3 : Measurement protocol near runway at CDG

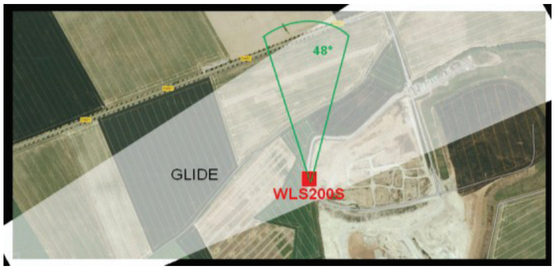

Figure 4 : Measurement protocol under the glide at Villeneuve

For all the scenarios, the scanning duration was 4 seconds to go down, this is the measuring phase and 3 seconds to go up and process the signals.

The scanning area was 48° for take-off in CDG, 12° for landing in CDG and 48° under the glide. The size of the scanning was limited by the software and computing capacities in order to keep the real time measurements: the scenarios have been adapted to the area of Wake Vortex potential location in the different configurations.

4. RESULTS AND DISCUSSION

Some examples of Wake Vortices detections for each scenario with different aircrafts are presented hereafter.

4.1.1 Take-Off at CDG

The wake vortices of small, medium and heavy aircrafts have been detected and monitored during about one minute when the lidar was installed near the runways. One can notice the turbulent background velocity field behind the wake vortices.

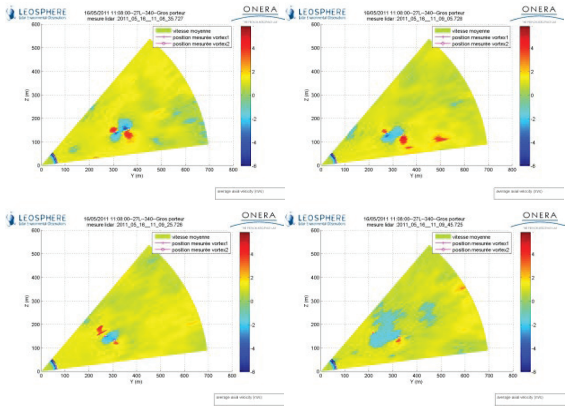

Figure 5 – Detection of Wake Vortex the 16/05/11 for a A340

In this example, the two vortices of the aircraft are clearly detected by the lidar. The wake vortices are followed up to 1'30" when their structures are no more relevant to the presumed wake model. These wake vortices are dissipated by the atmospheric turbulence.

4.1.2 Landing at CDG

Positioned 700 m away from the runway, the WINDCUBE 200S has been able to detect wake vortices of landing aircrafts with cross winds. Here, the ground effect is predominant but its influence can also vary with the wind conditions. When there is cross wind, one of the wake vortices is rapidly destroyed whereas the second one rebounds and is transported by the wind.

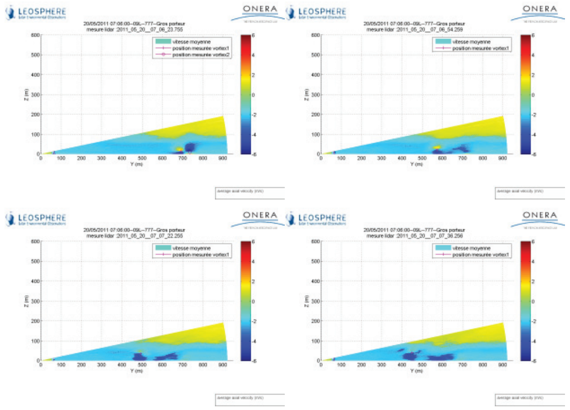

Figure 6 – Detection of Wake Vortex the 20/05/11 for a B777

In this example, the left wake vortex is destroyed after 1’30’’ but the right one is destroyed in less than 20’’.

4.1.3 Take-Off at Villeneuve

The WINDCUBE 200S has also been installed below the glide of Charles de Gaulle airport. This configuration is much more favourable to detect the pair of wake vortices and to follow the vortices during a long period.

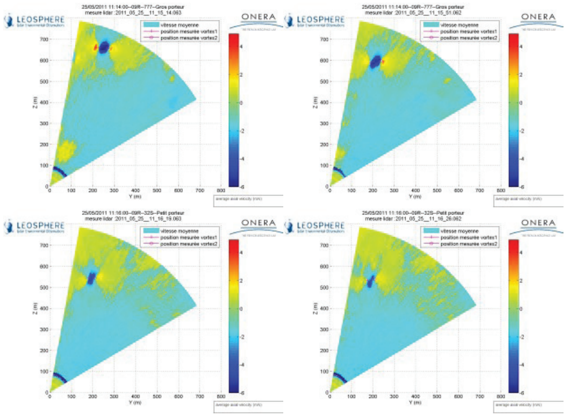

Figure 7 – Detection of Wake Vortex the 25/05/11 for a B777

In this example, the wake vortex is destroyed after 1’30’’. We can see that the wind was low because the wake vortex goes down straightly.

4.1.4 Landing at Villeneuve

Detection of landing aircrafts in the glide, is the easiest configuration because the aircraft crosses the detection plane always at the same location.

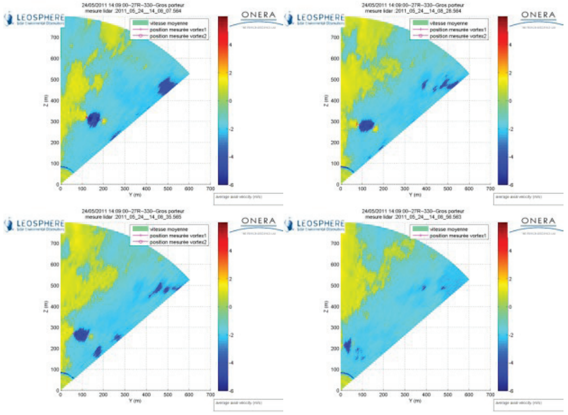

Figure 8 – Detection of Wake Vortex the 24/05/11 for A330

In this example, the wake vortex is destroyed after 1’ and it stayed almost at the same altitude.

4.1.5 Circulation and cores position computations

The circulations of the pair of wake vortices for several aircrafts for landing and take-off configuration have been plotted. The circulations of the different classes of aircrafts seem to be very close. The dissipation of the wake vortices varies a lot from day to day, so with weather conditions (wind in particular) and it is not monotonous as expected. This can be explained by the wind conditions. The analysis of the complete data base will help to understand the wake vortices dynamics and its dependence to weather conditions especially for on ground conditions for which very recently developed models have to be validated [5].

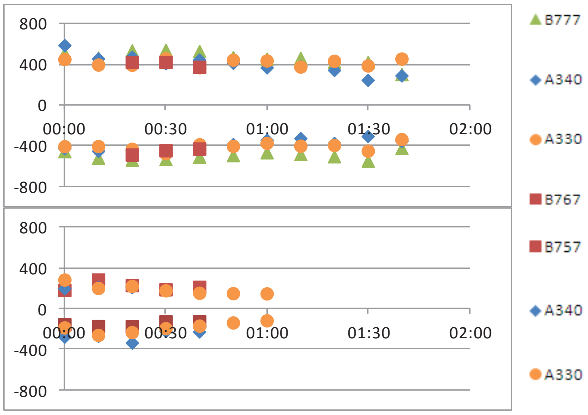

Figure 9 – Circulation Values for Villeneuve Take Off (at the top) and Landing (at the bottom)

An analysis has also been performed on the positions of the vortex cores and their trajectories in the scanning plane of the lidar. The trajectories of the wake vortex cores are updated every 7 seconds.

Figure 10 presents the wake vortices trajectories for three different landing aircrafts, at Villeneuve, measured on the same day. The cores trajectories are similar, oriented towards the lidar and fallen down. The wind was oriented the 24th of May from the North. For the A340 measurement the wind had increased during the first three scans dragging the vortex toward the lidar more rapidly than for the other measurements

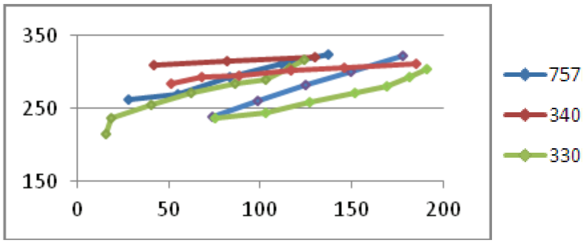

Figure 10 – Trajectories in an Y-Z plane of the vortex cores for three planes during landing at Villeveuve the 24/05/11. NB: (scale is in meters). The lidar position is Y=0 Z=0

5. CONCLUSION AND PERSPECTIVES

During this campaign, we've demonstrated the capacity of a WINDCUBE 200S scanning lidar to detect Wake Vortices. From the lightest to the heaviest aircrafts, for landing or takeoff, the two wake vortices generated by aircrafts have been detected by the algorithm and monitored for 1' to 1'30 by the Lidar with an accuracy on velocity about 1 m/s.

In the future, many improvements are planned so as to adapt the scanning angles to flight configuration (take-off or landing) and to the type of aircrafts. Another point is to improve the algorithm in order to increase the monitoring duration of wake vortices, and to provide reliable and real time information in terms on wake vortex position and circulation. Finally, further analyses will be very interesting in order to understand the influence of the wind direction and speed and eddy dissipation rate on wake vortices trajectories, since the measurement database that has been created during the XP0 campaign of SESAR is huge.

ACKNOWLEDGMENTS

The authors would like to thank Thalès Air system and the SESAR project for their support and involvement in these advanced research activities.

REFERENCES

1. Dolfi-Bouteyre A. & al, 2007: CLRC 14th conference, "1.5 µm all fiber pulsed lidar for wake vortex monitoring".

2. Koëpp F, S. Rahm, I., 2007: Journal of aircraft, **vol. 44, no3,** pp. 799-805, "Characterization of aircraft wake vortices by airborne coherent Doppler lidar".

3. Cariou J.P. & al., 2011: CLRC 16th conference, "Long range scanning pulsed Coherent Lidar for real time wind monitoring in the Planetary Boundary Layer".

4. A. Dolfi-Bouteyre & al, 2009: Aerospace Lab, Issue **1**, December, "Aircraft Wake Vortex Study and Characterization with 1.5 µm Fiber Doppler Lidar".

5. Holzaepfel F, 2012: 4th wakenet3 workshop, http://wakenet.eu/index.php?id=185. "Wake Vortex Decay in Ground Proximity - Physical Mechanisms and Artificial Enhancement",

MONITORING OF THE BOUNDARY LAYER WITH A POLARIMETRIC WSR-88D RADAR

Valery M. Melnikov[1], **Richard J. Doviak**[2], **Dusan S. Zrnic**[2], **and David J. Stensrud**[2]

[1]*Cooperative Institute for Mesoscale Meteorological Studies, University of Oklahoma, 120 David Boren Blvd., Norman, OK, USA, valery.melnikov@noaa.gov.*
[2]*NOAA/OAR, National Severe Storms Laboratory,120 David Boren Blvd., Norman, OK, USA*
dick.doviak@noaa.gov, dusan.zrnic@noaa.gov, david.stensrud@noaa.gov.

ABSTRACT

Enhancements to signal processing and data collection in the dual-polarization WSR-88D to increase its sensitivity to observe echoes from clear air are described. Applications of the covariance estimators, angular and range oversampling, coherent summation, and noise despeckling allow measurements of weak echoes from Bragg scatterers with equivalent reflectivity factors as low as -25 dBZ at distance of 10 km. This level of sensitivity allows revealing a fine structure of refractivity fields in the boundary layer and corresponds to a refractive index structure parameter $Cn^2$of about $8x10^{-15}$ $m^{-2/3}$, a typical magnitude found in maritime air. The features of signal processing to get fine radar sensitivity are described. Further increase of sensitivity to a level of -35 dBZ at 10 km is discussed.

To distinguish between Bragg scatter in clear air and echoes from atmospheric biota, the polarimetric spectral processing has been used. The polarimetric spectral analysis provides information on convective boundary layer depth. This allows monitoring of convection in the boundary layer. Different types of refractivity fields in the boundary layer are demonstrated and discussed. The WSR-88D's data from clear air are compared with data obtained from the wind profilers and rawinsondes.

1. INTRODUCTION

Bragg backscatter from refractive index perturbations $\Delta N(\boldsymbol{r}, t)$, at scales half the centimetric and metric wavelengths of atmospheric radars, return sufficient energy to be useful in measuring wind and the refractive index structure parameter Cn^2 (e.g., [1-3]). Cn^2 is strongly dependent on turbulent mixing in gradients of mean potential refractive index ([3, 4]; these gradients are typically strongest at boundaries of water vapor layers. For example, large values of Cn^2 typically occur at the top of the CBL (e.g., [5, 6]) where there is strong mixing of moist and dry air.

In absence of echoes from atmospheric biota, radar wind profilers measure height profiles of Cn^2above their sites but they do not map the horizontal structure of this parameter. If there are many biotic scatterers within the resolution volume, profilers cannot distinguish Cn^2 from reflectivity due to biota. Migrating birds and insects cause problems with interpretation of radar wind profiler [7] and WSR-88D wind measurements [8-10]. However, the scanning polarimetric WSR-88D has the capability to distinguish echoes from atmospheric biota and Bragg scatterers and thus the potential to provide information on the temporal and spatial structure of Cn^2. Thus one of the main goals of our study is to determine the polarimetric properties of Bragg scatter associated with refractive index perturbations.

2. RADAR DATA COLLECTION AND SIGNAL PROCESSING

To make quantitative measurements of Cn^2, the dimensions of the radar resolution volume must be smaller than the outer scale of inertial subrange turbulence, which is in interval 10-200 m so that the short-pulse resolution of 82 m has been chosen to collect data. Data presented herein have been collected with the S band dual polarization WSR-88D KOUN located in Norman, OK.

To enhance detectability of weak echoes and to reduce parameter estimate variance at weak signal, the following data collection and signal processing procedures were implemented on KOUN: 1) Increased the dwell time (i.e., 0.1s, yielding 128 samples at the pulse repetition frequency of 1280 Hz), 2) Collected data at smaller elevation increments (i.e., 0.25^o), 3) Doubled the range sampling rate, 4) Implemented a two-dimensional noise speckle remover to reduce the occurrence of false echoes 5) Used covariance products to estimate differential reflectivity Z_{DR} and the correlation coefficient ρ_{hv}, 6) Collected data in vertical scans to elevations higher than 20^o to better resolve and interpret the fine details of reflectivity layers at close range, 7) Implemented ground clutter filtering at all elevation angles, and, 8) Coherently summed signals from the horizontal and vertical channels [11].

By combining expressions for Z and reflectivity η of Bragg, $\log_{10} [Cn^2 (m^{-2/3})]$ can be expressed in terms of Z (dBZ) measured with WSR-88D radars as,

$$\log_{10} [Cn^2 (m^{-2/3})] = 0.1 Z(dBZ) - 11.6.$$

Minimal Cn^2_{10} at 10 km for KOUN is 3.5x10^{-15} $m^{-2/3}$ in the short-pulse mode of operations. This level is more than two orders of magnitude below the mean Cn^2 value of 5x10^{-13} $m^{-2/3}$ measured with radar and an airborne refractometer in maritime boundary layer air over Oklahoma [12]. Utilization of the long-pulse radar mode with the pulsewidth of 4.5 µs can give additional 9.5 dB in sensitivity so the minimal detectable reflectivity can be of -35 dBZ that correspond to Cn^2_{10} of 4x10^{-16} $m^{-2/3}$.

Removal of ground clutter. To detection weak scatter, we needed to implement a filter that strongly suppresses ground clutter. A notch filter centered on zero velocity and having a width of 4 m s^{-1} was applied. To avoid inadvertently filtering Bragg backscatter, data were collected in azimuth directions where airborne scatterers had radial velocities outside the notch. Although a 4 m s^{-1} wide notch should theoretically eliminate all ground clutter, spectral leakage, due to the large spectral sidelobes of the clutter signal samples, can cause clutter power to appear outside the notch as residues. For example, effects of such clutter residues can be seen in Figs. 1-3 within 4 km at elevation angles to 30^o, and in the regions below 1 km where large negative and positive Z_{DR} values are seen. Nevertheless residues of ground clutter do not cause noticeable problems with interpreting echoes from clear air as it is seen in the figures.

Distinguishing Bragg scatter from clutter due to biota. Using polarimetric radar, echoes from atmospheric biota can be distinguished from returns from turbulent air because biota echoes typically have large positive differential reflectivity, Z_{DR} (dB), in contrast to reflections from turbulent air where Z_{DR} = 0 dB. Bragg scatterers have Z_{DR} and ρ_{hv} properties similar to drizzle, these properties can then be used to distinguish Bragg and biota scatter.

In winter seasons, or for echo layer heights above the freezing level, it is assumed biota echoes are absent, and thus echoes are likely due to Bragg scatterers. For such layers, our observations show mean ρ_{hv} is larger than 0.98, and comparisons of vertical profiles of $Cn^2$from KOUN and those obtained from a 74.3 cm wavelength profiler from _N_OAA's _P_rofiler _N_etwork (NPN) show good agreement in altitudes of maximums of Cn^2 from the profiler and KOUN and reasonable agreement in the magnitude of Cn^2 when conditions of horizontally homogeneity apply (e.g., Figs 1 a and c). This comparison supports the premise that Bragg scatter is observed.

In warm seasons, the boundary layer in Oklahoma is filled with biota. Sometimes layers of clear air echoes are observed above the biota. Using data from wind profilers, echoes from these elevated layers can more reliably be associated with Bragg scatter. Our analysis suggests that to distinguish Bragg backscatter from biota clutter, data needed to be acquired from those regions of the clear atmosphere that satisfy the following conditions: 1) Profiler data reveal peaks in the height profile of Cn^2 corresponding to peaks seen in the vertical cross sections of Cn^2 measured with KOUN. 2) Skies are cloud-free. 3). Rawinsonde data show strong vertical gradients of water vapor/humidity. These conditions have been applied to select layers where echoes are assumed to be exclusively from Bragg scatterers. Under these conditions, the polarimetric properties of Bragg scatterers can be determined. Condition 1) is the strongest, and if satisfied should insure by itself echoes are exclusively from Bragg scatterers. In some cases Bragg scatterers are imbedded in layers of biota and we apply polarimetric spectral analysis to identify regions of Bragg scatter [11].

Profiler and rawinsonde data. Some data derived from KOUN observations have been accompanied with profiler data from the NPN site at Purcell, OK located 29 km SSW from KOUN. In the profiler graphs (e.g., Fig. 1c), the signal power P is that measured with the vertical beam. ZDR in the elevated layer in Fig. 1(a) is close to zero dB thus we conclude there is no contamination from biota. For the vertical cross section nearest the profile, both the profiler and radar show two layers of Cn^2 at nearly the same height and with the same order of magnitude. These data support the hypothesis that KOUN observes Bragg scatterers.

Polarimetric properties of Bragg scatterers. Medium differential reflectivities of Bragg scatterers, using enhanced data collection and processing procedures on KOUN, lie in the interval -0.08 to 0.06 dB . Thus it is concluded Bragg scatter at 10-cm wavelengths has Z_{DR} ≈ 0 dB; this is as expected based on theoretical grounds (section 4.1). The distributions of the measured Bragg scatter correlation coefficients ρ_{hv} have peaks between 0.998 and 1.0 with a median value of 0.995. Having ρ_{hv} so close to 1.000 confirms the good polarimetric quality of the WSR-88D's antenna for polarimetric measurements.

3. TYPES OF RADAR ECHOES

Three types of radar echoes from clear air are apparent from observations with KOUN radar. The first one is in a form of a layer (Fig. 1a). Closest in time rawinsonde profiles (Fig. 1b) exhibit a strong gradient of relative humidity and the wind speed at the height of strong radar echo. The height of maximal reflection obtained from the NPN profiler (Fig. 3c) is in an accord with the height of maximum reflection obtained from KOUN.

The second type of radar echo is shown in Fig. 2. It is in a form of strong convective plumes above 1 km. The temperature profile in Fig. 2(b) exhibits an inversion at height slightly above 4 km. There is a very strong layer of reflection just above the ground up to height of 1 km.

In the third type of echo shown in Fig. 3, one can see a weakly reflecting layer up to 2 km in which more strong layered reflections at height of 1.5 km are seen. This stronger layer coincides with the height of strong gradient of relative humidity (Fig. 3c) capped with a temperature inversion.

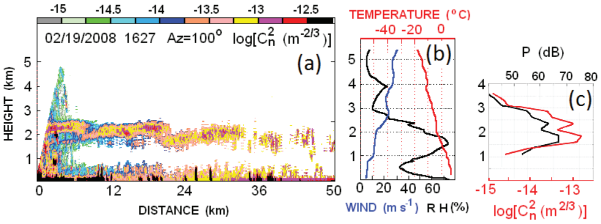

Fig. 1. Layered echo. (a): log(C_n^2) obtained from radar at 1627 Z. (b): Rawinsonde profiles of temperature, wind speed (W, m s^{-1}), and relative humidity (RH) in % at Norman, OK at 12Z 02/19/2008. (c): Profiles of the reflected power (P) from the wind profiler and derived log(C_n^2).

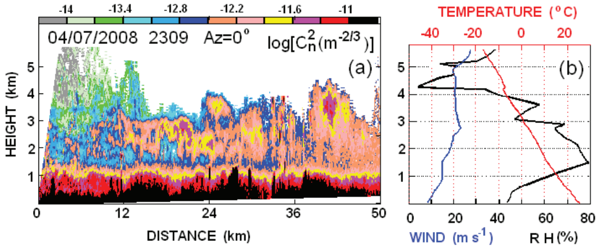

Fig. 2. Convective echo. Rawinsonde profiles were obtained at 0Z 04/08/2008 at Norman, OK.

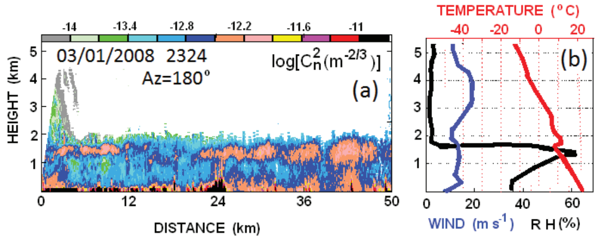

Fig. 3. Layered echo imbedded into a weak and steady reflections. Rawinsonde profiles were obtained at 0Z 03/02/2008 at Norman, OK.

4. DISCUSSION

Observations with a dual polarization WSR-88D (KOUN) show the capability to measure Cn^2 as low as $3.5x10^{-15}$ $m^{-2/3}$ at a range of 10 km; this is about two orders of magnitude below the mean $Cn^2$of $5x10^{-13}$ $m^{-2/3}$ measured with an airborne refractometer in maritime boundary layer air over Oklahoma [12]. Observations with KOUN show significant advantage of having a scanning capability to map the horizontal extent and structure of Cn^2. In cases where "clear air" returns to KOUN are thought not to have been contaminated with airborne biota clutter, a good correspondence was found between the properties of echo layers observed with KOUN and with longer wavelength wind profilers. Thus the NPN profiler and WSR-88D networks have the potential to provide, by working in a coordinated approach, more reliable meteorological data.

Maximal Cn^2measured with KOUN from January to April 2008 was $2.5x10^{-12}$ $m^{-2/3}$. This agrees markedly well with peak values of $3x10^{-12}$ $m^{-2/3}$ documented in [12] with a 10-cm wavelength radar for maritime air over Oklahoma.

Medium differential reflectivities of Bragg scatterers, are near 0 dB. The correlation coefficients ρ_{hv} have the median value of 0.995. These polarimetric properties can be used to distinguish Bragg scatter from atmospheric biota that has large differential reflectivity and ρ_{hv} less than 0.95. Layers of Bragg scatterers have also been observed within layers of biota. In some such cases slightly positive Z_{DR} (0.2 – 0.3 dB) and decreased ρ_{hv} (as low as 0.977 for the median value) are attributed to the presence of biota. In one case a layer of Bragg scatter was present at the top of the CBL, with biota both below and above. But, as shown [11], polarimetric spectral analysis has the potential to better distinguish the two types of scatterers, even when both are present within the radar's resolution volume.

Because Bragg scatter $Z_{DR} \approx 0$ dB and $\rho_{hv} \approx 1$, coherent summation of signals from the H and V receiver channels can add as much as 3 dB to the signal-to-noise ratio [11], thus enhancing radar capability to observe Bragg scatter. This could enlarge the area of radar measurement and/or reduce the standard deviations of Cn^2 and Doppler velocity estimates.

Results suggest that one potential meteorological application of Bragg scatter mapping is monitoring the temporal and spatial changes in the depth of the CBL. Detection of the CBL top is likely more reliable if the upper boundary of CBL is being mixed by strong turbulence as is so often the case when daytime surface heating creates thermal plumes. Furthermore, results show that the NPN wind profiler and WSR-88D weather radar networks have the potential to provide, by working in a coordinated approach, a more reliable measure of the top of the CBL. However, much more routine data collection is needed to establish the reliability of this approach throughout the daytime portion of the diurnal cycle, during partly cloudy and cloudy conditions, during all seasons of the year and across a spectrum of different environmental conditions.

Given that the WSR-88D can be used to monitor the temporal and spatial changes of water vapor near the earth using backscatter from fixed ground objects [13, 14], additional information on the depth of the CBL from a polarimetric WSR-88D could provide an important constraint on the changes in water vapor, pollutants and turbulence within the boundary layer. This combined information would be valuable to forecasters concerned about convection initiation and evolution, air quality, hazardous releases and wildfires and could be used in the initialization of rapidly-updating numerical weather prediction models. Current model predictions of CBL depth often differ from observations by a factor of 2 [15, 16], suggesting that estimates of CBL depth would provide new information that could be used advantageously in data assimilation systems. Convective boundary layer depth observations would also allow forecasters to assess the model forecasts of CBL depth and alter their expectations of moisture depth, convective inhibition and instability, thereby improving forecasts of the timing and likelihood of storm initiation.

5. REFERENCES

1. Hardy, K. R., D. Atlas, K. M. Glover, 1966: Multiwavelength backscatter from the clear atmosphere, *J. Geophys. Res.,* **71**, pp. 1537–1552.

2. Gossard, E.E., and R.G. Strauch, 1983: *Radar observations of clear air and clouds*. Elseiver, 280 pp.

3. Doviak, R. J. and D. S. Zrnic, 2006: *Doppler radar and weather observations*, 2nd ed., Dover Publication, 562 pp.

4. Ottersen, H. 1969: Atmospheric structure and radar backscattering in clear air. *Radio Sci.,* **4**, 1179-1193.

5. Wyngaard, J. C., M. A. LeMone, 1980: Behavior of the refractive index structure parameter in the entraining convective boundary layer. *J. Atmos. Sci.*, **37**, 1573–1585.

6. Fairall, C. W., 1991: The humidity and temperature sensitivity of clear-air radars in the convective boundary layer. *J. Appl. Meteor.*, **30**, 1064–1074.

7. Wilczak, J. M., and Coauthors, 1995: Contamination of wind profiler data by migrating birds: Characteristics of corrupted data and potential solutions. *J. Atmos. Oceanic Technol.*, **12**, 449–467.

8. Wilson, J.W., T.M. Weckwerth, J. Vivekanandan, R.M. Wakimoto, and R.W. Russel, 1994: Boundary layer clear-air radar echoes: Origin of echoes and accuracy of deriving winds. *J. Atmos. Oceanic Technol*., **11**, 1184-1206.

9. Bachmann, S., and D. Zrnic, 2007: Spectral density of polarimetric variables separating biological scatterers in the VAD display. *J. Atmos. Oceanic Technol.,* **24**, 1186-1198.

10. Holleman, I., H. van Gasteren, W. Bouten, 2008: Quality assessment of weather radar wind profiles during bird migration. *J. Atmos. Oceanic Technol.*, **25**, 2188–2198.

11. Melnikov, V.M., R. J. Doviak, D. S. Zrnic, and D.J. Stensrud**,** 2011: Mapping Bragg scatter with a polarimetric WSR-88D. *J. Atmos. Oceanic Technol.*, **28,** 1273- 1285

12. Doviak, R.J, and M.J. Berger, 1980: Turbulence and waves in the optically clear planetary boundary layer. *Radio Sci*., **15**, 297-317.

13. Fabry, F., C. Frush, I. Zawadzki, and A. Kilambi, 1997: On the extraction of near-surface index of refraction using radar phase measurements from ground targets. *J. Atmos. Oceanic Technol.,* **14,** 978–987.

14. Fabry, F., 2006: The spatial structure of moisture near the surface: Project-long characterization. *Mon. Wea. Rev.,* **134,** 79–91.

15. Bright, D. R., and S. L. Mullen, 2002: Short-range ensemble forecasts of precipitation during the Southwest monsoon. *Wea. Forecasting*, **17**, 1080–1100.

16. Stensrud, D. J., and S. J. Weiss, 2002: Mesoscale model ensemble forecasts of the 3 May 1999 tornado outbreak. *Wea. Forecasting*, **17**, 526–543.

SPACE-TIME STRUCTURE OF WEAK FLOWS IN THE LOWER ATMOSPHERIC BOUNDARY LAYER USING GROUND-BASED ACOUSTIC REMOTE SENSING

Christoph K. THOMAS

Physics of Oceans & Atmospheres, College of Earth, Ocean & Atmospheric Sciences, Oregon State University, 104 CEOAS Admin Bldg, Corvallis, OR, USA, 97331, chthomas@coas.oregonstate.edu

ABSTRACT

In the calm boundary layer, recent studies have shown that near-surface wind variability is large and submeso-scale motions dominate dispersion and diffusion of constituents. Currently, there is insufficient understanding of the underlying physics generating these motions and of their spatiotemporal scales. Several recent studies have reported that Taylor's hypothesis, which states that temporal and spatial scales are related by the mean speed of the flow, may apply for the intermittent turbulence, but not for the governing submeso-scale motions (Mahrt, et al., 2009; Thomas, 2011).

We present a study investigating the space-time dynamics of the weak boundary-layer flow in the lowest several hundred meters above ground primarily for nocturnal conditions. A pair of ground-based acoustic sensing systems (SODARs) was used to collect height dependent wind speed, direction, and turbulence data at fine temporal resolution over several months in 2010 in the bottom of the Willamette Valley in Oregon. The objectives were to describe the bulk statistics of motions present in the weak-wind boundary layer, as well as to identify possible external forcing mechanisms of the submeso-scale motions. Data were subject to stochastic analysis using the spectral multi-resolution decomposition technique yielding statistics including two-point correlation coefficients and structure functions between the paired stations and multiple measurement heights.

1. MOTIVATION

When winds are weak near the surface, the wind direction variability is large (Fig. 1) and sub-meso scale motions dominate dispersion and diffusion of constituents. Sub-meso scale motions are defined here as flow modes occupying scales just larger than the turbulence, but smaller than meso-gamma. Currently, there is insufficient understanding of their associated time and space scales, their generating mechanisms, as well as their interactions with turbulence in the surface layer. Recent research suggests that Taylor's hypothesis, which states that temporal and spatial scales are related by the mean speed of the flow, applies for turbulence, but not for sub-meso motions (Mahrt, et al., 2009; Thomas, 2011). Although always present in the atmospheric boundary layer (ABL), these motions become only important for momentum and scalar transport when the synoptic-scale flow is negligible leading to very weak surface flows typically ≤ 2 ms^{-1}. The objectives of this study are to i) describe the bulk statistics of weak flow near the surface as well as the vertical extent of weak wind variability, and ii) investigate possible external forcing mechanisms impacting the near surface flow.

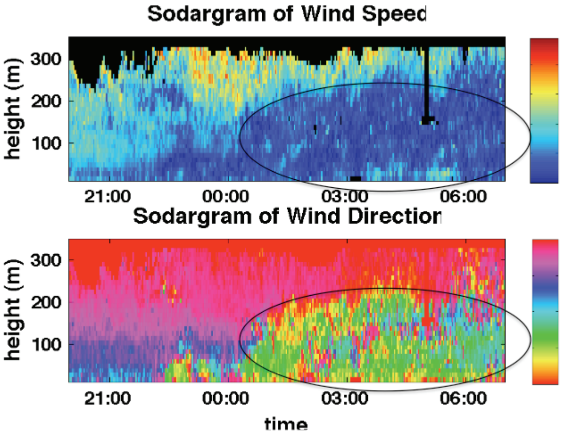

Figure 1: Circled areas depict the weak winds and high directional variability of the near-surface flow. The top color bar indicates wind speed in ms^{-1}, the lower wind direction in degrees from north. Date: Aug 16-17, 2010.

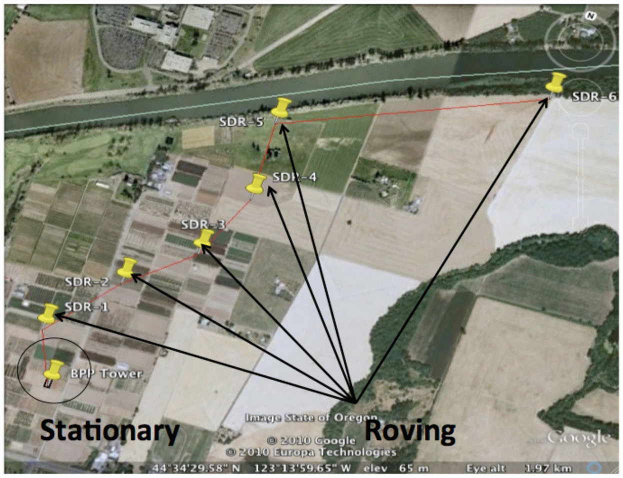

Figure 2: Map of experimental site and locations of the stationary and roving Sodar units. Separation distance was sequentially increased from 240 to 1740 m.

2. EXPERIMENT

The experiment was conducted in the flat bottomlands of the Willamette Valley in the Pacific Northwest in Oregon, USA. The site is of moderate surface heterogeneity that arises from small patches of crops of different heights. In order to obtain information related to horizontal scale, observations of Doppler and non-Doppler quantities were collected using a pair of SODARs (Model PCS-2000-24/LP, Metek, Elmshorn, Germany) deployed in different spatial configurations. One station remained stationary while the roving station was relocated to a new position every 10 to 14 days increasing the separation distance from initially 240 m to 1740 m over the course of the experiment (Fig. 2). Data were sampled from to 15 to 295 m above ground level (agl) averaged over 10 m gates and 2 min intervals. The time to complete one sampling sequence using all 5 virtual antennae of the phased-array was approximately 12 s, resulting in about 10 instantaneous samples to construct the 2 min average. Two sonic anemometers (Model USA-FHN, Metek, Elmshorn, Germany) at 1.5 and 7 m agl were deployed in close proximity to the stationary sodar to supplement the observations.

3. TIME-SPACE ANALYSIS

Data were sorted into two different velocity classes according to the hourly horizontal wind speed, *U*, measured with the sonic anemometer at 7 m agl: the first class contained periods with weak winds defined as $U \leq 1.5$ m s^{-1}, while the second class contained stronger flows with $U > 1.5$ m s^{-1}. This threshold was chosen based on comparing the directional shear between the two sonic anemometers to the mean speed of the flow (not shown here). For $U \leq 1.5$ m s^{-1}, the directional shear increased significantly, which indicated a dominance of sub-meso motions leading to meandering flows with abrupt wind direction changes (Anfossi et al., 2005). The total number of data in both classes equaled 385 hours collected over several months. The selected data for each gate and station were then decomposed using the Multi-Resolution Decomposition (MRD; Howell and Mahrt, 1997), which decomposes a signal into a series of unweighted averages of dyadic width referred to as MRD modes or time scales (2, 4, 8, 16, 32, and 64 min). MRD is an orthogonal technique and is equivalent to a HAAR-basis wavelet transform. The advantage of MRD over other spectral techniques such as the Fast Fourier Transform is that it obeys Reynolds averaging on all scales and is a local transform.

Subsequently, the decomposed data for all MRD modes were used to compute correlation statistics using the following equations:

$$R_u = \sum_{k=1}^{N} \frac{u_{ik}' u_{jk}'}{\sigma_{ui}\sigma_{uj}}, \qquad (1)$$

$$R = \sqrt{\frac{R_u^2 + R_v^2}{2}}, \qquad (2)$$

where u and v represent zonal and modal wind speed, i and j represent different stations or measurement heights, k represents the interval, prime indicates a deviation from the mean, sigma is the standard deviation, and R is the correlation coefficient. The combined correlation coefficient, *R*, is divided by the squared-root of 2 for normalization purposes.

4. RESULTS

4.1 Statistics between gates for each station

Correlating the data of the lowest gate (15 m) with those of higher gates for each station showed that the correlation coefficient for motions on short time scales decays rapidly with increasing vertical separation distance, while the correlation for larger time scales decay more gradually (Fig. 3). A strong initial decorrelation for motions on time scales ≤ 32 min was observed for separation distances < 40 m independent of the station. The latter finding suggests that sub-meso motions are predominantly confined to a thin layer with an extent on the order of 50 m. Correlations for data on longer time scales > 16 min were greater for the strong wind class, which is consistent with the expectation of large overturning eddies resulting from the speed shear. In contrast, correlations of motions on short time scales were insensitive to the wind speed class.

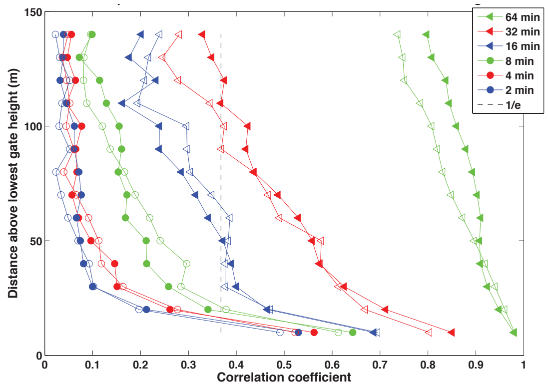

Figure 3: Correlation between winds at the lowest gate (15 m agl) and higher gates as a function of time scale (MRD mode, see Section 3 for details) for the weak wind class. Filled and open symbols are for the stationary and roving station, respectively. The dashed line marks a correlation of 1/e.

4.2 Statistics for gates between stations

Correlating the wind speeds for all gates between 15 and 155 m between stations averaged over all separation distances yielded that motions on longer time scales maintain a significant correlation $R > 1/e$ independent of gate height, while those on short time scales showed only weak correlations (Fig. 4). Complementary to the findings in the previous section, a decorrelation of wind speeds was observed within the lowest 50 m for motions on longer time scales. This observations suggests that the local topography and moderate surface heterogeneity may become important for these weak flows since they may give rise to local density currents despite the fact the slopes were very gentle. Correlations were generally greater for the strong wind speed class as in the previous analysis.

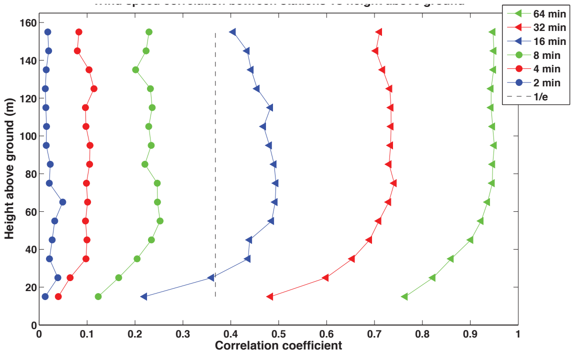

Figure 4: Correlation between winds at all gates between the two stations averaged over all separation distances as a function of time scale. Data are shown for the stationary sodar and the weak wind class only. For orientation purposes, the dashed line marks a correlation of 1/e.

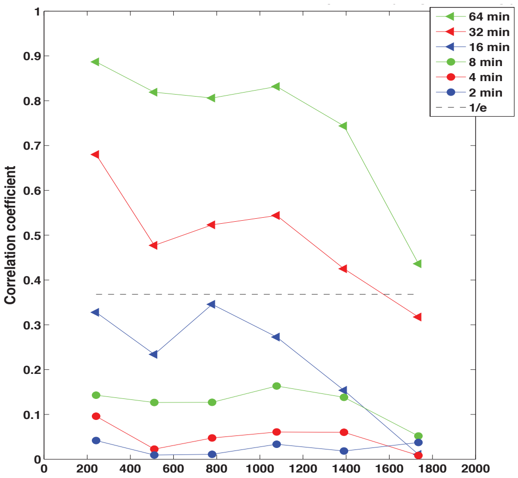

Figure 5: Correlation between winds observed at the 15 m gate between the two stations as a function of horizontal separation distance and time scale. Data are shown for the stationary sodar and the weak wind class only. For orientation purposes, the dashed line marks a correlation of 1/e.

4.3 Sensitivity to separation distance

The height-dependent correlation of wind speeds was sensitive to the horizontal separation distance showing a decline with increasing horizontal scale for motions on time scales ≥ 8 min (Fig. 5). Shorter motions showed no dependence on station spacing, suggesting that they occupy scales smaller than the minimum separation distance of 240 m. In contrast, transient motions occupying larger spatial scales are expected to maintain a high correlation irrespective of their short time scales measured by a fixed observer. Higher gates maintained a higher correlation compared to lower gates. These findings suggest that longer motions occupy larger spatial scales and preferentially exist outside of the near-surface layer.

5. PRELIMINARY CONCLUSIONS

The following conclusions can be drawn from the bulk statistics presented for the analysis of weak flows in the lower ABL:

The spatial and temporal scales of the dominant nocturnal motions are generally positively correlated for time scales between 2 to 64 min, i.e., longer motions occupy larger spatial scales. However, the ratio of space to time for these weak wind conditions remains uncertain. One obstacle for the determination of this relationship is the significant scatter. This large scatter is a common feature for calm, nocturnal boundary layers that are subject to a variety of forcing mechanisms, most of which are poorly understood or unknown. Future work will need to identify and include analysis of different external forcing mechanisms in addition to wind velocity classes.

Motions in the layer extending approximately 40 to 50 m vertically from the surface ground showed a high degree of variability leading to small correlations. We therefore conclude that this is the layer where sub-meso motions are most active. Here, the flow may be sensitive to even gentle slopes and individual flow obstacles such rows of trees etc. These terrain features may initiate local, but systematic flow modes including cool pools, density currents, and waves that lead to a large spatial and temporal variability of the weak surface winds.

ACKNOWLEDGMENTS

This research was funded by the National Science Foundation, CAREER award AGS 0955444, and the Army Research Office, contract W911NF-09-1-0271.

REFERENCES

1. Anfossi, D., Oettl, D., Degrazia, G. and Goulart, A., 2005. An analysis of sonic anemometer observations in

low wind speed conditions. *Boundary-Layer Meteorol.*, 114: 179-203.

2. Howell, J. F., Mahrt, L. (1997). Multiresolution Flux Decomposition. *Boundary-Layer Meteorol.,* 83, 117-137.

3. Mahrt, L. (2010). Computing Turbulent Fluxes Near the Surface: Needed Improvements. *Agric. For. Meteorol*., 150, 501-509.

4. Mahrt, L., Thomas, C. K., Prueger, J. H. (2009). Space-time Structure of Mesoscale Motions in the Stable Boundary Layer. *Q. J. R. Meteorol. Soc*., 135, 67-75.

5. Thomas, C. K. (2011). Variability of Sub-Canopy Flow, Temperature, and Horizontal Advection in Moderately Complex Terrain. *Boundary-Layer Meteorol.*, 139, 61-81.

RETRIEVAL OF THE TEMPERATURE AND VELOCITY STRUCTURE PARAMETERS FROM SODAR DATA WITH ALLOWANCE FOR THE EXCESS TURBULENT ATTENUATION

Nikolay P. Krasnenko[1, 2], **Liudmila G. Shamanaeva**[3]

[1]*Institute of Monitoring of Climatic and Ecological Systems SB RAS, 10/3, Akademicheskii Ave., Tomsk 634055, Russia,*
[2]*Tomsk State University of Control Systems and Radioelectronics, E-mail: krasnenko@imces.ru*
[3]*V.E. Zuev Institute of Atmospheric Optics SB RAS, 1, Akademicheskii Ave., Tomsk 634055, Russia E-mail: sima@iao.ru*

ABSTRACT

A closed iterative algorithm of sodar data processing for retrieval of simultaneous vertical profiles of the temperature and velocity structure parameters under convective conditions is described in the report. The algorithm allows the excess turbulent attenuation of a sound pulse propagating from the transmitter to the sounding volume and back to the receiver to be taken into account. The algorithm was used to process data of simultaneous sodar measurements of the wind velocity vector and backscattered signal power with the Zvuk-2 three-channel monostatic Doppler sodar. The vertical profiles of C_T^2 and C_V^2 were simultaneously obtained, and their synchronous and antiphase altitude behavior was established. A comparison of the results obtained with *in situ* measurements of the temperature and velocity structure parameters using a micropulsation sensor demonstrate their good agreement.

1. INTRODUCTION

In [1], the vertical velocity and echo intensity measurements with a vertically oriented monostatic Doppler sodar were used to retrieve simultaneously the velocity and temperature structure characteristics $C_V^2(z)$ and $C_T^2(z)$. However, in [2] it was indicated that under unstable conditions, sodars underestimated $C_T^2(z)$ due to the neglect of turbulent attenuation of sodar signals. In [3] it was also pointed out that the ratio of the average sodar to mast values of C_T^2 changed from ~0.1 to ~10 depending on the atmospheric conditions. In [4–6] an iterative closed data processing algorithm considering the excess turbulent attenuation of an acoustic signal propagating from the transmitter to the sounding volume and back to the receiver was described that allows $C_T^2(z)$ and $C_V^2(z)$ to be reconstructed simultaneously from the data of acoustic sounding with a three-channel monostatic Doppler sodar capable of measuring the backscattered signal power. In the present paper, this algorithm is used to study the simultaneous behavior of the temperature and velocity structure characteristics.

2. SODAR-RETRIEVED TEMPERATURE AND VELOCITY STRUCTURE CHARACTERISTICS

The average vertical profiles of the temperature and velocity structure characteristics $\left\langle C_T^2(z)\right\rangle$ and $\left\langle C_V^2(z)\right\rangle$ were retrieved from simultaneous Doppler sodar measurements of vertical profiles of the three wind velocity components $V_{i,j}(z)$ and backscattered signal power $P_j(z)$ using a closed iterative data processing algorithm described in [6]. Here $i = x, y, z$, $j = 1, \ldots, N$ is the serial number of measurement run, N is the number of runs in a series, and angular brackets designate averaging over a series of N measurements.

The archived data of measurements performed with the Zvuk-2 sodar in 1996–1997 were processed. The Zvuk-2 sodar [7] operated at a frequency of 1700 Hz, its pulse repetition period was $11.5\ \text{s}$, and its pulse duration was $\tau = 150\ \text{ms}$. One transceiving antenna of the Zvuk-2 sodar was pointed vertically, and two others were tilted at angles of 20° to the vertical in two mutually orthogonal planes.

The results of processing of 5 series of sodar measurements are presented in this study. The corresponding values of the surface temperature T_s, relative air humidity u_s, air pressure p_s, and average horizontal wind velocity $|\langle V_h \rangle|$ measured with an ultrasonic meteorological complex are tabulated in Table 1. It should be noted that the average horizontal wind speed on September 26, 1996 was too light to have a reading.

Figure 1 shows the first and last iterations of the vertical profile of the temperature structure characteristic reconstructed from a series of sodar measurements on September 26, 1996 from 10:00 to 10:10, Tomsk local time. Values of the temperature structure characteristic were normalized by $C_T^2(z_{1T} = 66\ \text{m}) = 1.27 \cdot 10^{-2} \text{K}^2/\text{m}^{2/3}$.

It can be seen that the contribution of the turbulent attenuation becomes significant for $z \geq 100\ \text{m}$. This is in agreement with the data of [3]. Good agreement of the results can be seen with allowance for the $z^{-4/3}$ dependence. A comparison of 10-min average values of $C_T^2(z)$ and *in situ* measurements with the ultrasonic micropulsation sensor performed in [8] for 3 successive series of sodar measurements also confirmed their good agreement.

Table 1. Meteorological parameters measured with the ultrasonic meteorological complex at the measurement site.

Parameter	T_s, °C	u_s, %	p_s, hPa	$\lvert\langle \boldsymbol{V}_h \rangle\rvert$, m/s
September 26, 1996, 10:00-10:10	7.38	86	1013	–
June 20, 1997, 16:00-16:10	19.2	53	988.3	5
June 25, 1997, 10:00-10:10	20.2	64	983.5	4
July 2, 1997, 10:00-10:10	17.5	66	992.2	3

From Fig. 1 it can be seen that the temperature structure characteristic first decreases with altitude, following the dependence $z^{-4/3}$ predicted theoretically, up to $z_{\min} = 250$ m, and then increases with altitude. During our measurements, $z_{\min} = 113 - 250$ m. Analogous altitude dependences were observed by Neff [9] and Coulter [10] (2002); from their data, $z_{\min} = 130 - 330$ m. An increase in C_T^2 above the minimum was related in [11] with the presence of a capping inversion above the mixing layer, and the altitude of the minimum was related with the inversion altitude. According to Fig. 1, the upper boundary of the surface layer for this series of measurements was 150 m.

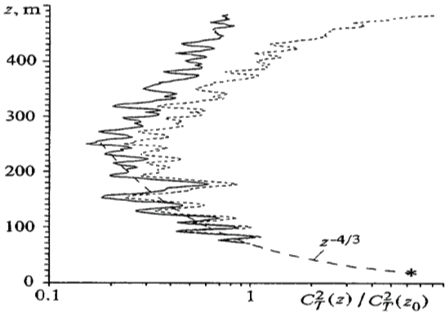

Figure 1.The first (the solid curve) and the last (the dashed curve) iterations of the profile $C_T^2(z)$ above Tomsk calculated by the suggested algorithm. The dotted curve shows the model $z^{-4/3}$ dependence, and the asterisk shows C_T^2 measured independently with the ultrasonic micropulsation sensor placed 17 m above the ground.

Figures 2–3 show 10-min average vertical profiles of the three components of the wind velocity vector and average wind velocity (a) and temperature (b) and velocity structure characteristics (c). Here crosses indicate $V_{x.\text{av}}(z)$, squares $V_{y.\text{av}}(z)$, triangles $V_{z.\text{av}}(z)$, and the solid curve shows the average wind velocity profile $\lvert\langle \boldsymbol{V}(z) \rangle\rvert$.

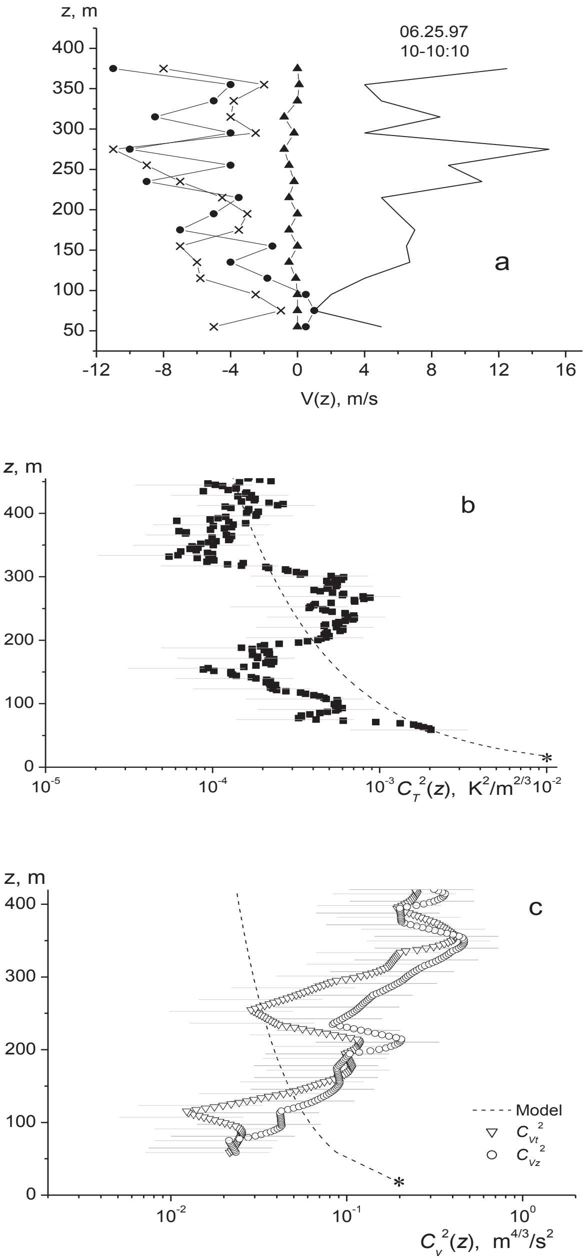

Figure 2. Vertical profiles of the three components of the wind velocity vector (a) and temperature (b) and velocity structure characteristics (c) reconstructed from measurements with Zvuk-2 sodar on June 25, 1997 from 10:00 till 10:10, Tomsk local time. The asterisks indicate the data of in situ measurements of C_T^2 and C_V^2 with the ultrasonic micropulsation sensor placed 17 m above the ground.

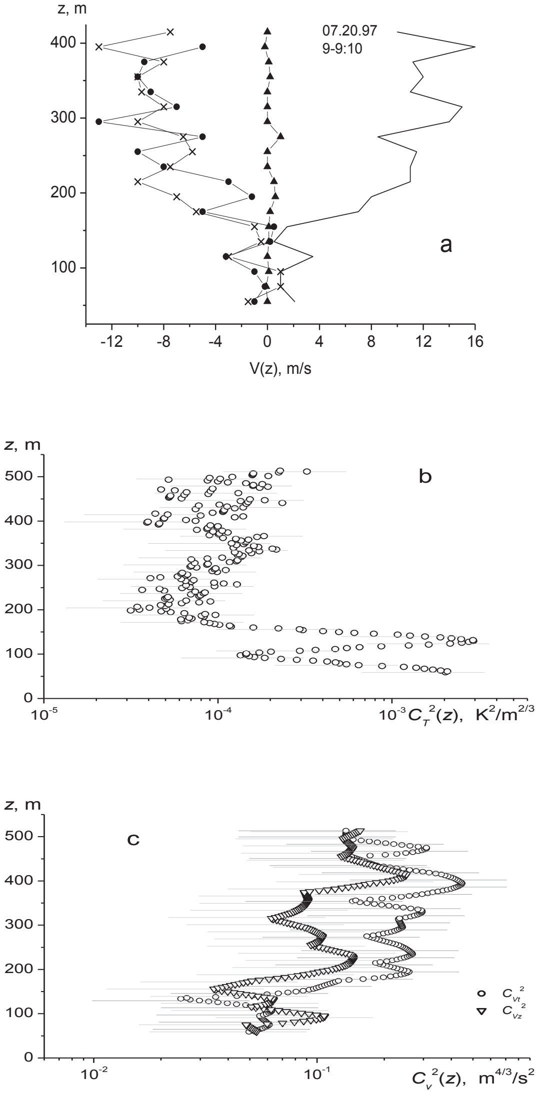

Figure 3. Vertical profiles of the three components of the wind velocity vector (a) and temperature (b) and velocity structure characteristics (c) reconstructed from measurements with the Zvuk-2 sodar on July 2, 1997 from 9:00 till 9:10, Tomsk local time.

A wind shear region is clearly seen in Fig. 2 (a) between 215 and 315 m, in which $|\langle V(z)\rangle|$ increases from 5 to 15 m/s at $z = 295$ m and then subsequently decreases to 4 m/s. A broad maximum in the vertical profile $C_T^2(z)$ in Fig. 2 (b) indicates the presence of an elevated temperature inversion. Below the inversion, C_T^2 follows $z^{-4/3}$ dependence typical of convection. Above the inversion, C_T^2 first sharply decreases and then increases again. According to [1, 11, 12], such altitude behavior is typical of a capping inversion above a convection layer that develops in the morning hours. According to [12], $z_{\max} = 260$ m is a sodar estimate of the base of inversion with a thickness of ~70 m. The asterisk here shows the temperature structure characteristic measured with the ultrasonic mucropulsation sensor placed 17 m above the ground.

A minimum in the vertical profile $C_T^2(z)$ is seen at $z_{\min} = 113-250$ m. Below $z_{\min}$, C_T^2 decreases with altitude. Above $z_{\min}$, it increases with altitude. In accordance with [13], such vertical behavior of C_T^2 is explained in the context of the convection theory, according to which the regions with intense temperature pulsations alternate with no-pulsation regions: the first are observed inside the plumes and the second are related with descending air flows. This results in spatial intermittence of the atmospheric turbulence. Petenko *et al.* [14] established that the difference between C_T^2 inside and outside of the temperature plumes reached 10–100 times, which also agrees with the data presented here.

Analogous vertical profiles $C_T^2(z)$ can be seen in Fig. 4 (a) which shows simultaneous profiles of the temperature (a) and velocity structure parameters (b).

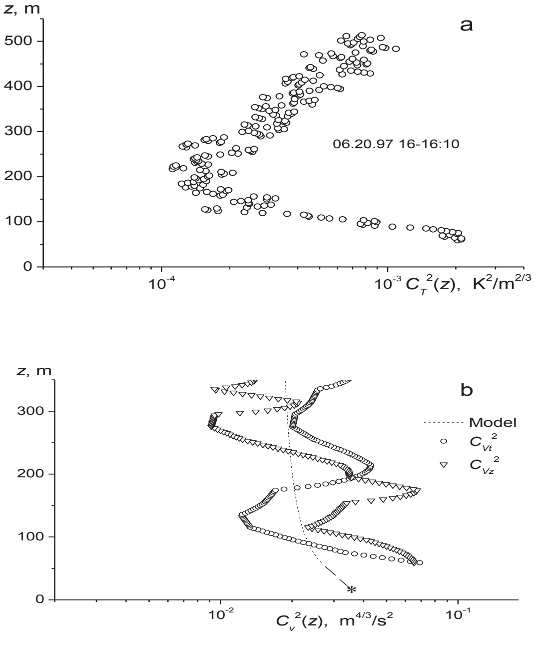

Figure 4. Vertical profiles of the temperature (a) and velocity structure characteristics (b) reconstructed from measurements with the Zvuk-2 sodar on June 20, 1997 from 16:00 till 16:10, Tomsk local time.

Figures 1, 3 (b), and 4 (a) show examples of typical sodar-derived altitude profiles of C_T^2 under convective conditions with a capping inversion [10] with $z^{-4/3}$ power dependence in the convective boundary layer. At the top of the mixing layer, C_T^2 increases due to turbulent mixing from thermals within the mixed layer that penetrate into the stratified layer above; this provides a measure of the mixing height. As can be seen from Fig. 1, the height of the capping inversion here is 150 m; it is 200 m for Fig. 3 (b) and 220 m for Fig. 4 (a), which is in agreement with the data of long-term sodar measurements in this region [7], according to which the mixing layer height is 161.9 ± 62.1 m.

The profiles $C_V^2(z)$ shown in Figs. 2 (c) – 3 (c) and 4 (b) were calculated for vertical (designated by C_{Vz}^2) or horizontal (designated by C_{Vt}^2) separation of the observation points, respectively. The altitude behavior of $C_{Vt}^2(z)$ and $C_{Vz}^2(z)$ was synchronous. The asterisk in Figs. 2 (c) and 4 (b) shows C_V^2 measured with the ultrasonic mucropulsation sensor placed 17 m above the ground. As can be seen from Figs. 2 (c) – 3 (c), both $C_{Vt}^2(z)$ and $C_{Vz}^2(z)$ increase with altitude. In Fig. 4 (b), they follow the $z^{-2/3}$ model dependence.

As can be seen from Figs. 4 (a) and (b), on June 20, 1997, $C_T^2(z)$ changes synchronously with altitude with $C_{Vt}^2(z)$ and $C_{Vz}^2(z)$ (except $135 \le z \le 275\,\text{m}$, where a minimum in $C_T^2(z)$ corresponds to maxima in $C_{Vt}^2(z)$ and $C_{Vz}^2(z)$). Synchronous altitude behavior of the structure characteristics was also indicated in [4, 14]. On June 25, 1997, the antiphase behavior of the structure characteristics, noted also in [4, 5], can be seen. On July 2, 1997, the altitude behavior of $C_T^2(z)$ anticorrelated with $C_{Vt}^2(z)$ and $C_{Vz}^2(z)$. Thus, a minimum in $C_T^2(z)$ at $z_{\min} = 240\,\text{m}$ corresponded to maxima in $C_{Vt}^2(z)$ and $C_{Vz}^2(z)$.

REFERENCES

1. Asimakopoulos, D. N., C. G. Helmis, and J. A. Kalogiros, 1996: Quantitative estimation of CBL parameters using the vertical velocity and echo intensity measurements of an acoustic sounder, *8th Int. Symp. on Acoustic Remote Sensing and Associated Techniques of the Atmosphere and Oceans (Proceedings)*, Moscow, Russia, pp. G.85-G.96 .
2. Coulter, R. L. and M. A. Kallistratova, 2004: Two decades of progress in sodar techniques: A review of 11 ISARS proceedings, *Meteorology and Atmospheric Physics*, **85**, pp. 3-19.
3. Rusakov, Yu. S., 2007: On the turbulent sound attenuation in vertical sounding of the atmosphere, *19th Session of the Russian Acoustical Society (Proceedings)*, Nizhnii Novgorod, Russia, Vol. **2**, pp. 144-148.
4. Shamanaeva, L. G., 1999: New method of acoustic sounding of the parameters of atmospheric turbulence, *Proc. SPIE*, **3983**, pp. 344-349.
5. Shamanaeva, L. G., 2000: Interpretation of the data of simultaneous sodar measurements of vertical profiles of C_T^2 and C_V^2 in the atmospheric boundary layer, *Proc. SPIE*, **4341**, pp. 316-322.
6. Shamanaeva, l. G., 2008: Acoustic sounding of the temperature and velocity structure characteristics with allowance for the turbulent attenuation, *Russian Physics J.*, **51**, pp. 1208-1215.
7. Krasnenko N. P., 2001: Acoustic Sounding of the Atmospheric Boundary Layer*, Vodolei*, Tomsk, Russia, 278 pp.
8. Krasnenko, N. P. and L. G. Shamanaeva, 1998a: Sodar measurements of the structural characteristics of temperature fluctuations and the outer scale of atmospheric turbulence, *Meteorol. Z.*, **7**, pp. 392-397.
9. Neff, W. D., 1975: Quantitative evaluation of acoustic echoes from the planetary boundary layer, *NOAA Tech. Rep. ERL 322-WPL 38*, Boulder, Colorado, 34 pp.
10. Coulter, R. L., 2002: Remote sensing of micrometeorological quantities, *11th Int. Symp. on Acoustic Remote Sensing and Associated Techniques of the Atmosphere and Oceans (Proceedings)*, Rome, pp. 321-327.
11. Coulter, R. L., 1990: A case study of turbulence in the stable nocturnal boundary layer, *Boundary-Layer Meteorology*, **52**, pp. 75-91.
12. Kaimal J.C., Wyngaard J. C., Haugen D. A., Cote O. R., Izumi Y., 1976: Turbulence structure in the convective boundary layer, *J. Atmos. Sci.*, 33, No. 11, pp. 2152-2169.
13. Andrianov, V. A., Vetrov V. I., 1987: Inhomogeneities of the lower 500-m layer of the atmosphere from the data of acoustic sounding, *Preprint No. 9, Institute of Radio Engineering and Electronics of the Academy of Sciences if the USSR*, Moscow, 35 pp.
14. Petenko I. V., M. A. Kallistratova, and A. N. Bedulin, 1996: Wind turbulence measurements with a mono-bistatic sodar, 8^{th} *Int. Symp. on Acoustic Remote Sensing and Associated Techniques of the Atmosphere and Oceans (Proceedings)*, Moscow, Russia, pp. 3.55-3.60.

AIRBORNE AND GROUND-BASED MEASUREMENTS WITH THE NCARS GVHSRL

Bruce Morley[1], Scott Spuler[1], Jothiram Vivekanandan[1], Matthew Hayman[1], Edwin Eloranta[2]

[1]*National Center for Atmospheric Research, 3450 Mitchell Lane, Boulder, CO, USA, bruce@ucar.edu*
[2]*University of Wisconsin, 1225 W. Dayton St., Madison, WI, USA*

ABSTRACT

The National Center for Atmospheric Research (NCAR) Gulfstream V High Spectral Resolution Lidar (GVHSRL) is an eye-safe calibrated lidar system that can measure the atmospheric backscatter cross section, extinction and depolarization out to a maximum range of 30 km. The instrument is capable of operation from the NCAR GV aircraft and a customized container on the ground. We will present results from the recent airborne deployment in the Tropical Ocean tRoposphere Exchange of Reactive halogen species and Oxygenated VOC (TORERO) field campaign which was conducted over remote ocean regions of the Pacific coast of Central and South America. The lidar measurements – obtained from aircraft altitudes ranging from 0.3 to 15.5 km were collected over a wide range of atmospheric conditions and include cases of: marine boundary layer, cirrus outflow, mid-tropospheric pollution and stratospheric haze. Additionally, ground-based results from Boulder, CO, will be presented. Vertical pointing data – processed with a particle identification algorithm under development – will be shown, along with preliminary results from the modified lidar system to identify and characterize oriented scatters (ice crystals).

1. INTRODUCTION

NCARs GVHSRL is an eye-safe lidar system built by the University of Wisconsin's Space Sciences Engineering Center lidar group led by Dr. Edwin Eloranta. The principals of high spectral resolution lidar are described by Eloranta in [1]. Shipley [2] and Sroga[3] describe an early HSRL system. The evolution of the current system is described by Razenkov [4; 5]. Figure 1 is a simplified block diagram of the transmitter, receiver and wavelength control systems. There are two key features in the design of GVHSRL that lead to an eye safe beam at the exit of the transmit/receive telescope. The first is that the transmit laser is a high pulse rate - 4000 Hz - micro-pulse laser and the second is the expansion of the laser beam to the full 40 cm aperture of the telescope. These two design features are the major reason that the laser energy density meets the eye safety criteria of the American National Standards Institute (ANSI) and NCAR has received a Letter of Determination (LOD) from the Federal Aviation Administration that allows zenith pointing unattended operation from NCARs Foothills location day and night. There are two other airborne HSRLs, the NASA system is described in Hair [6] and the German DLR system is described in Esselborn [7].

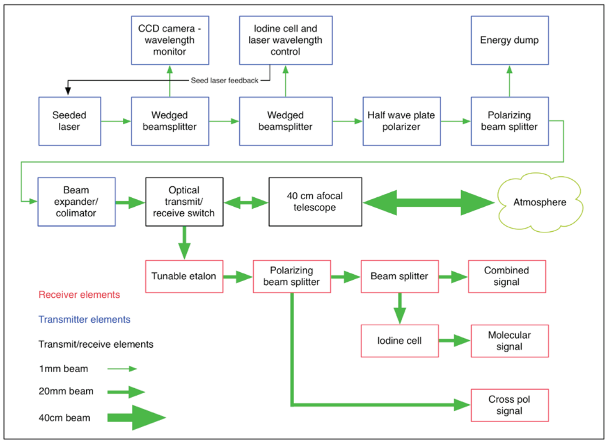

Figure 1. Simplified block diagram of GVHSRL.

The use of a single transmit/receive telescope gives both the same field-of-view (FOV) and makes the lidar less sensitive to misalignment than lidar systems that steer the transmit beam into the receiver FOV. These design features allow the telescope to be rotated between zenith and nadir pointing in few seconds during flight. A safety interlock insures that the outgoing laser shutter is open only when the telescope is locked in either the nadir or zenith position.

GVHSRL uses the method described by Piironen [8] and Eloranta [9] that uses an iodine absorption line to separate the aerosol return signal from the molecular return signal. Laser light that has undergone Brillouin scattering in a single mode fiber is used in the wavelength control subsystem. The light is wavelength shifted from the 1109 iodine line to the side of the 1105 line. The wavelength shifted signal is split into two beams with one beam going through an iodine cell before hitting a detector and the other passing directly to a detector. The ratio of these two signals is used in a feedback control circuit to keep the laser locked to the center of the 1109 line.

2. GROUND BASED MEASUREMENTS

The lidar has been operated from NCARs Foothills campus in Boulder, CO since September 1, 2010. On September 6 a wildfire broke out in the Four Mile Canyon just west of Boulder and burned out of control for several days. Smoke from the fire drifted over the GVHSRL between 17:00-23:45 UT. The top image in Figure 2 is the atmospheric backscatter cross section signal above the lidar. No smoke is present in the return signal at the start and end of the time period displayed. The lidar is able to see the boundary layer aerosols that extend to about 2 km. In the 2 km to 10 km altitude above the lidar the backscatter cross section is one to two orders of magnitude smaller with weak aerosol layers. The smoke from the fire is quite evident with backscatter cross sections one or two orders of magnitude stronger than that of the urban aerosol layer.

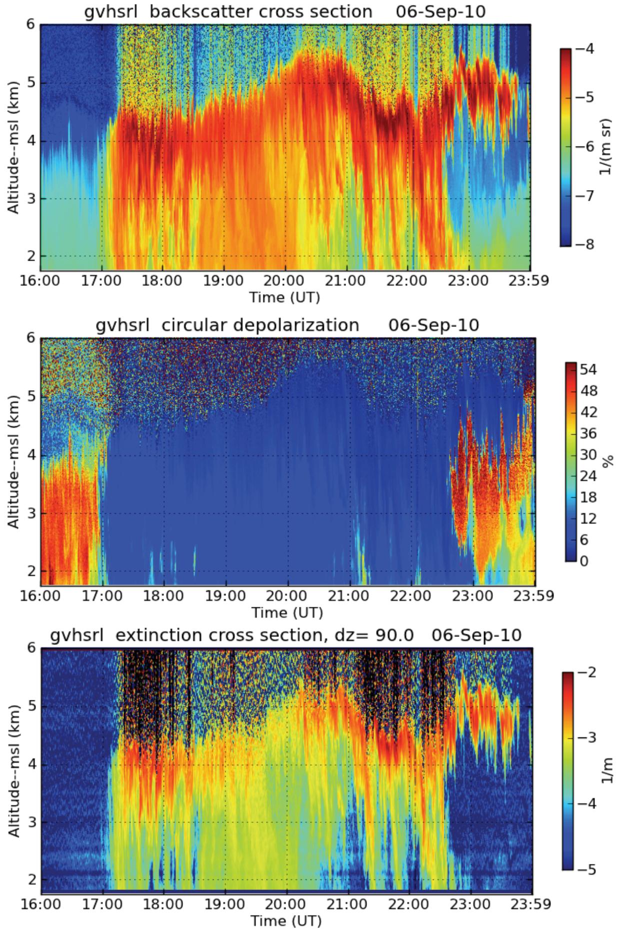

Figure 2. Backscatter cross section (top), circular depolarization ratio (middle) and extinction cross section (bottom) from the ground-based GVHSRL as smoke from the September 6, 2010, Four Mile Canyon fire was advected over the lidar.

The middle image is the depolarized return signal for the same time period. The optical properties of the Four Mile Canyon fire smoke are quite different than that of the boundary layer and higher tropospheric aerosols. The boundary layer aerosols have a much higher depolarization than that of the smoke. There are several possible reasons for this. The first is that the high winds responsible for the rapid spread of the wildfire were also responsible for elevated levels of large irregular dust particles which are depolarizing. The authors speculate that the smoke consisted of small hygroscopic particles which are round and do not depolarize the return signal. The bottom figure of extinction cross section also points out another significant difference between the smoke and other aerosols. The smoke had an extinction cross sectin two orders of magnitude stronger than the near surface aerosol seen before and after the smoke was over the lidar.

3. AIRBORNE DATA - TORERO

The TORERO field program was conducted from two locations: Anafagasta, Chile from January 19-29 and San Jose, Costa Rica from January 29 to February 26, 2012. Seventeen research flights were flown over remote regions of the Pacific Ocean. Figure 3 shows seven flight plans from TORERO. The altitudes flown varied widely from 100 m to over 15 km. On several flights the GV would rendezvous with the Japanese Research Vessel Hakuho Maru or the NOAA Research Vessel Ka'imimoana that was servicing buoys along the 95 W longitude.

The TORERO data in Figure 4 were taken off the coast of Chile on February 12 during a typical flight sounding. The lidar was used to determine atmospheric layers of interest and the PI then directed the GV to fly into them for *in situ* measurements. The GV is descending to an altitude of 300m for boundary layer sampling leg and then climbs to an altitude of over 10 km. This figure is an example of a typical TORERO flight profile. The calibrated backscatter cross section is available in real-time as are all GVHSRL data products. The color bar scale is logarithmic with the number being the exponent. As the GV changes altitude the retrieved cross section of the elevated aerosol layers and the marine boundary layer does not change. The orientation of the GVHSRL - nadir or zenith - does not alter the retrieved backscatter cross section. Any FOV or gain differences between the four receivers have been well characterized and removed during data processing.

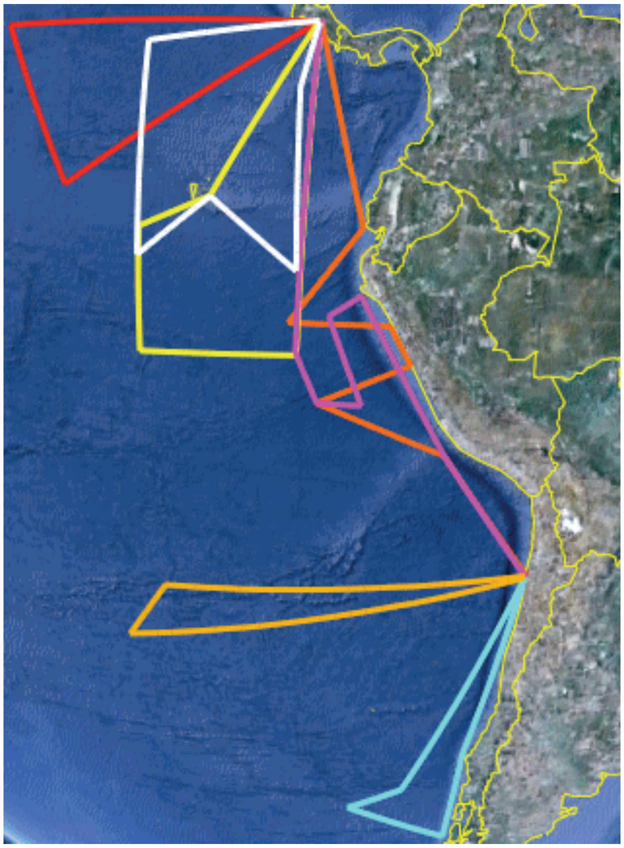

Figure 3. Seven representative flight plans from TORERO. All the research flights were flown out of Anafagasta, Chile or San Jose, Costa Rica over remote regions of the eastern Pacific Ocean.

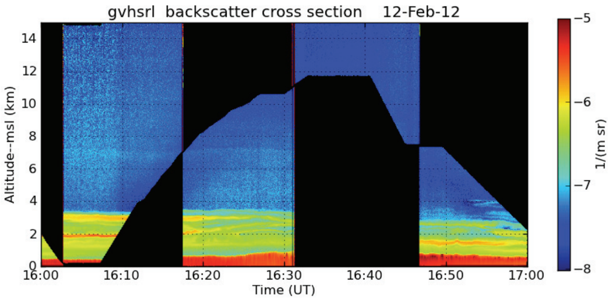

Figure 4. Backscatter cross section image taken on 12 February 2012 as the aircraft was profiling the atmosphere and the lidar was being switched between zenith and nadir pointing.

Figure 5 is an extinction profile from a 10-minute segment of data from 16:20 to 16:40 shown in Figure 4. The vertical resolution of extinction profile is 300m. The Rayleigh extinction cross section is shown by the black line near 10^{-5} m^{-1}.

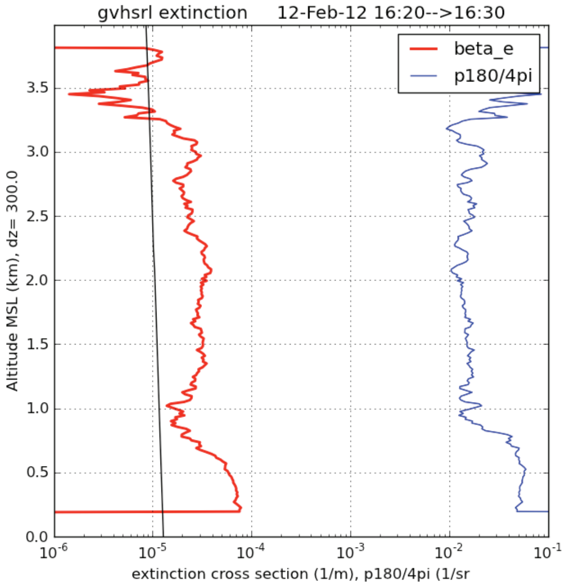

Figure 5. Extinction cross section profile using data from the 10-minute segment of data from 16:20 to 16:30. The aircraft was climbing from 8 to over 10 km.

4. PARTICLE IDENTIFICATION AND FUTURE PLANS

Shupe [10] describes a method for delineating regions of cloud liquid, ice and aerosol using backscatter and depolarization ratio. It uses thresholds, or hard boundaries, to identify particle classes. The use of hard boundaries can lead to misclassification because there is a fair amount of overlap between observables for various particle types. Boundaries between most of the observables are "fuzzy" as there is a smooth transition from one article type to the next as demonstrated by Vivekanandan [11]. In a fuzzy logic scheme measurement membership functions are used to define boundaries between various particle types. Values of backscatter and depolarization ratio are passed to membership functions to determine the degree to which each observation belongs to a particular particle type. Hard boundaries between various particle types were "fuzzified" for classifying particles. Preliminary results based on the above described classification scheme are shown in Figure 6.

A rotating half wave plate has been added to the GVHSRL receiver to add the capability of detecting oriented scatterers (ice crystals).

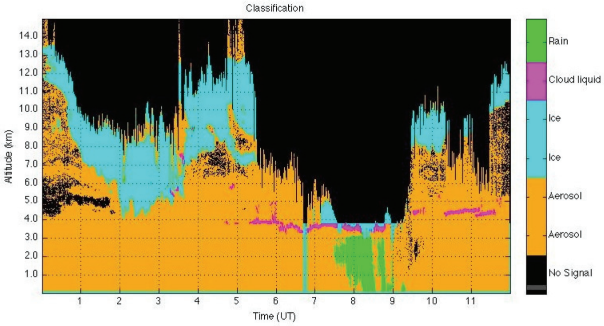

Figure 6. Particle ID from 18 July 2010 Boulder CO.

5. CONCLUSION

The GVHSRL has been demonstrated to collect calibrated boundary layer aerosol data from the ground and the GV aircraft. GVHSRL is available to researchers through the NSF Lower Atmospheric Observing Facilities [12].

ACKNOWLEDGMENTS

The authors would like to thank Dr. Igor Razenkov for sharing his intimate knowledge of the GVHSRL design with us. The authors also thank Mr. Joseph VanAndel and Mr. Joe Garcia for their help with software for GVHSRL. It is a very complex system and they have contributed significantly to the operation and maintenance of the instrument. The authors also thank Mr. Kyle Holden and Mr. Richard Erickson for their technical support of GVHSRL on the TORERO field deployment. NCAR is sponsored by the National Science.

REFERENCES

1. Eloranta, E. W., 2005: Lidar: Range-Resolved Optical Remote Sensing of the Atmosphere, Claus Weitkamp ed., pp. 143-164, Springer Science+Business Media Inc*, New York, USA, 2005.*

2. Shipley, S. T., D. H. Tracy, E. W. Eloranta, J. T. Trauger, J. T. Sroga, F. L. Roesler, and J. A. Weinman, 1983: High spectral resolution lidar to measure optical scattering properties of atmospheric aerosols. 1: Theory and instrumentation, *Applied Optics*, **22**, pp. 3716-3724.

3. Sroga, J. T., E. W. Eloranta, S. T. Shipley, F. L. Roesler, and P. J. Tyron, 1983: High spectral resolution lidar to measure optical scattering properties of atmospheric aerosols. 2: Calibration and data analysis, *Applied Optics*, **22**, pp. 3725-3732.

4. Razenkov, I. A., E. W. Eloranta, J. P. Hedrick, R. E. Holz, R. E. Kuehn and J. P. Garcia, 2002: A High Spectral Resolution Lidar Designed for Unattended Operation in the Arctic, *21st International Laser Radar Conference}, July 8-12, 2002, Quebec, Canada*, pp. 57-60.

5. Razenkov, I. A., E. W. Eloranta, J. P. Hedrick and J. P. Garcia, 2008: The Design of a New Airborne High Spectral Resolution Lidar, *24th International Laser Radar Conference}, June 23-27, 2008, Boulder, CO, USA.*

6. Hair, J. W., C. A. Hostetler, A. L. Cook, D. B. Harper, R. A. Ferrare, T. L. Mack, W. Welch, L. R. Isquierdo and F. E. Hovis, 2008: Airborne high spectral resolution lidar for profiling aerosol optical properties. 2, *Applied Optics*, **47**, pp. 6734-6752.

7. Esselborn, M., M. Wirth, A. Fix, M. Tesche, and G. Ehret, 2008: Airborne high spectral resolution lidar for measuring aerosol extinction and backscatter coefficients., *Applied Optics*, **47**, pp. 346-358.

8. Piironen, P., and E. W. Eloranta, 1994: Demonstration of a high-spectral-resolution lidar based on an iodine absorption filter. *Optics Letters*, **19**, pp. 234-236.

9. Eloranta, E. W. and I. A. Razenkov, 2006: Frequency locking to the center of a 532 nm iodine absorption line by using stimulated Brillouin scattering from a single- mode fiber., *Optics Letters*, **31**, L22809, doi:10.1029/2007GL031008.

10. Shupe, M. D., 2012: A ground-based multi-sensor cloud phase classifier. 2007:,*GRL*, **34**, pp. 25-30.

11. Vivekanandan, J., D. S. Zrnic', S. M. Ellis, R. Oye, A. V. Ryzhkov and J. Straka 2011: Cloud microphysics retrieval using S-band dual-polarization radar measurements., *Bull. Amer. Meteor. Soc*, **80**, pp. 381-388.

12. http://www.eol.ucar.edu/deployment/request-info/contact-information-for-nsf-lower-atmospheric-observing-facilities

Session 5 – Oral Presentations

SODAR OBSERVATIONS OF SUMMERTIME KATABATIC FLOWS AT ABOA, ANTARCTICA

Rostislav Kouznetsov[1,2], Priit Tisler[1] Timo Palo[1], 3, Timo Vihma[1]

[1] *Finnish Meteorological Institute, Erik Palmenin aukio 1 PL 503, 00101 Helsinki, Finland*
[2] *A. M. Obukhov Institute of Atmospheric Physics, Moscow, Russia*
E-mail: rostislav.kouznetsov@fmi.fi
[3] *University of Tartu, Estonia*

ABSTRACT

The three-axes Doppler sodar Latan-3 was operated at the Finnish Antarctic station Aboa (73°03'S, 13°25'W) in summer 2010-2011. The measuring site is located at practically flat slightly sloped (about 0.5 deg.) surface of the glacier about 10 km away from the station. The sodar was operated in multiple frequency parallel mode with 20-800 meters sounding range, 20 m vertical and 10 s temporal resolution. To reveal the wind and temperature profiles below the sounding range as well as turbulent fluxes at 2 and 10 meters, the data of 10-m meteorological mast were used.

During the measurements the atmospheric boundary layer was most of the time within the sounding range of the sodar. A large variety of katabatic wind speed profiles has been observed. The thickness of the katabatic flow varied from few tens to several hundreds of meters, the wind speed maximum could be as low as 5 meters. Such situations pose a major challenge for meteorological models, since the surface layer in these cases appears just within the lowest meters.

1 INTRODUCTION

Katabatic winds are air flows that occur above a cold sloped surface. They are driven by gravity that causes colder and more dense airmasses to move downhill. As velocity increases, the Coriolis force decline the flow from the downhill direction. After Vihma et al. [6] we define the katabatic wind as a downslope wind initially generated by surface cooling.

The katabatic winds occur near a surface in the stably stratified atmospheric boundary layer (ABL) and have a maxima in a range from few meters Barry [2] to few hundreds meters [1]. This makes a sodar a convenient tool to observe them.

Below we show a few examples of katabatic flows observed with a sodar near the Finnish Antarctic station Aboa during the summer campaign in December 2010 – January 2011.

2 MEASURING SITE AND EQUIPMENT

The station Aboa is located at Basen nunatak in west Dronning Maud Land (Fig. 1). The measurements were carried out at practically flat snow surface about 10 km south-east of the station (73.106095 S, 13.170151 W). The inclination of the surface around the measuring site is about 10 m/km. The surface is practically homogeneous for more than hundred kilometers in the south-eastern sector of the measuring site thus the katabatic flows (mostly Eastern), thus,can be considered undisturbed. The measuring site was equipped with sodar, meteorological mast, snow-temperature profiling system and tethered balloon system. Also various snow measurements were carried out. Only the data of the sodar and of the meteorological mast are used for this study.

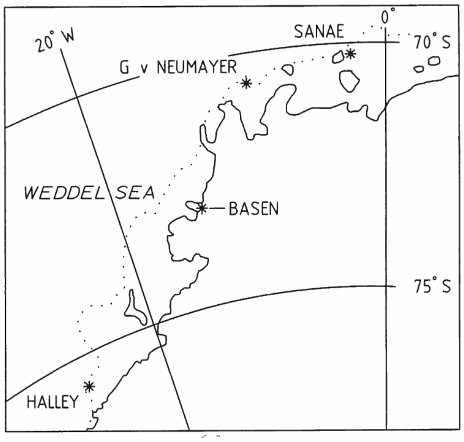

Figure 1: The location of the Basen nunatak

2.1 MAST

A 10-m meteorological mast was erected at the measuring site to provide the measurements in a surface layer. The mast was equipped with Campbell 107-type temperature probes at 5 levels (0.5, 1.2, 2.4, 4.7, and 10 m), 2D Gill WindSonic anemometers at same 5 levels, Kipp&Zonnen CNR4 radiation budget probe at 2 m, Väisälä HMP45AC temperature and humidity probe at 2 m and two Campbell CSAT3 3D sonic anemometers at 2 and 10 m.

The data of temperature, humidity and radiation sensors were acquired, preprocessed and stored by means of Campbell CR3000 data logger with 10-minute averaging time. The raw data from anemometers were ac-

Figure 2: The sodar antennas in a shield

quired by the sodar computer and processed off-line. 2D anemometers were sampled at 4 Hz and 3D anemometers at 20 Hz.

2.2 SODAR

We used the 3-component Doppler sodar LATAN-3m developed at the Obukhov Institute of Atmospheric Physics, Moscow [3]. The sodar was operated nearly continuously from 17.12.2010 to 22.01.2011. During the operation time, the most of the data losses occurred due to strong winds causing noise and due to power failures. No major problems caused by sound attenuation, experienced with a single-antenna version of LATAN-3m in Antarctica earlier [4], were found due to lower frequencies used and higher humidity.

The sodar was operated with 120 cm dish antennae at sounding frequencies 1600-2200 Hz. The operating mode with frequency-coded sounding pulse [5], and the parallel operation of the antennae was used to achieve high temporal resolution. The different frequency codings were used for the antennas to avoid crosstalk, each antenna used an individual set of 6 frequencies emitted as a series of 100-ms pulses, which resulted in 20-m vertical resolution. Tree antennae were mounted on wooden stands drilled into the hard snow surface, one vertically-pointing and three inclined to 30^o off-zenith with azimuths 190^o and 275^o. The sounding interval was set to 10 s, and sounding range was set to 20–800 m. The acoustic shields, needed to suppress the side lobes of the antennae and protect them from the wind, were constructed from snow blocks (Fig. 2).

In Latan-3 sodars the echo-signal from each sounding is processed separately and the information of signal and noise intensities, and on along-beam velocity component is stored for each range gate. During the campaign the raw echo-signals were stored as well for further reprocessing, should it be necessary.

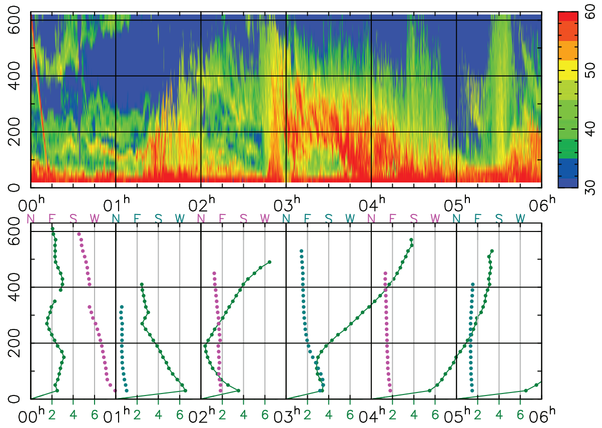

Figure 3: The sodar echogram and corresponding vertical profiles of wind speed (lines) and direction (dots) obtained 09.01.2011, 00-06 UTC. The wind speed profiles are shown in m/s. Y axis shows height above the surface in meters, the echo-intensity is given in dB

3 RESULTS

During the measurements, the net radiation flux under clear sky had very clear diurnal cycle from about -60 W/m^2 during night time to +200 W/m^2 during the day time. The steady katabatic flows were observed practically every cloudless night and lasted typically form about 10 pm till 10 am UTC. This, the appearance of katabatic flow had about 5 hours of hysteresis with respect to the radiative forcing.

The thickness of the katabatic flows varied from 5 to 100–200 meters above the surface. In most cases the katabatic flows were interacting with synoptic-scale phenomena producing rather complex and variable structure of the ABL (Fig. 3). The majority of wind profiles as well as the sodar echogram patterns observed during the campaign could hardly be classified into small number of types.

Below we consider two of few clear cases of katabatic flows on 15.01 and 16.01 2011, observed at practically same synoptic situation, but with different core heights and speeds.

When the katabatic layer is deep enough, the characteristic wind profile is clearly seen in the sodar data (Fig. 4). The wind speed is high near the ground and then gradually decreases to nearly zero above the flow core. The turbulent mixing occurs both below and above the wind speed maximum resulting in a strong return signal, which decreases as well. The clear directional shear is seen above the core.

The lower part of the flow is seen in the data of the

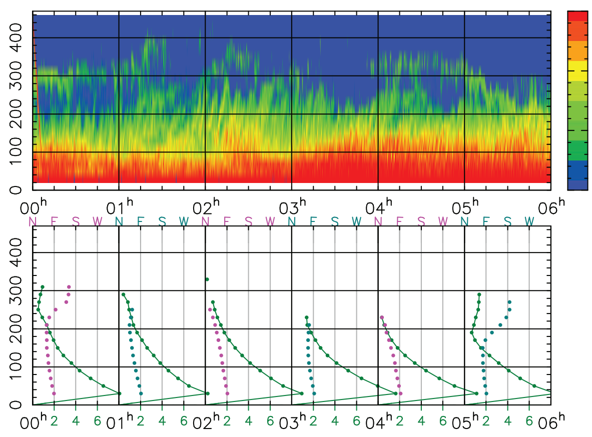

Figure 4: Same as in Fig. 3, but for 15.01.2011

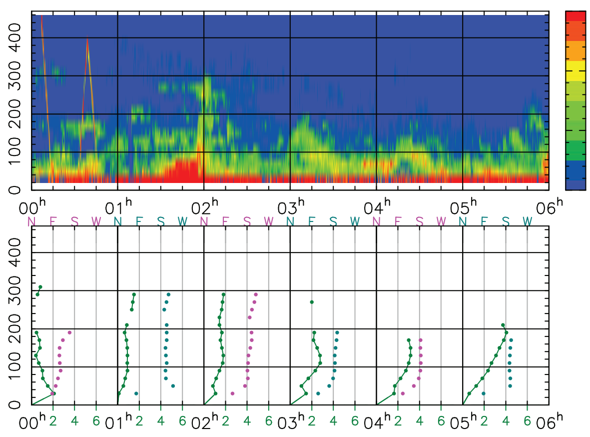

Figure 6: Same as in Fig. 4, but for 16.01.2011

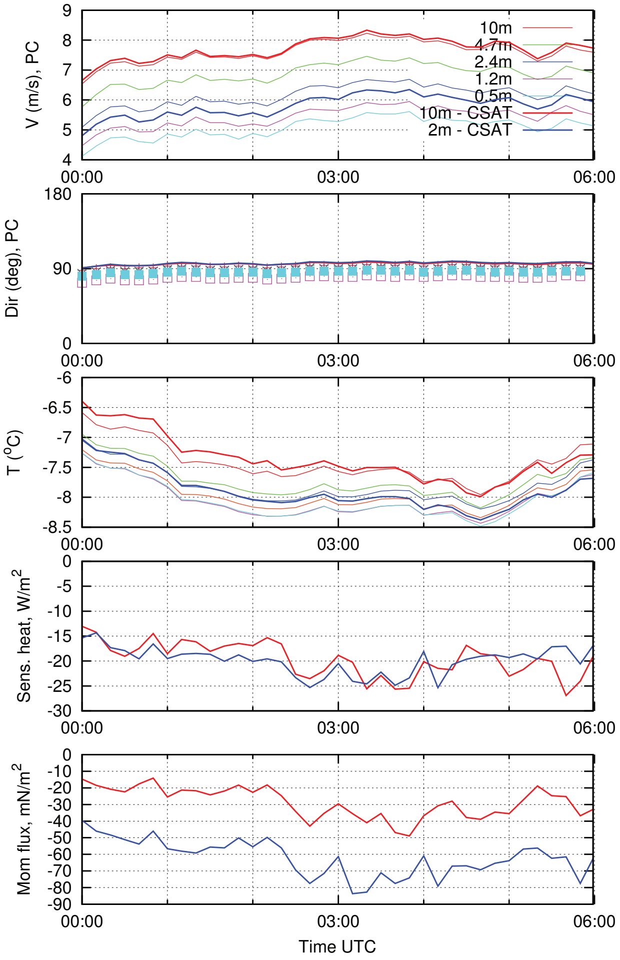

Figure 5: The time series of the data from the meteorological mast. 15.01.2011, The data of the CSAT3 anemometers are shown with bold lines

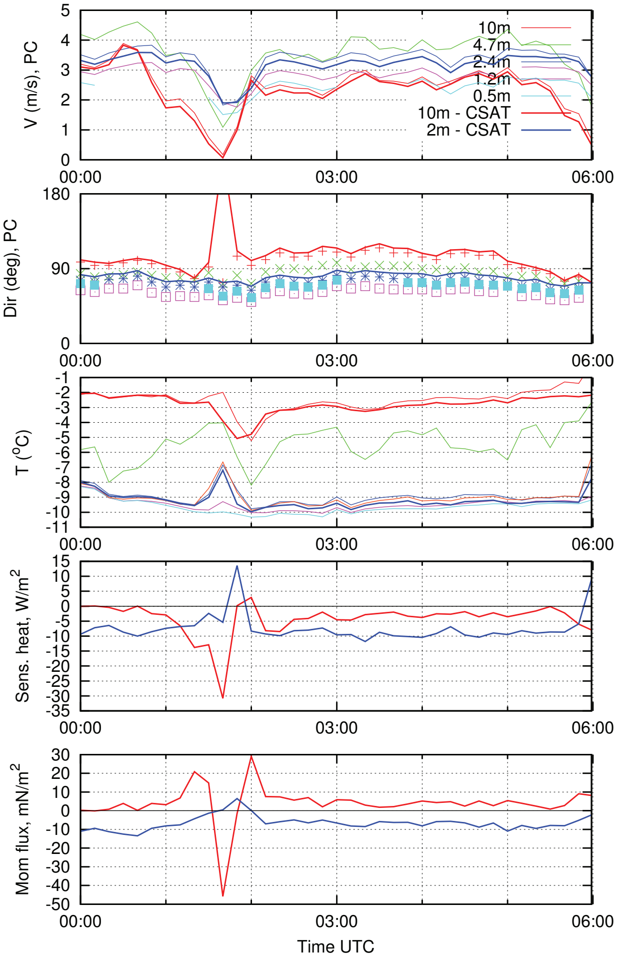

Figure 7: Same as in Fig. 5, but for 16.01.2011

anemometers (Fig. 5). The wind speed increases within the mast range. The directional shear is small. The temperature gradient is nearly linear within the tower range and is about 0.1 K/m. The sensible heat flux is practically same at 2 and 10 m, whereas the momentum flux differs rather strongly.

In the second selected case the katabatic layer was very shallow, well below the sodar range, however the wind shear and vertical diffusion are still enough to produce the sodar echo up to few hundred meters (Fig. 6). The maximum of the wind speed (∼3 m/s) was observed around 5-m height (Fig. 7). Such situations were characterised by very strong temperature gradients near the surface, but with much weaker sensible heat flux than in former case. The sensible heat flux practically vanishes already at 10 m. The directional shear is significant. The upward momentum flux is clearly seen above the jet core.

4 CONCLUSION

The ABL over slightly inclined snow-covered surface near Finnish antarctic station Aboa has been observed by means of a sodar and a meteorological mast during 1.5 months in austral summer 2010-2011. Despite the complex structure of the ABL during the field campaign, few clear cases of katabatic winds were identified. The same radiative cooling might result in different thickness of katabatic flow. Thinner katabatic flows have lower wind speed and weaker near-surface mixing, which results in stronger near-surface temperature gradients, but smaller heat fluxes. The collected dataset can be used for development and verification of simple models and parameterisations of the stable ABL.

ACKNOWLEDGEMENTS We are grateful to the staff of the Finnish Antarctic Research Program for managing and assistance in the field work. This study has been supported by the EC FP7 project ERC PBL-PMES (No. 227915), by Academy of Finland (ASTREX and AMICO projects).

References

1. Argentini, S., G. Mastrantonio, A. Viola, P. Pettré, and G. Dargaud (1996). Sodar performances and preliminary results after one year measurements at Adelie coast, East Antarctica. *Boundary-Layer Meteorol. 81*, 75–103.
2. Barry, R. G. (2008). *Mountain Weather and Climate*. Cambridge, U. K.: Cambridge Univ. Press.
3. Kouznetsov, R. D. (2007). Latan-3 sodar for investigation of the atmospheric boundary layer. *Atmospheric and Oceanic Optics 20*(8), 684–687.
4. Kouznetsov, R. D. (2009a). The multiple-frequency sodar with high temporal resolution. *Meteorol. Z. 18*(2), 169–173.
5. Kouznetsov, R. D. (2009b). The summertime ABL structure over an antarctic oasis with a vertical Doppler sodar. *Meteorol. Z. 18*(2), 163–167.
6. Vihma, T., E. Tuovinen, and H. Savijärvi (2011). Interaction of katabatic winds and near-surface temperatures in the Antarctic. *J. Geophys. Res. 116*, D21119.

VERTICAL WIND PROFILES AT A COASTAL SITE IN THE CENTRAL MEDITERRANEAN REGION.

A.M. Sempreviva[1,2], C.R. Calidonna[1], T. Lo Feudo[3], S. Federico[1], E. Avolio[1,3], L. De Leo[3], R. Wagner[2], MS Courtney[2]

[1]ISAC-CNR, U.O.S. Lamezia Terme, Comparto 15, I-88046 Lamezia Terme Cz (Italy)

[2] DTU, Frederiksborgvej 399, 4000 Roskilde, Denmark.

[3]Crati s.c.r.l., Lamezia Terme, Comparto 15, I-88046 Lamezia Terme, CZ (Italy),

ABSTRACT

An experiment was carried out during July 2009 to add new data on the vertical structure of the coastal flow at the coastal discontinuity. The coastal site is located 600m from the west coast of the Italian Region Calabria in the central Mediterranean. Here, we present the study of the vertical wind profile evolution in different weather regimes. A lidar Doppler, WLS7-0012-LEOSPHERE, was used to obtain time series of vertical profiles of wind speed and direction; the height of the Planetary Boundary Layer (PBL) was retrieved from a Vaisala CL30 ceilometer. The reflectivity of a sodar DSDPA90-24-METEK complemented the information from the lidar and characterizing the vertical thermal structures of the PBL. A surface standard meteorological station provided measurement of wind speed and direction, temperature, relative humidity, and solar radiation. An ultrasonic anemometer provided turbulent fluxes for estimating atmospheric stability. During summer, the site is characterized by both main synoptic flow and sea-land breeze system oriented along west-east. Sea breeze always develops due to the solar heating modulating the synoptic wind with its daily cycle. The sodar reflectivity before sunrise and after sunset helped in classifying the weather regimes in sea-land breeze, synoptic flow and a combination of the two. During the night, weak low level jets develop and the wind profile shows a daily variation. During synoptic flow, stability is near neutral and the wind vertical profile does not show a change in shape all day long. The most interesting surface turbulent features are detected during transition periods or during night and classified using the lidar, ceilometer and sodar signals.

1. INTRODUCTION

New ground-based remote sensing devices based on optical (lidars) and acustic (sodars) technology have been shown to be of use to study the vertical structure of the atmospheric boundary layer on land and offshore. Coastal areas, as where our site is located, (Figure 1) are particularly challenging environments due to the sharp discontinuity in the surface properties that demands high resolution models to resolve flows induced by the coastal discontinuity.

Doppler lidars as well as sodars are able to retrieve the vertical profiles of wind speed and direction based on different principles but can also provide complementary information because Doppler lidars are based on the backscatter by the aerosol content in the atmosphere and sodars are based on the backscatter due to dis-homogeneity of the atmospheric thermal structure.

However, in a preliminary analysis of the experiment, (Wagner et al.[1] and Lo Feudo et al. [2]) wind speed and directions from a lidar Doppler, WLS7-0012-LEOSPHERE and a sodar DSDPA90-24-METEK were compared and we found much spreading between the two instruments at the different levels.

Therefore, we choose to use the reflectivity of the sodar to complement the information from the Doppler lidar characterizing the vertical thermal structures of the PBL (Neff et al [3]). A surface meteorological station with standard and turbulent parameters provided the information on the surface atmospheric stability conditions.

Following, we present some cases of the evolution of the daily cycle of the vertical wind profile in different weather regimes.

2. EXPERIMENTAL SET-UP

An experimental summer campaign was organized in collaboration with the Wind Energy Department of the Technical University of Denmark (DTU) (former Risoe National Laboratory) from July 12 to August 5th 2009. The purpose of the experiment was to add new data on the vertical structure of the coastal flow at the coastal discontinuity in areas where atmospheric stability and sea breeze play a crucial role, in contrast to the sites available in Denmark.

The site proposed for the experiment is located in a coastal experimental research center were CNR - ISAC personnel operates a research coastal center in synergy with CRATI srl, an Italian SME working in meteorology applied to environmental and energy field.

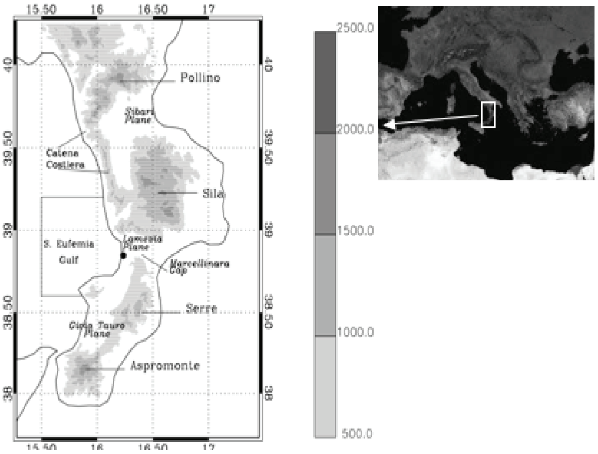

Figure 1. Calabria region in the central Mediterranean. Left: topography (m, gray shading) with topographical features cited into the text. The black dot shows the location of the experimental field.

The site is uniquely located at 600 m from the coastline with almost unobstructed onshore flow.

A combination of remote sensing devices based on different working principles were located at the site: a Lidar Ceilometer (CL31 VAISALA), a Pulse Doppler Lidar (Windcube WLS7-0012- LEOSPHERE) and a mini-sodar (DSDPA.90-24 METEK).

A standard meteorological station provided measurement of wind speed (U) and direction (DIR), temperature (T) at 10m a.g.l., relative humidity (RH), and solar radiation (R) at the surface. An ultrasonic Gill R3 anemometer provided turbulent fluxes for estimating atmospheric stability. Temperature differences between 2m and 5m (ΔT_{5_2}) and between 5m and 10m (ΔT_{10_5}) where measured by two Risoe inhouse devices to monitor the temperature structure in the lowest part of the surface layer.

The sodar and the meteorological station operated routinely. The ceilometer and the pulse Doppler Lidar were set up for the campaign period.

The Windcube, is a Doppler Lidar with a fixed focus, operating at the 1.5 μm wavelength. It has a 30° prism to deflect the beam from the vertical but here the prism does not rotate continuously. Instead, the prism holds still whilst the lidar sends a stream of pulses (5000-10000) in a given direction, recording the backscatter in a number of range gates (fixed time delays) triggered by the end of each pulse. After sending the required number of pulses, the prism rotates 90 degrees to the next azimuth angle to be scanned. A full rotation takes about 6s.

At each direction step, the Windcube combines the four most recent radial speeds at each height in order to obtain the horizontal and vertical speed and wind direction.

The sodar is a sounder for vertical profiles of wind and atmospheric turbulence and operates ranging from 45m to 405 m height with a working frequency at 1280 Hz. Data are retrieved averaging every 10 minutes.

Figure 2 shows the time series of DIR, U, T, the virtual heat flux <w'T'>, and the Monin Obukhov stability parameter z/L, where L is the Obukhov length and z is the height a.g.l.. Data are collected by the surface meteorological station at the height of 10m and for the whole period of the experiment.

We note periods characterized by 1) well developed sea-breeze regimes with wind direction along west-east. 2) un-complete sea-breeze i.e. where wind direction during night comes from South and 3) synoptic wind from west. During summer, the synoptic wind is modulated by the breeze: an example is shown in Figure 3.

Figure 3 shows an example of vertical wind profiles of wind speed and directions in case of synoptic flows followed by one and a half day of un-complete sea breeze.

Figure 4 shows vertical profiles of wind speed and direction for three days 28-29-30 July 2009 of consecutive breeze regime. Note the de-coupling of the wind profile during night at a height of 100m where wind speed decreases seen also in Figure 5.

Figure 5 shows wind speed vertical profiles and time series of T from the sonic anemometer for 7 half an hours from 01:00 LT to 07:00 LT on 16 July 2009. Sodar reflectivity is shown for the whole day. Note the structure of the temperature signal and the wind profile following the change in stability during the night. Also, from 5:30 am LT to 7 am LT, thermal plumes develop and the temperature rises from 21^{o}C to 23^{o}C. At 7 am LT, thermals are fully developed and convection starts. The development of the thermal structure throughout the day can be followed by the sodar reflectivity signal.

3. FINAL REMARKS

We have presented examples of the development of the wind profile at a coastal site in different meteorological situations using ground-based remote sensing and surface measurements collected during an experiment carried out in July/August 2009.

From previous study (Lo Feudo et al 2010 [2] we have seen that during consecutive days with a stationary sea-land breeze regime, after the onset of the sea breeze at the Windcube's maximum obtainable measuring height is often limited to 180 m. However, as the sea breeze intensity increases and become stationary around 14:00

UTC, the maximum height reached by the Windcube increases. The ceilometer signal shows a decrease of the height of the discontinuity in aerosol concentration before and an increase after. We suppose that the sea breeze advection of marine aerosols, confirmed also by the ceilometer signal, is the cause of the LIDAR low signal-to-noise ratio at high levels.

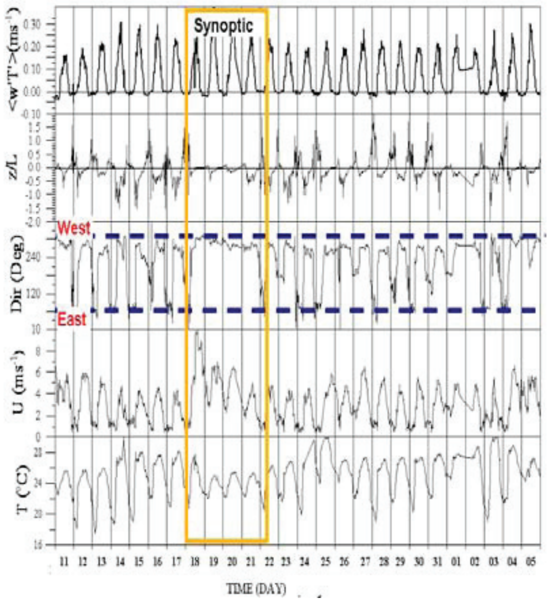

Figure 2. From top to bottom, time series of 15 minute average of mean kinematic virtual heat flux w'T', Monin Obukov stability parameter z/L, wind direction DIR, wind speed U and air temperature T. Note that positive values indicate downward heat flux. The orange box indicates three days of continuous synoptic flows. Note the modulation of the wind speed by the sea/-land breeze.

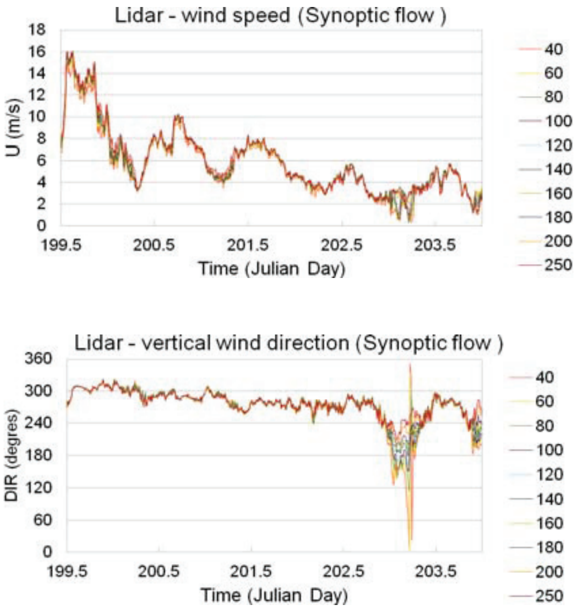

Figure 3. Vertical profiles of wind speed and direction for the four and a half days from 12:00 am of 18 July 2009: three of synoptic flow (orange box in Figure 2) and one and a half day with half sea breeze regime.

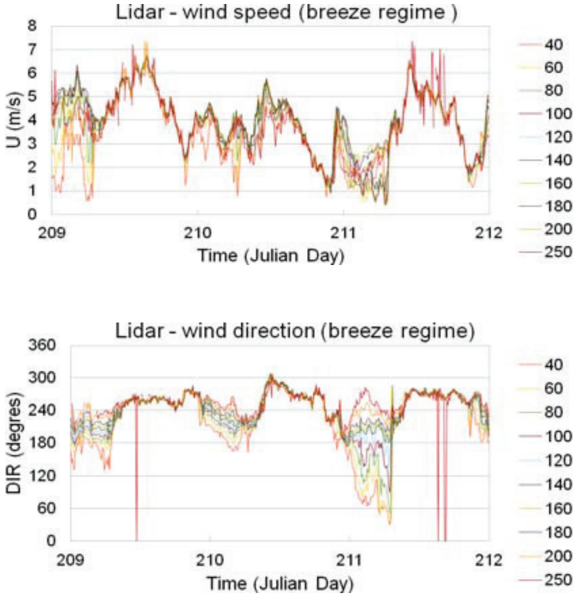

Figure 4. Vertical profiles of wind speed and direction for three days 28-29-30 July 2009 of consecutive breeze regime. Note that a weak low level jet like structure develops during night at a height around 100m where wind direction changes and wind speed decreases. (See also Figure 5)

During night time, the surface layer is stable and the land breeze is light, often contrasted by the synoptic westerly flow conditions. Night time in breeze conditions is characterized by stable stability and low level jets and a change in wind direction develop at a height of around 100m.

ACKNOWLEDGMENTS

We acknowledge funding from the FP6 Marie Curie Research Network, ModObs MRTN-CT-2006-019369. Rozenn Wagner was recipient of a grant and Anna Maria Sempreviva the coordinator. We thank ISAC-CNR and CRATI who supported the infrastructure expenses. We warmly thank Leosphere for lending us free of charge a new Windcube for the experiment.

References

1. R. Wagner, C. Calidonna, M. Courtney, Lo Feudo, L. De Leo, A. M. Sempreviva: 2010 Use of Doppler LIDAR for measuring the vertical profiles of wind speed at a coastal site Poster. ISARS 2010, International Symposium for the Advancement of

Boundary Layer Remote Paris, France, 28-30 June 2010.

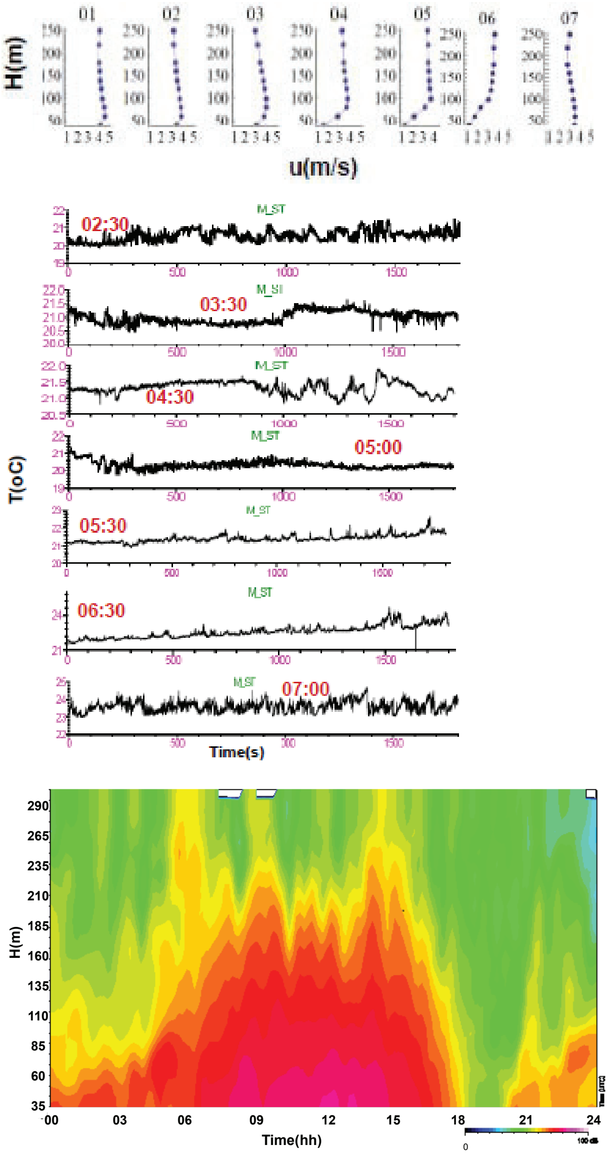

Figure 5. 16 July 2012 from 01:00LT to 07:00LT. Wind speed vertical profiles (Upper). Time series of T from the sonic anemometer for 7 runs of half a hour (Middle). Sodar reflectivity (Lower). Note the structure of the temperature signal and the wind profile following the change in stability during the night. At 5:30 LT thermal plumes develop and the temperature rises from 21°C to 23°C in one and a half hour. At 7 am LT, thermals are fully developped and convection starts. The development of the temperature structure can be followed by the sodar reflectivity signal.

2. T. Lo Feudo, C. Calidonna, A. M. Sempreviva, M. Courtney, L. De Leo, S. Federico, R. Wagner, and C. Bellecci: Flow evolution at a coastal site in the Central Mediterranean. Oral Presentation. ISARS 2010, International Symposium for the Advancement of Boundary Layer Remote Paris, France, 28-30 June 2010.

3. Neff, W. D., and R. L. Coulter, 1986: Acoustic remote sensing. Probing the Atmospheric Boundary Layer, D. H Lenschow, Ed., Amer. Meteor. Soc., 201–239.

4. Federico S., Pasqualoni, L., Sempreviva A.M., De Leo L., Avolio E., Calidonna C.R., and Bellecci C. The seasonal characteristics of the breeze circulation at a coastal Mediterranean site in South Italy, Adv. Sci. Res., 4, 47-56, 2010. www.adv-sci-res.net/4/47/2010/ doi:10.5194/asr-4-47-2010.

5. De Leo L., Federico S., Sempreviva A.M., Pasqualoni L., Avolio E., Bellecci C. (2008). Study of the development of the sea breeze and its micro-scale structure at a coastal site using a Multi-Tone Sodar system. Earth Environmental Science, 1, 2008. doi:10.1088/1755-1307/1/1/012054.

COASTAL BOUNDARY LAYER WIND PROFILE BASED ON SODAR DATA – BULGARIAN CONTRIBUTION TO COST ACTION ES0702

Ekaterina Batchvarova[1], **Damyan Barantiev**[1], **Mikhail Novitzky**[2]

[1]*National Institute of Meteorology and Hydrology, Blvd Tzarigradsko chaussee No. 66, 1784 Sofia, Bulgaria,*
Ekaterina.Batchvarova@meteo.bg, Damyan.Barantiev@meteo.bg
[2] *Research and Production Association 'Typhoon' - Obninsk, Russian Federal Service on Hydrometeorology and Environmental Monitoring, Russia, novitsky@typhoon.obninsk.ru*

ABSTRACT

Three years of sodar (SCINTEC MFAS) data at Ahtopol meteorological observatory (Bulgarian Black Sea coast) allowed climatological analysis of the wind profile under different conditions: breeze circulation (sharp onset of the sea breeze after nocturnal land breeze), combination of local and synoptic forcing (gradual onset in wind speed and wind direction for the sea breeze) and no sea breeze (at synoptic flow from the sea and flow the land). The novel results are possible for first time in Bulgaria, as the meteorological service and the country as whole have no network of remote sensing instruments.

For use in atmospheric composition studies, the height of the internal boundary layer is estimated based on turbulence eddy correlation measurements at 500 m inland from the coast and is compared to the internal boundary layer estimated from the sodar wind profile under sea breeze conditions.

The sodar and turbulence observation programmes start a climatological record for the structure of the boundary layer at the Bulgarian Black Sea coast. The monitoring will develop further to cover temperature and humidity profiles, ozone and aerosol concentrations, etc. The location is for the moment as a regional background air pollution station. Although in Bulgaria the surroundings are Natural park area, future industrial development are possible there and also in the neighbouring country.

1. INTRODUCTION

During the last two decades of XX century, a number of experimental campaigns were carried out worldwide using Doppler wind radars, lidars, sodars, instrumented tall masts, mesoscale networks of ground and aerological stations as described in papers [1 – 5]. The aim of such studies was to provide data for evaluation of mesoscale models performance in coastal areas and to develop further the parameterisations used in these models. As discussed in [6], the variety of physical, geographical and climate conditions related to sea breeze circulations, as well as weather patterns in coastal regions is huge, so mesoscale models need to be constantly and vastly evaluated. As noted in [7], the sea breeze is well known and well studied boundary-layer phenomenon, but there still remain issues for investigation about its structure and dynamics, especially in regions of complex or sloping topography.

For this reason, conducting detailed meteorological observations in coastal areas is very important issue both from scientific and practical point of view. Moreover, the present day remote sensing technologies developed robust instruments allowing continuous monitoring and new quality of data for model evaluation [8 -10].

2. COST ACTION ES0702

The use and importance of ground based remote sensing instruments for the weather and climate studies and operational work at the meteorological offices was recognized at European level by the COST Office through the funding of the COST Action ES0702 EG-CLIMET in 2007. The action gathered the efforts of leading meteorological services in Europe in the task of setting up networks of ground based remote sensing instruments. The technology in scope includes aerosol lidars of various types (ceilometers, backscatter aerosol lidars, Raman lidars, etc); Doppler lidars, radars, sodars; microwave rain radars; microwave radiometers. COST Action ES0702 aims also at developing procedures for assimilation of the data from these instruments in the weather prediction and climate models, a task on which ECMWF is collaborating in the action.

For a 4-year period, COST Action ES0702 succeeded in identifying the existing types of instruments and measuring sites in the 20 participating countries and to start common research on the wider and more effective use of them. One of the main achievements currently is the connection of the ceilometers across Europe in a network and the studies on the wider and multipurpose use of these instruments.

Another major achievement COST Action ES0702 has been the data supplied by these new unmanned lidars in the detection of Icelandic volcanic ash in April-May 2010. They have been able to establish that the ash is present in thin layers which are well captured by the models of the Met Services. This work has been pivotal in decisions to reopen air space over Europe.

In Bulgaria, the economic conditions have not allowed yet the operational use of the new technology. One sodar is operation since 2008 at a remote site on the Black Sea coast within a Bulgarian – Russian collaborative project [11, 12] and a Jenoptic (CHM-15k) ceilometer is operation at the Sofia University under a project of the Bulgarian National Science Fund since 2008 [13, 14].

These instruments are currently used for atmospheric boundary layer research, but through the participation of Bulgaria in COSTES0702 are included in wider international effort on studies of height and structure of the atmospheric boundary layer in Europe.

3. SITE AND INSTRUMENTS

The remote sensing observations started at the meteorological observatory of Ahtopol (southeast Black Sea coast of Bulgaria) in July 2008 under a joint research project between the National Institute of Meteorology and Hydrology - Bulgarian Academy of Sciences (NIMH-BAS) and the Research and Production Association (RPA) “Typhoon” in Obninsk - Russian Federal Service on Hydrometeorology and Environmental Monitoring (Roshydromet). The site is located in flat grassland, 30 m above sea level, about 500 m inland from a steep about 10 m high coast. The coast line is stretching out from north-north-east to south-south-west direction, therefore the winds from the sector 0 – 150 degrees are representing marine conditions. For about 20 years (1970 - 1990) the site was used for the launch of stratospheric rockets and therefore was and still is remote, Figure 1.

As shown in Figure 2, in addition to standard synoptic station equipment, an ultra sonic anemometer and a solar radiation sensor are mounted on a meteorological mast at height of 4.5 m; air temperature and humidity sensors are installed at 2 m height within a thermometer screen. These sensors form an automatic meteorological station named MK-15 assembled by “Typhoon”. The first prototype of the sonic anemometer was used during the International turbulence comparison experiment (ITCE-81) as described in [15]. The frequency of measurements of MK-15 is 0.5 Hz and records are made every 10 seconds.

The sodar is located on the roof of the administrative building at about 4.5 m high, Figure 3. It is a SCINTEC Flat Array middle range instrument (MFAS) with frequency range 1650 – 2750 Hz; 9 emission/reception angles (0°, ±22°, ± 29°); maximum 100 vertical layers; range between 500 – 1000 m; accuracy of horizontal wind speed 0.1 – 0.3 ms-1; range of horizontal wind speed ± 50 ms-1; accuracy of vertical wind speed 0.03 – 0.1m/s; range of vertical wind speed ± 10 ms-1; accuracy of wind direction 2 -3 degrees.

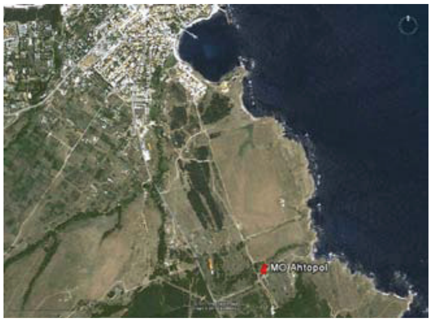

Figure 1. Google view of the surroundings of the Meteorological Observatory (MO) Ahtopol (42.08N, 27.95E).

Figure 2. The site for standards synoptic and turbulence measurements (left) and the SCINTEC sodar (right).

The sodar was set to measure in regime “optimized pulses for resolution” at 47 levels from 30 to 500 m with resolution of 10 m. The averaging time is 20 minutes and the records are made every 10 minutes, thus presenting running 20-minute averages.

Concerning data availability, problems with MK-15 occurred in winter 2008/2009, in spring 2011 and 2012.

Apart from electricity shut down problems, the sodar data are available during the days for the entire period since July 2008. In summers of 2008 and 2009 the night operation was suspended. Full diurnal operation and more stable electricity network were achieved since October 2009. The availability of sodar data at different heights was analysed for the period July 2008 – June 2009. At 50 m height, data are available between 83% of the time in December 2008 and 97 % of the time in May 2009. At 200 m height, the availability is between 82 % (March 2009) and 96 % (May 2009).

4. BREEZE CLASSIFICATION

Based on sonic anemometer and other surface data, the sea breeze days in 2009 were divided in 3 classes, Table 1 and Figures 3 and 4. The measurements started late July 2008, but some very clear breeze days were captured later in 2008. During the summer of 2009, weak pressure fields were observed over the Bulgarian Black Sea coast and therefore the local circulation has developed during most of the days.

The main goal of the studies is to reveal the vertical structure of the atmospheric boundary layer at the Black Sea coast connecting it to the surface observations.

Table 1. Breeze classification for summer 2009

Mont	July	Aug.	Sept.
Number of days with sonic anemometer data	30	30	26
Number of days with sea breeze	28	18	16
Number of days with sea breeze front in the morning (Class 1)	16	15	13
Number of days with sea breeze front in the morning and in the evening (Class 2)	6	2	2
Number of days with gradual wind direction change (Class 3)	6	1	1

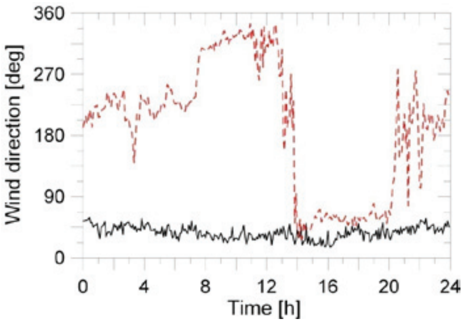

Figure 3. A day with no breeze (black line, 2 August 2008) and day with combined local and synoptic forcing (red line, 6 August 2008) which cause late onset of the sea breeze of Class 2.

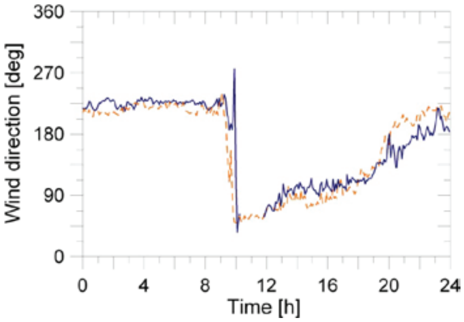

Figure 4. Days with pronounced breeze front and sharp onset of the sea breeze (blue line, 5 August 2008; orange line, 5 September 2008). These days are classified in Class 1, as the evening change to land breeze is gradual.

5. SODAR DATA ANALYSIS

The sodar data at Ahtopol allow enriching the sea breeze studies in Bulgaria and Russia [16, 2, and 3]. As seen in Figures 5 – 8, the coastal boundary layer structure and the formation of internal boundary layer can be studied based on wind and turbulence data derived from the sodar. As example, on 7 May 2009, clear breeze cell has formed within 500 m above sea level. There is evidence for a thermal internal boundary layer (TIBL) that reaches up to about 100 m at 11:20 and 200 m at 13:20 (Figure 9) in the field of the standard deviation of the vertical wind velocity. Further analysis will reveal if it is possible to use only sodar for TIBL retrieval, or temperature profiles are also needed.

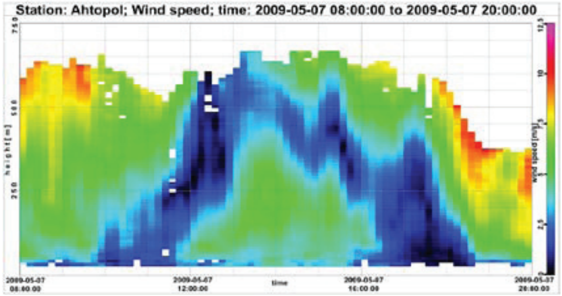

Figure 5. Wind speed on 7 May 2009, a day when almost the entire sea breeze cell is captured in the sodar data.

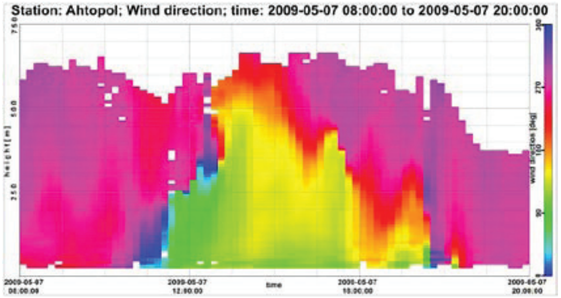

Figure 6. Wind direction on 7 May 2009.

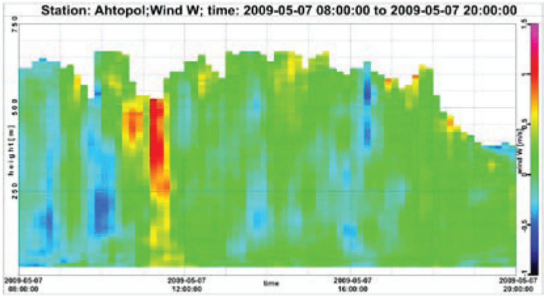

Figure 7. Vertical wind speed on 7 May 2009.

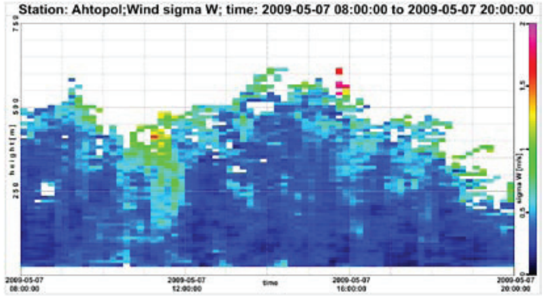

Figure 8. Standard deviation of the vertical wind speed on 7 May 2009.

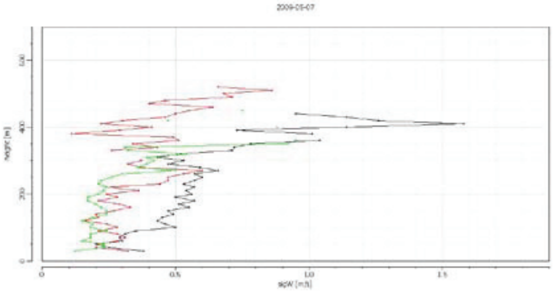

Figure 9. Profiles of the standard deviation of the vertical wind speed on 7 May 2009 at 11:20 (black), 13:20 (red) and 19:20 (green) local time.

ACKNOWLEDGMENTS

This work is part of scientific cooperation between the meteorological services of Bulgaria and Russia. The work is part of the activities within COST Action ES0702 (EG-CLIMET) and also related to COST ES1002 (WIRE).

REFERENCES

1. Alpert, P. and Rabinovich-Hadar, M., 2003: Pre- and post-sea-breeze frontal line – a meso-γ-scale analysis over South Israel, *J. Atmos. Sci*., **60**, 2994-3008.

2. Batchvarova, E. and Gryning, S.-E., 1998: Wind climatology, atmospheric turbulence and internal boundary layer development in Athens during the MEDCAPHOT – TRACE experiment, *Atmos. Environ.*, **32**, 2055-2069.

3. Batchvarova, E., Cai, X., Gryning, S.-E., and Steyn, D., 1999: Modelling internal boundary layer development in a region with complex coastline, *Bound.-Layer Meteor.*, **90**, 1-20.

4. Wilczak, J. M., Dabberdt, W. F., and Kropfli, R. A., 1991: Observations and numerical model simulations of the atmospheric boundary layer in the Santa Barbara coastal region, *J. Appl. Meteorol*., **30**, 652-673.

5. Zhong, S. and Takle, E. S., 1992: An observational study of sea- and land-breeze circulation in an area of complex coastal heating, *J. Appl. Meteorol*., **31**, 1426-1438.

6. Simpson J. E., 1994: Sea breeze and local wind. Cambridge: Univ. Press, 234 pp.

7. Wilczak, J. M., Gossard, E. E., Neff, W. D., and Eberhard, W. L., 1996: Ground-based remote sensing of the atmospheric boundary layer: 25 years of progress, *Bound.-Layer Meteor*., **78**, 321-349.

8. Floors, R., Batchvarova, E., Gryning, S.-E., Hahmann, A. N., Peña, A., and Mikkelsen, T., 2011: Atmospheric boundary layer wind profile at a flat coastal site – wind speed lidar measurements and mesoscale modelling results, *Adv. Sci. Res*., **6**, 155-159.

9. Novitzky M. A., Mazurin N. F., Kulijnikova, L. K., Tereb L. A., Kalinicheva, O. U., Nechaev, D. R., and Safronov, V. L., 2010: Comparing measured wind and temperature profiles using commercial sodar and tall meteorological mast observations in Obninsk. *Problems of hydrometeorology and environmental monitoring*, ISBN 978-5-901579-21-3, **4**, 122-136. (In Russian)

10. O'Connor, E. J., Illingworth A. J., Brooks, I. M., Westbrook, C. D., Hogan, R. J., Davies, F., and Brooks, B. J., 2010: A method for estimating the turbulent kinetic energy dissipation rate from a vertically pointing Doppler lidar, and independent evaluation from balloon-borne in situ measurements, *J. Atmos. Ocean. Technol*., **27**, 1652-1664.

11. Barantiev D, Novitsky M, Batchvarova E, 2011: Meteorological observations of the coastal boundary layer structure at the Bulgarian Black Sea coast, *Adv. Sci. Res.*, **6**, 251-259, 2011.

12. Novitskii M. A., Kulizhnikova L. K., Kalinicheva O. Yu., Gaitandzhiev D., Barantiev, D, Bachvarova E, and Krysteva, K., 2012: Characteristics of wind speed and wind direction in the atmospheric boundary layer on the southern coast of Bulgaria, *Russian Meteorology and Hydrology*, **37**, 159-164.

13. Kolev N, Grigirov I, Evgenieva T, Donev E, Ivanov D, Kolarov G, Kolev I, Stoyanov, D, 2012: Combined lidar-ceilometer measurements in the troposphere over Sofia (Bulgaria), *Comptes rendus de l'Acad´emie bulgare des Sciences,* 65, 4, 491-498.

14. Evgenieva T, Wiman B. L. B., Kolev I., Savov P. B., Donev E. H., Ivanov, D. I., Danchovski V., Kaprielov B. K., Grigorieva, V. N., Iliev I. T., Kolev, N., 2011: Three-point observation in the troposphere over Sofia-Plana Mountain, Bulgaria *International Journal of Remote Sensing,* 32, 24, 9343–9363.

15. Tsvang, L. R., Zubkovski, S. L., Kader, B. A., Kalistratova, M. A., Foken T., Gerstmann, V., Przadka, A., Pretel, Ya., Zeleny, Ya., and Keder, J., 1985: International turbulence comparison experiment (ITCE-81), *Bound.-Layer Meteor*., **31**, 325-348.

16. Novitsky, M. A., Reible, D. D., Corripio, B. M., 1992: Modeling the dynamics of the land-sea breeze circulation for air quality modelling, *Bound.-Layer Meteor*., **59**, 163-175.

THE IMPACT OF LIQUID BEARING CLOUDS ON SURFACE BASED INVERSIONS ABOVE THE GREENLAND ICE SHEET

Nathaniel Miller[1], David Turner[2], Ralf Bennartz[3], Mark Kulie[4]

[1]*AOS/UW and SSEC/UW, 1225 W. Dayton Street*
Madison, Wisconsin 53706 USA, nate.miller@ssec.wisc.edu
[2]*NOAA/NSSL, 120 David L Boren Blvd.*
Norman, OK 73072 USA, dave.turner@noaa.gov.edu
[3]*AOS/UW and SSEC/UW, 1225 W. Dayton Street*
Madison, Wisconsin 53706 USA, bennartz@aos.wisc.edu
[4]*AOS/UW and SSEC/UW, 1225 W. Dayton Street*
Madison, Wisconsin 53706 USA, mskulie@wisc.edu

1. INTRODUCTION

The Greenland ice sheet (GIS) currently rises to over 3200 meters at its summit. A NSF funded project, dubbed ICECAPS (An Integrated Characterization of Energy, Clouds, Atmospheric state, and Precipitation at Summit), deployed an integrated suite of remote sensing instruments to answer questions concerning the current atmospheric state above the GIS, investigate factors that drive the mass balance, and characterize the energy budget at the atmospheric/ice interface.

The growth or decline of the Greenland ice sheet is dependent on the atmospheric state, which provides the context for the dynamical processes that transfer energy and mass to and from the surface. By investigating the interface between the free atmosphere and the surface, the factors leading to GIS change can be understood. Temperature inversions are characterized by increasing temperatures with altitude up to the top of the inversion layer and are an indicator of the stability of the boundary layer. Surface based inversions constrain vertical mixing, thereby providing a limit to the degree the surface can interact with the atmosphere.

2. MWR RETRIEVALS

A pair of microwave radiometers (MWRs) covering the spectral range from 22.24 to 150.0 GHz were installed at Summit Station as part of the ICECAPS project. Using calibrated brightness temperatures from the MWRs, retrievals were developed for this extremely cold and dry environment. A statistical retrieval of precipitable water vapor (PWV) was developed utilizing the 23.84 and 31.4 GHz channels similar to [1]. A four channel (23.8, 31.4, 90.0, and 150.0 GHz) physical retrieval [2] was implemented in order to resolve the low liquid water paths (LWP) that occur at Summit. A statistical retrieval was developed to retrieve temperature profiles every 40 minutes using 48 pseudo-channels (6 frequencies, 8 elevation angles). Eliminating the bias in the calibrated V-band brightness temperatures improves both the bias and RMS error of the MWR temperature retrievals compared to radiosonde profiles taken within a half an hour of the MWR retrieval (Fig 1).

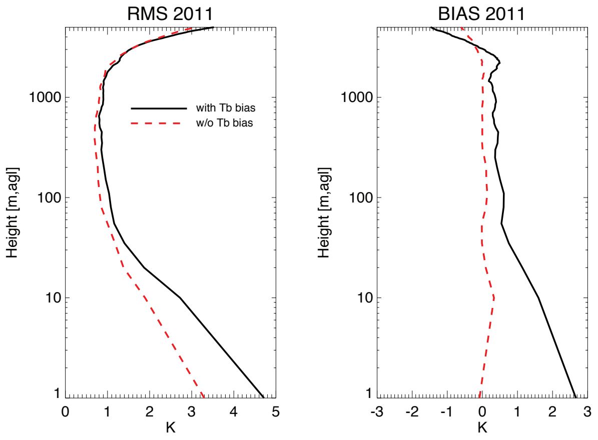

Figure 1. MWR retrieved temperature profiles compared to radiosonde profiles for 623 cases over the course of 2011. The RMS error (left) and bias (right) for the original calibrated brightness temperatures (Tb) is shown in black solid lines. Retrievals using bias corrected calibrated Tb values are represented by the red dashed lines.

3. RESULTS

MWR retrievals were used to characterize monthly distributions and mean values of PWV, LWP and temperature profile features for the year 2011. The retrieved PWV values are below 8 mm for the year with the largest average values occurring in July. In addition, July and August show an increase in the number of liquid bearing clouds with elevated LWP values (Fig 2).

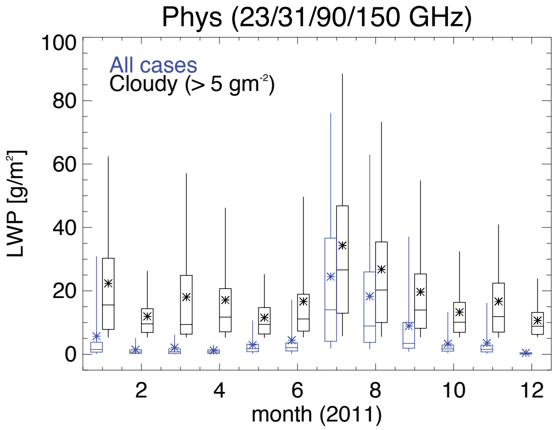

Figure 2. Liquid water path over the course of 2011 calculated via a physical retrieval [2] utilizing four frequencies (23.8, 31.4, 90.0 and 150.0 GHz). The box indicates 25% and 75%, the whiskers 5% and 95%, the horizontal line inside the box is the median, and the * indicates the mean. The monthly distributions on the left (blue) are for all cases and the distributions on the right (black) are for the subset of cases where the LWP is over 5 g/m².

Surface based inversions (SBI) are a predominant feature across the GIS. Figure 3 shows the monthly values of depth, intensity, and occurrences for 2011.

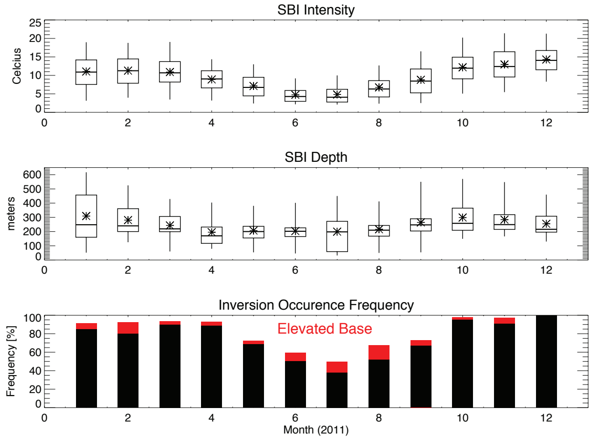

Figure 3. Surface based inversion intensity (top) and depth (middle) monthly averages (*) with box and whisker plots. The box indicates 25% and 75%, the whiskers 5% and 95%, and the horizontal line is the median. In order to be considered a surface based inversion the base must at the surface and the intensity must be greater than 2 K. The lower panel shows the percentage of MWR temperature profiles that meet these criteria over the course of 2011. The occurrence frequencies of surface based inversions are in black and inversions with an elevated base (> 0 m) are shown in red.

The monthly occurrence of SBI is above 80% during the winter months and is less frequent during the time period from May-September where the minimum in July is 38%. The SBI intensities have average values above 10°C during the winter with decreasing intensities in the summer months. The SBI depths vary the most in January and July with average inversion depths of about 200 meters from April to August and increased depths in the winter months. Although the atmospheric state is measured twice daily at Summit via radiosonde soundings, the advantage of using the MWRs is headlined by their close-to autonomous data collection at high temporal resolution. The MWR scanning strategy allows a temperature profile to be retrieved every 40 minutes, where a majority of the information content originates from the lowest 1 km. The high temporal resolution of the MWR temperature retrievals is utilized in a case study.

3.1 Case Study

The evolution of the temperature inversion is investigated for a case on February 20, 2011 (Fig 4). Within a matter of a few hours the presence of a liquid bearing cloud corresponds to a warming of the surface and decay in the strength of the inversion thus changing the stability of the boundary layer. Later in the day the strength of the surface based inversion steadily grows during clear sky conditions.

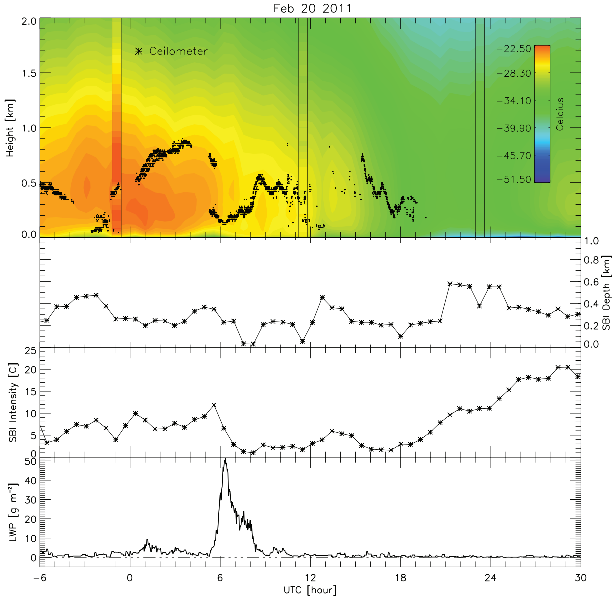

Figure 4. A case study during February 20, 2011 (+/- 6 hours). The top panel shows the MWR retrieved temperature profiles (color) with the cloud base height as determined by the ceilometer (black dots) and 3 radiosonde temperature profiles between the vertical solid black lines. The evolution of the depth (second panel from the top) and intensity (third panel from the top) of the inversion is shown in conjunction with the liquid water path (bottom panel).

3.2 SBIs and LWP

The data from 2011 shows that SBI strengths tend to decrease as the LWP values increase (Fig 5).

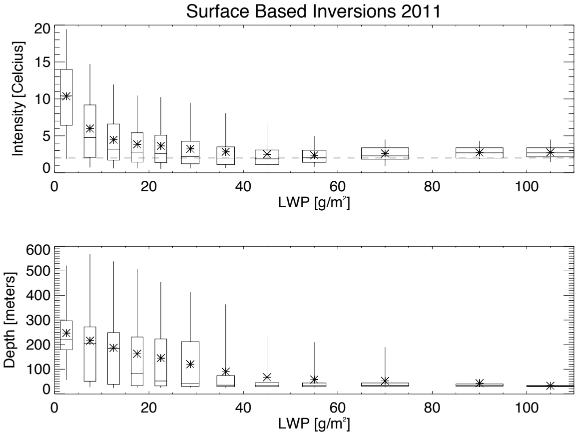

Figure 5. Surface based inversion intensity (top) and depth (bottom) as a function of the mean LWP five minutes before temperature retrieval. Only cases where the mean wind for the day is less than 10 m/s are shown. The box indicates 25% and 75%, the whiskers 5% and 95%, the horizontal line inside the box is the median, and the * indicates the mean.

For clear sky cases, when the LWP is between 0-5 g/m^2, over half of the inversions were deeper than 200 meters and the majority had a intensity of over 10°C.

4. CONCLUSION

Since the case study suggests that the presence of liquid bearing clouds lead to the decay of surface based inversions while the subsequent clear sky scene leads to the formation of a stronger and deeper inversion, the SBI metrics were investigated under the influence of LWP. The decrease of SBI intensity is presumably due to the limited radiative cooling of the surface by the presence of liquid in the cloud, which serves to increase the downward long-wave flux compared to the initial clear sky value. Without a temperature inversion the stability above the surface is threatened allowing for a deeper mixed layer which would enhance the interaction between the GIS surface and the atmosphere.

A possible increase in cloud frequency and/or change in cloud microphysics above the GIS would further inhibit inversions and lead to changes in the atmosphere/ice interaction in the boundary layer and warmer temperatures at the surface.

ACKNOWLEDGMENTS

The National Science Foundation is acknowledged for the provision of funding under grant No. 0904152.

REFERENCES

1. Liljegren, J. C., E. E. Clothiaux, G. G. Mace, S. Kato, and X. Dong, 2001: A new retrieval for cloud liquid water path using a ground-based microwave radiometer and measurements of cloud temperature. *J. Geophys. Res.*, **106 (D13)**, pp. 14485–14500.

2. Turner, D. D., S. A. Clough, J. C. Liljegren, E. E. Clothiaux, K. E. Cady-Pereira, and K. L. Gaustad, 2007: Retrieving liquid water path and precipitable water vapor from the atmospheric radiation measurement (ARM) microwave radiometers. *IEEE Trans. Geosci. Remote Sens.*, **45 (11)**, pp. 3680–3690.

Session 6 – Oral Presentations

PLANETARY BOUNDARY CHARACTERISTICS IN COMPLEX TOPOGRAPHY MEASURED WITH GROUND-BASED REMOTE SENSING SYSTEMS

***Christine Ketterer*[1], *Martine Collaud Coen*[2], *Alexander Haefele*[2], *Olaf Maier*[2], *Dominique Ruffieux*[2], *and Ernest Weingartner*[3]**

[1]*MeteoSwiss, currently at Meteorological Institute, Werthmannstrasse 10, 79085 Freiburg, Germany*
[2]*MeteoSwiss, Ch Aerologie, 1530 Payerne, Switzerland, dominique.ruffieux@meteoswiss.ch*
[3]*Paul Scherrer Institute, Laboratory of Atmospheric Chemistry, 5232 Villigen, Switzerland*

ABSTRACT

During the CLoud and Aerosol Characterization Experiment (CLACE) at the Jungfraujoch (3580 m asl) in summer 2010, various in-situ (at Jungfraujoch) and ground-based remote sensing systems (at Kleine Scheidegg, 2061 m asl, at the foot of Jungfraujoch) were installed in this high-alpine location. The main goal of this experiment was to study chemical and physical properties of aerosols in order to investigate their effects on cloud characteristics. The local meteorology is an important driving factor for cloud formation. Horizontal and vertical wind motions a well as the presence of a planetary boundary layer at these altitudes are critical factors to better understand the cloud formation and the aerosol behavior of this region.

At the Kleine Scheidegg, which is located in the vicinity of the WMO Global Atmosphere Watch (GAW) Jungfraujoch station (horizontal distance of ~4.5km), several remote sensing measurement devices were installed, including a low-tropospheric wind profiler and a ceilometer (Figure 1). These systems were operated during the entire 2-month campaign in July and August 2010.

The paper will focus on the analysis of ground-based remote sensing data. The planetary boundary layer (PBL) detection and its possible effect on aerosol concentrations in such a complex topography will be presented. Depending on the weather situations, an increase of the aerosol scattering and absorption coefficients measured at the top of the Jungfraujoch were correlated to the presence of the PBL measured with the ground-based remote sensing systems. During these events, the Jungfraujoch location cannot be considered as a free tropospheric site but is influenced by injections of the PBL, which include pollution transported from the Swiss Plateau by updraft motions.

1. MOTIVATION

Planetary boundary layer research is still a relatively young field with many unsolved issues [1], [2]. One of them is precisely the development of PBL in mountainous terrain [2] as well as the development of algorithm to detect the planetary boundary layer using remote sensing instruments as lidar ceilometers or wind profilers.

It is particularly interesting to correlate PBL height and aerosol measurement at the Jungfraujoch. During most of the time background concentration of chemicals and aerosols of the free troposphere are measured at the Jungfraujoch, which is not directly influenced by anthropogenic pollution. Nevertheless, PBL reaches the Jungfraujoch during fair-weather days in summer [3] and thus affects aerosol measurements as absorption coefficient which is mostly sensitive to black carbon, or scattering coefficient and particle number, which are also sensitive to new particles.

2. EXPERIMENT SETUP

The operational WMO GAW station of the Jungfraujoch was used as a place for in-situ measurements during CLACE 2010. Beside the operational surface meteorological station, a nephelometer, an aethalometer, and a CCNC (cloud condensation nuclei counter) were measuring the main characteristics of aerosols and clouds characteristics (Figure 1). Several remote sensing measurement devices were located at Kleine Scheidegg, including a low-tropospheric wind profiler, a microwave radiometer and a ceilometer. Furthermore a sonic anemometer, a sun- and aureole-spectrometer, a polarimeter and scanning UV backscatter lidar were installed at Kleine Scheidegg (Figure 1).

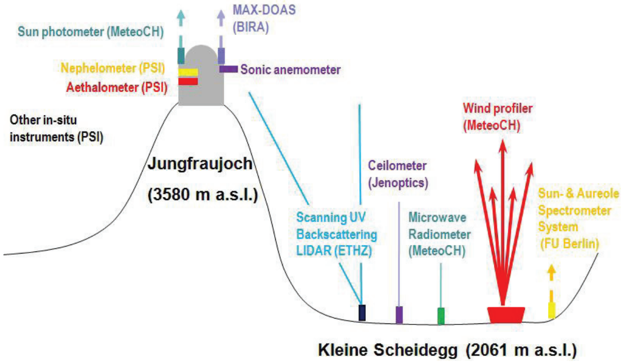

Figure 1. Measurement setup for the CLACE 2010 Experiment.

3. PLANETARY BOUNDARY LAYER

The ceilometer and the wind profiler were installed at the Kleine Scheidegg to investigate the origin of the air masses and the cloud development, but also to analyze the PBL height. As the wind profiler provider's software was unable to detect planetary boundary layer even during fair-weather days, a new algorithm was developed to monitor the PBL height.

A typical example of PBL determination is shown in Figure 2. Phenomenon, which can be detected in several datasets are two declining layers within around 2am. Generally not much is known about the decay of the PBL. It is probably influenced by the mountain-valley circulation. The lower curve shows the decay of PBL above the Kleine Scheidegg, while the second curve may show aerosols transported by downdrafts from Jungfraujoch.

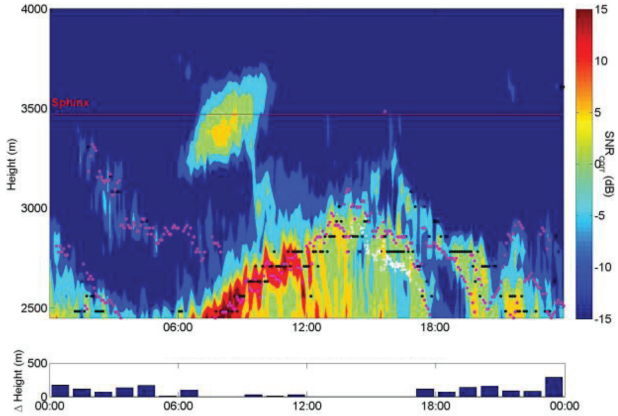

Figure 2. Temporal evolution at Kleine Scheidegg, 7 July, 2010. Top panel: range-corrected signal to noise ratio derived from wind profiler, wind profiler PBL (black dots), ceilometers PBL (purple dots) and clouds (white). The red line labeled "Sphinx" corresponds to the altitude of the Jungfraujoch station. Bottom panel: height difference between hourly averaged determined PBL of both measurement devices.

Ceilometer detects the presence of PBL by calculating aerosol gradients, corresponding to an aerosol layer while wind profiler detection is based on moisture and turbulence gradients. Nevertheless the ceilometer PBL and the wind profiler PBL agree well, especially under cloud free conditions and during day time (Figure 3). Meanwhile the ceilometer seems to be less performing in presence of clouds while the wind profiler has detection problems during the night.

When the PBL exceeded around 2800 m asl, injections of the PBL are transported upwards by slope winds. This was confirmed by aerosol measurements at the Jungfraujoch. The measured aerosol absorption and scattering coefficients showed an increase during the afternoon.

The results of the comparison between PBL heights derived by the NWP model COSMO-2 and retrieved from wind profiler and ceilometer measurements showed that COSMO-2 underestimated the PBL height at that site and time (not shown).

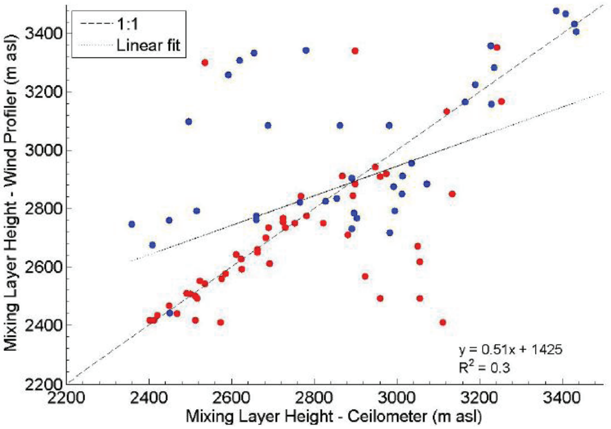

Figure 3. Scatterplot of the mixing layer height derived from ceilometer and wind profiler (daytime hourly means) for 8 fair-weather days. Red points are the PBL without clouds and blue dots PBL with clouds.

4. COMPARISON BETWEEN METEOROLOGY AT KLEINE SCHEIDEGG AND AEROSOL MEASUREMENTS AT JUNGFRAUJOCH

Comparison between PBL temporal evolution estimates and in-situ measurements at Jungfraujoch is shown in Figure 4. PBL air reaches Jungfraujoch on 8, 9, 12, and 20 July, 2010. This is reflected in the absorption coefficient (b_{abs}) measurements. Attention should be paid to spikes that are locally created by snow groomer and other human activities most of the time around 8-9 am and 1pm. On 7 July, the PBL remains below 3000 m , so that neither the absorption coefficient nor the scattering coefficient (b_{scat}) increases. It is to conclude that no PBL air reaches Jungfraujoch, even though the number of new particle (N) increases, probably due to new particles formation and subsequent growth at the Jungfraujoch. In contrast, b_{abs} and b_{scat} increase with an maximum in the late afternoon on 8, 12, and 20 July, 2010. b_{abs} and b_{scat} rise suddenly in the evening on 9 July, 2010. From wind profiler measurements, it can be deduced that a strong updraft lifts air pollutants to the Jungfraujoch. During these days, subsidence was predominant. On the other fair-weather days, PBL air does not reach the height of the Jungfraujoch.

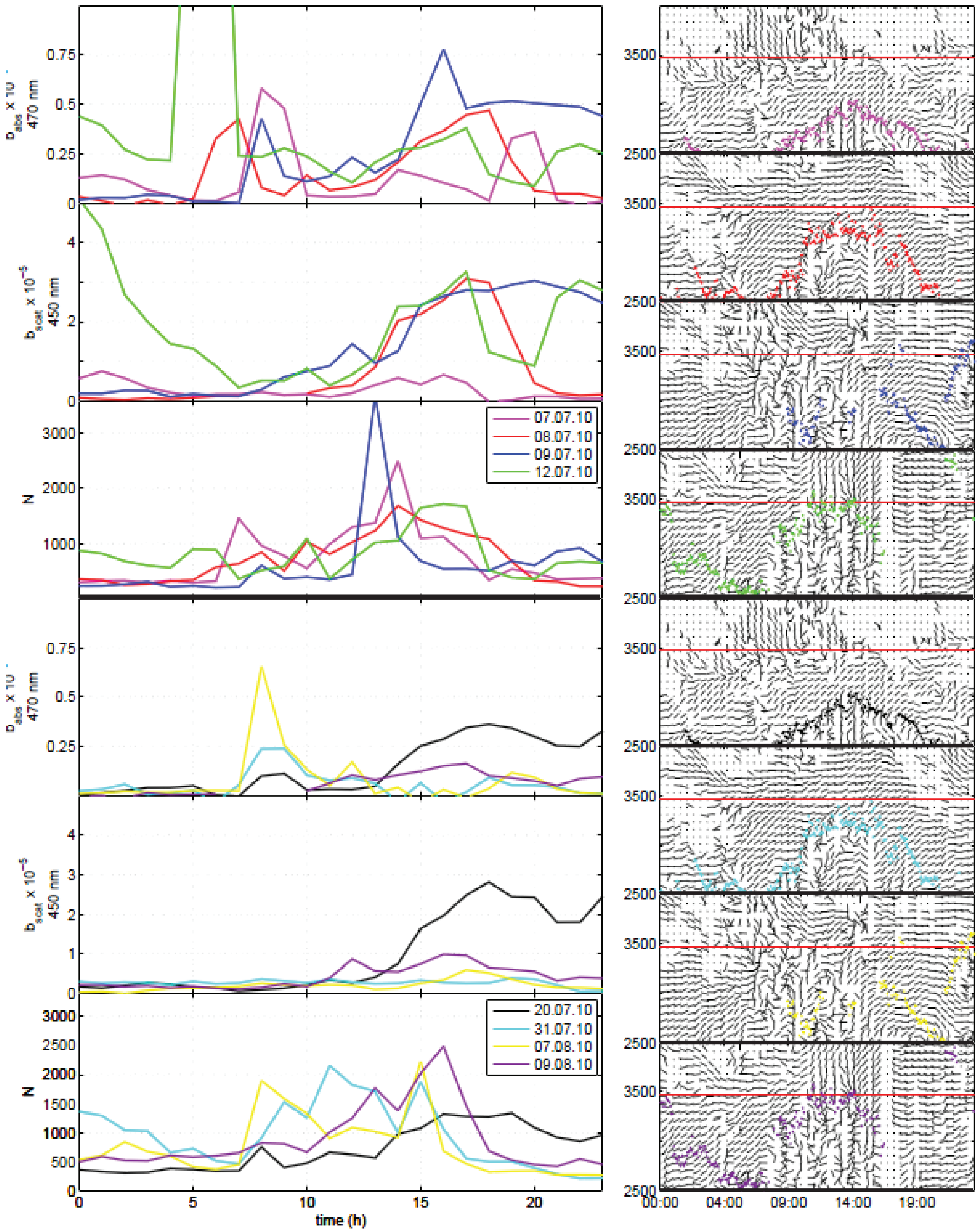

Figure 4. Left panels: Absorption coefficient (b_{abs}), scattering coefficient (b_{scat}) and new particles (N) measurements at the Jungfraujoch. Right panels: corresponding wind field and PBL height derived by the wind profiler. Colors correspond to 8 typical days with well-defined PBL evolution.

5. SUMMARY

The goals of the CLACE campaign were to study chemical and physical characterization of aerosols, to investigate the direct and the indirect aerosol effect on clouds at the GAW Jungfraujoch station (3508 m asl). As cloud characteristics strongly depend on meteorology, several remote sensing measurement devices were installed nearby (Kleine Scheidegg, 2061 m asl), including a low-tropospheric wind profiler and a ceilometer. Results from an analysis on the ability of these instruments to detect the PBL evolution were presented in this paper.

The diurnal variations of the PBL are well estimated by both the wind profiler and the ceilometer. The wind profiler PBL agrees well over daytime with Ceilometer PBL.

Transport from down-valley aerosols to Jungfraujoch were detected by in in-situ measurements, like the nephelometer and the aethalometer. These cases often correspond to summer convective situations when PBL estimated by ground-based remote sensing reaches altitudes corresponding to the Jungfraujoch. During these periods, the high-altitude station cannot be considered as a free-atmosphere location.

ACKNOWLEDGMENTS

We thank the International Foundation High Altitude Research Stations Jungfraujoch and Gornergrat (HFSJG) for providing the excellent infrastructure at the Jungfraujoch. We also acknowledge the Jungfraubahnen for providing the infrastructure at the Kleine Scheidegg. We thank Holger Wille and Steffen Frey (Jenoptics) for their support and for lending the ceilometer.

This work was financially supported by the EC-projects European Supersites for Atmospheric Aerosol Research (EUSAAR, contract 026140) and Global Earth Observation and Monitoring (GEOMON, contract 026140), as well as by the European Space Agency's Climate Change Initiative (aerosol cci) and by MeteoSwiss within the Global Atmosphere Watch programme (GAW) of the World Meteorological Organization (WMO).

REFERENCES

1. Wallace, J. M. and P. V. Hobbs, 2006: Atmospheric Science. An introductory Survey. Academic Press. London. 480 pp.
2. Weigel, A., 2005: On the atmospheric boundary layer over highly complex topography. Diss. ETH No 15972.
3. Collaud Coen, M., Weingartner, E., Furger, M., Nyeki, S., Prevot, A. S. H., Steinbacher, M., and Baltensperger, U. 2011: Aerosol climatology and planetary boundary influence at the Jungfraujoch analyzed by synoptic weather types, Atmos. Chem. Phys., 11, 5931–5944, doi:10.5194/acp-11-5931-2011, 2011. 11110.

BRAID PATTERNS OF KELVIN-HELMHOLTZ BILLOWS IN SODAR RETURN SIGNAL: A COMPOSITE ANALYSIS

V.S. Lyulyukin

A.M. Obukhov Institute of Atmospheric Physics, RAS, Pyzhyovskiy 3, 109117, Moscow, Russia,
lyulyukin@gmail.com

ABSTRACT

The structure and dynamic characteristics of the Kelvin-Helholtz billows (KHB) observed with a sodar are studied by means of a composite analysis. We used data from continuous sodar measurements in the Moscow region (2008–2011 years) to select the events of most pronounced KHB. The composite patterns of KHB have been constructed for a few cases of clear inclined-stripes echogram patterns to derive typical fine-scale structure of billows, and spatial distribution of wind speed and shear within them. The interconnection between echo-intensity and wind shear variations within such patterns is shown. The typical distributions of velocity fluctuations within various forms of billows are shown.

1. INTRODUCTION

Shear waves in a layer of stable-stratified environment is one of the most beautiful hydro-dynamic phenomena. Such waves, named the Kelvin-Helmholtz billows (KHB), occur in the presence of a vertical shear of the wind velocity, which generates a dynamic instability. KHB have highly varied shapes (Fig. 1).

Figure 1: Schematic shapes of KHB observed in different conditions in laboratory experiments and in the atmosphere. a – billows; b – braids; c – cat eyes [1].

For a long time the pictures of the clouds were the main source of information about KHB in the atmosphere. In the 1970-s the ground-based remote sensing tools (such as radars, sodars, lidars) began to develop. Such tools can visualize the structure of inhomogeneity of the air density and at the same time measure the profiles of wind speed. At the end of the last century a lot of new experimental data on KHB in the atmospheric boundary layer were obtained. These data can be found in the reviews [2, 3] and in the references therein. Over the last years, interest in experimental and theoretical studies of KHB has increased due to their great role in the generation of turbulence and vertical exchange of mass and heat in stably stratified ABL [4, 5, 6]. Information on the structure and properties of the KHB is required to modernize the models of diffusion and pollutants spread.

The objective of this work is to determine the dynamic structure of KHB with composite analysis of braid-type patterns observed by sodar.

2. MEASUREMENT SITE AND EQUIPMENT

We used data from the year-round sodar measurements at the Zvenigorod Scientific Station (ZSS) of the Obukhov Institute of Atmospheric Physics in 2008–2010. ZSS (55.70 N, 36.78 E) is located in weakly inhomogeneous rural area 45 km west of Moscow. The three-antenna monostatic Doppler sodar LATAN-3, used at the station, has the following system parameters [8]: carrier frequency – 1700 Hz, vertical resolution – 20 m, altitude range – from 40 m to 200 ÷ 500 m (depending on the stratification and the level of acoustic noise), time resolution – 10 ÷ 20 sec.

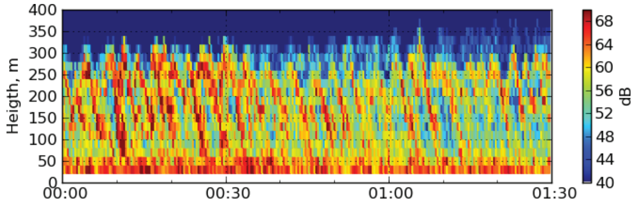

(a) 29 Jan 2010

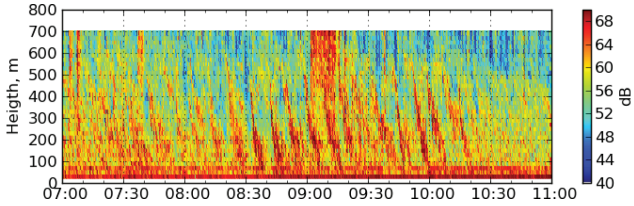

(b) 9 Nov 2010

Figure 2: Examples of return signal of vertical sodar antenna in coordinates height-time for two episodes of KHB.

Samples with clear braids were selected by visual inspection of sodar echograms (Fig. 2). There were selected 15 samples with time duration of 10–60 minutes totally.

3. DATA PROCESSING METHOD

Preprocessed data of the signal (the intensity of sodar echo, noise and radial speed) were used for averaging. Data processing consisted of several stages.

3.1 Composite analysis

A need for averaging arises primarily due to high level fluctuations of the instantaneous wind speed. Time averaging is complicated by the inhomogeneity of KHB amplitudes and wave periods. We have adopted the method of constructing a composite shape and structure, described by Williams and Hacker [7]. The method consists in the averaging of samples containing the event of interest, selected according to certain criteria and normalized in scale. A low resolution of sodar data makes impossible an averaging by normalizing of billows of various scales. The composite form was built separately for each of the selected samples, and waves included in the averaging were similar in scale and wave periods.

We used a Python script with an interface that allows us to manually mark the position and amplitude of the billows on the echograms (Fig. 3). Selected periods of KHB were averaged using preprocessed data of the echo signal from each of the three antennas. Points with S/N ratio less than 4 dB were omitted. Parameters of the averaging (position and number of selected periods, locked part of billows, the critical S/N ratio) were selected in way to maximize the sharpness of the average echograms.

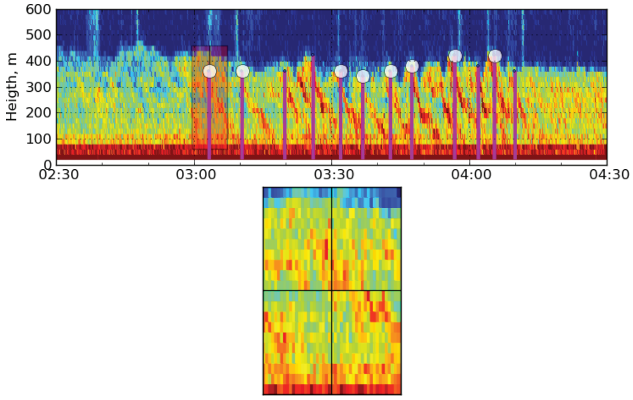

Figure 3: Interface for averaging over specific periods of KHB. Top: an echogram from the vertically directed antenna. The vertical lines show the position and amplitude of clear billows. Bottom: the scaled echogram.

An example of the composite shape of sodar echograms is shown in Fig. 4. The difference in the signal levels at the maximum and minimum of the scattering structures (10 ÷ 15 dB) is slightly less than in the original echograms (15 ÷ 20 dB).

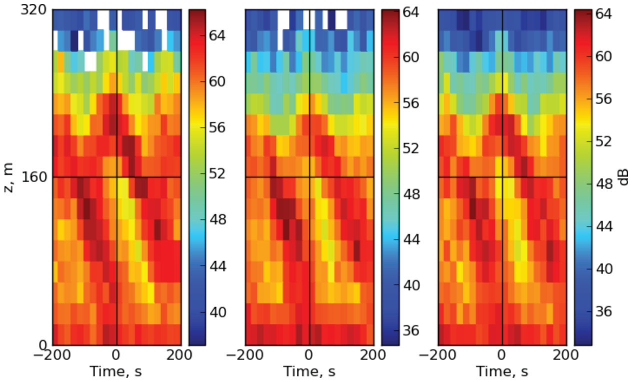

Figure 4: The composite shape of KHB obtained by averaging the echo signal of three antennas (the first and second are tilted, the third is vertically directed). 29 Jan 2010.

3.2 Vertical velocity distribution

A typical composite shape of space-time distribution of the vertical velocity within KHB, and vertical velocity shear profiles are presented in Fig. 5. The profiles were constructed by averaging over time (20–100 s) and associated with the averaged echogram of vertical antenna. Such figures allows us to trace the evolution of the profile within the billow.

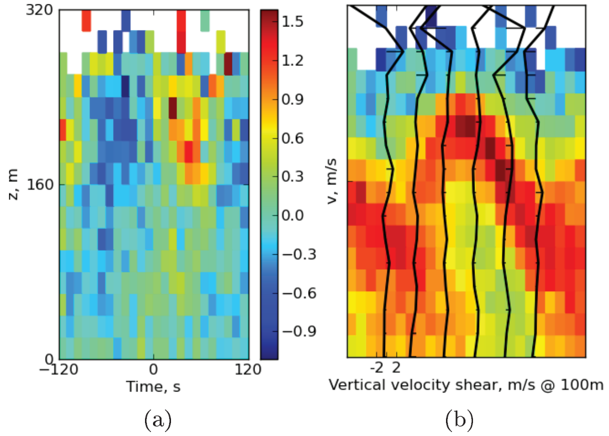

(a) (b)

Figure 5: The composite structure of the vertical velocity in the KHB. a - space-time distribution of vertical velocity; b - profiles of vertical velocity shear, attached to a vertical antenna echogram, averaging time – 30 s. 9 Aug 2008.

The resulting pictures show a high correlation between the vertical velocity distribution and turbulent structure within KHB. The height of the maximum of velocity shear well coincides with the height of the maximum intensity of the echo signal.

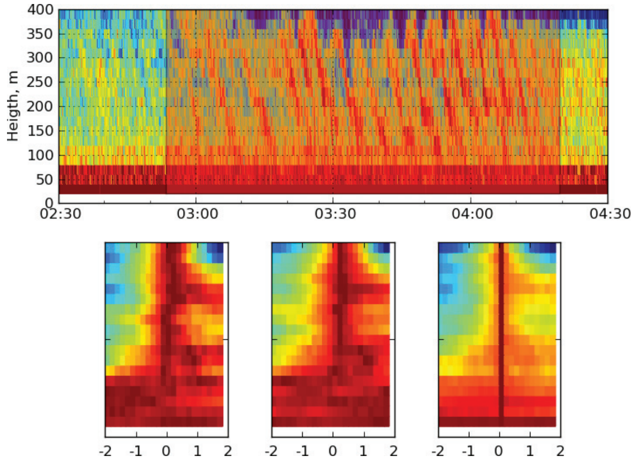

Figure 6: Correlation analysis of antenna signals. 5 Nov 2008.

3.3 Horizontal velocity distribution

To determine the time shift between the KHB structures on the echograms of the three antennas the correlation analysis was held (Fig. 6). Correlation functions of signals of the vertical and tilted antennas shows that the time shift does not exceed the resolving capacity of the sodar. Therefore the calculation of the horizontal velocity according to the data of three-point measurement can be performed without taking into account the shift.

The value of speed at a maximum of constructed profiles (Fig. 7a - 9a) exceeds the value obtained by time averaging. This fact demonstrate that the vertical location of the billows is connected with the maximum of the jet.

3.4 Velocity field

For each case the velocity field within KHB was obtained (Fig. 7 - 9b). The fields were constructed according to the average values of velocities in a cross section of KHB by a vertical plane tangential to the average wind speed vector. The deviation from the average was considered as a horizontal speed. Since the echograms are represented in time (not spatial) sweep, we need the normalization factor for the correct scale proportion of horizontal and vertical speeds:

$$k = \frac{\Delta t}{\Delta h \cdot \langle V \rangle}, \qquad (1)$$

where Δt is time resolution, Δh – height resolution, $\langle V \rangle$ – average wind speed.

4. TYPICAL STRUCTURES OF THE WIND FIELDS

Obtained wind distributions show that the structure of the wind velocity within KHB is strongly connected with the average wind profile. Several types of KHB dynamic structures under different meteorological conditions were selected.

4.1 Influence of the wind profile

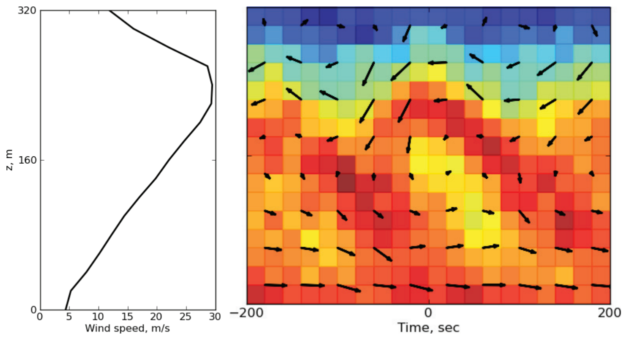

(a) (b)

Figure 7: The wind velocity field within KHB in the presence of monotonic wind profile. 29 Jan 2010.

The structure of the wind velocity field in the presence of monotonic wind speed profile is represented in Fig. 7. The turbulent structure has the shape of braid. The vortex located within the billow is seen in the velocity field.

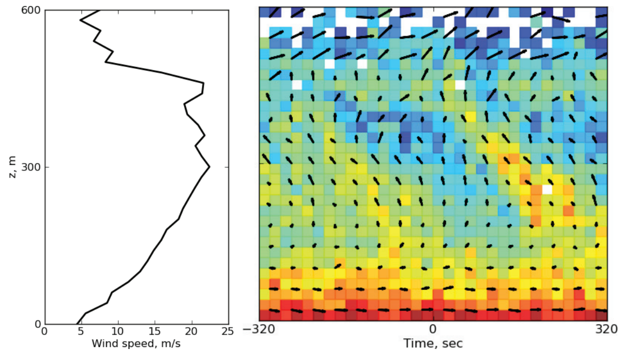

(a) (b)

Figure 8: The wind velocity field within KHB in the presence of LLJ. 3 Dec 2008.

In the case of low level jet stream (LLJ) with the speed maximum located within KHB layer, the wind field looks different (Fig. 8). Two counter-rotating vortexes can be shown in the wind structure. Therefore the turbulent structure at the echogram looks more like a series of inclined stripes than a braid.

4.2 Influence of the air temperature profile

Significant part of selected cases with clear KHB falls on the morning hours (7 - 12 AM) and on the evening hours (7 - 10 PM). The changing of vertical temperature distribution generally happens at these periods. A comparison of data (is not shown) of the temperature profiler with the echogrames shows that KHB arise under the short range of values of vertical temperature gradient. For example, under the value of wind speed shear $\sim 0.05s^{-1}$ KHB arises under the changing of temperature gradient value in range

$$\frac{0.3^\circ K}{100m} \leq \frac{\Delta T}{\Delta z} \leq \frac{0.6^\circ K}{100m}. \qquad (2)$$

These conditions approximately agree to criterion $Ri \leq 0.25$, theoretically obtained in [9] and confirmed experimentally [4].

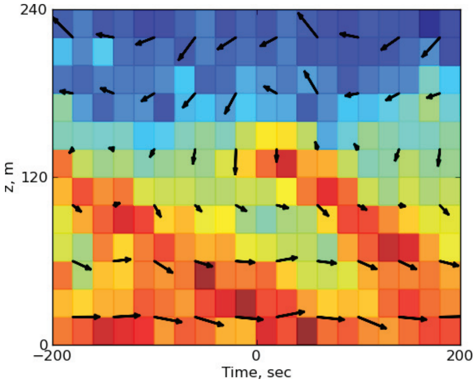

(a) 31 Jan 2010

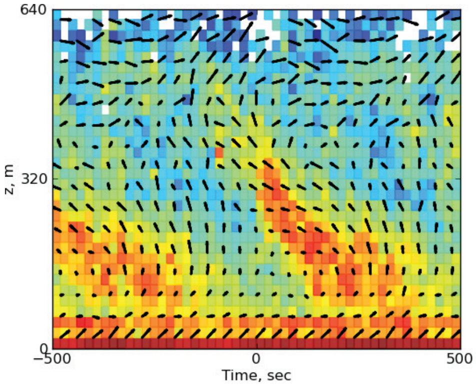

(b) 09 Nov 2010

Figure 9: The examples of the wind field in KHB under critical parameters of stratification. a – in the presence of monotonic wind profile; b – in the presence of LLJ.

The shape of KHB depends on the ratio of the gradients of temperature and wind speed. Fig. 9 shows composite shapes of KHB and related wind fields in cases, when the wave crest is less visible, and when the wind vortexes are shifted vertically relative to turbulent structures on echograms.

5. CONCLUSION

Data processing with composite analyses allow us to obtain distributions of wind speed fluctuations in KHB. The vortexes typical for Kelvin-Helmholtz instability are seen in the wind fields. The variety of KHB forms in the ABL is connected with parameters of atmospheric stability.

ACKNOWLEDGMENTS

The author thanks R.D. Kouznetsov and M.A. Kallistratova for suggesting the topic of research, permanent attention to the work, and useful discussions. The work was supported by the Russian Foundation for Basic Research through grant 10-05-00802.

REFERENCES

1. Gossard E.E., W. Hooke, 1975: Waves in the Atmosphere, *Elsevier, NY.*, pp. 532.
2. Readings C.J., D. Atlas, C. Emmanuel, Y.-H. Pao, S. Thorpe, 1973: The formation and break down of Kelvin - Helmholtz billows (Working Group Report VI), *Bound.-Layer Meteor.*, **5**, pp. 233-240.
3. DeSilva I., H. Fernando, F. Eaton, D. Hebert, 1996: Evolution of Kelvin-Helmholtz billows in nature and laboratory, *Earth Planet. Sci. Lett.*, **143**, pp. 217–231.
4. Newsom R.K., R. Banta, 2003: Shear-flow instability in the stable nocturnal boundary layer as observed by Doppler lidar during CASES-99, *J. Atmos. Sci.*, **60**, 16-33.
5. Cushman-Roisin B., 2005: Kelvin - Helmholtz instability as a boundary-value problem, *Env. Flu. Mech.*, **5**, pp. 507-525.
6. Fukao S., H. Luce, T. Mega, M. Yamamoto, 2011: Extensive studies of large-amplitude Kelvin-Helmholtz billows in the lower atmosphere with VHF middle and upper atmosphere radar, *Q. J. R. Meteor. Soc.*, **137**, pp. 1019-1041.
7. Williams A.G., J. Hacker, 1992: The composite shape and structure of coherent eddies in the convective boundary layer, *Bound.-Layer Meteor.*, **61**, pp. 213-245.
8. Kouznetsov R.D., 2007: LATAN-3 sodar for investigation of the atmospheric boundary layer, *Atm. and Oceanic Opt.*, **20(8)**, pp. 684-687.
9. Baas A.F., A. Driedonks, 1985: Internal gravity waves in a stably stratified boundary layer, *Bound.-Layer Meteor.*, **31**, pp. 303-323.

CONFIDENCE LEVELS AND ERROR BARS FOR CONTINUOUS DETECTION OF MIXING LAYER HEIGHTS BY CEILOMETER

Christoph Münkel[1], Klaus Schäfer[2], Stefan Emeis[2]

[1]*Vaisala GmbH, Schnackenburgallee 41d, 22525 Hamburg, Germany, christoph.muenkel@vaisala.com*
[2]*Karlsruhe Institute of Technology, Institute for Meteorology and Climate Research, Atmospheric Environmental Research Division (IMK-IFU), Kreuzeckbahnstr. 19, 82467 Garmisch-Partenkirchen, Germany,*
klaus.schaefer@kit.edu, stefan.emeis@kit.edu

ABSTRACT

The mixing layer height (MLH) is an important factor which influences exchange processes of ground level emissions. Thus, the continuous knowledge of MLH is required.

The Vaisala ceilometers LD40 and CL31 which are eye-safe commercial lidar systems are operated to detect the MLH in Augsburg since 2006. Special software for these ceilometers provides routine retrievals of lower atmosphere layering from vertical profiles (vertical gradient) of laser backscatter density data. The performance of the ceilometers is sufficient to detect convective layer depths exceeding 2000 m and nocturnal stable layers down to 50 m. The profile behaviour of relative humidity (strong decrease) and virtual potential temperature (inversion) of radiosondes in Oberschleissheim about 50 km away agree mostly well with the MLH indication from ceilometers during cloud-free conditions mainly.

Based on the gradient method, an automatic algorithm for online retrieval of boundary layer depth and additional residual structures has been developed. This robust all weather algorithm is part of the Vaisala boundary layer reporting and analysis tool BL-VIEW. The data averaging intervals used depend on range and signal noise; detection thresholds vary with signal amplitude. All layer heights reported are accompanied by a quality index. In most cases the lowest of these layers is a good measure for the MLH. The utility of MLH values for air quality forecast could be increased if the current quality index would be enhanced by more significant parameters like confidence levels and error bars. This is discussed for a measurement campaign at Athens airport.

1. INTRODUCTION

Eye-safe lidar ceilometers are reliable tools for unattended boundary layer structure monitoring around the clock up to heights exceeding 2500 m ([1] - [3]). Comparison to temperature, humidity, and wind profiles reported by RASS, sodar, radio soundings, and weather mast in-situ sensors has confirmed their ability to detect convective or residual layers ([4] - [8]). In addition, ceilometers with a single lens optical design enable precise assessment of inversion layers and nocturnal stable layers below 200 m [9]. This design has been chosen for the Vaisala Ceilometers CL31 and CL51.

An automatic algorithm for online retrieval of boundary layer depth and additional residual structures has been developed that covers not only ideal boundary layer diurnal evolution, but all situations involving clouds, fog, and precipitation. This algorithm is part of the Vaisala boundary layer reporting and analysis tool BL-VIEW.

There have been several publications regarding the issue of boundary layer investigation with ceilometer. Within the scope of the EG-CLIMET COST action there is a general agreement on a European level to use existing ceilometer networks for automatic layer height reports [10]. To further increase the applicability of these reports, statistically meaningful values like confidence levels and error bars should be added.

This paper is a first step in this direction. The method proposed has been tested on a large variety of recorded ceilometer profiles and validated with co-located soundings.

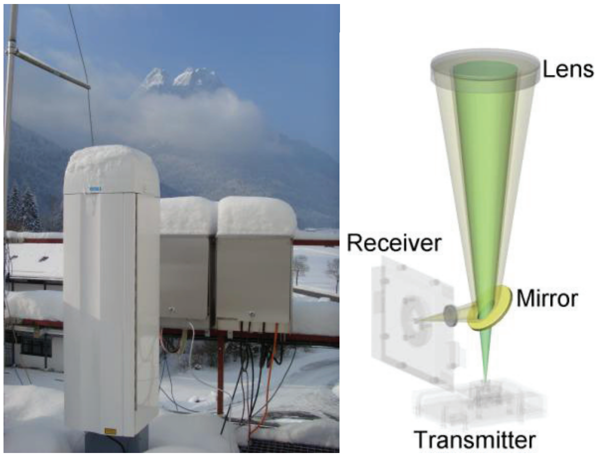

Figure 1. Vaisala Ceilometer CL51 installed on the roof of IMK-IFU, Garmisch-Partenkirchen, Germany and its single lens optical concept.

2. METHODOLOGY

2.1 Ceilometer

The ceilometers used within the measuring campaigns described in this paper are the Vaisala Ceilometers CL31, CL51 (Fig. 1) and LD40 [11]. The single lens optical design of all current Vaisala Ceilometers uses the inner part of the lens for transmitting and its outer part for receiving light (Fig. 1). This provides overlap of the transmitter light cone and the receiver field-of-view over the whole measuring range and allows reliable detection of also the very low nocturnal stable layers below 200 m not seen by other instrument types like the two lens system LD40.

2.2 BL-VIEW algorithm

A standard method to identify the vertical extent of aerosol layers within the boundary layer is the gradient method that searches the backscatter profile for local gradient minima. Sliding time and height averaging is essential for its success (Fig. 2, up), but precipitation and clouds call for a more sophisticated treatment. The resulting algorithm (Fig. 2, down) involves cloud and precipitation filter, noise and range dependant time and height averaging intervals, and signal strength dependant detection thresholds [12].

The current BL-VIEW algorithm gives a quality index from 1 to 3 to each gradient minimum detection. It is based on gradient amount (a low gradient minimum results in a high quality index), detected cloud bases (clouds detected in the vicinity of a boundary layer reduce its quality index), and distance to other gradient minima (high distance results in high quality).

2.3 Confidence levels and error bars

In most cases the lowest of the layers reported by the BL-VIEW algorihm is a good measure for the MLH. The continuous knowledge of this atmospheric parameter is supporting the understanding of processes directing air quality. The utility of MLH as a parameter for air quality forecast or dispersion calculation would be enhanced if the quality index described in the preceeding section could be quantified by calculating confidence levels (how sure are we that there really is an aerosol layer at that height?) and error bars (what is the uncertainty of the detected value?).

The algorithm introduced in this paper to estimate confidence levels and error bars is based on the available single profile messages that are averaged in time in the course of the BL-VIEW algorithm. The recommended message interval for BL-VIEW is 16 s. Depending on signal noise, the number of past messages N averaged for the detection of a gradient minimum height GM varies from 50 to 100.

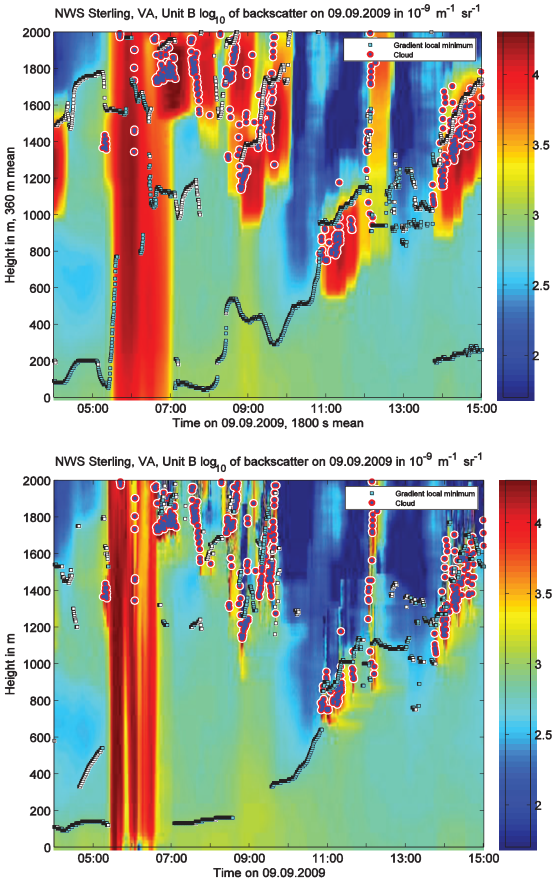

Figure 2. Up: Density plot of backscatter profiles recorded by a CL31 ceilometer at the US-National Weather Service test site Sterling, VA on 9 September 2009. The fixed sliding averaging parameters used do not reveal all aerosol layers; clouds and precipitation might even cause false layers. Down: The same data set treated with all steps of the BL-VIEW algorithm.

Confidence level and error bar calculation performs gradient minima search for the 16 s messages used in the averaging process and examines the results in the following way:

a) Gradient minima calculation for each of the *N* single messages. Result: up to 3 gradient minima heights for every 16 s profile examined.

b) Count of gradient minima detected that differ not more than the greater of 200 m and 20 % from *GM*. Result: *C*.

c) Confidence level *CL*: $CL = C / N$.

d) Uncertainty of *GM* (half error bar length): Standard deviation of the *C* gradient minima heights calculated in steps b) and c) from their arithmetic mean.

Fig. 3 gives an example of a convective layer at 870 m and a residual layer at 1580 m. Due to the fast rise of the convective layer only 37 out of the 52 examined

16 s profiles fulfill the criteria of b) above. Its confidence level is 71 %; that of the residual layer reaches 100 %. Fig. 4 shows the layer evolution for the whole day.

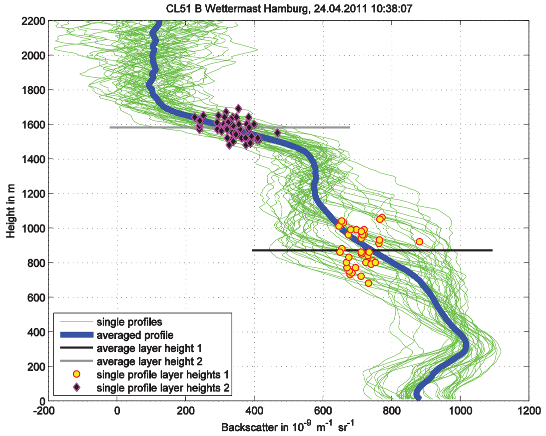

Figure 3. 52 single backscatter profile messages (green) recorded from a CL51 ceilometer at Hamburg, Germany, and their average (blue) covering the time interval 10:24:31 till 10:38:07 on 24 April 2011. The strong variation of the green curves in the range of the lower gradient minimum height at 870 m results in a confidence level of 71 % and a half error bar length of 105 m. These values are 100 % and 52 m for the residual layer at 1580 m.

3. RESULTS

3.1 Tall Wind 2011 experiment, Hamburg

The Tall Wind experiment involves continuous monitoring of boundary layer heights with ceilometer at Hamburg weathermast [7].

Fig. 4 shows the good agreement of the results of the algorithm introduced in Section 2.3 for two co-located CL51 ceilometers. Daylight signal noise generally increases the length of the error bars.

A five days intensive campaign during Tall Wind 2011 saw 2-hourly launches of Vaisala RS92 radiosondes. Weather conditions where not favourable for boundary layer detection during those days; there were a lot of periods with low clouds or precipitation. On 15 June 2011 there were some gaps in the clouds. The 09:30 and 11:00 soundings on that day show relative humidity drops and potential temperature rises at heights where the CL51 reports upper edges of aerosol layers (Fig. 5).

3.2 ECATS measuring campaign 2007, Athens

An LD40 ceilometer was involved in a measuring campaign conducted at Athens International Airport in September 2007 in the framework of the European Network of Excellence ECATS project. Fig. 6 gives an example that shows the applicability of the enhanced BL-VIEW algorithm to older ceilometer types.

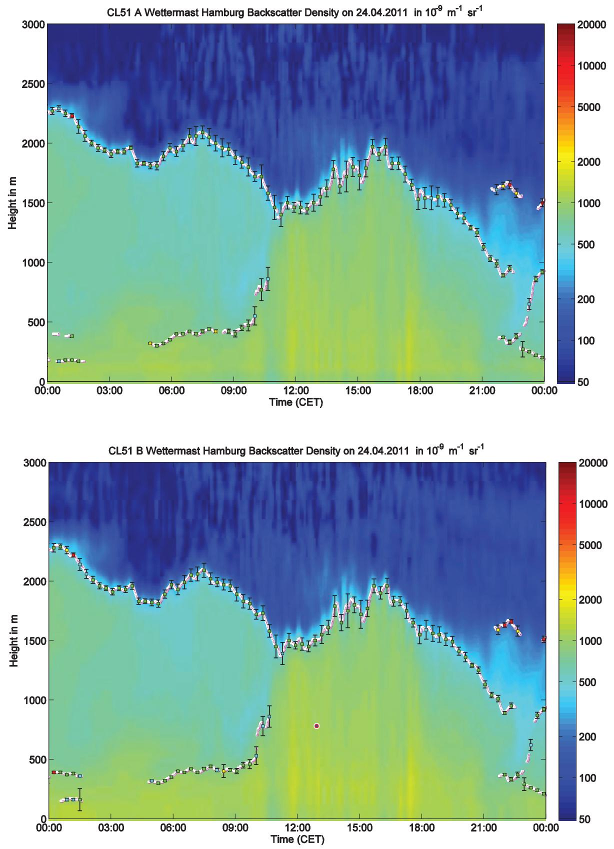

Figure 4. Density plots of backscatter profiles recorded by two co-located Vaisala CL51 ceilometers on 24 April 2011 at Hamburg weathermast. This nearly cloudless day shows the typical diurnal evolution of residual, convective and nocturnal layers.

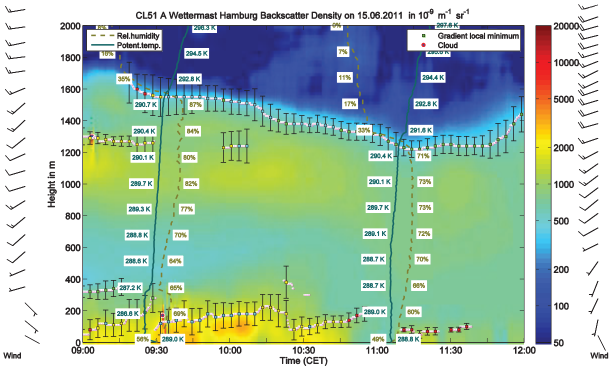

Figure 5. Density plot of backscatter profiles recorded by a CL51 ceilometer on 15 June 2011 at Hamburg weathermast. Relative humidity (dashed curve) and potential temperature profiles from soundings launched at 09:30 and 11:00 CET are plotted as well. Wind barbs of the 09:30 sounding are plotted on the left hand side, those of the 11:00 sounding on the right hand side of the plot. The south-easterly wind below 300 m is transporting dust from a close-by gravel pit. Large error bars reflect frequent change of dust concentration. At 11:00 wind direction has turned to south and thus less dust is transported.

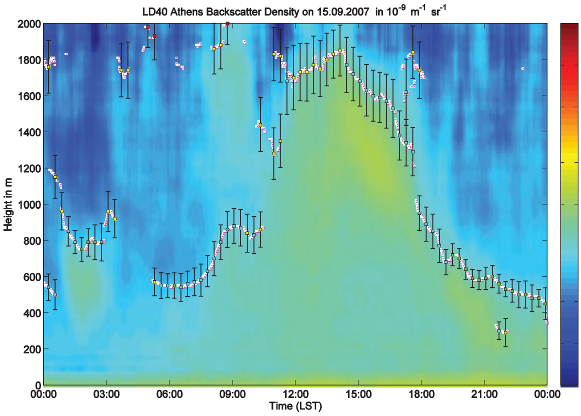

Figure 6. Density plot of backscatter profiles recorded by a Vaisala LD40 ceilometer on 13 July 2011 at Athens International Airport, Greece.

4. CONCLUSIONS

The method outlined in this presentation shows satisfactory results for the three ceilometer types CL31, CL51, and LD40. There is a good agreement with mixing layer heights derived from relative humidity and potential temperature profiles reported by soundings launched close to the ceilometers.

Evaluation of extensive databases from ongoing and projected measuring campaigns will be used for analysis and refinement of the proposed algorithm. These campaigns involve the Tall Wind 2011 experiment and the TERENO campaign with three CL51 ceilometers. TERENO is a Helmholtz Research Initiative in the field of environmental research and is expected to run for at least 10 years.

ACKNOWLEDGMENTS

The Tall Wind study is supported by the Danish Council for Strategic Research, Sagsnr 2104-08-0025.

REFERENCES

1. Münkel C., 2007: Mixing height determination with lidar ceilometers - results from Helsinki Testbed, *Meteorol. Z.*, **16**, pp. 451-459.

2. Heese B., H. Flentje, D. Althausen, A. Ansmann, S. Frey, 2010: Ceilometer lidar comparison: backscatter coefficient retrieval and signal-to-noise ratio determination, *Atmos. Meas. Tech.*, **3**, pp. 1763-1770.

3. McKendry I. G., D. van der Kamp, K. B. Strawbridge, A. Christen, B. Crawford, 2009: Simultaneous observations of boundary-layer aerosol layers with CL31 ceilometer and 1064/532 nm lidar, *Atmos. Environ.*, **43**, pp. 5847-5852.

4. Emeis S., K. Schäfer, C. Münkel, 2008: Surface-based remote sensing of the mixing-layer height - a review, *Meteorol. Z.*, **17**, pp. 621-630, http://imk-ifu.fzk.de/downloads/Emeis_et_al_2008_Rem_Sensing_of_MLH_-_review.pdf.

5. Haman C., B. L. Lefer, M. E. Taylor, G. Morris, B. Rappenglueck, 2010, Comparison of Mixing Heights using Radiosondes and the Vaisala CL31 Mixing Height Algorithm, *15th Symposium on Meteorological Observation and Instrumentation at the 90th AMS Annual Meeting*.

6. Emeis S., K. Schäfer, C. Münkel, 2009: Observation of the structure of the urban boundary layer with different ceilometers and validation by RASS data, *Meteorol. Z.*, **18**, pp. 149-154, http://imk-ifu.fzk.de/downloads/Emeis_et_al._MetZet_2009_Ceilometer_RASS.pdf.

7. Tsaknakis G., A. Papayannis, P. Kokkalis, V. Amiridis, H. D. Kambezidis, R. E. Mamouri, G. Georgoussis, G. Avdikos, 2011, Inter-comparison of lidar and ceilometer retrievals for aerosol and Planetary Boundary Layer profiling over Athens, Greece, *Atmos. Meas. Tech.*, **4**, pp. 1261-1273.

8. Emeis S., K. Schäfer, C. Münkel, R. Friedl, P. Suppan, 2011, Evaluation of the interpretation of ceilometer data with RASS and radiosonde data, *Bound.-Lay. Met.*, **143**, pp. 25-35.

9. Münkel C., S. Emeis, K. Schäfer, B. Brümmer, 2009, Improved near-range performance of a low-cost one lens lidar scanning the boundary layer, *Proc. SPIE*, **7475**, 74750O.

10. Haeffelin M., F. Angelini, Y. Morille, G. Martucci, S. Frey, G. P. Gobbi, S. Lolli, C. D. O'Dowd, L. Sauvage, I. Xueref-Rémy, B. Wastine, D. G. Feist, 2011: Evaluation of Mixing-Height Retrievals from Automatic Profiling Lidars and Ceilometers in View of Future Integrated Networks in Europe, *Bound.-Lay. Met.*, **143**, pp. 49-75, http://www.macehead.org/index.php?option=com_docman&task=doc_download&gid=1412&Itemid=73.

11. Haij M. J. de, H. Klein Baltink, W. M. F. Wauben, 2007, Continuous mixing layer height determination using the LD-40 ceilometer: a feasibility study, Scientific Report WR 2007-01, KNMI, De Bilt.

12. Münkel C., R. Roininen, 2010, Automatic monitoring of boundary layer structures with ceilometer, WMO Technical Conference on Meteorological and Environmental Instruments and Methods of Observation (TECO-2010), P2(17), http://www.wmo.int/pages/prog/www/IMOP/publications/IOM-104_TECO-2010/P2_17_Muenkel_Germany.pdf.

AN AUTOMATED ALGORITHM FOR DERIVING MIXING-LAYER DEPTH FROM A 1D SODAR IN HELSINKI

Curtis Wood[1*], Rostislav Kouznetsov[1,2], Ari Karppinen[1]

[1] *Finnish Meteorological Institute, Erik Palmenin Aukio, 00101 Helsinki (Finland)*

[2] *A. M. Obukhov Institute of Atmospheric Physics, Moscow (Russia)*

[*] *curtis.wood@fmi.fi*

ABSTRACT

The depth of the mixing layer (MLD) is important for models of air quality (AQ) and numerical weather prediction (NWP). Hence, observations of MLD are needed to provide the data for evaluation, assessment and improvement of urban submodels/ parameterizations in NWP and AQ models.

At high-latitudes it is not trivial to observe a long time series of MLD because of the prevalence of shallow MLDs (which lidars, e.g., typically cannot diagnose). Thus, sodar is an ideal tool (given its low first sampling region). In Helsinki, a Latan-3 1D sodar operated continuously on the roof of the Finnish Meteorological Institute from 14-Aug-09 to 05-Sep-11.

For 7 of those months, MLD was manually estimated from echograms (time-height plots of intensity). An automated algorithm was developed for the diagnosis of MLD. The automated algorithm is simply based on finding the height of the greatest reduction in intensity within the sensing range.

Within the sampling range, MLD was diagnosed in neither system (e.g. deep ML) for 31% of 30-min periods, and in both for 35% (the rmse was 53 m; bias was automatic < manual by 4 m). Some 30-min periods only had MLD diagnoses for one system (8% only manual, 26% only automatic).

1 INTRODUCTION

The mixing layer, used inter-changeably with “atmospheric boundary layer” (ABL), is the layer of atmosphere adjacent to the ground surface, where an intensive turbulent mixing occurs on timescales minutes–hours. Quantitative definitions of the mixing layer depth (MLD) are based on various methods [1,2].

MLD is used in many air quality and pollution dispersion models. Thus it needs to be reliably derived from basic meteorological quantities provided by NWP models.

In Helsinki, we have a network of urban observations (http://urban.fmi.fi), including sodar, lidar, scintillometers, infrared cameras and eddy-covariance flux stations. We use data from a sodar installed on the roof of the Finnish Meteorological Institute (in Helsinki) for the present study.

The automated procedures of mixing height determination from sodar echo intensity profiles are often neither straightforward nor robust [1]. So we develop our own automatic algorithm in Helsinki and compare to manual estimates of MLD.

2 EXPERIMENTAL DATA

The reference sodar used in the study is located in Helsinki, about 5 km north of downtown atop a small hill.

A Latan-3m 1D sodar operated continuously on the roof of the Finnish Meteorological Institute from 14-Aug-09 to 05-Sep-11 [3]. The sodar has range 20–400 m and resolution of 10 m. The sodar has a single vertically-pointing dish antenna of 60 cm in diameter. It is operated at 3400 Hz carrier frequency with 50 ms burst signal and pulse repetition rate 0.2 Hz.

For 7 months (Sep09–Mar10), the MLD was manually estimated from sodar echograms (time-height plots of intensity). We thus compare MLD as derived manually [4] to the automatic algorithm [present paper].

During some times the MLD was either above the sounding range (> 400m), or could not be detected due to weak temperature turbulence within ABL, or due to technical problems with sodar (wind and/or rain causing strong acoustic noise, heavy snowfall covering the antenna, etc.).

Data are recorded in two channels: A (‘signal+noise’ channel) and B (noise channel). We define **relative signal** as the difference between the channels (A–B); this is done in the 30-min mean data.

The automatic algorithm is under development. We present the latest version.

3 PRESENT ALGORITHM

Quality control (QC):

- Replace the 5-second data with "NaN" if exactly zero velocity is recorded (which is a QC flag).
- A fixed echo problem in range-gates 15 and 16. Reject and interpolate vertically if the 30-mean mean has an intensity peak in channel A compared to surrounding (gates 14 and 17).
- Define velocities as "NaN" for every gate where the relative signal < +4.5dB
- Sodar data were often affected by fixed echoes in the lowest range gates (highly variable in space and time) which would require a rather intelligent automated procedure for automatic MLD retrieval.
- Hence, do not use the lowest few gates for defining the MLD. So, define a lowest usable gate (LG) as the maximum of:
    - range-gate 4; or
    - the greatest height where the relative signal is above +10dB.

First iteration of MLD estimate:

- Find the height in the profile (from LG:top) of the **most negative vertical gradient in relative signal. This height is then defined as the MLD**, unless the conditions are deemed to be unsuitable for sodar-derived mixing height (see below).

Do not define MLD if:

- There might be **snow**: 30-min-mean velocity < -0.5 m s^{-1} across range-gates 3:10.
- There might be daytime **convection deeper** than the sodar's sampling range (applies at 0500–1700UTC only):
    i. mean velocity variance is increasing with height at the top of the data availability layer (defined as range gates 2:6 below top limit of data availability) <u>**&**</u> the variance is > 0.8 m s^{-1} for every gate in that layer; OR
    ii. the maximum 30-min-mean vertical-velocity variance > 1.7 m s^{-1} in any gate in that availability layer; OR
    iii. the minimum 30-min-mean vertical velocity > +1.0 m s^{-1} in any gate in that availability layer.
- All gates are **dominated by noise** (i.e. relative signal < +4.5dB).
- If the minimum gradient (LG:end) is not clearly negative (–1.5dB limit): this would mean that there is **no inversion**.
- There is a strong return (>+35dB in channel A) for all gates from LG:end [**probable rain**].
- There is a bulk increase in relative signal with height (e.g. **rain, convection**): gradient of gates 10:22 compared to 23:end.

Finally:

- Allow some temporal consistency of MLD (e.g. avoid flipping frequently between levels) by applying a 3-point running median through the time-series.
- Do not diagnose MLD for temporally-isolated periods (≤ 1 hr); make these "NaN" values.
- Apply a data flag (999.99 m) if the MLD was undefinable due to probable deep convection (such as high vertical velocity variance values).

4 RESULTS

We show example cases from the database (Appendix).

There are 3570 30-min periods available for inter-comparison (Figure 1) between manual and automatic methods, which is 35% of the dataset (whilst 31% was not diagnosed in either). There were 8% diagnoses only in the manual and 26% only in the algorithm.

If one considers only the 3347 (out of 3565) cases where the difference is less than ±80m (in order to check the comparison for cases when the same inversion is seen in both methods), then the statistics are $r = 0.9$, rmse = 29m, bias = +3m (see legend for definition).

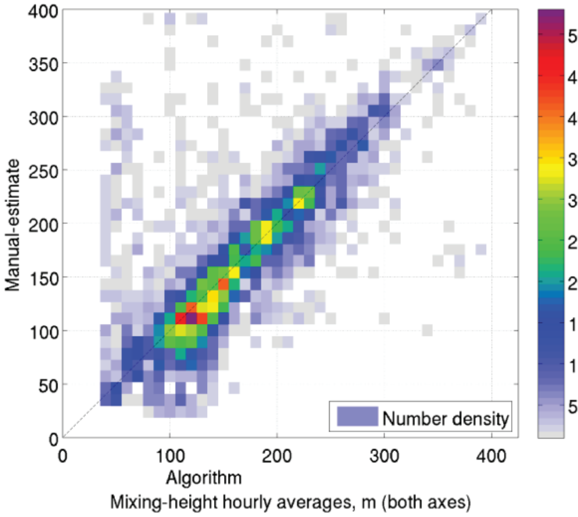

Figure 1. Comparison of automatic and manual MLD estimation. Height bins are 10m. Number density shown in colorbar. The correlation coefficient (r) is 0.7, rmse is 53 m, and the bias is –3.6m (automatic minus manual).

5 DISCUSSION

The presently-developed automated procedure has shown some promising results, but there are a few limitations:

- no recognition of very shallow boundary layers (e.g. < 60 m) due to cases of fixed echoes in lower range gates;
- sodar was on a building, on a hill—even more likely to miss the very shallow MLDs;
- perhaps predict too many mixing heights below 400 m, even though they are somewhat weak and there could be a ‘more relevant’ inversion aloft;
- no comparison to other (e.g. manual) MLD estimates for summer months.

Acknowledgements

This work has been supported by the EC FP7 project ERC PBL-PMES (No. 227915).

References

1. Beyrich, F., 1997: Mixing height estimation from sodar data – A critical discussion. Atmospheric Environment, **31**, pp. 3941–3953. doi:10.1016/S1352-2310(97)00231-8.

2. Emeis, S., Schäfer K., Münkel C., 2008: Surface-based remote sensing of the mixing-layer height – a review. Meteorologische Zeitschrift, **17**, pp. 621–630. doi:10.1127/0941-2948/2008/0312.

3. Kouznetsov R. D., 2007: Latan-3 sodar for investigation of the atmospheric boundary layer. *Atmospheric and Oceanic Optics*, **20**, pp. 684–687.

4. Kouznetsov R., Wood C. R., Sofiev M., Soares J., Karppinen A., and Fortelius C., 2012: In *Proc. 16th Int. Symp. for the Advancement of Boundary Layer Rmeote Sensing*, Boulder, CO, 5–8 June 2012.

Appendix

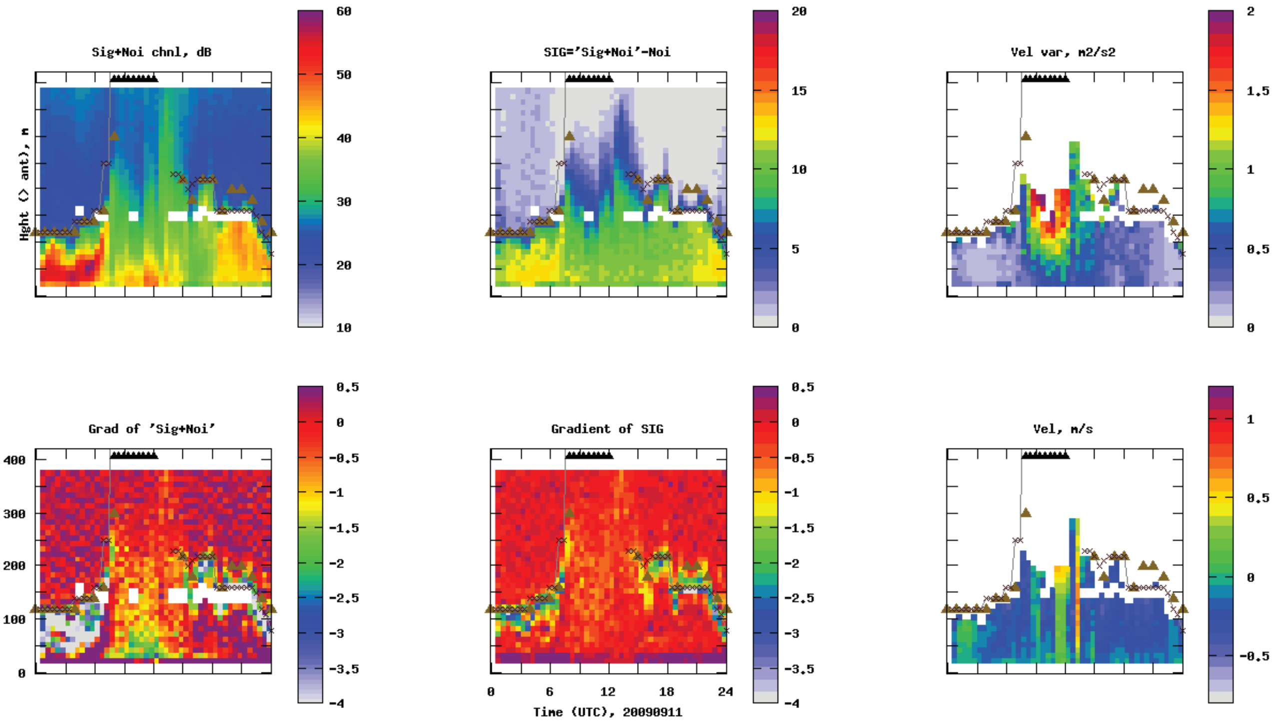

Figure 2. Example plot panel from the database for 11th September 2009. The subplots (clockwise) are channel A, relative signal, variance of vertical velocity (m^2 s^{-2}), vertical velocity (m s^{-1}), gradient of relative signal, gradient of channel A. Time in hours UTC. Golden triangles are manually-estimated MLD. Black line and crosses are automatic algorithm (black triangles are probable deep convection).

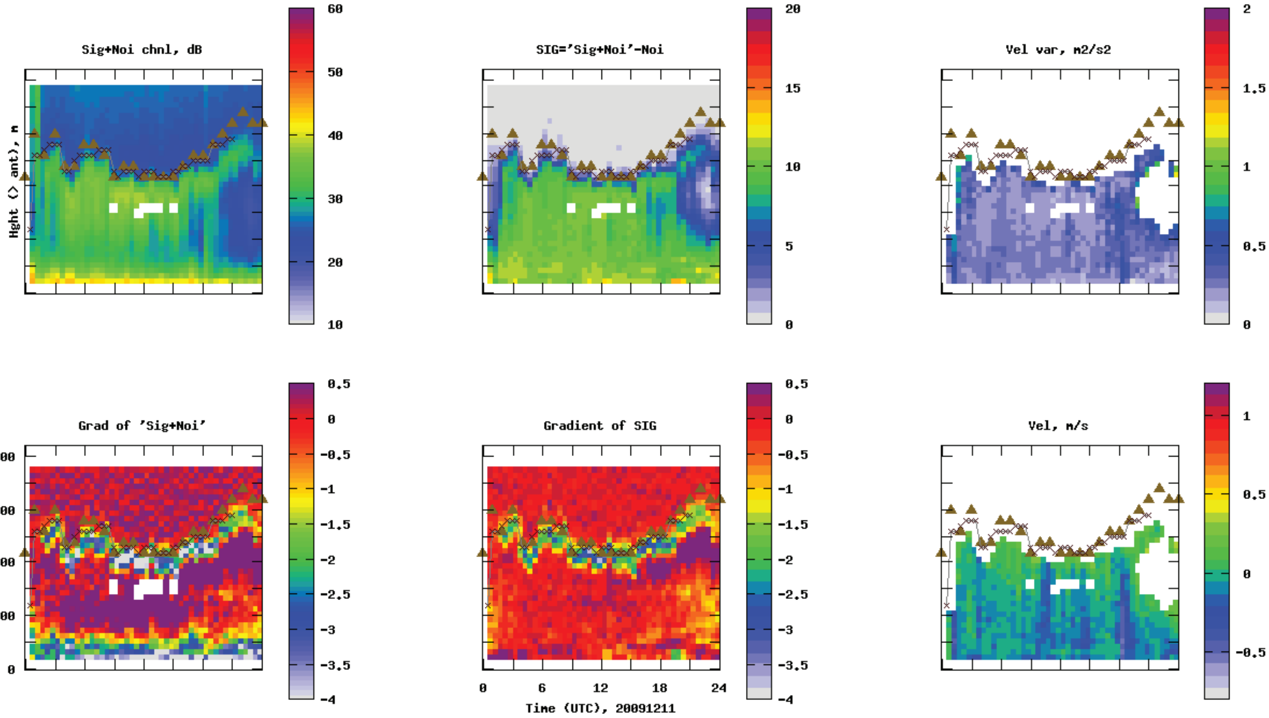

Figure 3. Example plot panel from the database for 11th December 2009. (See Figure 2 for further descriptions.)

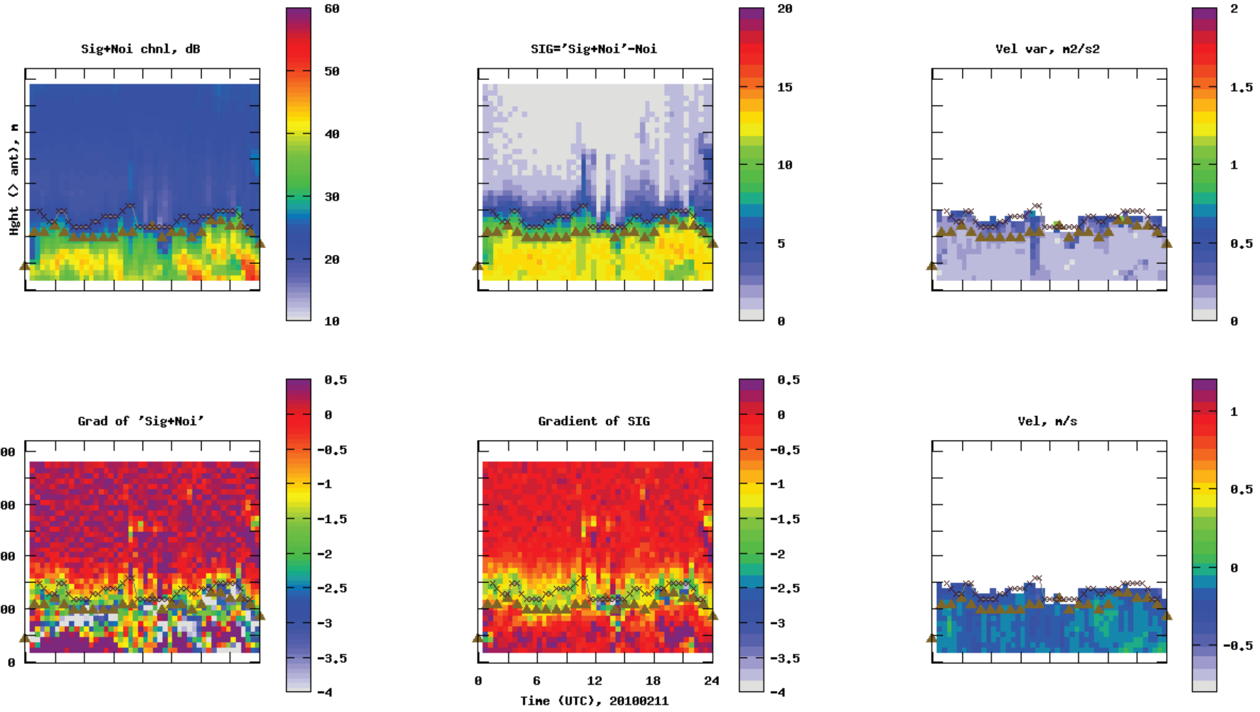

Figure 4. Example plot panel from the database for 11th February 2010. (See Figure 2 for further descriptions.)

Mixing Layer Heights and Aerosol Properties over Hampton, Virginia, USA

Neda Boyouk, Kevin R. Leavor[1], **M. Patrick McCormick**[2]

[1and2]*Department of Atmospheric and Planetary Sciences, Hampton University, 23 Tyler St., Hampton, VA 23668,USA ([1]nedaboyouk@gmail.com)*

ABSTRACT

The mixing layer height (MLH) over Hampton University (HU), Hampton, Virginia, United States (37.02°N, 76.33°W), was obtained using several methods over the course of 2 years by lidar measurements. The HU lidar has operated at 3 wavelengths (1064, 532 and 355nm) since June 2006, and is part of the CREST Lidar Network (CLN) to monitor aerosols in the troposphere and stratosphere. The network has operated on a routine basis since February 2009.

In this study we have used the 532 nm signal. The MLHs obtained from 532 nm lidar signal have been compared to the calculated MLHs of radio sounding measurements taken over Wallops Island, Virginia (37.93°N, 76.33°W).

This paper will describe the combination of 2 years of MLH measurements, aerosol optical properties and mass concentrations which help to relate the columnar optical properties to ground based measurements of mass concentration. Further, the impact of the variability of MLH on aerosol optical properties and mass concentration has been studied and will be described. The lidar provides detailed vertical profiles of aerosol-related information, potentially illustrating the structure of the boundary layer. This paper shows a difference between the methodologies when the boundary layer exceeds 1 km and the atmosphere is unstable. Hampton exhibits a high seasonal variability of average MLH, as in summer the mixing layer exceeds 2km while falling below 2km in winter.

1. INTRODUCTION

Understanding the development and extent of the planetary boundary layer (PBL), the lowest portion of the atmosphere, and knowing the temporal and vertical distribution of aerosols are important for the assessment of the climatic impact of aerosols.

The complexity and variability of boundary layer structure are well known [1-3]. The vertical extent of mixing within the boundary layer and the exchange level with the troposphere are characterized by the height (depth) of the PBL[4]. Traditionally, studies of PBL have been localized and of short duration[5]. Lidar signals can provide information related to boundary layer height and aerosol optical properties. Long-duration lidar measurements also provide the structure of the planetary boundary layer and vertical profiles of extinction and backscatter coefficients on a long time scale. However, retrieval of aerosol optical properties by elastic backscatter lidar suffers from the well-known problem that two quantities are measured from one signal, thus requiring an accurate estimate of the lidar ratio as an input parameter [6-8].

In this study we explore some issues related to boundary layer height using the different methods. We analyze the characteristics of aerosols and we relate these characteristics to boundary layer height structure. We interpret the PBL heights obtained in nontraditional ways such as ground-based lidar measurements of aerosols. We understand the variability and long-term changes in PBL structure and aerosol properties for clear sky days. A global PBL height climatology will, perforce, be based on automated algorithms applied to a very large data set. Such an approach is different from the careful and detailed examination of lidar profiles and short-duration micrometeorology PBL studies. The goals of this investigation are to study the variation of boundary layer height and aerosol properties over Hampton and to evaluate the automated algorithm to retrieve aerosol properties and boundary layer height.

2. DATA AND METHODS

The 48-inch lidar with its enormous collecting area provides the vertical structure of boundary layer height and aerosol optical properties. The HU lidar operates at 1064, 532 and 355 nm using a Nd:YAG laser with a repetition rate of 20 Hz. Under normal operation each measurement consists of a 100s (2000 shots) average. However, for the purposes of this study, only elastic retrievals of 532 are presented.

To calculate the aerosol optical properties we have used the Klett method [6].

The boundary layer height obtained from a radiosounding measurement depends on the degree of the convection prevailing over the region. We have used the Bulk Richardson number which is a dimensionless parameter. The critical value of the Richardson number is 0.25. Above this value the turbulent flow becomes laminar flow. The PBL height is the height at which the value of Richardson number exceeds the critical value. Two different methods are used to calculate the boundary layer height from the lidar signal. The first is an inflection point method. The absolute minimum of the second derivative of the lidar signal is considered to be the mixed layer height [9], and this height is related to the middle of the transition zone (the interface between the mixed layer and the free troposphere). The second method used in this study is based on fluctuations in the signal. This method uses the maximum of the standard deviation of the lidar signal [10, 11]. Both of these methods consider that most of the pollutants, such as aerosols, are concentrated in the PBL. Thus, at the boundary between the mixing layer and troposphere (or the residual layer), a large decrease in the concentration of aerosol is observed as a steep decrease of the range- corrected signal. A summary of seasonal variability of aerosol properties and boundary layer height and aerosol optical properties is presented in this study.

3. BOUNDARY LAYER HEIGHT RETRIEVED FROM LIDAR SIGNAL

The boundary layer heights have been calculated using 2 methods; inflection point method and standard deviation method. The temporal variability of boundary layer height during 2010 and 2011 is analyzed. A comparison of the different methods is shown in Figure 1. It can be observed from the figure that variation of height of boundary layer occurs more during daytime when most of the convection process helps the development of the boundary layer height. The STD method shows lower values of PBL height compared to the second derivative method.

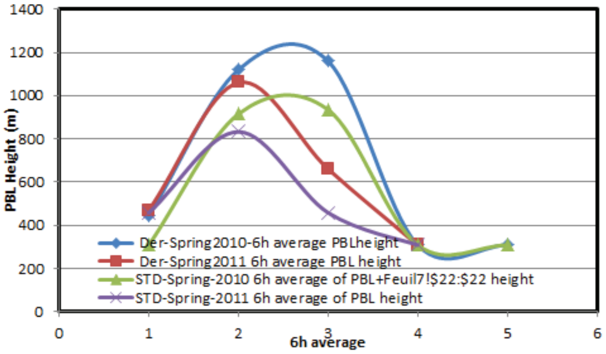

Figure 1. 6 h average of boundary layer height for spring 2010 and 2011. The height of the boundary layer is obtained using standard deviation method (STD) and second derivative of the signal (DER). 1 is the first average between 0:0 to 6:00, 2 between 6:00 and 12:00, 3 is the average between 12:00 and 18:00 and 4 is the average between 18:00 and 23:00 and 5 is at midnight.

Figure 2 shows the seasonal variation of planetary boundary layer based on derivation method. The PBL top is higher in summer compared to winter. The variation of PBL height is more remarkable at the time interval of 12:00 to 18:00.

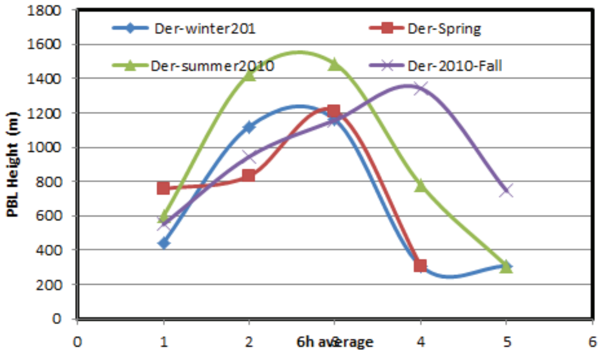

Figure 2. Seasonal variability of PBL height calculated using the second derivative of Lidar signal.

4. COMPARISON OF PBL HEIGHT OBTAINED BY LIDAR AND RADIO SOUND

A comparison of PBL height obtained by lidar signal and radiosonde measurement is shown in Figure 3.From the figure we observe that the low level atmosphere condition is highly dependent upon local weather and meteorology conditions. We cannot easily base PBL height on radiosonde data from Wallops Island which is a distance of over 150 km from Hampton.

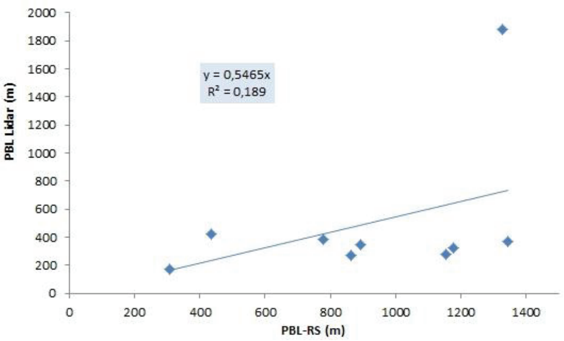

Figure 3. PBL height comparison Lidar and Radio sounding.

5. AEROSOL OPTICAL PROPERTIES

We have considered summer and winter as the two main seasonal variation periods for comparison of the 2010 and 2011 aerosol extinction coefficients. From Figure 4 both winter and summer 2011 show high aerosol concentrations and aerosol extinction coefficient values within the boundary layer height. In 2011 aerosols are also observed at high altitudes, especially in summer.

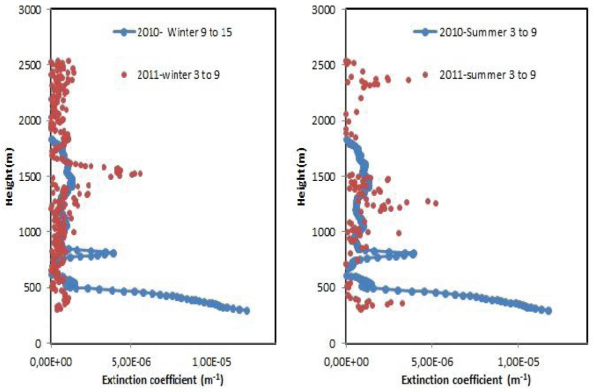

Figure 4. Vertical profiles of aerosol extinction coefficients at 532 nm for 2010 and 2011. For each summer month we have chosen days with a measurement duration of at least 12 hours and averaged. The aerosol extinction coefficient is calculated based on Klett method and using a proper Lidar ratio.

6. AEROSOL MASS CONCENTRATION

The mass concentration of aerosols is measured at NASA Langley, which is approximately 10 km from Hampton University. The seasonal variability of PM2.5 (aerosol with diameter less than 2.5) aerosol mass concentration on 2011 is analyzed. Figure 5 shows the summer and winter comparison of PM2.5 mass concentration.

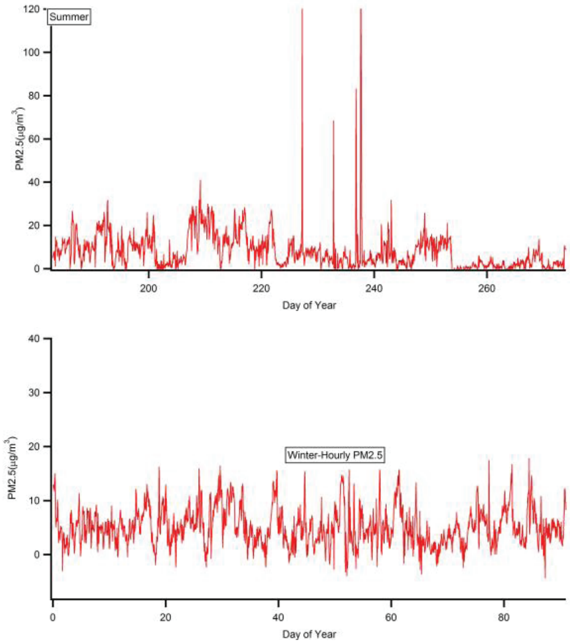

Figure 5. PM2.5 mass concentration for 2011 summer (top) and winter (bottom).

7. RELATIONSHIP BETWEEN MASS AND BOUNDARY LAYER HEIGHT

The impact of the boundary layer on mass concentration and aerosol optical properties has been shown by Boyouk et al [12]. Figure 6 shows the relationship between boundary layer height and mass concentration. The boundary layer height obtained in Hampton from lidar measurements is well correlated to the particle mass concentration. From the figure it is clear that in low level of atmosphere the Wallops PBL height using radio sounding is not well correlated to PM2.5.

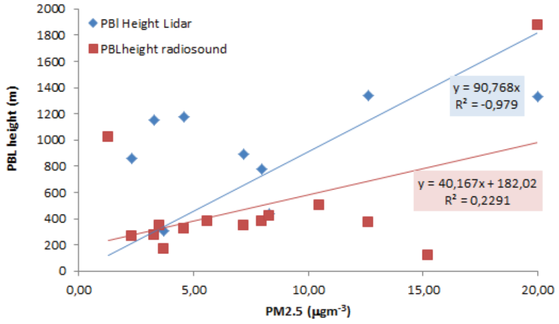

Figure 6. PM2.5 and boundary layer height relationship.

8. SUMMARY

We performed lidar observations over Hampton, VA, USA that allows for better understanding of aerosol characteristics and boundary layer structure. We have calculated the boundary layer height using two different methods and retrieved aerosol extinction and backscatter coefficients and aerosol optical properties. Boundary layer structure can impact the characterization of aerosols. The study of boundary layer height over Hampton shows that continental-coastal winds in this area are the prominent process impacting the height of boundary layer. The climatology of aerosol extinction coefficient exhibits higher values above the boundary layer in summer and spring.

ACKNOWLEDGMENTS

This project is supported by the PIRT project funded by US Army Research, Development, and Engineering Command (AQC) Center (DOD) under HU PIRT Award # 551150-211150) and by NASA under Grant #NNX10AM23G.

REFERENCES

1. Stull, R.B., *An introduction to boundary layer meteorology* 1988, Dordrecht, Boston, London Kluwer Academic Publishers.
2. Garratt, J.R., *The atmospheric boundary layer.* Cambridge Atmospheric and Space Science Series. 1992, Cambridge: University Press.
3. Oke, T., *boundary layer climate*. 1978: Methuen.
4. Seibert, P., Frank Beyrich, Sven- Erik Gryning, Sylvain Joffre, Alix Rasmussen, Philippe Tercier, *Review and intercomparison of operational methods for the determination of the mixing height* 2000, 2000. **34**(Atmospheric Environment): p. 1001-1027.
5. Holzworth, G.C., *Mixing depths, wind speeds and air pollution potential for selected locations in the united states.* J. Appl. Meteoro., 1967. **6**(1039-1044).
6. Klett, J.D., *Stable analytical inversion solution for processing lidar return signal.* Appl. Opt., 1981. **20**: p. 211-220.
7. Klett, J.D., *Lidar inversion with variable backscatter/extinction ratios.* Appl. Opt., 1985. **24**: p. 1638-1643.
8. Fernald, F.G., Herman, B. M., and Reagan, J. A. (1972)., D.o.a.h.d.b. lidar., and J. Appl. Meteorol., 482489., *Determination of aerosol height distributions by lidar.* J. Appl. Meteorol., 1972. **11**(3): p. 482-489.
9. Menut, L., et al., *Urban boundary-layer height determination from lidar measurements over the Paris area.* Appl. Opt., 1999. **38**(6): p. 945-954.
10. De Tomasi, F. and e. al, *The growth of the planetary boundary layer at a coastal site* Boun. Lay. Meteo, 2011. **139**: p. 521-541.
11. Bosenberg, L.A.a.J., *Determination of the convective boundary layer height with laser remote sensing.* Boundary-Layer Meteorology 2006. **119**: p. 159-170.
12. Boyouk. N, et al., *Impact of the mixing boundary layer on the relationship between PM2.5 and aerosol optical thickness* Atmos. Enviro, 2010. **44**: p. 271-277.

Session 7 – Oral Presentations

A SCALABLE RADAR WIND PROFILER FOR BOUNDARY LAYER, TROPOSPHERE, AND LOWER STRATOSPHERE OPERATIONS

Scott A. McLaughlin[1], Bob Weber[1], Frank Pratte[1], David Merritt[1], Tim Wilfong[2], Daniel C. Law[3]

[1]*DeTect, Inc., 117 S. Sunset Ste L, Longmont, CO 80504, USA, scott.mclaughlin@detect-inc.com*
[2]*Tim Wilfong and Associates LLC, 468 Brook Circle, Boulder, CO 80302, USA, timwilfongllc@gmail.com*
[3]*NOAA ESRL, 325 Broadway R/CSD2, Boulder, CO 80305, USA, daniel.c.law@noaa.gov*

ABSTRACT

Stratosphere-Troposphere (ST) radar wind profilers (RWPs) are typically built in the 400 – 500 MHz range and often use coaxial-collinear (COCO) antenna elements and monolithic transmitters. COCO elements are large and fragile, limit sidelobe control, and limit antenna sizes. Monolithic transmitters are not easily reconfigured for different powers and are difficult to maintain. The lack of scalable antennas and transmitters has meant that ST systems have limited configurations.

A new wind profiler model from DeTect, Inc. (RAPTOR FBS-ST), is scalable in both the antenna and the transmitter. The antenna uses Yagi-Uda elements, each with a solid-state phase shifter to allow Full Beam Steering (FBS) and uses “thinning” to control sidelobes. The transmitter is constructed of 2-kW blocks allowing configurations from 2 thru 16 kW and higher. These features allow the system to be produced with various antenna and transmitter sizes to create a power-aperture product (or cost target) to match the user’s needs (e.g., boundary layer through full ST radars).

In 2010 the DeTect RAPTOR FBS-ST was competitively chosen by the US National Weather Service (NWS) to replace the NOAA Profiler Network (NPN) systems. The Next Generation NPN (NGNPN) Demonstration unit has been operating in Longmont, CO since mid-2009. The first production system is installed at the NWS Radar Operations Center (ROC) in Norman, OK. Three more units will be installed in 2012 (see Figure 1).

1. SYSTEM SPECIFICATIONS

The RAPTOR FBS-ST can be built with various configurations for the antenna and the transmitter. Radar health and status monitoring is built-in throughout the system.

For the NWS, the RAPTOR FBS-ST was designed to have the same performance as the original 404 MHz systems, installed for the NOAA Profiler Network (NPN) in the early 1990’s. Table 1 lists specifications for the RAPTOR 449 MHz FBS-ST 256e-12kW used for the NPN.

Figure 1: RAPTOR FBS-ST installed in Norman, OK.

Table 1: RAPTOR FBS-ST Specifications for NPN Model

Transmit Frequency	449 MHz (for USA)
Transmit Power	12 kW (peak)
Duty-Cycle (max)	15%
Antenna Diameter	12 m
Number Elements	256
Element Type	3-element Yagi-Uda
Amplitude Taper	30-dB Taylor weighting
Antenna Gain	31 dBi
Beamwidth	< 5°
Steering	Anywhere in cone ± 20°
Transceiver	Single conversion heterodyne
DAC & ADC	16-bit transmit and receive
Lowest Range Gate	170 m

2. ANTENNA

The antenna array is composed of 256 Yagi-Uda elements, each fed the same power, but arranged in a computed thinned pattern to create the desired amplitude taper, in order to control sidelobes. Random thinning is used, which creates unsymmetrical random sidelobes. See [1] for information on antenna thinning. Figure 2 shows the antenna array element layout.

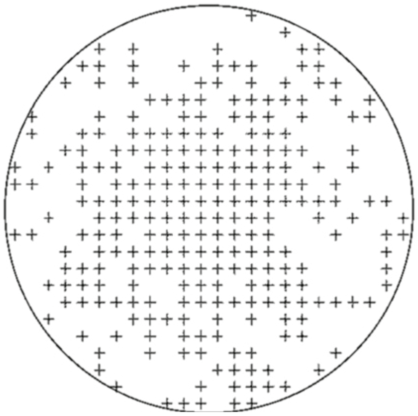

Figure 2: Antenna array layout, showing random thinning

For antenna steering, each Yagi element utilizes its own 4-bit PIN diode phase shifter. This allows for Full Beam Steering (FBS), meaning the array can be pointed anywhere in a cone above the radar. This allows for normal Doppler Beam Steering (DBS) (i.e., 5 beam: N-S-E-W-V) or more complex steering such as zenith angles tailored for each mode, rotating the azimuth to avoid clutter, and also Velocity-Azimuth Display (VAD) pointing (and processing). The FBS ability also allows for sun-tracking (for antenna and receiver verification) any time of year (depending on site latitude). The phase shifters are solid-state and therefore have no moving or wearing parts and conceivably could last for the life of the radar itself. An installed phase shifter assembly is shown in Figure 3.

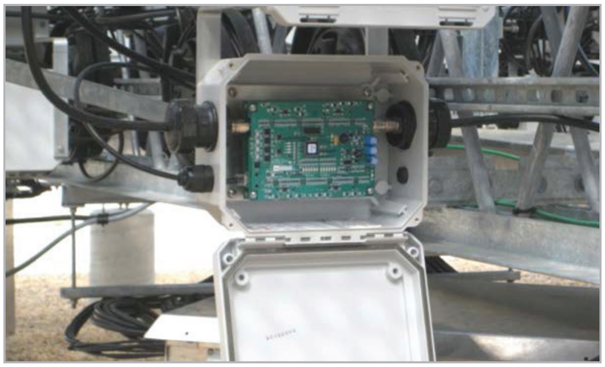

Figure 3: Phase shifter in NEMA 4X enclosure under the antenna.

Antenna pointing is accomplished via serial communication's commands originating from the Wind Profiler Computer (WPC). These serial commands are converted from RS-232 to RS-485 and distributed to the Phase Driver Units (PDUs), along with DC power for the phase shifters. There are 8 PDUs for the 256 element array, each powering and controlling 32 phase shifters. All phase shifters and the PDUs are monitored for operation. Figure 4 shows a Secondary Divider Enclosure with open door.

Figure 4: Secondary Divider Enclosure (SDE) under the antenna showing 64-way divider and PDU. Door is normally closed and enclosure is water-tight.

Since array thinning is used to control sidelobes, unequal RF power dividers are not required for the antenna feed system. This allows a highly simplified feed system composed of a single 4-way divider and four 64-way dividers.

The overall design of the antenna allows for graceful degradation of almost any component. For example, individual phase shifters, Yagi's, cables or PDUs can fail and the antenna will still form the main beam (pointed in the correct direction), albeit, with potentially higher sidelobes and a wider beam width. The efficacy of this point can be best illustrated by noting that this thinned array originated by thinning a filled 448 element array by about 57%.

All RF and DC connections for the antenna array are located within NEMA 4X housings, so there is no risk of water intrusion and no need for vulcanizing tape or other water-proofing aids on RF connections.

3. TRANSMITTER

The 12-kW transmitter is composed of 2 kW base units combined in a high-power RF combiner. Redundant DC power supplies are also used. The design specifically allows for higher or lower powers and soft-fail capability. Figure 5 shows the transmitter in a 12-kW configuration (i.e., 6 2-kW power amplifiers).

To fully protect the transmitter and always allow 50-Ohm operations, the Transmit/Receive (T/R) Switch utilizes an isolator composed of a ferrite circulator with the 3rd port terminated to a higher power load. After the isolator a duplicate circulator is used along with a high power PIN diode passive limiter to protect the receiver.

At the output of the 2nd circulator a harmonic filter is used, finally a high-power dual directional coupler for monitoring forward power and antenna VSWR, and finally a high power lightning arrestor.

Figure 5: RAPTOR FBS-ST transmitter stack showing 6 2-kW units, 3 redundant power supplies and RF divider/combiner.

4. PROFILER DATA SYSTEM

The Profiler Data System (PDS) utilizes (a) optimized sampling strategies, (b) a modern digital transceiver, and (c) advanced signal processing for the generation of reliable and accurate meteorological data products.

The sampling strategies include the use of 4-beam antenna pointing (which has been shown by Adachi [2] and others to significantly improve data quality) and the use of several radar modes in order to optimize atmospheric sampling. One mode utilizes a single short non-coded pulse to provide spatial sampling with the highest resolution as low as possible, just above ground level. Since radar sensitivity limits the maximum altitude of these observations, another radar mode uses a 4-bit code version of this short pulse in order to extend these high-resolution observations to greater altitudes in the lower troposphere. A third mode uses a 4-bit code with a long pulse in order to maximize radar sensitivity and to extend observations to 16 km and higher above ground level.

4.1 Digital Intermediate Frequency Transceiver

The digital transceiver employs an off-the-shelf Software Defined Radio (SDR) card, which is composed of a Field Programmable Gate Array (FPGA), a 16-bit digital-to-analog converter (DAC) for creating the transmit waveform, and a 16-bit analog-to-digital converter (ADC) for digital sampling the radar return signal.

Through the use of the programmable FPGA and the DAC, shaped waveforms are transmitted which specifically maximize use of available frequency spectrum yet can be perfectly processed with the radar matched filter. For example, raised-cosine pulses are easily created and used for the complimentary bi-phase pulse coding.

4.2 Signal Processing

Time series data from the SDR Card are processed using long Fast Fourier Transforms (FFTs), with 16k or more points in order to minimize aliasing of out-of-band noise and radio frequency interference (RFI). Estimates of incoherently averaged radar Doppler spectra are generated using a technique that minimizes effects of intermittent clutter as shown in [3] and [4]. Nevertheless, these radar spectral estimates generally will include, in addition to noise and radar return from the atmosphere, some contaminating signals from other sources (i.e., ground clutter, RFI, bird and aircraft echoes, hydrometeor echoes in antenna sidelobes, etc.). Therefore, noise and all signals present in these spectra are detected and measured.

This multiple-signal spectral information is processed to identify and to separate the atmospheric radar return signals from radar spectral noise and from any unwanted contaminating signals that may be present. That process includes using the time-height continuity and the consistency across four radar antenna beams, which are expected for most radar return from the atmosphere. In addition, the properties of spurious signals are also used to identify and to discriminate against their contribution to meteorological data products. Finally, quality controls are utilized [5] to screen out any remaining outliers in the wind data. The entire signal processing chain provides a high degree of immunity to RFI, birds, planes, ground clutter, and other sources of interference to wind profiler operations.

5. SCALABILTIY

As noted in the antenna and transmitter descriptions, each can be scaled for various sizes and powers. This allows the radar to be built for BL through ST use.

The antenna is built utilizing 64-element sections. This allows for 64, 128, 192, 256, 320, 384…512 element arrays. Each size only requires a new layout and a smaller or larger ground plane. The functionality and operations of the antenna is identical any configuration.

The transmitter is similarly designed to allow simple scalability. The 2-kW base units can be pared down to only one unit, or increased to 8 or more, depending on the antenna size. Again, the functionality and operations are identical no matter what size is used.

These features allows for a high degree of system tailoring depending on user requirements or budget. This design also allows a system to be easily upgraded in the future if a smaller less-powerful system was initially installed.

6. DATA RESULTS

Data collected from the RAPTOR FBS-ST was shown to meet NWS objective accuracy requirements (in the original procurement) of 0.5 m/s. Data comparisons were conducted between local Rawinsondes, the Rapid Update Cycle (RUC) model hourly analyses and a nearby NPN profiler in Platteville Colorado (PLCT2). A small discrepancy was noted between modes but has been attributed to mode-specific pulse-width range weighting.

During the month long test, the Raptor wind profiler operated in three modes – Lo-low, Low and High to provide altitude coverage from 165 meters to 16,265 meter above the ground level (AGL). The operating parameters are shown in Table 2 below. Note the modes overlap slightly. Figure 6 shows the data availability with height.

Table 2: RAPTOR Modes for NWS NPN Operations

Mode	LO-LOW	LOW	HIGH
Pulse Duration (µs)	1.4	1.68	6.81
Code Length (chips)	1	4	4
Sampling interval (m)	62.4	80.6	199.6
Lowest Range (m)	165.3	1894.5	4490.4
Highest Range (m)	2288.4	5844.8	16265.4
No. Range Gates	35	50	60

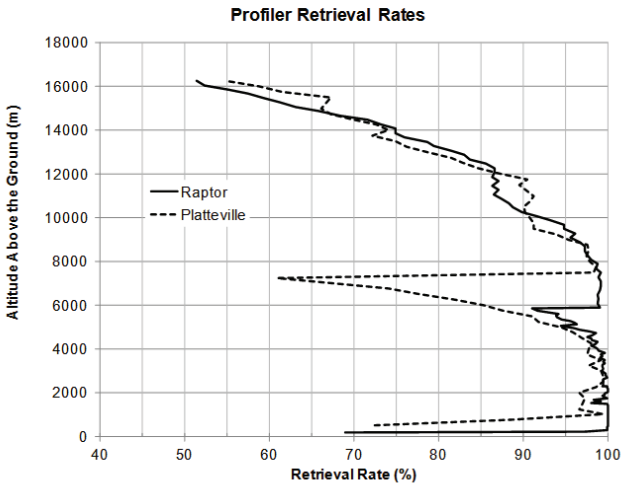

Figure 6: Altitude performance during winter 2009 testing period, comparing RAPTOR and nearby NPN system.

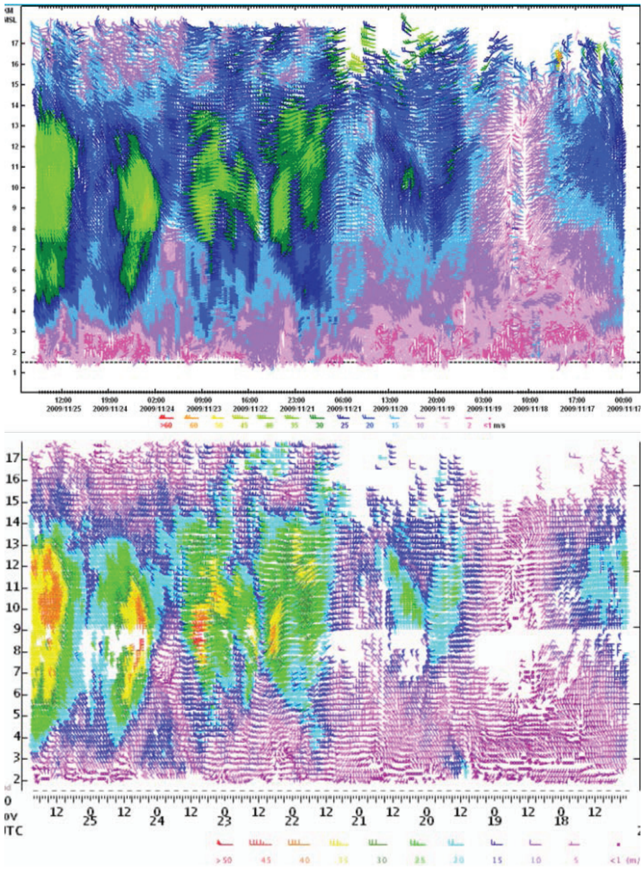

Figure 7: Comparison data showing RAPTOR FBS-ST data on the top and an older NPN system (data is shown above MSL).

REFERENCES

1. Skolnik, M.I., *Introduction to radar systems, 2nd ed,* (Ch 7)*,*1980, NY: McGraw-Hill Book Company.

2. Adachi, A., et al., *Evaluation of Three-Beam and Four-Beam Profiler Wind Measurement Techniques Using a Five-Beam Wind Profiler and Collocated Meteorological Tower.* Journal of Atmospheric and Oceanic Technology, 2005. **22**(8): p. 1167-1180.

3. Lehmann, V. and G. Teschke, *Advanced intermittent clutter filtering for radar wind profiler: signal separation through a Gabor frame expansion and its statistics.* Ann. Geophys, 2008. **26**(4): p. 759-783.

4. Merritt, D.A., *A statistical averaging method for wind profiler Doppler spectra.* J. Atmos. Ocean. Tech., 1995. **12**: p. 985-995.

5. Weber, B., et al., *Quality controls for profiler measurements of winds and RASS temperatures((radio acoustic sounding system)).* Journal of Atmospheric and Oceanic Technology, 1993. **10**(4): p. 452-464.

TURBULENCE MEASUREMENT USING A PULSED DOPPLER LIDAR AND THE CONTRIBUTION OF VERTICAL BEAM ON ITS ACCURACY FOR SHORT RANGE LIDARS

Mehdi MACHTA, Matthieu BOQUET[1]

[1]*LEOSPHERE, 76 rue de MONCEAU,75008,Paris, France, mmachta@leosphere.fr*

1. ABSTRACT

Assessment of climatic conditions for a wind farm project includes the study of the wind characteristics on a particular site. It concerns not only mean wind speed and direction statistics but also other wind parameters like shear values over the whole rotor area, flow-inclination and turbulence intensities. If long considered as secondary parameters, these values are now becoming more and more critical to develop and optimize a wind farm project.

With the spread of the remote sensing Lidar technologies in concrete resource assessment program, it should be clearly investigated the accuracy of Turbulence Intensity measurement with Lidars and how it compares to traditional anemometry. This paper aims to study this purpose on Pulsed Lidars and propose an alternative method to improve remote sensor accuracy.

2. TURBULENCE INTENSITY AND TURBULENCE CURVE.

Turbulent diffusion is generally characterized by its second order moments. In the wind energy industry, one wants more specifically to study the wind regimes with the Turbulence Intensity (TI) parameters given by the standard deviation over the mean value of the wind speed $TI = \frac{std(HWS^{10minutes})}{mean(HWS^{10minutes})}$. TI is usually measured over a period of 10 minutes.

Starting from this measurement of temporal intensity, it is possible to determine turbulence curve which is characteristic of the field. This curve depends on altitude and direction sector and is calculated by averaging occurrences of TI corresponding to Wind speeds values between $V_h = N\, m.s^{-1}$ and $V_h = (N+1) m.s^{-1}$ (Example in figure 4 and 5). This curve can help choosing the most appropriate wind turbine and forecasting its power curve as well as its service life.

3. PULSED LIDAR CLASSICAL METHOD

Accurate measurement of TI is necessary, mainly for site suitability analysis. Several Lidar to cup comparisons have however shown a deficit in the ability to accurately retrieve this parameter especially on complex field (see blue scatter plot in Figure 3) and the reasons of that are being closely investigated on WINDCUBE Pulsed Doppler Lidar system.

Usually, Wind pulsed lidar measures turbulence intensity using the algorithm below where $V_0, V_{90}, V_{180}\ and\ V_{270}$ are the radial speeds measured by the Lidar in North, East, South West respectively (Figure 1).

Every second, the WINDCUBE Lidar calculates two horizontal wind speed components U and V. The retrieval process mixes two opposite radial wind speeds from the four measured for each of the U and V components. Example below for one sample i of $U(i)$:

$$U_{lidar}(i) = \frac{V_0 - V_{180}}{2\sin\theta} = \frac{u_0 - u_{180}}{2} + \frac{w_0 - w_{180}}{2\tan\theta}$$

Therefore, the standard deviation estimated by the WINDCUBE on the *x-axis* for example is given by:

$$std(u_{lidar})^2 = \frac{std(u_{true})^2 + < u'_0 | u'_{180} >}{2} + \frac{std(w_{true})^2 + < w'_0 | w'_{180} >}{2(\tan\theta)^2} + \frac{< u'_0 + u'_{180} | w'_0 - w'_{180} >}{2}$$

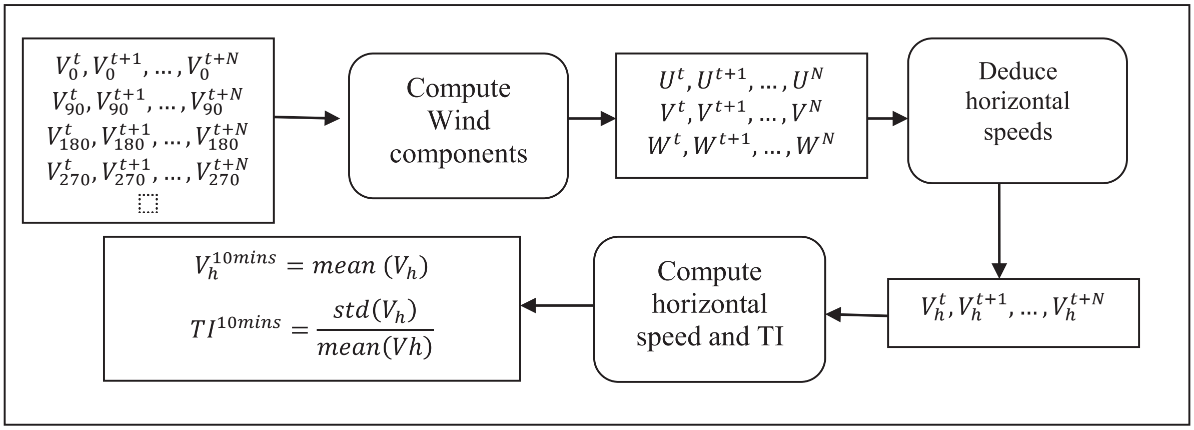

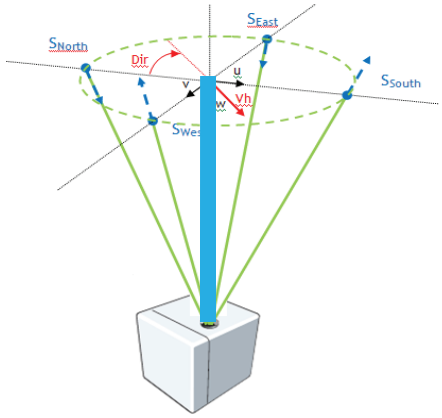

Figure 1 : Windcube lidar design and reconstruction vectors

While the correct parameter to retrieve is $std(u_{true})$, on the above expression it is seen that the vertical component influences the turbulence intensity measured by the Lidar through its second order moments: variance and covariance.

In simple field, vertical components $W_0$and W_{180} are usually weakly correlated especially on high altitude, therefore measuring turbulent intensity is accurate using the classic method (figure 6 and 7). On the other side, in complex field, vertical component is highly correlated to radial measurement, especially for low altitudes; therefore the measurement of turbulent intensity is highly noisy (figure 6 and 7).

4. ENHANCED METHOD

The study of turbulence intensities with Lidars requires a good estimation of the vertical wind speed and standard deviation of it. For this reason the configuration of WINDCUBE® V2 Lidar has been improved by adding a vertical beam that measures directly W wind speed component (Figure 1, blue beam).

Unlike the classical method where wind components variances where noised by each other $\sigma_{HWS} = f(\sigma_W)$, the new design provides an accurate measurement of W wind component. Through this direct measurement of vertical speed, decoupling verticals variation from horizontal variation (σ_{HWS}) is made in order to improve TI measurement accuracy. This method was tested on complex and simple fields with the aim to quantify the contribution of vertical shooting. The results are shown in the following section.

5. RESULTS

In order to validate the effectiveness of the vertical beam, two measurement campaigns were held in Risoe's test field in Hovsore (Simple terrain) from June 2011 to September 2011 and in CRES's test field in Lavrio (Complex field) from August 2010 to October 2010. During these campaigns, WINDCUBE TI measurements were compared to Mast cup anemometer on different altitudes.

In complex field, conventional method is inefficient (Figure 3). Correlation factor is low (0.3 to 0.5) and root mean error (rmse) is high (0.08). Furthermore, turbulence curve is overestimated and error can reach 50% (Figure 5). Contrariwise, the conventional method provide acceptable results on simple field (rmse= 0.02 and R^2=0.8) and turbulent curve is accurately estimated with average error <15% (Figure 4).

Using a vertical beam to measure W wind component allows "de-biasing" the measurement of horizontal turbulent intensity. This measurement results on better accuracy of turbulence accuracy (Figure 3) where error percentage is decreased by 30% in average (Figure 5) and permitted better correlation coefficient: 0.88 using the vertical beam compared to 0.34 using classic method (Figure 3). This can also be seen on root mean square which decreased from 0.1 to 0.02.

This improvement is observed on all altitudes (Figure 6 and 7) and allowed to obtain constant rmse of 0.02 which does not depend on altitude nor field complexity.

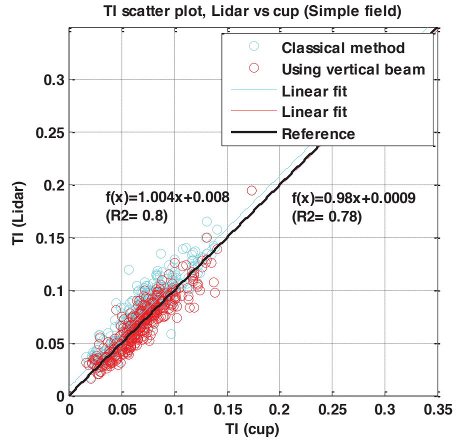

Figure 2 : Comparing TI measurement methods efficiency on Simple field (Direction 150° to 180°, Altitude 80m)

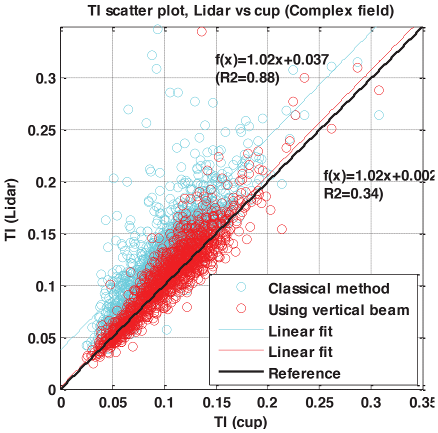

Figure 3 : Comparing TI measurement methods efficiency on Complex field (Direction 0° to 30° , Altitude 76m)

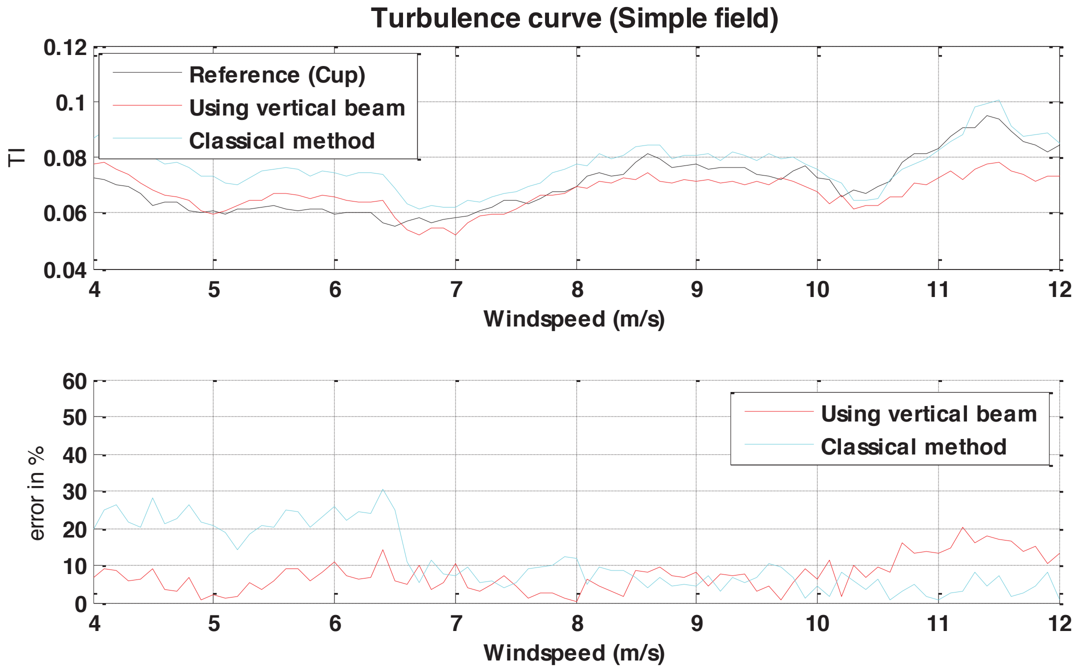

Figure 4 : Turbulence curve on Simple field compared to reference (Direction 150° to 180°, Altitude 80m)

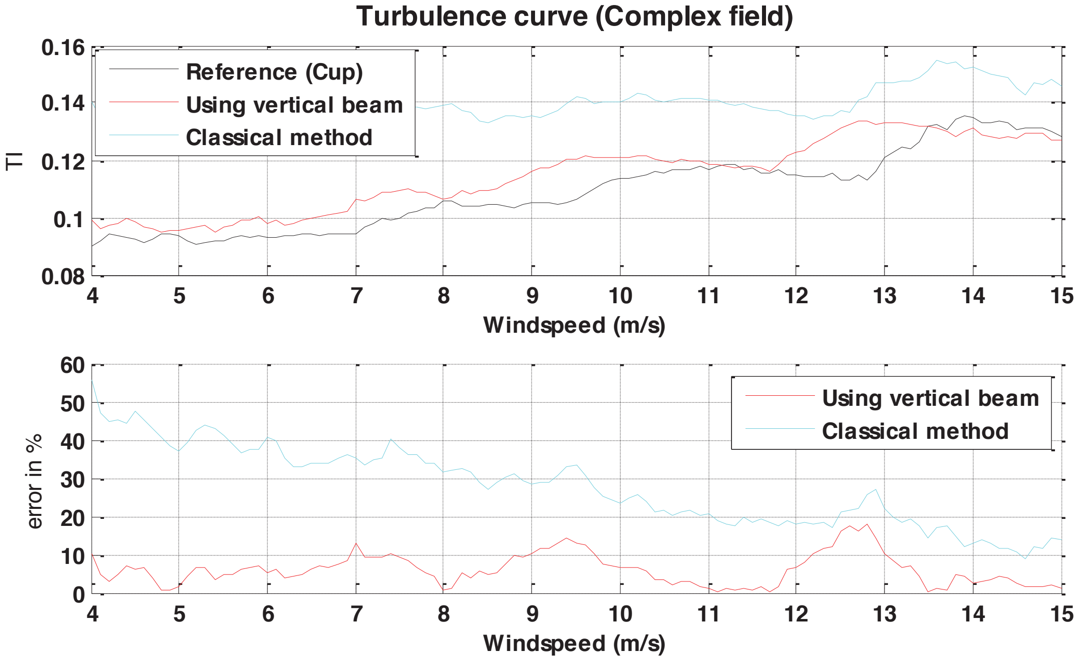

Figure 5 : Turbulence curve on Complex field compared to reference (Direction 0° to 30° , Altitude 76m)

Thanks to direct vertical wind speed measurement, turbulence curve error was reduced from 30% to 8% in the complex terrain of CRES and from 15% in average to 8% in the simple terrain of Risoe. In order to validate this method, more measurement campaigns are scheduled in other terrains.

.

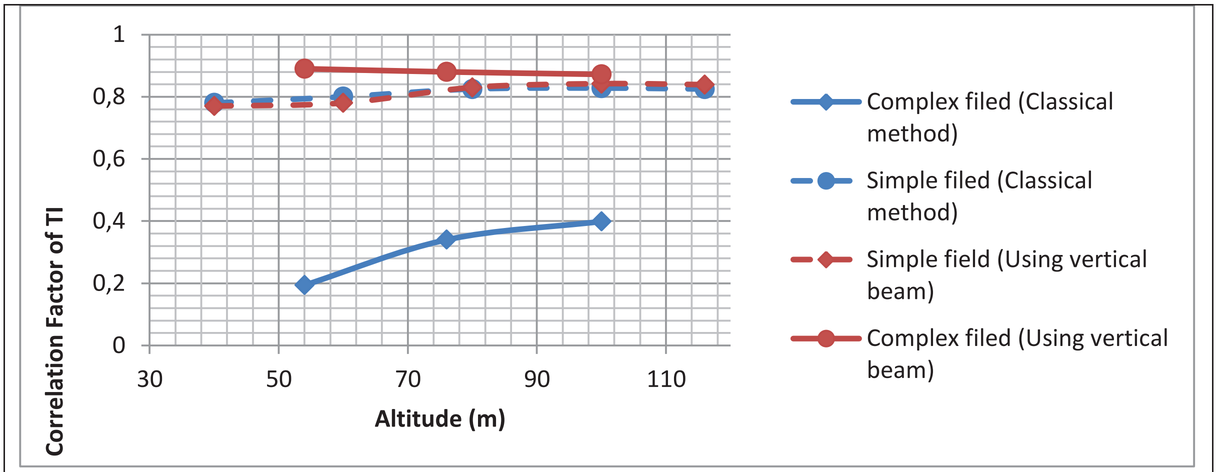

Figure 6 : Correlation Factor of Lidar TI measurement compared to Cup reference.

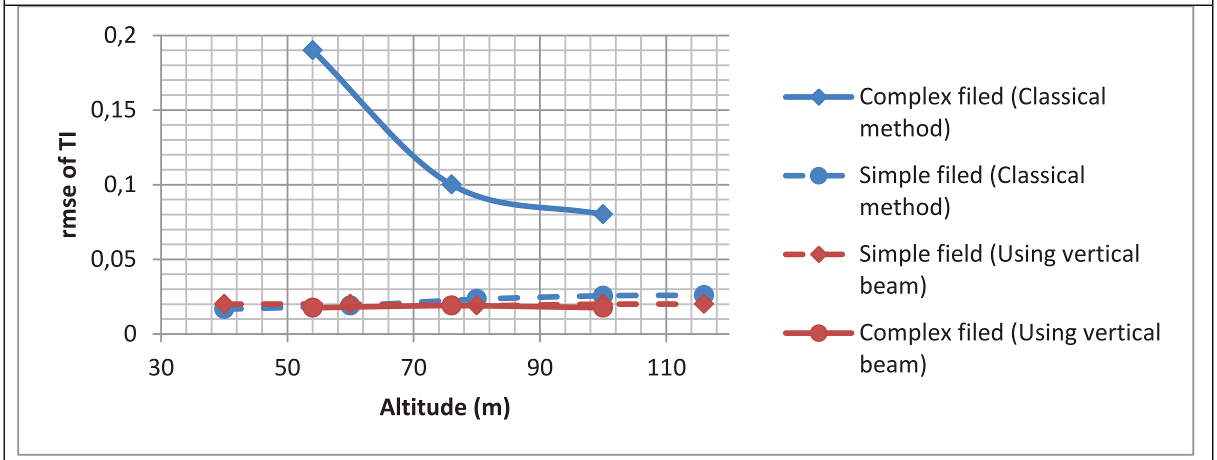

Figure 7 : rmse of Lidar TI measurement compared to Cup reference.

6. CONCLUSION AND PERSPECTIVE

The turbulence measured by the Cup anemometer differs from the turbulence reconstructed by the Lidar because of the Lidar reconstruction process. This process mixes the vertical and horizontal turbulences. To access the horizontal turbulence, we improved our WINDCUBE V2 design by adding a vertical beam which provides direct measurement of W wind component and we established a new turbulence reconstruction algorithm. This algorithm uses the second order moments of the vertical wind speed to obtain a new estimation of the horizontal turbulence intensity. We have succeeded in enhancing TI measurement accuracy and minimizing the error on turbulence curve on simple and complex terrain.

Ongoing effort is on the improvement of this method to reach higher quality estimations of turbulence intensities and validating this method on new measurement campaigns.

7. ACKNOWLEDGEMENT

The authors want to sincerely acknowledge Dimitri Foussekis from CRES and Rosenne Wagner from Risoe for their cooperation in providing wind data.

FIELD RESULTS FROM A NEW MINIATURE BISTATIC SODAR

Alexander Strehz[1], Stuart Bradley[1], Kenneth Underwood[2]

[1]*Physics Department, University of Auckland, Private Bag 92019, Auckland, New Zealand,*
a.strehz@auckland.ac.nz, s.bradley@auckland.ac.nz
[2]*Atmospheric Systems Corp., 26017 Huntington Ln., Unit F, Valencia, CA 91355, USA, ken@minisodar.com*

ABSTRACT

Field results from a new bistatic receiver are described. The receiver has 16 rows of 4 low-noise electret microphones (64 total) with very low power consumption. The receiver receives all scattered sound from a single vertical transmission made by a transmitter about 40m distant. Phasing of the microphone rows via FFT methods allows, in virtually real-time, for a wind component profile to be obtained. Two new bistatic receivers, together with a central monostatic receiver, allow wind vector profile to be obtained from a single atmospheric column: each wind vector is obtained from a 'common volume', thus avoiding the problems inherent in monostatic lidar and sodar systems. In practice it is possible to detect where in space the transmitted sound pulse is, or alternatively range gate according to time. The new receivers are 100x480x50 mm, and extremely light, so fit readily into a small suitcase, although they do need mounting on a tripod. The receivers can be solar-powered, with wireless communication to a central PC.

Comparisons are made with an ASC monostatic sodar. It is found that the new bistatic receiver has a range comparable or exceeding the monostatic system. Individual ten-minute profiles are compared. The correlations are similar to those typically reported for monostatic sodars being compared with masts. The difficulty then is in knowing whether the small differences are due to the spatially distributed sampling volumes of the monostatic instrument. Unfortunately we are not fully convinced that this will be elucidated by comparison with mast instruments.

1. MOTIVATION

Lidars and sodars measure the Doppler shift due to the radial component of wind along off-vertical beam directions. Measurements from 3 or more beam directions are used to build up the 3 components of the wind vector at each height, as shown in Fig. 1. The assumption in this method is that the same wind is present in each of the volumes sampled by the various beam directions [1].

Very good wind estimates are obtained by both lidars and sodars if this assumption is true. Numerous comparisons with mast-mounted instruments, on flat terrain, and with steady flow, have shown correlations with $R2 > 0.985$ for either lidars or sodars.

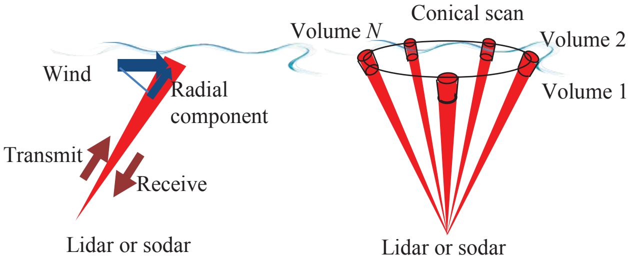

Figure 1. Wind vectors are assembled at each height layer by estimating the radial Doppler shift from a number of sampling volumes in a conical scan.

When wind flow is not horizontally homogeneous (in complex terrain), the radial wind equations contain different wind components (Fig. 2). For example, a 3-beam system sampling 3 separate volumes at a particular height will have u_1, u_2, and u_3 for the easterly wind component instead of just u, and 9 wind components in total, instead of just 3 [2].

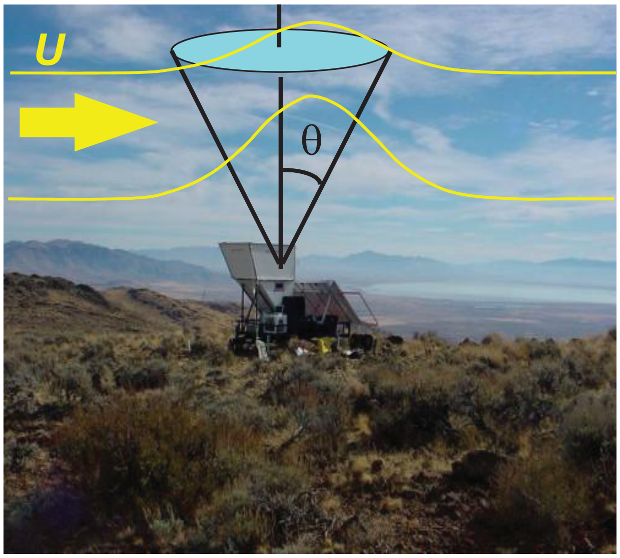

Figure 2. Different volumes in a conical scan contain different winds, especially in complex terrain.

Measurements using conventional lidar or sodar technology show up to 6% errors in wind speed estimates in complex terrain, when compared with mast-mounted instruments (Fig. 3). In this situation, the mast instruments measure in a single volume at a particular height, and so do not show errors due to horizontal variability of the wind [3][4].

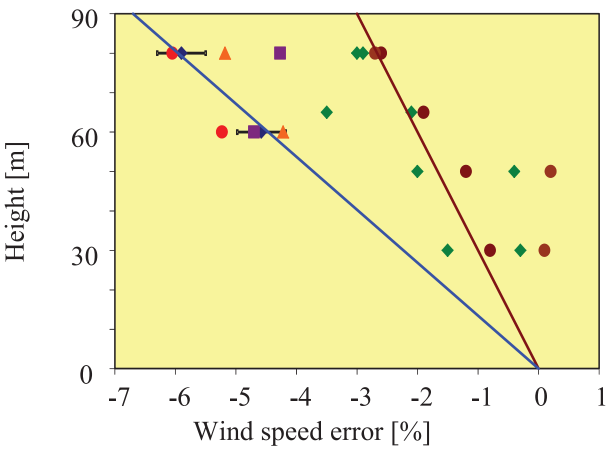

Figure 3. Measurements at a moderate hill site (ZephIR lidar measurements in green, AQ500 sodar measurements in brown), and at a complex site (Metek sodar measurements in blue). Model results are shown for a bell-shaped hill potential-flow model (orange), WindSim (purple) and OpenFOAM (red) for the complex site.

2. COMMON VOLUME SCANNING

Doppler shift, the signal which gives wind information, occurs when there is a component of the wind along either of the transmitted and received beams. A geometry having vertical transmission and oblique reception will give Doppler shift (Fig. 4).

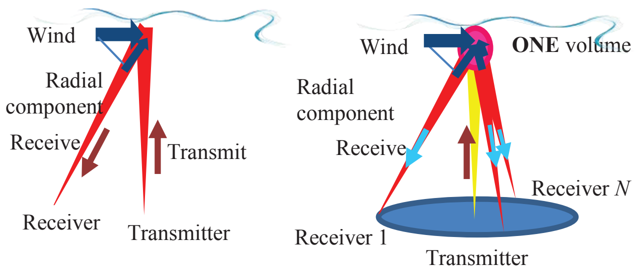

Figure 4. The common volume configuration is based on a conical scan of receivers, so that all the Doppler shift components originate from a single volume.

Previous common-volume systems, also known as 'bi-static', have directed the receiver beams to a single volume [5]. Here we describe a scanning common volume system, in which the receiver beams track the acoustic pulse which travels vertically upward from the central transmitter [6].

3. A NEW MAST-LIKE SODAR

The new scanning common-volume system consists of a central transmitter, directed vertically, and 2 inclined phased-array receivers, each at a distance of around 40m from the transmitter, as shown in the photograph in Fig. 5.

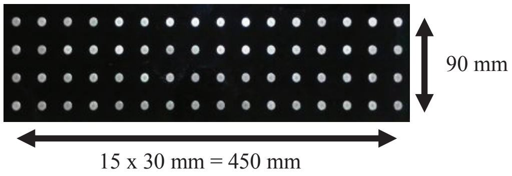

Figure 5. Photograph of a receiver front panel showing the 64 electret microphones. The overall dimension is 500 x 100 x 50mm.

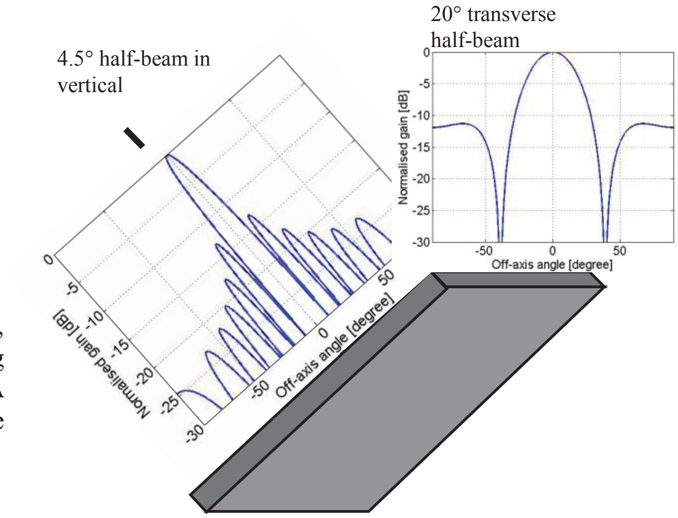

Figure 6. The beam configuration has 4.5º half-beam width in the vertically scanning plane, and a 20º half-width laterally.

This gives a narrow beam in the vertical (scanning plane) and a broad beam in the lateral direction (which facilitates alignment with the columnar transmitted beam.

Results from scanning the array in both the vertical plane and in frequency are shown in Fig. 7. The position of the transmitted pulse in space can be clearly seen. With this system it is possible to track the pulse as it ascends the sampled column. A typical received spectrum is also shown in Fig. 8.

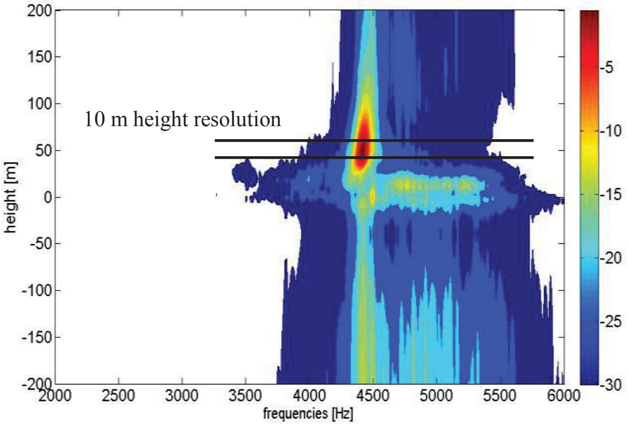

Figure 7. Scan over height and frequency by phasing the microphone rows. The position of the transmitted pulse at the time of the scan can be clearly identified.

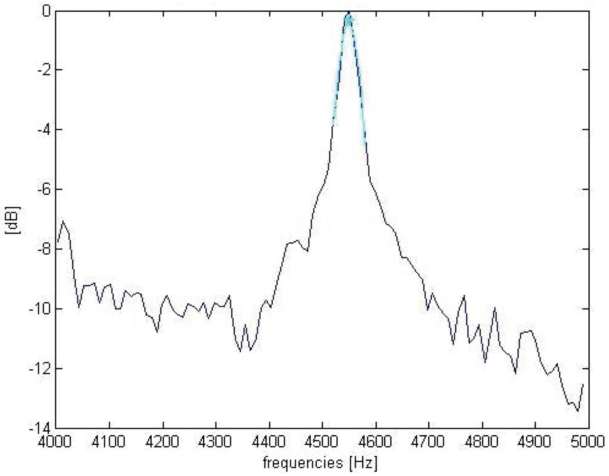

Figure 8. Measured received spectrum from 120 m. height. Signal-to-noise ratio is about 10 dB, but this will vary with conditions.

4. WIND DRIFT DOPPLER CORRECTIONS

When tracking the transmitted pulse we found that its position drifts a little with the wind [7]. The geometry is shown in Fig. 9. The receiver is sensitive to a narrow field of view at zenith angle θ_0 and measures a spectrum from a short time interval centered on time t_0 from the time of transmission. The horizontal wind u carries the sound downwind a distance ut_0. The sound which reaches the receiver, coming from zenith angle θ_0 has originated upstream from the transmitter a distance $z\tan\theta_1$, where z is the height of the scattering volume, as shown in Fig. 9. A measurement of fractional Doppler shift is made

$$\frac{\Delta f}{f_T} = \frac{u}{c}\left(\sin\theta_0 + \sin\theta_1\right) = \frac{u_0}{c}\sin\theta_0 \qquad (1)$$

or

$$\sin\theta_1 = \left(\frac{u_0}{u} - 1\right)\sin\theta_0 \qquad (2)$$

where f_T is the transmitted frequency, c is the speed of sound, and u_0 is the inferred wind speed if wind drift corrections are not made. From the figure,

$$z\left(\tan\theta_0 - \tan\theta_1\right) = D - ut_0 \qquad (3)$$

and

$$z\left(\frac{1}{\cos\theta_0} + \frac{1}{\cos\theta_1}\right) = ct_0 \qquad (4)$$

Eliminating z from (3) and (4), and assuming to first order $\cos\theta_1 = 1$ and

$$\frac{\sin\theta_0}{1+\cos\theta_0} = \frac{D}{ct_0} \qquad (5)$$

then

$$\frac{u}{u_0} = 1 - \frac{u_0}{c}\,\frac{1+\cos\theta_0}{\sin\theta_0\cos\theta_0} \approx 1 - 2\frac{u_0}{c}\frac{z_0}{D} \qquad (6)$$

where $z_0\tan\theta_0 = D$. For $u_0 = 3.4$ m s^{-1}, D =40 m, and z_0 = 100 m, the correction is 5%, and so is significant. The difference between z and z_0 is less than 1 m.

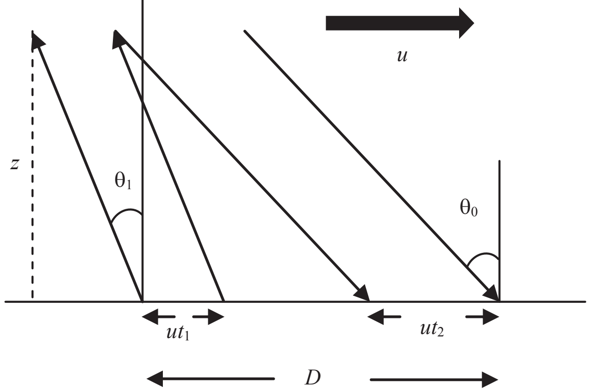

Figure 9. The geometry in a single vertical plane showing the transmitted beam drifting to the right with the wind and the received beam also drifting.

5. FIELD MEASUREMENTS

The central transmitter was provided by an ASC4000 monostatic sodar, and the common-volume receivers synchronized with its transmit pulse. This configuration allowed both monostatic and common-volume Doppler profiles to be obtained simultaneously. Fig. 10 shows a succession of 10-minute average profiles from both instruments.

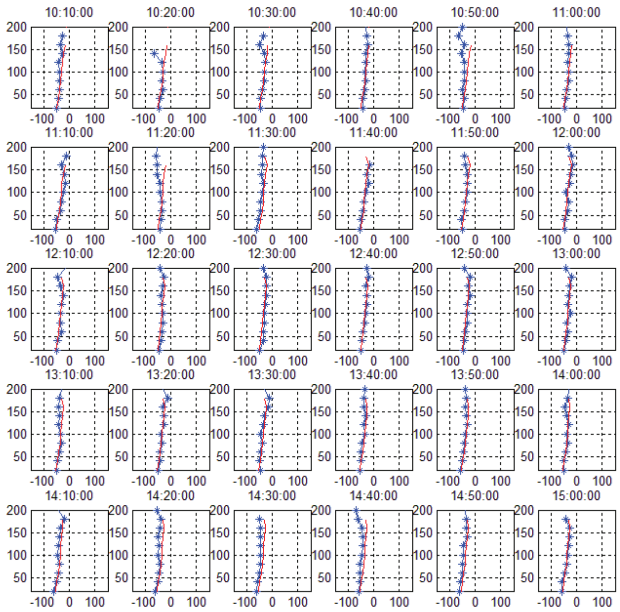

Figure 10. A succession of Doppler profiles, every 10 minutes, for an ASC4000 monostatic sodar (red) and one common volume receiver (blue). The monostatic profiles are corrected to allow for the different Doppler formula in the bistatic mode.

These Doppler measurements are readily converted to wind speeds. A scatter plot is shown in Fig. 11.

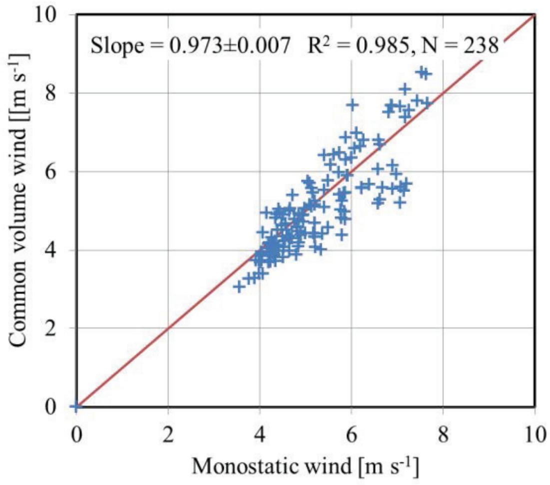

Figure 11. Raw data scatter plot of wind speeds measured during a short period of a few hours by an ASC4000 monostatic sodar and a common volume receiver.

This is a raw data plot. The only filtering which has been applied is to reject data points which have unphysical vertical wind shear. This simple filter mostly rejects data from the uppermost ranges, where signal-to-noise ratio is lower. The filter is applied only on the basis of single-instrument data.

6. CONCLUSIONS

Ideally wind measurements by ground-based remote sensing instruments are, at each height, from a single well-defined volume. Current lidars and sodars combine measurements from several volumes at each height.

We are designing a common volume system, in which all wind data at each height comes from a single well-defined volume. This system scans within a vertical column, so that winds are obtained from a similar geometry to those from a tall well-instrumented mast. Field results show, on flat homogeneous terrain, close agreement with wind profiles obtained by conventional instrumentation. Results shown here are essentially without any data quality control or filtering, apart from a very simple extreme error filter. Once the usual data filtering is implemented, of the type which is operationally applied in all sodar and lidar systems, it is expected the agreement between instruments will be much closer. The new common-volume scanning receivers are extremely light, very compact (can be carried in one hand) and, being passive, consume very low power.

ACKNOWLEDGMENTS

ASC is acknowledged for the provision of funding.

REFERENCES

1. Bradley, S. G., 2007: *Atmospheric Acoustic Remote Sensing*. Florida, CRC Press/ Taylor and Francis Group, 328pp.. ISBN 978-0-8493-3588-4.

2. Bingol, F., J. Mann, and D. Foussekis, 2009: Conically scanning lidar error in complex terrain. *Meteorologische Zeitschrift*, **18**, pp. 189–195.

3. Behrens, P., J. O'Sullivan, R. Archer, and S. Bradley, 2012: Underestimation of mono-static sodar measurements in complex terrain. *Bound. Layer Met.*, **143**, 97-106.

4. Bradley, S. G., Y. Perrott, and A. Oldroyd, 2012: Corrections for Wind-Speed Errors from Sodar and Lidar in Complex Terrain. *Bound. Layer Met,* **143**, 37-48.

5. Mikkelsen, T., 2007: The Bistatic Sodar "Heimdall" – You blow, I listen, *Riso National Laboratory DTU*, ISBN 87-550-3250-8

6. Bradley, S. G., von Hünerbein, S., and T. Mikkelsen, 2012: A bi-static sodar for precision wind profiling in complex terrain. *JTech*., In Press.

7. Mathews, T., D. A. Bohlender and D. Smith, 1986: Effect of refraction of sound on bistatic doppler sodar measurements of wind profiles. *Atm. Res.,* **20**, 141-149.

Poster Session 1

ON THE NONSTATIONARY ANALYSIS OF WIND-WAVE AND SWELL INTERACTIONS

Venkata Jampana[1], James B Edson[2], Christopher W. Fairall[3]

[1] *jampana.raju@gmail.com*
[2] *Marine sciences, University of Connecticut, CT, USA, james.edson@uconn.edu*
[3] *ESRL/NOAA, Boulder, Colorado, USA, Chris.Fairall@noaa.gov.in*

ABSTRACT

Wind waves and swell complement each other as a coupled system. The degree of modulation of each because of the other depends on a host of variables. While short waves adjust rapidly to the changing environmental conditions, swell on the other hand can propagate across large distances without much loss of momentum and are independent of the local wind conditions. Recent investigations and remotely sensed spatial data show that waves propagate in groups and energy is concentrated over a small range of wave numbers and wave groups of different wave numbers can coexist. The influence of non-stationarity and interaction of wind waves with swell is analyzed using wavelet transforms. The effect of the directionality and magnitude of swell must be considered to understand local small scale interactions. The long wavelength of the waves absorbs momentum from the wind leaving the short wavelength waves exposed to smaller wind stress. The coupling between the wind waves and swell affects both the growth rate and frequency of waves at the peak of the wind wave spectrum. As part of the study, simultaneous measurement of surface wave fields and turbulence were carried out using laser altimeters and sonic anemometers mounted on the ASIT tower during the CBLAST experiment. Directional properties of the waves and swell are analyzed using a morlet wavelet. From the differences in phase of wave records, wave number and wind-wave and swell directions are derived. Wave energy densities are computed as a function of wavenumber and direction. Good time frequency resolution is seen with the use of use of wavelets in resolving wind-wave swell direction

1. INTRODUCTION

Over the oceans wind waves and swell interact as a dynamically coupled system. While the wind waves adjust rapidly to the changing environmental conditions, swell does not respond to changing wind conditions as fast as local winds. The net momentum flux transfer at the air-sea interface depends on the magnitude and propagation direction of winds, swell and wind waves.

The wind-wave interaction is often described within the stochastic framework wherein the randomly changing waves are considered to be a part of a stochastic process. The random fluctuations of the sea surface are attributed to the transfer of energy across the air-sea interface. It is assumed that the wave field can be represented statistically by an average wave spectrum and is a realization of sum of infinitesimal waves propagating with random phases and directions such that distribution of energy in direction and frequency agrees with the observed spectrum. The spectral density function (wave spectrum) gives the magnitude of the time average of wave energy as a function of wave frequency. This is the basis of the stochastic description of the waves in random seas and assumes stationarity and ergodicity of the wave field [7]. However, the assumption of an equilibrium sea which is the basis for obtaining wave statistics from the wave spectrum is rarely valid over the open oceans.

An alternative model for the description of the random sea is that the sea surface can be represented as a superposition of wave groups of different amplitudes, shape and velocities [5]. The wave groups are assumed to be Gaussian envelops and the permanency of the group, their evolution and dispersion depend on the amplitude and phase. The steepest groups show stokes-like harmonics and it was found that steep groups propagate energy over short periods of time without significant loss of shape [8]. The balance between the stokes like harmonics and the free waves depend on the intensity of wind forcing. Recent field data, radar imagery as well as acoustic mapping of the sea surface indeed show the presence of wave groups which propagate over several periods in a given direction. Waves propagate in groups and their energy is concentrated in a small range of wave numbers along specific space time trajectories [9]. The observed spectrum is the result of random distribution of the amplitude, propagation direction and phases of these groups.

Non linear interactions is believed to be the primary mechanism for the directional spreading of the wind-wave and swell coupled system [1]. Directional distribution of waves over the ocean is taken in general to be uni-modal. On the other hand, bi-modal distributions are primarily seen at the short wave portion of the spectrum, and are attributed to the directional characteristics of wind input and breaking dissipation terms. From a modeling perspective, non-linear ocean wave models rely upon accurate determination of the directional distribution of the waves. These models show minimum spreading at the peak frequency. Away from the peak frequency the spreading increases both across the lower and higher frequencies. Non linear influence decreases as the directional spreading of the wave energy increases. However, it is often found that observed phase speed of the waves is higher than those from numerically computed ones [3]. This is partly attributed to limitations in correctly modeling the directional wave spectra.

How wave directionality influences wave development and its propagation is not yet fully resolved for complex mixed sea states and this forms the crux of the paper. Section 2 describes the wavelet method to study wave directionality over the oceans. In section 3 the experimental setup is briefed. In section 4 the wavelet method to extract the wind wave direction using the phase of a complex wavelet is briefly described. Results on the wave directionality and conclusions follow in the next two sections

2. WAVELET ANALYSIS

Wavelets are arbitrary functions $\psi(t)$, such that $\psi(t) \in L^2(\mathbb{R})$ and satisfies the admissibility condition. A scaled and translated representation of $\psi(t)$ given as $\psi_{b,a}(t)$ is

$$\psi_{b,a}(t) = \left(\frac{1}{\sqrt{a}}\right) \psi^* \left(\frac{t-b}{a}\right) \qquad (1)$$

where a represents scale and b is the translation of the signal [4, 10]. Further when$\psi(t) \in L^2(\mathbb{R})$; $\psi_{b,a}(t) \in L^2(\mathbb{R})$. The Morlet wavelet $\psi_M(t)$ is

$$\psi_M(t) = e^{i\omega_o t} \, e^{-|t|^2/2} \qquad (2)$$

where ω_o is in the range 5.3 - 6 to give good time and frequency resolution. Morlet wavelet is well localized in time and frequency. The Gaussian envelope $e^{-|t|^2/2}$ of $\psi_M(t)$ makes it a natural choice to analyse surface wave records.

The Continuous wavelet transform (CWT) of a signal $x(t)$ is given by the integral.

$$W_{\psi,x}(b,a) = \int_{-\infty}^{\infty} x(t)\ \psi_{b,a}(t) dt$$

$$= \frac{1}{\sqrt{a}} \int_{-\infty}^{\infty} x(t) \, \psi^* \left(\frac{t-b}{a}\right) dt \qquad (3)$$

The amplitude of CWT is the modulus of $|W_{\psi,x}(b,a)|$ and the phase is defined as

$$\varphi = \tan^{-1}[\ \mathrm{imag}(W_{\psi,x}(b,a))/\ \mathrm{real}(W_{\psi,x}(b,a)] \quad (4)$$

Large values of $W_{\psi,x}(b,a)$ imply that the signal $x(t)$ is well correlated with $\psi_{b,a}(t)$. CWT is thus a time-scale representation rather than a time – frequency representation of the signal. The peak in $\hat{\psi}_{b,a}(s\omega)$ which is the Fourier transform of the scaled and translated wavelet does not necessarily occur at frequency s^{-1} [10]. The relation between wavelet scale and Fourier period is nearly same for Morlet wavelet. The wavelet power spectrum of the signal $x(t)$ is defined as $|W_{\psi,x}(b,a)|$^2. The original signal $x(t)$ is recovered from $W_{\psi,x}(b,a)$ using the relation (ref…)

$$x(t) = \frac{1}{C_\psi} \int_{-\infty}^{\infty} \int_{-\infty}^{\infty} W_{\psi,x}(b,a) \, \psi_{b,a}(t) \, \frac{da}{a^2} \, db \qquad (5)$$

where C_ψ a constant and its value is depends on the type of wavelet that is convolved with the signal. Convolution of the signal with the scaled and translated wavelet in Equation (1) can be implemented in an efficient manner in the Fourier domain. Convolution in the time domain is equivalent to multiplication in the Fourier domain. The Parseval relation which relates the time and frequency equivalence holds for the wavelet as well.

$$\int_{-\infty}^{\infty} \psi_{b,a}(t) = \int_{-\infty}^{\infty} \hat{\psi}_{b,a}(\omega) \, d\omega \qquad (6)$$

3. EXPERIMENTAL SETUP

Wave height measurements were carried out using three downward looking Reigel make laser altimeters mounted on the ASIT during the OHATS experiment. The lasers are leveled on the ASIT platform such that they are perpendicular to the sea surface and they sample the waves at simultaneously at 50 Hz. This data is further downsampled to 5 Hz., after a suite of data processing procedures to obtain high quality data The horizontal separation of the altimeters is approximately 2m and this distance between the lasers determine the minimum wavelength of surface waves that can be resolved.

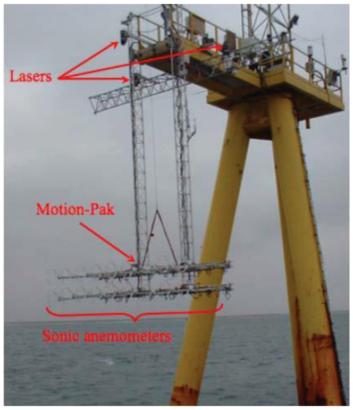

Figure 1. The position of the laser altimeters on ASIT

4. PHASE EXTRACTION AND DIRECTION PROPAGATION

At any given instant of time the three lasers sample the same surface at three intersections between the lasers and the sea surface can be represented with the same amplitude but different wave phase. The phase difference φ_{ij} of a wave across two points $\hat{x}_i$ and $\hat{x}_j$ $(i, j =$ 1 2 3…- caret implies a vector) is given by

$$\varphi_{ij} = \hat{k}.\hat{x}_{ij} \tag{7}$$

where $\hat{k}$ is the wave-number vector. $\hat{k}$ has magnitude $|\hat{k}|$ and propagation direction θ . Similarly the separation vector between the laser altimeters r_{ij} can be assigned a magnitude $|\hat{r}_j - \hat{r}_i|$ and directionβ_{ij} . The phase difference between laser 1 and laser 2 (φ_{12}) and between laser 2 and laser 3 (φ_{32}) can be recast from Equation (7) as

$$\varphi_{12} = k\, r_{12} \cos(\theta - \beta_{12})$$

$$\varphi_{32} = k\, r_{32} \cos(\theta - \beta_{32})$$

The individual phase from each wave record is directly obtained by the wavelet transform using Equation (4). r_{12} , β_{12} r_{32} β_{32} are computed from the configuration of laser altimeters. These two equations are solved to obtain the propagation direction θ and wavenumber vector $\hat{k}$ [2].

5. RESULTS

Figure 2 shows the time series of wind speed, wind, swell and wind waves direction for Julian Days 282-283 during the OHATS field experiment. This data was obtained from the nearby Martha Vineyard Coastal Observatory. During this period, the wind direction was nearly steady and from the open oceans. The wind speed increased from ~ 3ms^{-1} to 6 ms^{-1} and came back to ~3 ms^{-1}. This period is of gradual increase in wind speed and then a subsequent decay at nearly similar rate. When the winds are persistent, currents are induced at the surface by wind stresses [3]. This implies higher propagation speed for the dispersive waves. This is further analyzed in the later figures. Top panel of Figure 3 shows representative time series of wave heights obtained by the laser altimeters. The lower panel is the plot of wavelet transform which gives a time-scale representation of the ocean waves.

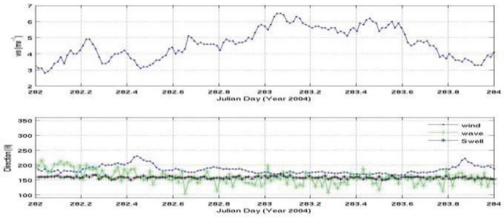

Figure 2: Time series plot of wind speed (Top panel) and wind direction, swell and wind waves direction (Lower panel).

As energy is a conserved property on the time-frequency-time plane, the modulus of the wavelet coefficients provide an instantaneous spectral description and is useful to analyze transient intermittent signals. It is seen that the distribution of energy is highly intermittent with groups, propagating along different directions with varying amplitudes. Groups may coalesce or disperse depending on the phase of component waves. The waves propagate in groups with energy concentrated in a narrow wavenumber band.

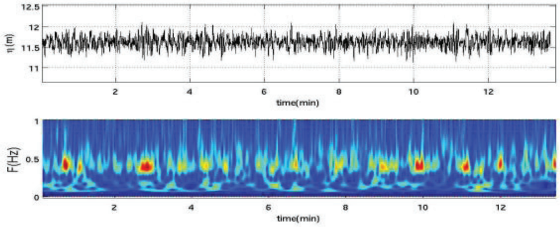

Figure 3. Wave height and its wavelet transform

Within the group the wavenumber magnitude and direction is confined to a narrow range. Wave groups of different range of wavenumbers can coexist. As a group passes by, change in local energy and increase in frequency. The directional spectrum gives the statistical average of the propagation characteristics of the sea. At any given instant or position, energy may be concentrated at a particular wavenumber The variability is due to the passage of groups with various amplitudes and vector wavenumbers. Wave directional spectra are computed for each 20 minute data records for the mentined period. It is found they show a fair of variability in the swell and wind wave direction which is not seen in regular spectra. Here we focus on three classes of wind-waves interaction. In the first case, winds are steadily blowing leading to growing wave field and higher wind speeds. We compute the energy

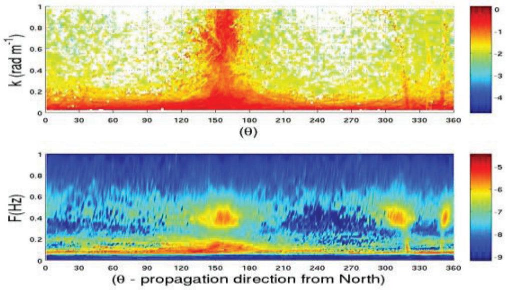

Figure 4 shows the wavenumber-direction (Top panel) and frequency-direction (lower panel) representation of the energy density of wind-wave swell system for Julian Day283.0694. The wind speed above the waves is ~ 6.5 ms^{-1}

density corresponding to wind speed of ~ 6.5 ms^{-1} on Julian Day 283.0694 on a wavenumber-direction plane. The wave energy density as a function of wave number and direction of propagation is obtained by averaging the wave energy at all the resolved wavelet scales which has the same wave number and direction. We see that much of the energy is confined along the swell propagation direction over a large range of wave numbers. The lower panel shows direction-frequency representation of the same data. A clear bi-modal distribution of energy is seen in the direction of propagation. Next in Figure 5 we consider a decaying wind field over a period of six hours and plot the wavenumber-frequency corresponding to Julian Day 283.93. Unlike Figure 4 much of the energy is across the lower waves and no bimodal distribution is seen. Thus amplitude dispersion and Doppler shifting of higher wave numbers is much more pronounced for the decaying wind fields.

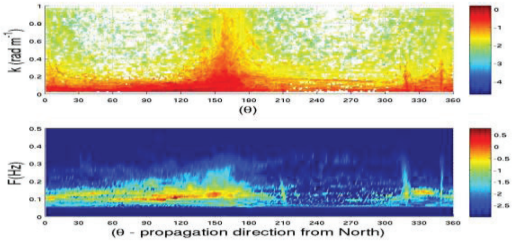

Figure 5 shows the wavenumber-direction (Top panel) and frequency-direction (lower panel) representation of the energy density of wind-wave swell system for Julian Day 283.93. The wind speed was ~ 3.5 ms^{-1}

In Figure 6 we consider a wave record for Julian Day 290.5 where the winds are sufficiently high(>10 ms^{-1}) and swell wind wave frequencies were closer to each other. In this data record, over a short period of time the winds increased from 4 ms^{-1} to 14 ms^{-1}. Also the wind direction was not steady compared to the previous Figures 4 and 5. This is reflected in the presence of some energy at 30^{o} . In this case the energy in the low wave numbers is much more focused and there is change in direction of propagation of swell. The non-linear energy transfer between swell and wind waves is strongly affected by the location of the frequencies of swell and wind waves.

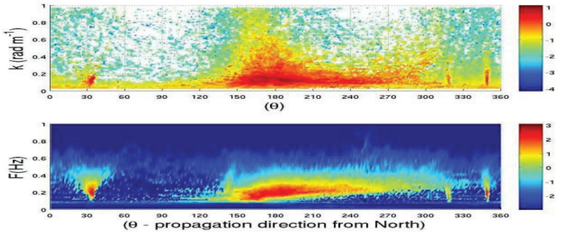

Figure 6: Same as Figure 5 but for wind speed greater than 10 ms^{-1} but without a gradual persistent increase in wind speed.

6. CONCLUSIONS

The sea surface as a random collection of groups propagating along different direction and amplitudes is easily seen by time-frequency transformations. Wavelet transforms are a convenient tool to elucidate many of the small scale processes over the air-sea interface. A persistent moderate wind field results in a bi-modal frequency distribution. Amplitude dispersion is much more pronounced over decaying wind fields. Changing swell direction and frequency modulation is a result due to closely located swell and wind wave frequencies.

ACKNOWLEDGMENTS

The first author acknowledges the funding and facilities provided by Dr James Edson to carry out this work.

REFERENCES

1.Banner, M.L., and I.R. Young, 1994: Modeling Spectral dissipation in the evolution of wind waves. Part I: Assesment of existing model performance. *J. Phy. Oceangr*., 24. pp 1550-1571.

2. Donelan,M.A., W.A.Drennan and A,K. Magnusson 1996: Nonstationary Analysis of the Directional Properties of Propagating Waves. *J. Phy. Oceangr*., 26 , 1901-1914.

3. Huang, N.E., and C.C. Tung, 1977: The influence of directional energy distribution on the non-linear dispersion relation in a random gravity wave field. *J. Phy. Oceangr*., 7. pp 403-414.

4. Kaiser, G., 1994: A friendly guide to wavelets, Birkhauser, 330pp.

5. Mollo-Christensen, E., and A Ramamonjiarisoa, 1978: Modeling the presence of wave groups in a random wave field. *J. Geophys. Res.* 83, 4117-4112.

6. Masson, D., 1993 : On the nonlinear coupling between swell and wind waves. *J. Phy. Oceangr*., 23. pp 1249-1258.

7. Ochi, M.K., 1998: Ocean Waves : The stochastic approach, Cambridge University Press, pp 319.

8. Pierson, Jr. W.J., M.A. Donelan and W.H.Hui 1992: Linear and non linear propagation of water wave groups. *J. Geophys. Res.* 97, 5607-5621

9. Poulter, E.M., M.J. Smith and J.A. McGregor, 1995: S-band FMCW radar measurements of oceanic surface dynamics. J. Atmos. Oceanic Technol., 12, 1271-1286.

10. Torrence, C., and G.P. Compo, A practical guide to wavelet analysis, Bull. Am. Meteorol. Soc., 79, 61-78, 1998.

Profiles of wind direction and studying of the ground air layer height by use of the sodar sounding

Lokoshchenko M.A. and Nikitina N.G.

Department of Meteorology and Climatology, Faculty of Geography,
Lomonosov Moscow State University. 119991, Lengory, Moscow, Russia
Phone: +7-495-9394284; Fax: +7-495-9392479; E-mail: loko@geogr.msu.su

ABSTRACT

The height of the ground air layer has been studied with the use of the sodar data about monthly-averaged profiles of wind direction in Moscow city for period 2004-2010. This parameter was supposed to be equal to the first level at which stable wind turning with a height is observed on a profile. As it is shown nearly at one third of cases this height was equal to 60 m or, sometimes, even higher – 80 or 100 m. In the rest of cases wind turning has been found at whole the range of the sodar data above 'dead-zone' of the sodar which is equal to 40 m. Thus, in the most of cases the ground air layer height is equal probably to 40 m or less. At the diurnal course the height of the ground air layer in average of several summer months is the most in the afternoon (from 80 to 100 m) and the least – at night (40 m or less).

1. INTRODUCTION

The acoustic remote sensing of the atmosphere allows measurements of vertical profiles both of wind velocity and of wind direction with high spatial and temporal resolution ([1] and others). Among others, the sodar data about wind direction profiles may be used for determination of the air ground layer height. Accordingly to classic theory one of possible criteria of this height is beginning of steady right turning. As it is known, Coriolis force $F_c = -2 \cdot [\Omega \times V]$, where Ω is the angular velocity vector and V is the velocity of an air particle. This force, being gradually increased inside the ground air layer, becomes comparable with other forces (frictional force and the force of baric gradient) which act to an air particle just above the ground air layer, i.e. in Ekman layer. At this layer which represents the upper part of the ABL, all these forces are of the same order. Unlike it, in the ground air layer below Ekman layer the Coriolis force is significantly less than other forces so that, as a result, a wind direction here remains nearly constant [e.g., 2]. Thus this simple criterion may be used for detection of the ground air layer height.

Of course, wind direction inside the ground air layer may be a bit changed with a height at any moment due to the influence of atmospheric stratification, relief or some local air flows. However, any changes of wind direction there are random, i.e. non-systematic and, hence, have a tendency to be mutually compensated by each other under averaging of sufficiently long time. Thus, the wind direction has a tendency to be nearly constant in average of long periods.

It should be noted that both empirical data, and theoretical estimations of the ground air layer height H in the literature are equal usually to 50-100 m, but sometimes, under some specific conditions, this parameter H may be found in wide range: from 30 to 200-250 m [e.g., 2-3]. Nevertheless, real estimations of the ground air layer height H remain questionable yet. Thus, any new measurements of this parameter seem to be an actual task for improvement of our knowledge about structure of the lower atmosphere.

2. MEASUREMENTS AND METHODICAL QUESTIONS

The acoustic remote sensing with the use of Doppler sodar 'MODOS' of METEK German firm production is carrying out at Meteorological observatory of Moscow University since 2004. The operative frequency of the sodar is 2000 Hz, the vertical resolution consists of 20 m. The first level of wind measurements is 40 m (that is the middle of the first air layer from 30 to 50 m above 'dead-zone' of the sodar which is available for measurements). Temporal resolution consists of 10 min that is the smallest time for calculation of reliable wind profiles. Monthly-averaged vertical profiles of wind direction for period from 2004 to 2010 were calculated using special program and analyzed precisely for each month of sodar observations.

Some methodical questions should be noted regarding wind direction profiles. Their calculation is not trivial task because of cyclicality of a direction value. Evidently, values of 2º and 362º represent the same direction. However, any profile of wind direction may demonstrate multiple passing across 360º value so that automatic algorithm has been created for account of this effect. Recalculation of all direction values may be made in vicinity either of 0º, or of 360º. There is no principal question what edge of the range of possible direction values is chosen as a base, but it is important to have homogeneous sampling of the data which were received at the same time (i.e. across one profile). So, some automatic filter (critical value of maximal possible difference between initial values of direction on two neighbouring levels) was added at our program to exclude any passes across cycle and, hence, to ensure homogeneity of each separate direction profile.

However it was found that sometimes real wind turning is unexpectedly strong. The sharpest changes of a direction both in time and in height are connected as a rule with nearly calm conditions at anticyclone center or at a saddle where values of wind velocity are extremely small. At these conditions wind direction at different levels is chaotic and does not demonstrate any clear tendency. At some cases sharp changes of wind direction, up to 200º and even more, take place both at different levels below 300 m height at the same profile and at the same level from one profile to another (i.e. after 10 min).

Besides, one more specific situation is passing of atmospheric fronts or ridge axes. At these zones wind direction is as a rule quite ordered at various levels but change very quickly in time. Thus, at these specific conditions an additional manual control of automatic calculations of wind direction profiles is needed.

A height H of the wind turning beginning was indicated not only visually from profiles, but using two criteria. Firstly, a turning value α was used:

$$\alpha = D_i - D_{i-1} \tag{1}$$

where D is wind direction, i – any height level.
However, so simple criterion is evidently insufficient. Then an additional co-efficient K of the turning change between two neighbouring height levels was applied:

$$K = \frac{D_{i+1} - D_i}{D_i - D_{i-1}}, \tag{2}$$

In cases of almost constant wind direction with a height (i.e. in limits of the ground air layer) a value of α consists of 0.4º in average whereas a value of K is from 1.0 to 1.5 in average (as a rule, not more than 2). Above the ground air layer height H a value of α is usually higher than 1º inside every separate interval of 20 m. At the level of H a value of K at the most of cases is higher than 3 (in average is nearly of 5). Thus, great difference between values of both α and K below and above the level of H confirms objective base of this analysis.

3. RESULTS

Preliminary results of this work as separate examples have been published in [4]. The most of results have been published by authors later in [5].

It was found that nearly in one third of cases (in 19 from 59 months) for period from 2004 to 2010 a direction was nearly the same (with an accuracy of 1º) inside the lowest part of a profile whereas steady right turning took place above (see Fig.1 and Table 1). The 'vertical' low part of profiles is marked on Fig.1 by bold points. As a rule a top of this 'vertical' part of profile consists of 60 m (Fig.1 b, c) and only sometimes it was found to be a bit higher –80 m (Fig.1 d,e).

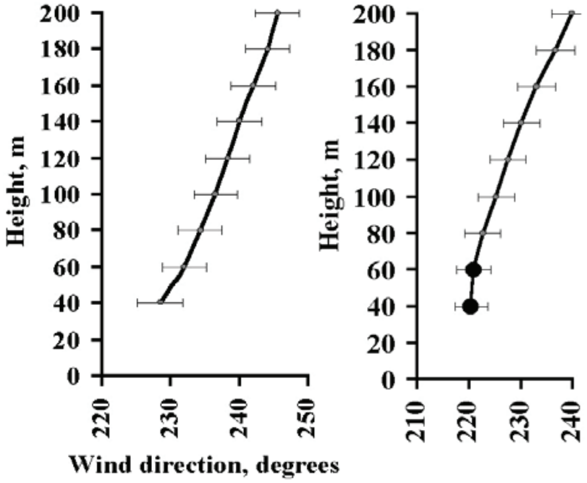

a) August 2008; b) July 2009;

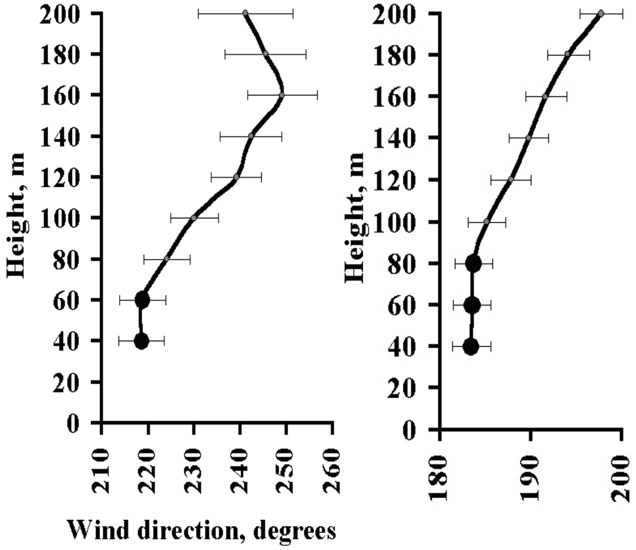

c) February 2007; d) November 2009;

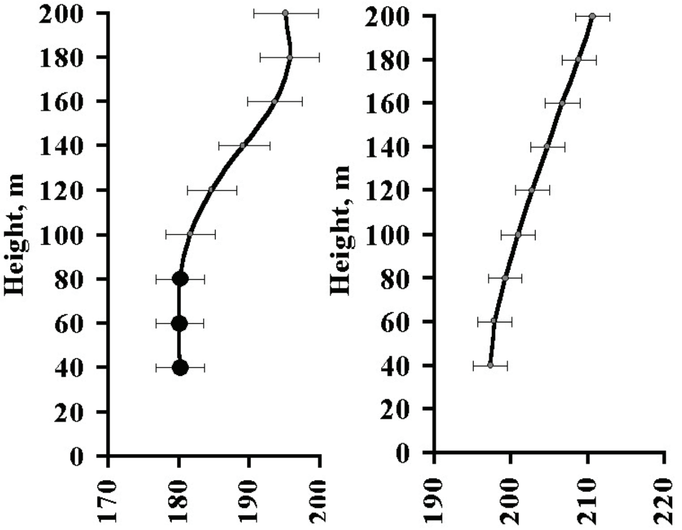

e) December 2010; f) January 2008

Fig.1. Examples of monthly-averaged wind direction profiles. Moscow. Confidence intervals are calculated with probability of 0.95.

Table 1. The ground air layer height (m) by the sodar data in Moscow in average of every month in 2004-2010.

Month:	Jan	Feb	March	Apr	May	June	July	Aug	Sept	Oct	Nov	Dec
2004	No data										≤40	**60**
2005	**60**	no data										≤40
2006	**60**	≤40	≤40	≤40	≤40		≤40	≤40	≤40	**100**	no data	
2007		**60**	≤40	≤40	≤40	≤40	≤40	≤40	≤40	**60**	≤40	**60**
2008	≤40	≤40	≤40	≤40	≤40	≤40		≤40	≤40	≤40	**60**	**60**
2009	≤40	≤40	**60**	≤40	≤40	**60**	**60**	**60**	≤40	**80**	**80**	**60**
2010	≤40	≤40	**60**	≤40	≤40	≤40	≤40	≤40	≤40	≤40	**80**	**80**

Table 2. Diurnal course of the ground air layer height (m). Moscow, period from June to August of 2009.

Time:	0-3 a.m.	3-6 a.m.	6-9 a.m.	9-12 a.m.	0-3 p.m.	3-6 p.m.	6-9 p.m.	9-12 p.m.
Height:	**≤ 40**	**≤ 40**	**60**	**80**	**80-100**	**80**	**80**	**≤ 40**

Evidently, in the rest 40 months the air ground layer was masked by 'dead zone' of the sodar so that its height was equal either to 40 m or less (Fig.1 a, f). A priory we expected that cases of values of $H \leq 40$ m must be found mainly in summer. However, they are surprisingly distributed almost evenly all over the year so that comparatively tall H may be observed at any season. Of course, for more detailed measurements of this parameter it is necessary to use a mini-sodar with less 'dead-zone'. Evidently, we can't calculate now an average height of H for Moscow city because of great uncertainty of its values inside 'dead-zone' in the most of cases. In Ekman layer above H wind turning is right as a rule, except only some cases (e.g., above 160 m on Fig.1 c) – possibly, due to specific thermal wind during that month.

The daily course of H was studied separately for summer time of 2009. As it is seen from Table 2 the ground air layer height is the highest in the afternoon (up to 100 m) and the smallest at night (40 m or even less). This result confirms classic theory about influence of the thermal stratification on the ABL structure.

CONCLUSIONS

1. At the most of cases the ground air layer height in Moscow city accordingly to the sodar data is inside of 'dead-zone' of the sodar that means value of 40 m or less. However, during nearly third of months this parameter consisted of 60 m or even a bit higher.
2. At the diurnal course the ground air layer height is the highest in the middle of a day and the lowest at night.
3. The most difference between wind direction at various levels in the ABL may be equal sometimes up to 200-250º in conditions of either extremely light winds close to calm at center of anticyclone, at ridge axis or at a saddle, or during front passing above the sounding site.
4. In average right wind turning is absolutely predominated in Ekman air layer that confirms classic Ekman theory.

ACKNOWLEDGEMENTS

This work has been supported by Russian Basic Research Foundation (project No. 10-05-01130).

REFERENCES

1. Krasnenko N.P., 1986: *The Acoustic Remote Sensing of Atmosphere,* in Russian. Novosibirsk, Nauka, Siberian division, 168 p.
2. Matveev L.T., 1967: *Fundamentals of General Meteorology, Physics of the Atmosphere* (translated from Russian by IPST, published by Dept. of Commerce and NSF, Jerusalem, Israel), 699 p.
3. Khromov S.P. and Mamontova L.I., 1974: *Meteorological Glossary*, in Russian. Leningrad, Gigrometeoizdat, 568 p.
4. Lokoshchenko M.A., 2010: Wind structure of lower atmosphere above Moscow by the sodar data. *Proceedings of the 15th ISARS, Paris, France.*
5. Nikitina N.G. and Lokoshchenko M.A., 2011: Height of the ground air layer in Moscow by the data of the acoustic remote sensing of the atmosphere. *Proceedings of XV All-Russian school-conference of young scientists "Air composition. Atmospheric electricity. Climatic processes"*. Borok, pp.45-46, in Russian.

BOUNDARY LAYER DEPTH ESTIMATION AND CHARACTERIZATION AT GEOSUMMIT STATION USING A SODAR AND MICROMETEOROLOGICAL DATA

B. Van Dam[1], **W. Neff**[2], **D. Helmig**[1]

[1]*INSTAAR, University of Colorado, Boulder, CO, USA, brie.vandam@colorado.edu*
[2]*NOAA Earth System Research Lab, Physical Sciences Division, Boulder, CO, USA*

ABSTRACT

Boundary layer conditions in polar regions have been shown to have a significant impact on chemical exchanges between the snow/ice surface and the atmosphere. The ability to properly describe boundary layer characteristics (e.g. stability, depth and variations on a diurnal and seasonal scale) is essential in understanding the processes controlling these exchanges. Boundary layer depths at GEOSummit Station, Greenland have been described for a previous spring and summer season using near surface turbulence data [1], but direct measurements of the boundary layer for comparison were lacking.

In this study, boundary layer depths for stable to weakly stable conditions are estimated using surface turbulence quantities derived from three 3-D sonic anemometers as well as gradient measurements of wind speed and temperature, all located on a 10 meter tower at GEOSummit Station, Greenland. These estimates are compared with direct boundary layer depth measurements from a sodar that was located approximately 50 meters from the tower. During this same campaign, measurements of ozone and nitrogen oxide concentrations and fluxes were undertaken at several heights on the 10 m tower. In addition to testing the diagnostic equations used for boundary layer depth estimation, this comparison of near-surface turbulence data, sodar observations and surface chemistry assists in the understanding of how surface processes influence the boundary layer development and surface layer gas exchanges at this site.

1. METHODOLOGY

Surface turbulence quantities from 3-D sonic anemometers and gradient temperature and wind speed measurements on a 10 meter meteorological tower were used to estimate boundary layer depths for stable to weakly stable conditions at Summit Station, Greenland. To obtain these estimates, two diagnostic equations were implemented. Previously, the authors in [2] used the following expression derived by [3] to estimate boundary layer depth at South Pole with good result:

$$H = 1.2 u_* (f N_b)^{-1/2}, \qquad (1)$$

Where f is the Coriolis parameter, N_b is the Brunt-Väisälä parameter and u_* is the friction velocity.

An alternative used in this study is an equation described by [4]:

$$H = C_s^2 (u_* L / |f|)^{1/2}, \qquad (2)$$

Where C_s^2 is ~0.7 and L is the Obukhov length.

2. INITIAL RESULTS AND CONCLUSIONS

As shown in Figure 1, equation (1) overestimated the boundary layer depth at Summit Station during June 2010. This expression was shown to work well at an environment such as South Pole, where conditions are quasistationary and highly stable (unlike Summit, an environment subjected to diurnal cycles). Boundary layer depth calculations using equation (2) provide a better estimate during the summer season. An investigation of ozone and nitrogen oxide concentrations during the same June 2010 period indicate that because sustained high stability conditions were not observed at Summit in June 2010, we do not see periods of elevated nitric oxide corresponding to sustained, low boundary layer depths as was observed in several studies (such as [2]) at South Pole.

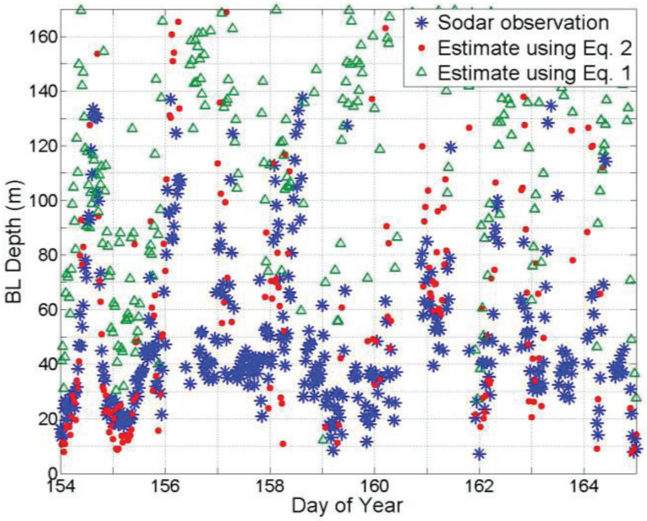

Figure 1: Sodar observations (blue stars) and boundary layer depth estimates using expressions (1) and (2) (green triangles and red dots, respectively) for the period 3-14 June 2011.

ACKNOWLEDGMENTS

This research is funded through the National Science Foundation Office of Polar Programs grant NSF-OPP-07-13992. Additional thanks go to the excellent support of the Summit Station science technicians and the logistical support of the 109th Air National Guard and CH2MHill Polar Services, as well as the Danish Commission for Scientific Research for providing access to Summit.

REFERENCES

1. Cohen, L., D. Helmig, W. Neff, A. Grachev, C. Fairall, 2007: Boundary-layer dynamics and its influence on atmospheric chemistry at Summit, Greenland, *Atmospheric Environment*, **41**, pp. 5044-5060.

2. Neff, W., D. Helmig, A. Grachev, D. Davis, 2008: A study of boundary layer behavior associated with high NO concentrations at the South Pole using a minisodar, tethered balloon, and sonic anemometer, *Atmospheric Environment*, **42**, pp. 2762-2779.

3. Pollard, R., P. Rhines, R. Thompson, 1973: The deepening of the wind-mixed layer, *Geophys. Fluid Dyn.*, **3**, pp. 381-404.

4. Zilitinkevich, S., A. Baklanov, 2002: Calculation of the height of the stable boundary layer in practical applications, *Boundary Layer Meteorology*, **105**, pp. 389-409.

THE HEIGHTS OF THE ATMOSPHERIC BOUNDARY LAYER AT A COASTAL REGION USING REMOTE SENSING AND IN SITU MEASUREMENTS

Gilberto Fisch

Institute of Aeronautics and Space (IAE/DCTA), São José dos Campos, Brazil, fisch.gilberto@gmail.coml

ABSTRACT

We have estimated and compared the heights of the ABL at the Alcantara Space Center (located at tropical region) using a data-set comprising of *in situ* rawinsoundings and from temperature profiles extracted from microwave radiometer. The measurements were collected during the wet season do 2010. The numbers of soundings used were 72 (made each 6 hours) and the meteorological values were interpolated for each 50 m height. The microwave profiles used were 4130 profiles (a single profile made at 15 min) with measurements each 50m up to 500 m and then each 100. The heights of the ABL have been computed with potential temperature profiles as the first level where the potential temperature gradient is positive for 3 consecutive layers. Considering the altitudes up to 1000 m, there is a tendency for the in situ measurements to be higher than the remote sensing to a value up to 1.0-1.2 °C at 400-500 m. Also, there is a pronounced diurnal cycle as the maximum differences occurred during daytime measurements (12 and 18 GMT). Considering the whole period, almost 60% of the results from the microwave radiometer presented the level 600 m as ABL height and this value can be assumed as typical value. The presence of the rainfall can alter the determination of the ABL height, mainly using the microwave radiometer.

1. INTRODUCTION

The space launching centers are usually located at coastal areas due to the safety reasons. Examples are the Kennedy Space Center (KSC) at Florida, Centre Spatial Guyanense at French Guiana and this is also true for the Alcantara Space Center (Centro de Lançamento de Alcântara – CLA in Portuguese) which has its launch pad at around 150 m from the seashore.

The atmospheric boundary layer (ABL) is the lowest portion of the atmosphere which is coupled with the surface being modifying by its characteristics (thermal characteristics, topography, types of vegetation, roughness, etc). Consequently, the winds and temperature and humidity profiles are studied in very detail in order to give support for the space activities. For instance, for KSC, the sea breeze climatology using a mesonet towers (44) and 5 wind profile radars observations was analyzed by [1] while the reference [2] studied the rapid temporal variation of the winds using wind profilers. For the CLA, the reference [3] studied the climatology of the winds inside the ABL thorough out 5 years of data from an anemometric tower. All the cited studies characterized the wind flow regime in order to improve the flight trajectory and safety conditions for the launchings.

Applications of this knowledge are very important in others branches of space meteorology. Recently, the reference [4] describe the use a software to study the dispersion of pollutants (or toxic gases) released at CLA, which depends strongly to the wind flow regime / turbulence characteristic. The height of the ABL is one of the input parameters for this dispersion study.

The goal of this paper is to investigate the behavior of the Atmospheric Boundary Layer developed at the Alcantara Space Center (CLA) using different instrumentation. The results can be used for an ongoing activities associated with the developing of a software / algorithm to describe the dispersion of a gas released by rockets during its launch.

2. DATA-SET AND METHODOLOGY

During the wet season of 2010, a meteorological field campaign named GPM 2010 was held in CLA, in order to collect meteorological data for future validation studies of the Global Precipitation Mission (GPM) constellation. During 25 days, meteorological soundings were conducted at 00, 06, 12 and 18 GMT using sondes RS92SVG from Vaisala Oy (Helsinki, Finland). Besides this data, a microwave radiometer MP3000 from Radiometric (Boulder, USA) collected simultaneous temperature and humidity profiles (one profile each 15 min). The Radiometrics MP3000 is a microwave radiometer designed to retrieve continuous temperature, humidity and cloud profiles in the lower troposphere, mounted on a tripod, as shown in Figure 1. For this study, only the temperature retrieval was used. It is nominally a 12-channel instrument, although in practice any combination of channels can be selected within the following bands: 22 – 30 GHz (K-Band) and 51 – 59 GHz (V-Band). Each band is received and detected independently, although all channels use a common frequency synthesizer, which must be switched to observe each channel. In the current hardware configuration, it takes ~2 s to switch frequencies, although this may be reduced substantially in the future. This results in the observations not being coincident in all channels and taking ~40 s to sample a set of 12 channels.

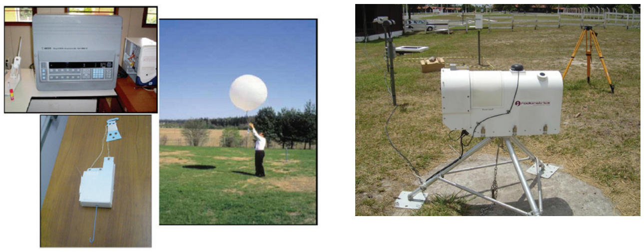

Figure 1. The instruments used: rawinsounding with a receiver Digicora, sonde and balloon (left) and MP3000 radiometer (right).

Although the field campaign was held during the wet season 2010, it was an abnormal period, being very dry in the first 18 days, with almost no rainfall (which is unusual for this time of the year). From March 19 onward, the rainy season started and there were a lot of events of rain. Usually this rain is a mixed between shallow cumuliform (e.g. Cumulus) and stratiform (e.g. Stratus and/or Stratocumulus) clouds. The peak of rain is in March-April during the austral summer and it is due to the presence of the Inter Tropical Convergence Zone (ITCZ) around 5 S. There is no daily cycle of the rain. The time series of the rainfall is presented at Figure 2.

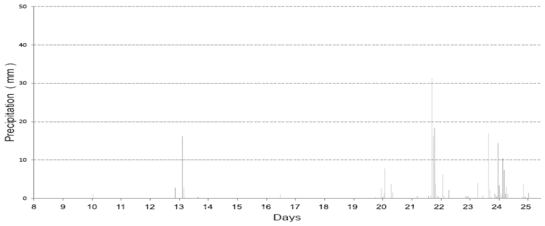

Figure 2. Time series of the rainfall during the March 2010.

Initially, potential temperature profiles for each profile (from rawinsoundings and from the MP3000) were computed and the height of the ABL was determined as the first level where the potential temperature gradient is positive (higher than 2 K/km) for 3 consecutive layers. The rawinsoundings have measurements typically around 10-20 m vertical resolution while the MP3000 presented his values at each 50 m (from the surface up to 500 m) and each 100 m from this level upward. According to reference [5], the estimates of the height of ABL from rawinsoundings are the best operational procedure.

3. RESULTS

Initially, the profiles of temperature were compared by the two measurements: in situ measurements made with rawinsoundings and estimates using the microwave radiometer for all profiles (average) and classified by time (00, 06, 12 and 18 GMT). The results are shown in Figure 3. Considering the altitudes up to 1000 m (which is a typical height for the ABL layer), there is a tendency for the in situ measurements to be higher than the remote sensing up to a value ranging from 1.0-1.2 °C at 400-500 m. Also, there is a pronounced diurnal cycle as the maximum differences occurred during daytime measurements (12 and 18 GMT). This could be a positive bias for the temperature sensors from the soundings due to radiation errors.

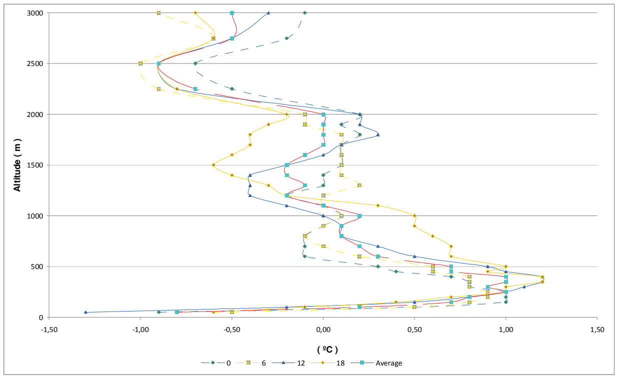

Figure 3. The differences between measurements of temperature (using rawinsoundings) and estimates (using the microwave radiometer).

The Figure 4 presents the time series of the height of ABL using both methods. The rawinsounding estimates were split in daytime (soundings from 12 and 18 GMT) and nighttime (00 and 06 GMT) due to the temperature bias. Also, the dynamics of daytime and nighttime boundary layer are very different as well the methods to estimate the ABL height. It is easily to observe that the most frequent height using the radiometer is the level of 600 m, which encompasses approximately 60% of the values. It should be mentioned that a level of 600 m means that the height can be in the range 600-650 m. It is interesting to notice that very few estimates (only 13 values, see Figure 5) from the MP3000 is higher than this critical value (600 m). Even during the night, the MP3000 showed heights of the ABL at level 600, probably the surface thermal inversion (characteristics of the nocturnal boundary layer) is not strong enough to backscatter the signal and the instrument is measuring the thermal inversion layer separating the turbulent boundary layer and laminar free atmosphere. During the daytime, this layer is really the top of the ABL (specifically the convective boundary or mixed layer) but at nighttime, it is the top of the residual layer. Comparing the Figures 2 (time series of rainfall) and 4 (time series of the height of ABL), it can be observed that the presence of the rainfall modify the determination of the height of the ABL. When there is a dry situation (no rain), the matching between the two estimates are much better.

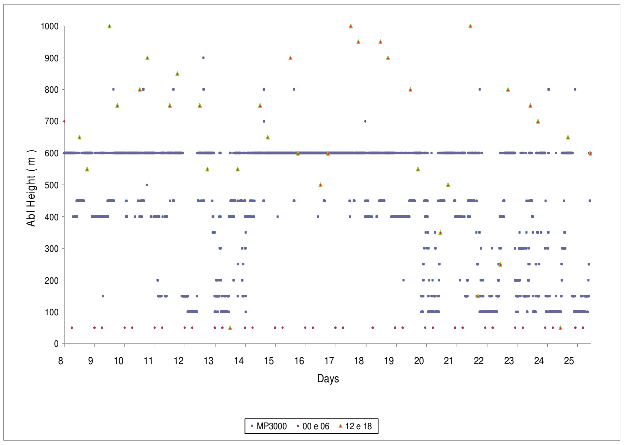

Figure 4. Time series of the ABL height during the field campaign.

Finally, at Figure 6, the dispersion between the estimates from rawinsoundings and from MP3000 was plotted for both daytime and nighttime. It is clearly that the nighttime values were underestimated from MP3000 comparing with the rawinsoundings due to the points described earlier.

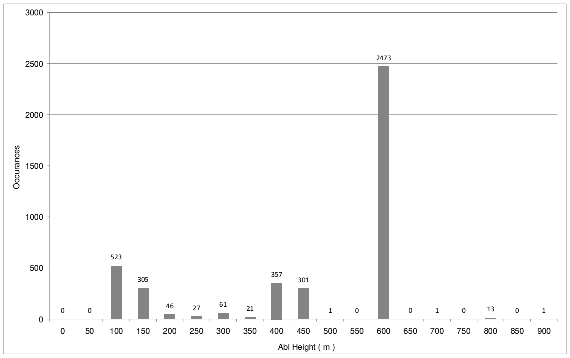

Figure 5. Frequency distribution from the occurrence of ABL heights using estimates from MP3000.

4. CONCLUDING REMARKS

The height of the ABL was compared using two different techniques during a field campaign at Alcantara (wet season 2010). The heights of ABL derived from the rawinsoundings are higher than observed by the microwave radiometer, but both measurements are consistent with a value of 600 m. This value is typical from oceanic or marine boundary layer. These results will be used for the ongoing research associated with the dispersion of gases exhausted from rockets (see [4]).

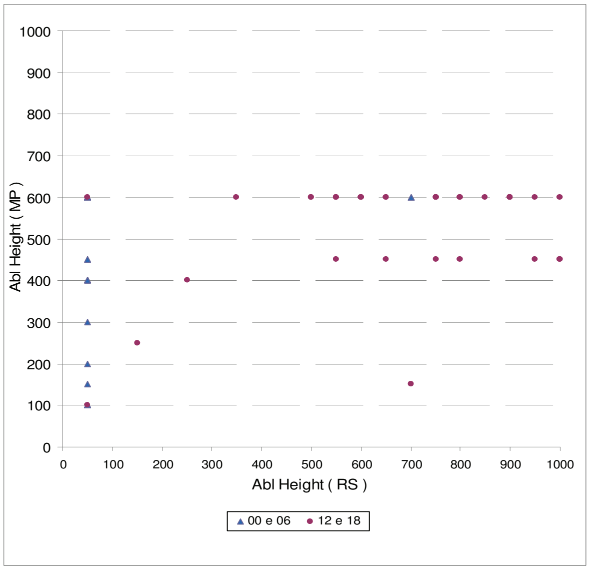

Figure 6. Dispersion plot between ABL heights derived from rawinsoundings and MP3000.

ACKNOWLEDGMENTS

The author is pleased to acknowledge the Conselho Nacional de Desenvolvimento Científico e Tecnológico (grants PQ 303720/2010-7 and 559949/2010-3) and Fundação de Amparo a Pesquisa do Estado de São Paulo (2009/15235-8) for financial support.

REFERENCES

1. Case, J. L., M. M. Wheeler, J. Manobianco, J. W. Weems, W. P. Roeder, 2005: A 7-yr climatological study of land breezes over the Florida Spaceport, *Journal of Applied Meteorology*, **44**, pp. 340-356.

2. Merceret, F. J., 2006: Rapid temporal changes of boundary layer winds, *Journal of Applied Metorology and Climatology*, **45**, pp. 1016-1020.

3. Gisler, C. A. F., G. Fisch, C. S. Correa, 2011: Análise estatística do perfil de vento na camada limite superficial no centro de lançamento de Alcântara, *Journal of Aerospace and Technology Management*, **3**, pp. 193 – 202 (doi: 10.5028/jatm.2011.03022411).

4. Moreira, D. M., L. B. Trindade, G. Fisch, M. R. de Moraes, R. M. Dorado, R. L. Guedes, 2011: A multilayer model to simulate rocket exhaust clouds, *Journal of Aerospace and Technology Management*, **3**, pp. 41-52 (doi: 10.5028/jatm.2011.03010311).

5. Seibert, P., F. Beyrich, S. E. Gryning, S. Jofre, A. Rasmussen, P. Tercier, 2000: Review and intercomparison of operational methods for the determination of the mixing height, *Atmospheric Environment*, **34**, pp: 1001-1027.

SODAR VERIFICATION OF BOUNDARY-LAYER HEIGHT SCHEMES FOR THE OUTPUT OF METEOROLOGICAL MODELS

Rostislav Kouznetsov[1,2], **Curtis Wood**[1] **Mikhail Sofiev**[1], **Joana Soares**[1], **Ari Karppinen**[1] **and Carl Fortelius**[1]

[1] *Finnish Meteorological Institute, Erik Palmenin aukio 1 PL 503, 00101 Helsinki, Finland*
[2] *A. M. Obukhov Institute of Atmospheric Physics, Moscow, Russia*
E-mail: rostislav.kouznetsov@fmi.fi

ABSTRACT

We use the data of 12-month continuous sodar monitoring of the atmospheric boundary layer over Helsinki, Finland, to evaluate the performance of different methodologies to diagnose the mixing-layer height (MLH) from the data of numerical weather prediction (NWP) models. The reference values of MLH were determined manually from the echogrammes of vertically pointing Latan-3M sodar. The data are compared to the results of three diagnostic procedures from NWP and chemical transport models. We apply different diagnostic procedures to the same set of meteorological fields obtained from European Centre for Medium-Range Weather Forecasts (ECMWF).

The diagnostic procedures that account for surface fluxes were found to be more accurate than those relying on mean meteorological quantities. The latter, however, are much less sensitive to the quality of the surface schemes used in the model. None of the diagnostic routines tested is suitable for very shallow mixing layers that often occur in high latitudes.

1 INTRODUCTION

The mixing layer, also known as the atmospheric boundary layer (ABL), or planetary boundary layer, is a layer of atmosphere adjacent to the ground surface, where an intensive turbulent mixing occurs. The quantitative definitions of the mixing layer height (MLH) are quite diverse and are based on various parameters to characterize it [1]. Moreover, even with a fixed determining parameter (e.g. temperature profile, or bulk Richardson number profile) slightly different definitions for MLH often lead to very different values of MLH.

Despite these problems, the concept of MLH is extensively used in all kinds of pollution dispersion modeling from very simple box models to sophisticated global chemical transport models. Thus it has to be reliably derived from the basic data of NWP models.

Modern numerical weather prediction (NWP) models do not rely on the concept of MLH, since in most cases they explicitly resolve the vertical structure of the exchange coefficients within and above mixing layer. Often they provide the mixing layer height (MLH) as an output parameter, however, since the MLH is not directly used in NWP, its quality varies in different models.

Earlier study [3] have shown that the accuracy of MLH diagnostics in provided by NWP models differs dramatically, and that some models perform quite well. However it was not clear if this difference is caused by differences in MLH diagnostic schemes, or by general model performance. The goal of the current study is to examine the different schemes with the same meteorological input, and thus to evaluate the the schemes as such. We consider the schemes of the mixing height diagnostic of ECMWF (European Centre for Medium-Range Weather Forecasts) and HIRLAM (High Resolution Limited-Area Model) operational NWP models and of SILAM (System for Integrated modeLing of Atmospheric coMposition) CTM. The data of Latan-3m sodar [4]installed at the roof of Finnish Meteorological Institute (Helsinki) were used as a reference. With the sodar data one can detect MLH within the range of 40-350 meters a.g.l. (~400 m a.s.l.). For the present study, mixing heights were derived manually from the sodar echogrammes.

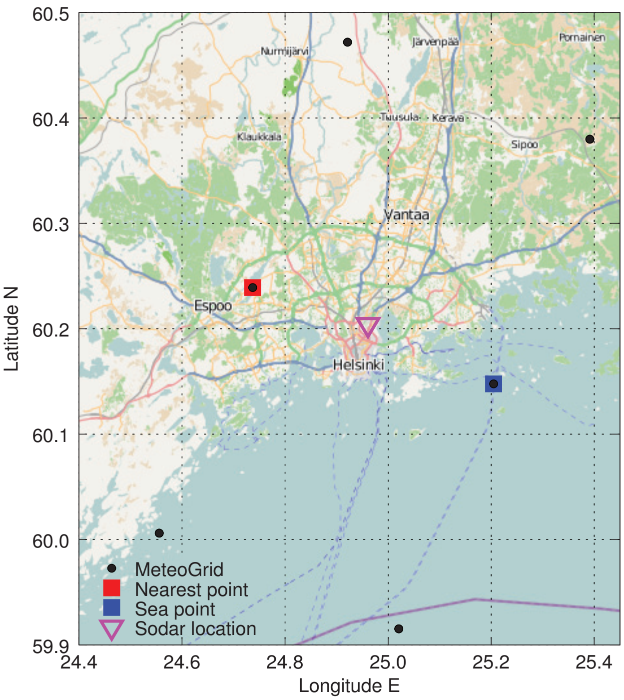

Figure 1: The map of the Helsinki area with model grid points and sodar location marked. The mesh is approximately 10x10 km. The map base from `http://openstreetmap.org`

2 DATA AND MODELS

The reference sodar used in the study is located in Helsinki, about 5 km north from down town at the top of a small hill (Fig. 1). The grid points extracted from ECMWF model and used for meteorology pre-processing are shown with dots. Two grid-points closest to the sodar location are at nearly same distance from it, thus the modeled MLHs were evaluated at both.

Sodar The sodar LATAN-3m in the configuration used for this study has sounding range up to 400 meters a.g.l. The sodar has a single vertically-pointing dish antenna of 60 cm in diameter. It is operated at 3400 Hz carrier frequency with 50 ms burst signal and pulse repetition rate 0.2 Hz. For this study we use the 12-month dataset collected between 1.09.2009 and 31.08.2010.

The MLH can be derived from sodar dara in various ways. The methods are based on different features of vertical profiles of mean meteorological or turbulent parameters [1]. Different methods sometimes result in substantially different MLH values for the same situation. However, in most cases the concept of MLH works well and the choice of particular method is not of importance.

The automated procedures of mixing height determination from sodar echo intensity profiles are often neither straightforward nor robust [1]. In case of the Helsinki measurements the sodar data were sometimes affected by fixed echoes in the lower range gates, especially during low ground-based inversions, which would require an automated procedure to be quite intelligent. Recently developed automated procedure [8] have shown some promising results, but still does not recognize shallow boundary layers in case of fixed echoes in lower range gates. Therefore, for this study we used the mixing height derived manually from the sodar echogrammes. The MLH was derived only for situations when the echo intensity had a clear drop-out at certain height which was identified as MLH.

Totally around 8760 hourly intervals were processed. The mixing height was identified within the range of the sodar for about 4300 hourly intervals. During the remaining time the MLH was either above the sounding range, or could not be detected due to weak temperature turbulence within ABL, or due to technical problems with sodar (wind and/or rain causing strong acoustic noise, heavy snowfall covering the antenna, etc.).

Modelled MLH The data from archives of operational NWP models output in most cases cannot be directly used to evaluate meteorological quantities that require both mean profiles and turbulent fluxes as an input; the mean quantities are stored as instantaneous quantities, the fluxes are stored as cumulative or time-averaged values. Given the large output time step (3 hours in our case), this results in the inconsistency between the mean profiles and turbulent fluxes. To overcome this difficulty we used the SILAM model as a pre-processor to harmonize the meteorological data and to downscale them to hourly temporal resolution of the experimental data. The horizontal grid used for the pre-processing is the same as in the initial meteorological data. The vertical levels for the pre-processing were chosen differently from those of the input meteorological data due to the limitations of the SILAM implementation. The SILAM output is given at fixed heights above ground, whereas the ECMWF meteorological data are in hybrid levels. The vertical interpolation leads to somewhat uneven histograms, however this does not compromise the conclusions.

There are two strategies for the estimation of the stable MLH [6]: the one based on surface fluxes, and one based on bulk Richardson number. The surface fluxes are poorly verified in the meteorological models, and the latter approach is more reliable since it relies on mean profiles of meteorological quantities. The surface bulk Richardson number as a function of height z is given by:

$$\mathrm{Ri}_{bs}(z) = z\frac{g}{\langle\theta\rangle}\frac{\theta(z)-\theta_s}{U(z)^2}, \qquad (1)$$

where g is acceleration due to gravity, θ is potential temperature and U is wind speed. Then a height of a mixing layer h is calculated as a height, where $\mathrm{Ri}_{bs}(h)$ exceeds it critical value Ri_c.

Vogelezang and Holtslag [7] proposed to use instead of (1) the bulk Richardson number with wind shear and temperature gradient between two elevated levels:

$$\mathrm{Ri}_b(z) = (z-z_l)\frac{g}{\langle\theta\rangle}\frac{\theta(z)-\theta(z_l)}{(\Delta U(z,z_l))^2}, \qquad (2)$$

where $\Delta U(z,z_l)$ is a (vector) of wind velocity difference between heights z and z_l, z_l is some height within few tens of meters. The resulting values of h were found to have no significant sensitivity to the choice of z_l between 20 and 80 m [7]. Excluding the surface layer from the computation makes the resulting values of Ri_b less dependent on uncertainties and/or local variations of surface-layer temperature.

The rational expressions like (2) result in highly uncertain values when the gradients are small. Thus various regularizations are applied in models.

The scheme used in NWP model HIRLAM (`http://www.hirlam.org`) uses the modified formulation of Ri_b proposed by Vogelezang and Holtslag [7]:

$$\mathrm{Ri}_b = (z-z_1)\frac{g}{\langle\theta\rangle}\frac{\theta(z)-\theta_1}{(\Delta U(z,z_1))^2+100u_*^2}, \qquad (3)$$

where z_1 is the lowest model level and height and u_* is a friction velocity. h, $\theta(z)$ is the virtual potential temperature at height z, and u_* is the friction velocity at the surface. Such formulation essentially forces $\mathrm{Ri}_b(z_1=0)$, not allowing the MLH to be lower than the lowest model level. For the comparison we have also used the values of MLH extracted from the data of operational runs of

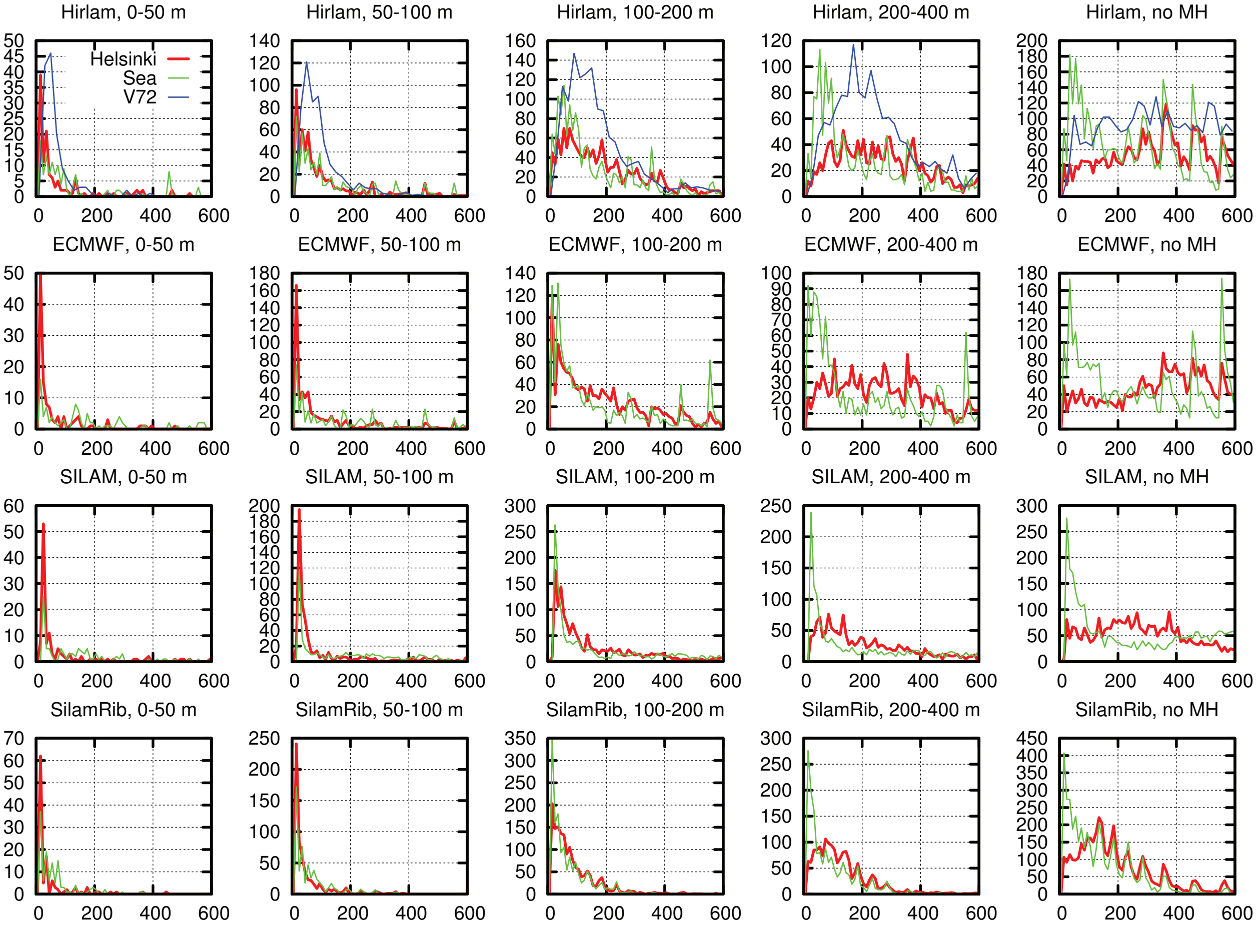

Figure 2: The histograms of forecasted MLH (in meters) for different ranges of measured those. The rightmost column correspond to cases when no mixing height could be detected by sodar. Y-axis shows the number of hourly intervals

Hirlam V72 setup (Europe, 15x15 km grid) for the location of the sodar, i.e. native Hirlam MLH scheme evaluated with Hirlam meteorology.

The ECMWF model is a global spectral NWP model uses slightly different formulation for Ri_b [2]:

$$\mathrm{Ri}_b = (z - z_1)\frac{g}{\langle\theta\rangle}\frac{\theta(z)-\theta_1-0.5\ \mathrm{K}-8.5T_*}{(\Delta U(z,z_1))^2}, \qquad (4)$$

where T_* is a surface-layer temperature scale. The correction for the temperature difference accounts for the entrainment in a convective boundary layer.

The SILAM preprocessor uses a combination of the critical bulk Richardson number (2) and the dry parcel methods to evaluate the mixing height from the temperature and wind profiles. The dry parcel method derives MLH as a height at which the virtual potential temperature equals to that at the surface plus some constant excess ΔT ($\Delta T = 0.5$ K for stable and 1.2 K for unstable stratification). Upon computation of MLH via both methods, the maximum of the two estimates is taken. According to experience of the operational model application, in most of cases the dry parcel method provides the higher value and its outcome is used as the final MLH estimate. Whenever run with the Hirlam input, SILAM utilizes the Hirlam native MLH estimate [5].

For comparison we used four procedures: Hirlam (3), ECMWF (4), SILAM (described above), and SilamRib (1). Note, that Hirlam and ECMWF procedures account for the humidity of air to calculate the potential temperature, whereas SILAM and SilamRib do not. The value of $\mathrm{Ri}_c = 0.25$ is used in all procedures considered here.

3 RESULTS

The main criterion of the quality of the MLH diagnostic was the probability of the model prediction to fall into a certain range centered around the measured value. We also calculated the histograms of modeled MLH corresponding to the different ranges of the measured one.

The measured values of MLH were classified into six classes: 0-50 m range, 50-100 m, 100-200 m, 200-400 m, and the unknown (including poorly pronounced MLH, MLH above the sodar range, technical problems, etc). For each class, the histogram of the corresponding modeled MLH was computed with above-mentioned schemes from the same ECMWF meteorological fields preprocessed with SILAM (Fig. 2). The

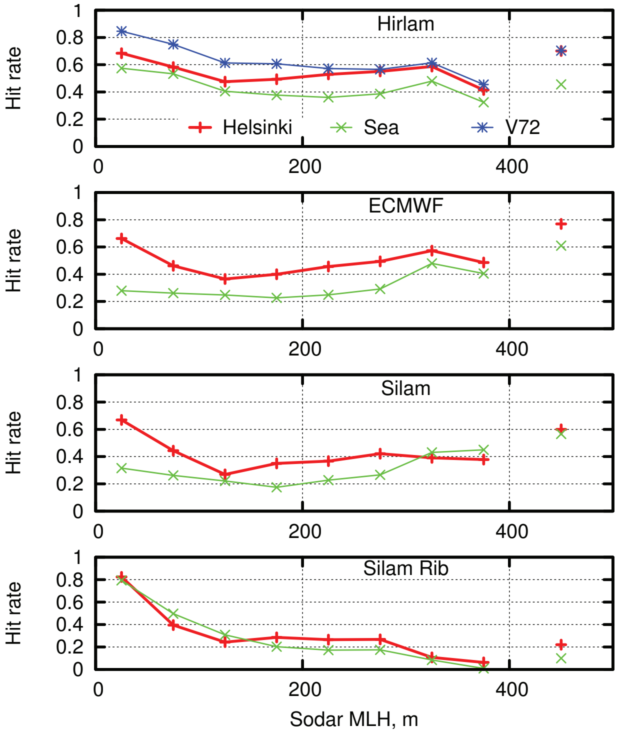

Figure 3: The hit-rates as functions of measured mixing height. Hit rate is a fraction of modeled MLHs that were within 50% or 100 m from the measured values

results are shown from two grid points ("Helsinki" and "Sea", Fig. 1) adjacent to the sodar site.

For 0-50 m range of the measured MLH, all procedures overwhelmingly report the MLH below 50 m, which is seen as sharp peaks of the corresponding histograms. The Hirlam V72 produces somewhat larger peak, which is likely to be caused by more accurate u_* than in SILAM pre-pocessor. For the ranges 50-100 m and 100-200 m all procedures result in wider peak, however all, except for Hirlam, tend to put MLH far too low. In the range 200-400 m, Hirlam produces a wide peak slightly biased towards low MLH. The peak is smaller and wider for ECMWF procedure. SILAM and SilamRib still tend to underestimate MLH. The distributions for "no MLH" class are quite different in the models. Hirlam produces almost uniform distribution for this case. ECMWF distribution shows a clear plateau beyond the sodar range for "Helsinki" grid point. SILAM and SilamRib tend to put MLH within the sodar range.

Computations of the hit-rate were based on two thresholds. The modeled value of MLH was considered to hit the measurements if it was within 50% or within 100 meters from the measured one (Fig. 3). For "not detected" case a model estimate was considered successful if it is above 350 m (corresponding value is shown as a separate point). For low MLH the diagnostics is better for the grid point which is closer to the measuring site, for higher MLH the effect of spatial separation is less pronounced. The higher performance of Hirlam native diagnostics is caused by better spatial and temporal co-location.

Our attempt to account for the entrainment in formula (3) by means of including terms with surface-layer temperature scale T_* or additional offset into the numerator of Ri_b did not improve the performance of the Hirlam diagnostics with respect to the data used. Moreover, alteration of the numerator in (3) reduced the performance of the scheme for low MLH.

4 CONCLUSION

Even with u_* diagnosed by SILAM pre-processor from 3-h meteorological data, the performance of Hirlam procedure is noticeably better than of other considered schemes. It was found to be robust for very low MLH and to work well for MLH within the sodar range. The Hirlam scheme can be recommended for application in chemical transport models.

ACKNOWLEDGEMENTS This work has been supported by the EC FP7 project ERC PBL-PMES (No. 227915), by Academy of Finland (projects ASTREX and IS4FIRES), and by the Russian Foundation for Basic Research (10-05-00802 and 11-05-00305).

References

1. Beyrich, F. (1997). Mixing height estimation from sodar data – a critical discussion. *Atmos. Environ. 31*(23), 3941–3953.
2. ECMWF (2011). IFS Documentation – Cy37r2, Part 4: Physical processes. Technical report, European Center for Medium-range Weather Forecasts.
3. Kouznetsov, R., M. Sofiev, J. Soares, and C. Fortelius (2010). The height of a shallow mixing layer in models: performance of different schemes. In *Proc. 15-th Int. Symp. for the Advancement of Boundary Layer Remote Sensing*, Paris, 28-30 June 2010, pp. 1–4.
4. Kouznetsov, R. D. (2007). Latan-3 sodar for investigation of the atmospheric boundary layer. *Atmospheric and Oceanic Optics 20*(8), 684–687.
5. Sofiev, M., P. Siljamo, I. Valkama, M. Ilvonen, and J. Kukkonen (2006). A dispersion modelling system SILAM and its evaluation against ETEX data. *Atmos. Environ. 40*, 674–685.
6. Vickers, D. and L. Mahrt (2004, November). Evaluating Formulations of Stable Boundary Layer Height. *Journal of Applied Meteorology 43*, 1736–1749.
7. Vogelezang, D. H. P. and A. A. M. Holtslag (1996, December). Evaluation and model impacts of alternative boundary-layer height formulations. *Boundary-Layer Meteorol. 81*, 245–269.
8. Wood, C., R. Kouznetsov, and A. Karppinen (2012). An automated algorithm for deriving mixing-layer depth from a 1d sodar in helsinki. In *Proc. 16-th Int. Symp. for the Advancement of Boundary Layer Remote Sensing*, Boulder, CO, pp. ???

MIXING HEIGHT RETRIEVALS BY MULTICHANNEL MICROWAVE OBSERVATIONS: POTENTIAL FOR INSTRUMENT SYNERGY

Domenico Cimini[1], Jean-Charles Dupont[2], Martial Haeffelin[2], Francesco De Angelis[3]

[1]*IMAA-CNR and CETEMPS, C.da S.Loja, Potenza, Italy, cimini@imaa.cnr.it*
[2]*IPSL/LMD/SIRTA, Palaiseau, France, jean-charles.dupont@ipsl.polytechnique.fr, martial.haeffelin@lmd.polytechnique.fr*
[3]*University of L'Aquila, Via Vetoio, L'Aquila, Italy, fradea89@alice.it*

ABSTRACT

The mixing layer height (MLH) defines the top of the layer near the surface where turbulent mixing is occurring. In the recent years, new algorithms have been developed for estimating MLH, though the automatic detection of the top of the mixing layer still remains challenging. For example, when the MLH is estimated from lidar data, the lidar overlap limit may mask the early growth of the mixing height under stable conditions. Thus, a synergetic approach, considering different techniques based on different aspects of the boundary layer, may be explored to improve the MLH estimate in all conditions. Here we show the preliminary results of a method developed to estimate MLH from multichannel microwave radiometer data.

1. INTRODUCTION

The atmosphere boundary layer is characterized by turbulent fluctuations that induce mixing. During daytime the mixing layer tends to be unstable as a result of convection and is capped by an entrainment zone. At night a shallow stable layer forms near the surface in which mixing occurs through intermittent turbulence, leaving a residual layer above. The mixing layer height (MLH) defines the top of the layer near the surface where turbulent mixing is occurring. The MLH is a key parameter for boundary layer applications, including meteorology, weather prediction and air quality. The determination of the MLH is crucial to study exchanges between the surface and the atmosphere. In the recent years, new algorithms have been developed for estimating MLH, though the automatic detection of the top of the mixing layer still remains challenging, with frequent missing estimates when the mixing layer is not well defined. Mixing layer height can be determined either using temperature, humidity, and wind profiles from insitu vertical profiles or by tracing gradients in atmospheric constituents or structures using remotely sensed vertical profiles (lidar, wind profiling radar, sodar). For example, MLH can be estimated from detection of the aerosol layers by the detection of the inflection points of the lidar signal. However, the mixing height is specially difficult to estimate in stable boundary layer conditions. In fact, the lidar overlap limit causes an offset in the measures of the MLH because stratifications below this height cannot be detected. In case of very low MLH, which may occur under stable conditions, this offset can actually mask the early growth of the mixing height. Thus, a synergy between different techniques, based on different aspects of the boundary layer, may be useful to improve the MLH estimate in all atmospheric conditions.

2. DATA SET

In this work, we show the potential of ground-based multichannel microwave radiometers (MWR) to estimate MLH. The data set considered here was collected at the Site Instrumental de Recherche par Télédétection Atmosphérique (SIRTA), a French national atmospheric observatory dedicated to cloud and aerosol research. SIRTA is located at Palaiseau (49N, 2E), 20 km south of Paris (France) in a semi-urban environment. At SIRTA, a suite of state-of-the-art active and passive remote sensing instruments is operated, including a multi-channel MWR and a backscatter lidar [1].

2.1 MWR

The multi-channel MWR deployed at SIRTA is a humidity and temperature microwave profiler (HATPRO) manufactured by RPG. It senses brightness temperatures (Tb) at 14 channels (22.24, 23.04, 23.84, 25.44, 26.24, 27.84, 31.4, 51.26, 52.28, 53.86, 54.94, 56.66, 57.3,58 GHz) and 7 scan elevation angle (90, 42, 30, 19, 10, 5, 0°).

2.2 LIDAR

The lidar deployed at SIRTA is a 355nm ALS450 backscatter lidar developed by Leosphere. The MLH is derived from lidar backscattering data using the STRAT2D algorithm [2].

3. PRELIMINARY RESULTS

Two approaches have been tested to retrieve the MLH from MWR data:

1) estimate MLH from MWR-retrieved temperature and humidity profiles [3].
2) estimate MLH from MWR-observed Tb.

The first approach is useful because it can deploy the tools developed for temperature and humidity profiles from radiosonde observations [4]. However, the MLH much depends on the different definition (i.e. tool) that is applied. The second approach is a “direct” estimate from Tb measurements. Here it was used a simple multivariate regression (other methods can be used, e.g. neural networks), with in input Tb at all 14 channels and 6 elevation angles (90-42-30-19-10-5°). The training was performed assuming the reference “truth” taken from MLH estimates from backscatter lidar data, following the STRAT2D algorithm. Two different sets of coefficients are determined for night- and day-time retrievals and these were used alternatively depending on local time. Preliminary results of MLH estimated from direct MWR observations are compared with MLH estimates based on other instruments. Figure 1 shows preliminary results obtained for March 2012 at the SIRTA site, obtained from MWR and lidar observations. It is evident that the MWR-based estimate is able to follow the diurnal cycle indicated by the lidar data. Figure 2 shows a statistical comparison performed on a test set that was not used during the training. Statistics of 1-hour average MLH estimates from MWR show a root-mean-square (rms) error of 162 m with respect to STRAT2D MLH estimates.

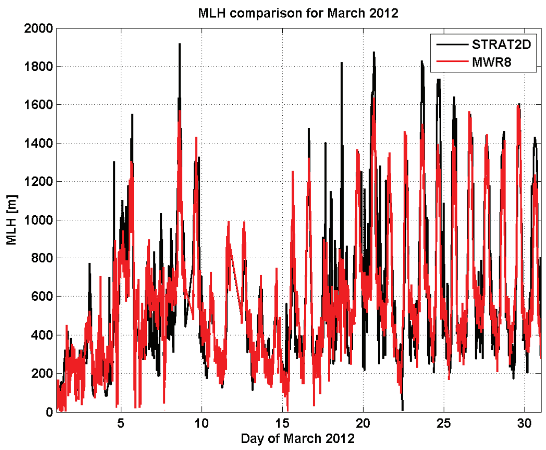

Figure 1. Time series of MLH derived from MWR (red line) and from STRAT2D algorithm (black line) for March 2012.

4. SUMMARY AND CONCLUSIONS

In this paper we demonstrated the potential for deriving MLH directly from MWR observations. Statistics of 1-hour average show rms error equal to 162 m with respect to estimates based on backscattering lidar data. Note that MLH estimates from MWR are expected to be specially valuable for shallow MLH during stable boundary layer conditions. Thus, the combination of MWR and lidar data, as well as data from other remote and in situ sensing instrumentations, seems crucial for studying the MLH in all stability conditions. Future work includes the development of an automatic procedure to identify stable and convective regimes (currently based on local time only), the extension of the dataset to increase the variability of MLH during winter and summer periods, and the use of other retrieval methods that do not require external reference truth for training.

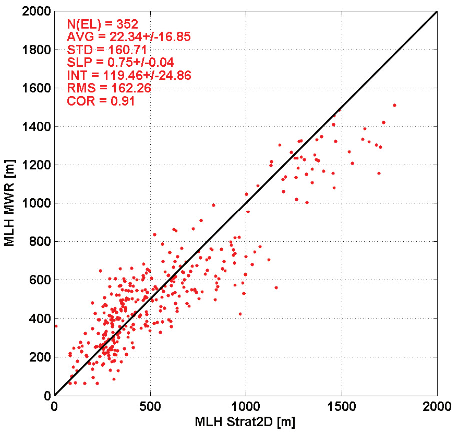

Figure 2. Scatter plot of 1-hour averaged MLH derived from MWR (Y-axis) and Strat2D (X-axis) for March 2012 at the SIRTA site. Number of elements (N(EL)), average X-Y difference (AVG), standard deviation (STD), root-mean-square difference (RMS), correlation coefficient (COR), slope (SLP) and offset (INT) of a linear fit are included. N(EL), SLP, and COR are dimensionless, while AVG, STD, RMS, and INT are in meters.

ACKNOWLEDGMENTS

This work has been partially supported by EU COST ES0702 EG-CLIMET.

REFERENCES

1. Haeffelin M. et al., 2005: SIRTA, a ground-based atmospheric observatory for cloud and aerosol research. *Ann. Geophysic.*, **23**, 253-275, doi:10.5194/angeo-23-253-2005.

2. Morille Y., Haeffelin M., Drobinski P., Pelon J. 2007: STRAT: an automated algorithm to retrieve the vertical structure of the atmosphere from single-channel lidar data. J. Atmos. Ocean. Tech. 761–775.

3. Cimini, D., T. J. Hewison, L. Martin, J. Güldner, C. Gaffard and F. S. Marzano, 2006: Temperature and humidity profile retrievals from ground-based microwave radiometers during TUC, *Meteorologische Zeitschrift*, Vol. 15, No. 1, 45-56.

4. Seidel, D. J., C. O. Ao, and K. Li, 2010: Estimating climatological planetary boundary layer heights from radiosonde observations: Comparison of methods and uncertainty analysis, *J. Geophys. Res.*, 115, D16113, doi:10.1029/2009JD013680.

A 21ST-CENTURY OBSERVING NETWORK FOR CALIFORNIA

Allen White[1], Mike Anderson[2], Mike Dettinger[3,4], Marty Ralph[1], Art Hinojosa[2], Dan Cayan[4]

[1]*NOAA Earth System Research Laboratory, R/PSD2, 325 Broadway, Boulder, CO, USA*
(allen.b.white@noaa.gov, marty.ralph@noaa.gov)
[2]*California Department of Water Resources, Sacramento, CA, USA*
(manderso@water.ca.gov, hinojosa@water.ca.gov)
[3]*U.S. Geological Survey, La Jolla, CA, USA*
[4]*Scripps Institution of Oceanography, University of California at San Diego, La Jolla, CA, USA*
(mdettinger@ucsd.edu, dcayan@ucsd.edu)

ABSTRACT

The NOAA Earth System Research Laboratory (ESRL) and the Scripps Institution of Oceanography (SIO) are implementing a five-year Memorandum of Agreement with the California Department of Water Resources (CA-DWR) to create a 21st-century observing, modeling, display, and decision support system to help address California's flood protection and water resource issues. This work is based on nearly a decade of scientific research into the forcings of extreme precipitation and runoff events along the U.S. West Coast conducted under NOAA's Hydrometeorology Testbed (HMT; http://hmt.noaa.gov). In order to take full advantage of the observing networks being implemented and to provide extended lead time for extreme events, a numerical modeling system focused on the U.S. West Coast is underway. This paper will describe the overall project and will demonstrate how the observing and modeling systems are providing integrated tools for improved monitoring and prediction of the extratropical storms that batter California each winter.

1. OBSERVING NETWORKS

1.1 Soil Moisture Sensors

Because antecedent soil conditions can determine whether a storm produces a flood, soil moisture sensors are being placed at 43 sites across the state (see Fig. 1). CA-DWR is partnering with SIO to install soil moisture sensors in the upper elevations of California by taking advantage of existing infrastructure at interagency Remote Automated Weather Station (RAWS) sites. ESRL is installing soil moisture sensors at lower elevation sites and primarily adjacent to California Department of Forestry fire station (CalFire) facilities. An example of an ESRL deployment is shown in Fig. 2.

1.2 GPS--Integrated Water Vapor

Water vapor fuels precipitation, and GPS technology provides a viable method of measuring the vertically integrated water vapor (IWV; [1]). Hundreds of GPS receivers exist in California for geodetic science. By installing surface meteorology sensors with the GPS receivers and by upgrading real-time communications, these GPS receiver sites can provide water vapor measurements in real time. ESRL is partnering with UNAVCO, the operators of the Plate Boundary Observatory (PBO; http://pbo.unavco.org/) where many GPS receivers already exist, to provide IWV measurements from 37 locations across the state (see Fig. 1).

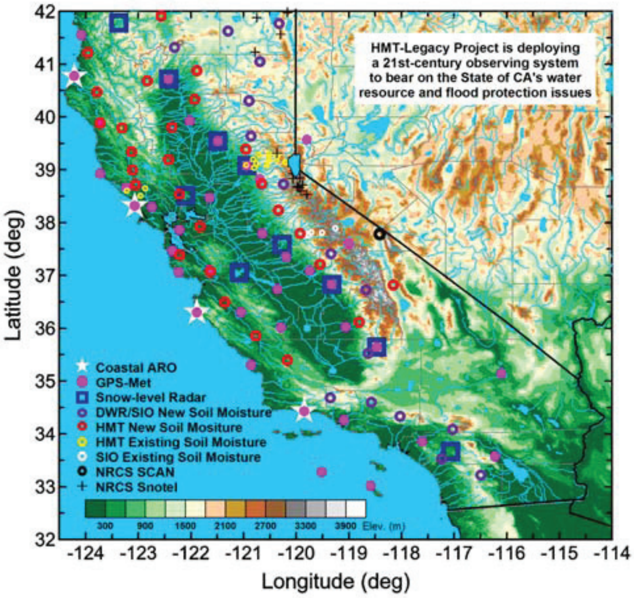

Figure 1. Map of California showing locations where instruments are being deployed as part of the observing network in the HMT Legacy Project.

1.3 Snow Level Radars

The snow level is also a significant variable with respect to flooding in mountainous watersheds because it determines the surface area throughout the watershed that is exposed to snow versus rain [2]. Engineers at ESRL have invented a new compact, frequency-modulated, continuous-wave (FM-CW) radar at S-band (Fig. 3; [3]) designed to measure the snow level at much reduced cost compared to the traditional pulsed-Doppler radars used by ESRL scientists for this purpose. These "snow-level radars" (SLRs) are being installed in ten key watersheds across the state (see Fig. 1). An example SLR deployment is shown in Fig. 3. A data display of snow-level observations from the SLR network is demonstrated in Fig. 4.

Figure 2. An example of an ESRL soil moisture monitoring site. Probes to measure the soil temperature and volumetric moisture content are buried in the ground at depths of 10 and 15 cm. The tripod mast holds a temperature/relative humidity probe and a tipping bucket rain gauge. The tripod also holds a data logger and a solar panel to provide electrical power.

Figure 3. The snow-level radar deployed at Pine Flat Dam in the central Sierra of California. The four-foot diameter radar transmit and receive antennas are at the bottom of the sloped antenna enclosures. The radar electronics and data acquisition computer reside in the environmentally controlled cabinet placed between the two antenna enclosures. Additional surface meteorological sensors (e.g, Fig. 2) are shown to the left. A GPS receiver antenna (far left) allows retrievals of integrated water vapor above the site.

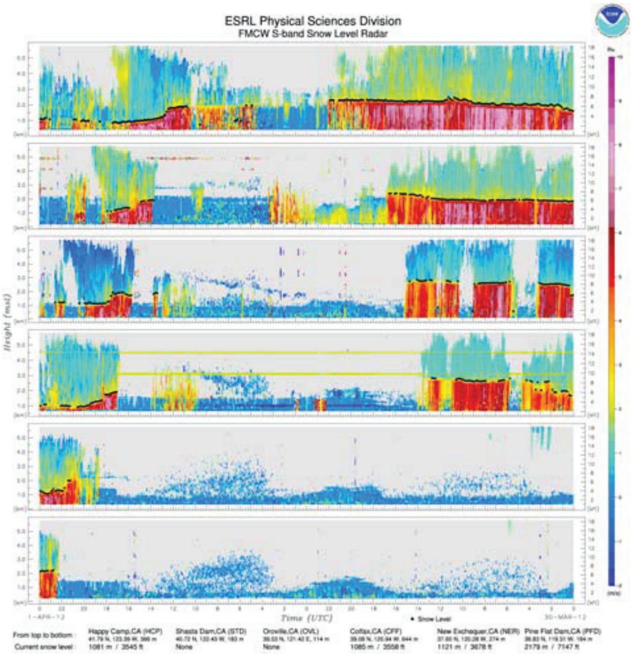

Figure 4. A time series of the snow levels (km MSL; black dots) overlaid on colored contours of Doppler vertical velocity (m s^{-1}; color scale on right) observed by six of the Snow-level Radars deployed along the California Sierra Nevada (see Fig. 1).

1.4 Coastal Atmospheric River Observatories

The winds contained in the low-level jets of landfalling winter storms contribute to the heavy orographic precipitation on the windward slopes of the coastal mountain ranges of California [4]. These jets are often accompanied by enhanced water vapor in the so-called warm conveyor belt of extratropical storms. The narrow band of enhanced water vapor is also referred to as an atmospheric river (AR).

HMT research has shown that ARs are responsible for flood-producing rains along the U.S. West Coast (e.g., [5]). ARs also have been recognized for producing floods in Western Europe (e.g., [6]) and elsewhere around the world. Microwave satellite technology, such as the Defense Meteorology Satellite Program's Special Sensor Microwave Imager (SSM/I), has allowed scientists to look more in depth into the global extent of ARs (see Fig. 5). Still, satellites measure only the water vapor in ARs, while the winds, especially in the storm's low-level jet, are not measured. In addition, the microwave technique used with satellites does not work over land, which explains why the continents are black in Fig. 5.

In response to this observing gap, HMT scientists have developed the concept of an Atmospheric River Observatory (ARO), a unique collection of instruments that monitors the atmospheric forcings associated with

ARs as they make landfall along the coast. The two key instruments in the ARO are a wind-profiling radar and a GPS receiver for IWV measurements. For this project CA-DWR has chosen to use the ¼-scale 449-MHz wind profiler technology for the four coastal AROs that are being implemented along the California coast (see Fig. 1). This choice was based on HMT experience gained in testing and evaluating wind profiling technology in the coastal environment (see http://www.esrl.noaa.gov/psd/psd2/programs/ioos/).

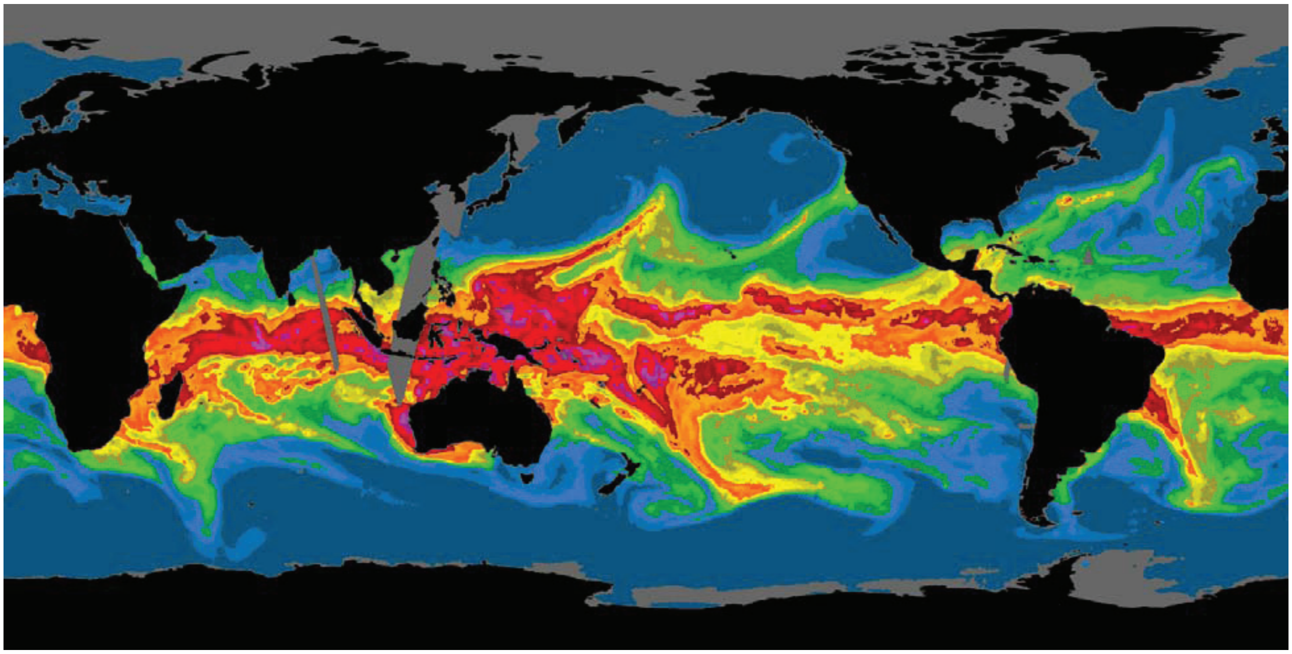

Figure 5. A global composite SSM/I satellite image of integrated water vapor (warmer colors indicate higher water vapor concentration) from 16 February 2004. Several ARs are evident, including one impacting the west coast of the U.S.

One of the real-time displays from an ARO is referred to as the water vapor flux tool and is available to weather forecasters and the public (www.esrl.noaa.gov/psd/data/obs/). It uses thresholds for IWV, upslope wind, and bulk IWV flux that identify AR conditions. For example, [7] showed that, in order to produce orographic rain rates > 10 mm hr^{-1} in California's coastal mountains, an IWV flux exceeding 25 cm m s^{-1} is required. An example display from the prototype ARO at Bodega Bay is shown in Fig. 6.

2. OTHER PROJECT COMPONENTS

To take full advantage of the observing networks being installed and to provide advanced lead time of high impact weather, this project involves a numerical weather prediction component using the HMT WRF ensemble ([8]; HMT weather forecasts are available at http://laps.noaa.gov/forecasts/). Special display systems that can provide this value-added information in the NWS Weather Forecast Offices and River Forecast Center are also being demonstrated (e.g., the Advanced Linux Prototype System development at ESRL). Finally, decision support tools, that will allow water managers and other decision makers to make optimal use of the new observing and modeling information, are being developed. An example is the water vapor flux tool shown in Fig. 6.

3. SUMMARY

ESRL and SIO are in the midst of a five-year Memorandum of Agreement with CA-DWR to install and operate a 21st-century observing system to detect and monitor the forcings associated with landfalling winter storms and the floods they create. To advance the forecast lead time of these important storms, the project takes advantage of advances in numerical weather prediction made by ESRL and HMT. Finally, display and decision support tools are being developed that eventually may allow water managers in California to more reliably make decisions based on forecast information.

ACKNOWLEDGMENTS

CA-DWR is acknowledged for the provision of direct funding for this project. Funding for this project is also leveraged from NOAA's Hydrometeorology Testbed. The authors commend the talented engineering and technical teams located at the ESRL Water Cycle Branch, CA-DWR Hydrology Branch, and the SIO Department of Climate Atmospheric Science and Physical Oceanography for developing, installing, operating, and maintaining the instrumentation in this project.

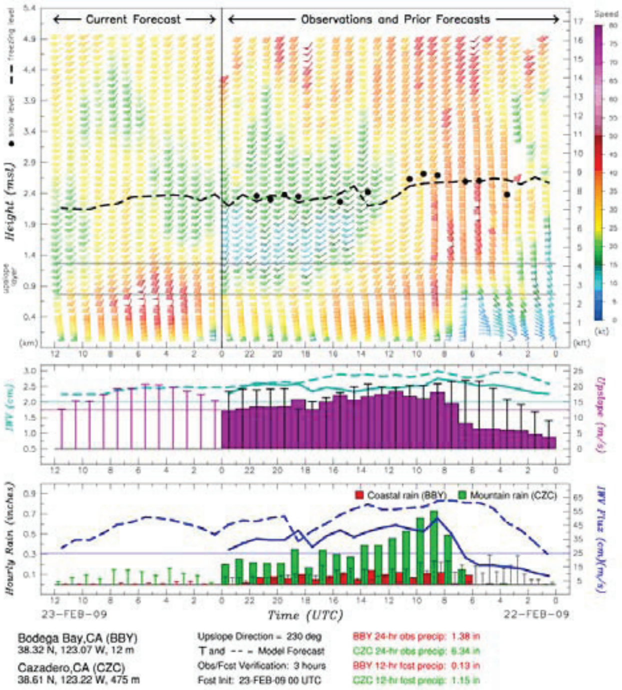

Figure 6. Example from 22-23 February 2009 of the atmospheric river water vapor flux tool displayed on the Internet (www.esrl.noaa.gov/psd/data/obs). Time moves from right to left along the horizontal axis. The current time is indicated by the vertical line in the top panel. Data plotted to the left of this line in each panel display the current HMT rapid-refresh mesoscale model forecast only (i.e., no observations), whereas data plotted to the right of the line in each panel are a combination of observations and model output (described next). (top) Wind profiler hourly averaged observations of the snow level (bold dots) and retrospective hourly HMT model forecasts of the freezing level (dashed line) at 3-hr verification time along with time-height section of hourly averaged wind profiles (flags = 25 m s^{-1}; barbs = 5 m s^{-1}; half-barbs = 2.5 m s^{-1} – wind speed color coded) observed by the ARO at Bodega Bay. (middle) Time series of hourly averaged upslope flow (m s^{-1}; from 230°) observed (histogram) and predicted (T posts) in the layer between 750 and 1,250 m MSL (bounded by the dashed lines in the top panel), and IWV (cm) observed (solid line) and predicted (dashed line) by the HMT forecast model. (bottom) Time series of hourly averaged IWV flux (cm m s^{-1}) observed (solid line) and predicted (dashed line) by the HMT forecast model, and hourly rainfall histogram from Bodega Bay (mm; red) and Cazadero (mm; green), in the coastal mountains. Minimum thresholds of upslope flow, IWV, and IWV flux for the potential occurrence of heavy rain (> 10 mm h^{-1}) in atmospheric river conditions defined by [7] are indicated by the thin horizontal lines in the middle and bottom panels.

REFERENCES

1. Bevis M., S. Businger, T. A. Herring, C. Rocken, R. A. Anthes, and R. H. Ware, 1992: GPS meteorology: Remote sensing of the atmospheric water vapor using the Global Positioning System. *J. Geophys. Res*, **97**, No. D14, 75–94.

2. White, A. B., D. J. Gottas, E. T. Strem, F. M. Ralph, and P. J. Neiman, 2002: An automated brightband height detection algorithm for use with Doppler radar spectral moments. *J. Atmos. Oceanic Technol*., **19**, 687–697.

3. Johnston, P. E., D. A. Carter, D. M. Costa, J. R. Jordan, and A. B. White, 2012: A new FM-CW radar for precipitation and boundary-layer science. *16th Intern. Sym. for the Advancement of Boundary-Layer Remote Sensing*, 5-8 June 2012, Boulder, CO (this issue).

4. Neiman, P. J., F. M. Ralph, A. B. White, D. E. Kingsmill, and P. O. G. Persson, 2002: The statistical relationship between upslope flow and rainfall in California's coastal mountains: Observations during CALJET. *Mon. Wea. Rev*., **130**, 1468–1492.

5. Ralph, F. M., P. J. Neiman, G. A. Wick, S. I. Gutman, M. D. Dettinger, C. R. Cayan, and A. B. White, 2006: Flooding on California's Russian River: The role of Atmospheric Rivers. *Geophys. Res. Lett*., **33**, L13801, doi:10.1029/2006GL026689.

6. Lavers, D. A., R. P. Allan, E. F. Wood, G. Villarini, D. J. Brayshaw, and A. J. Wade, 2011: Winter floods in Britain are connected to atmospheric rivers. *Geophys. Res. Lett*., **38**, L23803, doi:10.1029/2011GL049783.

7. Neiman, P. J., A. B. White, F. M. Ralph, D. J. Gottas, and S. I. Gutman, 2009: A water vapour flux tool for precipitation forecasting. *Proc. Institution of Civil Engineers – Water Management*, **162**, 83–94.

8. Yuan, H., J. A. McGinley, P. J. Schultz, C. J. Anderson, and C. Lu, 2008: Short-range precipitation forecasts from time-lagged multimodel ensembles during the HMT-West-2006 Campaign. *J. Hydrometeor.,* **9**, 477–491.

Thermodynamic Remote Sensing of the Boundary Layer and Above, A Network Approach

John Bosse[1], David Oberholzer[1], Marta Nelson[2], Randolph Ware[2,3,4]

[1]*Earth Networks,14210 Milestone Center Dr., Germantown, MD, 20876USA, jbosse@earthnetworks.com*
[2]*Radiometrics,4909 Nautilus Court North, Suite 110, Boulder, CO80301 USA, ware@radiometrics.com*
[3]*Cooperative Institute for Research in the Environmental Sciences*
[4]*National Center for Atmospheric Research*

ABSTRACT

Observations of the boundary layer, from the ground up to about 1,000 m, are critically important to the accuracy of atmospheric forecast and research models. But traditional sensors are typically limited in time and space, and insufficient to support the forecast accuracy desired by the renewables, utilities, aviation, air quality and water management industries. Microwave radiometers provide continuous all-weather boundary layer temperature and humidity profiles with radiosonde-equivalent assimilation accuracy. Radiometers also provide unique liquid profiles to 10 km height. A full suite of traditional forecast tools and indices can be generated if the thermodynamic profiles are combined with wind profiles. In addition, the profiles can be assimilated in numerical weather models.

The Earth Networks Boundary Layer Network (ENBLN) is the first monitoring network for continuous collection of planetary boundary layer data up to around 10 km height. The ENBLN will use radiometers from Radiometrics to provide round-the-clock temperature, humidity and liquid profiles of the boundary layer and above. Earth Networks will combine observations from these instruments with information from its global weather network of more than 8,000 weather stations.

ENBLN PILOT NETWORK BUILDOUT

To build a boundary layer network it was first critical to ensure the venture would be commercially viable. Several potential stakeholders were contacted for feedback on the ENBLN Network concept. Initial targets surveyed were Investor Owned Utilities, Independent System Operators (ISOs), Air Quality Districts, and Private Meteorological Firms. In this investigative stage, several atmospheric issues of concern were identified.

For cost feasibility, a wide scale deployment of the ENBLN was not an option. Too many sensors would be required to cover a large geographic region, and if the density of the sensors was not sufficient, the value of the data could be diminished. The companies settled on an initial network of 10 sensors to be deployed in the State of California, with concentration from the San Francisco Bay area southward.

PROPOSED NETWORK OPERATION

To facilitate easy data distribution to potential customers of the BLN, a centralized data processing approach was devised. Earth Networks is collecting the data from the 10 sensors centrally. This data will be made available from each sensor at an update frequency of 6 minutes. Daily archive files of hourly data will be maintained.

To ensure data quality and robust network operation, each site location will be visited a minimum of twice per year for complete field calibration. All sites will be monitored from a central Networks Operations Center. Here both data availability and data quality will be scrutinized and flagged. Field Technicians located in California will be dispatched to address any problem sites, with the goal of maintaining 99.5% availability during the pilot phase of network build-out.

ATMOSPHERIC TARGETS FOR PILOT

To address the business needs of our target customer base in Electric Utilities, Air Quality, and Federal Government, we focused on placing the radiometers at locations that would yield gains in understanding atmosphere phenomena that plague efficient electric utility operation, impact air quality, or could hinder operations at federal government facilities. The following atmospheric regimes we deemed most critical:

- Marine Layer Inversions
- Boundary Layer Stability near Wind Farms
- Santa Ana and Monsoonal Wind Flow

In all cases, the radiometer is adept at determining both the temperature and humidity profiles that enable forecasters to monitor the data in real-time for their operational purposes, and also allows for the data to be fed into Rapid Update Cycle models for an improved view of initial boundary layer conditions, and therefore improved forecast output.

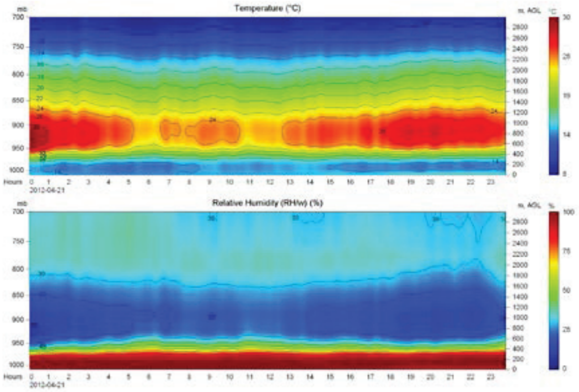

Figure 1. Top profile image shows the sharp temperature contrast over time between the cool surface in the marine cloud layer vs. the warmer air aloft. The bottom profile from the same time period illustrates the vertical extend of the cloud layer moisture, and the drier air aloft. This Data is from a 24 hour period covering 4/21/2012 from a radiometer based at LAX.

NEXT STEPS

The BLN is now moving from concept phase to deployment phase, with a target of late June for 80% network deployment. Once deployed, Earth networks and Radiometrics will be working to bring several customers of this information on-line. Significant efforts will be made to quantify operational usefulness of the data, and model output improvements as a result of better boundary layer initial condition data.

REFERENCES

1. K. Friedrich, J. Lundquist, M. Aitken, E. Kalina and R. Marshall, 2011: Stability and turbulence in the atmospheric boundary layer: An intercomparison of remote sensing and tower observations, GRL.

2. R. Hoff, R. Hardesty, F. Carr, T. Weckwerth, S. Koch, A. Benedetti, S. Crewell, N. Cimini, D. Turner, W. Feltz, B. Demoz, V. Wulfmeyer, D. Sisterson, T. Ackerman, F. Fabry, K. Knupp, R. Carbone and R. Serafin, 2011: Thermodynamic Profiling Technologies Workshop, NSF-NWS Workshop Report.

FEATURES OF KELVIN–HELMHOLTZ BILLOWS IN A STABLE ABL DERIVED FROM SODAR DATA

Lyulyukin V.S., Kuznetsov D.D.

Obukhov Institute of Atmospheric Physics, RAS, Pyzhyovskiy 3, 109117, Moscow, Russia,
lyulyukin@gmail.com

ABSTRACT

Continuous 4-year Doppler sodar measurements in the Moscow region provide the opportunity to obtain statistical information on Kelvin-Helmholtz billows (KHB) in the lower troposphere in this area. Sodar data were examined to select the cases of inclined-stripes echogram patterns. The features of observed KHB were derived by visual inspection of the echograms and used to obtain the statistical properties of KHB. Using the hypothesis of frozen turbulence the relation between the billow wavelength and height is shown to be close to theoretically predicted.

1. INTRODUCTION

The shear instability and Kelvin-Helmholtz billows (KHB) to which it leads are generally accepted to be the major cause of turbulence in a stably stratified ABL (see, eg, [1, 2] and references therein). However, turbulence is always observed in the stable ABL, while observations of KHB are rather rare. Indeed, only a few dozen descriptions of KHB in the ABL have been published, with some publications been devoted to the description of only one or two episodes [3, 4]. Available statistics on the frequency of KHB occurrence, and the distributions of KHB parameters, are scarce, if any.

The purpose of this study was to use the results of long-term continuous sodar measurements to obtain the statistics on the occurrence of KHB, their duration, amplitude, time period and wavelength, etc. Statistical comparisons of some parameters of the ABL obtained from sodar measurements, with KHB features were made.

2. MEASUREMENT SITE AND EQUIPMENT

We used data from continuous sodar measurements at the Zvenigorod Scientific Station (ZSS) of the Obukhov Institute of Atmospheric Physics in 2008–2010. ZSS (55.70 N, 36.78 E) is located in weakly inhomogeneous rural area 45 km west of Moscow. The three-antenna monostatic Doppler sodar LATAN-3, used at the station, has the following system parameters [5]: carrier frequency – 1700 Hz, vertical resolution – 20 m, altitude range – from 40 m to 200 $\div$ 500 m, time resolution – 10 $\div$ 20 sec.

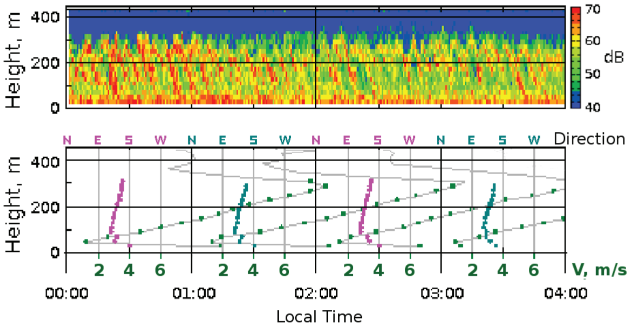

Figure 1. The episode of KHB. Top: the sodar echogram. Bottom: the corresponding wind speed (points with lines) and direction (points) profiles. Lines without points – data with lower reliability. Jan 29, 2010.

The features of observed KH billows were derived by visual inspection of sodar echograms. An example of echogram in case of KHB is shown in Fig. 1.

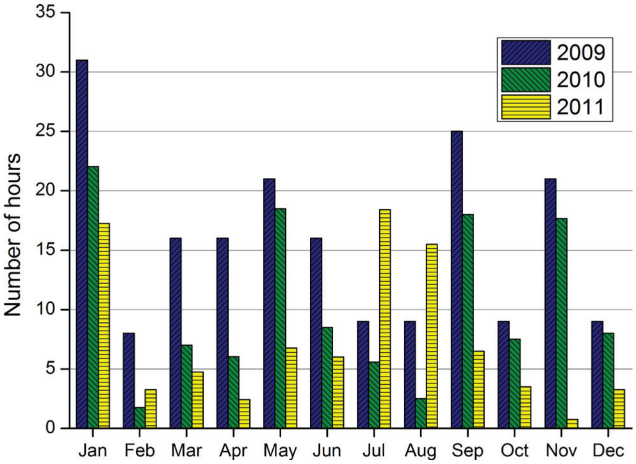

Figure 2. Record of the number of sodar KHB observation hours per month.

3. RESULTS

Figure 2 displays the total numbers of KHB observation hours per month. 344 cases of the occurrence of the billows, a total of 400 hours were counted by inspection of the echograms of 3 year-measurements. KHB were observed about 6% of the time of nocturnal hours from 00:00 till 06:00, which can be associated with the presence of the inversion.

Statistics on the wind speed shear in 2009 are presented in Fig. 3. Comparison of the time distributions of wind shear during nocturnal hours and in the cases of KHB, shows that the presence of the wind shear is not the only condition for arising of KHB. The distributions are similar in general and are close to the normal distribution.

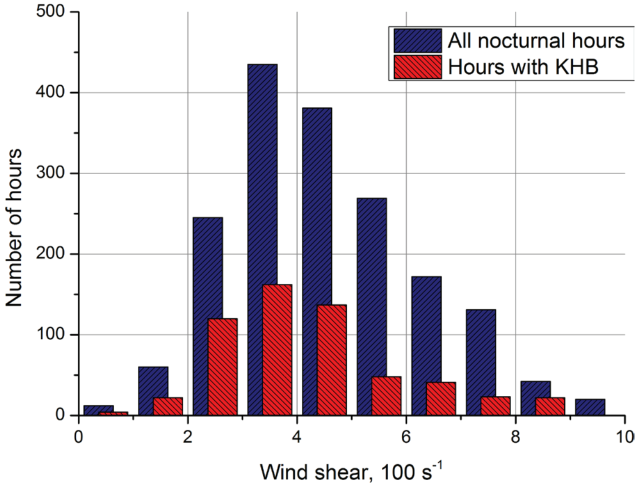

Figure 3. Statistics on the wind shear in 2009 year by sodar data.

The frequency distribution of the time periods of the billows is presented in Fig 4. The distribution is close to the normal distribution and 80% of the cases fall in the range between 2 and 4.5 minutes.

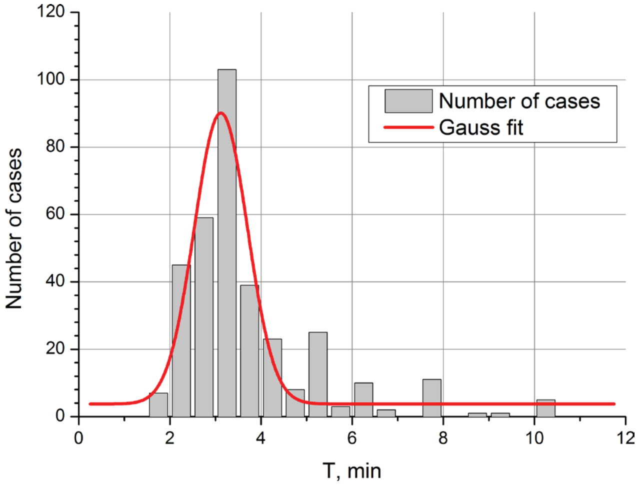

Figure 4. Statistics on the time period of KHB by three years of measurements.

Using the hypothesis of frozen turbulence we can estimate the wavelength of KHB as

$$\lambda \approx T \cdot \langle v \rangle\,, \tag{1}$$

where T is the time period of KHB, derived from the sodar echograms, and $\langle v \rangle$ is the average wind speed during KHB. It is possible to compare the billow wavelength λ, and the thickness of the billow layer or the billow amplitude H, to theoretical and model-derived values of λ/H. A plot of the derived wavelengths versus amplitudes is presented in Fig. 5. In several cases, KHB period can not be obtained with sufficient accuracy by visual inspection. Such fuzzy cases are marked in Fig. 5 with crosses. Using data on the clear cases (233 totally) we derived the average wavelength-to-height ratio from a linear fit:

$$\lambda = (8.5 \pm 0.3) \cdot H, \tag{2}$$

where H is the amplitude of the billows. This ratio corresponds to theoretical predictions and laboratory experiments (can be found in [6] and in the references therein). According to [7, 8] the ratio λ/H is within range $2 \div 20$ depending on the stage of development of the billows, and on the value of Ri. The ratio range is plotted in Fig. 5 with dash lines.

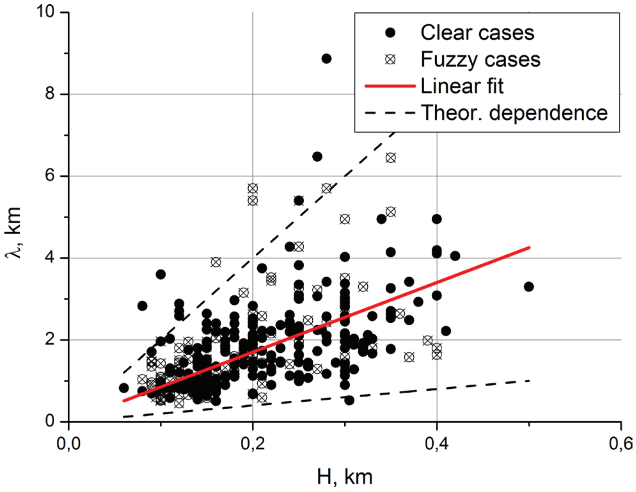

Figure 5. Relation between the height and the wavelength of KHB.

4. CONCLUSION

Continuous sodar measurements provide the opportunity to obtain statistical information on Kelvin-Helmholtz billows. We obtained the statistics on the frequency of KHB occurrence, and on the time period of the billows. The time distribution of wind shear in the presence of KHB is similar to general wind shear distribution at night and is close to the normal distribution. The statistics on the wavelength-to-height ratio are shown to be in agreement to theoretical predictions and experimental data. An exceeding of the predicted λ/H ratio range in several cases (Fig. 5) can be explained by the difference between the KHB forms in the presence of monotonic wind speed profile and in the presence of low level jet. Various structures of KHB are analyzed in details in [9].

ACKNOWLEDGMENTS

Authors thank R.D. Kouznetsov and M.A. Kallistratova for suggesting the topic of research, permanent attention to work and useful discussions. The work was supported by the Russian Foundation for Basic Research through grant 10-05-00802.

REFERENCES

1. DeSilva I., H. Fernando, F. Eaton, D. Hebert, 1996: Evolution of Kelvin-Helmholtz billows in nature and laboratory, *Earth Planet. Sci. Lett.*, **143**, pp. 217–231.
2. Cushman-Roisin B., 2005: Kelvin-Helmholtz instability as a boundary-value problem, *Env. Flu. Mech.*, **5**, pp. 507–525.
3. Newsom R.K., R. Banta, 2003: Shear-flow instability in the stable nocturnal boundary layer as observed by Doppler lidar during CASES-99, *J. Atmos. Sci.*, **60**, 16–33.
4. Fukao S., H. Luce, T. Mega, M. Yamamoto, 2011: Extensive studies of large-amplitude Kelvin-Helmholtz billows in the lower atmosphere with VHF middle and upper atmosphere radar, *Q. J. R. Meteor. Soc.*, **137**, pp. 1019–1041.
5. Kouznetsov R.D., 2007: LATAN-3 sodar for investigation of the atmospheric boundary layer, *Atm. and Oceanic Opt.*, **20(8)**, pp. 684–687.
6. Blumen W., R. Banta, S.P. Burns, D.C. Fritts, R. Newsom, G.S. Poulos, J. Sun, 2001: Turbulence statistics of a Kelvin–Helmholtz billow event observed in the night-time boundary layer during the Cooperative Atmosphere–Surface Exchange Study field program, *Dynamics of Atmospheres and Oceans*, **34**, pp. 189–204.
7. Thorpe S.A., 1973: Experiments on instability and turbulence in a stratified shear flow. *J. Fluid Mech.*, **61**, p. 731.
8. Atsavapranee P., M. Gharib, 1997: Structures in stratified plane mixing layers and the effects of cross-shear, *J. Fluid Mech.*, **342**, pp. 53–86.
9. Lyulyukin V.S., 2012: Braid patterns of Kelvin-Helmholtz billows in sodar return signal: A composite analysis, *This collection*.

RELATIONSHIPS BETWEEN PARTICLE NUCLEATION AND RADIATIVE FORCING AT A FOREST SITE IN THE SOUTHEAST US

Priya Pillai[1], Andrey Khlystov[2], John T Walker[3], Viney P Aneja[1]

[1] Department of Marine, Earth, and Atmospheric Sciences, North Carolina State University, Raleigh, NC, USA 27695, prpillai@ncsu.edu and viney_aneja@ncsu.edu
[2] Research Triangle Institute, 3040 Cornwallis Rd., Durham, NC, USA 27709, akhlystov@rti.org
[3] US Environmental Protection Agency, RTP, NC, USA 27711, Walker.Johnt@epamail.epa.gov

ABSTRACT

Aerosol particles modify the earth's radiation budget through direct (scattering and absorption) and indirect radiative effects (modifications in cloud physical and microphysical properties). Nucleation is an important source of atmospheric aerosol particles.

This study aims at calculating the aerosol and cloud radiative forcing at Duke Forest for different nucleation event classes. Continuous particle size distribution measurements were made from November 2005 to September 2007, using Scanning Mobility Particle Sizer (SMPS), at the Duke Forest Site, Chapel Hill, NC. The size distributions from 10 nm to 250 nm (aerodynamic diameter) are analyzed to identify nucleation events and classify these events into different event classes A, B, or C based on the behavior of particle size distribution and the particle growth pattern. Present study suggests that new particle formation is frequent in this region. The average total particle number concentration on nucleation event days is 8684 cm^{-3} ($10 < D_p < 250$ nm) and 3991 cm^{-3} ($10 < D_p < 25$ nm) with a geometric mean diameter of 35 nm and mode diameter of 28 nm and for non-nucleation days these values are 2143 cm^{-3}, 655 cm^{-3}, 49.6 nm, and 44.5 nm respectively.

Shortwave flux data from Clouds and Earth's Radiant Energy System (CERES) instrument onboard Earth Observing System (EOS) Terra and Aqua satellites are utilized for radiative forcing calculation. Cloud screening is performed using Moderate Resolution Imaging Spectro-radiometer (MODIS) cloud data. The measured particle number concentration will be analyzed using MODIS derived total column aerosol optical depth to find the contribution of these freshly nucleated particles on the total solar radiation extinction. Variations in aerosol and cloud radiative forcing may have important implications through their role as climate feedback mechanisms.

1. INTRODUCTION

Nucleation is the process of forming dispersed nuclei from the homogeneous phase under super saturation of vapor. It may produce very high concentrations of particles with diameters < 10 nm [1]. Nucleation involves the formation of initial nuclei and their growth through condensation and/or coagulation. Depending on the prevailing chemical and meteorological conditions, the dominant nucleation mechanism may differ [2], [3]. Primary emission, nucleation, and subsequent growth of pre-existing particles by condensation and coagulation are responsible for maintaining atmospheric aerosol concentrations and size distribution [4].

Atmospheric aerosols modify the earth's radiation budget through its role on earth's radiative balance. Radiative effects can be direct by scattering incoming solar radiation and absorbing outgoing long wave radiation or indirect by acting as cloud condensation nuclei to modify cloud micro-physical properties [5]. Aerosol radiative forcing is the anthropogenic contribution in aerosol radiative effect and a variety of studies have attempted to quantify the Top of the Atmosphere (TOA) direct radiative effect based solely on multi spectral information gathered from different space borne instruments [6],[7].

The purpose of this study is to detect and classify the new particle formation events and identify their role on aerosol number concentration and subsequent radiative forcing at the DF site.

2. EXPERIMENTAL

2.1 Site description

Particle size distribution, total number concentration, chemical, and meteorological measurements were conducted at Duke Forest, Chapel Hill, North Carolina. Duke Forest (35.98^{0}N, 79.09^{0}W), considered a suburban forest site, is surrounded by the cities of Chapel Hill (7 km to the south-southeast), Durham (17 km to the east-northeast), Raleigh (40 km to the southeast), and Burlington (33 km to west-northwest). Interstate-40 passes approximately 2.4 km to the northeast of the site. A detailed description of the site is provided by [8] Geron (2009). Measurements were conducted over a Loblolly pine plantation with an approximate tree height of 18 m.

2.2 Measurements

The particle size distribution measurements were conducted using a Scanning Mobility Particle Sizer

(SMPS) consisting of a TSI series 3080 Electrostatic Classifier with a 3081 Differential Mobility Analyzer (DMA), and a 3010 Condensation Particle Counter (CPC). A TSI Model 3025 CPC was used for a brief period early in the study. After accounting for periods of instrument malfunction and maintenance activities, a total of 364 observation days were available for analysis during the period November, 2005 – September, 2007.

2.3 Multi-spectral information from space

We use spatially and temporally coincident aerosol and cloud information derived from the Moderate Resolution Imaging Spectroradiometer (MODIS) and the Clouds and Earth's Radiant Energy System (CERES) instrument onboard Earth Observing System (EOS) Terra and Aqua satellite to calculate aerosol radiative forcings owing to new particle formation under cloud free conditions at a forest site in the Southeast US. By combining CERES and MODIS data, we take advantage of the more accurate cloud property retrieval of MODIS sensor because of its finer spectral resolution (36 narrowband spectral channels) compared to the broad band channels of CERES instrument. We use the TOA SW and LW fluxes from CERES SSF data product reported at 20 km spatial resolution at nadir. CERES instrument onboard Terra and Aqua Satellite observes TOA radiances and are converted to fluxes using the angular distribution models [9].

3. METHODOLOGY

3.1 Growth Rate and Condensation Sink

Particle growth rate indicates size changes of nucleated particles with time. A log-normal fit is applied to the data to identify the peaks in each size distribution. GR in nm hr^{-1} was calculated from the difference between diameters corresponding to the peaks for each instant of time by dividing it with the corresponding difference in time.

$$GR = \frac{\Delta D_{\mathrm{peak}}}{\Delta t}, \tag{1}$$

GR is a function of the condensable vapor concentration and the condensation sink (*CS'*). *CS'* quantifies the loss rate of molecules in the entire size spectrum due to condensation of condensable vapors on pre-existing aerosols [10]. The *CS'* in cm^{-2} is calculated as follows

$$CS' = \frac{2\pi \mathrm{D} \int_{10\mathrm{nm}}^{250\mathrm{nm}} D_{\mathrm{p}}\, \mathrm{n}(D_{\mathrm{p}})\ \mathrm{dlog}(D_{\mathrm{p}})}{2\pi D}, \tag{2}$$

3.2 Detection and Classification of Events

The observation days are categorized into nucleation event classes based on 2D size distribution and the particle growth rate plots. We adopted the nucleation event classification scheme by [11] Boy et al. (2008). For each observation days, the particle number concentration for each size bins (N_i) were plotted as a function of particle diameter and time. The periods of increasing N_i were assessed to identify potential nucleation event classes. The typical size distribution behavior for each of these event classes are shown in Figure 1.

Class A: Increased concentrations of nucleation mode (NM) particles ($D_p \leq 25$nm) with well-defined and uninterrupted growth to about 100 nm or greater.

Class B: Increased NM particle concentrations are observed followed by particle growth to about 100 nm. The highest concentrations of new particles are found not at the lowest size bins.

Class C: Shows local nucleation episode characteristics with increased NM particles at lower size bins with consequent particle growth that does not exceed 40 nm.

Non-Nucleation: Observation days with particle size distributions devoid of increased NM concentration and their subsequent growth to larger particles.

Unclassified: Days that do not fit into the described event classes or for which the growth rates are extremely fluctuating.

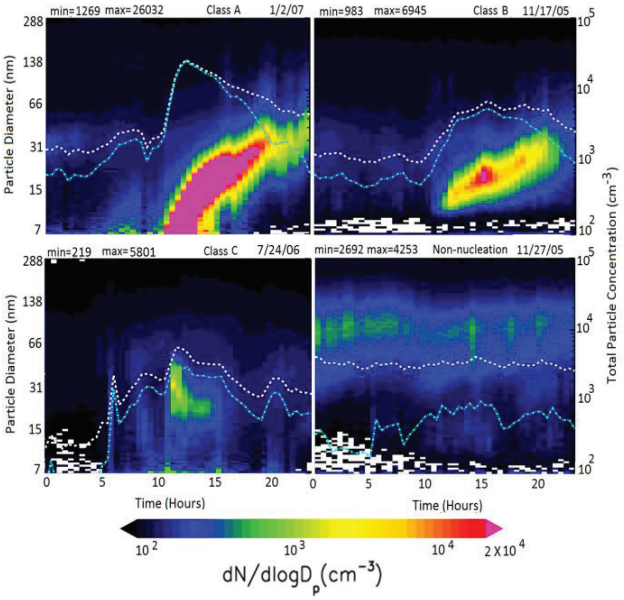

Figure 1. Examples aerosol size distributions for Class A, B, C and Non-nucleation event classes are shown along with total particle number concentration (white) and NM particle concentration (cyan).

3.3 Aerosol Radiative Forcing during Nucleation

We examined the impact of new particle formation on the radiative balance at the Duke Forest Site, by selecting the cloud free nucleation days for July, 2006.

To calculate the aerosol SW and LW radiative forcing, we separated the CERES data into two groups, cloud clear and cloud contaminated, based on the spatially and temporally coincident MODIS derived aerosol and cloud information. If the MODIS cloud fraction is greater than the threshold (5%), then that pixel is classified as cloudy otherwise cloud clear. For aerosol radiative forcing calculation, we selected CERES fluxes only if the MODIS pixels within the CERES instrument footprint has a percentage cloud fraction < 5%. We further separated the cloud cleared CERES data into two groups based on the MODIS aerosol optical thickness and the DF particle size distribution data. If the MODIS 550 nm AOD < 0.15, then we classified that pixel into aerosol and cloud free and any pixel for which the MODIS 550 nm AOD ≥ 0.15 is classified as aerosol.

The SW and LW TOA aerosol radiative forcing is defined as

$$SWRF_{nucl} = SWFlux_{clear} - SWFlux_{aerosol}, \quad (3)$$

$$LWRF_{nucl} = LWFlux_{clear} - LWFlux_{aerosol}, \quad (4)$$

$Flux_{clear}$ is the TOA SW or LW flux observed under cloud free (MODIS pixel cloud fraction < 5%) and aerosol free (MODIS AOD at 550nm < 0.15) conditions and $Flux_{nucl}$ is the flux observed for cloud free nucleation days. For the radiative forcing calculation, we ensure that the selected CERES pixels are confident cloud free, by selecting those pixels for which the spatially and temporally coincident MODIS pixel percentage cloud cover < 5%.

4. RESULTS

4.1 Statistics

Nucleation events are observed on approximately 79% (237 days) of days with complete measurements. The observed nucleation frequency at Duke Forest site is significantly higher compared to that observed at forested areas elsewhere. From the total valid observations, 46% of the days at a mixed deciduous forest in southern Indiana [12], 35% of the days at a deciduous central Virginia [13], and 53% of the days [14] at the Pittsburg boreal forest exhibited new particle formation characteristics.

The average total particle number concentration on nucleation event days is 8684 cm^{-3} (10 < D_p < 250 nm) and 3991 cm^{-3} (10 < D_p < 25 nm) with a geometric mean diameter of 35 nm and mode diameter of 28 nm and for non-nucleation days these values are 2143 cm^{-3}, 655 cm^{-3}, 49.6 nm, and 44.5 nm respectively.

4.2 Nucleation Radiative forcing for July, 2006

Total 8 nucleation days and 6 non-nucleation days are cloud free at the time of MODIS scanning and included in the calculation aerosol direct radiative forcing. Total 10 days are detected as cloudy days. By the close examination of particle size distribution, it is evident that even though there is no sign of new particle formation, particles that are nucleated and grown on the previous day still exists at the site for the following days. For this reason, we grouped such days as nucleation days for TOA flux calculation for which aerosol particle concentration is impacted by nucleation. But majority of those days (7 days out of 9 days) are associated with percentage cloud cover well above the threshold value and are thus not involved in further analysis and subsequent radiative forcing calculation. However, the association between new particle formation and cloud fraction is that new particle formation followed by days with cloud fraction much greater than the applied threshold and may indicate the role of newly formed particles in aerosol indirect radiative forcing as cloud condensation nuclei.

As stated earlier, new particle formation is frequently observed in relatively dryer air with low background aerosols [13] owing to lower competition for condensable vapors.

Table 1. The TOA aerosol SW and LW upward flux at Duke Forest site for July, 2006.

Nucleation Day	SW Flux Wm^{-2}	LW Flux Wm^{-2}	MODIS AOT 550nm	Cloud Fraction %
Aerosol	198.23	292.44	0.43	0.75
Clean	183.96	295.67	0.107	1.43

The SW and LW fluxes and MODIS aerosol optical depth at 550 nm and percentage cloud fraction for low and high aerosol loading conditions are listed in Table 1. The shortwave and long wave aerosol forcings are calculated for nucleation days (Table2) as in equation 1 and 2.

Table 2. The TOA SW and LW direct radiative forcing at the DF site for July, 2006.

Nucleation	SW Forcing Wm^{-2}	LW Forcing Wm^{-2}
	-14.27	3.23

In regions dominant of fine mode aerosols, the LW RF is far less compared to SW RF. However, regions dominant of coarse mode aerosols, the LW radiative forcing become significant [15]. At the DF site the nucleation day SW direct radiative forcing is partially offset by LW radiative forcing (23%) and is same as the offset reported by [16] Nair et al. (2008) for case 2 with higher aerosol loading and low values of angstrom exponent.

5. SUMMARY AND CONCLUSIONS

Particle size distributions were measured from November, 2005 to September, 2007 at Duke Forest near Chapel Hill, North Carolina. Observations indicate that new particle formation is frequent in this region, with class A and B events occurring on 35% of valid measurement days. The estimated SW direct radiative forcing during nucleation events was -14.27% and the LW RF offset SWRF by 23%. Our study shows that the frequent nucleation events at the Duke Forest Site are associated with significant SW and LW radiative forcing and thus necessitates the detailed understanding of the new particle formation events and subsequent impact on radiative balance.

6. REFERENCES

[1] Ehn, M., T. Petja, W. Birmili, H. Junninen, P. Aalto, and M. Kulmala, 2007: Non-volatile residuals of newly formed atmospheric particles in the boreal forest, *Atmos. Chem. Phys*., **7**, pp. 677–684.

[2] Kulmala, M., P. Korhonen, I. Napari, A. Karlsson, H. Berresheim, and C.D. O'Dowd, 2002: Aerosol formation during PARFORCE: Ternary nucleation of H2SO4, NH3, and H2O,*J. Geophys. Res.*, **107**, pp. 8111.

[3] Zhang, R., I. Suh, J. Zhao, D. Zhang, E.C. Fortner, X. Tie, L.T. Molina, and M.J. Molina, 2004: Atmospheric new particle formation enhanced by organic acids, *Science*, **304**, pp. 1487–1490.

[4] Stanier, C.O., A.Y. Khlystov, S.N. Pandis, 2004a: Ambient aerosol size distributions and number concentrations measured during the Pittsburgh Air Quality Study (PAQS), *Atmos. Environ.*, **38**, pp. 3275–3284.

[5] Ramanathan, V., P.J. Crutzen, J.T., Kiehl, and D. Rosenfeld, 2001: Aerosols, climate, and the hydrological cycle, *Science*, **294**, pp. 2119–2124.

[6] Zhang, J., S. A. Christopher, L. A. Remer, and Y. J. Kaufman, 2005: Shortwave aerosol radiative forcing over cloud-free oceans from Terra: Seasonal and global distributions, *J. Geophys. Res.*, **110**, D10S24.

[7] Patadia F., P. Gupta, S. A. Christopher, 2008: First observational estimates of global clear sky shortwave aerosol direct radiative effect over land, *Geophys. Res. Lett.*, **35**, pp. 5.

[8] Geron, C., 2009: Carbonaceous aerosol over a pinus taeda forest in central North Carolina, USA, *Atmos. Environ.*, **43**, pp. 659-969.

[9] Loeb, N. G., and N. Manalo-Smith, 2005: Top-of-atmosphere direct radiativeeffect of aerosols over global oceans from merged CERES and MODIS observations, *J. Clim.*, **18**, pp. 3506– 3526.

[10] Dal Maso M., M. Kulmala, K.E.J. Lehtinen, J.M. Makela, P. Aalto, and C.D. O'Dowd, 2002: Condensation and coagulation sinks and formation of nucleation mode particles in coastal and boreal forest boundary layers, *J. Geophys. Res.*, **107**.

[11] Boy, M., Karl, T., Turnipseed, A., Mauldin, R. L., Kosciuch, E., Greenberg, J., Rathbone, J., Smith, J., Held, A., Barsanti, K., Wehner, B., Bauer, S., Wiedensohler, A., Bonn, B., Kulmala, M., and Guenther, A.: New particle formation in the front range of the Colorado Rocky Mountains, Atmos. Chem. Phys. Discuss., 7, 15581-15617, 2008b.

[12] Pryor S.C., A.M. Spaulding, R.J. Barthelmie, 2010: New particle formation in the Midwestern USA: Event characteristics, meteorological context and vertical profiles, *Atmos. Environ.*, **44**, pp, 4413-4425.

[13] O'Halloran, T.L., J.D. Fuentes, D.R. Collins, M.J. Cleveland, and W.C. Keene, 2009: Influence of air mass source region on nanoparticle events and hygroscopicity in central Virginia, U.S., *Atmos. Environ.*, **43**, pp. 3586–3595.

[14] Stanier, C.O., A.Y. Khlystov, S.N. Pandis, 2004b: Nucleation events during the Pittsburgh Air Quality Study: description and relation to key meteorological, gas phase, and aerosol parameters, *Aerosol Sci. and Tech.*, **38**, pp. 253–264.

[15] Ackerman S.A., H. Chung, 1992: Radiative effects of airborne dust on regional energy budgets at the top of the atmosphere, *J. Appl. Meteor.,* **31**, pp. 223-233.

[16] Nair, V.S., S.Suresh Babu, S. K. Satheesh and K. K. Moorthy, 2008: Effects of sea surface winds on marine aerosols characteristics and impacts on longwave radiative forcing over the Arabian Sea, *Atmos. Chem. Phys.-D*, **8**, pp. 15855-15899

ACKNOWLEDGMENTS

The authors would like to acknowledge that the Duke Forest meteorology data was obtained from Brookhaven National Laboratory under the U.S. Department of Energy Contract No. DE-AC02-98CH10886. This research was supported in part by the Office of Science (BER), U.S. Department of Energy, Grant No. DE-FG02-95ER62083. CERES SSF data was obtained from the Atmospheric Science Data Center at the NASA Langley Research Center.

LIDAR OBSERVATIONS OF FINE-SCALE GRAVITY WAVES IN THE NOCTURNAL BOUNDARY LAYER ABOVE AN ORCHARD CANOPY

Shane D. Mayor[1], **Elizabeth R. Jachens**[2], **Tyson N. Randall**[3]

[1]*Department of Physics, California State University Chico, sdmayor@csuchico.edu*
[2]*Department of Civil Engineering, California State University Chico, ejachens@mail.csuchico.edu*
[3]*Department of Geosciences, California State University Chico, trandall4@mail.csuchico.edu*

ABSTRACT

Fifty-two episodes of micrometeorological gravity wave activity were identified in data collected with the Raman-shifted Eye-safe Aerosol Lidar (REAL) near Dixon, California, during a nearly continuous 3-month period of observation. The internal waves, with wavelengths ranging from 40 m to 100 m, appear in horizontal cross-sectional elastic backscatter images of the atmospheric roughness sublayer between 10 m and 30 m AGL. All of the episodes occur at night when the atmosphere tends toward stability. Time-series data from in situ sensors mounted to a tower that intersected the lidar scans at 1.6 km range reveal oscillations in all three wind velocity components and in some cases the temperature and relative humidity traces. We hypothesize that the lidar can reveal these waves because of the existence of vertical gradients of aerosol backscatter and the oscillating vertical component of air motion in the wave train that displace the backscatter gradients vertically.

1. INTRODUCTION

The atmospheric boundary layer (ABL) is that part of the troposphere that is directly influenced by the presence of the earth's surface, and responds to surface forcings with a timescale of about an hour or less [1]. During the daytime and over land, the ABL is usually hundreds of meters to a kilometer or more in depth and is characterized by large eddies that mix heat, moisture, trace gases, pollutants, and momentum very effectively in both the horizontal and vertical dimensions. At night, radiant energy from the sun is no longer available to warm the surface and drive convective thermals. As a result, the nocturnal ABL tends towards static stability supporting stratification, vertical wind shear, gravity wave activity, and intermittent turbulence confined to shallow layers. This complex nocturnal flow regime presents significant observational and modeling challenges. In this paper, we report on new atmospheric lidar observations of what appear to be fine-scale waves within 20 m of the top of an orchard canopy.

Observations in the form of time-series and limited amounts of spatial sampling from previous studies have revealed wave-like oscillations at night in this shallow region above forest canopies [2 - 8]. However, we could find no papers on lidar observations of canopy waves. This may be due to the difficulty of observing the waves in the very shallow layer immediately above tree tops. Herein we report on our preliminary investigations of what appear to be "canopy waves" observed with the Raman-shifted Eye-safe Aerosol Lidar (REAL) [9] during the 2007 Canopy Horizontal Array Turbulence Study (CHATS) [10]. The REAL is a ground-based elastic backscatter lidar operating at a wavelength of 1.54 microns.

2. EXPERIMENTAL SETUP

CHATS took place in Dixon, California, from mid-March through early-June of 2007. The main part of the experiment was a horizontal array of sonic anemometers located approximately 100 m south of a 30 m tall vertical instrumented tower in a walnut orchard. The REAL was located 1.61 km directly north of the tower (see Fig. 1) and scanned at a sufficiently low elevation angle as to intersect the vertical tower at about 18 – 20 m AGL (see Fig. 2). "Wide scans" covered 60-degrees of azimuth and "narrow scans" 10-degrees of azimuth. The update rate for scan images depended on the azimuthal range and scan rate and ranged between 10 s and 40 s per scan.

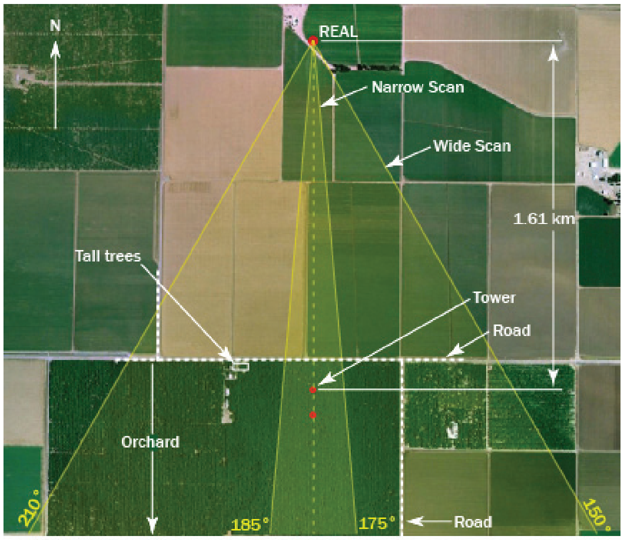

Figure 1. Plan view of the experimental area for the 2007 CHATS. The REAL was located 1.61 km directly north of the 30-m tall NCAR ISFF tower.

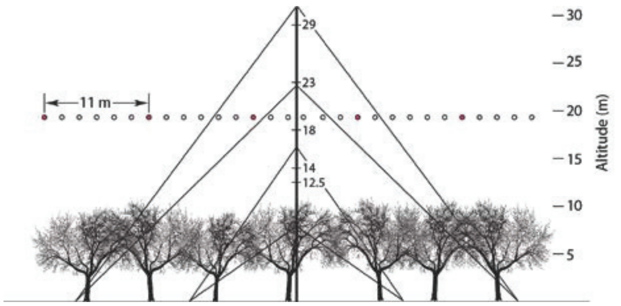

Figure 2. Side view of NCAR ISFF tower at CHATS and the approximate altitude, size, and spacing of laser pulses from the REAL (horizontal row of circles.) when looking north (or south). The circles filled in red show the east-west spacing of the laser pulses (11 m) at the range of the tower based on a 10 Hz pulse rate and 4 degrees per second azimuthal scan rate.

3. HYPOTHESIS

The first question that we wish to address is “Why is the REAL capable of detecting canopy waves?” We hypothesize that during the evening and night, as the earth’s surface cools and the atmospheric surface layer tends toward stability, the lower atmosphere becomes stratified with layers that are horizontally homogeneous in terms of temperature, relative humidity, and aerosol However, the variation in these properties may change significantly with height. (See Fig. 3.) These aerosol “strata” may then be displaced vertically as internal gravity waves form. (Fig. 4.) The horizontally scanning lidar beam may then penetrate and reveal the waves as shown in Fig. 5.

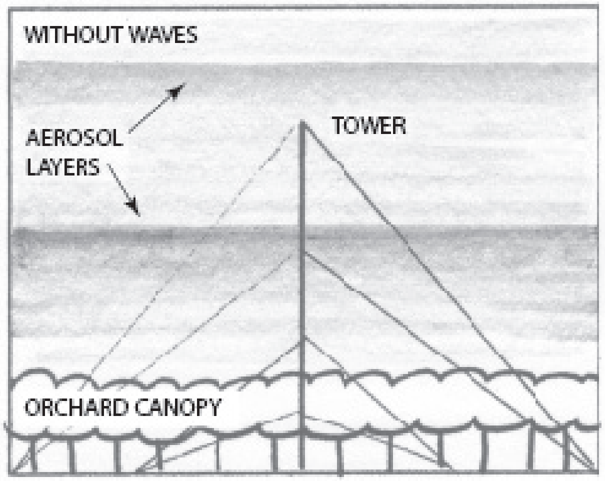

Figure 3: Sketch of a vertical cross-section of the lower atmosphere (from the surface to about 40 m AGL) that may occur at night during quiescent conditions. Stable stratification and weak flow result in the formation of vertical gradients of aerosol backscatter that are horizontally invariant.

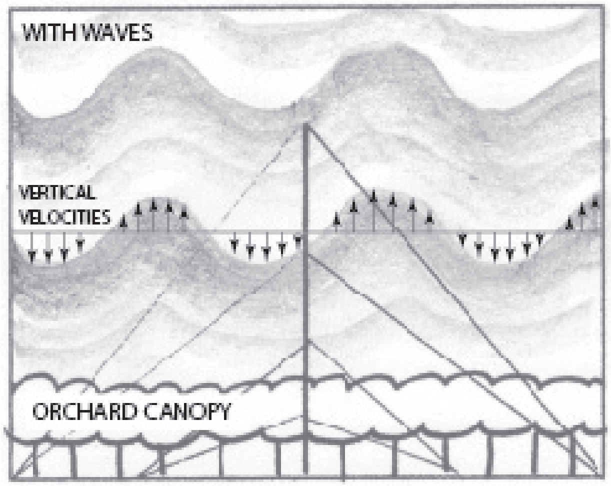

Figure 4: Sketch of a vertical cross-section of the lower atmosphere showing how the vertical wind component *w* caused by internal gravity waves (as observed in the bottom traces in Fig. 6 and all levels in Fig. 7) can vertically displace the horizontal aerosol strata shown in Fig. 3 and enable the elastic backscatter lidar to observe the wave structure in a near-horizontal plane as shown in Fig. 5. The horizontal line above is the approx. altitude of the horizontal lidar scans in Fig. 5.

4. OBSERVATIONS

Time-lapse animations of more than 1800 hours of high-pass filtered REAL images from the entire CHATS data set were created. The animations of nearly-horizontal scans were carefully examined for the presence of fine-scale wave packets. A wave packet is distinct from other flow features observed in the lidar images in that the linear bands of enhanced backscatter intensity tend to be oriented perpendicular to the wind direction and the direction in which they propagate. Furthermore, they appear to have a high degree of spatial and temporal coherence compared to plumes and wind parallel streaks sometimes observed during periods of turbulent flow. For a wave packet to be included in this study, it must have passed through the tower (located 1.6 km directly south of the lidar) and have a lifetime longer than one minute. Our subjective judgments of the coherence of the wave packets were based on the clear identification of crests and troughs and movement together as a group. Fifty-two wave episodes met the criteria. All cases had one thing in common: none of the wave packets were present during daylight hours. All cases existed between 5:00 and 14:00 UTC, which corresponds to 20 PST to 6 PST. During data collection, the average time of sunset was at 19:44 PST and sunrise at 6:09 PST. On the next page we present just one of the 52 cases.

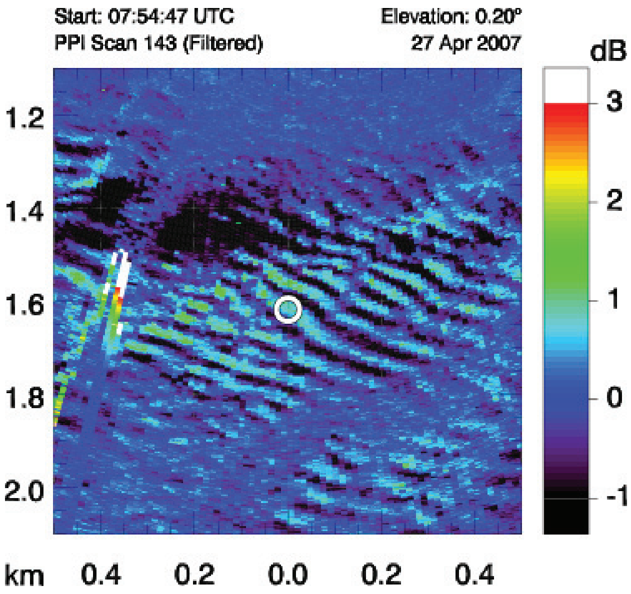

Figure 5: 1 km^2 section of a single, nearly-horizontal, lidar scan through gravity waves on 27 April 2007 at 7:54 UTC. The white circle at the center is the location of the tower. The bright marks on the left side are the result of a grove of trees that stood higher than the orchard trees. Color represents backscatter intensity. The canopy wave wavelength above is about 70 m.

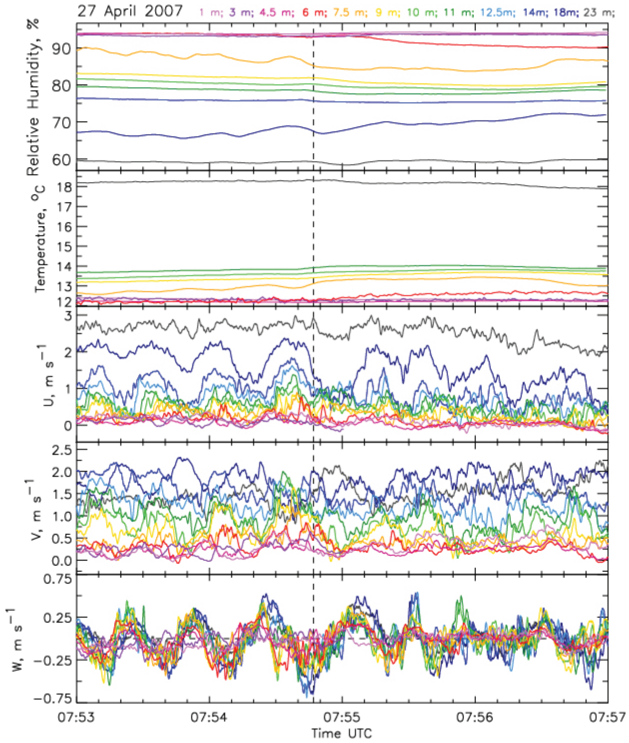

Figure 6. Four minutes of relative humidity, temperature, and three wind components (*u*, *v*, and *w*) from 12 altitudes on the tower for 27 April 2007 between 7:53 and 7:57 UTC. The wave period is approx. 30 s. The vertical dashed line is placed at the time corresponding to the image in Fig. 5.

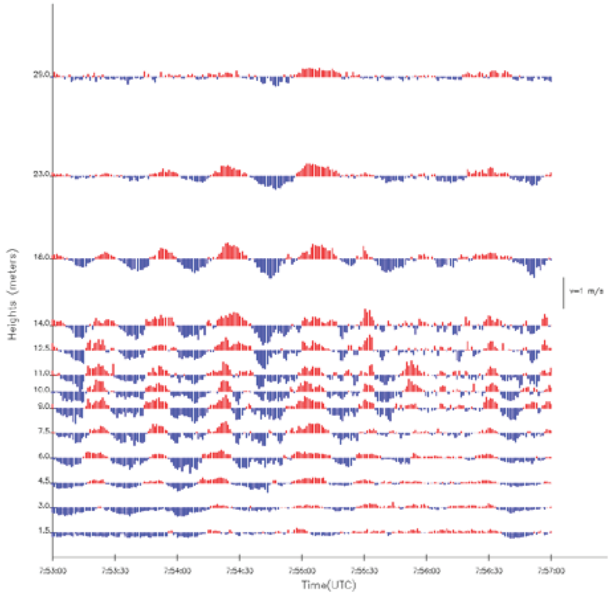

Figure 7: Vertical velocity *w* from tower-mounted sonic anemometers as a function of time and height for 27 April 2007 between 7:53 and 7:57 UTC. Upward air motion is colored red and downward air motion is blue. The plot suggests the waves have a strong vertical coherence and do not tilt appreciably within this span of altitudes.

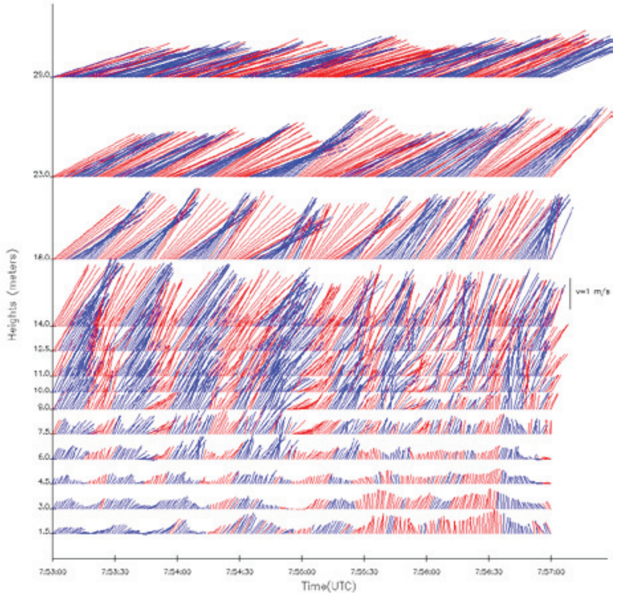

Figure 8: Horizontal wind vectors (resulting from *u* and *v* components) from tower-mounted sonic anemometers as a function of time and height for 27 April 2007 between 7:53 and 7:57 UTC. The vectors are colored according to the direction of *w* as in Fig. 7. The plot reveals oscillations in speed and direction as well as vertical shear in the mean speed and direction.

5. DISCUSSION

The lidar can provide the wavelength of the waves. When the lidar scan "frame rate" is fast enough it can also provide a direct measurement of the wave phase speed. However, for the wide scans the frame rate is a little too slow. In that case however, the phase speed can be computed by taking the wavelength and dividing by the period of the oscillations as obtained from in situ measurements. For the 27 April 2007 case presented, the lidar data reveal a wavelength of about 70 m and the tower data reveal a period of about 30 s resulting in a wave phase speed of about 2.3 m s^{-1}. This is approximately the same speed as the wind speed at the 18 and 23 m altitudes. Additional cases in the CHATS data set were observed with narrow scans and faster frame rates thereby enabling direct measurement of the phase speed.

6. CONCLUSIONS

The horizontally scanning eye-safe elastic backscatter lidar can identify and confirm the presence of fine-scale gravity waves over forest canopies. The lidar images contain quantitative spatial information such as wavelength that is not available from in situ time-series data. Key requirements for such lidar measurements is eye-safety, horizontal scanning, high spatial resolution images and sensitivity to small changes in aerosol backscatter. Radial high-pass median filtering is used to clarify the presence of the waves in the images. We note the spacing of backscatter data points in the radial direction of the REAL data is 1.5 m. This enables the instrument to resolve these wave structures that occur on scales of tens of meters.

ACKNOWLEDGMENTS

This work was supported by NSF AGS 0924407.

REFERENCES

1. Stull, R. B. An Introduction to Boundary Layer Meteorology. Kluwer Academic Publishers, Dordrecht, The Netherlands, 1988.

2. Cava, D., U. Giostra, M. Siqueira, and G. Katul, 2004: Organised Motion and Radiative Perturbations in the Nocturnal Canopy Sublayer Above an Even-Aged Pine Forest, *Boundary-Layer Meteorol.*, **112**, 129-157.

3. Van Gorsel, E., I. N. Harman, J. J. Finnigan, and R. Leuning, 2011: Decoupling of Air Flow Above and in Plant Canopies and Gravity Waves Affect Micrometeorological Estimates of Net Scalar Exchange, *Agr. Forest Meteorol.*, **151**, 927-933.

4. Lee, X., 1997: Gravity Waves in a Forest: A Linear Analysis, *J. Atmos. Sci.*, **54**, 2574-2585.

5. Lee, X., 1997: Gravity Waves in a Forest: A Linear Analysis, *J. Atmos. Sci.*, **54**, 2574-2585.

6. Fitzjarrald, D. R. and K. E. Moore, 1990: Mechanisms of Nocturnal Exchange between the Rain Forest and the Atmosphere, *J. Geophys. Res.*, **95(D10)**, 16,839-16,850.

7. Lee, X., and A. G. Barr, 1998: Climatology of GravityWaves in a Forest, *Q. J. Roy. Meteorol. Soc.*, **124**, 1403-1419.

8. Bergström, H. and U. Högström, 1989: Turbulent exchange above a Pine Forest. 2. Organized Structures, *Boundary-Layer Meteorol.*, **49**, 231-263.

9. Mayor, S. D., S. M. Spuler, B. M. Morley, and E. Loew, 2012: Polarization lidar at 1.54-microns and observations of plumes from aerosol generators, *Opt. Eng.*, **46**, DOI: 10.1117/12.781902.

10. Patton E. G., et al., 2011: The Canopy Horizontal Array Turbulence Study (CHATS), *Bull. Amer., Meteor. Soc.*, **92**, 593-611.

ANALYSIS OF PHYSICAL FACTORS FORMING THE RECEIVED SIGNAL AT SODAR SOUNDING OF ABL

Alexander Panchenko[1], **Nikolai Slipchenko**[1], **Liu Chang** [2]

[1]*Kharkov National University of Radioelectronics, Ukraine, panchenko-a-yu@yandex.ru*
[2] *Heilongjiang Bayi Agricultural University, China, sumalagu@gmail.com*

ABSTRACT

The approximations traditionally used in the ABL modern theories exclude a number of factors from consideration. Among these, for example, there is a turbulent flow incompressibility assumption.

The established practice of sodars design also has a number of settled propositions, requiring analysis.

Results of the theoretical research on the sodar's antennas optimizations, taking into account properties of the reflecting volume, on the analysis of physical mechanisms of Doppler frequency shift and the reflected signal intensity under conditions of the developed turbulence and the stable state of ABL, are generalized.

1. INTRODUCTION

At present the acoustic sounding gives the image of the local meteorological condition, but it does not make it possible to present its details and single out the main meteorological parameters. Basically, it is associated with the lack of an adequate mathematical description both of the atmospheric boundary layer (ABL) dynamics and conditions of a sound scattering in it [1]. Despite a long period of research on this subject and considerable efforts of many prominent scientists, the complexity of the processes prohibits them to give sufficiently rigorous description to the present days.

The approximations traditionally used in the ABL modern theories exclude a number of factors [2] from consideration. Among these, for example, there is a turbulent flow incompressibility assumption. The established practice of sodars design also has a number of settled propositions, requiring analysis and, in some cases, even a significant finishing.

Thus, there are problems which should be solved to rise efficiency of the sodars and systems of sounding based on them. To do this it is required to single out step-by-step the most significant obstacles limiting obtaining of a useful information. A number of such obstacles are shown in [3-5]. Their complex analysis is needed to develop the propositions on the further modification.

2. ESTIMATION OF THE MODERN CONCEPTS OF THE NFORMATION COMPONENTS OF THE ABL AS SIGNAL

Several states of the ABL significantly dissimilar can be singled out on the basis of long-standing experience of carrying out the meteorological measurements using a complex of meteorological sensors, placed near the ground and meteorological mast (50m), a system for radio acoustic sounding and acoustic radar as well as analysis of the data cited in the modern literature.

At present the most perfect models are created for dynamic turbulence [2].But when designing sodars the results of previous work in this field are not considered completely. This, in particular, relates to the choice of the radiation pattern (RP) width of the acoustic antennas.

2.1 Choice of the sodar antenna radiation pattern width

In [3] the estimate of the RP width necessary for sounding at a period of the developed dynamic turbulence was substantiated on the strength of the known statements of the antenna theory and wave optics. When analyzing the similarity theory was used. Estimation of the structural function of the random field of the turbulent pulsing of wind velocity makes it possible to derive a relation between the vortexes dimensions at the height variation. The minimal dimension of the turbulent vortex immediately near the surface is estimated in accordance with Reynolds theory.

On the other hand, particularities of information obtaining at the stable ABL sounding were taken into account. The possibility to separate information at interaction of spherical acoustic waves with the plane temperature-inhomogeneous layers was considered.

On the basis of simple geometrical relations for an effective estimation of the spatial and energy characteristics turbulence, fluctuations of parameters of the air mass one can derive dependence of the optimal RP width on the assumed height of sounding (Fig.1).

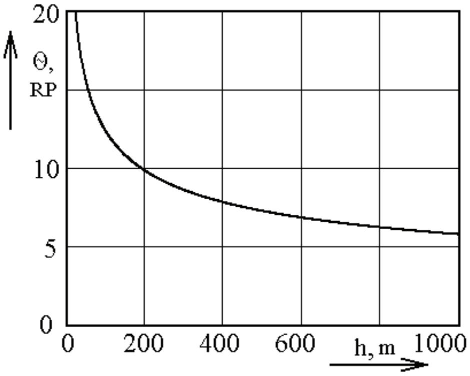

Figure 1. Estimation of the sodar RP needed width.

2.2 About accounting of the reflecting volume dimensions action

Formation of the return signal remains no less important. Either statistical representation of the reflector is used or the problem in one dimension is solved.

The reflecting volume has significant dimensions increasing at drift from the sodar that is why the receiver is in the Fresnel zone, and in some cases even in the near zone of such a reflector. Wave properties of the field in this case have a definite value. The analysis is complicated by the statistical nature of the reflector. That is why it is necessary to use previous results obtained earlier in deals with the Fresnel the statistical theory, particularly in that part of it, which deals with the Fresnel zone. But this theory is sufficiently complicated by itself, its application to the given problems requires much efforts. But this work is necessary. The known problems on estimation of parameters of the reflected waves in the turbulent atmosphere are formulated under conditions of the specified turbulence [2]. Immediate conversion of their results will be incorrect, as initially a lot of simplifications and heuristic assumptions have been done

2.3 Formation of the received signal frequency Doppler shift

The most successful sodar methods are used to measure wind velocity. But the complexity of the measurements object requires further work on perfection of methods and technical means in this field as well.

At present wind measuring sodars are created according to the three-component scheme. Doppler shift of the received signal frequency f_D is used as a primary information. Firstly, in this case the initial value of f_D has the fluctuation component Δf_D. Estimation of the value Δf_D assumes a particular significance. Secondly, the velocity vector components vary in the points where the correlation is close to the minimal one. These factors result in a considerable dispersion of the calculated value of the mean velocity. The analysis of physical factors of the signal f_D Doppler shift formation, particularly of its fluctuation component, is shown in [4].

The emergence of f_D in transverse waves is defined at once by the reflector movement. Mechanism of f_D emergence is much more complicated in the longitudinal waves whose field moves together with the medium. The total velocity of the acoustic waves includes movement velocity of the medium which is mobile and fills all possible space (Fig.2). At movement of the hard boundary the medium moves together with an obstacle and movement velocity of the medium $\vec{V}$ near the obstacle boundary is equal to its movement velocity $\vec{V}_0$.

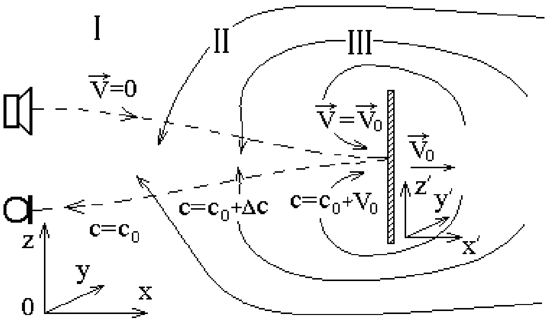

Figure 2. Scheme of waves and medium movement at the reflector movement.

This results in that the boundary conditions for acoustic waves can't include the material boundary movement. The sound velocity in the first region (I) c_0 in the immobile coordinate system x, y, z depends on the scalar parameters of the medium. Just near the obstacle (region III) the sound velocity in the system of coordinates x', y', z', moving together with it, is also equal to c_0. It is equal to $c = c_0 + V_0$ relative to the immobile system. Velocity Δc variation takes place in the region II due to the traverse influx and removal of the medium. Thus, the problem of defining of Δf_D fluctuations should be solved in the system of three dimensions or with the simplification of the problem in two dimensions and should take into account the trial turbulence.

2.4 Dynamic component of the reflection coefficient in the turbulent ABL

The next information parameter is the return signal amplitude. Generally the amplitude values field is built in the height-time coordinates. The processes taking place in ABL are judged by the form of the field. Such usage of this information can't be considered as a complete one. The reflection coefficient module is the information parameter for any radar systems but not always its physical origin is interpreted adequately. The qualitative relations require even more modification

When developing methods for separation of the information from the AS signals the notion of the sound reflection, mainly from the temperature nonhomogeneities, prevails. Such approach describes well the case of temperature inversions or thermal turbulence. The models of backward reflection for dynamic turbulence are developed rather weakly and sometimes they are even negated. Nevertheless, random motion of the continuous medium is possible only with the availability of random field of forces resulting in the local variations of velocity. If there are no external nonhomogeneous force fields then such field of forces can be stipulated only by a random pressure field. It is demonstrated in [5] by the digital example that with fluctuations of the flow velocity, inherent to the turbulent ABL, the pressure and density drop attendant to them will result in emergence of the return audio signal the level of which is comparable with the signal reflected from the temperature nonhomogeneities. But it should be taken into account that the range of the meteorological values fluctuations in ABL - wind velocity, aqueous vapor content, temperature and pressure pulsations – can be of several orders. That is why the relation of their contribution also changes in a wide range of values when forming the signal being received.

3. CONCLUSIONS

The presented results of the analysis show that the complex of methods adapted to different states of ABL should be created. It will require creation of several types of antenna systems and sodar receiving-transmitting paths optimized for different conditions and solution of different problems. Complexity of physical processes stipulates the necessity of thorough separation of the process of information extraction breaking into a number of stages.

It is necessary to include measurement of parameters which do not receive proper attention at present in particular such an important parameter as humidity into the circle of the prospective problems. The fundamental possibility to solve this problem is defined by sufficient distinctions between conditions of a sound propagation in a dry and humid air.

As a whole it is possible to consider that the development of the ABL dynamics theoretical foundations, methods for acoustic signals analysis and progress of technical means of sounding will make it possible to increase significantly the volume of information received by the acoustic sounding systems.

ACKNOWLEDGMENTS

We would like to express our gratitude to Mr. Ulianov Yu.N. for help in preparation of this manuscript.

REFERENCES

1. N.P. Krasnenko, *Acoustic sounding of atmosphere boundary layer,* Tomsk Publishing house SD RAS, 2001. (in Russian)

2. A.S. Monin, A.M. Yaglom, *Statistical hydromechanics,* vol.1, Moscow Science, 1965. (in Russian)

3. Panchenko A. Yu., V. Maryukh, 2009. Action of the wave properties of the directed acoustic beam sodars when forming the reflected waves field in ABL, *Systems for navigation and communications,* **4(12**), pp. 42-46. (in Russian)

4. Panchenko A.Yu., 2010. Analysis of physical factors forming parameters of the return signal at acoustic sounding of the atmospheric boundary layer *Radiotechnika: All-Ukr. Sci. Interdep. Mag.* N**160**. pp. 184-188. (in Russian)

5. Panchenko A.Yu., 2011. On estimation of acoustic waves intensity in ABL in absence of the heat sources on the surface *Radiotechnika: All-Ukr. Sci. Interdep. Mag.* N**164**. pp. 53-57. (in Russian)

A TURBULENT BUBBLE MODEL FOR ACOUSTIC SCATTERING

Stuart Bradley[1]

[1]*Physics Department, University of Auckland, Private Bag 92019, Auckland, New Zealand,*
s.bradley@auckland.ac.nz

ABSTRACT

We describe a new model of turbulent scattering of sound, based on Rayleigh scattering from small turbulent cells. The acoustic refractive index, arising from both temperature and velocity fluctuations, varies from cell-to-cell so as to give, to any arbitrary accuracy, agreement with theoretical spatial coherence or turbulent spectra. The scattering of sound is the sum of the Rayleigh scatter from all turbulent bubbles, and is shown to agree, without numerical artifacts, with the expected theoretical treatment for scattering of continuous monotonic sound from a large volume. Having demonstrated that the turbulent scattering model matches expectations for both turbulence and scattering, we then concentrate on finite volumes. The motivation is two-fold. We are interested in how much sodar 'noise' originates from the limitation of a finite volume in each range gate, and secondly we are moving toward step-chirp designs comprising many small sub-pulse of sound. The change in the scattering pattern with decreasing scattering volume is explored. The model also allows estimation of the variance of the scattering strength, and the variance of Doppler velocity estimation, which a attributable to a finite scattering volume. The implications for sodar design, and the interpretation of sodar correlations with other instrumentation, are discussed.

1. MOTIVATION AND BACKGROUND

The motivation for this work arises from earlier work on a linear-FM chirped sodar [1] and on a step-chirp sodar [2][3]. Both of these investigations are driven by a search for methods for improving sodar signal-to-noise ratio. Linear-FM (continuously changing frequency during a transmitted pulse) is common in radar systems, but does not work in a straight-forward manner for sodars because of the very much larger Doppler shift/transmitted frequency ratio. A step-chirp approximates linear-FM by transmitting successive discrete frequency pulses to make up the overall transmitted pulse. There remain a number of difficulties and concerns though, including the question of what happens to the turbulent scattering if the scattering volume becomes quite small. Our previous attempts to answer this question are incomplete [4].

The present model arose as a thought experiment. Turbulent scattering, from a volume of dimensions very much larger than a wavelength, is well established both theoretically and experimentally [5][6]. At the other extreme is scattering from a volume of dimensions very much smaller than a wavelength [7]. The scattering pattern and scattering cross section are very different for these two extremes of volume dimensions. Also, large volume scattering, so called Bragg scatter, is known to be extremely selective of the turbulent refractive index scales contributing to the scattering. Is this also true in the small volume (Rayleigh scatter) case? If so, then do problems arise with multi-frequency sodar designs because of scattering from scattering elements of different size?

A typical sodar pulse duration is τ = 50 ms. If this is divided into, say, 20 discreet frequency steps, then each step is of duration 2.5 ms and the relevant vertical extent in the atmosphere is 0.4 m. At a frequency of 4 kHz this corresponds to 5 wavelengths. So this example lies very much between the two extreme scattering models. A model is required which will cope with scattering in this regime.

2. SCATTERER FROM SMALL VOLUMES

The scattered acoustic pressure at large range r from a sphere of radius a (which is small compared with a wavelength) is [7]

$$p_s(r,\theta) = p_0 (k_0 a)^2 \left(\frac{e-1}{3e} - \frac{g-1}{2g+1} \cos\theta \right) \frac{a}{r} e^{-ik_0 r} \quad (1)$$

where $k_0 = \omega/c_0$, $g = \rho_1/\rho_0$, $h = c_1/c_0$, and $e = gh^2$, with k_0 the wavenumber in the surrounding air, g the ratio of the density ρ_1 in the sphere to the density ρ_0 in the surroundings, and h the ratio of the sound speed c_1 in the sphere to the sound speed c_0 in the surroundings. The angle between the incident and scatter directions is θ and p_0 is the incident pressure.

For small fluctuations $T' = T_1 - T_0$ in temperature

$$h = \sqrt{\frac{T_1}{T_0}} \approx 1 + \mu \, . \quad (2)$$

Assuming adiabatic processes

$$g = \left(\frac{T_1}{T_0} \right)^{\frac{1}{1-\gamma}} \approx 1 + \frac{T'}{(1-\gamma)T_0} = 1 + \frac{\mu}{1-\gamma} \quad (3)$$

where γ =1.4 is the ratio of specific heats for air. This gives

$$\frac{p_s(r,\theta)}{p_0} \approx \frac{7\mu}{4\pi}\frac{k_0^2 V}{r}\left(1-\frac{5}{7}\cos\theta\right)e^{-ik_0 r} \tag{4}$$

where V is the volume of the scatterer. In this Rayleigh limit, the scattered amplitude in (4) is proportional to volume, and to the square of frequency. For Bragg scatter, the *amplitude* dependence is on frequency to the power of 1/6. Fig. 1 shows the two scattering patterns, which are in fact very similar.

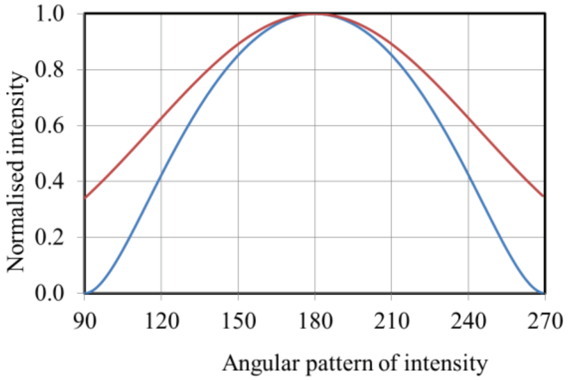

Figure 1. Angular scattering pattern for intensity in the backward direction for Rayleigh (red) and Bragg (blue) scattering.

The biggest difference in scattering pattern is that, for Bragg scatter, the intensity goes to zero at ±90°.

3. MODELLING LARGER VOLUMES

Rayleigh scattering amplitudes are proportional to volume V and, to first order, are independent of the volume shape. To model scattering form multiple small volumes, we set up a grid with cells of sides d and cell volume $V = d^3$. Two such volumes combined have a volume $2V$ and the amplitude of scattering is simply twice that from a single volume. So the scattering pattern is not at all specific on d as long as d is much smaller than a wavelength λ ($d < 0.1\lambda$ is a useful guide). Beyond that limit, phase effects begin to be important. For example, a long line of small volumes extending perpendicular to the sound propagation direction will produce scattered sound of many phase angles when summed at some distant receiver placed at 90°. This will lead to an intensity of zero at 90°, in keeping with the Bragg predictions.

In order to model turbulent temperature fluctuations, we must assign temperatures T_1 to cells. This requires a turbulence model. Finally, the scattered pressure at some point is the sum of all the individual scattered pressures, allowing for direction and phase. The advantage of this new approach that the scattering pattern is already established for the small turbulent patches, without needing to solve a more general wave equation.

4. RANDOM TURBULENT FIELD

Our model is an application of that in [8]. For temperature fluctuations T' about mean temperature T_0, the refractive index is

$$n = \frac{c_0}{c} \approx 1-\mu \tag{5}$$

where

$$\mu = \frac{T'}{2T_0}. \tag{6}$$

The correlation function for refractive index fluctuations is the time average

$$B(\underline{r}) = \overline{\mu(\underline{s}+\underline{r})\mu(\underline{s})} \tag{7}$$

and the three-dimensional spectral density is

$$\Phi(\underline{k}) = \frac{1}{(2\pi)^3}\int_{-\infty}^{\infty}\int_{-\infty}^{\infty}\int_{-\infty}^{\infty} e^{-i\underline{k}\bullet\underline{r}} B(\underline{r})d\underline{r}. \tag{8}$$

For a von Karman spectrum and wind flow in the +x direction

$$B(x,y,z) = \frac{\Gamma\left(\frac{1}{3}\right)(K_0 r)^{1/3}}{\pi 2^{2/3} K_0^{2/3}\sqrt{3}}\left[K_{1/3}(K_0 r)\frac{C_T^2}{4T_0^2} + \left\{K_{1/3}(K_0 r) - \frac{K_0\left(y^2+z^2\right)}{2r}K_{2/3}(K_0 r)\right\}\frac{C_v^2}{c_0^2}\right] \tag{9}$$

and

$$\Phi(k_x,k_y,k_z) = \frac{5}{18\pi\Gamma\left(\frac{1}{3}\right)\left(k^2+K_0^2\right)^{11/6}}\left[\frac{C_T^2}{4T_0^2} + \frac{11}{6}\frac{k^2}{k^2+K_0^2}\left(1-\frac{k_x^2}{k^2}\right)\frac{C_v^2}{c_0^2}\right] \tag{10}$$

where $K_0 = 2\pi/L$ and L is the outer scale of turbulence. The normalised structure parameter C_T^2/T_0^2 is generally in the range 2x10^{-10} to 6x10^{-7} $\mathrm{m}^{-2/3}$ and C_v^2/c_0^2 is generally in the range 1x10^{-9} to 2x10^{-6} $\mathrm{m}^{-2/3}$. $K_{1/3}$ is the modified Bessel function of the second kind of order 1/3.

A random μ value at position $\underline{r}$ can be found using

$$\mu(\underline{r}) = \sqrt{8\pi\Delta k}\sum_{n=1}^{N}\cos\left(\underline{k}_n \bullet \underline{r} + \alpha_n\right)\sqrt{\Phi\left(\underline{k}_n\right)k_n^2} \qquad (11)$$

where $\underline{k}_n = n\Delta k(\sin\theta\cos\phi,\ \sin\theta\sin\phi,\ \cos\theta)$, and α_n is a random angle uniformly distributed in 0 to 2π [8]. The angles θ and ϕ give the propagation direction.

Given a turbulent intensity represented by a value for C_T^2 / T_0^2, the three random numbers (θ, ϕ, α_n) allow a value to be found for the n^{th} term in the summation. Acoustic wavelength is typically around 75 mm, and spatial scales down to 1/10th of this should be resolved, so the maximum k value should be at least 800 m^{-1}. So choosing $\Delta k = 1\ \text{m}^{-1}$ and $N = 1000$ is reasonable. Fig. 2 shows a numerical simulation of a von Karman spatial correlation function for refractive index compared with the analytic solution. Here we have used a single line of refractive index elements, with $C_T^2 / T_0^2 = 10^{-7}\ \text{m}^{-2/3}$ and $K_0 = 0.1\ \text{m}^{-1}$.

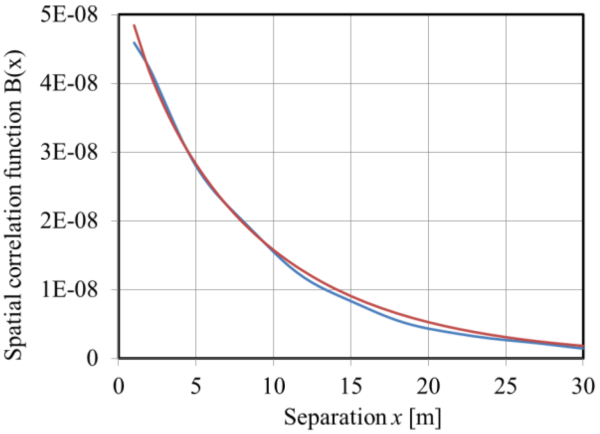

Figure 2. Comparison between modeled spatial correlation function (blue) and theoretical correlation function (red).

5. NEXT STEPS AND CONCLUSIONS

The above lays the ground-work for the model. We have validated the scattering model and the turbulence model. Now the two need to be merged. The geometry is that typical of a sodar with a cylindrical scattering volume where the radius is determined by beam width and height, and the depth is determined by the transmitted pulse length. The only new step is accounting for phase, which is very straight forward since it only depends on the scattering element position.

At the point of production of the Extended Abstracts this is still a work in progress. In our poster at ISARS we aim to complete the analysis and determine how the scattering cross section, angular pattern, and selectivity vary with cylinder height.

ACKNOWLEDGMENTS

Ellen Barnard helped with the early Matlab coding while the author was inescapably captured by bureaucracy as Head of Department.

REFERENCES

1. Bradley, S. G., Bottcher, F.M., Martin, A. , 2006: Broadband Acoustic Backscatter Response of the Atmosphere, *Proceedings ISARS 2006*, *Garmisch*, *July*, p.2-4.
2. Bradley, S.G., 2009: Atmospheric turbulent scattering of broad-band acoustic signals, *ICSV*, *Krakow*, 5-9 July, 2009 (Proceedings ISBN 978-83-60716-71-7)
3. Bradley, S. G., and S. von Hünerbein, 2008: Pulse coding for a new scanning bistatic acoustic wind profiler, *156th meeting of the Acoustical Society of America*, *Miami*, November 10-14.
4. Bradley, S. G., 1999: Use of coded waveforms for SODAR systems. *Met. and Atm. Phys* **71**, pp15-23.
5. Ostashev, V. E., 1997: *Acoustics in moving inhomogeneous media.* London, E & FN Spon.
6. Turbulent scattering, from a volume of dimensions very much larger than a wavelength, is well established both theoretically and experimentally
7. Bowman, J. J.; Senior, T. B. A.; Uslenghi, P. L. E., 1987: *Electromagnetic and acoustic scattering by simple shapes (Revised edition).* New York, Hemisphere Publishing Corp., pp747 .
8. Salomons, E., 2001: *Computational atmospheric acoustics*. Kluwer, London, 335pp.

Mechanism making it possible to use pulsed acoustic sounding for atmospheric temperature remote measurement

Delov I.A., Cand. Sc. (Technology), Slipchenko N.I. Dr. Sc. (Physics and Mathematics), Kartashov V.M. Dr. Sc. (Technology), Leonivod A.V. Eng.

Kharkov National University of Radio Electronics, E-mail: pnilsabsi@kture.kharkov.ua, Kharkov, Ukraine

INTRODUCTION

The use of the phased method of acoustic sounding for the atmosphere temperature remote measurement provoked a particular interest among the researches from the outset of the acoustic sounding application to the atmosphere parameters remote measurement.

The point is that the phase of the acoustic wave φ is related to the atmosphere temperature T° by rather simple equation [1]. This follows from the expression for the acoustic wave (1) and the expression for the acoustic wave phase (2):

$$A_t = A_m \cos\left(2\pi\Delta t/T - (2\pi/T)\cdot(\Delta h/c)\right), \qquad (1)$$

$$\varphi = 2\pi\Delta t/T - (2\pi/T)\cdot(\Delta h/c), \qquad (2)$$

here $\varphi = 2\pi\Delta t/T - (2\pi/T)\cdot(\Delta h/c)$ - is the acoustic wave phase; A_t - is the wave amplitude at any instant; T - is the sound wave oscillation period; Δt - is the time at the sound wave observation moment; Δh - is the height (distance) at which the sound wave, having passed the way from the radiation source to the height Δh, is observed at the given instance Δt; c - is the sound wave velocity which is related to the atmosphere temperature by the known equation $c = 20\sqrt{T^{\circ}}$.

Thus, we can easily find the value of c from the expression (2) by the measured phase φ of the echo-signal, if we know the time Δt, through which we have received the scattered acoustic echo signal, and the height (distance) Δh, from which we have received this echo-signal and, consequently, the value T°

But if the time, within which we have received the measured sound wave Δt, can be recorded by gating the receiver through the specified (known) time $\Delta t = t_{cmp}$, then the situation is different with the height Δh as at acoustic sounding the height (distance) Δh is not measured. Its value is defined as $\Delta h = \Delta tc$ and varies with variation of c. In this case, as according to (2) the spatial phase is defined as $\varphi = (2\pi/T)\cdot(\Delta h/c)$, then having substituted $\Delta h = t_{cmp}c$ in this expression instead of Δt we will receive $\varphi = (2\pi/T)\cdot(t_{cmp}c/c) = (2\pi/T)t_{cmp} = 2\pi t_{cmp}/T$, i.e. $\varphi = 2\pi t_{cmp}/T$. Here $\varphi = 2\pi t_{cmp}/T$ - is a number of the wave cycles T for the gating time t_{cmp}. As with the specified parameters t_{cmp} and T their values do not change, then, consequently, the spatial phase in this case will not change remaining equal to $\varphi = 2\pi t_{cmp}/T$ with any meaning of the value c, and, hence, the value of the atmosphere temperature T°. But in this case the height Δh varies with variation of the value of c, as the value Δh $\Delta h = t_{cmp}c$ is defined as $\Delta h = t_{cmp}c$, it will be varying in such a way that the wave phase φ will not change with variation of temperature T°.

Thus, any variations of the phase, associated with the acoustic velocity c variation (and, hence, the temperature), will always be compensated for the variation of the phase, associated with the height (distance) variation, and we will never observe the phase variations if we don't record the height.

Considering that with the pulsed sounding all the parts of the pulse change their height (distance) for one and the same value with the change in the sound wave velocity, then with the pulse sounding we will not observe the phase variation with the atmosphere temperature variation.

This conclusion was checked with the air balloon and the acoustic radar [2] and then [3]. The atmosphere temperature and the acoustic echo-signal phase were measured at the same height. But the author of [2, 3] did not find the mechanism making it possible to observe variations in the acoustic echo-signal phase with variation in temperature and made a conclusion that such a mechanism did not exist (though in the course of the experiment [2] a high correlation between the observed acoustic echo-signal phase and the measured temperature of atmosphere a high correlation had been received; the correlation coefficient had been equal to ~ 0,8).

But as a result of long-standing experimental and theoretical investigations we have found out the mechanism at the pulsed monostatic acoustic sounding of atmosphere, which makes it possible to observe variations in the acoustic echo-signal phase with a sufficiently high precision.

This mechanism is associated with existence of two effects at the pulsed acoustic monostatic sounding of atmosphere.

One of them testifies that the acoustic echo-signal, scattered by a whole area of the atmosphere heights, occupied by half of the sounding pulse duration $L = \tau c/2$, arrives simultaneously at the receiving antenna input at each instant. Thus, in this case we measure the echo-signal phase and amplitude, averaged for this whole area of heights, at each instant.

Another effect testifies that with the pulsed acoustic monostatic sounding of the atmosphere at the cost of changing the sound wave length, when the atmosphere temperature changes, variation of the spatial duration of the sounding pulse L takes place. The point is that the value L is related to the wave length λ by the equation $L = \tau c/2 = (\tau\lambda/T)/2$. As the value τ/T is not altered at the specified parameters τ and T, variation of λ will involve the change in duration of the sounding pulse L, and in the side opposite to the sound wave motion.

At the cost of these two effects presence the mechanism is formed, permitting us to watch a change of the acoustic echo-signal phase at variation of the atmosphere temperature and to measure these variations with a sufficiently high accuracy.

The essence of this mechanism is associated with the fact that at the pulse monostatic acoustic sounding at small changes of the atmosphere temperature the sounding pulses height is overlapped, i.e. the major area of not varying (coinciding) heights (A) is saved and there is a rather small area of varying heights (fig. 1), where the layout by height of two sounding pulses having speed $c_1 > c_2$ is represented schematically.

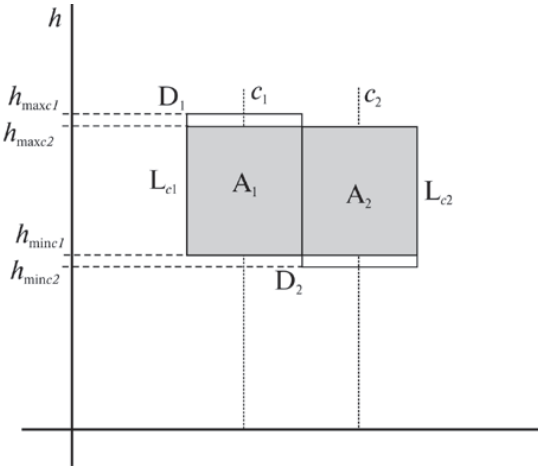

Fig. 1 - Layout by height of two sounding pulses for the identical value (t_{cmp})*, but for two different temperatures of the atmosphere* T_1° *and* T_2°*, so for two different values* c_1 *and* c_2 *(and* $c_1 > c_2$*)*

As the acoustic echo-signal arrives at the receiving antenna input simultaneously from the whole area of heights occupied by a half of the sounding pulse $L = \tau c/2$ duration at the expense of the first effect, we measure simultaneously an average value of the phase for this whole area of heights $L = \tau c/2$, which includes the area of not varying (A) and varying (D) heights. Then, as the area of not varying heights gives us a true value of the phase, associated with the change in the atmosphere temperature (as the average value of height for this area of heights does not vary with change in temperature), and the area of varying (not coinciding) heights, enters into the measured average value of the phase as a systematic error connected with a sounding pulse bias by height for the value $\Delta\Delta h$, corresponding to a difference in phase for waves c_1 and c_2, observed in points $h_{max_{c_1}}$ and $h_{max_{c_2}}$, i.e. the area D enters in this case as the systematic error equal to 100 %,

But as the area of varying heights D is much less than the area of not varying heights A, its specific gravity in the measured average value of the phase φ will be insignificant and, therefore, systematic error $\Delta\%$ at its expense will be insignificant and will be defined as $\Delta\% = 100\%/n$, where $n = (A + D)/D$.

Let's consider this problem in more details.

For this purpose we shall divide the expansion of the sounding pulse L, consisting of the area of coinciding heights A and distinct heights D, into sites, equal to the size of a site of distinct heights D. The number of such sites n will be defined as $n = (A_2 + D_2)/D_2 = A_2/D_2 + 1$.

As the mean value of a phase is measured as

$$\varphi_{cp} = \frac{\sum(\varphi_1 + \varphi_2 + \cdots + \varphi_n)}{n},$$

and the measured value D enters into a mean value as the systematic error $\Delta\%$ equal to $100\%/n$, then the measured mean value of a phase in this case will be overstated for the value of $100\%/n$.

But as on a site of the area D, i.e. on the site of $\Delta\Delta h = h_{max_{c_1}} - h_{max_{c_2}}$ the systematic error $\Delta\%$ varies from 100 % observed at the point $h_{max_{c_1}}$, up to 0 % observed at the point $h_{max_{c_2}}$ (at the point of the coinciding heights), then a mean value of the error $\Delta\%$ for this area can be taken equal to 50 %. But as at matching two measured values of phases φ_1 and φ_2 the phase for lower speed of sound will be underestimated at the expense of a site of distinct heights D_2 for the value of $\Delta = 50\%$, the systematic error $\Delta\%$ in this case for a measured difference in phases φ_1 and φ_2 will be defined as $\Delta\% = (2 \cdot 50\%)/n = (100\%)/n$, where $n = L/D_2$.

The value $L = A_2 + D_2$ is an expansion of a sounding pulse for two compared sound waves having the smaller value of speed $c_2 < c_1$. In this case $L_2 = \tau c_2/2$, as $D_1 = D_2$, then the value D is defined as $D = \Delta\Delta h = h_{max_{c_1}} - h_{max_{c_2}}$.

At the expense of the second effect, associated with the change in the sounding pulse L expansion, as a result of change in the acoustic wavelength λ at variation of the atmosphere temperature, the decrease in one of two (namely, lower one) areas of distinct heights D_2 takes place, this results in the decrease in systematic error $\Delta\%$ in the measurement of relative changes in the temperature of the atmosphere.

As the error $\Delta\%$ considered above is connected with existence of two areas of distinct heights D_1 and D_2, equal in value, then the action of the second effect at the expense of decrease in the lower area of the distinct heights D_2 cannot reduce the systematic error $\Delta\%$ more than by 50 %.

In this case the common systematic error $\Delta\%_{общ}$ will be presented as

$$\Delta\%_{общ} = \Delta\%_{I} - \Delta\%_{II} = \frac{100\%}{n} - \frac{50\%}{t_{cmp}/\tau}. \tag{7}$$

As $n = L_2/D = (\tau c_2/2)/(t_{cmp}\Delta c_{1,2})$, it follows from the expression, that the common systematic error $\Delta\%_{общ}$ decreases at the expense of the first and second mechanisms at the increase in duration of the sounding pulse τ and at the decrease in duration of the strobe t_{cmp}, and also at the decrease in the observable variations of the atmosphere temperature

ΔT° .

Therefore, from the point of view of reaching the minimum systematic error, it is expedient to carry out the sounding with the parameters t_{cmp} and τ close in value.

The carried out calculations of the value $\Delta\%_l$, connected with the first mechanism, for the following parameters of the equipment: $\tau = 0{,}1$ with, $t_{cmp} = 0{,}2$ s and for $L = \frac{1}{2}\tau c_2 = \frac{1}{2}\cdot 0{,}1\cdot 330{,}45 = 16{,}52$ have made 0,036 %; 0,36 %; 0,73 %; 2,62 %; 12,35 % at variation of the observed temperature of the atmosphere for $0{,}1^\circ$; 1°; 2°; 7°; 20°, respectively.

Taking into account the second mechanism this error will be moderated by the value of $\frac{50\%}{n^*} = \frac{50\%}{2} = 25\%$ for each value of ΔT° .

Applying the gating by height to the limiting admissible small sites $\Delta\Delta h$, i.e. for all $t_{cmp} = \tau$ it is possible to watch changes in the atmosphere temperature at any heights accessible at the acoustic sounding.

The method for measuring relative changes of the atmosphere temperature at the monostatic pulse acoustic sounding was developed on the basis of the described mechanism [5] This method was used in the developed acoustic radar applied to the long-term measurements of the atmosphere temperature relative changes carried out at different angles of elevation and azimuth and at different heights [5] with the aim to check the hypothesis about possibility of existence of the molecular processes anisotropy in the Earth's atmosphere (in its boundary layer**)**.

The obtained numerous results of the acoustic echo-signal phase under different weather conditions observed within a year, as well as comparison of the experimental data obtained through the use of the acoustic sounding with the data obtained by other means and at other heights when studying the molecular processes anisotropy phenomenon in the Earth's atmosphere, testify to a high reliability of the information about the changes of the atmosphere temperature obtained with the help of the phase method of the atmosphere pulse acoustic sounding**.**

The errors of a different origin are studied and the ways of their recording are defined.

Fig. 2 and fig. 3 demonstrate the fragments of the acoustic echo-signals phase measurements, obtained in [5] in the process of the echo-signals phase measurements simultaneously in three directions: in the vertical and in two directions, opposite in direction to the azimuth, at an angle of $\alpha = 22^\circ$ from the vertical. The results are obtained for two initial phases of the emitted acoustic package of waves differing by 180° **.**

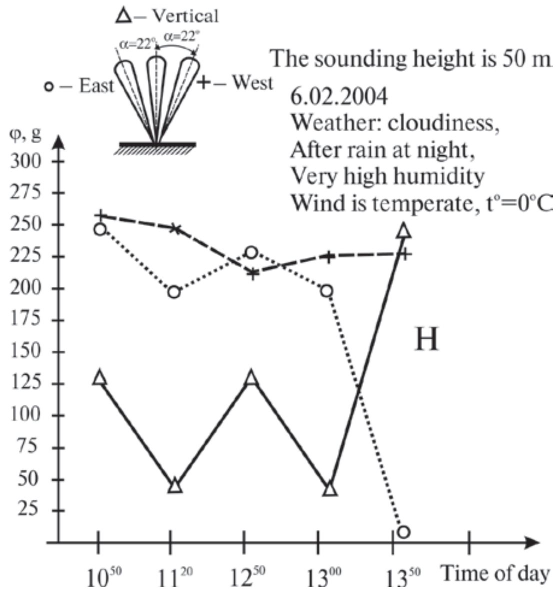

Fig. 2 - Dependence of the acoustic echo-signal phase on time for three angles of sounding: Δ *- for the vertical direction, + - for the western direction at the angle of* $\alpha = 22^\circ$ *,* O *- for the eastern direction at the angle of* $\alpha = 22^\circ$ *the rectified data according to [6], H – the phase of the radiated wave not inverted*

This correspondence between the initial phases was saved in the received echo-signals; this testifies that the phase of the acoustic wave, when passing the path there and back up to the scattering volume of the atmosphere, was not distorted in the given case.

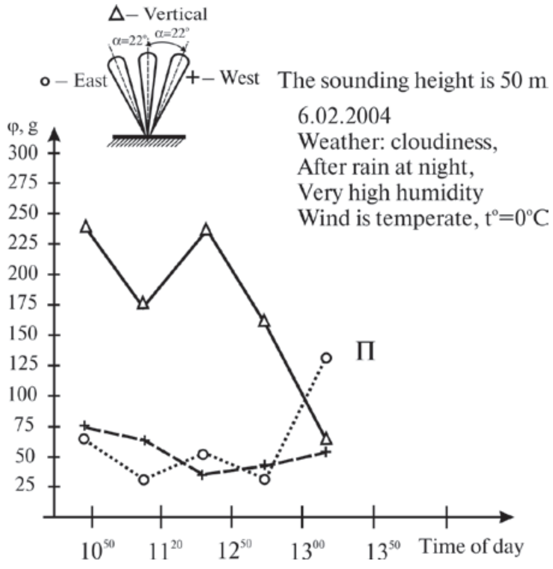

Fig. 3 - Dependence of the acoustic echo-signal phase on time for three angles of sounding: Δ *- for the vertical direction,* $+$ *- for the western direction at the angle of* $\alpha = 22^\circ$ *,* O *- for the eastern direction at the angle of* $\alpha = 22^\circ$ *, П – the initial phase of the radiated wave inverted by* 180° *.*

As the acoustic echo-signal phase φ is connected with a random speed v by the relation $\varphi = 1/v$, then the observed measured phase values close in magnitude for two directions, opposite in direction to the azimuth, testify to close values of molecules random speed, measured for these two directions, and the essential distinction between the measured values of the phase for these two directions at the angle of $\alpha = 22^\circ$ and the phase, measured for the vertical direction, is in the satisfactory consent with the experimental data obtained with other methods and at other heights, which testifies to the possibility of existence of the molecular processes anisotropy phenomenon in the Earth's atmosphere.

CONCLUSION:

The mechanism, considered in the report, creates broad possibilities for development of acoustic radars of a new generation, making it possible to measure the atmosphere temperature remotely with rather hair accuracy; earlier it was considered impossible in principle.

The presented above mechanism can become a new trend in the atmosphere acoustic sounding.

REFERENCES

1. Savekiev I.V. Course of common physics. - M.: Nauka. - 1973. - 511 p. (in Russ.)
2. Surridge A.D. On a phase sensitive acoustic sounder. J. Atmos. Terres. Phys., 49, P.105-110, 1978.
3. Bradley S.G., Hipkin V.J. and Underwood K. The relationship between the phase of a sodar signal and atmospheric temperature // Proc. 10th Intern. Sympos. On Acoustic Remote Sensing and Associated Techniques of the Atmosphere and Oceans Auckland, 2000, New Zealand, P. 13-18.
4. Delov I .A., Slipchenko N. I. Method of remote measurement of relative changes of the air temperature with acoustic sounding of atmosphere. Patent of Ukraine № 76538 A, 15.08.2006. (In Russ.)
5. Delov I .A., Slipchenko N. I. Outcomes of experimental researches into anisotropy of molecular processes of atmosphere with acoustic sounding // Applied radio electronics, 2004, №3. Kharkov. – P. 27-36. (In Ukr.)

PULSE COMPRESSION IN SODAR

Paul Kendrick[1], **Sabine von Hünerbein**[1]

[1]*Acoustics Research Centre, University of Salford, The Crescent, Salford, Greater Manchester, M54WT, UK,*
p.kendrick@salford.ac.uk

ABSTRACT

Pulse compression techniques have been applied to SODAR technology in both, simulations and on an experimental device. The increase in transmission power associated with a longer pulse is expected to extend SODAR range at the same range resolution as a shorter simple pulse. A bank of matched filters is used for correlation with the backscattered signal. It is shown that in principal pulse compression using a stepped chirp signal is successful, however the expected gains in range are not apparent due to a suspected lack of a coherence in the response to a stochastically varying atmosphere. Novel post processing techniques using Gaussian Mixture Modelling (GMM) enable reliable identification and rejection of fixed echoes and noise contributions.

1. INTRODUCTION

In a trade-off between SODAR range and resolution a longer pulse increases transmission power and range and decreases the range resolution. Pulse compression provides an alternative approach to the typical single frequency pulse. By modulating the signal, the transmission bandwidth is decoupled from the transmission length. As the transmitted signal is known a priori, a matched filter can be used which maximizes the signal to noise ratio (SNR) of the scattered sound within the presence of noise. The filter response that achieves this is a time reversed replica of the transmitted pulse. Pulse compression refers to the use of a waveform designed with excess bandwidth together with a matched filter specifically designed to 'compress' the returned signal into a shorter time. The greater the bandwidth of the transmitted signal the more the returned signal can be compressed in time, this is known as the pulse compression ratio. Pulse compression is used extensively in radar and communication applications. For SODAR signals, its use has been proposed as an attractive method. But to date its use in SODAR devices has been limited to a number of theoretical investigations [1] [2], an experimental device which uses extremely long pulses with continuous linear frequency modulation [3] and multi-frequency SODAR has been implemented using non-coherent spectral methods [4]. This paper presents work which has been carried out to investigate the applicability of pulse compression to wind velocity profiling with SODARs. Section 2 introduces the proposed pulse compression methodology, analyses the possible improvements that could be achieved, Section 3 presents some results from measurements on a real device. Section 4 presents a novel post processing scheme using GMM that can be applied to the matched filter output to reject reflections from fixed echoes and background noise.

2. PULSE COMPRESSION

A theoretical study [1] postulated an 11 dB SNR improvement when using a stepped chirp with SODARs. The stepped chirp modulation compared to other techniques such as phase modulation is an attractive choice as it provides the best velocity resolution, and is compatible with existing spectral methods. It has therefore been chosen for this work. In interpreting the scattered signal the range-velocity ambiguity problem needs consideration as a change in frequency can be due to either modulation, or Doppler shift. Careful coded waveform design can minimize the range-velocity ambiguity problem. For a stepped-chirp the ambiguity is easily understood. Consider a linearly increasing (in frequency) chirp. If the spacing of the frequencies is of the same order as the Doppler shift the matched filter will detect false returns at intervals related to the sub-pulse spacing.

2.1 Doppler estimation from matched filters

For SODAR the wideband matched filter is adopted due to the small wave speed to target speed ratio. The matched filter that maximizes the SNR of a reflected, Doppler shifted, noisy signal y(t) can be expressed as;

$$\Psi(t,a) = \left| \sqrt{\alpha} \int_{-\infty}^{\infty} y(t) x^{*}(a(t-\tau)) d\tau \right| \qquad (1)$$

Where *Ψ(t)* is the matched filter output and *α* is the Doppler stretch parameter which is a function of the radial velocity, *y(t)* is the returned signal and *x(t)* is the transmitted signal. The velocity detection algorithm is implemented as a bank of matched filters each with a different *α,* to represent a range of possible radial velocities. Maxima in the matched filter bank output represent positive identification of target at a particular range and velocity. A delayed Doppler shifted version of the step chirp representing an echo from a moving target can be expressed as:

$$x(t,\alpha)=\sum_{n=1}^{N}\sin(2\pi f_n(\alpha t-T))e^{\left(\frac{\alpha t-\tau_n+T}{\sigma}\right)^2} \quad (2)$$

Where T is the sub-pulse duration, f_n the chirp frequencies, and σ the subpulse width. The matched filter is implemented using FFTs as shown in the in Figure 1. The Hilbert transform is used to compute the analytic signal, so that the magnitude of the matched filter output is smooth. The matched filter yields two output parameters for each time lag, the magnitude $MF_{max}(t)$ and the Doppler stretch parameter $\alpha_{max}(t)$, which is converted to a radial velocity estimate $v_r(t)$ using.

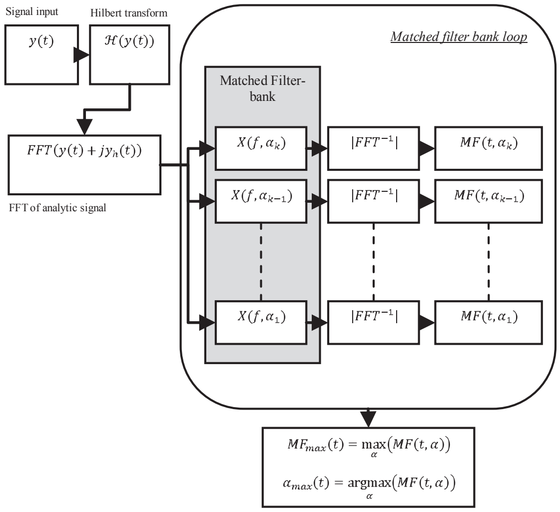

Figure 1. Matched filter bank algorithm

2.2 Waveform design

For a step chirp a range-velocity ambiguity is caused when there is a high degree of correlation for not only the zero-Doppler case, but also at a Doppler shift related to the frequency spacing, where for example the first frequency in the matched filter waveform, matches the second frequency of the returned signal and the second matches the third etc.. Assuming a maximum wind velocity of 20 m/s and a beam tilt of 20° the maximum radial velocity ($v_{r\max}$) is about 7 m/s. As Doppler shift scales with transmitted frequency, to optimize the transmission bandwidth, a non-linear frequency spacing is optimal. To prevent ambiguity, starting with a maximum transmit frequency of 6.5kHz and a minimum of 3kHz, the transmission bandwidth of the CHIRP experimental SODAR [5], this equates to an optimal non-linear frequency spacing of:

$$f[n-1]=f[n]-\left|f[n]\frac{c-2v_{r\max}}{c+2v_{r\max}}-f[n]\right| \quad (3)$$

This places a strict limitation on the pulse compression ratio that can be achieved. For the CHIRP SODAR, the maximum pulse compression ratio is 9 which is equivalent to a maximum transmission power increase of 9.54 dB.

To increase the pulse compression ratio, the bandwidth and ambiguity must be increased. The ambiguity function is a tool used to study the range-velocity ambiguity. It is implemented using (1) but replacing *y(t)* with *x(t)*. The level of range-velocity (RV) sidelobe relative to the main lobe informs on the ability of the waveform to differentiate between different ranges and velocities. The experimental CHIRP SODAR is bistatic where transmitter and receiver were located side-by-side allowing for a long pulse as simultaneous recording and transmission is possible. The blind range (the range where simultaneous transmission and measurement is not possible) is limited to a single sub-pulse length. This also allows the direct comparison of matched filter based methods with traditional in-coherent power spectrum methods as the chirp train can be processed in both ways. Chirp pulses of 9/-27 frequencies are used in this study where individual subpulses are between 30 and 5 m long.

To reduce the RV sidelobes the frequency order of the sub-pulses can be optimized e.g. by using Costas codes [6]. Measurements showed the ratio of direct to backscattered sound from 150 m is about 50 dB thus defining the required reduction in RV peak sidelobe level (PSL). Can this be achieved by decreasing the frequency spacing, by reducing $v_{r\max}$? Figure 2 a) shows the ambiguity function for a 9 frequency chirp c) for a 27 frequency Costas optimised chirp. Figures 2b) and d) provide more detail on the centre of the pulse. Both pulses are 180 m long overall. PSL in Figure 2d) is around -23 dB, while Figure b) shows no sidelobes but a lower effective range resolution. Also for both waveforms a strong thin central peak occurs when the matched filter matches in both range and Doppler scale. The level of the thin central lobe in relation to the wider central lobe is around 9 dB for the 9 frequency chirp. To ensure that the matched filter can detect Doppler shifted signals, the velocity resolution of the filter bank must be such that it can fully represent the thin central lobe in the ambiguity function. If the thin central lobe is not detected the system will perform like an incoherent spectral based method.

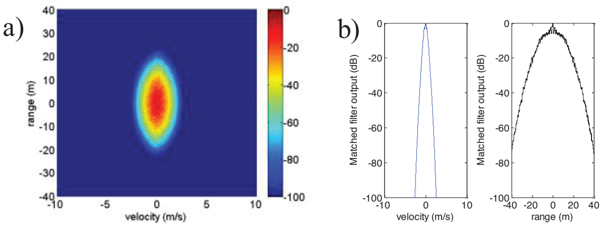

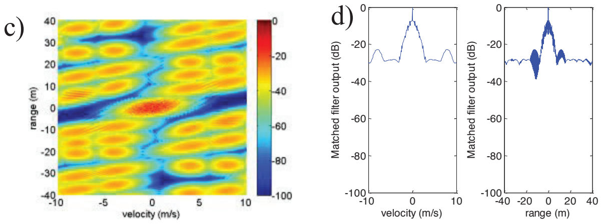

Figure 2. Ambiguity functions for a 9 frequency chirp (top) and a 27 frequency chirp (bottom). The centre line cross-sections in velocity (middle) and range (right) bring out the thin central lobe which determines matched filter performance.

The only way to increase bandwidth and decrease PSL below -50dB is to increase the length as v_{rmax} is decreased. The length must be increased to at least 200 s, with a v_{rmax} of 0.0005 m/s! This is extremely long and time variance of the atmosphere will cause a mismatch of returned signal with matched filter causing the detection to fail. Therefore the maximum achievable pulse compression ratio for a long chirp is 9. With a short chirp, the required sidelobe level is much lower as assuming a blind range is acceptable then the RV PSL need only be around 7 dB for 100 ms chirp, this is related to the rate of decay of the backscattered sound of this period. However the shortness of the pulse makes comparison with spectral methods difficult.

3. MATCHED FILTER RESULTS

Figure 3 A shows the overlaid matched filter results from ten minutes of sounding of the atmosphere using a tilted beam, a 9 frequency 180 m pulse, with a matched filter bank resolution of .05 m/s. The z axis is not shown but represents the matched filter output magnitude. Visual inspection indicates a steady decrease in radial velocity up to 70 m (the range of the device was generally limited by electronic noise), but within the presence of a number of scatters which vary around 0 m/s. These are fixed echoes due to a number of tall structures nearby. Figure 3 B shows the radial velocity computed using a standard FFT based method fitting a Gaussian to the spectrum including rejection of noisy spectra. This shows that there has been no obvious gain in using matched filtering to increase the range of the system. This result is consistent for numerous measurements. The expected 9 dB gain should show a clear extension in range, while it could be argued that the fixed echo response would appear to be extended the range of backscattered data is the same. The strong central peak shown in Figure 2 is not being detected but the points on the wider peak are. With Bragg scattering, scattering structures of scales related to ½ a wavelength dominate. Therefore different groups of scatterers contribute scattering for different wavelengths. This causes the phase relationship between the different frequency components of the scattered signal to be randomized. It can be shown that when an ambiguity function is generated as in Figure 2 but with the phases of simulated return signal randomized, the strong thin central lobe is lost. In this case the matched filter just detects peaks based on the wider central lobe, hence the range of the algorithm is the same as the incoherent method.

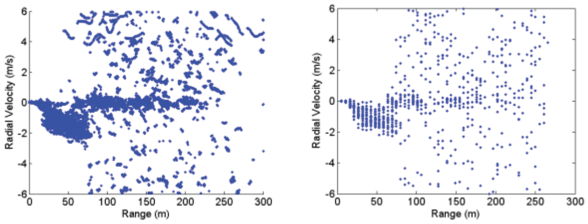

Figure 3. Radial velocities, a) matched filter, b) spectral estimates

4. POST PROCESSING USING GMM

4.1 Algorithm

Despite this result, the matched filtering still provides radial velocity estimates where multiple frequencies are automatically combined into single radial velocity estimates. Additionally the resulting data set contains radial velocity estimates on a finer range grid than is usual when using range gating. While the effective resolution due to the sub-pulse length is not increased, the location of the scattered sounds are not forced to originate from the range gated positions. By assuming that the backscattered signal is the result of the sum of a number of different hidden stochastic processes, a statistical model such as GMM, where data is assumed to be a sum of multiple multivariate Gaussian processes, can be used to recognize different random processes. An iterative algorithm is optimized to estimate the most likely set of model parameters including the number of mixtures, the component weights, the component covariance and the component means. The number of components is chosen via the Akaike information Criterion. Fitting a GMM to the data from Figure 3 yields Figure 4, where each Gaussian distribution is displayed as a 3D ellipse, whose position and shape are based on the optimized covariance **σ**, and mean **μ** matrices.

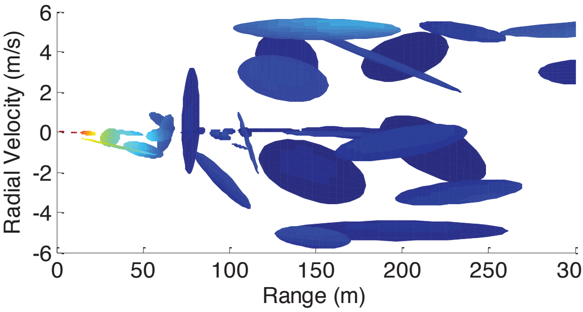

Figure 4. GMM fit to ten minutes of matched filter data

4.2 Fixed echo and noise identification and rejection

Rules are defined to classify each component as either, backscatter, fixed echo or noise, experience and details from [7] are used to help determine these rules.

Fixed echoes	The magnitude of the mean velocity μ_v is less than 0.1m/s – scatterers from stationary objects are not Doppler scaled. **And** Velocity standard deviation σ_v is less than 0.1m/s, backscatter may have a zero Doppler shift, but it will have a larger variance due to the turbulence.
Noise	The covariance matrix value which determines the slope between range and MF output is positive. – backscattered sound will always decay with range, noise may not.
Noise	Standard deviation of component in velocity direction is greater than 1m/s
Outliers	Component mean velocity value is more than 2 m/s away from the Mixture median value. – This identifies outliers and rejects them.

Table I. GMM classification rules

Components that display any of the described attributes, are rejected. Figure 5 shows the GMM after fixed echoes and noise have been rejected And shows that fixed echoes, direct sound and noise have been detected and rejected effectively even when backscattered sound is present at the same range as the fixed echoes.

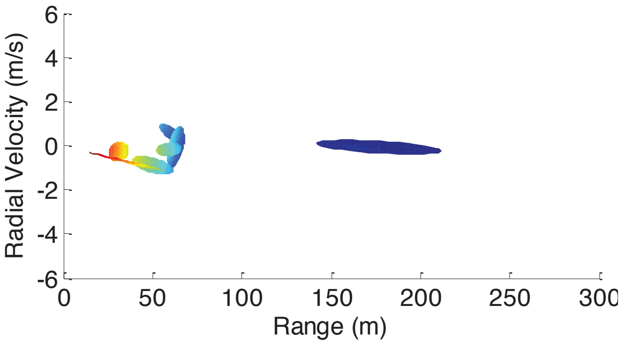

Figure 5. GMM components with fixed echoes and noise removed

A final radial velocity estimate can be produced by from the filtered GMM, by calculating the 50% percentile of the distribution mixture and the confidence limits on that estimate can also be computed directly. Using the probability from the total mixture, ranges that exhibt a low probability ($p<0.05$) can be rejected as inaccurate. Figure 6 A shows 10 minute wind speed averages over a 15 h period computed using the matched filter method using 5 beams, (at 6 pm there was a cable failure).

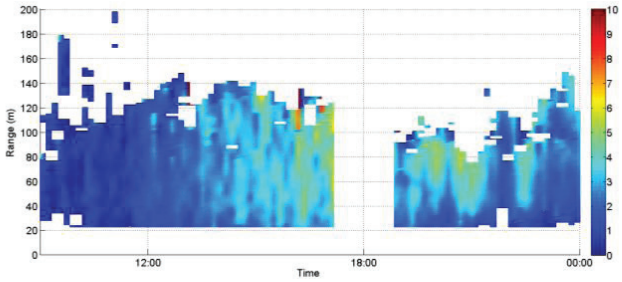

Figure 6. A GMM based estimate wind speed from a day's worth of data (ten minute averages)

5. CONCLUSIONS

Pulse compression for Doppler SODAR does not provide the expected gains that have been predicted. It is thought that this is because the nature of the scattering which can hide the phase relationship between different frequencies in the scattered signal. However the matched filter does provide an alternative approach to SODAR signal processing where different frequency components are automatically linked. The investigations have also inspired the development of an alternative post-processor where radial velocity estimates are computed using a GMM. This is able to categorize and separate components such as noise, backscatter and fixed echoes. Additionally by fitting a statistical model to the data, other statistical parameters, such as σ_w, are directly available. The GMM post processing method could also be applied to radial velocity estimates from standard spectral methods.

ACKNOWLEDGMENTS

The authors wish to acknowledge the UK Engineering and Physical Sciences Research Council for their support via grant EP/G003734/1

REFERENCES

1. Bradley, S. G., 1999: Use of coded waveforms for SODAR systems, *Meteorology and Atmospheric Physics,* **23**, pp 15-23.

2. Nagaraju, A., Kamalakumari, A., Purnachandra Rao, M., 2010: Application of Pulse Compression Techniques to Monostatic Doppler SODAR, *Global Journal of Researches in Engineering,* **10**, pp 37-40.

3. Martin, A., 2004: Very High Resolution Boundary Layer Profiling With Small Dead Zone for Measurements to 500m in Low Wind Conditions, *proc. ISARS 2004*.

4 Rao, I. S., Anadan V. K., Kumay, M. S., Multifrequency Decoding of a Phased Array Doppler SODAR, 2009: *Journal of Atmospheric and Oceanic Technology,* **26** (4), pp 759-768.

5. Kendrick, P & Hunerbein, S V & Bradley, S G & Bradley, S G, 2010: A flexible new SODAR design for chirped signals and conformable beam forming, *proc ISARS 2010, Versailles, France*

6. Bellegarda, J., Titlebaum E., 1988: Time-Frequency Hop Codes Based Upon Extended Quadratic Congruences, *IEEE Transactions on Aerospace and Electronic Systems,* **24**(6), pp 726–742.

7. Peters, G., M. Latif, and W.J. Muller, 1984: Fluctuation of the vertical wind as measured by Doppler SODAR. *Meteorologische Rundschau,*. **37**(1), p. 16-19.

AN URBAN SODAR FOR STUDYING THE LONDON URBAN BOUNDARY LAYER

Stuart Bradley[1], **Janet Barlow**[2]

[1]*Physics Department, University of Auckland, Private Bag 92019, Auckland, New Zealand,*
s.bradley@auckland.ac.nz
[2]*Department of Meteorology, University of Reading, Box 243, Reading, RG6 6BB, UK, j.f.barlow@reading.ac.uk*

ABSTRACT

ACTUAL is a comprehensive study of the London urban boundary layer, with a wide selection of in situ and remote sensing instrumentation deployed. One of the instruments is a new urban sodar design, which we describe. The goal for this instrument is to provide information at heights between those sampled by instruments on small masts (generally at less than 10m above rooftops), and the data collected by a Doppler lidar at heights above around 80m. This is a very interesting and challenging region, since there is great complexity arising from the rough building/street structure. It was therefore necessary to design a sodar which had extended 'complex terrain' capabilities, particularly in having good spatial and temporal resolution, as well as not sampling in volumes which are widely separated spatially. Our solution is to use a single vertically-transmitted beam, of moderate beam-width, coupled with the use of a 'Doppler imaging camera'. The camera comprises a cluster of small very directional microphones which image the scattering from the across the width of the transmitted beam. The disadvantage of relatively low Doppler shifts is compensated by having many simultaneous samples of the Doppler components, essentially from a 'common volume'. The design will be discussed in detail along with field trials.

1. DISTRIBUTED SAMPLING VOLUMES

Sodars measure the Doppler shift due to the radial component of wind along off-vertical beam directions. Measurements from 3 or more beam directions are used to build up the 3 components of the wind vector at each height, as shown in Fig. 1. The assumption in this method is that the same wind is present in each of the volumes sampled by the various beam directions [1]. However, in an urban environment the radial wind equations contain different wind components. For example, a 3-beam system sampling 3 separate volumes at a particular height will have u_1, u_2, and u_3 for the easterly wind component instead of just u, and 9 wind components in total, instead of just 3.

The challenge for the design of an 'urban sodar' is therefore to *not* have spatially distributed sampling volumes. The solutions proposed for complex (hilly) terrain are either correction of the wind measurements using a complex terrain flow model, or implementation of a Common Volume Profiler, or bistatic sodar. However, neither of these options are available in an urban environment. Models with detail of a few meters simply do not exist (indeed, their absence is one of the motivations for measurements in an urban area). There is also difficulty finding suitable roof-top or open ground sites for a conventional sodar, let alone one with the necessary extended baseline of a bistatic sodar. An alternative approach is therefore needed.

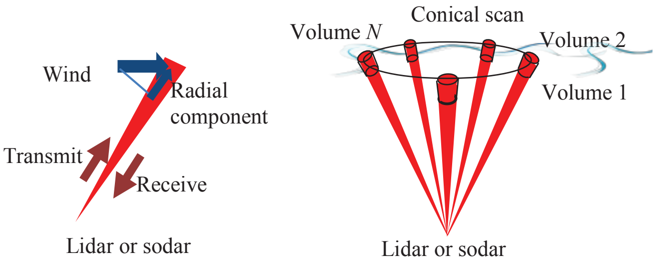

Figure 1. Wind vectors are assembled at each height layer by estimating the radial Doppler shift from a number of sampling volumes in a conical scan.

2. MONOSTATIC BEAM ANGLES

A typical monostatic sodar system comprises a planar phased array of many transducers or, alternatively, several parabolic dish antennas each having a single transducer at its focus. The transducers are used both as transmitters and receivers. Transmission is into three or more beams, one of which might be vertical, but the others offset from the vertical by 15º-20º. Two beams, each 15º from the vertical and in orthogonal vertical planes are separated by 38 m at a height of 100 m.

This geometry of N_b beams gives N_b equations at any particular height, which relate the measured radial Doppler shift to the three vector wind components. Clearly $N_b \geq 3$ to solve for the three vector components.

More beams should reduce the errors in solving for the three components, in a least-squares manner. But the difficulty is that transmission and reception is typically performed serially on the various beams, rather than in parallel, and this means that more beams take longer to sample and temporal variability degrades whatever advantages might have been expected.

Clearly the design aims for an urban sodar should be to have multiple simultaneous beams, and to have these clustered near the zenith. However, in its simplest form, the equation system to be solved is

$$\begin{aligned} D_1 &= u\sin\theta + w\cos\theta + \varepsilon_1 \\ D_2 &= v\sin\theta + w\cos\theta + \varepsilon_2 \\ D_3 &= w + \varepsilon_3 \end{aligned} \qquad (1)$$

where D are the scaled radial Doppler shift measurements, (u, v, w) is the vector wind, θ is the zenith angle for beams 1 and 2 (and beam 3 is vertical), and ε are the measurement errors which can be assumed to be distributed as $N(0, \sigma_m)$. Error propagation finds that

$$\sigma_u = \sigma_v = \left(\frac{1}{\sin^2\theta} + \frac{1}{\tan^2\theta} \right)^{1/2} \sigma_m \approx \frac{\sqrt{2}}{\sin\theta}\sigma_m \, . \qquad (2)$$

$$\sigma_w = \sigma_m$$

This means that there is error magnification for beams clustered at small zenith angles θ and, for such a system to be successful, the advantages of multiple beams must offset the disadvantages of small zenith angles. Since error reduction decreases roughly as the square root of the number of uncorrelated random error sources, 16 sensors will compensate for a change in zenith angle from 15º to 3.7º i.e. $\sin(15)/\sin(3.7) = 16^{1/2}$. At 100m height, two beams in orthogonal vertical planes and having zenith angles of 3.7º are separated by only 9 m, so spatial variability problems are much reduced.

3. DISH ANTENNA BASICS

Our design is based on the use of a parabolic dish antenna. The geometry is shown in Fig. 2. Two sensors are shown, one laterally displaced a distance r from the focal point. This lateral sensor has a beam with zenith angle

$$\theta = \tan^{-1}\frac{r}{f} \approx \frac{r}{f} \qquad (3)$$

where f is the focal length of the parabola. The same construction shows that the angular half-width of beam for a sensor which itself is of diameter d will be $d/2f$. We chose a commercial satellite receiving dish having f = 492 mm and used this as a mold for fiberglass copies (the fiberglass is acoustically 'dead'). For microphones we used d = 10 mm diameter omni-directional electret microphones which have low self-noise and good sensitivity. These have a geometric beam half-width with this dish of 5/492 radians or 0.6°. Being omni-directional, they nevertheless collect sound from the whole antenna area.

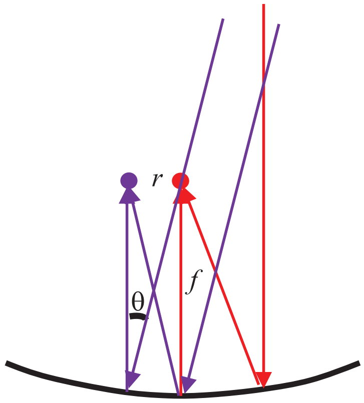

Figure 2. Dish geometry. One sensor is at the focal point (red) and the other a distance r laterally from the focal point.

A sensor displaced laterally by 32mm will have a beam zenith angle of 3.7°.

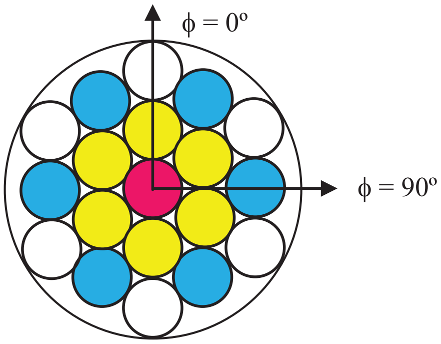

Figure 3. Sensor head geometry. The 18 sensors comprise one central (red), 6 with centers displaced d (yellow), 6 with centers displaced $3^{1/2}d$ (blue), and 6 with centers displaced $2d$ (white). The radius of the head unit is $2.5d$ = 25 mm.

A close-packed geometry is shown in Fig. 3. This will give opposing beam combinations in several directions and has over all angular symmetry (the beam pattern will look similar to the mirror image of the microphone head). The microphone head unit obscures a fraction of only 2% of the incoming sound for a 500 mm diameter dish.

4. THE DOPPLER CAMERA CONCEPT

Measuring the azimuth angle ϕ from the x axis shown in Fig. 2, the Doppler equations are

$$D_m = u\theta_m \cos\phi_m + v\theta_m \sin\phi_m + w + \varepsilon_m \qquad (4)$$

for microphone m = 1,2,..,18.

This set of 18 equations can be solved by least squares for the 3 wind components. Because of symmetry,

$$w = \frac{1}{M}\sum_{m=1}^{M} D_m \quad . \qquad (5)$$

the average of all the Dopplers.

What does a typical Doppler shift pattern look like, plotted visualizing the microphones as pixels? If plotted as a contour plot, it will have a preferred direction. This suggests a fitting procedure based on the typical scatter pattern for straight line regression. Eqn. 4 can be rewritten

$$ux + vy - D' = 0 \qquad (6)$$

where x and y are the Cartesian coordinates of microphones on the sensor head, and D' is the vector of D values minus the mean. This is the equation of a straight line, so linear regression can be used to find u and v.

5. EMERGING DESIGN

At this point we are first experimenting with a 3-sensor system. This is equivalent to conventional 3-beam sodars, except that we are using a single dish antenna for the 3 sensors. For this first version, the microphone units are very low noise 1.2-inch commercial microphones and, because of their size, we are using an offset focus parabolic dish, so that the sensor head is not within the sound path. This trial design allows us to experiment with various signal conditioning ideas, but it contains the essential ingredients of the Doppler camera in that all beams are transmitted and sampled simultaneously.

Figure 4. A photograph of a dish, single transmitter horn and driver, and acoustic baffles. One side of the acoustic enclosure is open.

The sodar transmitter dish is shown in Fig. 4. We measured the beam pattern for the horn without dish, as shown in Fig. 5. There is very little frequency variation, so this horn and dish arrangement can be used with complex signals such as chirps. When the dish is added, the beam half-width decreases to around 3º.

This system uses separate transmitter and receiver enclosures, as shown in Fig. 6

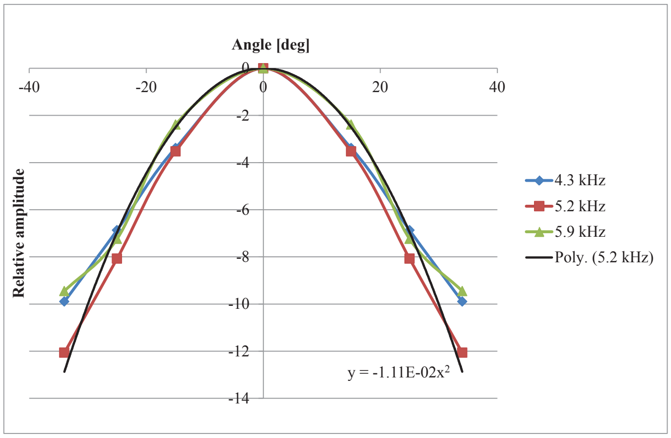

Figure 5. Measured beam patterns of the transmitting horn.

Figure 6. A photograph of the combined transmitter and receiver enclosures set up at the test site of the University of Reading. The metal box on the ground is a temporary power distribution box.

ACKNOWLEDGMENTS

This work is funded by a grant from EPSRC.

REFERENCES

1. Bradley, S. G., 2007: *Atmospheric Acoustic Remote Sensing*. Florida, CRC Press/ Taylor and Francis Group, 328pp.. ISBN 978-0-8493-3588-4.

SEA-LAND BREEZE OBSERVATION USING WIND LIDARS IN KOREA

Y.-S. Park, G.-H. Kim, T. Kwon, Y.-J. Choi

National Institute of Meteorological Research, KMA, Seoul, South Korea, sanpark@korea.kr

ABSTRACT

Two sets of wind lidar are installed perpendicular to the direction of the seashore in order to measure wind profiles in east coast of South Korea. The time lag of sea breeze initiation and heights of sea breeze are compared with distances from the coast and with time. The wind turnings from land breeze to sea breeze and vice versa are also analysed.

1. INTRODUCTION

Sea-land breeze is representative local circulation observed in coastal region. There have been many studies about sea-land breeze so far, but field studies for observation focused on vertical structure of sea-land breeze are relatively rare.

2. INSTRUMENTATION

In order to investigate the characteristics of land-sea breeze in east coastal area in South Korea, the wind direction and speed by height at two points were observed. Two sets of wind lidar were installed at two locations (points A and B in Fig. 1) and they are about 7km apart. There is a range of mountains parallel to the seashore in southwest region in the right hand side of the map in Fig. 1. There are 5 automatic weather stations at 10 m height. The observation period is from March 3 to June 10, 2011.

3. RESULTS

The horizontal characteristics of land-sea breeze in East Sea coast~~,~~ was that the wind direction of sea breeze was different for each area due to complex topographical effects despite its monotonous coastline. In order to investigate the characteristics of daily change of sea-land breeze, we analyzed the data for a number of days when it was clear and wind speed was low(cloud amount less than 5 and geostrophic wind less than 6 m/s), resulted in 4 days selected; April 17, May 2, May 8, and May 17. At point A near the coastline and at point B, which was about 7 km away from seashore to inland, there were differences in the beginning and development of sea breeze and the transition time into land breeze. Due to development of sea breeze, the wind was 6～12 ms^{-1} at point A while at point B, it was 3～4 ms^{-1}. The development of sea breeze started about an hour later in point B than in point A. Fig. 2 shows wind structure at two locations in May 17. The westerly blew until 7 in the morning at A and the winds turned to northeasterly/easterly since 9 am and the maximum wind speeds are 8 m/s at 5 in the afternoon at site A and 4 m/s at 3 pm at site B and then the winds turn clockwise in the direction at evening.

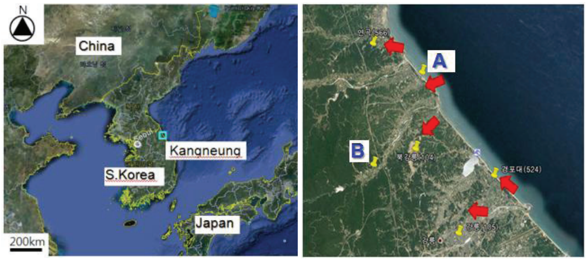

Figure 1. The location of observation experiment(top) and wind lidars installed(bottom, A and B). The wind directions(red arrows)are at surface level averaged from 13h to 18h on selected clear 4 days.

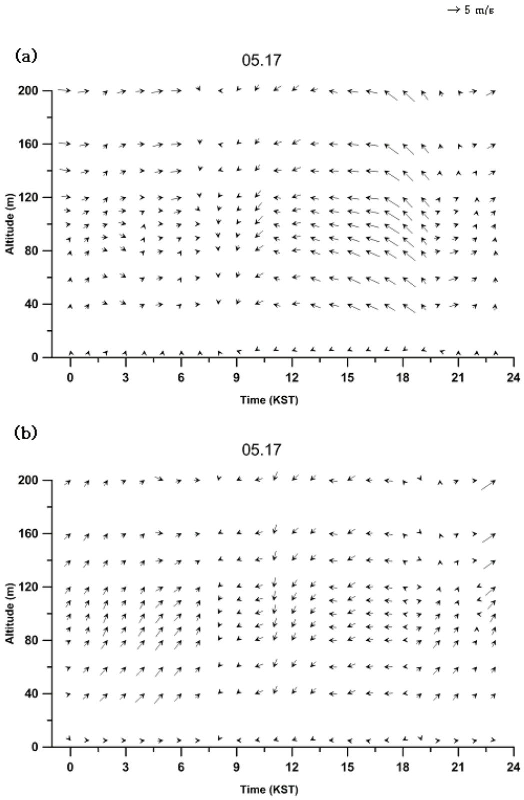

Figure 2. Diurnal variation of wind vector for 17 May, 2011 at (a) Site A, and (b) Site B.

SURFACE BASED REMOTE SENSING AND NEURAL NETWORKS FOR COMPLEX TERRAIN BASED DISPERSION MODELING

Kodilkar A.A[1], Murti M.V.R[1], Pillai J.S[2]

[1]*Center of Studies in Resources Engineering, IIT Bombay, India,* abhishekak@iitb.ac.in, mvrmurti@iitb.ac.in
[2]*Society of Applied Microwave Electronics Engineering and Research, India,* jspillai@sameer.gov.in

ABSTRACT

In this study the diurnal variation of different atmospheric parameters in the Atmospheric Boundary Layer (ABL) at different altitudes has been using from a ground based remote sensing instrument, Phased Array Doppler Sodar. The Phased Array Doppler sodar used in the study is developed by Society of Applied Microwave Electronics Engineering and Research (SAMEER), India. The sodar generates acoustic signal in three orthogonal directions using 8x8 phased array antenna with programmable frequency (1800 Hz to 2500 Hz). Most of the human activities take place within the atmospheric boundary layer (ABL) and it plays a vital role in modifying the atmospheric circulation and the dispersion of air pollutants. These studies are based on the data collected at hill side area Indian Institute of Technology (IIT), Bombay Campus, Mumbai which has complex terrain topography, the campus is spread about 500 acres (2023428 sq. m) over 19.08ºN Latitude, 72.55ºE Longitude. By analyzing the received signal from the atmosphere (scattering from atmospheric inhomogeneity due to temperature fluctuations), the individual components of the wind (two horizontal and one vertical; or u, v, and w) can be estimated. This paper also explores various parameters of acoustic radar data, which includes the site specific parameters such as Joint Frequency Distribution (JFD), Wind Rose (WR) and Echogram (reflectivity) for feature identification and analysis, which are some of the critical inputs provided for dispersion modeling. An Artificial Neural Network (ANN) model is proposed for dispersion modeling on basis of sodar data which will be used as input parameters for the study. With the help of site specific input parameters model can find out the hidden correlations between wind data required to carry out analysis of dispersion over complex terrain.

1. INTRODUCTION

Surface based remote sensing is one of the most trusted technique when it comes to mesoscale meteorology as compared to satellite based synoptic studies. The layer near the surface in which heat, momentum and moisture are exchanged between earth and atmosphere, and where pollutants are dispersed is popularly known as ABL [7]. Here, output which we get from the sodar system is wind field components, the components of the three-dimensional wind field (u, v, w) are derived by measuring the frequency shift of the backscattered acoustic pulse due to the Doppler effect [3].One of the fundamental problem which has to be addressed is whenever one wants to model the dispersion of atmospheric pollutants is to relate quantitatively the air concentration and deposition values of one or more pollutions species in space and timer to independent variables such as emissions into the atmosphere, meteorological variables and parameters, which describe removal and transformation processes. All these independent variables can also be functions of space and time, but need not all be mentioned relationship by mathematical and/or physical methods is called a 'model'. It is often necessary to establish objective techniques to predict or analyze the wind distributions. In complex terrain it is difficult to characterize wind patterns even experimentally, as the measured wind is often representative only to a horizontal scale of a few meters.

Available data show strong site-specific characteristics, but there is a clear need for more observational work to fully understand and quantify complex terrain influences on ambient air quality. In complex terrain, the wind field is strongly affected by topography, and thus the profiles strongly depend on wind direction [6]. Some models work on deterministic approach such as Gaussian diffusion model and time series model such as Box model which have their own assumptions and requirements which allows users to choose the parameters according to site selected [2].Statistical modeling with the help of ANN has eventually proved their impact on real time prediction with a greater accuracy [1].

These complex dispersion models simulate 3-D atmospheric fields to a certain level of accuracy; they also require detailed input conditions and significant computer effort that is not feasible for wide use in a variety of operational atmospheric applications now or in the near future. One of the alternatives is to use artificial neural networks (ANN) to assess the future impact of emission sources on the atmosphere by forecasting wind speed. The ANN methods have two major advantages: simplicity in use and low computational requirements [8]. In this study, we try to implement the feasibility of using ANN methods in simulating the transport and dispersion of wind components for both short-term averaged time series of input conditions (meteorological parameters) and output conditions (current simulated wind speed and direction).

2. ARTIFICIAL NEURAL NETWORK MODEL

ANN model has proven applications in acoustic remote sensing for atmospheric dispersion modeling and unknown air pollution sources [5]. The structure of a three layer neural network is shown in Fig. 4.The transfer function which will be used here is the sigmoidal function.

$$\mathbf{Y = [1 + \mathit{e}\ (-ax+b)]^{-1}} \qquad (1)$$

Where ‘a’ will determine slope of the sigmoid and ‘b’ is the threshold. The process of learning the training set of patterns means the determination of the optimum weights which will certainly minimize the mean square error between the outputs in the output layer and the desired values. Most commonly used “back-propagation learning algorithm” [9] is used or the training. Basically initial random weights between ±0.5 will be assigned to each weight as initial guesses. The weights are learned through an iterative process. During learning the weights are updated. When the network learns the training set of patterns well enough it can be used for determining the output values for the pattern with unknown outputs.

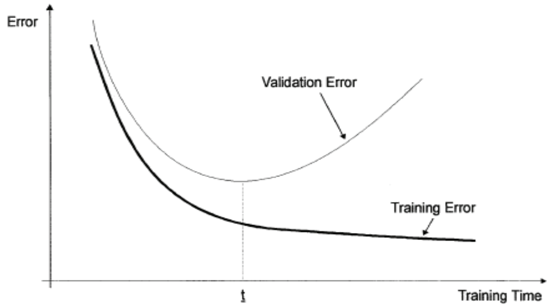

Figure 1: Training and validation errors with respect to training time.

As reported by [4] the backpropagation only refers to the training algorithm and is not another term for the multilayer perceptron or feed-forward neural networks. Output can be a tracer concentration or it can be correlations of wind profile data that depends generally on what input data is provided in addition to raw sodar data.

3. RESULTS

3.1 Study Area and Specifications of Sodar

The Phased array Doppler sodar instrument used in project is developed by SAMEER, India. The test analysis is carried out at SAMEER; IITB campus area which is a complex terrain area situated at hill side, the campus is about 500 acres (2023428 sq. m) over 19.08ºN Latitude, 72.55ºE Longitude.

Figure.2: Spatial location of experimental site on google map with the instrument.

No. of piezoelectric transducers	52
Frequency	1800-2500 Hz
Acoustic power (output)	100W
Wind speed accuracy	$0.1ms^{-1}$
No. of beams	3 (zenith, north and east)
Beam angle	16º
Maximum angle	1000m
Pulse width	Programmable
Pulse repetition frequency	Programmable
No. of FFT points	4096
Transmission Type	Reflecting mode
Beam width	5º
Range resolution	User defined

Table.1: Technical specifications of the SAMEER Sodar system used in the study.

3.2 Computation of Joint Frequency Distribution & Wind Rose

We have also computed JFD & display WR for different classes and analyze various features from Echograms on daily basis as well as analysis by means of T-H (Time vs. Height) plot; these parameters are required as an input to validate the models. All the parameters are site specific and can be utilized as per requirement for the research.

4.2.1 Methodology

Sodar systems collect wind data continuously for further processing through offline software. All wind files are for a given period located at a given directory and analysis can be daily, monthly, and yearly as per user specifications and these wind data is again preprocessed as per signal to noise ratio (SNR) values for data quality control.

Echogram observed for 13th Oct 2011, 24 hr period
[Time (x axis) Vs. Height (y axis)]

(a 0-8 hrs, b 8-16 hrs, c 16-24 hrs.)

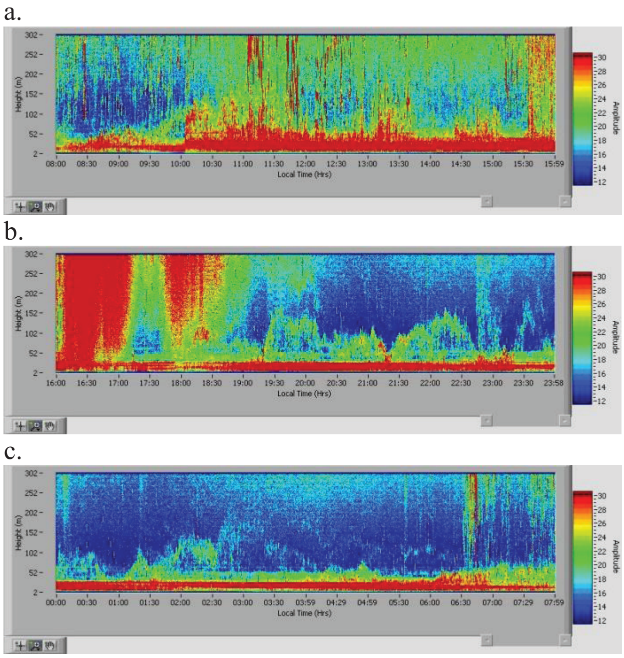

Wind Rose

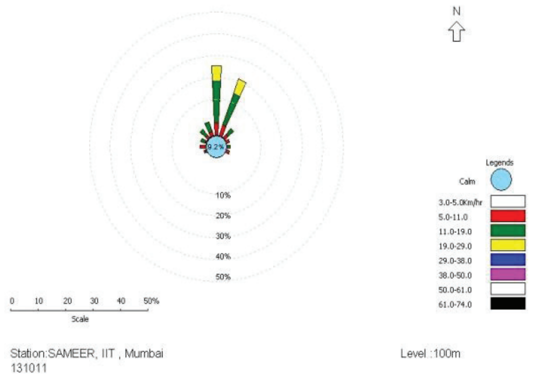

Figure.3: Corresponding echogram (received vertical acoustic signal intensity in relative units) and wind rose generated for 13^{th} Oct 2011.

- Only wind magnitude & wind direction data fields are extracted from wind file after prequalification using SNR value. These wind magnitudes are classified in 10 different classes of wind as per their magnitude.
- Similarly wind directions are distributed in 16 sectors of interval where each sectors are of 22.5 degree. These wind speed and direction values are distributed into suitable classes. Each class is divided by number of qualified data for the given period.
- This gives percentage difference of wind speed and wind direction of wind data collected over a given period by user. This data is arranged in tabulated form which is known as joint frequency distribution and graphically plotted as wind rose.

Here we have processed data for post monsoon season (i.e in the month of october) over mumbai region and the echogram observed is seen in the figure.3

4.2.2 Tools used for the Study:

Here the idea is to use input parameters as a height, u, v, w (two horizontal and one vertical) components and output is wind speed and wind direction parameters which are known as well as unknown. Unknown values indicate forecasting of the required data. The hidden layer in between is trained by weights which are adjusted according to the log-sigmoid function (eqn.1). We have used multilayer feed forward backpropogation for the data.

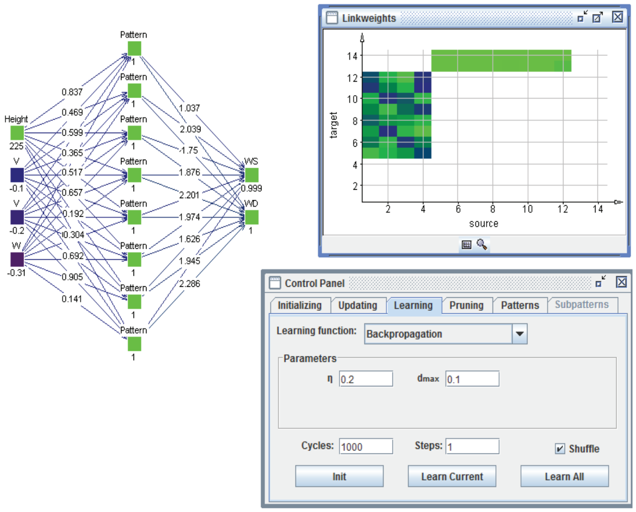

Learning function: Backpropagation

η 0.2 dmax 0.1

Cycles: 1000 Steps: 1 ☑ Shuffle

Figure.4: Proposed topology of the three-layered feed-forward neural network which is used in this study.

An error signal is basically described as the difference between the desired and actual output. In our case training uses the magnitude of this error signal to compute to what degree the weights in the network should be adjusted so that the overall error of the multilayer perceptron is minimized. The error values from the required test data is between 0.1-0.2%. JavaNNS [10] tool is used as a neural network simulator; it is based on its computing kernel, with a newly developed, comfortable graphical user interface written in Java set on top of it. It's free open source software developed by University of Tübingen. The output from the simulator further can be used to forecast the short term wind speed. JFD and WR software is MS window based software package. In order to provide textual and graphical analysis of wind data to wind profile users. It is designed and developed using NI Lab VIEW. This software provides provision for data quality control periodic analysis, ASCII, and image storage facility, analysis at different height levels and easily printed reports.

CONCLUSION

In this test analysis we have processed the wind components obtained from raw sodar data and given as a input to the JavaNNS simulator for short term wind speed prediction. Also post monsoon data processing and computation of joint frequency distribution, displaying wind rose for different stability classes and generation of echograms and feature identification based on input raw sodar data has been carried out. NI's Lab VIEW 7 software was used for processing data. These results can act as a preliminary input to the dispersion model proposed and further assumptions are made on its basis for atmospheric boundary layer meteorology.

ACKNOWLEDGMENTS

Authors are thankful to IIT Bombay and Atmospheric Radar Instrumentation Division, SAMEER Mumbai for providing resources whenever required and their support as well as encouragement to carry out the experiment.

REFERENCES

1. Bishop, C.M., 1995: Neural Networks for Pattern Recognition, *Oxford University Press*, Oxford.
2. Carruthers, D.J., R.J. Holyrod, J.C.R. Hunt, W.-S. Weng, A.G. Robins, D.D. Apsely, F.B. Smith, D.J. Thomson, B. Hudson, 1992: UK atmospheric dispersion modelling system. In: H. V. Dop, G. Kallos, eds., Air Poll. Modeling and its Appl. IX, Plenum Press, New York, *Proc. 19th CCMS/NATO ITM Ierapetra*, pp.15-28.
3. Coulter, R. L. and M.A. Kallistratova, 2004: Two Decades of Progress In Sodar Techniques: A Review of 11 ISARS Proceedings, *Meteorology and Atmospheric Physics.* **85**, pp.3-19.
4. Gardner M.W. & Dorling S.R., 1998. Artificial Neural Networks (The Multilayer Perceptron) - A review of applications in the atmospheric sciences, *Atmospheric Environment* Vol. **32**, No. 14/15, pp.2627-2636.
5. Gera B.S. & Neeraj Saxena, 1996: SODAR Data- A useful input for dispersion modeling, *Atmospheric Environment* Vol. **30**, No. 21, 3623-363.
6. Jens-Christopher Mayer, 2005: *Diploma Thesis* University of Bayreuth, Germany, (http://www.bayceer.uni-bayreuth.de/mm/de/top/diss/29352Thesis_final.pdf)
7. Martin Piringer, Sylvain Joffre, Alexander Baklanov, Jerzy Burzynski, Koen De Ridder, Marco Deserti, Ari Karppinen, Patrice Mestayer, Douglas Middleton, Maria Tombrou, Roland Vogt and Andreas Christen, 2004: The urban surface energy budget and the mixing height: Some results of recent European experiments simulated by the COST- ACTION715, *9th Int. Conf. on Harmonisation within Atmospheric Dispersion Modeling for Regulatory Purposes*.
8. Podnar, D., D. Koracin and A. Panorska, (2001). Application of artificial neural networks to modeling the transport and dispersion of tracers in complex terrain, *Atmospheric Environment*, Vol.**36**, pp. 561-570.
9. Rumelhart, D. E., Hinton, G. E., and Williams, R. J. 1986. Learning internal representations by error propagation, In *Parallel Distributed Processing*, MIT Press. Vol. **1**, pp.318-362.
10. JavaNNS open source software-(http://www.ra.cs.uni-tuebingen.de/software/JavaNNS/)

Session 8 – Oral Presentations

Wind velocity by the sodar data and its influence on air pollution in Moscow

Lokoshchenko M.A.[1], Trifanova A.V.[2], Elansky N.F.[3]

[1]*Lomonosov Moscow State University, Faculty of Geography, Department of Meteorology and Climatology.*
119991, Lengory, Moscow, Russia. Phone:+7-495-9394284; Fax: +7-495-9392479; E-mail:loko@geogr.msu.su
[2]*International University of Nature, Society and Man "Dubna". Dubna, Moscow region, Russia.*
[3]*Obukhov Institute of Atmospheric Physics of Russian Academy of Sciences. Moscow, Russia.*

ABSTRACT

The influence of wind velocity in the atmospheric boundary layer (ABL) on the ground concentrations of main air pollutants has been analyzed on a base of long-term sodar sounding in Moscow. As it is shown the most of minor atmospheric gases and even CO_2 demonstrate monotonously decreasing functions of the wind velocity both in the ground air layer and in Ekman layer above. However, ozone due to its specific (growth with a height in the lowest air layer close to the ground) has opposite dependence so that as a rule the higher is wind velocity the higher is the ground concentration of O_3. One more specific feature is function of SO_2 concentrations of the wind velocity which is non-monotonous and demonstrates intermediate maximum because this gas, unlike most other pollutants, is emitted mainly from high sources.

1. INTRODUCTION AND MEASUREMENTS

As one knows sodar sounding allows to measure wind profiles with fine spatial resolution and, besides, to determine a type of the lower atmosphere thermal stratification by analyzing of the classic sodar record (sodar echogram). Among others, inversion layers which prevent upward dispersion of air pollutants may be seen and recognized on this record. Both wind velocity and thermal stratification clearly influence on air pollution levels. Thus, results of the sodar sounding contain information about both these parameters, so that the air pollution monitoring is one of the most important applications of the sodar data since 1970s and 1980s [1, 2, etc.].

The acoustic remote sensing of the atmosphere is carrying out at Meteorological observatory of Moscow State University continuously since 1988. Firstly vertical sodar "ECHO-1" by GDR production was used, then – Doppler sodar "MODOS" of METEK company (Germany) production which operates there since 2004. Classic Doppler scheme of three beams with separate antennas for each beam, one vertical and two inclined, is used there (see Fig.1). Each antenna consists of seven equally-phased loudspeakers; totally – 21. Its operation frequency is 2000 Hz, total electric transmit power is 1 kW, the vertical range is from 40 to 500 m, spatial resolution is equal to 20 m, reliable wind profiles are measured in average of each 10 min. An accuracy of wind velocity V measurements by the sodar is ±0.24 m/s up to the value of 6 m/s and ±4 % if V is higher than 6 m/s. The main results of wind measurements by the sodar in Moscow are presented in [3 and others].

In 2002 a special ecological station was created by common efforts of IAP and Geographical faculty of MSU at the same location in the Observatory (at a distance of 70 m from the sodar). Since that time continuous measurements of the ground concentrations of a lot of minor air gases are carrying out there

Fig.1. Doppler sodar "MODOS" (of METEK production) at Moscow University.

Fig.2. Ecological station at Moscow University.

automatically on the 4 m level above the ground (Fig.2) during each minute with high accuracy: ±1 ppb for ozone, ±0.05 ppb for nitrogen oxide and for nitrogen dioxide, ±10 ppb for carbon oxide and ±0.5 ppb for sulfur dioxide [4]. Gas analyzers there are calibrated accordingly to standards of the WMO Global Atmospheric Watch. It should be noted as well that the station is situated at green park zone of the University on the South-Western periphery of the city. As a result, fortunately, none of strong sources of the atmospheric pollution presents in close locality of the station so that measurements there are quite representative for a great area of the city.

Thus, joining of results of both sodar and chemical measurements allows to study in details short-term dynamics of the air pollution and their relations with meteorological conditions. Among others, sodar data at Moscow University allowed to explain difference between morning and evening maxima of the diurnal courses of main urban air pollutants CO and NO which are primary products of fuel burning. As it was shown by authors using the sodar data the most probable reason of the highest concentrations in morning is usual existence of elevated inversion at that time [e.g., 4]. One more usage of the sodar data about thermal stratification was an explanation of structure of relations between main air pollutants [5].

It should be noted that there are a lot of examples of case-studying in literature which represent separate cases of extremely high air pollution incidents and their relations with meteorological conditions during several hours or, at least, several days. However, any example may demonstrate some occasional effects which may be not typical and do not reflect common tendencies. Evidently, for better understanding of these tendencies it is necessary to analyze and compare not only separate cases, even interesting, but long-term sampling of simultaneous data as well.

2. MAIN RESULTS

Common database of synchronous chemical, sodar and ground meteorological measurements during each hour has been created for period since 2004. On its base an influence of different meteorological parameters on the air pollution dynamics has been studied, including, among others, hourly-averaged wind velocity by the sodar data at various heights. The first preliminary result for the period from 2004 to 2007 was presented briefly in [6]. Now we represent more detailed and extended statistical results which contain all simultaneous hourly-averaged data of chemical measurements of the air composition and sodar measurements of wind velocity at Moscow University for the period since November the 11th of 2004 till June the 30th of 2008. The average ground concentrations of six gases have been calculated under different values of V at four heights: 40 m, 60 m, 100 m and 200 m. Total sampling of hours of simultaneous measurements consists nearly of 15.000 hours at 40 m and at 60 m. As one knows the number of reliable sodar measurements decreases with a height so that at the level of 100 m a sampling is equal nearly to 14.500 whereas at 200 m height – nearly to 11.500 only. The results for the levels 40 and 200 m are presented below on Fig.3 and 4 correspondingly.

The main tendency of almost all gases, except only ozone, is decrease of their concentrations with a growth of wind velocity. Some primary products of fuel combustion such as nitrogen oxide and carbon oxide demonstrate monotonous dependencies which are close to hyperbolic functions so that the more is wind velocity the less is in average their ground concentration. It is a result of combined action both of wind velocity and of thermal stratification because calm conditions are connected usually with surface inversions at night. Evidently, sources of NO and CO are low (mostly, urban traffic close to the ground). So, both these factors lead to slow dispersion of NO and CO. Similar dependence is seen for the secondary pollutant NO_2.

Unlike them SO_2 which is mainly product of high sources (city heating, plants, etc.) demonstrates non-monotonous function with maximal values of concentrations under wind velocity in a range from 1 to 2 m/s – both at 40 m, and at 200 m. It means that in calm conditions smoke-plumes from chimneys move as a rule upward above the ground. Ozone due to its specific (increase with a height due to dry absorption of this gas by the ground, especially at night in conditions of surface inversions) has a contrary dependence so that the more is wind velocity the higher is ground concentration of O_3 because more intensive vertical mixing leads as a rule to downward transport of this gas from upper air layers to the ground.

The only exception from this total tendency is a bit lower average concentrations of the ground ozone under intermediate values of V in range from 7 to 9 m/s at 40 m height (and, correspondingly, under values of V from 14 to 17 m/s at 200 m height) in the comparison with both less and more velocity values.

One more gas which ground concentration was analyzed among others is carbon dioxide. Unlike other mentioned above gases, CO_2 is not an air pollutant because it represents constant part of even ideal clean air. Nevertheless, even carbon dioxide demonstrates the same total dependence on the wind velocity as minor gases except ozone: the more is V the less is CO_2 concentration as a rule. However, it should be noted that its function at the height of both 40 m, and 200 m is not monotonous because there is an increase of CO_2 concentration under strong winds (from 7 to 12 m/s at 40 m and from 15 to 18 m/s at 200 m).

All mentioned above empiric functions are statistically meaningful at least with probability of 0.95 with the account of confidence intervals.

For more detailed analysis of possible changes of these tendencies with a height Figure 5, in addition to Figures 3 and 4, represents for three gases (ozone, nitrogen oxide and sulfur dioxide) dependencies of

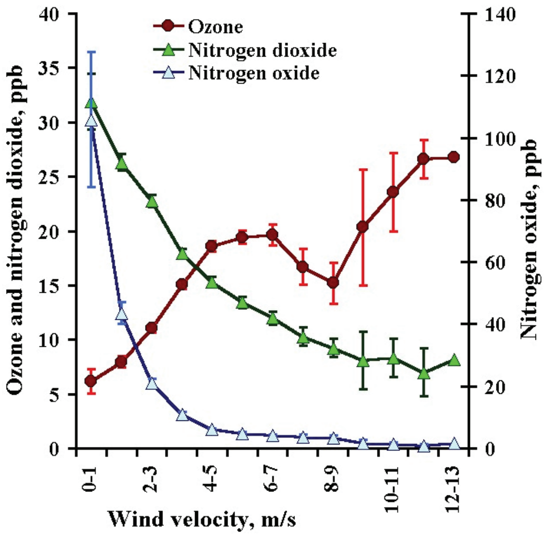

a) Ozone and nitrogen oxides;

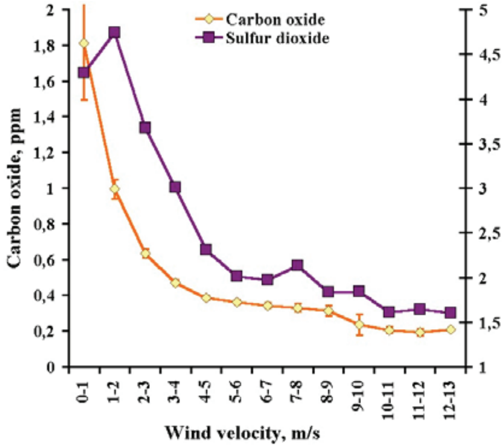

b) Carbon oxide and sulfur dioxide;

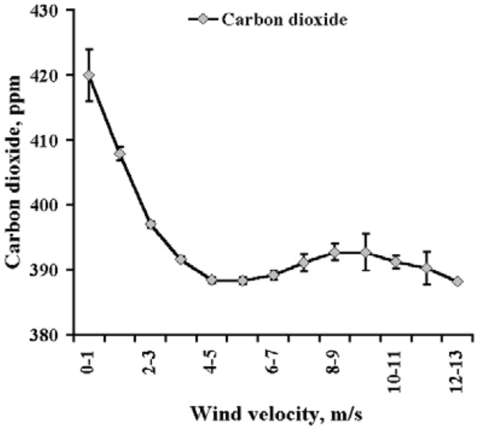

c) Carbon dioxide.

Figure 3. Influence of wind speed at 40 m height on the ground concentrations of minor gases by hourly-averaged data in 2004-2008.
Confidence intervals are calculated with significance level of 0.05.

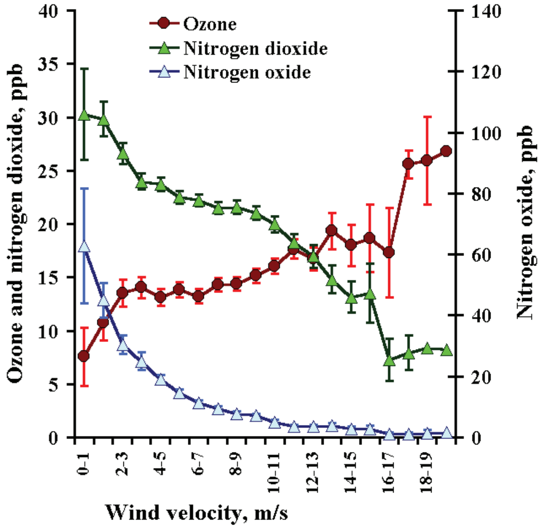

a) Ozone and nitrogen oxides;

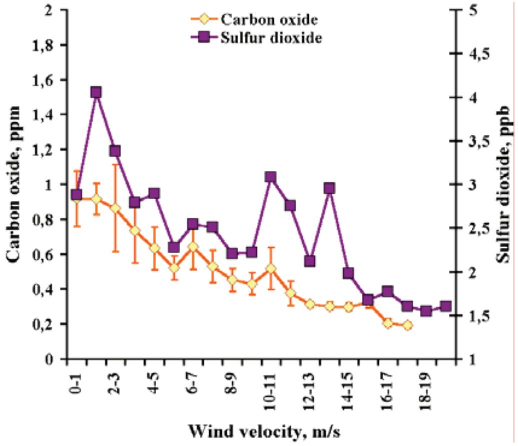

b) Carbon oxide and sulfur dioxide;

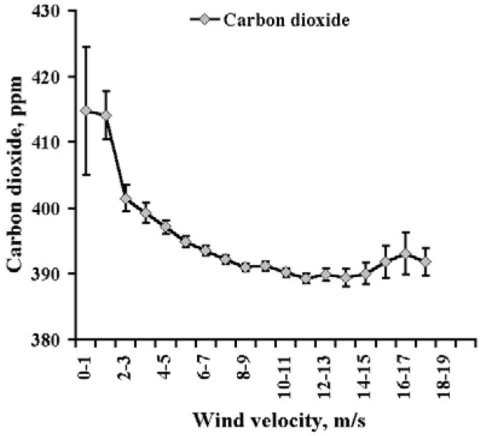

c) Carbon dioxide.

Figure 4. Influence of wind speed at 200 m height on the ground concentrations of minor gases by hourly-averaged data in 2004-2008.
Confidence intervals are calculated with significance level of 0.05.

their concentrations on the wind velocity at all four heights. As it is seen mentioned above functions for each gas are principally the same everywhere.

For instance, dependences of NO on V demonstrate simple and close to hyperbolic functions at all heights. Function of O_3 is complicated and non-monotonous but in general it demonstrates a growth of its ground concentrations under strong winds at any height. The highest concentration of SO_2 is observed under V in range from 1 to 2 m/s at any height as well.

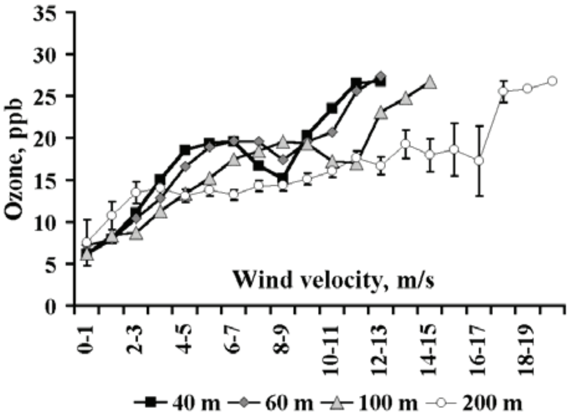

a) Ozone;

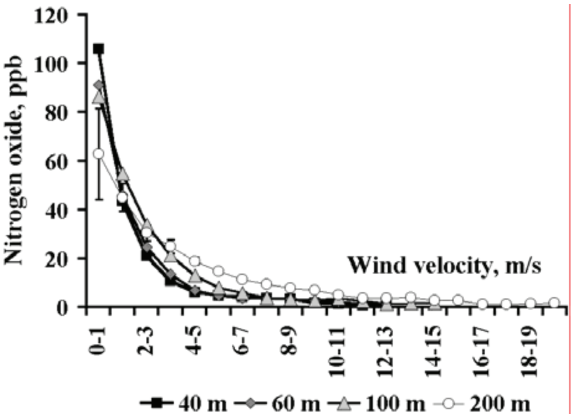

b) Nitrogen oxide;

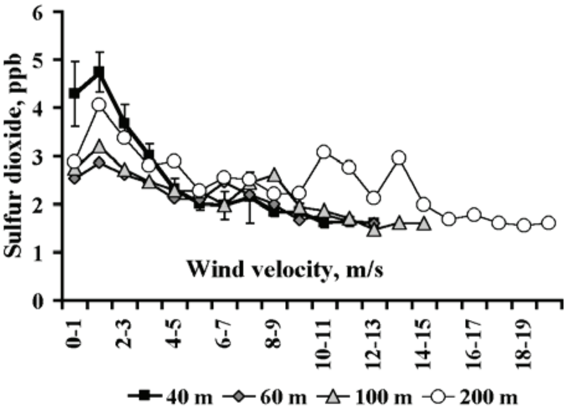

c) Sulfur dioxide.

Figure 5. Influence of wind speed on the ground concentrations of a gas at different heights. Hourly-averaged data for period of 2004-2008 were used. Confidence intervals are calculated with significance level of 0.05.

3. CONCLUSIONS

The ground concentrations both of minor gases and of carbon dioxide are clearly dependent on the wind velocity in the ABL. For NO, NO_2, SO_2, CO and CO_2 functions of velocity are decreasing whereas for O_3 it is mainly increasing.

ACKNOWLEDGEMENTS

This work has been supported by Russian Basic Research Foundation (projects No. 10-05-01130 and 10-05-00272).

REFERENCES

1. Russell P.B. and Uthe E.E., 1978: Acoustic and direct measurements of atmospheric mixing at three sites during an air pollution incident. *Atm. Environment*, **12**, pp.1061-1074.
2. Prater B.E, and Colls J.J., 1981: Correlations between acoustic sounder dispersion estimates, meteorological parameters and pollurion concentrations. *Atm. Environment*, **15**, No.5, pp.793-798.
3. Lokoshchenko M.A., Yavlyaeva E.A. and Kirtzel H.-J., 2009: Sodar data about wind profiles in Moscow city. *Meteorologische Zeitschrift*, **18**, No. 3 (June), pp.321-330.
4. Elansky N.F., Lokoshchenko M.A., Belikov I.B., Skorokhod A.I., and Shumskii R.A., 2007: Variability of Trace Gases in the Atmospheric Surface Layer from Observations in the City of Moscow. *Izvestiya, Atmospheric and Oceanic Physics*, **43**, No.2, pp.219-231.
5. Lokoshchenko M.A. and Elansky N.F., 2008: Use of sodar data for analysis of relations between concentrations of minor atmospheric gases. In: Proceedings of the 14th ISARS, Riso National Laboratory, Denmark. IOP Conference Series: Earth and Environmental Science, **1**, No.012028. IOP Publishing, Bristol and Philadelphia.
6. Lokoshchenko M.A., 2011: Results of long-term sodar measurements of wind profiles above Moscow city. In: Proceedings of the European Geosciences Union (EGU) General Assembly, Vol.13, paper index: 13844 (published on-line as presentation).

COMPARING LIDAR ANEMOMETRY WITH OBSERVATIONS FROM SCINTILLOMETERS AND ULTRASONIC ANEMOMETERS; IN LONDON AND HELSINKI.

Curtis Wood[1,2], Lukas Pauscher[3], Helen Ward[3,4], Rostislav Kouznetsov[1,5], Ewan O'Connor[1,2], Anne Hirsikko[1], Ari Karppinen[1], Janet Barlow[2], Simone Kotthaus[3], Mariana Gouvea[3], Sian Lane[2], CSB Grimmond[3]

[1]*Finnish Meteorological Institute, Helsinki, Finland*
[2]*Department of Meteorology, University of Reading, United Kingdom*
[3]*Kings College London, United Kingdom*
[4]*Centre for Ecology and Hydrology, Wallingford, United Kingdom*
[5]*A. M. Obukhov Institute of Atmospheric Physics, Moscow, Russia*

Curtis Wood, curtis.wood@fmi.fi

ABSTRACT

Urban boundary-layers evolve a complex structure in response to urban surfaces. Within roughness sublayers there are typically a range of morphologies at different scales: comprising a mixture of building shapes, parks, trees and larger-scale features (e.g. rivers). Over such heterogeneous landscapes, it can be challenging to conduct representative micro-meteorological analyses from point measurements.

In London and Helsinki, comparisons were made between ultrasonic anemometry (a micro-meteorological standard) and two instrumental techniques providing wind speeds representative of larger scales (several hundred meters): a scintillometer (Scintec BLS 900) and a scanning Doppler lidar (HALO Photonics Streamline). Dual-beam scintillometry provides estimates of wind speed perpendicular to the beams; the lidar was configured with a novel scanning strategy, enabling an estimation of a horizontal transect of wind vectors.

Field tests began in October 2011 in Helsinki along a 4.2 km path at about 50 m height; sonic anemometry is available near both ends of the path. A field experiment in London (18th February to 17th May 2011) focused on an area of central London around the River Thames: an 808-metre scintillometer path crossed the river at about 20–35 m height and its wind speed was compared with wind-speed data from the lidar (plus, ultrasonic anemometry was available near one end of the path). These new lidar anemometry methods were verified against measurements from the scintillometer and ultrasonic anemometers. Furthermore, the path-resolved transect of wind vectors across the River Thames revealed interesting atmospheric flow features, such as channeling and flow speed-up.

ACKNOWLEDGMENTS

This work has been supported by the EC FP7 project ERC PBL-PMES (No. 227915), EPSRC EP/G029938/1, EUF7 MegaPoli (212520), EUF7 Bridge (211345), UK Met Office, NERC NE/H00324X/1. Guy Pearson advised on implementing LIDAR SNR quality control. Marc Stringer and Gary Robinson provided data support on the ACTUAL project. Rosy Wilson and John Lally provided technical support on the ACTUAL project. Thanks to all people/students at KCL who contributed to the data collection; KCL Directorate of Estates & Facilities for giving us the opportunity to operate the various measurement sites; funding support from KCL; Westminster City Council, BT, and Guy's Hospital. Related project websites: http://urban.fmi.fi and http://www.actual.ac.uk.

URBAN BOUNDARY LAYER STRUCTURE UNDER LOW LEVEL JETS AS OBSERVED OVER LONDON, UK: IMPLICATIONS FOR WIND ENGINEERING ASPECTS

Christos H. Halios, Daniel R. Drew, Siân E. Lane,

Janet F. Barlow

Department of Meteorology, University of Reading, Earley Gate, P.O. Box 243, Reading, RG6 6BB

ABSTRACT

Low Level Jets (LLJs), defined as wind speed maxima within the lowest several hundred metres above ground, influence the structure and dynamics of the atmospheric boundary layer. They are important due to practical implications for flight safety, air pollution and wind engineering, particularly with the potential wind loading on the structure of tall buildings. Yet, relatively few studies have examined LLJs over urban areas. The aim of this study is twofold: (a) to examine the structure and dynamics of the Urban Boundary Layer (UBL) over London, when LLJs are present, under low and high wind conditions related with stable and near neutral stratification respectively. And (b) to evaluate the wind profiles specified in the UK wind loading code under these conditions. Data were collected during the ACTUAL project (Advanced Climate Technology Urban Atmospheric Laboratory) which has established platforms of instrumentation in London for longer term observations of urban meteorology. The UBL vertical structure was monitored with a Halo-Photonics scanning Doppler lidar. Results were compared with (a) data obtained from an eddy correlation system, installed at the BT-tower (190.8 m agl) and (b) results from the Met Office's Unified Model (UKV, variable-resolution model that is run for the UK weather forecast). The LLJ origin was studied using model results. LLJs modification due to different aerodynamic characteristics of the urban area under different wind directions was examined with morphological data. Wind profiles were compared with predictions of the Deaves and Harris model which is used in the UK wind loading code.

1. INTRODUCTION

Low level wind maxima with the form of LLJs have attracted a great deal of interest due to their importance for air pollution studies, wind energy production, and aviation safety. Various criteria have been proposed for the identification of LLJs; also, a number of mechanisms have been suggested for the LLJ development. LLJs can develop due to inertial oscillations in the boundary layer (Blackadar 1957), baroclinicity over sloping terrain (Holton 1967), gap winds (Macklin et al. 1990), or flow separation (Oettl et al. 2001). In some cases several factors contribute to LLJ formation such as the combination of large scale processes with mesoscale forcing due to the complex terrain (Liu et al. 2000), or frontal events in the stable marine boundary layer (Helmis et al., 2012).

During the last years, a few studies have experimentally examined LLJs in the urban environments at Washington (Frehlich et al., 2006), Oklahoma City (Wang et al., 2007) and Moscow (Kallistratova and Kouznetsov, 2012). Results from the later study highlighted the role of thermal stratification and the LLJ modification over the urban area as a result of the thermal structure of the urban atmosphere.

The aims of this study are a) to examine the structure and dynamics of the UBL over London under a LLJ, and b) to compare observed wind profiles with the predictions of the models in the various wind loading codes: the Deaves and Harris model, the power law and the log-law. Comparisons aim to test whether a more detailed representation of the urban surface is needed to provide an improved estimate of the wind profile.

2. SITE AND METHODS

The UBL in London was monitored by three instrumentation platforms that were deployed in the frame of the ACTUAL project (Advanced Climate Technology Urban Atmospheric Laboratory). ACTUAL aims to develop the tools to monitor and simulate urban climate from city down to building scale. The vertical structure of the UBL was measured with a Halo-Photonics scanning Doppler lidar installed at the roof-top of the Westminster City Council's building (18m agl, lat. 51^{O} 31' 17'' N lon. 0^{O} 09' 40'' W). Two modes of operation were used: continuous vertical stare, and the Doppler beam swinging (DBS) method of wind profiling (Pearson et al., 2009). The instrument operates at 1.5 μm wavelength, the pulse repetition frequency is 20 KHz, the sampling frequency is 30 MHz (with integrated signals being outputed every 3.6 s), and the vertical resolution is 30 m. Only spurious returns are available within 90m of the lidar, therefore results are presented from heights of 100m upwards.

The heat and momentum fluxes were analyzed with measurements from two identical instrumentation platforms; they were equipped with eddy correlation systems (Gill Instruments R3-50 sonic anemometer, and Licor Li-7500 Hygrometer), net radiometers (Kipp and Zonen CNR4) and weather stations (Vaisala WXT520). They were installed at the Westminster City Council Library roof-top and at the BT-tower (190.8 m, agl lat. 51^{O} 31’ 17’’ W lon. 0^{O} 08’ 19’’ N). The BT-tower is the tallest building within several kilometres, with good exposure to winds in all directions. Data from the fast response sensors were logged at 20 Hz and were subject to quality assurance checks (Wood et al., 2010).

Following Barlow et al., (2011), mixing height (MH) was derived from lidar turbulence measurements by considering a threshold value of $\sigma_w^2 = 0.1 m^2 s^{-2}$. In order to check the sensitivity of the calculated height to changes in the threshold, a 30% perturbation of this threshold value was applied.

The UKV, a variable-resolution version of the UK Met Office Unified Model that is run for the UK weather forecast, was employed. The grid spacing is 1.5 km over most of the domain, including London. The model was run in operational configuration, thus the urban scheme and the boundary layer scheme that are used for forecasting were tested against observations. (Lean et al., 2011).

The neutral log-law mean velocity profile equation is given by:

$$V = \frac{u_*}{k} \ln \frac{z}{z_0} \qquad (1)$$

where u_* is the friction velocity, z_0 the aerodynamic roughness height and k = 0.40 is von Karman’s constant. The power-law model uses an empirical formula for the mean velocity profile of the form:

$$\frac{V}{V_{ref}} = \left(\frac{z}{z_{ref}} \right)^a \qquad (2)$$

where V_{ref} is the mean wind speed at some arbitrary reference height z_{ref} and a is the exponent of the power-law. The Deaves and Harris (1978) model is based on a modification of the classic logarithmic law:

$$V = \frac{u_*}{k} \left[\ln \frac{z}{z_0} + 5.75 \left(\frac{z}{h} \right) - 1.88 \left(\frac{z}{h} \right)^2 - 1.33 \left(\frac{z}{h} \right)^3 + +0.25 \left(\frac{z}{h} \right)^4 \right] \qquad (3)$$

where h is the equilibrium boundary layer height.

3. RESULTS

During the period from 28/9 to 2/10/2011 a high pressure system was centred over Europe, resulting in moderate southerly flow, cloudless skies and temperatures warmer than average over the UK. Conditions favoured an urban heat island over London, and the lack of clouds was advantageous when comparing model and observations. Strong temperature inversions were observed both at the surface overnight and capping the boundary layer, associated with anti-cyclonic subsidence. Results from 30/9 (see Fig. 1) are presented here, which was a typical day in terms of urban boundary layer evolution.

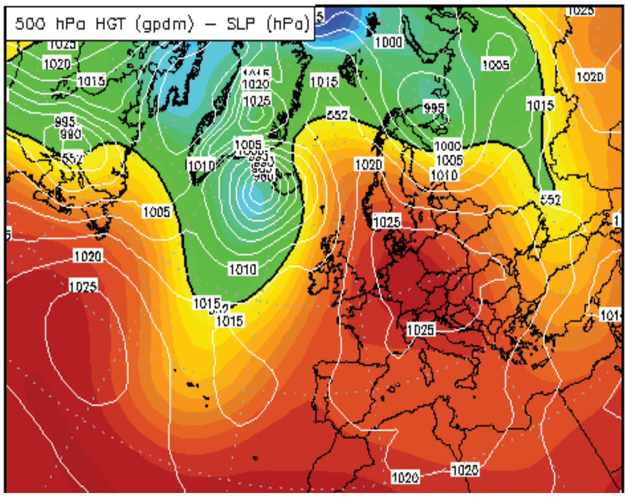

Figure 1. Geopotential height at 500 hPa (colourscale) and sea level pressure (white contours) for 30/9/2011.

Fig. 2 shows the Doppler lidar data: the nocturnal LLJ which was initially observed during the early night hours appeared again during the day-time from 10:00 – 13:00 at higher levels (approximately 600-700 m).

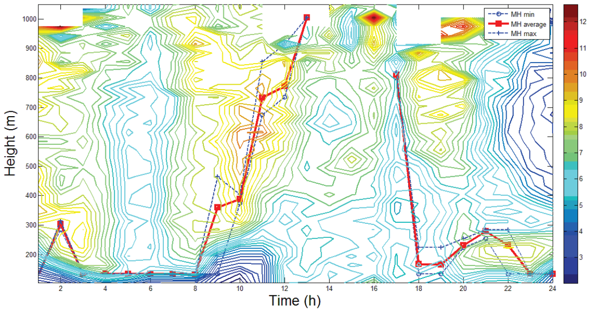

Figure 2: Contour plot of the wind speed (in m s^{-1}) and mixing height (MH) from lidar measurements. Minimum and maximum MHs are due to 30% perturbation in threshold criterion used in derivation.

During the night time the mixing height is lower than 150 m, except at 02:00, when the observed peak (close to 300 m) is probably associated with the appearance of the LLJ. A similar pattern repeats after 20:00 when wind maxima appear on the top (or very close to) the MH. It is evident that during the morning and noon hours the LLJ follows closely the development of the MH.

Comparison between data obtained from the DBS method with data from the BT sonic anemometer gave good agreement; good agreement was also found between the lidar and sonic estimated variance of the vertical wind speed component (not shown here).

Fig. 3 shows the development of the jet spatially, as simulated by the UKV. Results from the central (BT-tower), southern (Croydon - lat. 51^{O} 17' W lon. 0^{O} 7'N) and northern (Barnet - lat. 51^{O} 38' W lon. 0^{O} 7' N) London suburban areas are presented. By comparing Figs 2 and 3, it can be seen that the peak of the LLJ measured by the lidar was 100 – 200 m higher than the modeled peak. At the same time the model underestimates the boundary layer depth, possibly due to underestimated heat fluxes. Between 1200 and 1700 the LLJ is not visible in the lidar data, suggesting that it has either been broken down by convective mixing, or lifted above the range of the lidar.

Given the southerly flow, Croydon is approximately 18km upwind of London, whilst Barnet is approximately 15 km downwind. At Barnet the jet appears higher and is weaker, probably indicating the influence of the convective UBL. In Kallistratova and Kouznetsov (2012) significant differences between the rural and urban LLJs were observed, with urban LLJs being higher and weaker. They provided evidence that the LLJ mechanism was the inertial oscillation induced in the wind field by frictional decoupling during the evening transition. In our study evidence of inertial oscillations could not be deduced from hodographs (not shown here) at the height of the jet's core.

Comparisons between the measured and theoretically deduced (see eqn. 1-3) profiles for the first 500 m of the UBL are presented in Fig. 4, V_{ref} is taken to be the lowest measured windspeed, $z_0 = 0.8m$, $\alpha = 0.27$ and $h = 3250m$ (Cook, 1997).

It is clear that greater differences are observed when the convective UBL is still developing (09:00, 10:00), and when the LLJ is within the first 500 m. The agreement between the measured and theoretically deduced profiles is better under the fully developed convective UBL, when the LLJ is much higher.

4. CONCLUSIONS

This study presents a case study of the structure of the Urban Boundary Layer over London under the presence of a LLJ. The LLJ was determined from lidar measurements and was seen to persist from night-time into the day-time convective boundary layer.

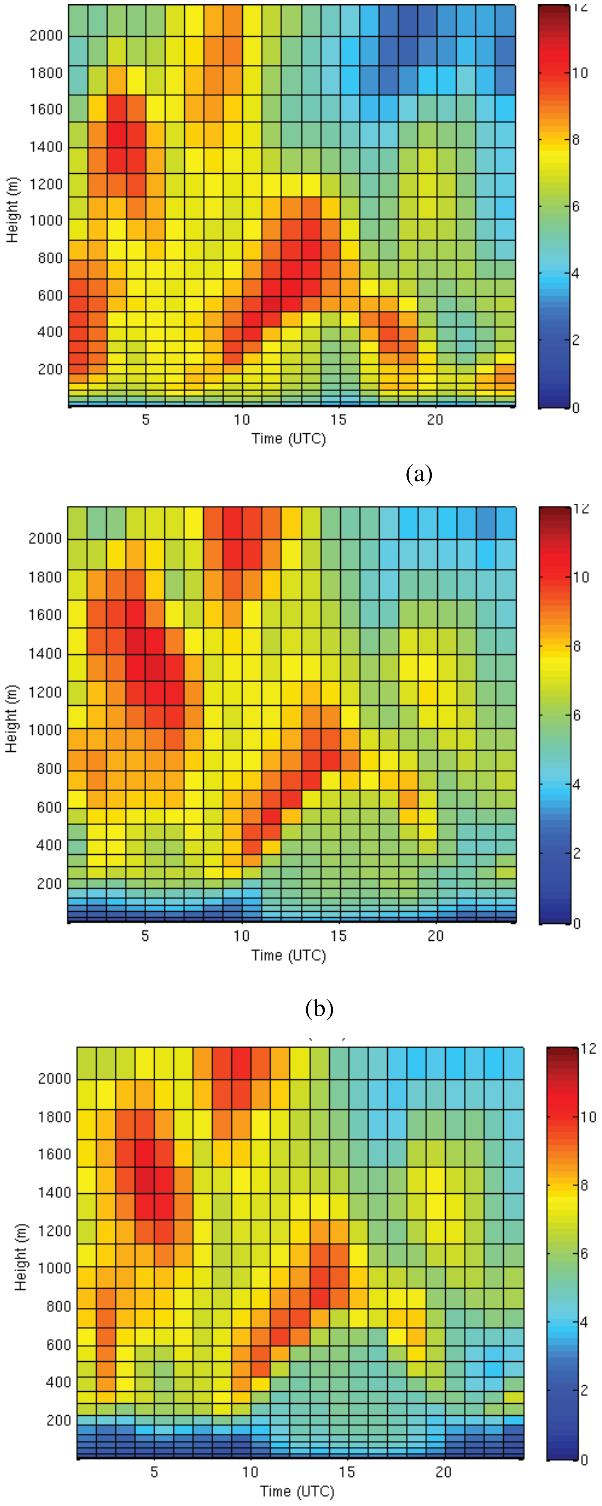

(a)

(b)

(c)

Figure 3: UKV model results for the upwind (a – Croydon) downwind (b – Barnet) and central (c – BT-tower) parts of London.

The jet maximum was located just above, and closely followed, the MH as determined from lidar turbulence measurements.

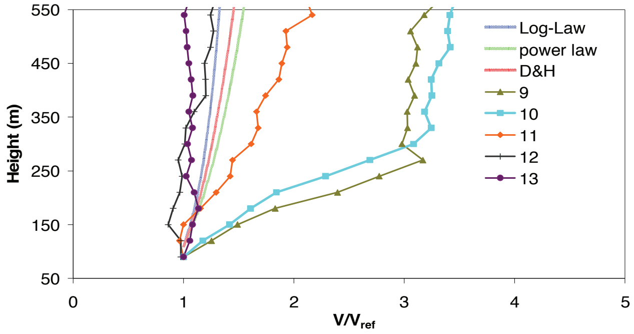

Figure 4: Measured and theoretically deduced normalized wind profiles. V_{ref} is at the first measurement height (90m) and D&H is the Deaves and Harris model.

Runs with the UK Met Office UKV model showed a shallower mixing height and lower jet, suggesting that urban heat fluxes may have been under-represented. The model runs also provided evidence that the convective UBL weakens the LLJ across London, as well as shifting the jet core upwards. It was found that the wind profile models which are usually employed in wind loading codes fail to predict the wind profile under the developing convective UBL, when the LLJ core is low. Further research is underway to examine the frequency of LLJs over the urban area, and the accuracy of the wind loading code in predicting urban wind profiles across a range of conditions.

ACKNOWLEDGEMENTS

The authors would like to acknowledge Rosy Wilson and John Lally for technical support, Humphrey Lean and Emilie Carter (UK Met Office) for providing the model data, and Curtis Wood for discussions about the research. The ACTUAL project was funded under EPSRC grant number EP/G022938/1 (www.actual.ac.uk).

REFERENCES

1. Barlow J.F., Dunbar T.M., Nemitz E.G., Wood C.R., Gallagher M.W., Davies F., O'Connor E. and Harrison R.M., 2011: Boundary layer dynamics over London, UK, as observed using Doppler lidar during REPARTEE-II, *Atmos. Chem. Phys.*, **11**, 2111–2125

2. Blackadar A.K. (1957) Boundary Layer Wind maxima and their significance for the growth of nocturnal inversions, Bull Am Meteorol Soc, 38:283-290.

3. Cook N.J., 1997: The Deaves and Harris ABL model applied to heterogeneous terrain Journal of Wind Engineering and Industrial Aerodynamics **66 (3)**, 197–214

4. Deaves D.M., Harris, R.I., 1978: A mathematical model of the structure of strong winds. Report No. 76. United Kingdom Construction Industry Research and Information Association.

5. Frehlich R., Meillier Y., Jensen M.L., Balsley B., and Sharman R., 2006: Measurements of Boundary Layer Profiles in an Urban Environment, *Journal of Applied Meteorology and Climatology*, **45**, 821-837.

6. Helmis C.G., Wang Q., Sgouros G., Wang S. and Halios C.H., 2012: Investigating the Summertime Low-Level Jet over 1 the East Coast of the United States: A case study. Submitted to *Boundary-Layer Meteorology*

7. Holton J.R., 1967: The diurnal boundary layer wind oscillation above slopping terrain., *Tellus,* **XIX, 2, pp.** 199 – 205.

8. Kallistratova M.A., Kouznetsov R.D., 2012: Low-Level Jets in the Moscow Region in Summer and Winter Observed with a Sodar Network, *Boundary-Layer Meteorology*, **143**, pp. 159-175.

9. Lean H.W., Bornemann J., Tang Y., Mittermaier M., Roberts N. and Trueman M., 2011: Experiences with a 1.5km version of the Met Office Unified Model for short range forecasting, 91st American Meteorological Society Annual Meeting, 25 Jan. 2011.

10. Lenschow, D. H., Wyngaard, J. C., and Pennell, W. T., 1980: Mean-field and second moment budgets in a baroclinic, convective boundary layer, *J. Atmos. Sci.* **37**, 1313–1326.

11. Liu M., Westfall L.D., Holt R. T., Xu Q., 2000: Numerical Simulations of a Low Level Jet over Complex Terrain in Southern Iran. *Monthly Weather Review*, **128**, pp. 1309-1327.

12. Macklin S.A., Bond N.A., Walker J.P., 1990, Structure of a Low Level Jet over Lower Cook Inlet, Alaska. *Monthly Weather Review*, **110 (12)**, *pp 2568-2578.*

13. Oettl D., Almbauer R.A., Sturm P.J., Piringer M., Baumann K., 2001: Analysing the nocturnal wind field in the city of Graz. *Atmospheric Environment* **35**, pp 379-387.

14. Sorbjan, Z. 1989: Structure of the atmospheric boundary layer. Prentice Hall, New Jersey, USA.

15. Wood C.R., Lacser A., Barlow J.F., Padhra A., Belcher S.E., Nemitz E., Helfter C., Famulari D., and Grimmond C.S.B., 2010: Turbulent flow at 190 metres above London during 2006–2008: a climatology and the applicability of similarity theory, *Boundary-Layer Meteorology*, **137**, 77–96.

Session 9 – Oral Presentations

SOME CHALLENGES OF WIND MODELLING FOR MODERN WIND TURBINES: THE WEIBULL DISTRIBUTION

Sven-Erik Gryning[1], Ekaterina Batchvarova[2], Rogier Floors[1], Alfredo Peña[1]

[1]*Wind Energy Department, Technical University of Denmark, Risø Campus, Roskilde, Denmark, sveg@dtu.dk*
[2]*National Institute of Meteorology and Hydrology, Sofia, Bulgaria, ekaterina.batchvarova@meteo.bg*

ABSTRACT

Wind power assessments, as well as forecast of wind energy production, are key issues in wind energy and grid related studies. However the hub height of today's wind turbines is well above the surface layer. Wind profiles studies based on mast data show that the wind profile above the surface layer depends on the planetary boundary layer (PBL) structure and height, thus parameters that are not accounted for in today's traditional applied flow simulation models and parameterizations.

Here we report on one year of measurements of the wind profile performed by use of a long range wind lidar (WSL 70) up to a height of 600 meters with 50 meters resolution. The lidar is located at a flat coastal site.

The applicability of the WRF model to predict some of the important parameters for wind energy has been investigated. In this presentation, some general results on the ability of WRF to predict the wind profile and the turning of the wind direction with height will be touched upon, but we mainly will discuss the long term distribution of the wind speed, which is often represented by a Weibull distribution. It was found that above 100 meters both the measured scale (A) and shape (k) parameter are larger than predicted by WRF. The under prediction of scale parameter is in accordance with the general underestimation of the wind speed by WRF. The consequence for wind energy is discussed and a simple parameterization for the shape parameter is put forward.

1. SITE AND MEASUREMENTS

The measurements were carried out at the Danish National Test Station of Wind Turbines at Høvsøre, which is located at the western coast of Jutland, Fig. 1. Except for the presence of the North Sea to the west, the terrain is flat and homogeneous consisting of grass, various agricultural crops and a few shrubs. The intensively instrumented 116.5 m high reference meteorological mast is located about 1.8 km east of the coastline and south of the closest wind turbine stands. Wind speed is measured at 10, 40, 60, 80, 100, 116.5 m with Risø cup anemometers and the wind direction at 10, 60 and 100 m. with wind vanes. Observations from the 160 m top level at the nearby light tower are also used. Both the light tower and the meteorological mast are instrumented with METEK Scientific USA-1 sonic anemometers installed at heights: 10, 20, 40, 60, 80, 100 and 160 m. The three-dimensional wind speeds are measured with a frequency of 20 Hz and then reduced to 10-min statistics of linearly de-trended mean values, variances and co-variances.

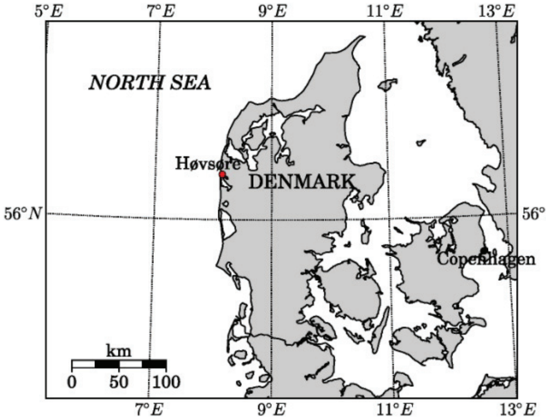

Figure 1 Geographical location of the Høvsøre site.

In addition a pulsed wind lidar (WLS70) has been operating near the meteorological mast between April 2010 and March 2011. The wind lidar is equipped with a rotating silicon prism providing an optical scanning cone of 15 degrees to zenith. The lidar scans the atmosphere at four azimuth angles separated by 90°. One 360 degree full scan (rotation) is performed about every 30 s. The wind lidars Doppler shift based measurements of the wind are available measures from 100 m above the ground and every 50 m up till 1 to 2 km height dependent on the attainable 10-min averaged Carrier to Noise (CNR) ratio. The upper measuring height is often determined by the cloud base where the lidar signal (1.55 nm) largely weaken.

2. NUMERICAL MODELLING

Wind profiles were predicted using a research real-time forecast system based on the WRF ARW model version 3.2.1, developed by the National Centre for Atmospheric Research (NCAR), [1]. It is a numerical weather prediction and atmospheric simulation system designed for both research and operational applications. Data for initial and boundary conditions come from the Final Analyses (FNL, Global Final Analysis Data) of the National Center for Environmental Prediction (NCEP, USA) global model. The physical options of model setup include the Noah land surface scheme [1] and the Thompson microphysics scheme [2]. The WRF model calculates the meteorological parameters at 41 vertical levels from the surface to pressure level 100 hPa. Eight of these levels are within the height range of 600 m that is analyzed in this study and the first model level is at 14 m.

When the model is run in analysis mode as in this study, it uses the NCEP Final Analysis (FNL) global boundary conditions that are available every 6 hours on a 1 x 1 degree grid. Two domains with a horizontal grid size of 18 and 6 km respectively are used. The simulations are initialized every 10 days at 12:00 and after a spin up of 24 hours a time series of 10 minutes simulated meteorological forecast data from 25 to 264 hours is generated. In order to prevent the model from drifting away from the large scale features of the flow, the model is nudged towards the FNL analysis. Nudging is applied for the wind, temperature and humidity above the 10th model level, which approximately corresponds to 1400 m, on the outermost model domain during the whole simulation period.

3. WEIBULL DISTRIBUTION

The long-term frequency distribution of the horizontal wind speed is often presented in the form of a two parameter Weibull distribution. This distribution has received considerable attention in relation to assessment of wind energy from meteorological observations.

The Weibull distribution of the horizontal wind speed can be expressed as:

$$f(u) = \frac{k}{A}\left(\frac{u}{A}\right)^{k-1} \exp\left(-\left(\frac{u}{A}\right)^{k}\right) \tag{1}$$

where $f(u)$ is the frequency of occurrence of the wind speed u. In the Weibull distribution the scale parameter A has units of the wind speed. It is proportional to the average wind speed $\langle u\rangle$ for the entire distribution. It is related to the wind speed through:

$$\langle u\rangle = A\,\Gamma(1 + 1/k) \tag{2}$$

where Γ represents the gamma function and k is the shape parameter in the Weibull distribution: for typical wind speed distributions over homogeneous terrain k is in the range 2 to 3. For decreasing k the mode of the distribution shifts towards lower values of the wind speed at the same time as the probability for higher wind speeds increases.

From the measurements and simulations of the wind speed the A and k parameters in the Weibull distribution were derived by use of the Climate Analyst which is a part of the Wind Atlas Analysis and Application Program (WAsP).

3.1 Scale parameter

The comparison of the modeled A parameter with measurements shows similarities with the wind speed. Below 60 meters the WRF predicts well the A parameter. Above 60 meters the simulated scale parameter is gradually underestimating the measurements more and more, Fig. 2.

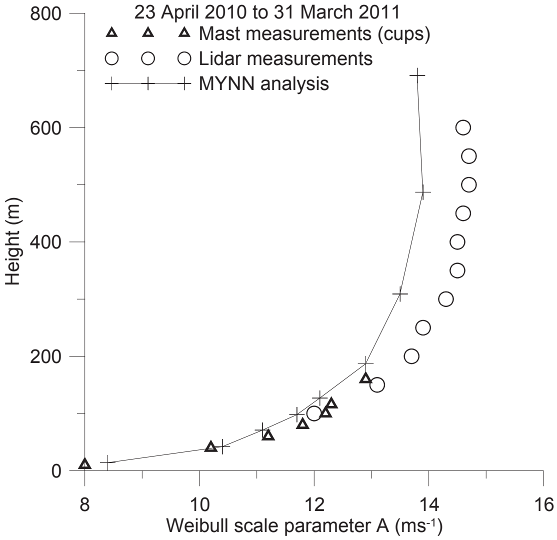

Figure 2. Profiles of the scale parameter in the Weibull distribution estimated from measurements and simulations.

3.2 Shape parameter

Contrary to the scale parameter, which has a rather smooth vertical profile, the shape parameter k has a very distinct form. Investigations over land have revealed [3] and[4] that k is controlled by 2 regimes of the atmosphere, the large-scale wind climate and the local boundary-layer. This results in a characteristic vertical profile of the shape parameter. It increases from its value near the ground up to a maximum located at around 100 to 200 meters height, in dependence of the balance between the diurnal variation of the local meteorological conditions and the variability of the synoptic conditions prevailing in the region. The height of the maximum in the k profile is associated with the height of the stable boundary-layer as well as the reversal of the wind regime that occur in stable nights where the diffusion of momentum is inhibited, resulting in low wind surface winds while the wind speed above the stable boundary-layer increases.

It is found that the WRF simulations agrees well with the measurements up to 100 meters, while above that height the model generally underestimates the k parameter. The height of the maximum in the k-profile from measurements is about 200 m while it is lower for the model simulations, being about 120m.

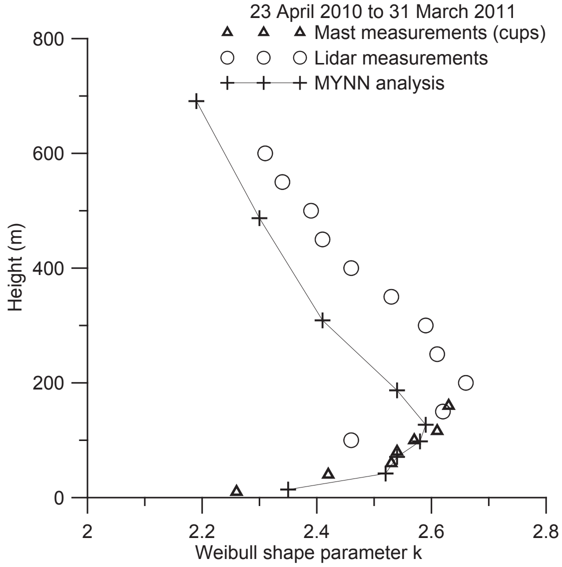

Figure 3. Profiles of the shape parameter in the Weibull distribution estimated from measurements and simulations.

3.3 Parameterization of k

Here is suggested a simple parameterization of the k-profile. Both the measurements and the modeling simulations show that the k parameter has a very distinct profile at Høvsøre. Similar profiles have been reported by [4]. The suggested relationship have 3 external parameters, the value of k in the surface layer, k_s, at a specific height z_s; the value of k in the free troposphere k_t and the height of the maximum in the k profile, z_r, sometime named the reversal height. The suggested simple parameterization for $z>=z_s$ reads:

$$k = c\,\frac{z-z_s}{z_r-z_s}\; exp\left(-\frac{z-z_s}{z_r-z_s}\right) + k_s - (k_s - k_t)\exp\left(-\frac{z_t}{z-z_s}\right) \qquad (3)$$

which has a maximum near z_r and will asymptotically approach the value of k_t in the upper part of the planetary boundary layer. The best fit value of c is near one, that of z_t is around 1000 meters and likely connected to the height of the convective boundary layer and the values of k_t is around 2, see Table 1. The application of the suggested parameterization is shown in Fig. 4.

Near the surface and well below z_r, the k-profile is almost linear, therefore for $z<z_s$ it is suggested to apply linear extrapolation. The derivative of the expression for the k profile reads:

$$\frac{dk}{dz} = c\,\frac{z_r - z}{(z_r - z_s)^2} exp\left(-\frac{z - z_s}{zr - zs}\right) \qquad (4)$$

where the right hand side of Eq. (3), the part dealing with the tropospheric adaption, has been neglected.

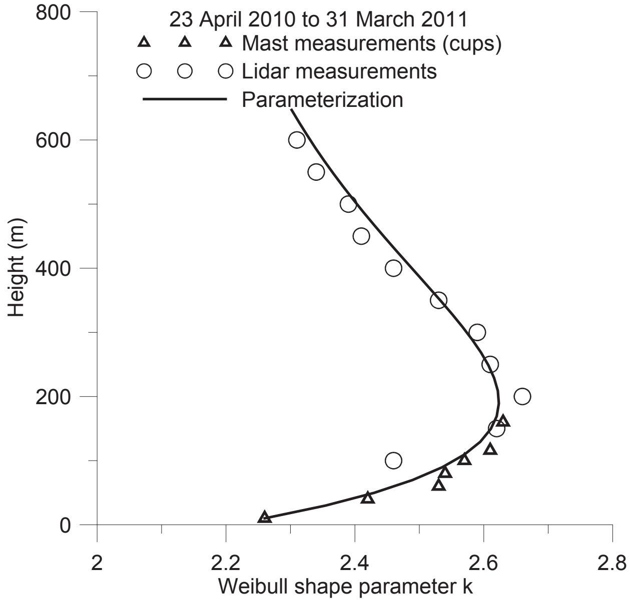

Figure 4. Measured k profile and the suggested parameterization in Equation (3). The parameterization is plottet for z_s=10 meter where k_s in this case can be seen to be 2.26, z_r=200 m and z_t is taken as 1000 m with k_t=2.

Table 2. Values of the parameters in Equation. (3) determined from the measurements.

c	k_t	z_r	z_t
1.0	2.0	200	1000

4. DISCUSSION

In this study a full year of measurements of the wind profile performed at a coastal site in a windy climate has been analyzed and compared to a simulations carried out with the WRF model. The measurements were carried out with a novel wind lidar that permitted wind profiles up to 2 km in favorable conditions in combination with a tall meteorological mast. Reference [5] found very good agreement with wind speed measurements carried out a with cup anemometer at 100 meters height and simultaneous wind lidar observations. The agreement deteriorates as the signal to noise become worse. A CNR ratio of -22 dB was found to be a fair compromise between the need for high quality measurements and a good height coverage of the wind profile. By filtering the observations with this CNR value and allowing for a number of technical problems resulted in data coverage of 31% where the missing data are distributed over the whole year. The wind rose from the wind lidar indicated predominantly westerly winds, i.e. from the sea.

The dominance of westerly winds has as consequence that the results from the analysis are influenced by the internal boundary-layer that forms downwind of the abrupt change between sea and land. The height of the internal boundary layer is typical 100 meters at the measuring site, it is shallower in stable conditions and higher at unstable atmospheric conditions [6] and thus comparable to the height of the maximum in the shape parameter in the Weibull distribution.

In this study the focus is on the wind profile and its Weibull distribution. Performing a WRF simulation requires a choice among the many parameterizations that are available in the WRF package. Presently there does not exists a generally accepted set of parameterizations for overall use, but the literature is still at a stage where specific set-up's is suggested in dependence of the climatic region and the specific parameters that the user wishes to model.

Other modeling aspects such as surface roughness, atmospheric stability and enhanced diffusion in the surface layer are discussed in [7]. Additional aspects rarely dealt although important for many practical applications are eddy diffusivity, turbulence kinetic energy, mixing length, temperature profiles and boundary-layer height just to mention a few [8].

The 1.5 order closure MYNN PBL scheme was used in this study and it was found that the WRF simulation predicts the general profile of the shape parameter quite well although it underestimates its value. It can be mentioned that the first order closure YSU PBL scheme is unable to predict the characteristic profile of the shape parameter, but this aspect is not shown here.

5. OUTLOOK

In the Tall Wind project one year data-sets of wind and aerosol profiles were created from measurements by remote sensing instruments and instrumented tall meteorological masts for two sites - Høvsøre in Denmark and Hamburg in Germany. The data are available for the COST ES0702 community through the participation of several Tall Wind project partners in EG-CLIMET. COST Action ES0702 aims at operational use of remote sensing technology in weather and climate models and all related applications. The present study is related to the evaluation of meso-scale models wind profile against long range wind lidar data at one of the sites. The outcome is important for the use of meso-scale models in wind climate applications and the downscaling studies on wind power potential.

ACKNOWLEDGMENTS

The study was supported by the Danish Council for Strategic Research, project number 2104-08-0025 named "Tall Wind". The study is a part of activities within the COST Actions ES1002 (WIRE) and ES0702 (EG-CLIMET). We would like to thank the Test and Measurements section of DTU Wind Energy for the maintenance of the Høvsøre database.

REFERENCES

1. Skamarock, W. C., Klemp, J. B., Dudhia, J., Gill, D. O., Barker, D. M., Duda, M. G., Huang, X.-Y., Wang, W. & Powers, J. G. (2008). A description of the Advanced Research. WRF version 3. NCAR/TN–475+STR, NCAR Technical note, Mesoscale and Microscale Meteorology Division, National Center for Atmospheric Research, Boulder, Colorado, USA, 113pp.

2. Thompson, G., Rasmussen, R. M., & Manning, K. (2004). Explicit forecasts of winter precipitation using an improved bulk microphysics scheme. part i: Description and sensitivity analysis. *Monthly Weather Review*, **132(2),** pp. 519-542.

3. Hellmann G. (1917) Über die bewegung der luft in den unteren schichten der atmosphäre. *Meteorol. Zeitschr.* **34**, pp. 273-285.

4. Wieringa J. (1989) Shapes of annual frequency distribution of wind speed observed on high meteorological masts. *Boundary-Layer Meteorology*. **47,** pp. 85–110

5. Peña, A., Hasager, C. B., Gryning, S.-E., Courtney, M., Antoniou, ., & Mikkelsen, T. (2009). Offshore wind profiling using light detection and ranging measurements. *Wind Energy*, **12,** pp. 105–124.

6. Floors, R., Gryning, S., Peña, A., & Batchvarova, E. (2011). Analysis of diabatic flow modification in the internal boundary layer. *Meteorologische Zeitschrift,* **20,** pp. 649–659.

7. Floors, R., Batchvarova, E., Gryning, S.-E., Hahmann, A. N., Peña, A., & Mikkelsen, T. (2011). Atmospheric boundary layer wind profile at a flat coastal site - wind speed lidar measurements and mesoscale modeling results. *Advances in Science and Research***, 6**, pp. 155–159.

8. Gryning, S-E., Batchvarova, E., Brümmer, B., Jørgensen, H. & Larsen, S. (2007). On the extension of the wind speed profile over homogemneous reaarion beyond the surface layer. *Boundary-Layer Meteorology*. **124,** pp. 251–268.

HIGH-RESOLUTION DOPPLER LIDAR MEASUREMENTS OF INLAND AND OFFSHORE WIND FLOW FOR WIND ENERGY APPLICATIONS.

Pichugina Y. L. [1,2], R. M. Banta[2], W. A. Brewer[2], J.K. Lundquist[3], R. M. Hardesty[2], Raul.Alvarez[2], and S. P. Sandberg[2]

[1]*Cooperative Institute for Research in Environmental Sciences (CIRES), 325 Broadway, Boulder, CO, 80305,U.S.A.*
Yelena.Pichugina@noaa.gov
[2]*Earth System Research Laboratory (ESRL), NOAA, 325 Broadway, Boulder, CO, 80305, U.S.A.*
Robert.Banta@noaa.gov, Alan.Brewer@noaa.gov, Mike.Hardesty@noaa.gov, Raul.Alvarez@noaa.gov,
Scott.Sandberg@noaa.gov
[3]*National Renewable Energy Laboratory (NREL), Golden, CO, U.S.A*
Julie.Lundquist@nrel.gov

ABSTRACT

Success in the Wind Energy (WE) industry depends on accurate information on wind properties in the turbine layer.

NOAA's High-Resolution Doppler Lidar (HRDL), a scanning, Doppler system, has been extensively used on land and at sea during the past two decades to obtain high-resolution profiles of wind speed, wind direction, and turbulence. Detailed analysis of these measurements can provide important insight into wind resources and wind-flow characteristics in different areas of the U.S., under different atmospheric and terrain-roughness conditions, and can be of great use in developing and evaluating wind-turbine and atmospheric models.

This paper will describe the HRDL ability to provide continuous measurements of wind flow with sufficient spatial and temporal resolution at turbine heights to study atmospheric processes that may impact the operational reliability and lifetime of wind turbines and their components.

Examples of the HRDL measurements during inland field programs in the Great Plains and offshore field programs in the Gulf of Maine will be shown illustrating wind characteristics which are important for the wind energy industry. These examples include low-level jet properties as well as time series and distributions of quantities such as wind speed, direction, and shear through the blade layer. HRDL was also used to obtain simultaneous measurements of vertical and horizontal wind flow features both upwind and downwind of a multi-megawatt wind turbine. Accounting for wakes is an important issue in the optimization of siting turbines in the wind farm, operational strategies to reduce wake effects, and improved design of wind turbines.

INTRODUCTION

The rapidly expanding wind-energy industry requires better characterization of wind flow at turbine heights, understanding of meteorological processes controlling boundary layer, and improved forecast of wind resourses. Wind measurements from tall (100-120 m) towers are limited inland and do not exist offshore. Due to the lack of data at turbine heights and the frequent decoupling of this layer from the surface, true climatologies of wind and turbulence at turbine heights are unknown. In the absence of observational data, the performance and accuracy of numerical weather prediction (NWP), computational fluid dynamics, and other numerical modeling outputs used for wind energy applications are unknown.

In this presentation we use wind measurements from NOAA High Resolution Doppler lidar (HRDL) during several field experiments to provide insight into the nature of the wind flows and illustrate the spatial and temporal variability of winds over land and over ocean. These studies have demonstrated the ability of this instrument to reveal the structure and evolution of the boundary-layer during nocturnal stable and Low-Level Jet (LLJ) conditions over the Great Plains [1]-[3] and off the US East coast [4].

During all experiments, the HRDL measurements of line-of-site (LOS) velocities were acquired twice per second with 30-m range resolution either in a fixed elevation (conical), or a fixed azimuth (vertical-slice) mode. Profiles of wind speed, wind direction, horizontal wind component, and turbulence with a vertical resolution of 5-15 m, and time resolution from 1min to 1 hour were computed from LOS measurements. These profiles extended from ~surface up to several hundred meters.

VARIABILITY OF WINDS

Time-height cross-sections of 10-min averaged wind speeds and wind directions are shown in Figure 1 for ship-borne lidar measurements in the Boston Harbor during the diurnal cycle, including the nighttime hours (0000-2400 UTC) on 13th and 16th of July 2004. Wind speeds on both panels are scaled from 0 to 14 m s^{-1}. The figure illustrates variability of winds during each night and in between these nights.

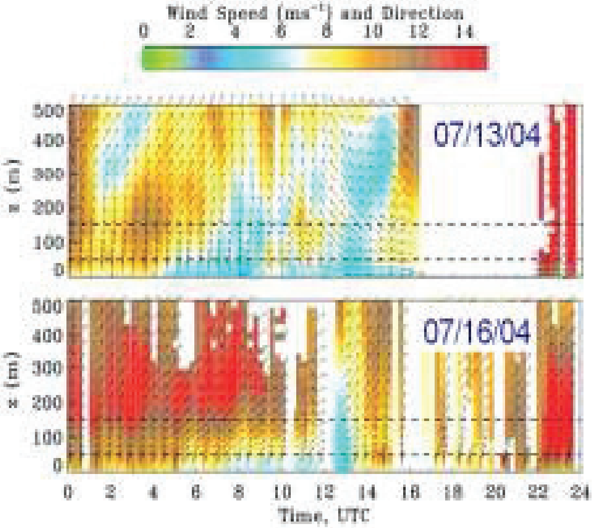

Figure 1. Mean wind speed (color) and direction (arrows), computed from HRDL measurements during two nights. Vertical axis is the height above sea level (m), and horizontal axis is the time in UTC. Two dotted horizontal lines indicate the layer of 50-150 m.

Concurrent air-chemistry measurements (not shown) indicate that the night of July 13th was characterized by transitional flow shifting from polluted continental to clean oceanic air: south-southwesterly winds shifted to southerly at ~0700 then to almost easterly during the morning transitional period (at ~1200 UTC). LLJs were observed during the period of 0200-0500 UTC with wind speed maxima reaching 10-11 m s^{-1} at 160-180 m. During the night of July 16th, LLJ winds with sustained west-southwesterly flow were several m s^{-1} stronger than those on the night of July 13th. LLJs having distinct maxima in the vertical were observed in 71% of 15-min profiles throughout the night, from 00 to 10 UTC.

The rest of the profiles showed more complex, layered structure [4] with strong shear in the lowest 200 m.

This plot shows that wind speeds in the rotor layer can vary over a wide range of values even on individual nights. As expected, shear magnitudes were larger during the stronger wind periods in general.

Accurate estimate of wind and directional shear across the entire rotor layer is an important issue for turbine operation, since modern turbine rotors are so large that wind conditions can differ above and below the turbine hub. Considerable variability of winds in time and height could be a big challenge for numerical model simulations of wind flow characteristics.

TURBINE WAKE MEASUREMENTS

The HRDL's ability to simultaneously measure upstream and downstream wind flow was used to estimate velocity deficits downwind of a research wind turbine, during the Turbine Wake and Inflow Characterization Study (TWICS) at the NREL National Wind Technology Center in the spring of 2011 [5].

Details of velocity reduction behind the wind turbine and wake meandering in the vertical plane, observed on April 23d at 0253 UTC are illustrated in Figure 2.

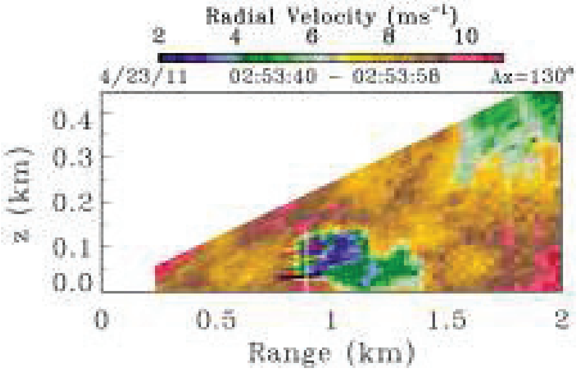

Figure 2. Vertical-slice scans, performed along the HRDL/turbine center line, illustrate velocity deficit downstream of the wind turbine, indicated on the plot by the white vertical line. The horizontal axes are the distance from the lidar.

The scan was performed with the elevation of laser beam from -1° to 12° and at azimuth angle of 129.5°. A velocity deficit of 6-7 m s^{-1} downstream of the wind turbine evident for more than 5 rotor diameters and extends from the top of turbine almost to the ground. Such scans provide information on wake characteristics in the vertical plane.

Enhanced detail on velocity deficit, wake width, length, and meandering can be seen in the horizontal plane from sector scans [5]. Such scans were performed at shallow (0°-6°) elevation angles over a narrow azimuth range of 115° -145°. The velocity deficit along each azimuth was estimated as a normalized difference between the reference inflow velocities (U_{IN}), averaged over 1200 m upstream of the turbine, and outflow velocities (U_{OUT}), measured every 30 m downstream. Initial results obtained from both vertical-slice and sector scans show velocity deficits up to 60-70%

extending up to 5-6 rotor diameters downstream, and are consistent with previous studies using lidars [6-9].

Occasionally, wider sector scans (90°-150°) were performed to observe the interaction of wakes behind several turbines as illustrated in Figure 3.

Wind turbines along with other obstacles located on the experimental site are shown in Fig.3 by the black bars. The velocity reduction can be seen on the scan as a green color area extending downstream of the wind turbines. This plot demonstrates the HRDL ability to study wakes of a large wind farm and provide detailed information needed for validation and improvement of the wind resource characterization and forecasting of turbine wakes and wake-interaction effects associated with arrays of operating turbines.

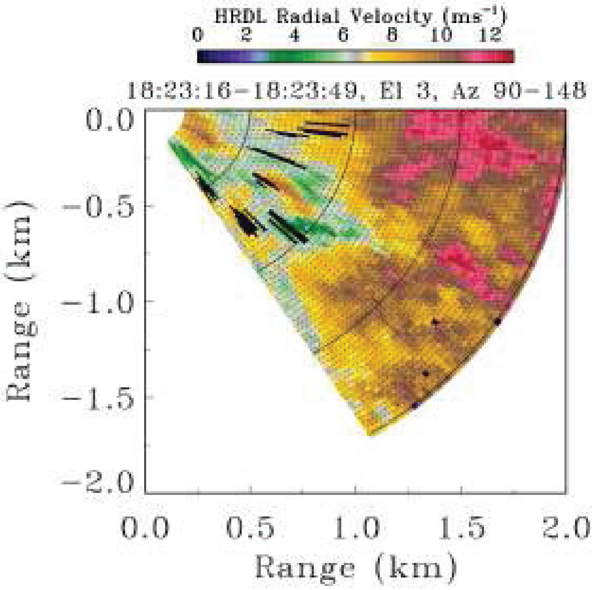

Figure 3. Example of wide (90°-150°) sector scan performed on April 15th at elevation of 3°. Black lines are hard target returns from different parts of wind turbines located at the test site. Wake interaction is evident behind two tallest turbines.

SUMMARY

The availability of accurate, high-resolution profile data gives a number of advantages in determining quantities of interest to wind energy. Profile data can also be used to assess the errors associated with using standardized (e.g., power-law) profiles to extrapolate wind-speed values from near the surface to turbine hub height, and to provide measured values of the speed and directional shear across the blade layer, often significantly underestimated using the standardized profiles, especially during LLJ conditions.

Presented results show the ability of the HRDL to provide continuous information about the vertical and horizontal structure of flow features and turbulence produced by an operational wind turbine. This information is necessary to optimize distances between turbines in wind farms and to improve modeling of wind turbine wakes for single turbines.

REFERENCES

1. Grund, C.J., R.M. Banta, J.L. George, J.N. Howell, M.J. Post, R.A. Richter, A.M. Weickmann, 2001: High-resolution Doppler lidar for boundary layer and cloud research. *J. Atmos. Oceanic Tech.,* **18**, 376-393.

2. Banta, R. M., Y.L. Pichugina and R.K. Newsom, 2003: Relationship between low-level jet properties and turbulence kinetic energy in the nocturnal stable boundary layer. *J. Atmos. Sci.*, **60**, 2549-2555.

3. Banta, R. M., Y.L. Pichugina and W.A. Brewer, 2006: Turbulent velocity-variance profiles in the stable boundary layer generated by a nocturnal low-level jet. *J. Atmos. Sci.*, **63**, 2700-2719.

4. Pichugina Y. L., R. M. Banta, W. A. Brewer, S. P. Sandberg, and R. M. Hardesty, 2012: Doppler-lidar-based wind-profile measurement system for offshore wind-energy and other marine-boundary-layer applications, Journal of Applied Meteorology and Climatology, **51**, pp. 327-349.

5. Pichugina Y.L., R. M. Banta, W. A. Brewer, J. K. Lundquist, R. M. Hardesty, R. J. Alvarez, J. D. M.L. Aitken[3], S. P. Sandberg[2], A. M. Weickmann[1, 2], N. D. Kelley[4] and J. D. Mirocha[5] 2012: Estimation of wind turbine wake characteristics from doppler lidar measurements, 26th *International Laser Radar Conference,* June 25-29, 2012, Porto Heli, Greece

6. Mann J., F. Bingöl and G. C. Larsen, 2006: Laser Doppler scanning of a wind turbine wake, *Geophysical Research Abstracts*, **8**, 06888.

7. Mikkelsen T., 2008: WINDSCANNER: A Facility for Wind and Turbulence Measurements around large Wind Turbines, *Nordic Conference on Global Challenges -Regional Opportunities,* Stockholm 12-13 Nov. 2008.

8. Käsler Y., S. Rahm, R. Simmet, and M. Kuhn, 2010: Wake measurements of a multi-MW Wind Turbine with coherent long-range pulsed Doppler wind lidar, *Journal of Atmospheric and Oceanic Technology*, **27**, pp. 1529-1532.

9. Clive J. M., I. Dinwoodie and F. Quail, 2011: Direct measurement of wind turbine wakes using remote sensing, *European Wind Energy Association,* March, Brussels, Belgium.

Session 10 – Oral Presentations

Coherent Doppler Lidar for Wind Farm Assessment

Raghu Krishnamurthy[1], R. Calhoun[1], A Choukulkar[1], K Barr[2]
[1]Environmental Remote Sensing Group, Arizona State University, Tempe, AZ
[2]Lockheed Martin Technologies, Louiville, CO

Abstract

Wind measurements are fundamental inputs for wind farm assessment and performance of wind farms. Three-dimensional scanning coherent Doppler lidar may provide a new basis for wind farm site selection, design and optimization. In this paper, the possibility of using lidar measurements to characterize the wind field is discussed, specifically, terrain effects, spatial variation of winds, power density, and the effect of shear at different layers within the rotor swept area. Vector retrieval methods are applied to lidar data, and results are presented on a terrain-following surface at hub height. In certain cases, the power law is used to estimate winds on the terrain-following surface below the horizon. Local stability, based on lidar measurements at higher elevations, is computed for estimating winds on the terrain-following surface. Wind speed and direction estimates from the lidar are compared to tower measurements, after interpolation to the appropriate level. Reasonable agreement between lidar retrievals and tower measurements in the mean and off-mean wind directions is observed. Doppler lidar measurements of winds at different vertical levels are used to estimate spatial power density at several heights within the rotor-swept area. Advanced vector retrieval algorithms are used to characterize extreme wind events which can have dramatic effects of wind power production. The vertical profiles of wind speed and direction during these events are presented.

1. Introduction

Wind energy is one of the fastest growing and currently practical forms of renewable energy (AWEA, 2011). In recent years, wind power has exhibited one of the highest growth rates among renewable energy sources. It can be considered as the most promising option for replacing a significant part of the electricity produced by conventional sources. Over the past two decades, the average turbine hub height has increased by 43%, while the average rotor diameter has increased by 76% (Wind Energy Technology Market Report, 2010). Further scaling, especially in rotor diameter, is expected in near future. There is a growing awareness of the inadequacy of current methods to measure the spatial variability of the winds, both vertically and horizontally, for wind assessment (Hannon et al. 2008). Due to the global growth of wind energy, short-range lidar profilers and sodars are proliferating and are increasingly being used to measure wind profiles (Smith et al. 2006, Barthelmie et al. 2006). A larger body of open literature is required to more fully understand the character of these and other remote sensing measurements for wind energy applications. Three-Dimensional (3D) scanning coherent Doppler lidars have been extensively used in meteorological studies for the past few decades (Gal-chen et al. 1992, Newsom et al. 2005). Modern 3-D scanning coherent Doppler lidars are well suited for characterizing wind farm airsheds, and may eventually form a new basis for real-time adaptive control of wind turbines (Laks et al. 2009). Lidars can measure the velocity deficit downstream of an individual wind turbine (Kasler et al. 2010), as well as the accumulated wakes from an array of turbines. Typical ranges of the current generation of commercially available coherent Doppler lidar (such as that used in this study, i.e., *WindTracer*, from *Lockheed Martin Coherent Technologies, Inc.*) are 10 ~ 20 km, depending on the atmospheric conditions. Various wind retrieval techniques have been developed to estimate 2D and 3D vector fields from Doppler lidar data (Chan et al. 2007, Choukulkar et al. 2012). Algorithms range from computationally intensive 4DVAR (four-dimensional variational data assimilation) techniques to simpler and faster methods based on volume velocity processing (VVP) (Krishnamurthy et al. 2012) and 2DVAR (Chan et al. 2007). This paper presents the results of a Doppler lidar deployment for a proposed wind energy development. The objectives of this research were:

1. To measure hub-height winds (and their variation spatially) over most of the wind farm domain,
2. To calculate (spatially varying) wind speed distribution, and spatial power density distribution over the wind farm,
3. To estimate power density on multiple vertical layers within the rotor swept area,
4. Apply advanced optimal interpolation retrieval algorithms to lidar data.

[See Krishnamurthy et al. 2012 for detailed description of experiment setup, lidar scanning strategy, and data filtering performed for the analysis.]

2. Wind Speed Retrieval

Since the basic Doppler lidar output is the *radial velocity,* interpretation and processing of the radial velocity fields can be complex, requiring the resolution of indeterminacy in the basic data through supplementary assumptions or information. Two advanced velocity retrieval algorithms were applied to the data set. VVP algorithm was applied to estimate the winds on a terrain-following surface at hub height. The *terrain-following surface at hub-height* is constructed by adding a vertical offset (in our case 80 m) to the surface which defines ground level over the domain (Krishnamurthy et al. 2012). Advanced Optimal Interpolation (OI) technique was used to characterize atypical wind flow events (Choukulkar et al. 2012).

a. Interpolation of winds to hub height

Winds obtained from the VVP algorithm at different heights are used to generate a terrain-following wind map at hub height. At each grid point, there are normally 13 velocity values at different heights which can be used to interpolate speeds to the appropriate level. However, due to the terrain-blocking at lower levels of the lidar scans, and noise caused by atmospheric conditions, the required scan levels were not always available. To overcome this problem, three different techniques were used to complete the interpolation:

1. At grid points where there are at least two available data points at different heights, and the interpolating level is in-between these data, a linear interpolation is used to obtain the wind speed.
2. At grid points where there are at least two available data points at different heights, but the interpolating level is below these data, wind speed at that level is obtained using the theoretical wind power law, with locally adjusted exponent value. The exponent value is calculated based on the velocity measurements available at the higher level scans.
3. At grid points where there is only one available data point in the vertical direction, the interpolating level is obtained by using the wind power law, where the power law exponent from the previous time period is used, assuming no change in atmospheric conditions. The time period between instances where wind speed data was available only at one vertical level was short (≤ 20 minutes). The stability conditions are not expected to change within the short period.

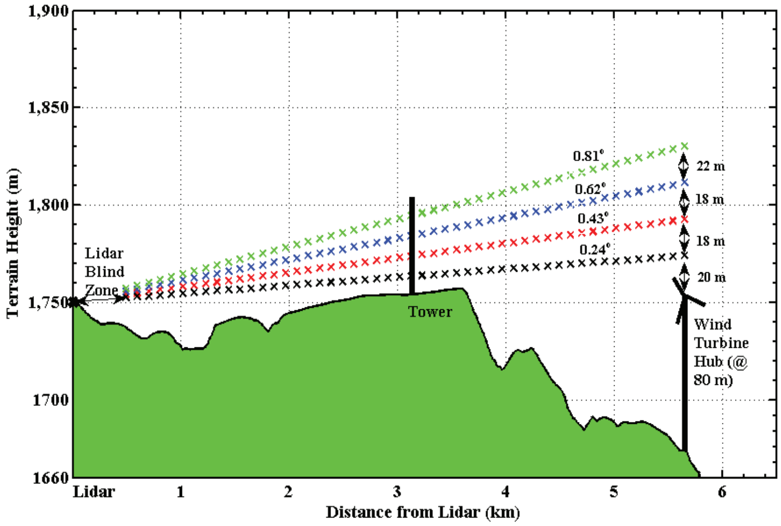

Figure 1. Terrain cross-section from lidar location, through the tower, till the end of scan radius is shown above. Lidar (x) and tower location are shown. Scans at various elevation angles are displayed. The power law 'dip' height used to estimate wind speed at terrain-following surface (80 m hub height) is approximately 20

This procedure is applied for the entire period of observation and the results are provided below. Note that for 90% of the data set, the power law is not required to estimate winds on the terrain-following surface. The maximum extrapolation distance used in power law calculations is approximately 20 m (as shown in Figure 1). The stability (power law exponent, α) is estimated at every grid point based on winds measured at different vertical levels. The errors associated from the usage of power law should be a subject of further research. The use of power law can be assumed viable for this case, since the extrapolation distance used is small and local stability conditions are used in calculating the winds at the interpolating level.

3. Data Validation

Near continuous wind measurements were collected over a period of one month. Two cup anemometers and vanes were positioned at 50 m, 50.2 m and 48 m, respectively, on a meteorological tower. The lidar measurements are interpolated to 50 m above ground level (AGL) and are compared to tower measurements for the entire period of observation. The 10 min integrated mean wind speeds/directions and standard deviations for both the tower and lidar measurements are presented in Table 1 and Table 2, respectively. The time series plots of wind speed and direction for tower and lidar are shown in Figure 2. It can be seen that the lidar and tower measurements are in close agreement with a mean wind differences equal to 0.06 ms^{-1}. The 10 min root mean square (RMS) error between the lidar and tower is estimated to be approximately 1.18 ms^{-1}. Because of the inherent differences in the data acquisition method, particularly the sampling frequency (over 10 minute period: 1200 tower measurements -- versus 1 lidar measurement), the RMS differences are dependent on the averaging time period. That is, increasing averaging times would yield reduced RMS differences (Krishnamurthy *et al.* 2012).

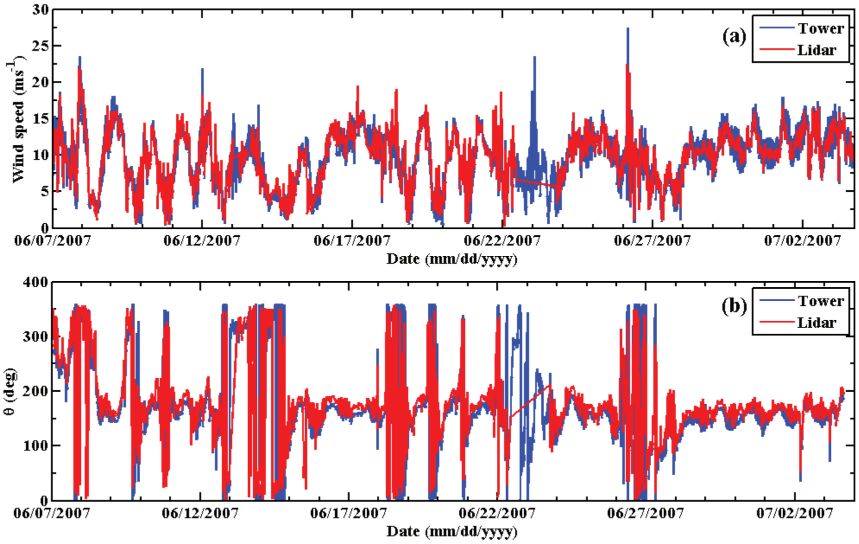

Figure 2. (a) Comparison between one minute averaged tower and ten minute interpolated lidar wind speed at 50m. (b) Comparison between one minute averaged tower and ten minute interpolated lidar direction at 50 m. A total of 3,459 ten minute periods are chosen for both figures. Gaps in the series correspond to bad signal-to-noise ratio at those time periods, and hence were neglected.

Table 1. Tower – Lidar wind speed statistics over the period of observation

Instrument	Mean (ms^{-1})	Standard Deviation (ms^{-1})	10 minute RMS Difference (ms^{-1})
Tower @ 50 m	9.67	3.60	1.18
Lidar @ 50 m	9.61	3.61	

Table 2. Tower – Lidar direction statistics over the period of observation

Instrument	Mean (deg)[a]	Standard Deviation (deg) [a]	10 minute RMS Difference (deg) [a]
Tower @ 50 m	168.24	36.94	19.40
Lidar @ 50 m	170.34	37.01	

[a] Data utilized between 60-300 deg

4. Results

a. Terrain-following Wind Maps

One of the key advantages of 3D scanning coherent Doppler lidar is to generate wind maps on a terrain-following layer at hub height for the region of interest. The wind speed data was placed on a 12 km x 12 km grid domain and overlaid on a digital terrain model. The resultant map covers a geographic area of 144 square kilometers and is comprised of approximately 9,150 data points on the terrain-following plane. Figure 3 shows the three dimensional image of the terrain-following wind field at 80 m hub height. Such spatially resolved wind maps (on terrain-following surfaces at hub-height) may aid developers to gain more complete understanding of the spatial variation of winds within a prospective wind farm. Based on visual inspection of the wind map, it is straightforward to locate the area with maximum winds.

b. Wind Distributions

Of course, the energy content of the wind depends not only on the mean wind speed but also on wind speed distribution. Lidar is capable of providing wind speed distributions at every point over the entire spatial domain. As observed in Figure 4A, tower and lidar distributions compare reasonably well. Radial and transverse wind speed distributions between lidar and tower are compared in Figure 4B and Figure 4C, respectively. To calculate the wind speed distributions in radial and transverse directions, wind speeds were binned into four 90° sectors based on the wind speed directions. Two sectors along the radial direction, *i.e.*, 170 ± 45° and 350 ± 45°, and two sectors along the transverse direction, *i.e.,* 80 ± 45° and 260 ± 45°. The distributions in the transverse directions are less converged, due to insufficient data points observed in the two sectors. These measurements could be used to estimate the error from current mesoscale, computational fluid dynamics (CFD) and linear wind resource prediction models (such as WAsP etc.).

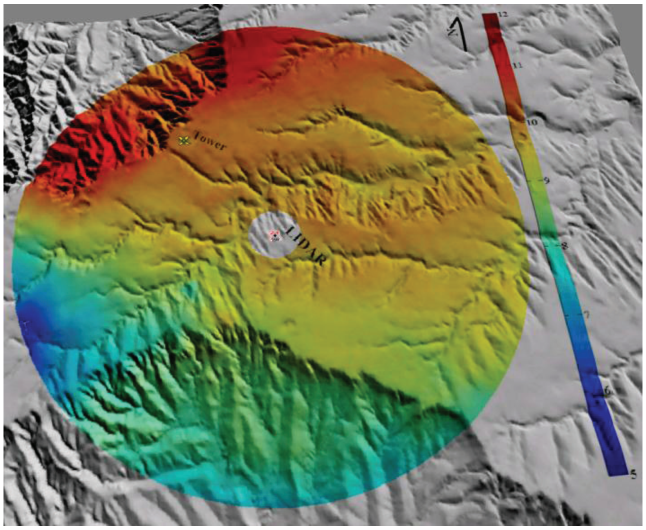

Figure 3. Lidar terrain-following averaged wind speed measurement at 80 m hub height. The colour bar represents wind speed from 5 to 12 ms^{-1}. The lidar is at the centre and the tower is located 3.42 km north-west of the lidar. The radius of the scan is 5.75 km.

Figure 4. (a) Distribution of wind speed comparison between tower and lidar measurements at 50 m (from all directions). (b) Wind speed distribution between the tower and lidar in the radial direction at 50 m. Wind speed data selected from directions 170 ± 45^{O} and 350 ± 45^{O} were chosen for this distribution (mean wind direction is 170^{O}). (c) Wind speed distribution between the tower and the lidar in the transverse direction at 50 m. Wind speed data selected from directions 80 ± 45^{O} and 260 ± 45^{O} were chosen for the distribution (mean wind direction is 170^{O}). The distribution is less well defined due to reduced amount of data perpendicular to the mean wind direction.

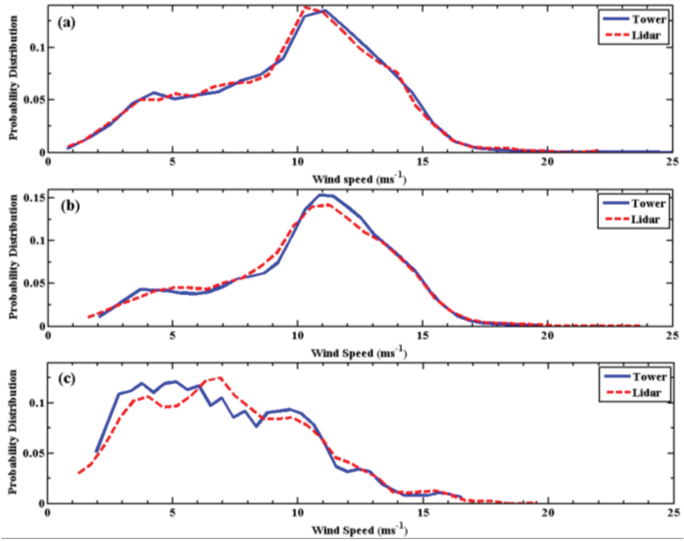

c. Wind Power Production

The wind resource or wind power production for a particular site can be estimated based on wind speed distribution for the given area. As shown in the previous section, the distribution of winds over the entire site has been measured. The total energy output is calculated at every location at hub height based on the distribution of wind speed and the power curve (assuming a standard 80 m hub 2.1 MW wind turbine power curve). Figure 5 shows the terrain-following wind power production at hub height.

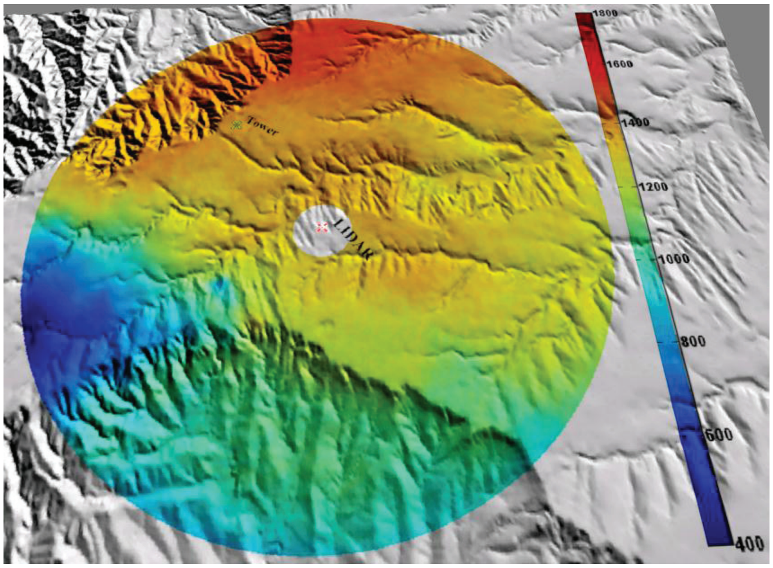

Figure 5. Lidar terrain-following machine power production at 80 m hub height. The colour bar represents the power in kW.

d. Layered Approach

To estimate the power output from a turbine, it is a general practice to assume that the mean wind speed at hub height is representative of the wind over the whole swept area. Since greater wind speeds and shear are often observed at the higher elevations associated with the largest wind turbines, there may be significant differences in wind speed within the rotor-swept area. Since the lidar can provide wind information at multiple levels, the approach of Wagner *et al. (2009)* is followed herein, and terrain-following average wind power is estimated at various vertical levels within the swept rotor area. Figure 6 shows the available wind power density estimated at the three individual layers and combined wind power density (all three layers together.) As observed in Figure 6, the power density changes significantly among the layers as well as the combined approach.

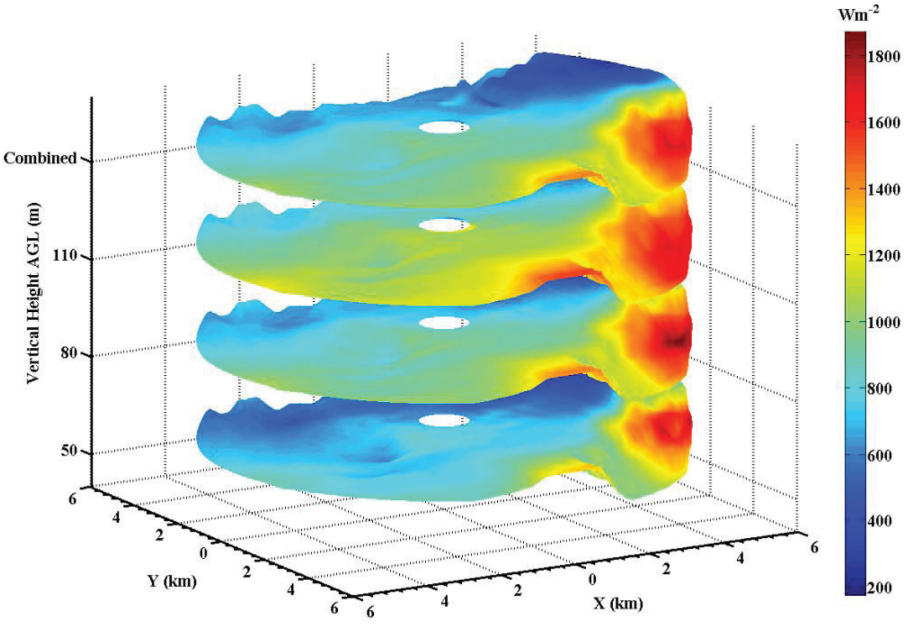

Figure 6. Terrain-following wind power density estimates at various heights of the rotor swept area. The "combined" wind power density estimated from all the three layers is also shown. Where X (km) and Y (km) is the distance from lidar in the respective directions

e. Advanced Vector Retrieval Methods

The wind energy methods given above depend upon the accuracy and degree of suitability of the vector retrieval methods for the domains of interest. Optimal interpolation methods (Choukulkar *et al.* 2012) have been applied to Doppler lidar data and are designed to preserve more local variation in wind vectors. An example of this type of vector retrieval which has been applied to the dataset studied above is given in Figure 7. It is expected that different uses of 3D scanning Doppler lidar (for example, if one were primarily interested in transient or more highly localized flow features) may require more advanced vector retrieval methods. An example retrieval of an extreme event which featured high velocity and directional shear is shown in Figure 8.

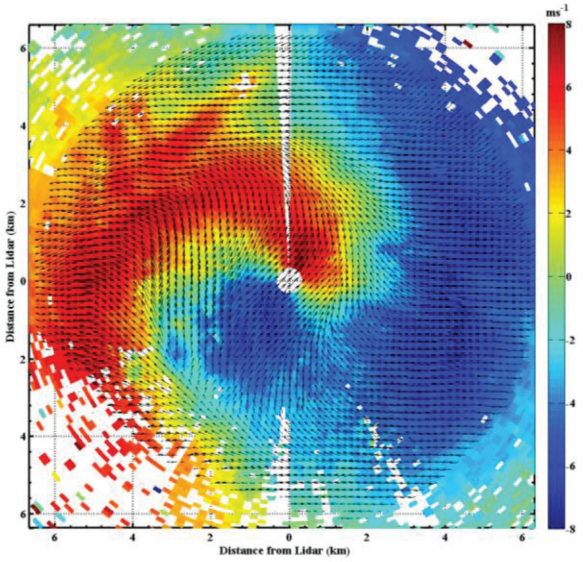

Figure 7. Horizontal velocity vectors from OI technique on a 3.5° elevation conical scan showing the rotation of winds with height. The scan takes approximately 38 seconds to complete one revolution shown. The colors on the plot represent radial velocity measurements by lidar. Red color (positive values) represent wind moving away from the lidar and blue color (negative values) shows wind moving towards the lidar. Data with low SNR is not shown (white regions).

Figure 8. Vertical profile of horizontal velocity vectors from OI technique on June 26 2007 from 0043 local time. Vector profiles plotted every 20 minutes.

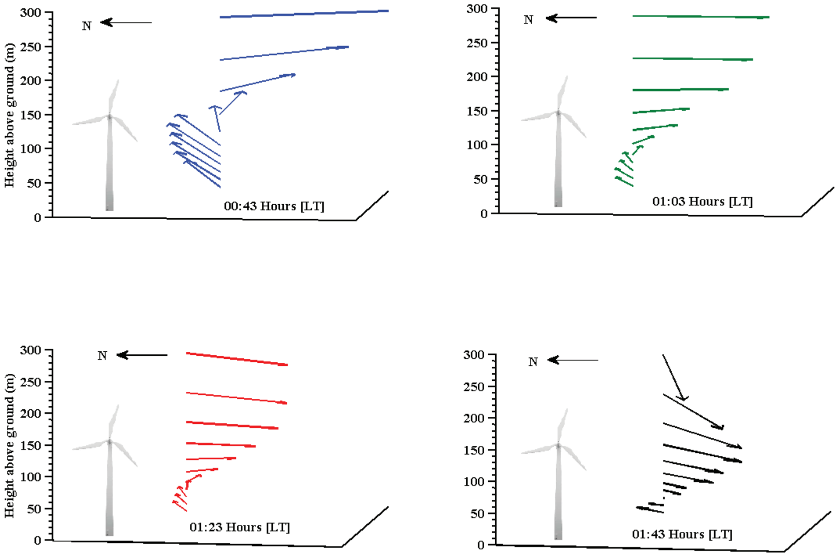

5. Summary

A Doppler lidar was used to obtain radial velocities over a wind farm domain. Mean wind speeds were obtained on a terrain-following surface at hub-height. The wind speed distributions were shown to be within reasonable accuracy with the given algorithms. For this site, the wind speed distribution was shown to vary significantly with spatial location. Therefore, a key result of this study is that (spatially varying) mean wind speeds and their distributions can be *measured* from one central location in the wind farm – although an important caveat is that more experimental data is required to fully define and understand the error structure of the products, particularly in the regions of the domain perpendicular to the mean wind. Field experiments which also deploy instruments capable of measuring winds and their distributions at multiple heights in the off-mean-wind direction would be a valuable next step for validating scanning Doppler lidar products for wind energy. 3D Doppler lidar data can be used to produce "layered" wind and power estimates, accounting for wind variations at different elevations of the rotor-swept area. Future work will focus on characterizing errors associated with lidar measurements and their retrieval algorithms for wind speed estimates.

Acknowledgements:

Support was also provided through the Army Research Office, sponsor awards W911NF0410146 and W911NF0710137 (Program Officer: Walter Bach) and the NSF grant 0522307 (Program Officer: Stephan P. Nelson) which made this work possible. The authors also would like to thank RES, Americas for providing the Doppler lidar and tower data.

References:

1. AWEA, http://www.awea.org, 2011
2. Barthelmie R, Folkerts L, Larsen G, Pryor SC, Frandsen ST and Schepers G. Comparison of wake model simulations with offshore wind turbine wake profiles measured by sodar, Journal of Atmospheric and Oceanic Technology, 2006; **23**(7), 888-901.
3. Chan PW, Shao AM. Depiction of Complex Airflow Near Hong Kong International Airport Using a Doppler LIDAR with a Two-dimensional Wind Retrieval Technique. Meteorologische Zeitschrift 2007; **16**: 491-504.
4. Choukulkar A, Calhoun R, Billings B, Doyle J (2012), Advanced optimal interpolation for lidar velocity retrieval" IEEE Remote Sensing Letters (In Press).
5. Gal-chen T, Xu M, Eberhard W. Estimations of atmospheric boundary layer fluxes and other turbulence parameters from Doppler lidar data. *Journal of Geophysical Research* 1992; **97**: 409-418.
6. Hannon SM, Barr K, Novotny J, Bass J, Oliver A and Anderson M. Large scale wind resource mapping using a state-of-the-art 3-D scanning lidar. *European Wind Energy Conference*, 2008.
7. Käsler Y, Rahm S, Simmet R, Kühn M. Wake Measurements of a Multi-MW Wind Turbine with Coherent Long-Range Pulsed Doppler Wind Lidar. *Journal of Atmospheric and Oceanic Technology*, 2010; **27**: 9, 1529-1532
8. Krishnamurthy, R., Choukulkar, A., Calhoun, R., Fine, J., Oliver, A. and Barr, K.S. (2012), Coherent Doppler lidar for wind farm characterization. *Wind Energ*.. doi: 10.1002/we.539
9. Laks JH, Pao LY, and Wright A. Control of wind turbines: Past, present, and future. In *Proceedings of American Control Conference* 2009; St. Louis, MO.
10. Newsom R, Ligon D, Calhoun R, Heap R, Cregan E, Princevac M. Retrieval of microscale wind and temperature fields from single- and dual-Doppler lidar data. *Journal of Applied Meteorology* 2005; **44**: 9, 1324-1345.
11. Smith DA, Harris M, Coffey AS, Mikkelsen T, JØrgensen HE, Mann J, Danielian R. Wind LIDAR evaluation at the Danish wind test site in HØvsØre. *Wind Energy* 2006; **9**: 87-93.
12. Wagner R, Antoniou I, Pedersen SM, Courtney MS and Jørgensen HE. The influence of the wind speed profile on wind turbine performance measurements. *Wind Energy* 2009; **12**: 348–362. doi: 10.1002/we.297
13. Wind Energy Technology Market Report, 2010

Model of the Correlation between Lidar Systems and Wind Turbines for Lidar Assisted Control

D. Schlipf[1], J. Mann [2], A. Rettenmeier[1], P. W. Cheng[1]

[1] *Stuttgart Wind Energy (SWE), University of Stuttgart, Germany*
[2] *DTU Wind Energy, Risø Campus, Denmark*

ABSTRACT

Investigations for lidar assisted control to optimize the energy yield and to reduce loads of wind turbines increased significantly in recent years. For this kind of control it is crucial to know the correlation between the rotor effective wind speed and the wind preview provided by a nacelle or spinner based lidar system. If on the one side the assumed correlation is overestimated, the uncorrelated frequencies of the preview will cause unnecessary control action, inducing undesired loads. On the other side the benefits of the lidar assisted controller will not be fully exhausted, if correlated frequencies are filtered out.

To avoid these uncertainties, this work presents a method to model the correlation between lidar systems and wind turbines using Kaimal wind spectra. The derived model accounts for different measurement configurations and for different turbine sizes. The method is evaluated in two steps: At first the model is compared to the results from a lidar simulator to prove that the model is able to reproduce the effect of volume measurement, limited measurement points and scanning time. In a second step the model is augmented by a model for the decay due to wind evolution and compared to real measurement data with promising results. In addition an example is given, how this model can be used to design an optimal controller for a lidar system with fixed parameters and a given turbine and how the pattern of a scanning lidar system is optimized for a given turbine to improve the correlation.

1 REQUIREMENTS FOR LIDAR ASSISTED CONTROL

Reducing fatigue and extreme loads of the structure is an important design goal for large wind turbines control. Transient events such as gusts represent an unknown disturbance to the control system. Conventional feedback controllers can only provide delayed compensation for such excitations, since the disturbance effects must propagate through the entire wind turbine before showing its effects in the measured outputs. This usually results in additional loads for the wind turbine and requires high actuator rates for the disturbance compensation. Those effects can be avoided, if the wind ahead of the wind turbine is measured by remote sensing techniques such as lidar and the information is fed to the turbine controller.

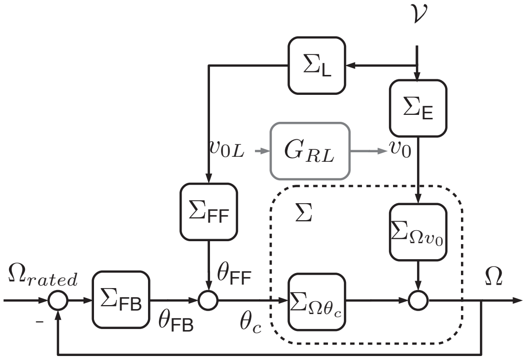

Figure 1: Feedforward control: The feedforward controller Σ_{FF} tries to compensate the effects of the wind field $\mathcal{V}$ to the rotor speed Ω.

The magnitude of load reduction depends on the quality of the wind preview expressed by the correlation of the Lidar measurements and the turbine reaction. In this section the requirements of the correlation for lidar assisted control are derived by a description of a feedforward collective pitch controller.

The feedforward controller (see Figure 1) is based on the work in [1] and combines the baseline feedback controller with a feedforward update. The main control goal of the collective pitch feedback controller Σ_{FB} is to maintain the rated rotor speed Ω_{rated}. The system Σ is disturbed by a wind field $\mathcal{V}$, which can be measured by a lidar system Σ_L in front of the turbine before reaching the rotor. If the wind would not change on its way ($\Sigma_E = 1$)

and in the case of perfect measurement the measured wind speed v_{0L} and the rotor effective wind speed v_0 are equal. The disturbance could be perfectly compensated by a feedforward controller $\Sigma_{\mathsf{FF}} = -\Sigma_{\Omega\theta_c}^{-1}\ \Sigma_{\Omega v_0}$, if the influence on the generator speed of the wind $\Sigma_{\Omega v_0}$ and the pitch angle $\Sigma_{\Omega\theta_c}$ is known and $\Sigma_{\Omega\theta_c}$ is invertible.
In reality v_0 cannot be measured perfectly due to the limitation of the lidar system Σ_L and the wind evolution Σ_E. Therefore the needed feedforward controller is:

$$\Sigma_{\mathsf{FF}} = -\Sigma_{\Omega\theta_c}^{-1}\ \Sigma_{\Omega v_0}\ \Sigma_L^{-1}\ \Sigma_E. \tag{1}$$

Due to the interaction with the turbine and missing technology, modeling and verifying the wind evolution Σ_E is very complicated. Also not all information of the wind field $\mathcal{V}$ can be reconstructed by the inverse of a real limited lidar system Σ_L. However, if the transfer function G_{RL} from the measured wind speed to the rotor effective wind speed can be used to exploit all information captured by the lidar system:

$$\Sigma_{\mathsf{FF}} = -\Sigma_{\Omega\theta_c}^{-1}\ \Sigma_{\Omega v_0}\ G_{RL}. \tag{2}$$

For real time applications the transfer function G_{RL} can be obtained from measurements and approximated by a standard low pass filter. Therefore the cut-off frequency ($-3dB$) of the corresponding filter can be considered as a quality criterion for the correlation. In the following sections a analytic way is presented to estimate the both the transfer function G_{RL}

$$G_{RL} = \frac{S_{RL}}{S_{LL}}, \tag{3}$$

and the coherence γ_{RL}

$$\gamma_{RL} = \frac{|S_{RL}|^2}{S_{RR}S_{LL}}. \tag{4}$$

2 ROTOR AVERAGED SPECTRUM

The model of the rotor averaded spectrum $S_{v_0v_0}$ is derived from Kaimal wind specra. The hub height power spectral density of the longitudinal velocity component is given in [2] by the equation:

$$\frac{fS_{HH,1}(f)}{\sigma_{HH,1}^2} = \frac{4fL_1/v_{HH}}{(1+6fL_1/v_{HH})^{(5/3)}}, \tag{5}$$

where and v_{HH} and σ_{HH} are the mean and standard deviation of the longitudinal velocity component on hub height. The spatial correlation of a longitudinal velocity component with distance r_{ij} of two points with coordinates (y_i, z_i) and (y_j, z_j) is defined as

$$\gamma_{ij}(f) = \exp(-\underbrace{12\sqrt{(f/v_{HH})^2 + (0.12/L_1)^2}}_{\kappa}\ r_{ij}) \tag{6}$$

The rotor averaged spectrum can be derived by an average of the cross and auto spectrum densities of all points and combinations in the rotor plane D with rotor radius R:

$$S_{RR}(f) = \frac{1}{(\pi R^2)^2}\int_{D_j}\int_{D_i} S_{ij}(r_{ij}, f)dy_i dz_i dy_j dz_j \tag{7}$$

An explicit solution of (7) can be found showing the complexity by

$$\begin{aligned} S_{RR}(f) = {} & 2(R\kappa(-9\pi\,{}_0\tilde{F}_1(;2;(R\kappa)^2)- \\ & 6\pi\boldsymbol{L}_2(2R\kappa) - 8R\kappa + 6\pi I_0(2R\kappa) + 3\pi)+ \\ & 3\pi\boldsymbol{L}_1(2R\kappa))/(3\pi(R\kappa)^3)\ S_{HH,1}(f) \end{aligned} \tag{8}$$

where ${}_0\tilde{F}_1$ is the regularized confluent hypergeometric function, $\boldsymbol{L}_n$ is the modified Struve function, and I_0 is the modified Bessel function of the first kind.
The discrete form of the averaged rotor spectrum can be calculated by with n points inside the rotor area

$$S_{RR}(f) = \frac{S_{HH,1}(f)}{n^2}\sum_{i=1}^{n}\sum_{j=1}^{n}\gamma_{ij}(f). \tag{9}$$

3 CORRELATION OF A PERFECT STARRING LIDAR

Ignoring the filtering effect of a lidar, assuming Taylor's Hypothesis to be fully valid (no wind evolution), the spectrum of a starring lidar can be modeled by

$$S_{LL}(f) = S_{HH,1}(f). \tag{10}$$

Then the cross spectrum between the starring lidar and the rotor is

$$S_{RL}(f) = \frac{1}{\pi R^2}\int_D S_{Hj}(r_{Hj}, f)dy_j dz_j, \tag{11}$$

where S_{Hj} means the cross spectrum of the hub and the point j with distance r_{Hj}.
This can be solved with

$$\begin{aligned} S_{RL}(f) &= \frac{S_{HH,1}(f)}{\pi R^2}\int_0^{2\pi}\int_0^R r\ \gamma_{Hj}(f)\ dr d\phi \\ &= \frac{2S_{HH,1}(f)}{R^2\kappa^2}\left(1 - \frac{R\kappa + 1}{\exp(R\kappa)}\right). \end{aligned} \tag{12}$$

With (3), (4) and

$$k = \frac{2\pi f}{\bar{u}} \tag{13}$$

the transfer function G_{RL} and the coherence γ_{RL} can be calculated over the wavenumber k, independent of the mean wind speed $\bar{u}$.

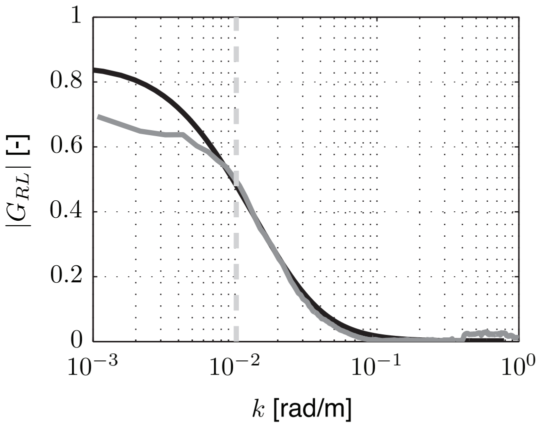

Figure 2: Transfer function for a nacelle anemometer and a turbine with $D = 116m$: analytic (black) and measured (gray). Maximum wavenumber $\hat{k} = 0.01\ rad/m$ (dashed).

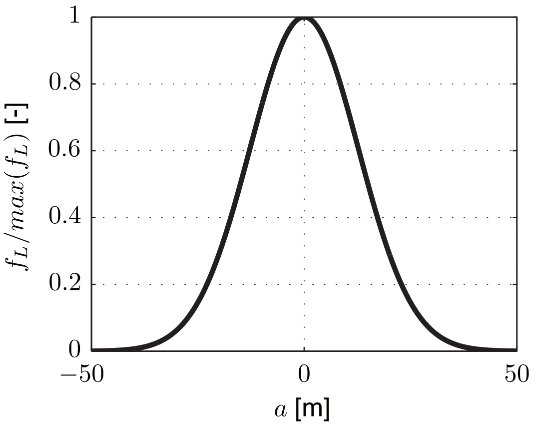

Figure 3: Normalized range weighing function $f_L(a)$ for the considered LIDAR system.

This model cannot be evaluated with a real lidar system, because wind evolution and volume measurement cannot be neglected. Therefore an anemometer on a 5 MW turbine is compared to a nacelle anemometer. Figure 2 shows that the modeled transfer function fits to the data.

4 CORRELATION OF A REAL SCANNING LIDAR

For real scanning lidar system the model has to be extended by a model for the volume measurement and wind evolution. Here the model [3] is used.
To model the volume measurement, a Gaussian shape weighting function $f_L(a)$ depending on the distance a to the focus point with full width at half maximum (FWHM) of $W = 30m$ is used, following the considerations of [4], [5] and [6]:

$$f_L(a) = \frac{e^{-4\ln 2(a/W)^2}}{\int_{-\infty}^{\infty} e^{-4\ln 2(a/W)^2} da} = \frac{2\ln 2 e^{-4\ln 2(a/W)^2}}{W\sqrt{\ln 2\pi}}. \tag{14}$$

With the weighting function it is possible to calculate the line-of-sight wind speed of each focus point with $f_L(a)$ by

$$v_{los} = \int_{-\infty}^{\infty} (l_x u(a) + l_y v(a) + l_z w(a)) f_L(a) da, \tag{15}$$

where $\begin{bmatrix} l_x & l_y & l_z \end{bmatrix}^T$ is the normalized laser beam vector and $\begin{bmatrix} u(a) & v(a) & w(a) \end{bmatrix}^T$ the wind vector at the distance a to the focus point.
As LIDAR systems measure only the wind speed in line-of-sight direction, the three dimensional wind vector is reconstructed using the assumption of perfect yaw alignment with the wind direction. If the turbine is perfectly aligned with the wind, the estimated lateral and vertical wind components are assumed to be zero and the longitudinal component $\hat{u}_{i_{fp}}$ for each focus point can be calculated as

$$\hat{u}_{i_{fp}} = v_{los}/l_x. \tag{16}$$

For each distance i_{fd} the longitudinal wind component $\hat{u}_{i_{fp}}$ is then averaged over the n_{fp} focus points of the last trajectory by

$$v_{i_{fd}} = \sum_{i_{fp}}^{n_{fp}} \hat{u}_{i_{fp}}/n_{fp} \tag{17}$$

for a rotor effective value and the obtained time series of the measurements $v_{i_{fd}}$ is time-shifted according to Taylor's frozen turbulence hypothesis and combined to the rotor effective wind speed:

$$v_{0L} = \sum_{i_{fd}}^{n_{fd}} v_{i_{fd}}/n_{fd} \tag{18}$$

The spectrum of a scannig lidar can then be found by a Fourier transform of (18), including (17), (16) and (15) using a weighting function such as (14) and a wind evolution model such as [3].

5 LIDAR SYSTEM OPTIMIZATION

The proposed model can be used to optimize a lidar system. To determine the optimum correlation of a lidar system with three independent beams on a turbine with $D = 40m$, the measurement distance x and the scan radius r is varied, see Figure 5. The value of maximum wavenumber $\hat{k}$ at $-3dB$ below the steady value of the transfer

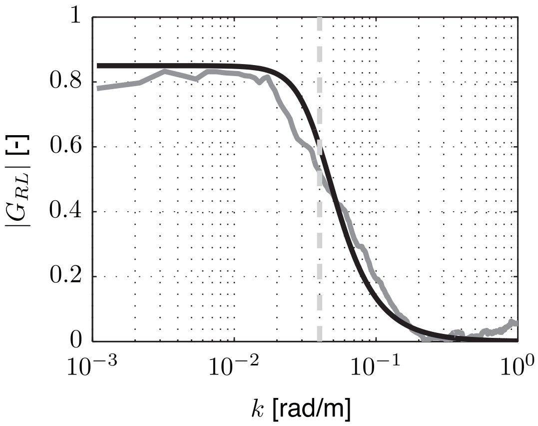

Figure 4: Transfer function for a scanning lidar and a turbine with $D = 116m$: analytic (black) and measured (gray). Maximum wavenumber $\hat{k} = 0.04\ rad/m$ (dashed).

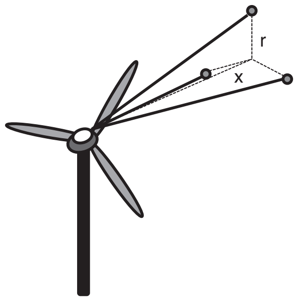

Figure 5: Scope of lidar with three beams.

function is shown in Figure 6. A optimum value ($\hat{k} = 0.03 rad/m$) can be found at $x = 40m$ and $r = 12m$.

6 CONCLUSION AND OUTLOOK

This work presents a model to estimate the correlation between a lidar and a turbine, considering volume measurements, different scanning patterns and wind evolution. A criterion for lidar assisted control is derived: for a collective pitch feedforward controller the transfer function from the measured wind speed to the rotor effective wind speed obtained from turbine data has to be used to filter the data. For real application this transfer function has to be fitted to a standard filter and therefore the $-3dB$ of considered as a useful criterion for the the correlation between a lidar and a turbine.
The model can be used to optimize the configuration of a lidar system such as probe volume and scan pattern.

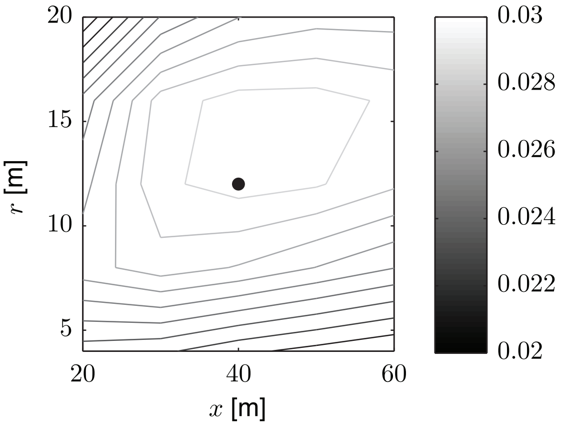

Figure 6: Maximum wavenumber of lidar with three beams on a turbine with $D = 40m$ (dashed) and different distances and radii.

ACKNOLEGEMENT

Part of this research is funded by the German Federal Ministry for the Environment, Nature Conservation and Nuclear Safety (BMU) in the framework of the German joint research project “LIDAR II - Development of nacelle-based lidar technology for performance measurement and control of wind turbines” (FKZ 0325216B).

References

[1] D. Schlipf, T. Fischer, C. E. Carcangiu, M. Rossetti, and E. Bossanyi, “Load analysis of look-ahead collective pitch control using LiDAR,” in *Proc. DEWEK*, 2010.

[2] *IEC 61400-1 third edition 2005-08 Wind turbines - Part 1: Design requirements*, IEC Std., Rev. third edition, 2005.

[3] L. Kristensen, “On longitudinal spectral coherence,” *Boundary-Layer Meteorology*, vol. 16, pp. 145–153, 1979.

[4] J. P. Cariou, “Pulsed lidars,” in *Remote Sensing for Wind Energy. Risøreport Risø-I-3184(EN)*. A. Peña and C. B. Hasager, June 2011, pp. 65–81, risø-DTU.

[5] P. Lindelöw, “Fiber based coherent lidars for remote wind sensing,” Ph.D. dissertation, Technical University of Denmark, 2008.

[6] V. A. Banakh and I. N. Smalikho, “Estimation of the turbulence energy dissipation rate from the pulsed doppler lidar data,” *Atmospheric and Oceanic Optics*, vol. 10, pp. 957–965, 1997.

POWER PERFORMANCE MEASUREMENTS OF THE NREL CART-2 WIND TURBINE USING A NACELLE-BASED LIDAR SCANNER

A. Rettenmeier[1], D. Schlipf[1], I. Würth[1], P.W. Cheng[1], A. Wright[2], P. Fleming[2], A. Scholbrock[2], P. Veers[2]

[1]*Stuttgart Wind Energy (SWE), University of Stuttgart, Allmandring 5B, 70569 Stuttgart, Germany,*
andreas.rettenmeier@ifb.uni-stuttgart.de
[2]*National Renewable Energy Laboratory, 1617 Cole Blvd.,Golden, Colorado 80401,USA,*
Alan.Wright@nrel.gov

ABSTRACT

By the use of a horizontally scanning, nacelle-based lidar it's possible to determine power curves without a met mast [1]. The new measurement technique seems to be promising for cost effective measurements particularly offshore. Due to the lack of a mast and mutual influences, fewer sectors have to be excluded for the certification process of a turbine. This leads to a faster measurement campaign which can be performed at on- and offshore sites.

The modified nacelle-based lidar system allows horizontal scanning of the incoming wind field at various points and distances [2]. Over the whole rotor disc shear and yawed flow can be taken into account which is a significant advance compared with the single-point measurement using an anemometer according to the IEC 61400-12-1 standard.

The measurements were performed on the CART-2 wind turbine at the National Wind Technology Center (NWTC), Colorado, USA. The turbine is 42m in diameter, with a rated output of 660 kW. Turbine inflow was measured horizontally from the nacelle simultaneously to measurements with a standard met mast. In order to calculate an averaged equivalent wind speed across a defined area, different lidar measurement points were taken into account. The comparison of power curves measured using a scanning, nacelle-based lidar with simultaneous measurements obtained from mast-mounted anemometers is shown.

1. INTRODUCTION

To get a worldwide comparability of a wind turbine's performance and to calculate the annual energy production of a turbine it is unavoidable to determine a power curve where the electric power output for the operating wind speeds is defined. Nowadays cost expansive metrological met masts have to be installed for this and equipped with anemometers, wind vanes, thermometers and barometers. This procedure is defined at the IEC 61400-12-1 standard. For offshore wind turbines the costs to determine a power curve increase, because of the complex construction of met masts at sea and the ever-increasing heights of the wind turbine's hub and therefore of the met masts. Thus, it is important to develop new methods for power curve determination.

One of the most promising techniques is the determination of power curves based on interpolated line-of-sight velocities of nacelle-based LiDAR measurements.

2. SITE DESCRIPTION

The measurements were performed on the National Wind Technology Center (NWTC), Colorado, USA. The test site is located approximately 8 km south of Boulder and consists of flat terrain with short vegetation. On the test site, two Controls Advanced Research Turbines (CART's) are installed. Both turbines are research turbines. The CART-2 turbine is two bladed with a diameter D of 42 m and a rated power output of 660 kW which is reached at a wind speed of around 12.6 m/s [3]. The site comprises not only the CART-2 turbine but also three neighboring turbines and their respective met masts. The valid measurement sectors according to the IEC 61400-12-1 for power performance testing are smaller and are shown in Figure 1.

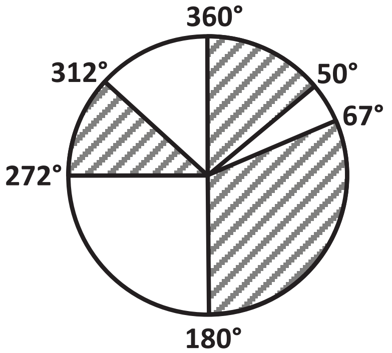

Figure 1. Measurement sectors of the CART-2 turbine; shaded: excluded sectors.

3. MEASUREMENT SETUP

On the nacelle of the CART-2 a Lidar system is installed to measure the inflowing wind field. The system comprises a customary Lidar device from the company Leosphere and a scanning system, specially developed at the SWE. The basic principle is that the pulsed laser beam emitted by the Lidar device can be deviated in any direction by the scanning system. A mirror can be positioned within a definite range horizontally and vertically and the laser beam follows a prescribed path. Thus the Lidar scanner makes it possible to scan the wind field at several discrete points, forming an arbitrary trajectory. Furthermore, as it is a pulsed laser beam, measurements can be taken at five focus distances simultaneously. Thus measurement with a high temporal and spatial resolution of the inflowing wind field is possible.

Figure 2 depicts the trajectory used for the the CART-2 campaign. The wind field is measured at five focus distances ranging from 1D to 2D in equidistant distances. The six measurement points at each focus plane form a circular trajectory. The diameter of the circle is the same as the rotor diameter in 2D.

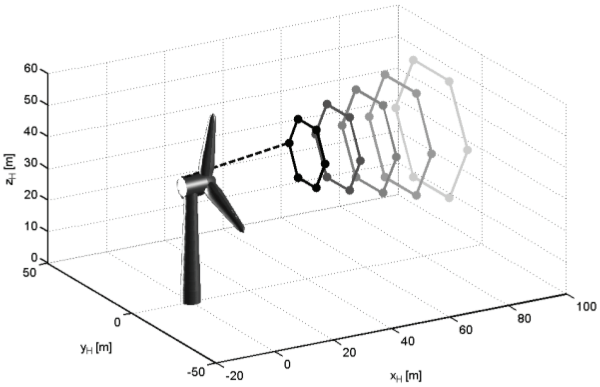

Figure 2. Circle trajectory used for the CART-2 campaign.

Simultaneously to the Lidar measurements, the wind speed is also measured using a cup anemometer mounted at hub height at the met mast which is located 2D in front of the turbine.

4. ROTOR EFFECTIVE WIND SPEED

To describe the power performance of a turbine in a power curve the electrical output is set into relation to the reference wind speed. In the case using a met mast, the wind speed is measured at one single point at hub height. With the new approach using a Lidar from the nacelle it is possible to take the whole swept rotor area into account. In this case the six measurement points of a circle are measured at each of the five focus distances. For quite good wind field information a high spatial and temporal resolution of the wind fields is needed. Therefore all of these thirty measurement points in space are taken into account and are calculated to one single speed, which is further called rotor effective wind speed v0: In [4] one describes how to calculate this rotor effective wind speed. The line-of-sight wind speeds are measured by the laser in six points at five different fixed distances. By the use of assumptions the wind speeds are corrected and averaged over the last trajectory at each focus distance. In a further step the resulting preview of the rotor effective wind speed v0(t) is a weighted average over all available vi available during time t (Fig. 3). That means that the five focus distances are shifted to one single distance. This shift can be done by the use of Taylor's frozen turbulence hypothesis which is valid for horizontally Lidar measurements [5].

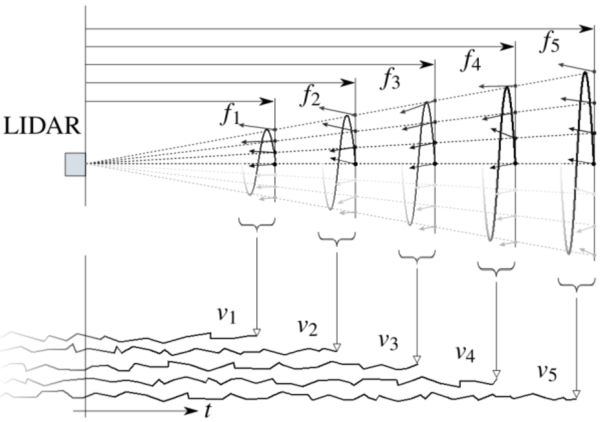

Figure 3. Schematic drawing of the incoming wind field measured by a Lidar at different focus distances.

In Figure 4 three different wind speeds are shown in a 10-min time series: one is measured by the anemometer on the met mast v_M, the other one shows the rotor effective wind speed v_{0L} measured with the Lidar. The third wind speed is recalculated from the turbine data as e.g. the pitch angle, rotor speed and power output data. Here the turbine represents a big horizontal axes anemometer with a rotor effective wind speed v_0. It is visible that the turbine's wind speed corresponds much better to the rotor effective wind speed of the Lidar than to the anemometer on the met mast.

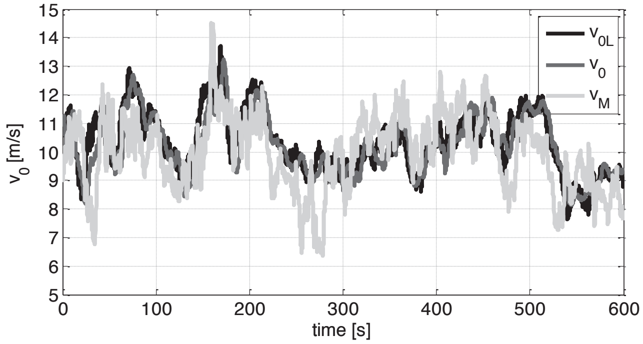

Figure 4. Time series of the rotor effective wind speed from Lidar and turbine and of the anemometer mounted on a mast.

In a further step, the power production of the CART-2 turbine was simulated with FAST. As input for the wind two different data sets were used: the real met mast data and the rotor effective wind speed measured with the Lidar. In Figure 5 the result of the simulated power output is shown together with the real electrical power from the turbine. As one can see, the simulation with the rotor effective wind speed corresponds very well with the real data.

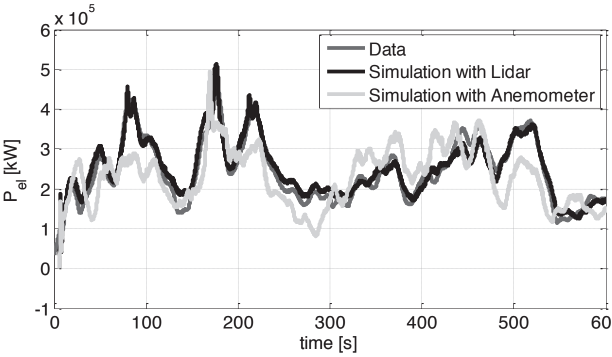

Figure 5. Simulation of the power production with met mast and Lidar data in comparison with the real production data.

5. POWER CURVES

According to the IEC 61400-12-1 standard, the measured wind speed and power data is supposed to be averaged over periods of 10 minutes in order to bin the data and plot the power curve. However, during the CART-2 campaign, the wind conditions are not optimal and subsequently not enough data is gathered to fill the required bins. Therefore it is decided to deviate significantly from the norm and to reduce the averaging period from 10 minutes to 10 and 30 seconds respectively. Thus enough data blocks are produced to plot meaningful power curves.

In Figure 6 and 7 the scatter plots of the 10 and 30 seconds averaged data of both the Lidar and met mast data is presented. In contrast to the Lidar data, the met mast data needs to be filtered according to the measurement sectors (cf. Figure 1). Hence more data blocks remain for the Lidar power curve. Comparing the 10 and 30 seconds averaged data, it is obvious that the scatter for both Lidar and met mast data increases by reducing the averaging period.

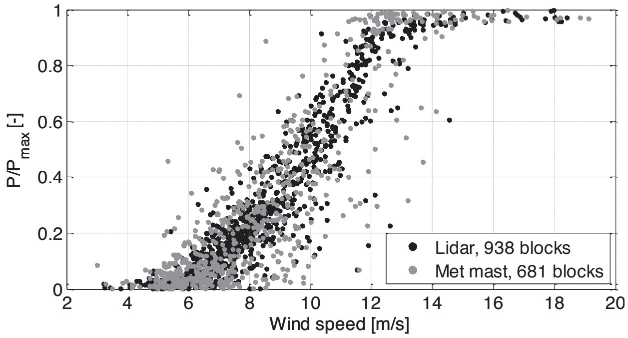

Figure 6. Scatter plot of Lidar and met mast power curves using 10 seconds average.

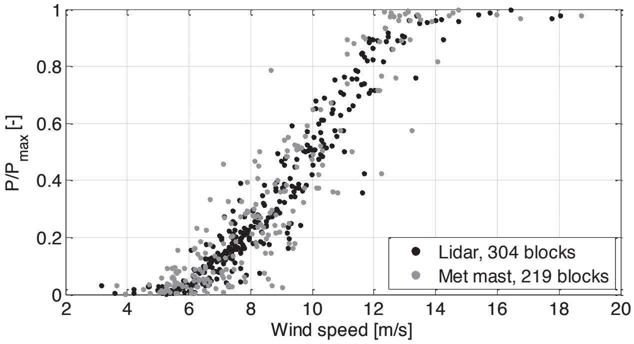

Figure 7. Scatter plot of Lidar and met mast power curves using 30 seconds average.

In Figure 8 and 9 the power curves are plotted. It becomes obvious that although the averaging period differs significantly from the norm, the quality of the power curves does not decrease likewise. Comparing the scatter of Lidar and met mast data of each wind speed bin, one can notice that the standard deviation of the power is always smaller for the Lidar measurements which are confirmed by the Figure 10 and 11.

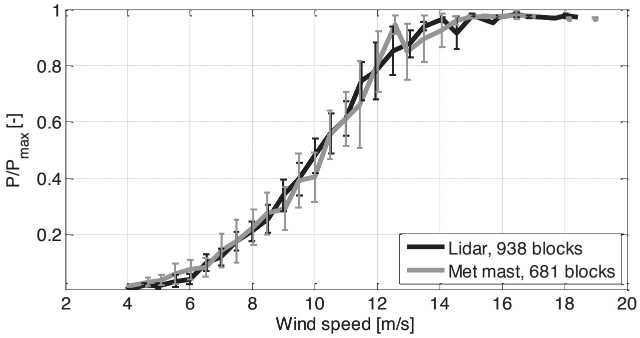

Figure 8. Power curve based on Lidar and met mast data using 10 seconds average.

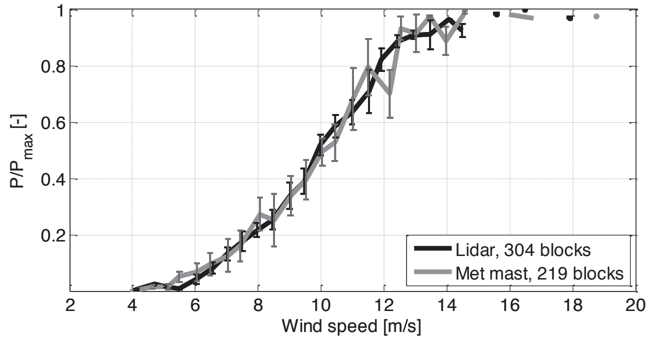

Figure 9. Power curve based on Lidar and met mast data using 30 seconds average.

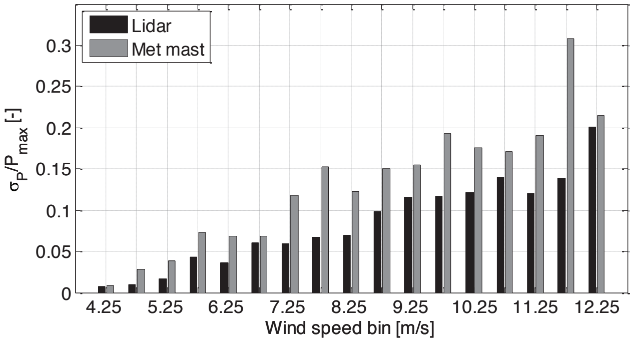

Figure 10. Ratio of the standard deviation and maximum power output over the wind speed BIN (10 seconds average).

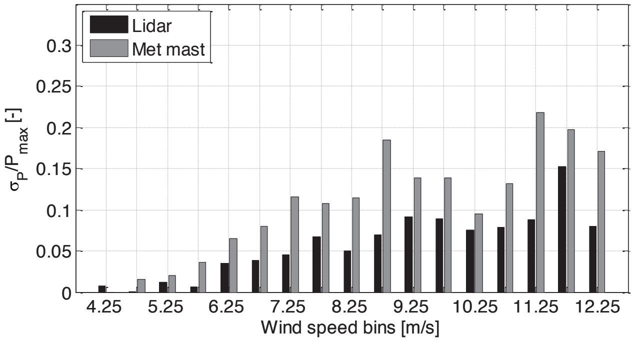

Figure 11. Ratio of the standard deviation and maximum power output over the wind speed BIN (30 seconds average).

ACKNOWLEDGMENTS

This work was performed at NRELs National Wind Technology Center (NWTC), Colorado, USA. The authors would like to thank all the people getting the Lidar systems and the different measurement campaigns working, special thanks to the further members Jan, Martin and Oliver of SWE Lidar group.

REFERENCES

1. Rettenmeier, A. et al., “Determination of power curves based on wind field measurements using a nacelle-based LiDAR scanner”, EWEA, Brussels, 2011

2. Rettenmeier, A. et al., “Wind field analyses using a nacelle-based LiDAR system”, EWEC, Warsaw, 2010.

3. Bossanyi, E., Wright A., Fleming P., “Controller Field Tests on the NREL CART2 Turbine”, NREL, 2010

4. Schlipf, D. et al, Nonlinear Model Predictive Control of Wind Turbines Using LIDAR, Wind Energy Journal, paper accepted

5. Schlipf, D. et al., Testing of Frozen Turbulence Hypothesis for Wind Turbine Applications with a Scanning Lidar System, ISARS, Paris, 2010.

SIMULATION OF LIDAR WIND SPEED MEASUREMENTS FOR WIND TURBINE CONTROL APPLICATIONS IN AN EVOLVING LES WIND FIELD

Eric Simley[1], Lucy Y. Pao[1], Edward G. Patton[2]

[1]*Dept. of Electrical, Computer, and Energy Engineering, University of Colorado,*
425 UCB, Boulder, CO 80309, USA , eric.simley@colorado.edu, pao@colorado.edu
[2] *National Center for Atmospheric Research, P.O. Box 3000, Boulder, CO 80307, USA, patton@ucar.edu*

ABSTRACT

Preview wind speed measurements from a forward looking LIDAR located in the hub of a wind turbine can be used by a feedforward blade pitch control system to mitigate structural loads. In addition to errors caused by LIDAR characteristics, the evolution of the wind as it travels between the upstream measurement location and the rotor will impact the preview measurement quality; this degradation can be described by a coherence loss between the remotely sensed wind and the wind at the turbine. Simulations of LIDAR measurements are performed in wind fields derived from a weakly stable high-Reynolds number numerical simulation. Results highlighting measurement scenarios that maximize coherence bandwidth are presented for effective wind speeds at the rotor using the WindPACT 1.5MW turbine model.

1. INTRODUCTION

Upstream LIDAR wind speed measurements can be used as input to a feedforward controller designed to reduce loads on the turbine structure. Past efforts [1,2] in simulating wind preview-based controllers have relied on Taylor's frozen turbulence hypothesis [3], which states that turbulent eddies advect downstream at the mean wind speed while remaining unchanged. The degree to which turbulence evolves between the upstream measurement point and the turbine rotor largely determines the effectiveness of LIDAR-based feedforward control. This research examines how wind evolution, or the deviation from Taylor's hypothesis impacts the correlation between upstream measurements and rotor effective wind speeds.

Rotor effective wind speed, as used in this research, is an average of the wind speeds at the rotor such that the power available to the turbine is given by the well-known equation $P = \frac{1}{2}\rho A C_p u_{eff}^3$ [4]. Rotor effective wind speed is calculated using

$$u_{eff} = \sqrt[3]{\frac{\sum\limits_{r=1}^{N_{rad}} \frac{C_p\left(r\right)}{N_{az}} \sum\limits_{\phi=1}^{N_{az}(r)} u^3\left(r,\phi\right)}{\sum\limits_{r=1}^{N_{rad}} C_p\left(r\right)}} \qquad (1)$$

where the wind is sampled at N_{rad} radial distances with N_{az} azimuth angles per radius and $C_p\left(r\right)$ is the power coefficient as a function of radial distance. Aerodynamic data are determined from the WindPACT 1.5MW turbine model with 70 m rotor diameter [5]. For this turbine, $C_p\left(r\right)$ is such that wind speeds from all rotor locations are weighted relatively evenly except near the hub and blade tips where root and tip losses occur.

2. LIDAR MEASUREMENTS

Measurements are simulated using a model of a continuous-wave ZephIR LIDAR [6] located in the turbine hub as shown in Figure 1. A hub height of 90 m is used, which is slightly higher than the WindPACT definition. The ZephIR can sample at a rate of 50 Hz.

Each LIDAR sample is a weighted line-of-sight velocity given by

$$u_{wt,LOS} = -\ell_x u_{wt} - \ell_y v_{wt} - \ell_z w_{wt} \qquad (2)$$

where $\vec{\ell} = \left[\ell_x, \ell_y, \ell_z\right]$ is the unit vector in the LIDAR beam direction. The weighted velocity vector, $\vec{u}_{wt} = \left[u_{wt}, v_{wt}, w_{wt}\right]$, is a weighted sum of velocities along the LIDAR beam given by

$$\vec{u}_{wt} = \int_0^\infty \vec{u}\left(R\vec{\ell}\right) W\left(F,R\right) dR \qquad (3)$$

where $W\left(F,R\right)$ is a range weighting function with focal distance F and range R from the LIDAR as arguments. More information about the ZephIR range weighting function is available in [7]. The line-of-sight velocity in Eq. 2 is divided by ℓ_x to yield an estimate of the streamwise *u* component of interest

$$\hat{u} = u_{wt} + \frac{\ell_y}{\ell_x} v_{wt} + \frac{\ell_z}{\ell_x} w_{wt}. \qquad (4)$$

Equation 4 reveals two sources of error in the LIDAR-based estimate of the *u* component: range weighting along the beam and the presence of transverse *v* and vertical *w* components.

In this research, the upstream estimate of the rotor effective wind speed is formed by measuring a circle of wind with radius *r* at a preview distance *d* ahead of the turbine as shown in Figure 1. The estimate of the effective wind speed is given by

$$\hat{u}_{eff} = \sqrt[3]{\frac{1}{N_{az}} \sum_{\phi=1}^{N_{az}} \hat{u}^3(\phi)} \tag{5}$$

where N_{az} is the number of measurement azimuth angles. It is assumed that all azimuth angles are sampled simultaneously.

3. MEASUREMENT COHERENCE

Several combinations of scan radius r and preview distance d are examined. The quality of each scan scenario is judged by the coherence between $\hat{u}_{eff}$ and the effective wind speed at the rotor, delayed by d/U seconds where U is the mean wind speed at hub height. Magnitude-squared coherence describes the correlation between two signals as a function of frequency and is calculated using

$$\gamma_{xy}^2(f) = \frac{\left|\overline{S_{xy}(f)}\right|^2}{\overline{S_{xx}(f) S_{yy}(f)}} \tag{6}$$

where $S_{xx}(f)$ and $S_{xy}(f)$ are the power spectral density (PSD) of signal x and cross-power spectral density (CPSD) between signals x and y respectively. All spectral densities are calculated using Welch's method [8] and $\overline{S(f)}$ denotes the average spectrum over all wind fields used for simulation.

4. LARGE-EDDY SIMULATION (LES)

4.1 Code and Simulation Description

The National Center for Atmospheric Research's (NCAR's) LES code [9] generates turbulent fields mimicking the weakly stable atmospheric boundary layer [10]. The code solves the incompressible Boussinesq equations using pseudo-spectral methods in the horizontal directions (x and y), second-order finite differences in the vertical (z), and a third-order Runge-Kutta scheme in time.

The simulation's general setup and forcing follows that described in Beare et al.'s intercomparison study [11], but a key difference is that the current simulation uses a 1 km^2 × 400 m domain resolved by 500^2 × 400 grid points. The flow is driven by imposed horizontal geostrophic winds (u_g, v_g) of (8, 0) m s^{-1}, which is also used as the initial wind profile. The initial virtual potential temperature profile is horizontally homogeneous and is specified as 265 K from the surface up to 100 m, and then increasing to the domain top at a rate of 10 K km^{-1}. The surface, which has a prescribed roughness length z_o = 0.1 m, is cooled at a rate of 0.25 K hr^{-1}. Turbulence initiates by imposing divergence free temperature fluctuations with a 0.1 K amplitude through the domain's lowest 50 m and the unresolved energy is initially set as 0.4(1-z/250)^3 m^{-2} s^{-2} throughout the domain's lowest 250 m. The generated flow field represents unobstructed flow without the presence of the turbine.

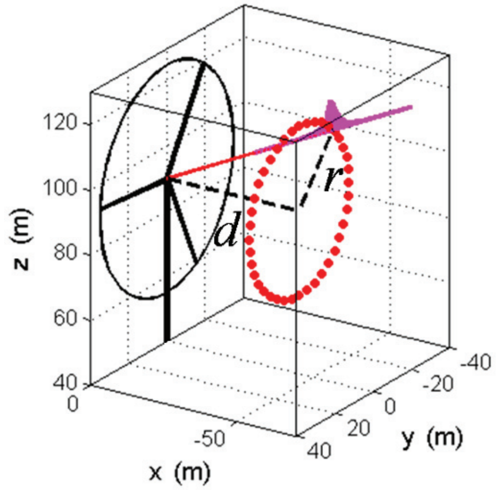

Figure 1. Hub-mounted spinning LIDAR scenario with scan radius r and preview distance d. The LIDAR range weighting function is illustrated in magenta.

Analysis of the data begins following an initial nine hour integration period, where the planetary boundary layer (PBL) depth (z_i) reaches approximately 200 m, with an inertial-oscillation-generated low-level wind maximum of about 9.6 m s^{-1} persisting just below z_i. Profiles of potential temperature, mean wind speed, and wind direction for heights between 50 m and 150 m are included in Figure 2.

4.2 LES Wind Fields

The four-dimensional LES wind field is divided into twenty smaller 200-second periods with dimension 200 m × 200 m in the xy plane, as shown in Figure 3,

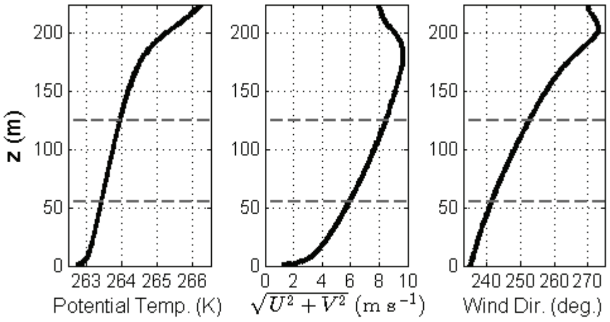

Figure 2. Profiles of potential temperature, mean streamwise wind speed, and wind direction. The gray lines indicate the boundary of the rotor plane.

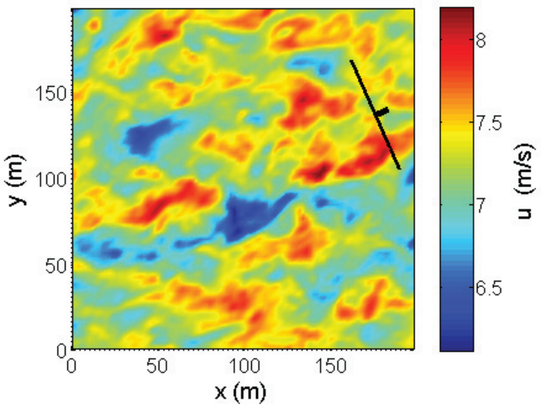

Figure 3. An instantaneous horizontal (*xy*) slice of the LES-derived wind field at 90 m hub height. The turbine rotor is aligned perpendicular to the mean wind direction.

spanning a height of 100 m. Spatial resolution is 2 m and the sample rate is 1.02 seconds.

4.3 Wind Evolution

The evolution of turbulence as it advects downwind can be quantified using the coherence between the time series of u at two points separated along the streamwise direction. Taylor's hypothesis is valid if the coherence is equal to 1 and the CPSD of the two time series has linear phase due to the finite transit time between points. Coherence functions for the LES-derived wind field are shown in Figure 4 for longitudinal separations at heights describing the top and bottom of the rotor disk. Although mean wind speed varies with height, the longitudinal separations for both heights yield the same eddy transit time delays: 2, 5, 11, and 23 seconds.

5. LIDAR SIMULATION RESULTS

Simulations of LIDAR measurements were performed to study measurement coherence for a variety of scan radii r and preview distances d. For each wind speed estimate, given by Eq. 5, N_{az} is chosen such that the circle scanned by the LIDAR is sampled every 2 m. Measurement coherence is affected by the measurement angle $\arctan(r/d)$, the focal distance F, and the intensity of wind evolution, which is a function of the preview distance d. For large measurement angles, the v and w components corrupt the estimate of the u component. As F increases, range weighting causes the LIDAR to sample a larger volume [12]. As d increases, coherence loss due to wind evolution becomes more severe.

Figure 5 summarizes the simulated measurement coherence for a variety of scan radii and preview distances. Four scan radii are used, representing r = 10%, 30%, 70%, and 90% of the rotor radius R = 35 m. Only preview distances beyond 1 R are simulated because of the distorted wind speeds in the induction zone of the rotor, which is prominent for $d < R$ [13].

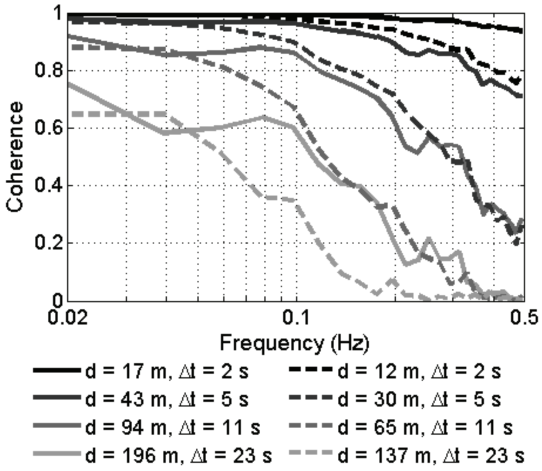

Figure 4. Longitudinal u component coherence curves for separations along the streamwise direction. **Solid**: z = 125 m, U = 8.4 m/s. **Dashed**: z = 55 m, U = 5.8 m/s.

Due to wind shear across the rotor plane (Figure 2) upstream winds measured at different heights do not reach the turbine at the same time. Similarly, due to wind veer, winds at different heights will not advect toward the turbine in the same direction. Figure 6 compares coherence curves for the basic scan geometry with r = 0.7 R and d = 37 m and 132 m with a more complicated scan geometry that corrects for shear and veer. The corrected scan geometry focuses the LIDAR differently at each height and azimuth so that wind at the measured locations reaches the turbine rotor at the intended points after the desired preview time based on hub height wind speeds.

6. DISCUSSION AND CONCLUSIONS

LIDAR simulation results show that for a circular scan pattern a scan radius close to 70% rotor radius provides the strongest measurement correlation. When considering that rotor effective wind speed is dominated by low frequencies, strong correlation is more important at the lower end of the spectrum. Small scan radii, such as r = 0.1 R, produce lower correlations because the measured winds are representative of a smaller portion of the rotor plane. For preview distances beyond 37 m, roughly equivalent to the rotor radius, the coherence drops as the preview distance increases due to wind evolution. However, preview distance must roughly double before coherence drops by more than 0.1. When knowledge of the wind speed and direction at heights other than hub height is used to determine the scan geometry, measurement coherence can be increased, but at most by 0.1 for r = 0.7 R and 37 m < d < 132 m. The modified scan pattern improves measurement quality more for longer preview distances.

Therefore, with knowledge of only hub height wind speed and direction, upstream wind measurements can still provide rotor effective wind speed estimates of acceptable quality.

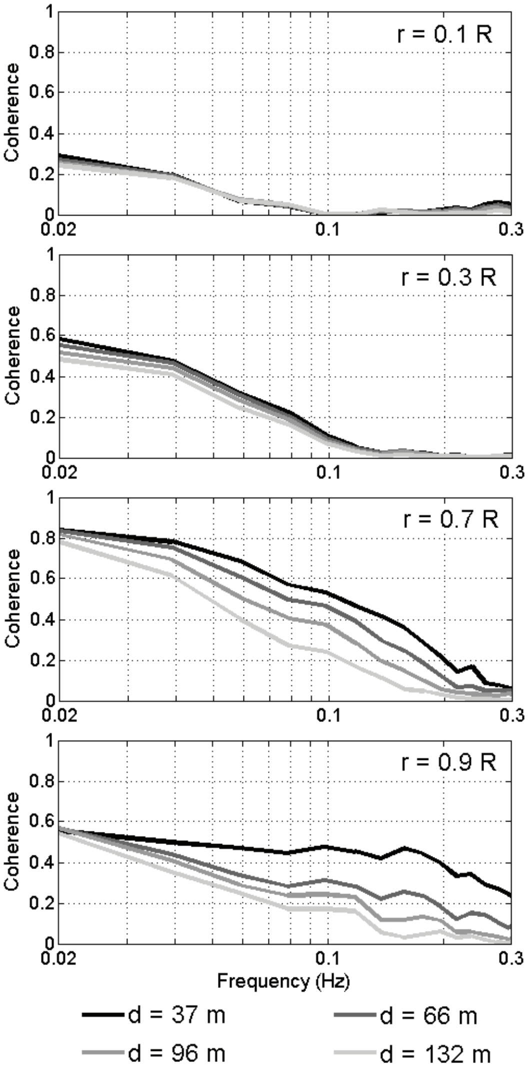

Figure 5. Coherence between LIDAR measurements and rotor effective wind speed for various *r* and *d*.

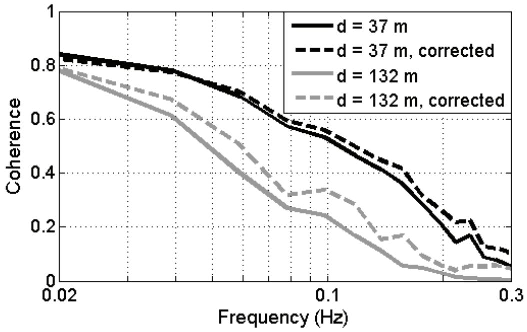

Figure 6. Measurement coherence for scan geometries that correct for wind shear and wind veer for *r* = 0.7 *R*.

Simulations were performed using a numerical simulation of the stable boundary layer. It is necessary to study neutral and unstable conditions to understand how wind evolution varies with atmospheric stability.

ACKNOWLEDGMENTS

This work was supported in part by the U.S. National Renewable Energy Laboratory. NCAR is sponsored in part by the National Science Foundation.

REFERENCES

1. Dunne, F. et. al., "Adding Feedforward Blade Pitch Control for Load Mitigation in Wind Turbines: Non-causal Series Expansion, Preview Control, and Optimized FIR Filter Methods," *Proc. ASME Wind Energy Symposium*, 2011.

2. Laks, J. et. al., "Model Predictive Control using Preview Measurements from LIDAR," *Proc. ASME Wind Energy Symposium*, 2011.

3. Taylor, G. I., "The spectrum of turbulence*," Proc. Roy. Soc. Lond. A*, **164**, 476-490, 1938.

4. Manwell, J.F., McGowan, J.G., and Rogers, A.L., *Wind Energy Explained: Theory, Design and Application*. West Sussex, England: Wiley, 2002.

5. Malcolm, D.J. and Hansen, A.C., "WindPACT turbine rotor design study," National Renewable Energy Laboratory, NREL/SR-500-32495, 2006.

6. Courtney, M., Wagner, R., and Lindelöw, P., "Commercial wind profilers for wind energy. A comparative guide," *Proc. European Wind Energy Conference*, 2008.

7. Simley, E., Pao, L.Y., Kelley, N., Jonkman, B., and Frehlich, R., "LIDAR wind speed measurements of evolving wind fields," *Proc. ASME Wind Energy Symposium*, 2012.

8. Stoica, P., and Moses R.L., *Introduction to Spectral Analysis*, Englewood Cliffs, NJ, Prentice-Hall, 1997.

9. Sullivan, P.P. and Patton, E.G., "The effect of mesh resolution on convective boundary layer statistics and structures generated by large-eddy simulation," *J. Atmos. Sci.,* **68**, 2395-2415, 2011.

10. Saiki, E.M., Moeng, C.-H., and Sullivan, P.P., "Large eddy simulation of the stably stratified planetary boundary layer," *Bound.-Lay. Meteorol.,* **95**, 1-30, 2000.

11. Beare, R.J. et al., "An intercomparison of large-eddy simulations of the stable boundary layer," *Bound.-Lay. Meteorol.*, **118**, 247-272, 2006.

12. Simley, E., Pao, L.Y., Frehlich, R., Jonkman, B., and Kelley, N., "Analysis of wind speed measurements using continuous wave LIDAR for wind turbine control," *Proc. ASME Wind Energy Symposium*, 2011.

13. Medici, D., Ivanell, S., Dahlberg, J.Å., and Alfredsson, P., "The upstream flow of a wind turbine: blockage effect," *Wind Energy*, **14**, 691-697, 2011.

Poster Session 2

AN ALGORITHM BASED ON THE STATISTICAL LEARNING THEORY FOR DENOISING AND GAP FILLING OF SODAR WIND DATA

Velayudhan Praju Kiliyanpilakkil, Sukanta Basu

Department of Marine, Earth, and Atmospheric Sciences, North Carolina State University, Raleigh, NC, USA
prajukv@gmail.com, sukanta_basu@ncsu.edu

ABSTRACT

Wind energy industries around the world have witnessed a significant surge in recent years. However, to make wind a cost-effective and reliable alternative energy source, the industry will need to make significant scientific advancements in several arenas of wind power meteorology. Modern-day utility-scale wind turbines have blade tips extending up to 150 m above ground level; new turbines are expected to extend even above 200 m. As the future wind turbines are designed with increasingly higher hub-heights and larger rotor diameters, accurate measurements of lower boundary layer wind fields will become more important. Given the high construction, operation, and maintenance costs associated with tall-tower-based wind measurements, the wind energy community is exploring standalone, and inexpensive alternatives. Active ground-based remote sensing instruments like sound detection and ranging (sodar) and laser imaging detection and ranging (lidar) are gaining popularity for various wind resource assessment, inflow characterization, and short-term forecasting [1]. Modern-day sodars are very portable and can measure vertical profiles of three-dimensional velocity components and turbulence characteristics with high spatial and temporal resolutions.

Susceptibility to ambient noise and data-loss with increasing altitude are two major weaknesses of contemporary sodars. In this paper, we are introducing a new algorithm for sodar data denoising and gap-filling. The algorithm based on the Vapnik-Chervonenkis Statistical Learning Theory [2] is designed to be fully automated. The effectiveness of this algorithm is tested by using sodar wind observations (Scintec SFAS system) along with a boundary layer profiler (Vaisala LAP-3000) from an ongoing field campaign in Texas, USA. In-situ wind observations from a collocated 200 m meteorological tower are utilized for validation. The proposed algorithm will complement the existing sodar/profiler noise reduction schemes by reducing the uncertainty associated with the missing data.

1. DESCRIPTION OF DATA

The testing and validation of the current algorithm is conducted using data collected in an ongoing field campaign, Wind Forecast Improvement Project (WFIP) (http://www.esrl.noaa.gov/psd/psd3/wfip/). We used wind speed and wind direction data from a Vaisala LAP-3000 boundary layer profiler, meteorological tower [3], and a Scintec Flat Array Sodar system (SFAS) [4] operational at Reese Technology Center near Lubbock, Texas, United States. Observations from15th July, 2011 to 5th May, 2012 are used for testing the denoising algorithm.

2. KEY RESULTS

Figures 1(a) and 1(b) show time-height plots of observed wind speed by sodar and profiler, respectively. The application of the proposed algorithm to merged sodar and profiler wind speed data is demonstrated in Figure 1(c). By visually comparing with collocated tower observations [Figure 1(d)], it is quite evident that the algorithm reasonably filters the noisy data and fills in the data gaps. However, it is not able to fill in the gaps when substantial amounts of observations are missing.

ACKNOWLEDGMENTS

This research was partially supported by the U S Department of Energy (subcontract from AWS Truepower) and the National Science Foundation. The authors gratefully acknowledge John Schroeder, Jeff Livingston, and Wes Burgett at Texas Tech. University, Lubbock, TX for their effort in making the profiler and met-tower data available.

REFERENCES

1. Bradley, S. G., 2008: *Atmospheric acoustic remote sensing*, Taylor and Francis group, FL, USA.

2. Cherkassky, V., F. Mulier, 2007: *Learning from data: Concepts, theory, and methods*, 2nd ed., John Wiley & Sons. Inc., Hoboken, New Jersey.

3. Walter, K., C. C. Weiss, A. H. P. Swift, J. Chapman, N. D. Kelley, 2007: Observations of extreme speed and directional wind shear in the US Great Plains, *the European Wind Energy Conference*, Milan, Italy.

4. Scintec Flat Array Sodar – Hardware Manual Version 1.00, 2010: Scintec AG, Wilhelm-Maybach-Str. 14, 72108, Rottenburg, Germany.

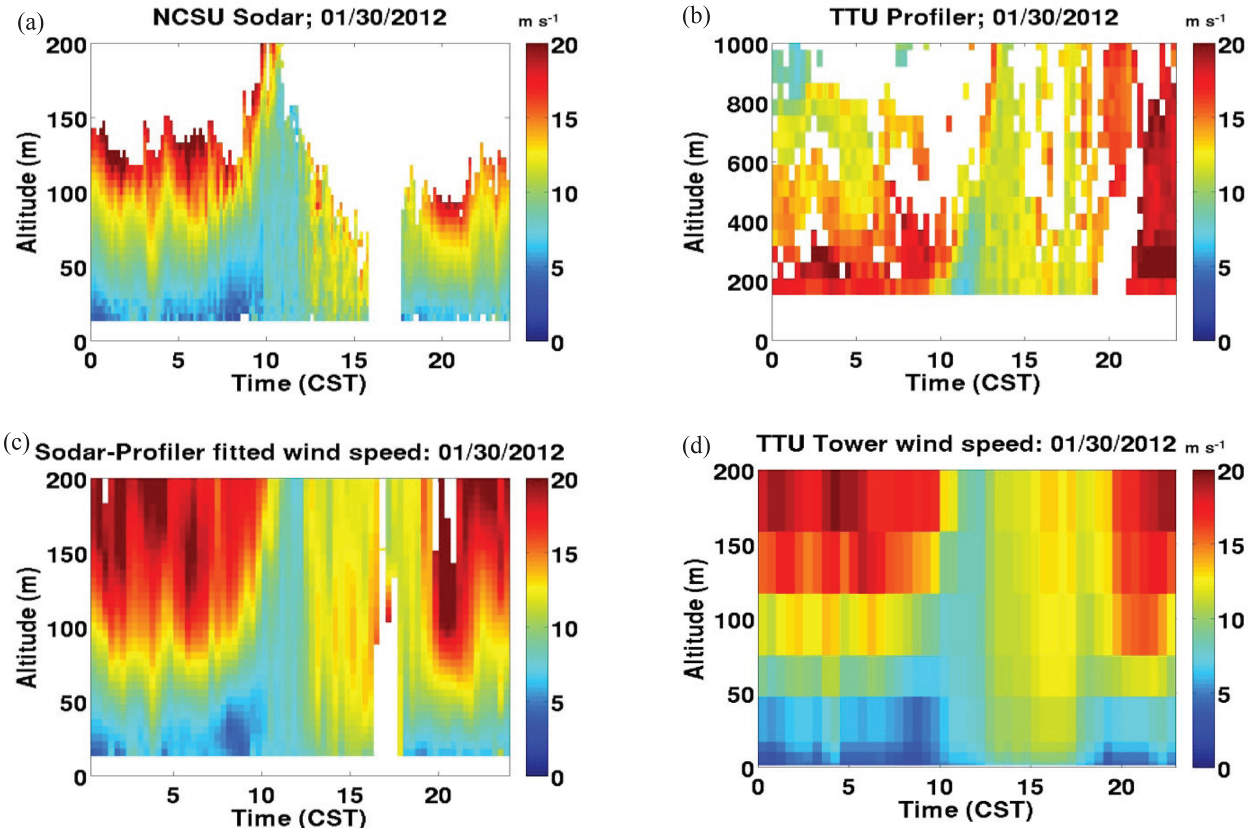

Figure 1. Time-altitude plots of wind speed for (a) sodar (b) wind profiler, (c) filtered and gap-filled merged sodar/profiler, and (d) tower data on 30th January, 2012. Central Standard Time (CST) = UTC - 6 hours

DATA ASSIMILATION TECHNIQUE FOR SHORT-TERM WIND FORECASTING

E. Avolio [1,2], S. Federico [1], A.M. Sempreviva [1,3], C.R. Calidonna [1], M. Courtney [3], R. Girard [4], G. Kariniotakis [4]

[1] *Institute of Atmospheric Sciences and Climate – National Research Council (ISAC-CNR), Lamezia Terme, Italy.*
e.avolio@isac.cnr.it
[2] *CRATI Scrl, c/o University of Calabria, Rende (CS), Italy*
[3] *Danish Technical University Wind Energy Department, Roskilde, Denmark*
[4] *MINES-ParisTech, Center for Energy & Processes, Sophia Antipolis, France*

ABSTRACT

The purpose of this work is to investigate the use of data assimilation of vertical profile of wind speed and direction by a Lidar Doppler to improve the performance of a Numerical Weather Prediction (NWP) model in short-term wind forecasting functional to wind energy integration. The work was in the framework of the COST Action ES1002 “Weather Intelligence for Renewable Energies” (WIRE) within collaboration between CNR-ISAC, the Mines–ParisTech, and the Danish Technical University. NWP model outputs represent the unavoidable input data for all wind power prediction systems and the Mines–ParisTech has developed the Armines Wind Power Prediction System (AWPPS) that provides short-term forecasts for the power output of onshore and offshore wind farms. The work was primarily focused to study the relationship between the meteorological information and the possible operational applications in term of power prediction.

An high-resolution state-of-the-art mesoscale model, operational at CNR-ISAC, was adopted for the simulations. Vertical profiles of wind speed and direction from a Windcube Lidar were used, for both the assimilation and the comparison with model simulations. The NWP model was run for 30 consecutive days and in two different configurations: with and without data assimilation scheme activated. The study area is a flat coastal area in Denmark, where both wind measurements and wind power data are available. Preliminary results show small improvements of the model runs in which the assimilation scheme is activated compared to the control runs, without data assimilation. The forecast is improved for some days by the data assimilation, but there are occasions in which the technique doesn’t improve or even worsen the forecast.

Work is in progress to better understand the error behaviour as a function of the synoptic circulation and of the height. Moreover, the analysis will be repeated for very-short term forecasts (up to 1 h) and for a longer period.

1. INTRODUCTION

Above a significant level of wind energy penetration it is crucial to rely on trustable wind forecast models for time horizons from minutes to days ahead and to be aware and quantify their uncertainties under different atmospheric conditions.

A main issue in improving weather forecast numerical models is to obtain an improved knowledge of the atmospheric state through the use of asynoptic data, in order to produce good initial and boundary conditions. Several remote sensing instruments, such as wind profilers i.e. sodars, lidars and radars, are able to provide continuous streams of data on the evolving atmospheric conditions, and atmospheric observations through a deep layer of the atmosphere.

Data assimilation is the procedure that consists to incorporate observational data into analysis or forecast provided by meteorological models [1]; in this work a Four Dimensional Data Assimilation (FDDA) technique, based on Newtonian Relaxation [2,3], is adopted to produce accurate meteorological simulations with a tailored version of a high-resolution state-of-the-art mesoscale model.

2. EXPERIMENTAL SITE AND MEASUREMENTS

The experimental site is the Danish National Test Station for Large Wind Turbines, located at Høvsøre in Western Jutland, Denmark, Figure 1 (picture from Google Earth). The site is in a flat terrain area, with low height variations (less than 5 m) near the coastline. This site is equipped with a line of five test stands for MW-class wind turbines.

Vertical profiles of wind speed and direction from Leosphere WLS-7 (Windcube) Lidar, were used both for data assimilation tests and for evaluating a model performance; the Lidar was located at the southern end of the turbine line.

The Windcube is a pulsed Doppler Lidar wind profiler operating at the eye-safe 1.5μm wavelength. The instrument measures the radial speed in 4 directions azimuthally separated by 90 degrees. The full 3-D wind speed vector is retrieved by combining the four last consecutive radial speeds. The maximum measuring height of the instrument was set to 300 m.

Figure 1. Høvsøre site.

The simulations and the verification procedures were performed for the available one-month period, from 20 April 2010 to 20 May 2010. The dataset consisted of 10-minute time series at the following levels: 40m, 60m, 80m, 100m, 116m, 130m, 160 m, 200 m, 250 m and 300 m.

3. MODEL CONFIGURATION AND PROCEDURES

A tailored version of the meteorological model Regional Atmospheric Modeling System (RAMS), in its version 6.0, was used in this work. A detailed description of the RAMS model is given in Cotton et al. [4].

The model is configured with four two-way nested grids (Figure 2). Horizontal resolutions are 27 km, 9 km, 3 km and 1 km, respectively. The fourth grid is centred over the Høvsøre experimental site; for this grid forty vertical levels are used and the spatial extension is 32 km.

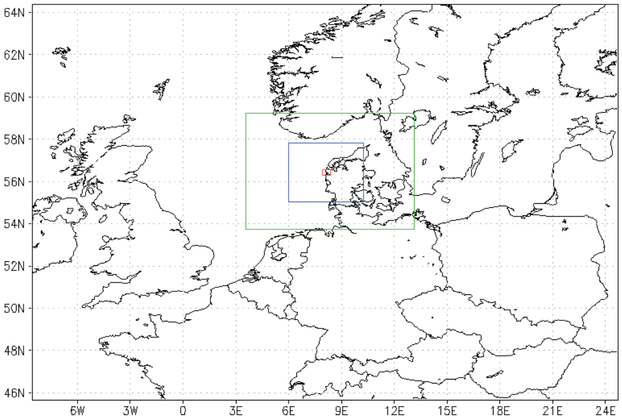

Figure 2. RAMS domains

RAMS model was run in two different configurations: a "normal forecast" (also 'NOAS', below) and a "data assimilation" (also 'AS12', below) run. The run duration is twenty-four hours for both configurations. For each configuration, simulations were performed for a one-month period from 20 April 2010 to 20 May 2010 (one simulation per day, starting at 12 UTC).

3.1 Assimilation Technique

For the assimilation procedure, a Newtonian relaxation (or nudging) was adopted [3,5]. The nudging technique consists of adding an extra tendency term, to the prognostic equations of the zonal and meridional wind components, which forces the variable toward the observations.

3.2 Statistical Analysis

To compare the NOAS and the AS12 runs, the Mean Absolute Error (MAE) and the Root Means Square Error (RMSE) for both wind speed WSP (ms-1) and direction WDIR (Deg) were computed for one, three, and six hours following the end of the nudging time, i.e. after the first 12 h of simulation.

4. RESULTS

Preliminary results are showed in terms of biases BIA and RMSE, for the whole study period, for all vertical levels, for both WSP and WDIR and for three different time steps: one, three, and six hours following the end of the assimilation procedure. Improvements are evaluated by comparing model errors for the NOAS simulations with model errors for the AS12 simulations. The results are summarized in Table 1. MAE and RMSE units for WSP are [ms^{-1}] and for WDIR are [Deg].

30 days	**NOAS**				**AS12**			
	WSP		**WDIR**		**WSP**		**WDIR**	
	MAE	*RMSE*	*MAE*	*RMSE*	*MAE*	*RMSE*	*MAE*	*RMSE*
6 HOURS	1.41	1.82	16	30	1.39	1.80	17	31
3 HOURS	1.40	1.82	18	31	1.37	1.79	18	32
1 HOUR	1.39	1.80	18	31	1.29	1.70	19	34

Table 1. One-month results (MAE and RMSE) for WSP (m/s) and WDIR (Deg)

Statistics show negligible improvement of the "data assimilation" run compared to the "control forecast" run. The wind speed RMSE of the NOAS (AS12), averaged over all levels, and for the whole period, is 1.80 m/s (1.70 m/s) for the one-hour forecast, 1.82 (1.79 m/s) for the three-hour forecast, and 1.82 (1.80 m/s) for the six-hour forecast. The wind direction RMSE of the NOAS (AS12), averaged over all levels and for the whole period considered is 31° (34°) for the one-hour forecast, 31° (32°) for the three-hour forecast, and 30° (31°) for the six-hour forecast.

For the one-hour forecast, the wind speed RMSE "error reduction" is of about 5%. For the same case, but for the wind direction RMSE, we found an "error increase" of about 8%. Anyway, all the errors and the results should be contextualized and examined in absolute terms. In fact, even in the "worst case", the difference between NOAS run and AS12 run (for the wind direction RMSE), is 3° (Tab. 1); this value, can be considered negligible with respect to the instrumental error of most wind sensors.

A subsequent step was the daily analysis of the one-hour forecast. This statistics (not showed) allows us to perform daily analysis and to study the error variability. It follows that there are days in which the forecast is improved by the data assimilation and days in which the technique does not improve or even worsen the forecast.

From the daily analysis follow some information: when the wind direction is forced by the synoptic scale, and it is well defined, the errors are low without data assimilation. In these cases, it is more difficult to improve the "control forecast", because the assimilation improvement is larger when the difference between the background and observation is large. Again, regarding the daily errors on WDIR, the RMSEs have significant fluctuations in connection with significant changes in wind direction.

Due to the problems related to the wind variability in the PBL, it has been necessary to perform some accurate analysis (not showed) taking into account the wind behaviour with height. From these analysis it follows that for WSP RMSE error is maximum at the first level, minimum at the second one, and generally tends to become smaller with height; this behaviour, confirmed both for the NOAS and for the AS12 run, is justified by the fact that in the surface layer there are several issues that make difficult to perform a good forecast.

For WDIR RMSE there is a different trend. Errors, both for the NOAS and for the AS12 run, are quite constant for the first six levels and almost twice at higher levels. This fact shows that the model has difficulties to forecast wind direction, likely because the RAMS PBL parameterization's scheme is not optimized for high resolutions used in this work.

5. CONCLUSIONS AND FUTURE WORK

A personalised version of the mesoscale model RAMS was tested to investigate the performances improvement by implementing a 4-dimensional nudging scheme. Assimilation and verification are performed using data from a Wind Lidar over one-month period available at a Danish site in flat terrain. Initial results show that the assimilation of wind profiles produces a negligible improvement of the model performances. At the same time, it was evident that for several days the initial (NOAS run) RAMS errors, both for WSP and for WDIR, were small, and for those days the improvements were lower. For WSP, it was found that the higher the wind, the bigger the errors. And near the surface (first vertical levels) errors are higher than above. For WDIR the error behaviour with the height is opposite, because errors become larger at higher vertical levels. Moreover, it is noticeable that errors have significant fluctuations when significant changes in wind direction occur.

Further work is planned (and is already in progress) in order to:

- Repeat numerical simulations (and analyses) for very-short term forecasts (up to 1 h) and for a longer period;
- Try to test the system in an orography complex terrain;
- Test different parameterization's scheme (PBL, surface, etc.); and
- Set up and use different assimilation schemes (3DVAR, 4DVAR).

ACKNOWLEDGMENTS

Elenio Avolio acknowledges funding from the COST Action ES1002 "Weather Intelligence for Renewable Energies" (WIRE) for his short-term mobility mission at *MINES-ParisTech.* DTU and MINES-ParisTech are also acknowledged for the scientific support and for providing data collected within the SafeWind project www.safewind.eu.

SELECTED REFERENCES

1. E. Kalnay, "Atmospheric Modeling, Data Assimilation, and Predictability", Cambridge Univ. Press, New York, 2002.

2. R. A. Anthes, "Data assimilation and initialization of hurricane prediction models", J. Atmos. Sci., 31, 1974, pp. 702–719.

3. D. R. Stauffer and N. L. Seaman, "Use of four-dimensional data assimilation in a limited-area mesoscale model. part I: Experiments with synoptic-scale data", Mon. Weather Rev., 118, 1990, pp. 1250–1277.

4. Cotton, W. R., Pielke, R. A. Sr., Walko, R. L., Liston, G. E., Tremback, C. J., Jiang, H., McAnelly, R. L., Harrington, J. Y., Nicholls, M. E., Carrio, G. G., McFadden, J. P. : RAMS 2001: Current status and future directions, Meteorol. Atmos. Phys., 82, (2003), 5-29.

5. Avolio E., S. Federico, A.M Sempreviva, C.R Calidonna, L. De Leo, C Bellecci: Preliminary Meteorological Results of a Four-Dimensional Data Assimilation Technique in Southern Italy. Atmospheric and Climate Sciences, 2011, 1, 134-141. doi:10.4236/acs.2011.13015

WIND PROFILE MEASUREMENT IN SEASHORE USING A WIND LIDAR AND A TOWER

Y.-J. Choi, Y.-S. Park, S.-W. Lee, G.-H. Kim, B.-K. Seo

National Institute of Meteorological Research, KMA, Seoul, South Korea, yjchoikma@korea.kr

Korea Meteorological Administration(KMA) developed high-resolution wind resource maps over entire Korean peninsula in 2010 and keeps improving them thereafter. The wind resource assessments over Korea are based on the results of mesoscale model, WRF. In order to validate the model results, vertical wind profiles are measured at levels of 80, 100, and 120 m above ground using conically scanning lidar installed at ground level and cup anemometers installed in a tower and they are compared. Measurements were performed at Gochang in seashore(see Fig. 1) located in southwest region of South Korea where it is close to one of 2 offshore wind farms planned to be constructed within 10 years in South Korea. The sea-land breezes are also observed and the vertical structures are investigated. The sea-land breezes observed in east coast and west coast are compared.

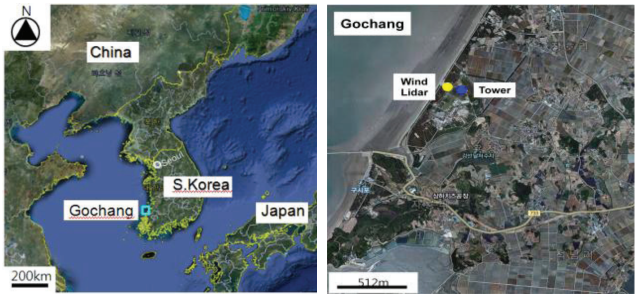

Figure 1. The location of observation experiment in South Korea.

WIRE: WEATHER INTELLIGENCE FOR RENEWABLE ENERGIES.
THE COST ACTION ES1002

Anna Maria Sempreviva[1], Alain Heimo[2], Foeke Kuik[3], Laurent Vuilleumier[4], Bertrand Calpini[4].

[1] *Institute of Atmospheric Sciences and Climate – National Research Council (ISAC-CNR), Lamezia Terme, Italy,*
am.sempreviva@isac.cnr.it
[2] *A METEOTEST| Fabrikstrasse 14, CH-3012 Bern, Switzerland, alain.heimo@meteotest.ch*
[3] *A Kipp & Zonen B.V. Delftechpark 36, 2628 XH Delft P.O. Box 507, 2600 AM Delft, The Netherlands*
Foeke.Kuik@kippzonen.com
[4] *Atmospheric Data Climate Division MeteoSchweiz, Case postale 316, CH-1530 Payerne, Switzerland,*
Laurent.Vuilleumier@meteoswiss.ch

ABSTRACT

The main goal of WIRE www.wire1002.ch is contributing enhancing methodologies for forecasting wind and solar power production from minutes up to several days ahead combining Numerical Weather Prediction (NWP) models and real-time surface and remote sensing measurements. The objectives are: to establish an understanding between the scientific and end user communities; to optimize the technical and economic integration of renewable energies and transferring knowledge across Europe and worldwide. WIRE consists of three Work Groups (WG):

WG1. Modeling and post-processing. Activities in progress are: the assessment of current research activities in Europe and current knowledge gaps to highlight the existing weaknesses for all components of the renewable energy forecast system and of the adequacy of NWP models and downscaling methodologies coupled with dedicated power conversion modules to deliver accurate power production forecast.

WG2. Measurements and Observations. The added value of the new observation techniques in developing power forecasting models will be quantified. In particular, the focus will be on space-borne and ground-based remote sensing technologies for determining i.e. cloud cover, vertical wind profiles, the vertical content of Liquid Water and Particle Size Distribution. Recommendations will be provided to the scientific and users communities. NWP benchmarking is being organized and results of post-processing improved forecasting systems will be evaluated selecting existing locations with wind farms and solar energy plants. Databases will be set up and formatted for direct use by the modeler's community.

WG3. Power Plants and Grid Management. End-users will be involved in developing improved forecasting systems assuring a good match between the scientific and the end-user's requirements.

1. INTRODUCTION

Due to climate change and shrinking fossil resources, the transition to more and more renewable energy shares is unavoidable. But, as wind and solar energy is strongly dependent on highly variable weather processes, increased penetration rates will also lead to strong fluctuations in the electricity grid, which need to be balanced. Proper and specific forecasting of 'energy weather' is a key component for this. Therefore, it is timely to scientifically address the requirements to provide the best possible specific weather information for forecasting the energy production of wind and solar power plants for the next minutes up to several days ahead.

Towards such aims, the COST action ES1002, *Weather Intelligence for Renewable Energies, WIRE* www.wire1002.ch has two main lines of activity: first to develop dedicated post-processing algorithms coupled with weather prediction models and measurement data especially remote sensing observations; second to investigate the difficult relationship between the highly intermittent weather dependent power production and the energy distribution towards end users. The second goal will raise new challenges as this will require from the energy producers and distributors definitions of the requested forecast data and new technologies dedicated to the management of power plants and electricity grids.

Twenty five European COST Countries and four non-cost countries, Australia, Canada, Japan, and USA, are participating to WIRE that is one of the largest actions in the Earth System Science and Environmental Management domain.

2. WIRE ACTIVITY

The main goal of the Action is to contribute enhancing methodologies of forecasting wind and solar power production in the time domain from a few minutes up to several days ahead. This will be achieved during the activity of three Working Groups by:

- Combining numerical weather models with suitable post-processing methods as well as real-time surface and remote sensing measurements.
- Establishing a common understanding between the relevant communities (wind and solar, meteorologists, energy engineers, grid managers) in order to optimize the technical and economic integration of these renewable energies into electricity grids and markets.
- Transferring knowledge across Europe, connecting the scientific and end user communities.

3. WORKING GROUP 1. MODELING AND POST-PROCESSING.

In the first phase of the project, a critical assessment of past and present research activities in different countries and of current knowledge gaps will be performed (State-Of-The-Art, SOTA). This has to highlight the existing weaknesses for all components of the renewable energy forecast system. In particular, it will allow evaluating the adequacy of numerical weather models coupled with dedicated power conversion modules to deliver accurate power production forecasts.

Furthermore, the potential of downscaling models towards higher spatial resolution will be analyzed in order to evaluate its impact when combined with appropriate post-processing applications.

If proved necessary, the project will promote the development of downscaling methodologies adapted to the need of wind and solar energy applications.

4. WORKING GROUP 2. MEASUREMENTS AND OBSERVATIONS

The activity in WG2 aims to quantify the added value of the new observation techniques in further developing power forecasting models. In particular, the focus will be on how including ground-based and space-borne (satellite) remote sensing technologies will improve the quality of the production forecasts including at the post-processing level. Recommendations will be provided to the scientific and users communities. Ground-based remote sensing systems include:

Weather radars, cloud radars, ceilometers, Total Sky Imagers, pyrgeometers, and combinations of these systems;

Wind profilers and LIDARs for the wind speed and direction fields, or combinations of them;

LIDAR and micro-wave systems for the determination of Liquid Water Content LWC (and possibly the Particle Size Distribution PSD) of the boundary layer - presently products of the model itself – which are required for improving the high resolution models.

The results of these post-processing improved forecasting systems will be evaluated and validated. Existing wind farm and solar energy plant locations will be selected for the verification and additional ad-hoc measurements will be installed whenever possible. Database (s) containing the validation data will be set up and appropriately formatted for direct use by the modelers' community.

5. WORKING GROUP 3. POWER PLANTS AND ELECTRICAL GRID MANAGEMENT

Finally, the development of improved forecasting systems will be done in cooperation with end users in order to guarantee a good match between the scientific developments and the user s' requirements. A tentative implementation of the forecasts into the operational strategies of the power plants and electrical grid operators will be evaluated. At this point, it is required to establish a high level interdisciplinary collaboration between science and industry. Secondary specific applications such as the influence of "thermal rating" and icing for power lines at selected test sites will also be performed.

6. MAIN ACHIEVEMENTS

Report on the current state of research and development related to measurement, modeling and forecasting technologies for renewable energy integration.

Gathering and preparation of datasets for various sites in order to benchmark existing modeling and forecasting approaches.

7. ONGOING ACTIVITIES AND EXPECTED RESULTS

- Analysis of the added value from ground-based and space–born remote sensing measurements techniques for nowcasting, weather forecast modeling and post processing tools
- Evaluation of the economic benefit for the power production resulting from improved high resolution forecasts in terms of efficiency and cost savings

- Assessment of the effects of the intermittent character of renewable energies on the electrical grid management.
- Roadmap for modeling of solar and wind power production for the management of power plants and electrical grids.
- Organization of the *Workshop on Remote Sensing Measurements for Renewable Energy.* 22-23 May 2012. Technical University of Denmark DTU, Risoe Campus, Roskilde, Denmark. http://www.wire1002.ch/index.php?id=24

ACKNOWLEDGMENTS

COST Office is acknowledged for the provision of part of the funding for attending the conference.

Figure 1. Diagramme summarizing the WIRE project.

Figure 2. Participants to the 1st Steering Committee Meeting and State-of-the art Workshop at MINES-ParisTech, Center for Energy & Processes, Sophia Antipolis, France. 22-23 March 2011.

COLUMBIA BASIN WIND ENERGY STUDY

Mikhail Pekour[1], Larry Berg[1], Jerome Fast[1], Rob Newsom[1], Qing Yang[1], Mark Stoelinga[2], and Catherine Finley[3]

[1] *Pacific Northwest National Laboratory, 902 Battelle Blvd., P.O. Box 999, Richland, WA, USA,*
mikhail.pekour@pnnl.gov, larry.berg@pnnl.gov, jerome.fast@pnnl.gov, rob.newsom@pnnl.gov,
qing.yang@pnnl.gov
[2] *3TIER, Inc., 2001 Sixth Avenue, Suite 2100, Seattle, Washington 98121, USA, mstoelinga@3tier.com*
[3] *WindLogics, Inc, 201 NW 4th Street, Grand Rapids, MN 55744, USA, cathy.finley@windlogics.com*

ABSTRACT

The Columbia Basin Wind Energy Study (CBWES) is a Department of Energy supported study focused on creating a multi-season data set that can be used to evaluate the ability of mesoscale meteorological models to predict low-level winds in the vicinity of an operating wind plant in a region of complex terrain. CBWES was conducted in 2011-2012 in an area of rolling hills near an operational wind farm in northeast Oregon and southwest Washington State. Instrumentation deployed included a 60 m instrumented tower equipped with ultrasonic and propeller and vane anemometers, a Doppler sodar, and a 915 MHz radar wind profiler. The final data product is single best estimate of wind profile over the site as a function of time. The obtained wind field is then used in two ways: (a) to evaluate Weather Research and Forecasting (WRF) model simulations for periods of interest, with an emphasis on wind ramp and wind shear events; and (b) to evaluate retrievals of horizontal winds from National Weather Service WSR-88D radar located in Pendleton, Oregon. All of the observations from this study will be made publically available at the conclusion of the study.

1. MOTIVATION AND GOALS

Mesoscale atmospheric models, such as the Weather Research and Forecasting (WRF) model, are useful tools for characterization of a perspective site, for operational wind forecasting, and for study of complex inflow conditions to the wind plant [1-3]. However, in general, there is a lack of publically available wind data sets focused on wind energy industry needs [4], especially those suitable for evaluation of mesoscale meteorological models abilities to accurately predict hub-height winds. The Columbia Basin Wind Energy Study (CBWES) is a US Department of Energy supported study designed to partially address this shortcoming and to provide data that can be used by the wider wind energy community to evaluate mesoscale model forecasts of winds, including speed and direction at the hub height, ramp events and wind shears.

This study utilized a number of remote sensing and *in-situ* probes to measure the profile of wind speed and wind direction from the surface to an altitude of several hundreds meters above the ground and to evaluate turbulent kinetic energy profiles in the lower boundary layer. Data from all instruments have been combined to form a single best estimate of the wind over the site as a function of time and height.

The suite of instruments has been deployed for a period of 8-12 months in order to obtain multi seasonal data set over a wide range of meteorological conditions.

The modeling component of the study includes a set of simulations using the WRF model that covers a range of surface-layer and boundary-layer parameterizations applied under variety of meteorological conditions. These simulations used a standard configuration of WRF and could be compared to “experimental” simulations completed by an interested third party. In addition, specific guidance on the selection and use of surface- and boundary-layer parameterizations in WRF has been developed.

2. FIELD SITE

The CBWES field site (45.955° N, 118.688° W) is located in northeastern Oregon in an area of rolling hills near the State Line Wind Energy Center. This plant consists of 454 turbines (660-KW, Vestas V-47) and has an installed capacity of 300-MW. This location is in a small area of wind power class 4, as identified in the *Wind Energy Resource Atlas of the United States* [4]; usually areas with a wind power class 3 or greater are considered for wind energy development.

Steep slopes and narrow gullies add to the complexity of the surrounding terrain. Overall height difference between the top of the local ridge and valley bottom is around 450 m.

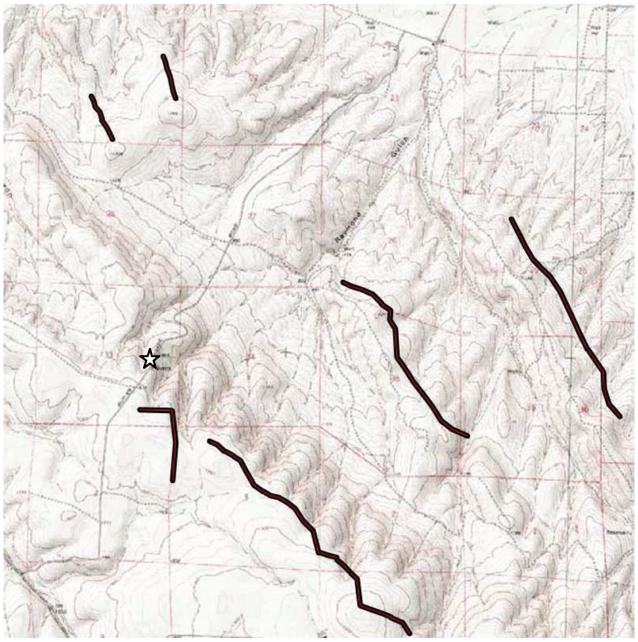

Figure 1. Topographic map showing the CBWS site (star) and approximate locations of the State Line Wind Project turbines (black lines).

A 65 m tall telecommunication tower is located on the site. Propeller and vane anemometers that are permanently installed at three levels on the tower are maintained by the Bonneville Power Administration (BPA) for use in their operations. Measurements from these BPA anemometers for the duration of the CBWES study are included into the data set.

Figure 2. The CBWES site.

Figure 3. View looking to the north-east of the site.

3. INSTRUMENTATION

The suite of deployed instruments (Table 1) was selected to be able to provide winds from the surface to the heights above the area swept by the blades of wind turbines, and to estimate the stability and the turbulence kinetic energy (TKE).

Remote sensing instruments deployed during various periods of the CBWES study were Scintec MFAS Doppler sodar, and a Vaisala 915 MHz radar wind profiler (RWP), the later has been supplied by the DOE Atmospheric Radiation Measurement Climate Research Facility [5].

Ultrasonic anemometers (ATI SATI/3K) have been deployed at two levels (30 m and 60 m) on the radio tower. The top level was instrumented with two sonic anemometers on booms pointing to the southeast and southwest in order to give redundancy in the event of a failure of one of the sensors. During initial phases of the study a single sonic anemometer mounted at a height of 3.1 m above the surface was used.

Table 1. Instruments deployed during CBWES

Instrument	**Deployment period**	**Nominal heights (m AGL)**	**Averaging (min)**
915 MHz RWP	16 Nov. 2010- 24 May 2011	89-1462 25 range gates	30
Doppler sodar	4 Dec. 2010- 21 Mar. 2012	30-410 40 range gates	15
Sonic anemometer(s)	21 Jan. 2011- 18 Apr. 2011	3.1	30
	23 Apr. 2011- 21 Mar. 2012	30, 60	30
Prop and vane anemometers	Permanent	30, 44, 62	10

4. DATA

The RWP was configured to run in three-beam, low-power mode with range gate spacing of 57 m and averaging time of 30 min. This configuration was chosen to get finest possible time/space resolution and minimize artifacts from adjacent radio tower and wind turbines.

The Doppler sodar was operated with 10 m range gate spacing and a maximum height of 400 m. The system operated with five beams in coded pulse mode (frequencies between 1650 and 2750) and used an averaging time of 15 min.

Sonic anemometers were operated with 10 Hz acquisition rate and the data were processed in 30-min periods. Data transmission from the anemometers to the acquisition computer was established via radio modem links in order to avoid long cables.

Routine measurements, data acquisition, and quality control of propeller and vane anemometers were performed by the Bonneville Power Administration. The winds were provided at three levels with 10 min averaging.

One of the reasons why this site was selected for CBWES field campaign was 65 m radio tower on the site, however this same tower, and powerful telecommunication equipment installed on it, had posed significant challenges to instrument operation, data collection, and post-processing.

Ground and intermittent clutter from the tower, tower guy wires, and from the rotating blades of the nearest turbine affected wind measurements from both remote sensing instruments. Sonic anemometer data links were disrupted during periods of intensive radio transmissions; radio frequency interference also affected sonic anemometers themselves, causing frequent spikes in the data.

Data processing and quality control procedures for the wind data from the remote probes and the tower anemometers included cleaning up various outliers and artifacts in a chain of “sanity” checks, averaging to a common time base of 30 min, filling small (less than 3 range gates or 3 hours) gaps using cubic spline interpolation, and then merging all data streams into one single best estimate of wind profile over the site as a function of time.

5. WRF SIMULATIONS

The WRF model has been configured to be consistent with applications within the wind industry. Our particular setup includes three nests, with 12, 4 and 1.3 km horizontal resolution and 55 vertical levels (with approximately 15 m spacing in the lowest 200 m). Three different boundary-layer parameterizations have been used: Mellor-Yamada-Janjic (MYJ), University of Washington (UW), and Yonsei University (YSU). Simulations have been completed for May 2011.

An example of WRF performance is shown in figure 4. The top panel shows the observed wind speed from 146 m AGL as well as the wind speed simulated by each of the three selected boundary-layer parameterizations. There are periods during which the all three simulations over predict the wind speed (between 00:00 and 12:00 on 16 May). The UW and YSU scheme do a better job capturing the up ramp on 15 May, and all three parameterizations capture the down ramp later in the day.

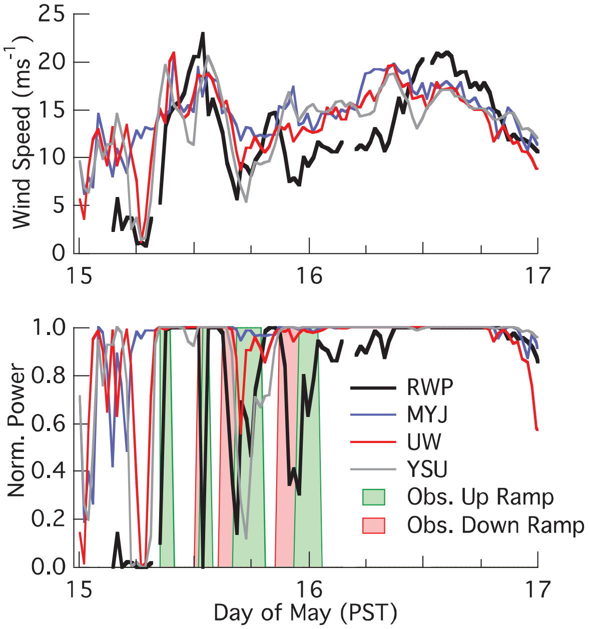

Figure 4. Wind speed (top panel) observed at the CBWES site (black) and simulated using the MYJ (blue), UW (red) and YSU (gray) parameterizations, and normalized power (bottom panel) calculated from the observed wind speed (black) and simulated using the MYJ (blue), UW (red) and YSU (gray) parameterizations. Shading indicates up (green) and down (red) ramps.

The power generated from a hypothetical wind turbine can be computed directly from the observed or simulated wind speed using a standard power curve. For convenience, the power has been normalized by the maximum power of the turbine, and therefore ranges between 0 and 1. The bottom panel in Figure 4 shows an example of the normalized power, along with periods of up ramps and down ramps highlighted. The MYJ scheme predicts nearly full power production during most of the period, while the UW and YSU scheme show a number of times during which the power produced by the wind turbine would be significantly reduced.

6. FUTURE WORK

CBWES is part of an ongoing project, future tasks include finalize wind data set and release it for use by the wider wind energy community. A new set of control WRF simulations with different resolutions and for other seasons is under development.

ACKNOWLEDGMENTS

This work was supported by DOE Department of Energy Efficiency and Renewable Energy. The Pacific Northwest National Laboratory (PNNL) is operated by Battelle for the DOE under contract DE-AC06-76RL0 1830. A portion of this research was performed using PNNL Institutional Computing .

REFERENCES

1. Landberg, L., Myllerup, L., Rathmann, O., Petersen, E. L., Jørgensen, B. H., Badger, J. and Mortensen, N. G. (2003), Wind Resource Estimation—An Overview. *Wind Energ.*, **6**: 261–271. doi: 10.1002/we.94

2. Landberg, L., Giebel, G., Nielsen, H. A., Nielsen, T. and Madsen, H. (2003), Short-term Prediction—An Overview. *Wind Energ.*, **6**: 273–280. doi: 10.1002/we.96

3. Holttinen, Hannele, Lemström, Bettina, Meibom, Peter, Bindner, Henrik, Orths, Antje, Hulle, Frans van, Ensslin, Cornel, Hofmann, Lutz, Winter, Wilhelm, Tuohy, Aidan, O'Malley, Mark, Smith, Paul, Pierik, Jan, Tande, John Olav, Estanqueiro, Ana, Ricardo, João, Gomez, Emilio, Söder, Lennart, Strbac, Goran, Shakoor, Anser, Smith, J. Charles, Parsons, Brian, Milligan, Michael & Wan, Yih-huei. (2007), Design and operation of power systems with large amounts of wind power (State-of-the-art report). VTT Working Papers 82, ISBN 978-951-38-6633-4 (URL: http://www.vtt.fi/publications/index.jsp)

4. Elliot, D.L., C.G. Holladay, W.R. Barchet, H.P. Foote, and W.F. Sandusky. 1986. Wind Energy Resource Atlas of the United States. DOE/CH10093-4. DE86004442. Solar Technical Information Program. Solar Energy Research Institute (now the National Renewable Energy laboratory). Golden, CO. Available online: http://rredc.nrel.gov/wind/pubs/atlas/.

5. Atmospheric Radiation Measurement Climate Research Facility. http://www.arm.gov/about/.

Short-term dynamics of the atmospheric boundary layer wind structure in Moscow city by the sodar data

Mikhail A. Lokoshchenko, Lyubov I. Alekseeva

Department of Meteorology and Climatology, Faculty of Geography,
Lomonosov Moscow State University. 119991, Lengory, Moscow, Russia
Phone: +7-495-9394284; Fax: +7-495-9392479; E-mail: loko@geogr.msu.su

ABSTRACT

Case studying of short-term dynamics of wind profiles in the lower 500-m height air layer in Moscow has been presented with the use of the sodar data. Quick changes of wind direction in time are connected as a rule with synoptic processes such as passing of atmospheric front, axis of ridge or axis of trough above a site of sounding. Usually wind turning in time is right although sometimes it may be left – e.g., during passing of ridge axis at its Northern periphery. Extremely quick and sharp changing of wind direction up to 360º during several hours may took place in close vicinity of an anticyclone center or a cyclone center. Some weather phenomena which are connected with Cb clouds (thunderstorms and others) are accompanied by quick acceleration of wind speed.

1. INTRODUCTION

The acoustic remote sensing is carrying out at Meteorological observatory of Moscow University since 1988, including measurements of wind profiles with the use of 'MODOS' sodar of METEK production since 2004 [1]. The operation frequency is 2000 Hz, the vertical range is between 40 and 500 m. The spatial resolution of these data is equal to 20 m and the temporal one (i.e. minimal time for measuring of reliable wind profiles) consists of 10 minutes. Thus, the sodar data allows studying of short-term dynamics of the wind fine structure in the atmospheric boundary layer, including any changes both of wind velocity and of wind direction in time range from 10 min to several hours. Evidently, most of these quick changes are connected either with synoptic events or with some specific meteorological phenomena. The main features of short-term wind dynamics have been studied on a base of a lot of examples using synoptic charts and the ground meteorological data. Among others, it has been found that quick turning of wind direction in time is connected as a rule with passing of either atmospheric fronts or ridge (or trough) axes.

2. RIGHT TURNING

Let us use below a term 'turning' as quick change of wind direction not with a height but in time – from one moment to another in all the range of the sodar data. The most typical case of quick right turning is well-known synoptic phenomenon of a front passing above the sounding site. One of examples is presented on Fig.1. As one can see before 06 a.m. at that day (November 29th, 2005) wind direction was South-Eastern at all the range of the sodar data from 40 to 400 m above the ground. However, at 06 a.m. direction sharply changed to South-Western so that right turning consisted of 70-80º. Intermediate zone of Southern winds was narrow – they were observed during nearly of one hour from 05 to 06 a.m. at the level

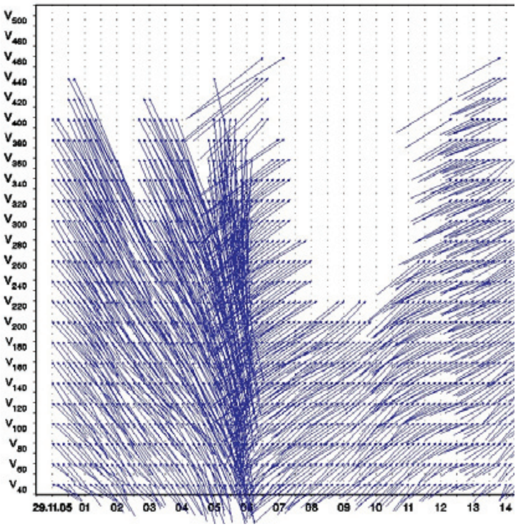

a) Sodar data about wind velocity and direction. Horizontal axis – time, hours; vertical axis – height, m.

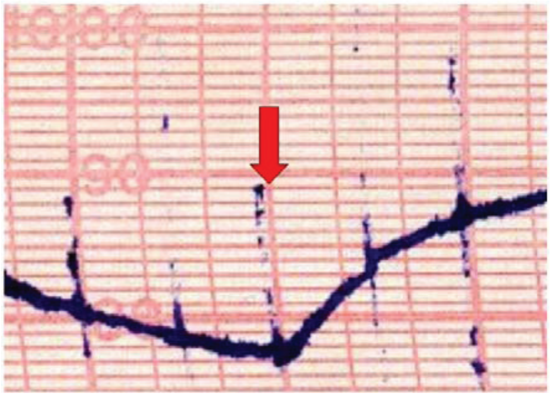

b) Barograph record of the air pressure for the period from 10 p.m. on November 28th to 02 p.m. on November 29th; the moment of cold front passing on 06 a.m. is shown by red arrow.

Fig.1. Right turning of the wind direction connected with front passing on November 29th, 2005. Moscow.

of 400 m and only during 20-30 minutes (from 05.30 to 06.00 a.m.) at the ground air layer. Thus, wind direction was gradually changing from South-Eastern to Southern downward. Both before, and later it was stable without of significant changes.

As it is seen on the barograph record (Fig.1 b) just at 06 a.m. the air pressure began to sharply increase that means, accordingly to classic synoptic analysis [e.g., 2], a passing of intensive cold front above Moscow. Indeed just at this moment the air temperature T began to fall: from +9.7 ºC at 06 a.m. to +5.6 ºC at 09 a.m. and, then, even to +0.9 ºC at 09 p.m.

This example of the wind direction right turning is quite typical for cases of front passing. Wind turning is, as a rule, quicker for cold fronts and slower for warm fronts which zones are usually wider in space.

3. MULTIPLE RIGHT TURNINGS

One more typical situation at the wind direction dynamics is two right turnings which take place during several hours, just one after another. As it is seen on Fig.2 a) East-South-Eastern winds were replaced by Southern after 08 a.m. (intermediate South-Eastern direction was detected by the sodar during only one hour from 07 to 08 a.m.). Then at 03 p.m. Southern winds were replaced by South-Western ones quickly (during only 20-30 minutes). Thus, two sharp right turnings took place at the same day. It should be noted as well that during periods before 07 a.m., from 08 a.m. to 03 p.m. and after 03 p.m. wind direction was stable and nearly the same.

The barograph record (Fig.2 b) indicates two critical points – at 07 a.m. when fall of the air pressure was finished and at 03 p.m. when its increase was suddenly accelerated. Usually these moments are connected with consequent passing of, firstly, warm and, then, cold front. True, synoptic chart on Fig.3 confirms a location of Moscow city inside warm sector of the cyclone with the centre above White Russia (although localization of the warm front at the chart pass a bit ahead of its real passing above Moscow).

This synoptic situation is confirmed by the ground meteorological data. Indeed, T at Moscow University was increased from –0.4 ºC at 06 a.m. to +1.4 ºC at 09 a.m. and to +2.3 ºC at noon. Later, after passing of the cold front, it decreased again up to +0.4 ºC at 09 p.m. True, these changes may be partially explained by usual diurnal course. However, change of the air mass type at this day is evident as well at dynamics of the humidity parameters (e.g., the water vapour partial pressure was equal to 4.5-5.0 hPa at the forepart of the cyclone before 07 a.m., to nearly of 5.5 hPa in warm sector and only to 4.0 hPa in the cyclone rear after 03 p.m. The method of such detailed kind of synoptic analysis was discussed in [3]. Thus, both right wind turnings on Fig.2 a) were connected with passing of two atmospheric fronts whereas the period between them with stable Southern winds was noted by warm sector of the cyclone.

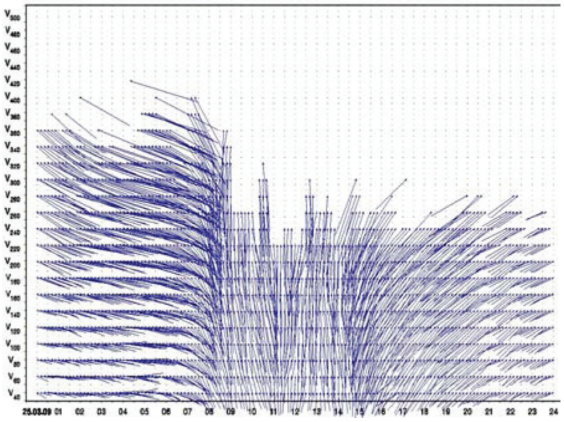

a) Sodar data about wind velocity and direction. Horizontal axis – time, hours; vertical axis – height, m.

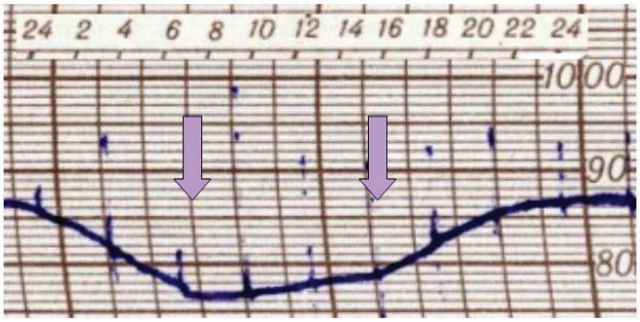

b) Barograph record of the air pressure; moments of passing of warm and cold fronts at 07 a.m. and at 03 p.m. are shown by violet arrows.

Fig.2. Two right turns of the wind direction connected with passing of cyclone warm sector of on March 25th, 2009. Moscow.

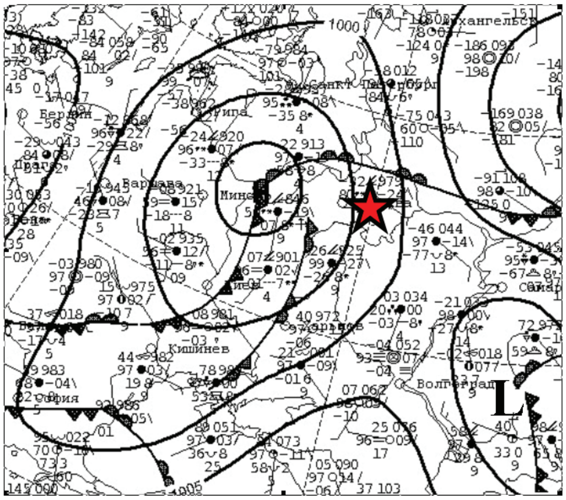

Fig.3. Surface synoptic chart for 03 a.m. of Moscow time on March 25th, 2009. Moscow city is shown by red asterisk.

4. LEFT TURNING

Significant left wind turning is observed not so often as the right one. It may take place, for instance, in time of passing of ridge axis at its Northern periphery. One example of such event is shown on Fig.4. At that time, on November 8th in 2008, the sodar operated in Obninsk town at a distance of nearly 100 km to the South from Moscow city. As one can see before noon wind was characterized by comparatively high speed (up to 12 m/s) and by North-Western direction. Then, wind speed significantly decreases up to only 1-2 m/s at 05 p.m. After 05 p.m. left wind turning occurred so that direction was changed from North-Western to South-Western. At the same time, wind speed was increased again in the evening up to 5-7 m/s at the level of 100 m height and up to 9 m/s at the level of 180 m height. This kind of turning is evident and strong but it is slower in the comparison with right turnings at frontal zones.

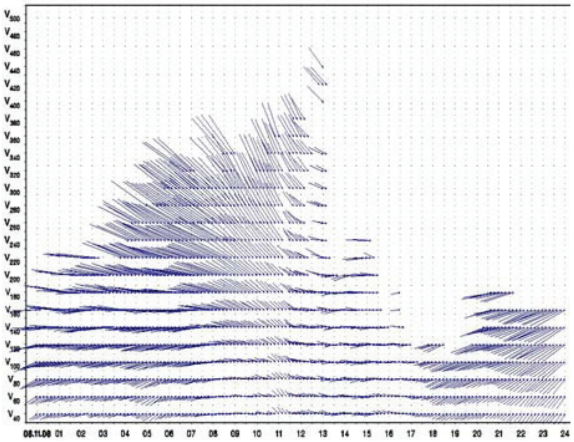

Fig.4. Left turning of the wind direction connected with passing of ridge axis on November 8th, 2008. Obninsk. Horizontal axis – time, hours; vertical axis – height, m.

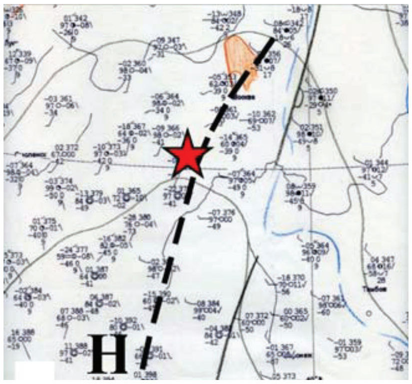

Fig.5. Surface synoptic chart for 06 p.m. of Moscow time on November 08th, 2008. Ridge axis is shown by dashed line; Moscow city – by red flag; Obninsk town – by red asterisk.

As it is seen on Fig.5, in the afternoon Obninsk was situated at zone of ridge axis of anticyclone with the center above Ukraine. This axis is shown by dashed line. In other words, before noon the site of sounding was located at the Eastern periphery of the ridge in conditions of North-Western winds which were replaced by South-Western winds at the ridge Western periphery after passing of its axis which is confirmed by maximum of the air pressure on the barogram.

5. GRADUAL CHANGE OF WIND DIRECTION

We discussed above several cases of more or less quick wind turnings in the lower troposphere. However, sometimes wind direction may be changed gradually, without sharp turnings. One typical example is demonstrated on Fig.6. One can see that at the first half of a day wind direction was changed from North-Western to Western and, then, to South-Western. In the afternoon, vice versa, South-Western winds were replaced by firstly Western and, then, by North-Western ones again. Thus, gradual wind turning was left before 09 a.m. and then became right.

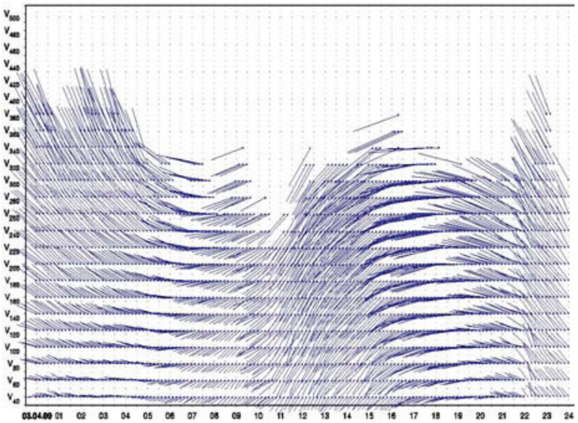

Fig.6. Gradual change of wind direction on April 3rd, 2009. Moscow. Horizontal axis – time, hours; vertical axis – height, m.

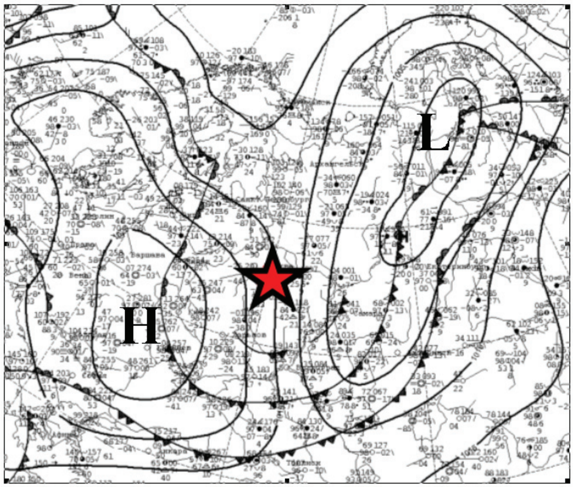

Fig.7. Surface synoptic chart for 04 p.m. of Moscow time on April 3rd, 2009. Moscow city is shown by red asterisk.

As it is seen on Fig.7 Moscow was situated at the Eastern periphery of anticyclone with the center above Western Ukraine. During whole the day anticyclone quickly replaced to the South-East and, simultaneously, became weaker, so that at midnight of April 4th its center appeared above Northern Caucasus. As a result, in the morning of April 3rd Moscow was situated at the ridge axis and then – at its Western periphery already. The consequence of this replacement was the left turning from North-Western to South-Western direction – similar to example mentioned above on Fig.4. In the afternoon Moscow was situated already at the Western periphery of trough which was appeared to the North from Russian capital, in conditions of cyclonic curvature of isobars. As a result, right wind turning took place at that time which renewed the initial North-Western wind direction.

Evidently, all changes of direction during the day were gradual (unlike previous examples on Figures 1 and 2) because of absence of frontal activity at locality of Moscow, in spite of significant transformation of the baric field.

6. THUNDERSTORMS

Some weather phenomena connected with quick development of strong Cb clouds lead to sharp increase of wind speed. Among others, this effect may be observed during thunderstorms (Fig.8).

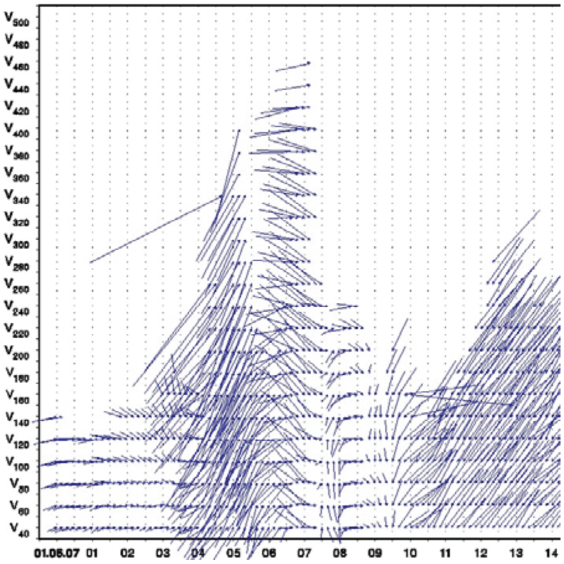

Fig.8. Wind increase during thunderstorm on June 1st, 2007. Moscow. Horizontal axis – time, hours; vertical axis – height, m.

At that day thunderstorm was started in vicinity of Moscow University at 04.19 a.m. Firstly it was weak but then it became strong since 04.35 till 05.30 a.m. Finally thunderstorm was finished at 06.15 a.m. At the same time, as it is seen on Figure 8, strong and quick increase of wind speed took place: before 03.40 it was very low (less than 2 m/s) whereas at 04.30 it increased already up to 13-14 m/s in the ground air layer below 100 m height and was equal even to 23.5 m/s at the level of 260 m height.

Evidently, a relation between weather phenomenon of thunderstorm and wind acceleration is indirect because common cause of both effects is development of a thundercloud. It should be noted that in some cases of remote thunderstorms or of summer lightning increase of wind speed doesn't be observed. Evidently, a closeness of thunderstorm cloud to the sounding site has principal meaning for wind increasing.

CONCLUSIONS

1. Significant short-term changes of the wind direction, including both quick and gradual turnings, may be explained as a rule by synoptic conditions and changes of common baric field. Right quick turnings are connected usually with passing of atmospheric front or trough axis; left turnings may be connected with passing of ridge axis at its Northern periphery.

2. Some weather phenomena such as thunderstorms and others which are connected with development of strong Cb clouds lead often to short-term acceleration of wind speed, but, as a rule, without stable change of wind direction in time.

ACKNOWLEDGEMENTS

Authors are grateful to Ms. N.G.Nikitina for her help. This work has been supported by Russian Basic Research Foundation (project No. 10-05-01130).

REFERENCES

1. Lokoshchenko M.A., E.A. Yavlyaeva, H.-J. Kirtzel, 2009: Sodar data about wind profiles in Moscow city. *Meteorologische Zeitschrift*, **18**, No.3, pp.321-330.
2. Khromov S.P., 1948: *Foundations of synoptic meteorology* (in Russian). – Gidrometeoizdat, Leningrad, 696 pp.
3. Lokoshchenko M.A., 1998: Application of sodar sounding to studying influence of synoptic conditions on thermal stratification. *Atmospheric and Oceanic Optics,* Tomsk, **11**, No.5, 419-427.

Investigation of the influence of synoptic conditions on the temperature stratification in the surface atmosphere

Krasnenko N. P, Buhlova G. V.
Institute of Monitoring of Climatic and Ecological Systems SB RAS
10/3, Akademicheskii Ave., Tomsk 634055, Russia
E-mail: krasnenko@imces.ru, galvik76@mail.ru

ABSTRACT

Influence of the synoptic conditions on the temperature stratification in the surface layer of the atmosphere above Tomsk is considered. The data of sodar sounding are presented. Simultaneously with these data, the synoptic situation is described that allows us to elucidate in more details changes in the temperature stratification at the moment of observation. For more objective estimation, special feature of the temperature stratification and weather conditions are given for different seasons of the year.

1. INTRODUCTION

The temperature stratification in the surface atmospheric layer, in addition to many factors such as inhomogeneity of the underlying surface, radiative heat inflows, and air humidity, is influenced by the synoptic conditions [1, 2]. The most convenient means for monitoring of the temperature stratification of the atmosphere is an acoustic radar also called sodar [3]. It allows continuous monitoring of the lower layer of the atmosphere to be performed in real time with high spatial and temporal resolution. Previously such investigations were performed on the example of Moscow [4] and Velikie Luki [5]. The present study is aimed at estimation of the degree and pattern of this influence for Tomsk located in the southeast of Western Siberian plain on the high right bank of the Tom' river.

Atmospheric sounding was performed with the Zvuk-3 monostatic sodar [3]. The sodar carried out vertical sounding and determined in real time the stratification type (class of the atmospheric stability), mixing layer height, height of temperature inversions, and convective flows.

2. DATA EMPLOYED

To estimate the influence of synoptic conditions on the temperature stratification in the surface layer of the atmosphere, weather maps coinciding in time with acoustic sounding periods were used to elucidate a dependence of the vertical temperature gradient on the air mass (AM) type and localization of baric formations and atmospheric fronts.

Cyclones and anticyclones in the process of their formation and motion influence the atmospheric circulation at mid-latitudes. Motion of cyclones and anticyclones and air circulation inside them lead to meridional air mass transfer and inter-latitudinal heat and moisture exchange. More often, peripheral parts of cyclones and anticyclones influence the weather in Tomsk.

Cyclones usually move in series; as a rule, a crest is formed in the rear part of each cyclone, and the series ends with an anticyclone formation. Sharp changes of weather in Tomsk are usually observed when cyclones have a meridional component from the Barentsev and Karskii Seas and cause sharp changes of the air temperature, strengthening of wind, and blizzard. Weather changes when atmospheric fronts of cyclonic origin passed by. In winter they are stronger than in summer, and their number is greater. The influence of the Asian anticyclone is traced in winter over the Tomsk Region. The crest of this anticyclone is extended toward the south of Western Siberia. Anticyclones can be very stable; therefore, strong frosts are sometimes observed for 10-15 days.

We must consider that the temperature stratification in the surface layer of the atmosphere varies continuously, which is also seen from the data of sodar sounding [6]. Comparing sodar facsimile records with weather maps, we were able to trace the influence of this or that atmospheric process on the temperature stratification. For our analysis, we used the weather maps from the site GU "Novosibirsk TSGMS-RSMTS" [7].

Since we must provide exact coincidence in time of the sodar data and synoptic processes, we considered only the periods when those or other air masses (AM) or baric formations were observed or when these masses approached at very short distances to the city, that is, we analyzed the sodar data recorded in the morning hours from 00 to 04 h, Tomsk LT.

3. INFLUENCE OF SYNOPTIC CONDITIONS ON THE STRATIFICATION OF THE SURFACE LAYER OF THE ATMOSPHERE

Sharp changes in the character of atmospheric circulation in the south of Western Siberia caused unstable weather in the first decade of March, 2011. Northwest AM transfer under conditions of high atmospheric pressure (in the region of the ridge of the Siberian anticyclone) was the reason for cold weather in the first half of the decade.

Then the southwest flows in the atmosphere and passage of warm cyclone sectors led to considerable warming, frosts were followed by the glazed frost phenomena and a thaw. At the end of the first decade, significant precipitations and fronts associated with them were observed in the deep cyclone region. From Fig. 1 it can be seen that the ridge of the Siberian anticyclone was situated over Tomsk, and light precipitations were observed, but not at the moment of observations.

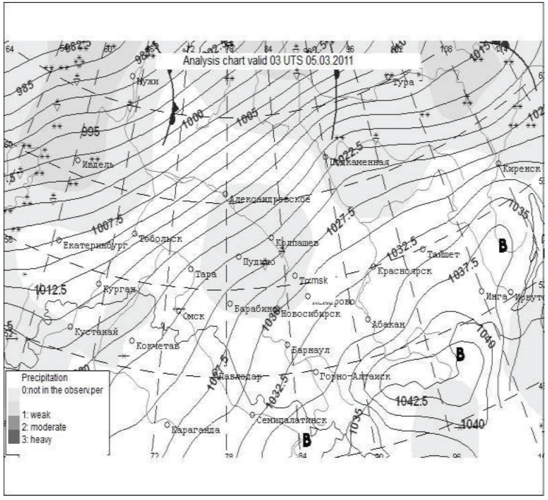

Figure 1. Weather map on March 5, 2011 at 03 h, Tomsk LT.

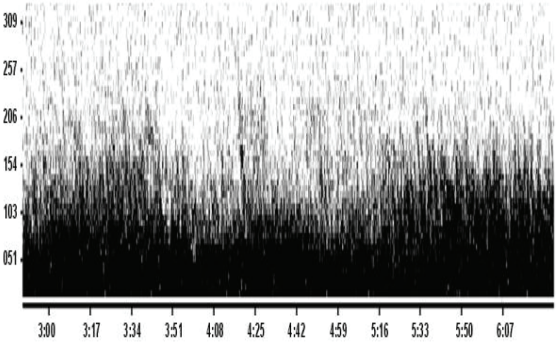

Figure 2. Sodar facsimile record of the ABL structure on March 5, 2011 (sounding height, in meters, is plotted on the vertical axis, and current time is plotted on the horizontal axis).

Essential changes in the character of atmospheric circulation caused unstable weather in the second decade of May, 2011. Prevalence of anticyclonic forms of baric fields in combination with western and southwest AM transfer contributed to the formation of the enhanced temperature background at the beginning (May 11-13) and end (on May 19-20) of the decade. In the middle of the decade, considerable cold spell was observed. At the end of the decade, the active cyclonic activity led to an increased frequency of rains with thunderstorms. From Figs. 3-4 it can be seen that during passage of fronts over Tomsk, when unstable stratification was observed, vertical plumes characterizing convection were observed on the sodar record.

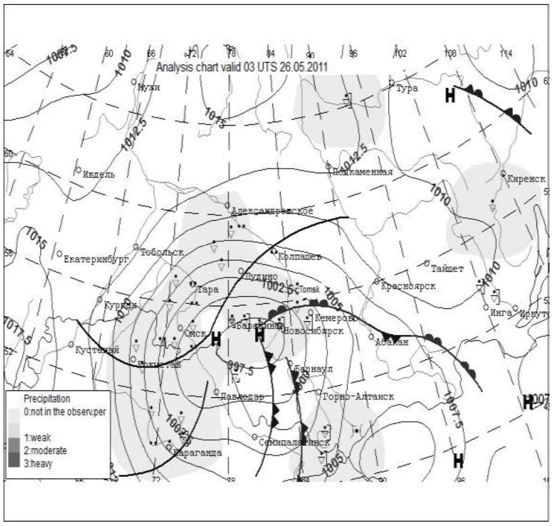

Figure 3. Weather map on May 26, 2011 at 03 h, Tomsk LT

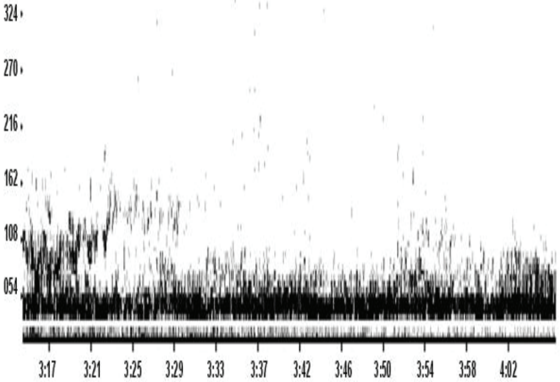

Figure 4. Sodar facsimile record of the ABL structure on May 26, 2011 (sounding height, in meters, is plotted on the vertical axis, and current time is plotted on the horizontal axis).

In July, the near-ground temperature inversions were most often observed in the process of heat advection or in warm air masses, but they were less pronounced and less stable in comparison with the cold season.

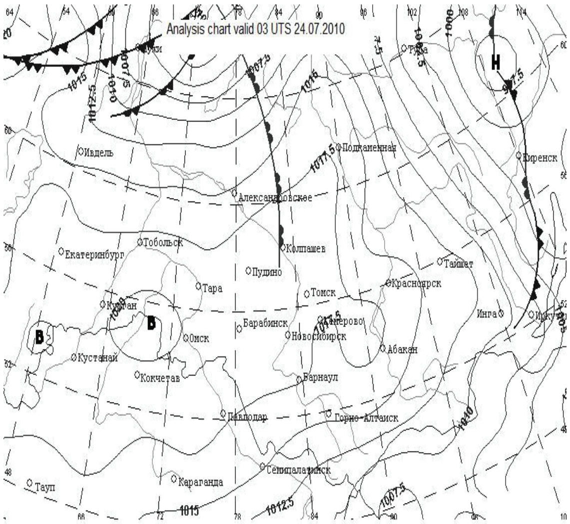

Figure 5. Weather map on July 24, 2010 at 03 h, Tomsk LT

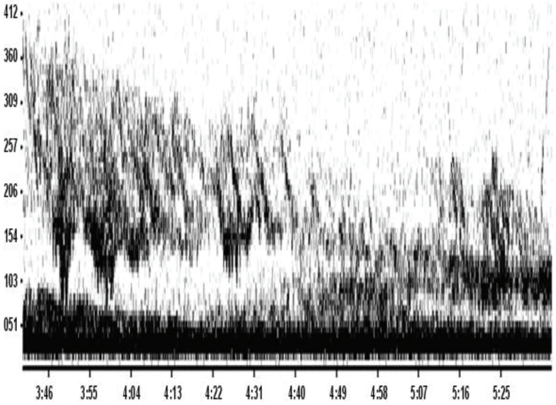

Figure 6. Sodar facsimile record of the ABL structure on July 24, 2010 (sounding height, in meters, is plotted on the vertical axis, and current time is plotted on the horizontal axis).

As can be seen from Figs. 5-6, an anticyclone was observed at night over Tomsk, and a warm front approached. On the sodar facsimile records at that time, elevated and ground inversions were observed, which in the morning, after 4 h, Tomsk LT, merged into one common ground inversion. In summer, convection was more often developed in cold air masses [7]. Previously we have already noted that ground inversions with synoptic patterns were less pronounced in the warm period in comparison with the cold period. This was also confirmed by the sodar facsimile records obtained during the cold period of the year.

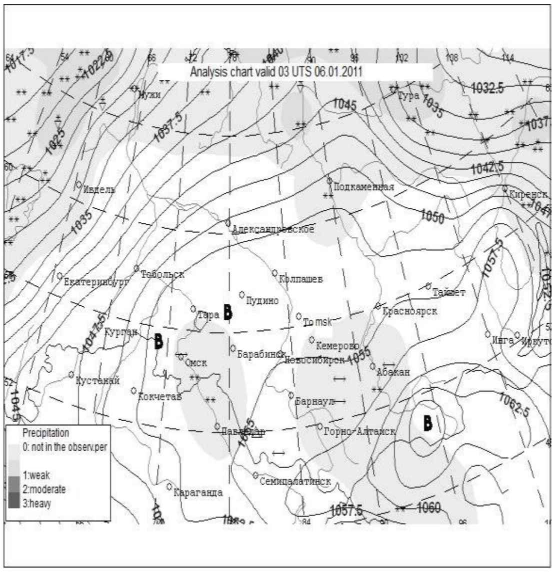

Figure 7. Weather map on January 6, 2011 at 03 h, Tomsk LT.

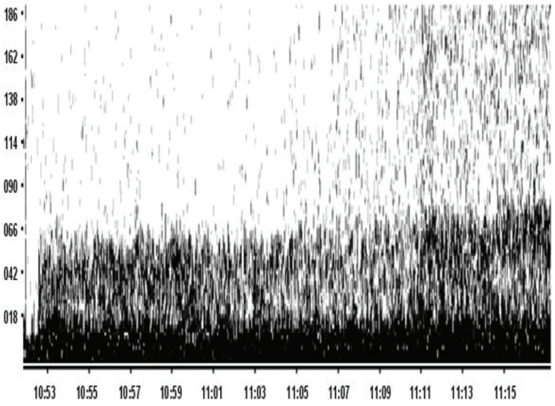

Figure 8. Sodar facsimile record of the ABL structure on January 6, 2011 (sounding height, in meters, is plotted on the vertical axis, and current time is plotted on the horizontal axis).

The weather in the first decade of January in 2011 was anomalously cold, a capping crest that hindered the motion of warm air from the Atlantic region was formed in the troposphere over Siberia. In this regard, the temperature in the afternoon in the first decade of January, 2011 was not higher than minus 24°C. At the end of the decade, decay of the capping crest over the Ural Mountains led to an increase in the temperature in the Tomsk region to minus 13 – minus 18°C. High atmospheric pressure was also observed in the second decade of January; the frosty weather that contributed to the formation of ground and elevated inversions was observed during this period in Tomsk. Figure 8 confirms this; a ground inversion is well seen in the sodar facsimile record.

4. CONCLUSIONS

Thus, as a result of joint analysis of weather maps and sodar data, some patterns of convection and temperature inversion observed in different seasons of the year in Tomsk were revealed. In summer months, convection was most often observed during passage of cold air masses, and without warming of the underlying surface, the stratification of the surface layer was either neutral or weakly stable; such pattern was characteristic for the passage of local fronts. In the cold period, the repeatability of convection was low. The ground temperature inversions were usually observed during heat advection or when a very cold AM was dominant. The elevated temperature inversions were much less often observed in the presence of such air masses. Of interest is the study of the structure of thermal stratification in the surface layer depending on the wind velocity. Preliminary data demonstrated that the stratification of the surface layer of the atmosphere was more variable for light winds. The influence of the synoptic conditions on the temperature stratification was also considerable, and elucidation of patterns of this influence calls for further investigations.

REFERENCES

1. Ivanov V. N., Byzova N. L. Coherent structures in the atmospheric boundary layer. – *Meteor. Gidrol.*, 2001, No. 1, pp. 5-25.

2. S. D. Koshinskii, L. I. Trifonov, Ts. A. Shver, eds., Climate of Tomsk. Leningrad, Gidrometeoizdat, 1982, 176 pp.

3. Krasnenko N. P., Kudryavtsev A. N., Mananko E. E., Stafeev P. G. “Zvuk-3”acoustic radar for sounding of the atmosphere. *Prib. Tekh. Eksp.* 2006, No. 6, pp. 144-145

4. Lokoshchenko M. A. Application of sodar sounding for investigation of influence of synoptic conditions on the temperature stratification. – Opt. *Atmos. Okeana,* 1998, v. 11, No. 5, pp. 480-489.

5. Lokoshchenko M. A., Shifrin D. M. Temperature stratification and vertical variability of ozone in the lower troposphere from the data of acoustic and balloon sounding. – *Meteorol. Gidrol.,* 2009, No. 2, pp. 14-28.

6. Krasnenko N. P. *Acoustic* Sounding of the Atmospheric Boundary Layer. – *Vodolei,* Tomsk, Russia, 2001, 278 pp.

7. *http://www.meteo-nso.ru/information.php?id=18*

REMOTE SENSING MEASUREMENTS OF THE URBAN BOUNDARY LAYER OF ROME UNDEF THE EU LIFE+ EXPAH PROJECT

C. Gariazzo[1], S. Argentini[2], I. Petenko[2], I. Pietroni[2], A. Pelliccioni[1]

[1] *INAIL Research Centre, Via Fontana Candida 1, 00040 Monteporzio Catote (RM), Italy, c.gariazzo@inail.it*

[2] *CNR-ISAC, Via Fosso del Cavaliere 100, 00133 Rome, Italy, s.argentini@isac.cnr.it*

ABSTRACT

The EC funded the EXPAH project (EXPAH "Population Exposure to PAHs") under the LIFE+ program. The aim of EXPAH is to identify and quantify the population exposure to Polyciclic Aromatic Hydrocarbon (PAH) in highly urbanized areas, and to assess the impact of the PAH on human health. A collection of meteorological measurements is required to feed the modeling system that simulate the emission, dispersion and transformation of PAH in the target studied area, which has been chosen to be the metropolitan area of Rome, Italy. Since December 2010 the project is collecting upper air and surface meteorological data. In addition to the existing monitoring network, four stations have been located in the city of Rome and its surroundings. Remote sensing systems are used in this intensive field campaign. A SODAR-RASS has been located in a urban park of the city to collect wind and temperature vertical profiles. A ceilometer is located in the same site to measure the vertical backscattering aerosol profiles which will be used to retrieve the PBL height and for monitoring the PBL aerosol structures. At CNR-ISAC Tor Vergata science park, located in the suburbs of Rome, the wind and temperature profiles are measured by means of respectively a SODAR and a microwave radiometer. The combination of these remote sensing techniques will allow to monitor the spatial extensions of the meteorological phenomena, identifying urban effects and the observation of both mountain-valley and sea-land circulations in the basin area. After the first year of measurements, preliminary results are presented.

1. THE POPULATION EXPOSURE TO PAH (EXPAH) PROJECT

1.1 Aim and objectives

In order to addresses the environmental and health problems induced by emission, dispersion and transformation of Polycyclic Aromatic Hydrocarbons (PAHs) compounds, the European Commission funded the "Population Exposure to PAH" (EXPAH) project (Oct 2010-Dec 2013; http://www.ispesl.it/expah) under the LIFE+ program. The overall goal of the project is to identify the sources and quantify the exposure of children and elderly people to particulate PAHs in highly urbanized areas, and to assess their impact on human health. More in detail the EXPAH objectives are:

- to develop a state-of-the-art PAH emission inventories for the city;
- to improve and integrate air pollution models to describe the emissions, diffusion, atmospheric transformations, and removal of PAHs;
- to estimate the actual concentrations of PAHs to assess the human exposure in different living places and to develop an outdoor-indoor infiltration model;
- to estimate the mean exposure of the target populations to particles and PAHs by means of an exposure model;
- to estimate the short-term and long-term health impact of particles and PAHs and to improve exposure-response relationships of PAHs;
- to evaluate the health impact in view of EU policies in order to provide recommendations for adaption and mitigation strategies.

The city of Rome (Italy) was chosen as study area due to its serious pollution problems, particularly for PM_{10}, NO_2 and O_3. Several studies have reported health effects due to air pollution in this city [1] and an increase of 10 $\mu g/m^3$ of PM_{10} is expected to be responsible for an increase of 1.1% in cardiovascular and respiratory mortality.

1.2 Meteorological monitoring under the EXPAH project

Upper air and surface meteorological measurements are being collected in the metropolitan and sub-urban areas of Rome in order to get information on the climatology of the target area. In particular the correlation of PM and PAHs concentrations with the local meteorology and circulation is the objective of our study. The existing monitoring network has been extended with four stations located in the city of Rome and its surroundings. An intensive experimental campaign started in January 2011 in which at two of the four stations were added ground based remote sensors. The first site, named Villa Pamphili, is located in one of the urban park of Rome, (North-west of the city). A Metek DSDPA-90 phased array SODAR-RASS was mounted in this station to measure wind and temperature vertical profiles. A Vaisala CL31 ceilometer was also running to get vertical back-scattering aerosol profiles to retrieve the Planetary Boundary Layer (hereafter PBL) height and investigate the aerosol structures. The second station is set at the ISAC-CNR facilities, located at Tor Vergata in the south suburbs of Rome. Wind and temperature profiles are measured respectively by means of a SODAR and a MTP 5-P microwave radiometer. Complementary turbulence measurements are also carried out at both sites using sonic anemometers. The turbulence information is fundamental for dispersion models. The local circulation regimes around the city of Roma has been studied by different authors [2]. The local circulation is characterized by two prevailing circulations: land and sea breezes, and drainage flows from the mouth of the Tiber valley. A strong seasonal dependence of the diurnal behavior of wind speed and direction were also found.

2. RESULTS

2.1 Statistical analysis

In order to characterize the urban site of Pamphili, a statistical analysis of the wind velocity derived by SODAR between 40-400 m was made. The measurements, averaged over a period of 10 minutes, refer to the year 2011. Figure 1 shows the wind rose for the entire year. The different colors represent the wind occurrences (in percent units). Two prevailing wind directions are shown: NE and W-SW. For both the directions the distribution presents a peak corresponding at a wind speed of about 5 m/s, with the NE direction more frequent than W-SW one. Detailed analyses indicate that these prevailing wind directions have a seasonal behavior as shown by the wind roses of Figure 2.

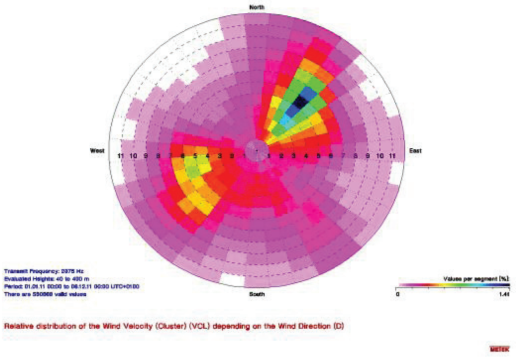

Figure 1. SODAR wind rose at the Pamphili urban park of Rome during year 2011.

The NE peak is observed during all the seasons (Figure 2). During the summer (left lower panel of Figure 2) the occurrence is lower and the sector interested is narrower than during the other seasons.

winter spring

summer autumn

Figure 2. Seasonal wind roses for the same site and period of Figure 1.

The presence of this peak is due , as shown in the paper by Petenko et al. [2], to a drainage flow from the Tiber valley. The W-SW peak, which occurs in spring and summer, is due to the sea breezes which normally develop in this area. In order to characterize this behavior the measurements were grouped into four time intervals: 0-6; 6-12; 12-18; 18-24 LT. Figure 3 shows the corresponding wind roses. Winds from NE are observed during both night and morning hours (upper and bottom right panels of Figure 3). The westerly winds are found instead during the warmest hours (bottom left panel) of the day confirming its sea breeze origin. The observations for the late afternoon evidence both the wind regimes, however a larger spread in the wind distribution occurs.

0-6 am 6-12 am

12-18 pm 18-24 pm

Figure 3. SODAR wind rose for different time intervals collected at Pamphili urban park during year 2011.

2.2 Detection of urban vertical structures by means of SODAR/RASS and MTP profiles

The SODAR measurements in Rome evidenced the existence of a consistent wind rotation during the early morning hours for cloudless days and stable conditions, in presence of an high pressure system. As an example Figure 4 shows this behavior for February 7th at the Pamphili urban park. More than 100 degrees of wind rotation from north to south is observed. The rotation starts from about 380 m on 0200 am LT and penetrates with time into the residual layer reaching the minimum height of 180 m at about 0700 am LT. This regime lasts up to about 1000 am when the heating of the sun removes its structure. A decreasing of the wind speed with height is observed during the same time interval.

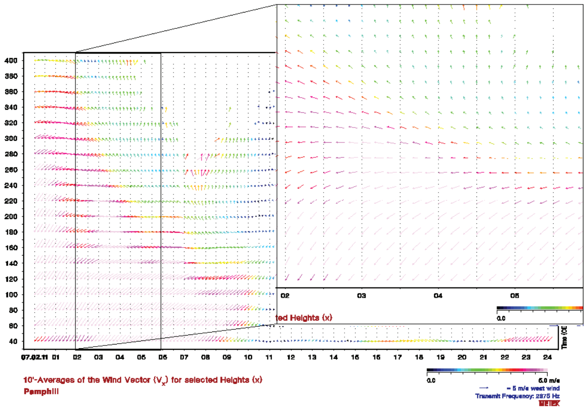

Figure 4. Wind profile structures detected at Pamphili urban park on February 7th, 2011.

The potential temperature profiles measured by a co-located RASS system (Figure 5), show the existence of a well defined stable layer with a depth of about 160 m in correspondence of the layer characterized by the highest wind velocities. The low height coverage of the RASS did not allow to detect the height of the residual layer, which was instead evidenced at 400 m by the MTP 5-P radiometer as shown in Figure 6. The availability of two temperature profiles might also be used to study the urban heat island effect in Rome.

The facsimile recording of the SODAR located at Tor Vergata, for February 7th is shown in Figure 7. The echogram confirms the presence of a very strong stratification in the low atmosphere with a shallow stable boundary layer of 200 m depth, which decrease up to 100 m in the early morning. The correspondent nighttime SODAR wind profiles are shown in Figure 8. A wind rotation with height is detected also at this site from 0230 am LT up to about 0400 am, but with weaker intensity than the Pamphili site. This behavior indicates that the urban boundary layer might introduce some effects in triggering this process. Early morning profiles exhibit stronger northern wind in the first 150 m respect to the wind above, confirming a decoupling of the local flow.

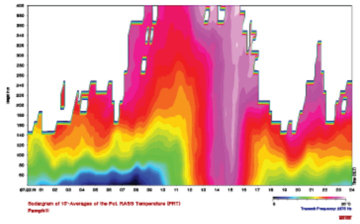

Figure 5. The RASS potential temperature profile measured at Pamphili urban park on February 7th . 2011.

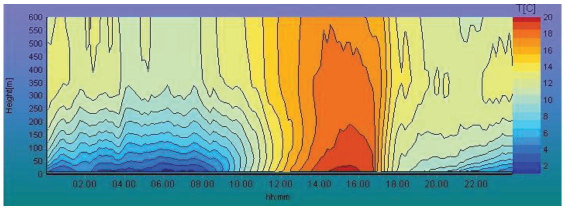

Figure 6. MTP-5P microwave radiometer temperature profile collected at Tor Vergata.

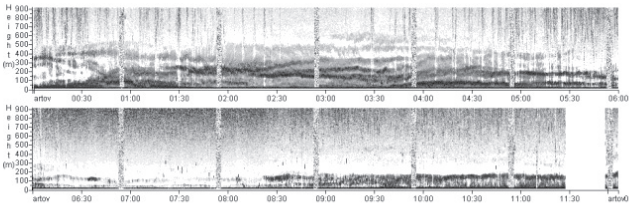

Figure 7. Facsimile representation on February 7th , 2011 given by ISAC SODAR located at Tor Vergata.

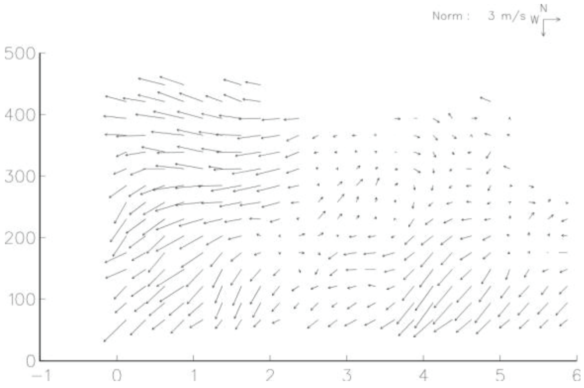

Figure 8. Wind profile structures detected at Tor Vergata on February 7th ,2011 0000-0600 am LT.

2.3 Backscattering aerosol profiles

The effects of the wind field and thermal structure on the vertical distribution of the aerosols can be observed in the signal provided by the Ceilometer located at the Pamphili site. Figures 9 and 10 show respectively the plot of the backscatter signal collected on February 7th and the correspondent PBL heights as estimated by means of the gradient detection algorithm embedded in the Vaisala BLVIEW software. The backscattered signal confirms the presence of a weak aerosol layer (dark green on Figure 9) which starts at 2 am from the upper part of the residual layer, penetrates progressively in the stable layer and ends at about 1000 am in correspondence of the wind rotation mentioned above.

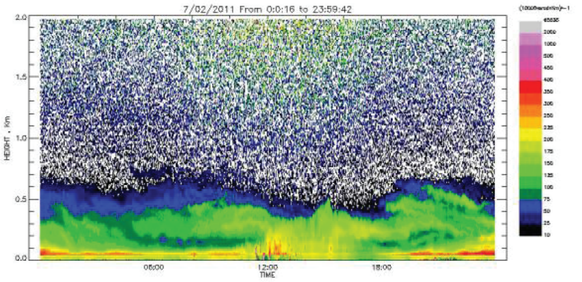

Figure 9. Backscatter signal of the Ceilometer collected at Pamphili urban park on February 7th, 2011.

The southern winds present in the upper layers might bring some less polluted air from outskirt areas of the city. The PBL heights (Figure 10) exhibit a strong stable layer 120 m high topped by a residual layer which extends up to 500 m for the whole day, confirming the strong stability conditions for this day.

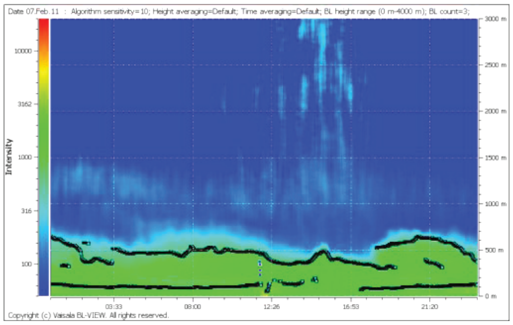

Figure 10. Intensity of backscatter signal and PBL heights (dots) of the Ceilometer collected at Pamphili urban park on February 7th, 2011.

2.4 Surface turbulence measurements

Both at Pamphili and Tor Vergata sites surface turbulence measurements were carried out. Figures 11a and 11b show respectively the time series of sensible heat (H_0) and turbulence kinetic energy (TKE) for February 7th 2011.

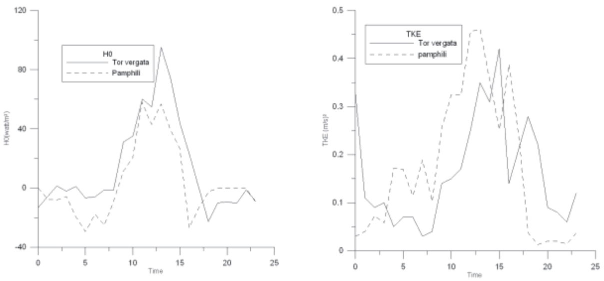

a) b)

Figure 11. Sensible heat fluxes (a) and turbulence kinetic energy (b) collected at Pamphili (black dotted line) and Tor Vergata (black full line) sites on February 7th, 2011.

The sensible heat flux measured at the Pamphili (black dotted line) shows negative values when the vertical structures mentioned above where detected. This downward fluxes might also produce the decoupling of the local atmosphere, which in turns might affect the observed wind vertical structures. An analogous behavior is not detected in the suburbs area of Tor Vergata (black full line). Similar behavior is shown by the turbulent kinetic energy which shows higher values at the urban site respect to the suburbs one.

3. DISCUSSION AND CONCLUSIONS

The complementary results provided by different remote sensors allowed to monitor the different features of the local atmosphere such as wind structures, PBL heights, thermal stratifications and aerosol vertical distribution. The long time serie of these measurements in the city of Rome have also made possible the identification of two prevailing wind regimes: one is linked to the drainage flows coming from the north of Tiber valley, the other is the sea-breezes circulation which develops in this area.

Wind vertical structures were often observed at the urban site late in the night and in the early morning in coincidence of very stable and cloudless nights under high pressure conditions. Thermals, as well as, aerosol structures are well correlated with these events. The availability of remote sensing systems at different city sites, allows to identify the main pattern of the urban circulation. The wind vertical structure at the urban site of Pamphili is generally more defined than the one of Tor Vergata site (south of Rome). This means that the city of Rome exhibits an urban circulation regime which might be driven by the larger thermal circulation pattern.

ACKNOWLEDGMENTS

The LIFE+ EU financial program (EC 614/2007) is acknowledged for the provision of funding for EXPAH project (LIFE09 ENV/IT/082).

REFERENCES

1. Forastiere F, M Stafoggia, G Berti, L Bisanti, A Cernigliaro, M Chiusolo, S Mallone, R Miglio, P Pandolfi, M Rognoni, M Serinelli, R Tessari, M Vigotti, C.A. Perucci; SISTI Group, 2008: Particulate matter and daily mortality: a case-crossover analysis of individual effect modifiers. *Epidemiology*. 2008 Jul;**19**(4):571-80.

2. Petenko I., Mastrantonio G., Viola A., Argentini S., Coniglio L., Monti P., Leuzzi G., 2011, Local circulation diurnal pattern and their relationship with large-scale flowin a coastal area of the Thyrrenian sea. *Boundary Layer Meteorology*. 139:353–366.

THE STRUCTURE OF THE ABL IN MOSCOW REGION DURING HIGH-POLLUTION EPISODES

Kramar V.F.[1], Baykova E.S.[2], Kallistratova M.A.[1], Kouznetsov R.D.[1,3], Kulichkov S.N.[1]

[1]*Obukhov Institute of Atmospheric Physics, 3 Pyzhevskii, 119017 Moscow, Russia, vkramar@list.ru*
[2]*Lomonosov Moscow State University, Faculty of Physics, GSP-1, 1-2 Leninskiye Gory, 119991 Moscow, Russia, baykova.e@mail.ru*
[3]*Finnish Meteorological Institute, 1 Erik Palménin, Helsinki, Finland, rostislav.kouznetsov@fmi.fi*

ABSTRACT

The structure of the atmospheric boundary layer (ABL) during high-pollution episodes in Moscow region has been revealed by means of sodars and microwave temperature profilers. The episodes were identified from the data on the concentrations of NO_x, SO_2 and CO collected by the air-quality monitoring network of 22 measuring sites. Few episodes of severe exceedance of the short-term exposure limits for one or more substances at several locations were identified during 2010-2012. The corresponding parameters of the ABL were obtained from the data of routine meteorological measurements and from the data of the ground-based remote sensing network. The network consists of three LATAN-3 Doppler sodars and three MTP-5 temperature profilers, located in Moscow downtown and in rural area.

The fine structure of the ABL recorded by the remote sensing network during high pollution episodes are analyzed. The bulk estimates of regional emissions are made for several species.

1. INTRODUCTION

The short-range transport of pollutants from the source to the point of measurement is driven by the wind field and the intensity of turbulent mixing in the atmospheric boundary layer (ABL).

To analyze meteorological conditions for local-scale air quality applications one has to estimate pollutant concentrations at the lower 50 – 100m. The important features of the layer are: small vertical variability of vertical fluxes of momentum and scalars (usually 10-20%), and significant variability of wind velocity, temperature, and turbulence intensity [1]. The stratification of the layer strongly influences its pollution. A stable stratification suppresses turbulence preventing the mixing of the polluted and clean air masses, whereas unstable stratification intensifies the mixing leading to decrease of pollutant concentrations from the surface sources. The sodar data provide the information on wind field, and intensity of turbulent mixing in the ABL.

2. NETWORK FOR ABL MONITORING

Obukhov Institute of Atmospheric Physics (IAPh) of Russian Academy of Sciences together with Physical Faculty of Lomonosov Moscow State University designed an experimental network of the ground-based remote sensing for monitoring of ABL parameters in the Moscow region. One of the main goals of the activity was to acquire data on parameters that affect short-range transport and dispersion of pollutants in the region.

LATAN-3 sodars [2] designed and produced in IAPh were placed at three sites: a) in the center of Moscow (IAPh), b) on the periphery of the city (MSU), and c) in rural area, 45 km West of Moscow at the Zvenigorod Scientific Station (ZSS) of IAPh. For this study only the data from IAPh and ZSS are used.

Surface concentrations of various pollutants in the region are measured by "Mosecomonitoring" network of automatic stations [3,4], arranged by the city council.

3. HIGH-POLLUTION EPISODES

Moscow has very intensive traffic with low mean vehicle velocity and frequent traffic jams. This makes the traffic a major source of air pollution in the city. At neutral or unstable stratification of the ABL or at moderate to strong winds the pollutants are efficiently removed from the urban air basin. The stably stratified ABL under calm conditions is shallow and poorly ventilated, which results in a poor air quality in Moscow.

Under conditions of a low pressure gradient or anticyclonic type of weather, the wind velocity is small, the clear sky leads to maximum solar radiation that creates favorable conditions for photochemical reactions. In the absence of precipitation pollutants are not washed out. Under such situations primary and secondary pollutants from near-surface sources get accumulated in urban air, leading to fast increase of the surface concentrations, often up to hazardous levels.

Bellow we consider one of such episodes, occurred on March 24-26, 2012.

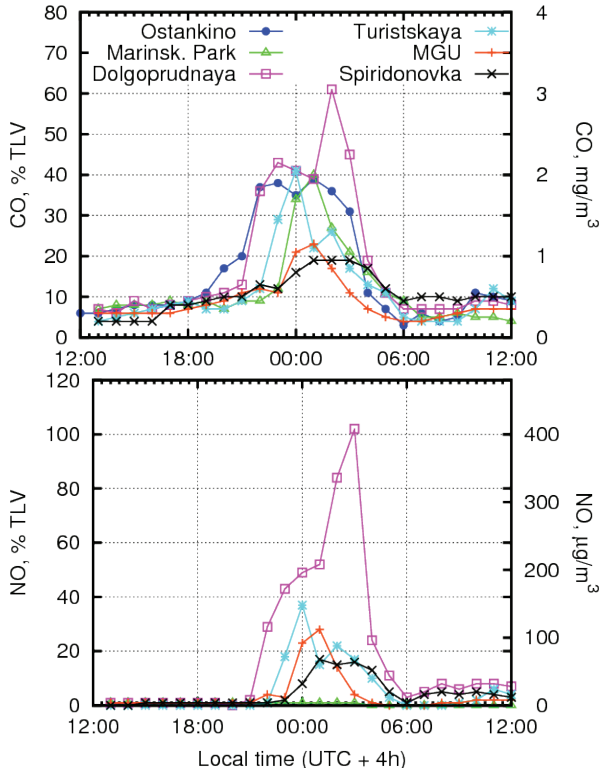

Figure 1. Time series of CO and NO concentrations for six automatic stations. March 24-25, 2012. TLV stands for threshold limit value

Carbon monoxide (CO), and nitrogen oxides (NO_x) are the main pollutants generated by vehicles. The time series of the normalized CO concentrations for several urban sites of Mosecomonitoring network [4] indicate a similar pattern during the episode for both city center and its outskirts (Fig. 1). The concentrations of pollutants during the episode raised up to about half of their Threshold Limit Values (TLV) for short-term exposure. According to the Russian standards TLVs for CO and NO in residential areas are 5 and 0.4 mg/m^3 respectively [4]. Typically observed concentrations of pollutants at the urban stations in Moscow are in the range of 0.01—0.05 TLV. The episode started at around 20:00 on March 25 and lasted for 6-8 hours. After the episode the concentrations returned to their typical levels.

The concentrations of NO indicate a similar behavior as those for CO. The maximum concentrations of NO (1 TLV) were registered at the same site as for CO ("Dolgoprudnaya").

The coherence in the variations of the pollutants concentrations at different sites indicate that the reasons causing such a behavior are common for the entire area of the megalopolis.

4. INTERPRETATION

The surface pressure maps for 00 UTC March 25, 2012 show that Moscow was in a low gradient area of pressure field (in the so-called "ridge"). This agrees with both the sodar data and the data of network of meteorological stations (e.g. No 27612 at night and in the early morning of March 25, 2012 reported the clear sky, haze and 0–1 m/s wind.)

During the day time on March 24 even under the weak mean horizontal wind the urban surface layer was efficiently ventilated by free convection. The updrafts of 1-2m/s and slightly slower downdrafts detected by the sodar are capable of mixing the pollutants in the whole ABL, within less than half an hour.

The concentration increase began after the sunset around 19:00. At that time the rush hour is not over yet. After the free convection ceased, the stable stratification arose and the wind speed in the ABL did not exceed 2m/s (Fig. 2). This resulted in a sharp increase of the surface pollutant concentration.

The rural station (ZSS) also recorded calm and very strong ground-based inversion during the episode. Thus the conditions were favorable for the accumulation of the pollutants at a substantial horizontal scale.

5. ESTIMATES OF EMISSION INTENSITY

The data on the near-surface concentrations together with the information from sodar network can be used to estimate the emission rates in the city.

Assume that at the maximum of the surface concentration of the pollutant, its emission is in equilibrium with the ventilation. For the whole city it means that for the period of time, in which the whole volume of the pollutant air over Moscow will be carried away through the city boundaries, the pollutant sources will emit the same amount of pollutants (the most simple balanced box model). The following parameters are assumes: the size of the city is about 50 km, the wind speed is 1 m/s, and the mixing layer height is 200m. To simplify the estimation let us consider that the pollutants in the mixing layer are distributed uniformly with height, because they were well mixed by free convection. The overall volume of polluted air in the layer is approximately equal to $4*10^{11}$ m^3. For such approximation the volume will be entirely replaced in $5*10^4$ s (14 hours). For the episode of March 25, 2012 the average CO concentration in the layer was

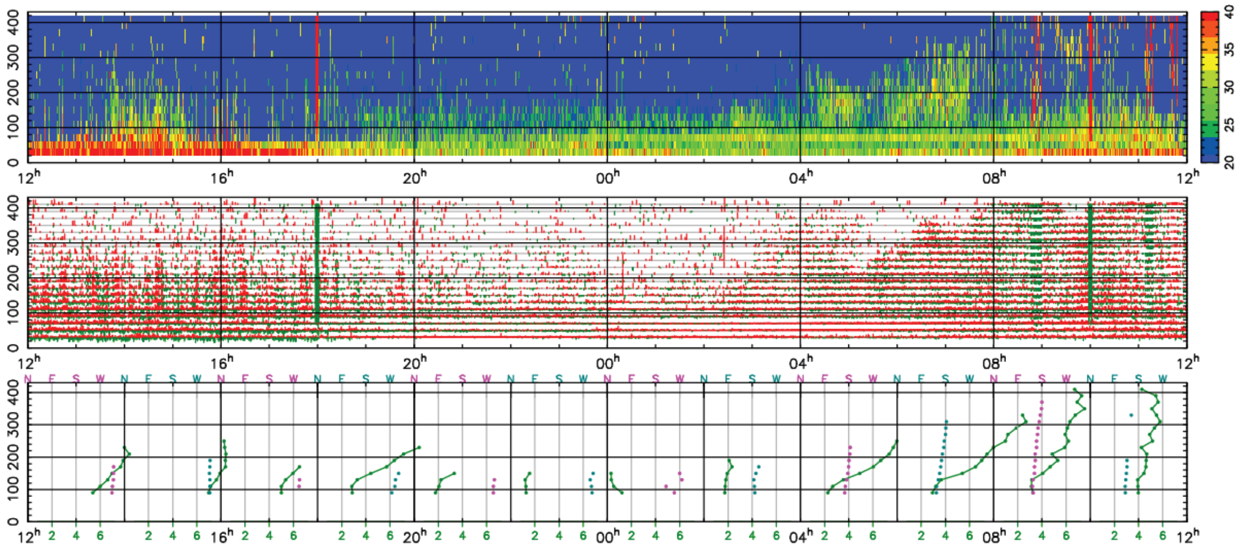

Figure 1. Moscow, IAPh, March 24-25, 2012. Top: The sodar echogram. Middle: instantaneous vertical velocity; red and green strokes show upward and downward motions, respectively. Bottom: profiles of horizontal wind speed and direction; The lowest part of the wind profile is discarded due to fixed echoes.

approximately 0.3 TLV that is equal to 5*0.3 = 1.5mg/m^3. Then the overall quantity of this pollutant exhausted during 14 hours into the city air basin will be approximately equal to 600 tonnes. Being converted into 1 square meter the intensity of CO sources will be about $Q_{CO} \sim 6$ µg/(m^{2}s). Analogous estimation for NO gives the value $Q_{NO} \sim 0.8$ µg/(m^{2}s) which is almost ten times lower.

To more accurate estimates a distribution of pollutants concentration with the height (up to zero value on the top boundary of the layer) should be accepted. In the case of linear law the estimates of pollutant source intensity will be twice lower.

A significant excess of pollutant concentration at site “Dolgoprudnaya” (Northern outskirt) over the values measured at other sites at night March 24-25, 2012 could be explained by the Southern wind in the lower 200-m layer.

6. CONCLUSIONS

In the conditions of megalopolis sodars can provide an important information for the air-quality evaluation. The measured vertical profiles of wind velocity, its direction and vertical velocity together with the measurements of the mixing height can be used in dispersion models.

In some meteorological situations sodar data along with regional pollutant concentration monitoring network data can be used to estimate intensity of uniformly distributed surface pollutant sources.

Usually, strong horizontal winds purify the air over Moscow so that values of pollutant surface concentrations are low. Nevertheless, in anticyclonic and analogous meteorological situations a strong vehicle traffic can cause the accumulation of pollutants near the surface. Under such conditions the pollutant concentration can exceed the threshold limit values within few hours.

ACKNOWLEDGMENTS

This study has been supported by the Russian Foundation for Basic Research, (grant No. 10-05-00802), by the EC FP7 project ERC PBL-PMES (No. 227915), and by Academy of Finland (ASTREX).

REFERENCES

1. Monin A.S., A.M. Yaglom, 2007: *Statistical Fluid Mechanics: Mechanics of Turbulence*, Dover Publications, 784 pp.

2. Kouznetsov R.D., 2009: The multiple-frequency sodar with high temporal resolution *Meteorol. Zeitschrift.*, **18**, pp. 169–173.

3. Gorchakov G.I., E.G. Semutnikova, E.V. Zotkin, A.V. Karpov, E.A. Lezina, A.V. Ul'yanenko, 2006: Variations in Gaseous Pollutants in the Air Basin of Moscow, *Izvestiya, Atmospheric and Oceanic Physics*, **42**, pp. 156-170

4. Mosecomonitoring web site (accessed 10.05.2012) http://www.mosecom.ru/air/air-today/

THE SIGNAL PROCESSING ALGORITHMS STUDY OF ATMOSPHERIC RADIOACOUSTIC SENSING SYSTEMS

V.M. Kartashov, D.M. Kulia

Kharkov National University of Radio Electronics, 42V 50-letiia VLKSM Ave., 61153 Kharkov, Ukraine, res@kture.kharkov.ua

Kharkov National University of Radio Electronics, 51A L.Svobody Ave., Apt. 519, 61174 Kharkov, Ukraine, d.kylay@mail.ru

ABSTRACT

Most of the known atmospheric radioacoustic sensing (RAS) systems are designed to measure the air temperature, which is functionally related to the velocity of sound in the medium. In the existing systems the sound velocity is determined according to the Doppler frequency shift of electromagnetic waves scattered at the sound premise. Therefore, signal processing methods of atmospheric radioacoustic sensing systems are designed as the Doppler frequency measuring devices and divided into methods that use frequency adjustment to provide the Bragg condition, and methods without frequency adjustment. The multi-channel correlation processing scheme is used to estimate the Doppler frequency.

The frequency adjustment method needs a considerable amount of time for sensing. The method without frequency adjustment is characterized by a significant magnitude of systematic errors because it does not take into account the scattered signal energy dependence on the speed of sound and shape changing of radiosignal reflected from a sound premise.

To eliminate systematic errors of measurement when multi-channel correlation processing scheme is used in channels it is necessary to form reference signals using a mathematical model of the scattering channel which determines a radiosignal shape dependence on the Bragg condition detuning if a radiosignal is reflected from acoustic premise. The Bragg condition detuning is functionally related to the velocity of sound and the reference signal energy depends on Bragg condition detuning.

The Bragg condition detuning measurement and accounting of reference signal energy dependence on Bragg condition detuning give a possibility to receive a more accurate estimate of sound speed.

1. THE SIGNAL PROCESSING METHODS OF ATMOSPHERIC RADIOACOUSTIC SENSING SYSTEMS

In practice, the measurement process, carried out by some atmospheric radioacoustic sounding systems, is performed by applying the adaptation. Adaptation is the adjustment of the frequency of acoustic or electromagnetic signals to provide a zero value of the parameter of Bragg condition detuning $q = 2k_e - k_s = 0$, where k_e is the wave number of the electromagnetic oscillations and k_s is the wave number of acoustic vibrations [1]. This is due to the fact that under the condition of equality $q = 0$, the Doppler measurements can be performed, because the frequency obtained in this case is exactly the Doppler and, consequently, in this case, you can use the usual technique of measuring and usual interpreting technique of the measurement results for finding the speed of sound and ambient temperature.

Signal processing algorithms include the sound radiation frequency change (most often by hand). When the value of the frequency of sound is changing, and the radiosignal frequency is constant, it changes the value of Bragg condition detuning parameter.

Frequency tuning is performed before the appearance of the maximum of the reflected signal or until the appearance of frequency coincidence of a sound signal with a Doppler frequency of the scattered signal. This approach stems from the fact that the condition of $q = 0$ is the reason of the amplitude maximum of the reflected signal and it is the reason of coincidence of the Doppler frequency shift of the scattered signal with the frequency of the radiated sound premise.

Adaptation methods greatly complicate the system and the process of sensing and significantly reduce the efficiency of sensing, because the adaptation is carried out, usually in manual mode.

A number of the other sensing systems determine the sound speed by the Doppler frequency shift of electromagnetic waves, scattered at the sound premise, without the frequency tuning of the sensing signals.

Processing devices of such atmospheric radioacoustic sounding stations, regardless of the types of the used acoustic and electromagnetic sensing signals, are built as the Doppler frequency meters, and the theoretical model of processing devices, that are used in the RAS systems, is the well-known multi-channel correlation or filtering scheme of informative parameter estimate. However, the results of measurements obtained with the use of such algorithms are accompanied by significant systematic errors: the obtained temperature of the atmosphere differs from the true value at 1-2 degrees [1].

2. THE REASON OF SYSTEMATIC ERROR

To find out the cause of the obtained errors it is necessary to write the posterior distribution of the received signal information parameter x [2]

$$P(x \mid y) = c'' \cdot P(x) \exp\left[-\frac{1}{N_0} \int_0^T y(t) \cdot u_c(t,x) dt \right] \times$$
$$\times \exp\left[-\frac{Q_x}{N_0} \right], \qquad (1)$$

where c'' is the constant that determines the scale on the ordinate, $Q_x = \int_0^T u_c^2(t,x) dt$ is the signal energy at a given value of the message x. A mixture of useful signal and noise at the input of processing and reproduction device of an informative parameter is represented as

$$y(t) = u_c(t,x) + u_n(t), \qquad (2)$$

where $u_c(t,x)$ is the signal of arbitrary shape which is known in the place of reception exactly, except for the unknown informative parameter x with a priori distribution $P(x)$, $u_n(t)$ is the Gaussian independent stationary additive white noise with known spectral density N_0.

For a broad class of location problems (including problems of velocity measuring of objects on the Doppler frequency), it is assumed that the signal form $y(t)$ does not differ from the shape of the reference signal $u_c(t,x)$, and the value Q_x is assumed independent of the informative parameter. In the formation process of the required estimation the value Q_x is not taken into account and it is included in the constant c''. Similar processing procedures are implemented to estimate the sound speed according to the Doppler frequency at the RAS systems. However, in reality, in the atmospheric RAS systems this condition is not performed. First, the scattering of radio waves on the sound is frequency-dependent: the level of the scattered signal Q_x depends on the sound speed, which is necessary to evaluate. Secondly, the scattering on the sound significantly changes the structure of the emitted signal, which acquires additional amplitude-angular modulation [1].

3. ELIMINATION OF ERROR

To eliminate systematic errors it is necessary to consider the signal shape change, when it interacts with acoustic oscillations. Using the scattering function (3) [3], the shape of the scattered signal can be determined.

$$F(r,q) = \int_{-\infty}^{\infty} E(2r'-r) \cdot S^*(r') \exp[jqr'] dr' \qquad (3)$$

where $q = 2k_e - k_s$ is the parameter of the Bragg condition detuning, $k_s = 2\pi f_s / c_s$ is the wave number for sound, $k_e = 2\pi f_e / c$ is the wave number of electromagnetic wave, r is the signal shift in the coordinate "distance", $E(2r'-r)$ is the space envelope of the radiosignal, $S^*(r')$ is the space envelope of the acoustic signal, f_s is the frequency of the acoustic signal, f_e is the frequency of the electromagnetic signal.

As for the information parameter it is necessary to use the parameter of the Bragg condition detuning q which is functionally related to the velocity of sound (4).

$$c_s = \frac{2\pi \cdot f_s}{4\pi \cdot f / c - q}, \qquad (4)$$

Forming the reference signals, it is necessary to take into account the generated signal energy dependence from q.

Thus, the signal processing device eliminating the systematic error (Fig. 1) must be a circuit consisting of the N correlators, where the reference signals $F^*(q)$ are the vibrations that is generated according to the scattering function.

The values of the correlation integrals are calculated between the received signal $F_y(q_m)$ and the reference vibration set $F^*(q)$. Further, the values of the correlation integrals are corrected by subtracting from the corresponding output value the corresponding value Q_x determined by the energy of the reference signal of the corresponding correlator. As a result, if the parameter of the Bragg condition detuning of the received signal, for example, is equal to zero, the correlator output signal is formed such as shown in figure 2, if you use signals with a rectangular envelope.

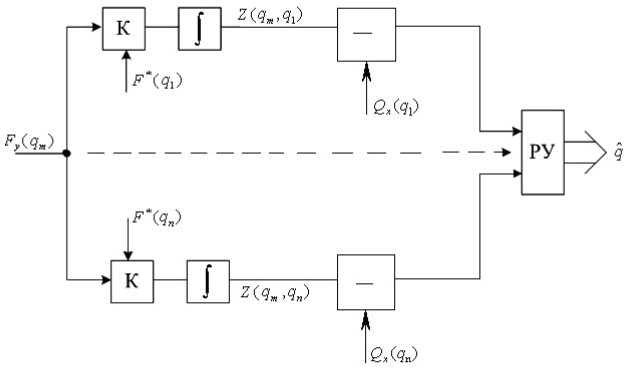

Figure 1. The signal processing device scheme without systematic error

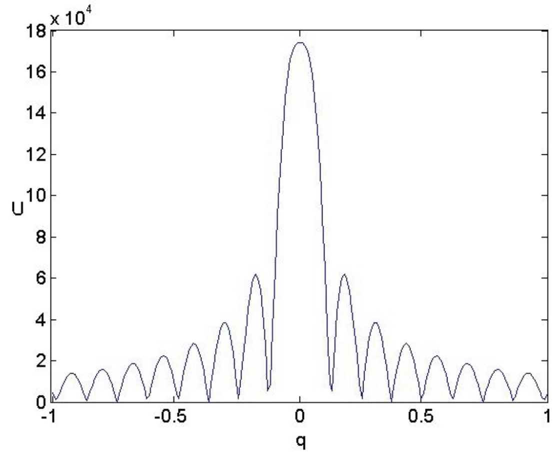

Figure 2. The output signal of the correlator after correction when the Bragg condition detuning of the received signal is equal to zero.

The output signal is described by the expression (5)

$$Z(q_m,q)=\left|F(q_m,q)\right|-\frac{1}{2}Q_x, \qquad (5)$$

where $F(q_m,q)=\int\limits_0^T F_y(r',q_m)\cdot F^*(r',q)dr'$ is the cross-correlation function of the input signal and reference signal, $Q_x=\int\limits_0^T F^{*2}(r',q)dr'$ is the energy of the reference signal.

The decision about the value of the estimated parameter q_m is taken at the higher values obtained after correction.

To evaluate the potential accuracy of the atmospheric parameter estimation by proposed algorithm it is necessary to compute the standard deviation (SD) of the Bragg condition detuning estimation from the Bragg condition detuning true value. Because in the proposed algorithm the evaluation of sound speed carried out by the energy parameter q, the standard deviation is [4]

$$D_q=\sqrt{\sigma_q^2}=\left[\sqrt{\frac{d^2S(q_1,q_2)}{\partial q_1\partial q_2}}\right]_{q_0}^{-1}, \qquad (6)$$

where $S(q_1,q_2)$ is the signal at the output of the optimum receiver (signal function). The signal function is a cross-correlation function of the input signal and the reference signal with different current values of the parameters q_1 and q_2.

CONCLUSIONS

In the report we have considered the signal processing algorithms used in radio acoustic sounding systems and analyzed defects of these algorithms. Optimal signal processing algorithm which eliminates the find defects is synthesized.

Reference signals for multi-channel correlation circuit according to the algorithm are formed in accordance with the influence, which is subjected to the signal at an acoustic radar channel. These reference signals are formed due to the scattering function.

The estimation of the sound speed in the proposed algorithm is performed out by the energy parameter, so the values of the correlation integrals in multi-channel scheme are corrected in accordance with the energy of generated reference signals.

REFERENCES

1. Kallistratova M.A., Kon A.I., 1985: *Radio Acoustic Sounding of the Atmosphere*, M.: Nauka, 195.

2. Tihonov V.I., 1983: *Optimal reception of signals*, M.: Radio and Communications, 320.

3. Kartashov V.M., 2011: *Models and Methods of Signal Processing of the Atmospheric Radio-acoustic and acoustic sounding*, Kharkov: KNURE, 234.

4. Kulikov E.I., Triphonov A.P., 1978: *Parameter estimation for signals on the background noise*, M.: Sov. Radio, pp. 69-77.

DOPPLER OR CORRELATION PROCESSING OF THE REFLECTED SIGNALS IN THE HARDWARE RASS: ERROR ANALYSIS

S. I. Babkin

Kharkov National University of Radio Electronics, 14, Lenin Ave., 61166 Kharkov, Ukraine;
pnilsabsi@kture.kharkov.ua

ABSTRACT

At the report it is performed the comparative analysis of the methodological and instrumental errors in recording of vertical profiles of air temperature by the atmosphere RASS instrumentation for the Doppler and correlation methods of the signal processing scattered. It is shown that the correlation processing method provides higher instrumental accuracy of the temperature measurement than the Doppler. However, the correlation processing method complicates the signal processing device and increases the number of the meteorological variables, which shaping methodological errors.

1. THE REGISTRATION ERROR OF AIR TEMPERATURE PROFILE BY THE DOPPLER METHOD

The Doppler method for detecting of the vertical air temperature profiles based on the speed measuring of the acoustic wave package in the atmosphere. Acoustic speed is related to temperature by the expression [1]

$$C_S = a\sqrt{T} \pm V, \qquad (1)$$

where T - is the absolute air temperature, V - is the wind speed projection on the sensing direction, a - coefficient for dry air depending on the composition of air,, $a = 20{,}0789 \cdot m \cdot s^{-1} \cdot K^{-1/2}$.

Evaluation of instrumental mean square error of the air temperature measurement by the Doppler radar performed by conventional circuitry, is performed earlier, the error of this kind depends on the stability of the frequency characteristics of the probing equipment and when the signal/noise ratio is not less than 10 is $\sigma T \approx 0{,}25 - 0{,}3K$. In some experiments the registration error of the air temperature vertical profiles by the Doppler method which is used in the radioacoustic sounding systems (RASS) of the atmosphere and by the staff gauges was properly investigated. The staff gauges were taken as a reference and were available on 13 balconies of high-rise 300-meter meteorological masts of the Experimental Meteorology Institute (Obninsk). Depending on the meteorological conditions, the mean-square deviation of the comparative measurements results were (0.1 - 0.5) K. Note that the obtained values of standard deviations include the methodical errors, which are caused by the influence of humidity and by the presence of vertical air flow (it is additionally changes the sound speed in the atmosphere). Methodical errors are also caused by the fluctuating nature of the received radio signals and the design antennas spacing of the radio channel.

The altitude variation existence of the air temperature in the atmosphere, which is especially noticeable in the boundary layer, leads to the violation of the Bragg condition. The violation of the Bragg condition leads to the following effects: the intensity of the scattering from the pack of acoustic waves radio waves decreases and the intensity decrease leads to the decrease in signal / noise ratio at the output of the radio receiver, especially when the package has a great length; the Doppler frequency shift of the received signal does not coincide with the frequency of the sinusoidal filling of probing acoustic package, the registering error of the temperature profile at the points, where the Bragg condition is violated, can reach 1-2 K.

The experimental study of the registration error growth of the air temperature profile as violation of the Bragg condition is shown that the error variation along the profile can be described by the tangent of the curve with the its minimum value at the altitude, where the Bragg condition is performed exactly.

2. THE REGISTRATION ERROR OF THE AIR TEMPERATURE PROFILE BY THE CORRELATION METHOD

By using the correlation method of the air temperature vertical profile registering the velocity of acoustic package in the atmosphere can be found by the formula [2]

$$C_S = (2\pi f_S)/[(4\pi f / c) - q], \qquad (2)$$

where f_S is the sinusoidal fill frequency of the acoustic package, f is the radar working frequency, c is the propagation velocity of radio waves, q is the parameter of the Bragg condition detuning.

Using (2), we can find an expression for the air temperature calculating. It is

$$T, K = \{(2\pi f_s)/a[(4\pi f/c)-q]\}^2. \qquad (3)$$

In the formula (3) we takes into account the expression (1), and it is assumed that the vertical component of wind velocity can be neglected because that is much lower then the speed of sound. After the experimental evaluation completing of the q detuning parameter across the road-sensing you can register the vertical profile of air temperature.

The relative mean square error of air temperature calculation by the expression (3) can be written in the total error equation form (when the error sources are uncorrelated), in which the partial derivatives with respect to all parameters is:

$$\partial T/\partial f_s = 8\pi^2 f_s / a^2 b^2;$$

$$\partial T/\partial f = 16\pi^2 f_s / a^2 b^3 c;$$

$$\partial T/\partial c = -16\pi^2 f_s f / b^2 c^2;$$

$$\partial T/\partial q = -4\pi f_s / a b^3;$$

$$\partial T/\partial a = -8\pi^2 f_s{}^2 / a^3 b^2,$$

$$b = 4\pi f/c - q. \qquad (4)$$

To estimate the relative mean square error of air temperature it is necessary to specify the parameter values which are included in the expression (4). For example, used in a series of comparative experiments, the 10-centimeter RASS had the following parameters: $f_n = 6800$ Hz, $f = 3\cdot 10^9$ Hz, $c = 3\cdot 10^8$ m/s, $a = 20{,}0789 m\cdot s^{-1}\cdot K^{-1/2}$, $q = 0{,}5$, $b = 125{,}1$ m^{-1}.

The values of influence coefficients in (4) in this case are as follows:

$$\partial T/\partial f_s = 8{,}5\cdot 10^{-2};\ \partial T/\partial f = 5{,}72\cdot 10^{-14};$$

$$\partial T/\partial c = -8{,}93\cdot 10^{-9};\ \partial T/\partial q = -2\cdot 10^{-3};$$

$$\partial T/\partial a = -23\cdot 10^{-2}. \qquad (5)$$

Analyzing the results (5), it is necessary to say that the frequency uncertainty of the probing sound, humidity uncertainty and detuning parameter uncertainty have a greatest influence on the mean square error of air temperature measurement. The sound frequency is formed by the technical devices of the sensing system and its stability can be achieved by using of the required stabilization methods. Humidity is a physical parameter of the atmosphere, details about which can be obtained in various ways (by synchronous measurements, model calculations and others). In some cases, for example, when the atmospheric boundary layer sensing is performed, the humidity can be adopted as a constant. The q parameter is the unknown quantity.

The majority values of the relative mean square error of the parameter measurements, which are included to the equation (4), can be evaluated by known methods:

$$\sigma f_s / f_s = 15\cdot 10^{-12}, \sigma f / f = 0{,}3\cdot 10^{-16},$$

$$\sigma a / a = 10^{-4} \text{ and } \sigma c / c = 0{,}5\cdot 10^{-6}. \qquad (6)$$

We do not have a common method of estimation error calculating yet, because, in fact, this quantity can not be measured, it is estimated by the correlation integral maximum obtained by the reference voltage multiplying by the real output voltage of radio receiver, which receives a signal from a given sensing height. The reference voltage is formed in accordance with some q value.

One place to start might be the error determination method coming from the opposite: at first you must ask the temperature measurement error that satisfies the specific requirements of meteorological practice (type of forecasting, scientific researches of the atmosphere physics, air pollution control, etc.). Next, it is necessary to find the resolution of the Bragg condition detuning parameter Δq and it is necessary to find the grade number of Bragg condition detuning parameter N. The last step of this procedure is the finding of the q magnitude determining error. In this case, as usual, you must separate the methodical and random components of error.

The random component of q determining error depends on the playback of the reference voltage and it depends on the level of output voltage of a radio receiver at the input of the correlator, which corresponds to the scattered signal, which is received from a given height. In this case we must assume that $\delta q \le \Delta q$ (δq is the q definition error) and $\sigma T \le \Delta T$.

Now we consider the role of the radio receiver in the formation of the error of the q detuning parameter definition. The main parameter that determines the accuracy of the q parameter fixed is the signal / noise ratio. We know, for example [3], that the power estimation of a random signal, when the correlation processing is performed, can be performed with an error of 10% when the signal/noise ratio is 10 dB. The received signal power P depends on the Bragg condition detuning parameter q. The received signal power dependence on Bragg condition detuning is described by the exponential form $e\left(-q^2\right)$ [1]. Bypassing the intermediate steps, we can write

$$\frac{\sigma q}{q} \approx \sqrt{\frac{1}{4(\ln P)^3}} \sqrt{\left\{\frac{\sigma P}{P}\right\}^2},$$

The Bragg parameter determining error strongly depends on the value of the received power and accuracy of its measurement. For the 10-centimeter RASS, which is used in comparative experiments, the level of the received power, which provides the acceptable accuracy of temperature measurements, lies in the 10^{-12} ... 10^{-14} W, or about 1 mW. Then

$$\sigma q / q \approx 1{,}4 \cdot 10^{-2}, \qquad (7)$$

Including (7), the relative mean square error of temperature measurement (note, instrumental), when the correlation processing is performed, is $\sigma T / T \approx 3 \cdot 10^{-5}$, and the relative mean square error of the air temperature measuring in the standard atmosphere is $\sigma T \approx 0{,}01K$.

Consideration of methodological error sources we start with the error, which depends on a given resolution of the vertical temperature profile recording in layers ΔT. It should be borne in mind the possible values of the vertical gradient of air temperature in the real conditions of sensing, the average value of this quantity for the standard atmosphere is $\gamma = 0{,}62$ K/100 m. In some cases, for example, when the breeze cells are appeared, the values of the vertical gradients can reach 1-2 K in the 100 meters. The maximum resolution of temperature measurement is necessary to the determination of vertical gradients of the refractive index for radio waves in the centimeter wavelength range. The vertical spatial resolution for temperature measurement is within $\Delta R = 25 - 30$ m. It means that to the reliable determination of the values of the vertical refractive index can it is necessary to provide ΔT = 0.25-0.3 K.

Very important issue, when the correlation method of the temperature vertical profile recording is used, is the number of gradations of the Bragg detuning parameter, which is required for the given resolution providing of the temperature, and the number of the correlation reception channels.

Depending on the number of wavelengths in the probing acoustic package, the range of q values (in other words, the width of the main lobe of the function $(\sin x / x)^2$, which determines the significant Bragg scattering) is [-1.8, 2.2] for $n = 10$ and it is [-0.0018 , 0.0022] for $n = 100$ [1]. If we assume that $n = 10$ and $\Delta q = 0{,}1$, the number of gradations N will be 40 and the temperature change ΔT will be $1{,}39K$. The obtained value of the temperature resolution casts doubt on the possibility of the effective atmosphere sensing by using the correlation processing method of the received signal, when the control of the atmospheric boundary layer by RASS is performed.

To provide the necessary resolution, when the atmospheric boundary layer sensing is performed, it is necessary to provide the condition $\Delta q \le 0{,}05$. Then the resolution ΔT is $0{,}2K$. Consequently, to implement this temperature measurement resolution by using the correlation method it is required 80 channels for the signal received processing. In comparative experiments on the sounding of the atmosphere in short and long acoustic packages we have found that by using long packets the fluctuations of the received signals are significantly increased and it did not relate to the fluctuations of the parameter q.

In determining the systematic error should also be noted and a number of physical factors existing in the atmosphere (the horizontal wind, vertical gradient of meteorological parameters, turbulence, the energy absorption of sound, etc.). These factors do not cause a change in setting q, but their effect on the acoustic package reduces the signal power P, and as a consequence, the determination of the error q.

To determine the methodical error it is necessary to note the number of physical factors existing in the atmosphere (the horizontal wind, vertical gradient of meteorological parameters, turbulence, the energy absorption of sound, etc.). These factors do not cause the change of q parameter, but their effect on the acoustic package reduces the signal power P and, consequently, this leads to the determine error.

The methodological errors that arise due to the lack of a priori information about the meteorological quantities and atmospheric processes in various sensing conditions by using different types of signal processing can be reduced by the involvement of relevant information received either from the respective meteorological sensors or from data of model calculations. This approach was used to study the possibilities of Doppler methods, when the experimental probing of the atmosphere in real weather conditions and the air temperature profile registering at different stages of the existence of warm fogs on the border of the land-sea are performed.

CONCLUSIONS

Our analysis allows the following conclusions.

1. The instrumental error of the air temperature measuring by using apparatus RASS, which is based on the using of the correlation processing of received signals, is lower than if we use the Doppler processing, but the correlation processing device needs to be made more complicated (in particular, the correlation processing device needs the number increasing of channels).

2. When the correlation signal processing is performed, the amount of the atmospheric variable factors in height is significantly increased. The atmospheric variable factors form the recording methodical error of temperature profiles. The recording methodical error of temperature profiles requires the further researches.

REFERENCES

1. Author1 A. B., C. Author2, D. Author3, 2011: Journal Article Title, *Journal Name*, **47**, pp. 25-30.

1. Kallistratova M.A., Kon A.I., 1985: *Radio Acoustic Sounding of the Atmosphere,* M.: Nauka, -195 p.

2. Kartashov V.M., 2011: *Models and Methods of Signal Processing of the Atmospheric Radio-acoustic and acoustic sounding,* Kharkov: KNURE. – 234 p.

3. Vladimir Orlov, 2003: *Estimation of the capacity of a random signal based on the correlation of spatial processing,* AAEKS, № 1 (11), Information-control equipment and systems.

DEVELOPMENT OF A NOISE-PROTECTED ACOUSTIC ANTENNA FOR A MONO-STATIC CITY SODAR

Ulianov Y.N.[1], Vetrov V.I.[2], Misailov V.L.[3]

[1]*National Technical University "KhPI. ", Kharkov, Ukraine, E-mail: ulianov.y@yandex.ua*
[2]*SIC «TRISTAN», Moscow, Russian Federation, E-mail: vetrov@1system.ru*
[3]*Kharkov Air Force University, Kharkov, Ukraine, E-mail: misaylov@ukr.net*

ABSTRACT

Wide application of sodars for ecological needs in cities is restrained now generally due to their high acoustic nuisance.

Methods and principles of the antenna system construction for mono-static city sodar are considered from the position of meeting the requirements of acoustic ecology with respect to city area

Particular attention has been paid to the development of rational design of hybrid horn-reflector acoustic antenna with phased array of piezoelectric transducers. Thereto the computer simulation has been performed by means of 3-d antenna system FE model to determine its vibration characteristics.

We have considered the acoustic characteristics of up-to-date construction and sound-absorbing composite materials and have justified their selection on basis of the criterion of efficiency-cost.

To adapt to the horizontal wind the sodar receiving pattern it has been set wider than the radiation one. To this effect the diagram formation functions for receiving and radiation are separated between the phased array and the guide horn.

Reduction of far-out sidelobes to the level of -60 dB is achieved at the expense of additional acoustic enclosure, structurally related to the guide system of the hybrid acoustic horn-reflector antenna. The level of near-in sidelobes additionally reduced by forming aperture tapering for receiving and radiation modes.

Separation of the piezoelectric array with the functional basis is allowed to reject the antenna switch, to reduce the "dead" zone of the sodar and to improve the noise characteristics of the receiving channel.

The paper presents data on experimental verification the directing properties of the developed noise-protected sodar antenna.

1. FEATURES OF SODAR ANTENNAS OPERATION

The efficiency, innocence of used acoustic radiation, and small cost of sounding equipment have, however, an essential antipode – noise pollution originated from sodar working. It is necessary also to take into account surrounding noise affecting on sodar and restricting its efficiency. The complicating circumstance here consists in the use of the audible sonic range which is practically coincided with the auditory human sensitivity. This fact causes restriction of using sodar in cities and in populated areas at all. It is connected with the irritating effect on a man by emitted sounding parcels acting from non-working directions of a sodar antenna (along its far sidelobes, usually close to 90º in relation to the main lobe).

A level of side lobe suppression, as well as of own acoustic unwanted radiation, for modern monostatic sodar antennas usually averages -30..35 dB at the angle close to 90^0 with respect to the horizontal, according to [1]. For using in city it cannot be considered as sufficient because the parasitic acoustic radiation remains considerable and comparable by the level with a loud speech or shout, what is inadmissible according to sanitary codes and requirements of acoustic ecology [2] especially at night.

In our opinion, a reserve of this parameter improvement consists in the account of dynamic properties of the sodar acoustic antenna design as a mechanical system.

It is possible to single out four approaches in the direction of the problem solution:

- reduction of a value of the disturbing force ;
- increasing of walls damping properties;
- tuning out frequencies of the resonance;
- providing such a shape of the resonant fluctuations, which down to the limit is orthogonal to the disturbing effect.

2. SODAR ANTENNA MECHANICAL RESONANCES

Taking into account that the correction by the first item is connected with both the deterioration of the antenna qualitative indices, the increase of the walls damping properties is finite and usually realized at the maximum possible level, so the latter two items take on special significance. They were not taken into account till now when designing and developing acoustic antennas intended for sodar and the radioacoustic equipment.

The factors causing occurrence of mechanical resonances of a sodar antenna are connected with the pulse mode of its functioning.

The program of the computational research of mechanical resonances included the following stages:

1) calculation of the strained state at static loading;
2) computation of the natural vibrations spectrum and corresponding natural modes;
3) definition of possible resonant modes;
4) estimation of vibration amplitudes at the modes.

In order to solve the task, the finite-element method has been used [3]. The feature of this method is that the required unknown functions describing its strained state are defined only at some points of a solid body, at so-called nodes. After dividing into finite-elements, the task of these deviations as functions of spatial coordinates is replaced by the equivalent task of finding these function values at the finite number of solid elements, that is at nodes.

According to the results [4] of natural frequencies computation, for sodar antenna horn-reflector antenna, it turned out that the second natural form is multiple to the repetition rate of sounding parcels. Therefore, occurrence of the superresonant mode with the amplitude of not less than the static deflection amplitude is possible. Arising infrasonic the antenna oscillations at influence very negatively upon the cardiovascular human system and it can lead to development of hypertensive disease. Natural frequencies spectrum analysis close to the working frequency have shown that natural frequencies are situated very compactly. For example, at the working frequency equal to 2.6 kHz there are 38 natural frequencies close to it. Exact coincidence (at the most dangerous multiplicity equal to unit) with the working frequency of the antenna shows the frequency of natural fluctuations # 767 (figure 1) that results in occurrence of the resonant mode.

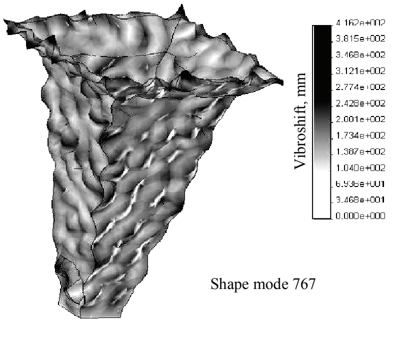

Figure 1. View of 767-th natural oscillation form of the sodar antenna directing system.

The proposed approach to studying the possible causes of spurious radiation occurrence for sodar antennas is based on the analysis of the natural frequencies spectrum and on the assessment of chances of excitation resonant operating modes for a given part of a design. Any sodar antenna design can be tested for the presence of resonant modes at its working frequency with the subsequent tuning out from them by changing mechanical parameters of the design. Estimation of absolute values of amplitudes for resonant oscillations with an error of about 20%, can be made by application of static loading from sound pressure upon the area of the radiating walls restricted by nodal curves. Calculation of their exact values is possible when carrying out the numerical research of the forced oscillation of the design subject to internal energy losses of oscillations.

For estimation of the acoustic antenna far sidelobes distortion caused by coincidence of emitted sound frequencies and frequencies of mechanical resonances in the antenna construction it is possible to apply, known electro-acoustic analog method. The antenna radiation pattern is represented as a sum of the horn direction diagram without mechanical oscillations of its case and the direction diagram of an acoustic radiation of a solid with external dimensions of the horn having surface mechanical motions like it is shown in figure 5.

The sodar horn antenna pattern with the unperturbed case is computed with electrodynamics methods taking into consideration that E-type electromagnetic waves correspond to sound tubes waves, and that H_{10} wave in E-plane horn creates the diagram in E-plane, in accordance to [5], with the help of its electric component – E_{00} wave. Acoustic radiation of the solid, can be considered as electromagnetic radiation of a hollow dielectric tube, whose diameter considerably exceeds a working wavelength. Such a dielectric antenna is practically undirected. Therefore the radiated power falling on walls of the basic sodar antenna horn during sounding acoustic parcels emitting, after partial sound absorption by wall material, is almost uniformly distributed in external space. Radiation created in such a way is similar to the evenly heated solid with the spatial distribution similar to Lambert's diagram. Calculations carried out on the basis of the proposed procedure show that acoustic radiation at angle of 90° to the axis of the basic acoustic horn, caused by the antenna mechanical resonance at the sound pressure upon internal walls about 100 dB is comparable to acoustic radiation in the same direction on the sidelobe of this antenna without mechanical resonance.

3. SODAR ANTENNA DESIGN

The special importance of the antenna system in the sodar chart results from its cost part in the total price of standard sodar assemblage. Thus, according to our price analysis of current sodar techniques, the price constituent of sodar antenna approaches a half of its overall system cost. Note should be taken that technical features of sodar in general and its noise protective properties in particular are determined by characteristics of the acoustic antenna system.

It is possible to improve significantly the value of the signal-to-noise at the output of the acoustic antenna by using piezoelectric acoustic transducers, instead of electromagnetic ones. Figure 2 shows the frequency responses which we obtained for piezoelectric transducer MPT-165, as well as the frequency dependence of urban daily noise [6]. In addition to the high values of efficiency and sensitivity, this transducer has another useful feature – its dead band coincides by frequency with the maximum of ambient noise.

Just this type of transducers we have chosen for construction the acoustic phased antenna array. Be guided by our experience in the development of acoustic phased arrays [7], we studied a group of 15 transducers and found that the phase differences do not exceed the permissible value of 12^0 for selected 10 specimens.

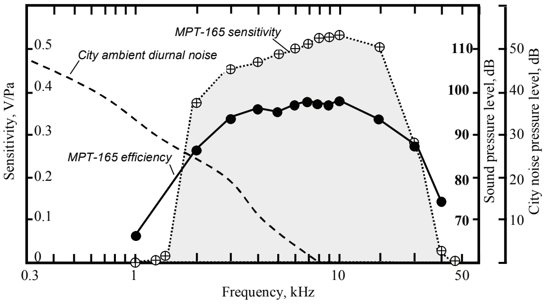

Figure 2. Capabilities of piezoelectric transducer MPT-165

The design of the developed acoustic hybrid antenna explains by its overall view in figure 3. The active phased array is placed in an upright position preventing horn piezoelectric transducers from ingress of water and different waste particles. Redirecting of the array radiation from the horizontal position to the vertical one is performed by a flat reflector mounted at the angle of 45^0 to the main optical axis of the array. There is mounted the diffraction cap with acoustic absorber along the perimeter of the antenna aperture. Horn directing system has inner acoustic absorber coating too to produce a tapered distribution of radiating acoustic intensity in the aperture. The directing system of the designed sodar antenna is constructively combined with external soundproof shell by the use of elastic antidrumming bridges. Such a double-walled construction of the antenna has improved its noise protection up to 30 dB. Mounting base provides tilt angle of the antenna up to 90^0 in order to work in an inclined position, and for maintenance.

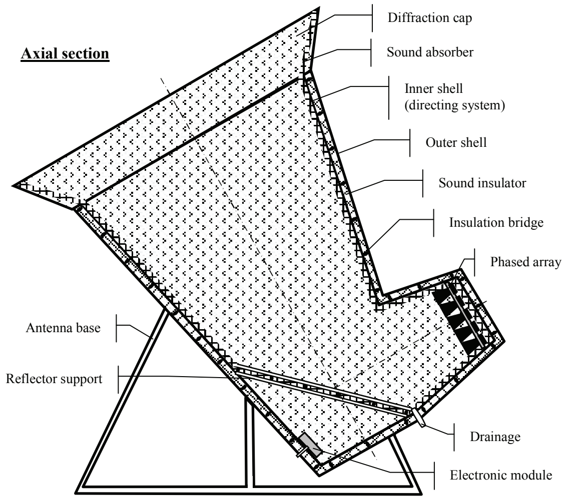

Figure 3. City sodar antenna construction

The placement of individual transducers in the array is illustrated by figure 4. Horn piezoelectric transducers (“a” ÷ “u”) operate in the mode of radiation acoustic parcels, and transducers (“v” ÷ “y”) are receiving elements and they operate in the microphone mode. Such a structure of the phased array ensures of different directivity patterns for radiation and reception, thereby it is minimized power losses of echo-signals due to wind influence at the scattering cross-section [8].

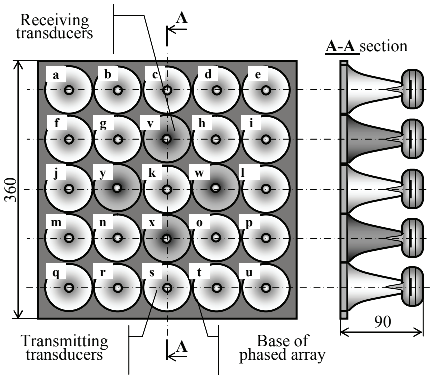

Figure 4. The principle of transceiving acoustic phased array construction.

Complex passive noise protection measures to the antenna includes the selection of construction materials such as Alucobest composite panels with high sound-insulation value, the choice of elements form, their thickness and methods of attachment which eliminate the resonant modes of the antenna construction. Impedance coating is made with “Isolon” sound-absorbing material. As a result, the developed acoustic antenna [9] insures the suppression of far-out sidelobes up to -70 dB. External view of developed experimental noise-protected acoustic antenna for a mono-static city sodar working at frequency of 3.0 kHz is shown in the figure 5. The resulting experimental and calculated radiation patterns of the designed antenna are shown in the figure 6.

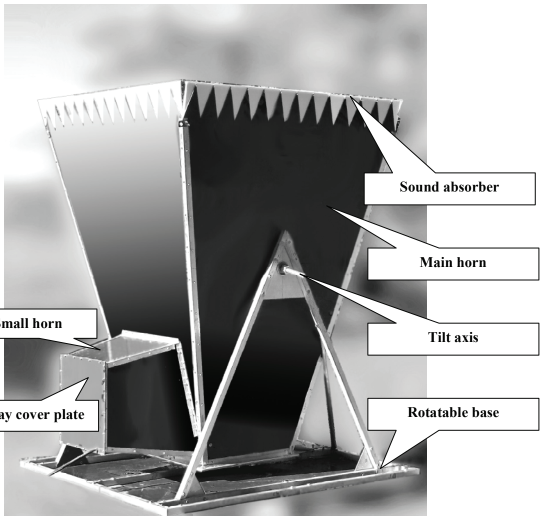

Figure 5. Appearance of the developed city sodar antenna.

In order to reduce the level of intra-system noise we have used the original scheme of the transmitter/receiver antenna array with the separation of piezoelectric transducers by the emission and reception of acoustic parcels. Circuitry from a traditional antenna switch on the acoustic receiver input it is retained the protection node against probable voltage overloads. Functionally important here is (used after preselecting), the summation four transducers output signals to achieve double increasing of the signal-to-noise ratio. These measures of noise suppression and protection for the designed SODAR antenna permit us to consider it as really noise-protected.

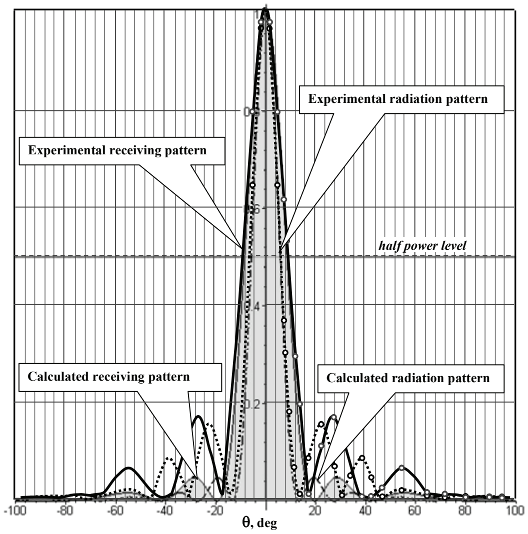

Figure 5. Directional diagrams of the developed acoustic antenna.

4. CONCLUSIONS

The main factor that limits the efficiency of any sodar is external acoustic noise and creating by working sodar the annoyance factor. This restriction removing requires, first and foremost, the development of special noise-protected acoustic antennas.

Usage of the hybrid type horn-reflector with transducers phased array sodar antenna system, with functional separation of acoustic piezoelectric transducers, equipped with inner sound-absorbing coating and the directing system which is constructively combined with external soundproof shell by the use of elastic antidrumming bridges, allows us to develop the effective sample of modern low-cost acoustic noise-protected acoustic antenna.

REFERENCES

1. Crescenti G.H., 1997: A Look Back on Two Decades of Doppler Sodar Comparison Studies, *Bull. of the Amer. Meteorol. Society*, Vol. 78, **4**, pp. 651-673.

2. Barry Truax, 1999: Handbook for Acoustic Ecology CD-ROM Edition. Cambridge Street Publishing, CSR-CDR 990

3. Moaveni S., 2008: Finite Element Analysis Theory and Application with ANSYS, Pearson, 868 p.

4. Butakova S.V., Martynenko G.Y., Smirnov M.M., Ulianov Y.N., 2004: Reduction of Spurious Sodar Antenna Radiation Basing on Structural Analysis of Resonance Modes, *Journal of the National Technical University "KhPI",***19**, pp. 33-60. (in Russian)

5. Butakova S.V. Using of the solution for a flat waveguide at the analysis of radiations for the open end of a rectangular waveguide, 2002: *Antenny,* Moscow,: IPRZhR, issue 12(**67**), pp. 48-54. (in Russian).

6. Krasnenko N.P., 2001: Acoustic sounding of the bound-ary atmospheric layer, Tomsk, "Vodoley", 278 p. (in Russian).

7. Shifrin Y.S., Ulianov Y.N., Maksimova N.G., 2008: Field statistics of antenna arrays of equipment for remote sensing of the atmosphere, *Proc. 14th Intl. Symp. Acoust. Rem. Sens.*, Denmark, P. 012037.

8. Bovsheverov V.M, Karykin G.A., 1981: To the Influence of Wind on Exactness of Determination of Structural Constant of Temperature by the Acoustic Sounding Method, *News of AS USSR. Physics of atmosphere and ocean,* v.17, **2**, pp. 205-207.

9. Shifrin Y. S., Ulianov Y. N., Vetrov V. I., Misaylov V.L., Noise-protected Antenna for a Pulse Acoustic Atmospheric Sounder, 2011: *Proc. of International Conference on Antenna Theory and Techniques,* , Kyiv, Ukraine, pp. 120-122.

Continuous and automatic measurement of atmospheric structures and aerosols optical properties with R-Man510 nitrogen Raman lidar

A. Bizard[1], P. Royer[1], L. Sauvage[1], M. Boquet[1], L. Thobois[1], M. Renaudier[1], B. Bennai[1]

[1] Leosphere, 16 Rue Jean Rostand, 91400 Orsay, France (abizard@leosphere.fr)

Introduction:

This ash component in the troposphere poses a variety of hazards to humans and machinery on the ground, as well as damage to aircraft that fly inadvertently through ash plumes. To mitigate such hazards, a combination of surface observations, satellite remote sensing, and aerosol dispersion model predictions are currently relied on. However, atmospheric clouds can obscure eruptions, and after initial transport and dispersion the volcanic plume will become too diffuse to be detectable using available satellite techniques.

Nitrogen Raman lidars R-Man510 (ground-based lidars) offer the opportunity to detect aerosol particle and retrieve independently particle extinction and backscatter coefficients contrary to Rayleigh-Mie lidars that require an assumption on aerosol type. The use of a cross-polarized channel gives additional information on aerosol depolarization ratio which enables the identification of aerosol type.

We will present here the first results obtained with this new commercial lidar system at Orsay (48°N, 2°E), FRANCE.

Instrumental set up:

A new compact and light nitrogen Raman lidar (R-Man510) has recently been developed by Leosphere company. This UV-lidar system is based on a low energy diode pumped Nd:YAG laser at 355 nm for elastic channel and 387 nm for Raman channel. Measurements are typically performed with a vertical resolution at 15 m and a temporal resolution between 30 seconds (for elastic channel) and 10 minutes (for Raman channel). The figure 1 shows the parallel-polarized channel at 355 nm, the cross-polarized channel at 355 nm and Nitrogen Raman channel at 387 nm.

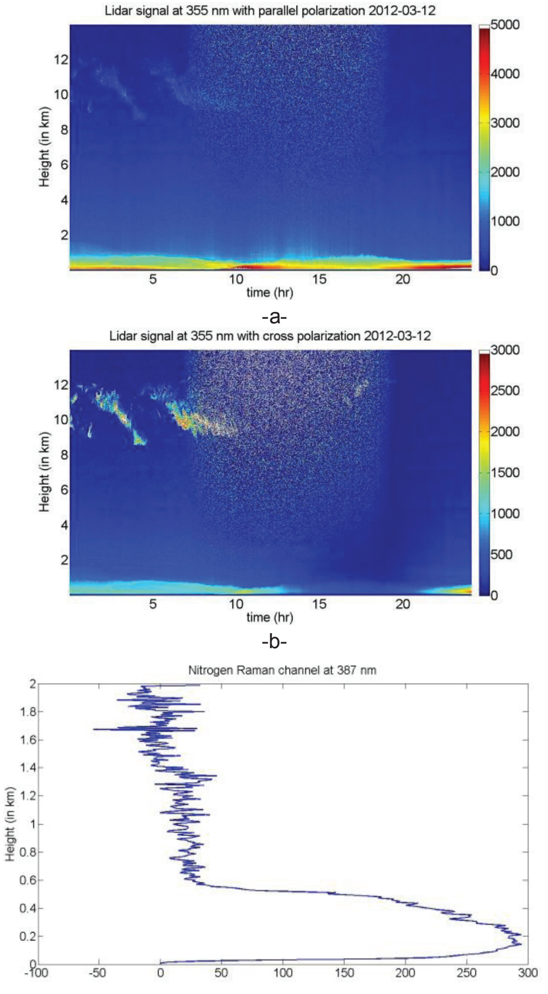

-a-

-b-

-c-

Figure 1: (a) parallel polarized channel at 355 nm, (b) cross polarized channel at 355 nm and (c) Nitrogen Raman profile at 387 nm

Table 1 presents a technical description of lidar systems R-MAN510.

TECHNICAL	
Laser source	Nd: Yag 355nm – diode pumped
Detection channels	-Parallel & cross polarized channel @ 355 nm -Nitrogen Raman channel @ 387 nm
Acquisition type	Analog and photon-counting on each channel
Power supply	100-240V AC/ 50-60 Hz
Electrical consumption	300W to 600W (in maximum heating mode)
Dimensions and weight	Dimensions (mm) : H1150 X L800 x W650 Weight(kg): 105kg

Table 1 : R-MAN510 technical spec

Data Processing:

The range-corrected signal Sk (corrected for the sky background, the solid angle and the overlap function) measured at wavelength λ_k and at altitude z with a vertically pointing lidar can be written under the form (Measures, 1984):

$$S_k(z) = K_k\beta_k(z)\exp\left\{-\int_0^z\left(\alpha_j^m(z')+\alpha_j^a(z')+\alpha_k^m(z')+\eta\alpha_j^a(z')\right)dz'\right\}$$

$$\text{with}\,\eta=(\lambda_k/\lambda_j)^{-a}$$

Using the three channels and lidar equation, an algorithm has been implemented to provide automatically both qualitative and quantitative information of the atmosphere.

In first, the planetary boundary layer (pbl) is retrieved with a 2D method. The gradient image of the elastic channel gives, with a new threshold method, an estimation of atmospheric boundary layer height and residual layer height. Figure 2 shows an example of final result of the pbl estimation.

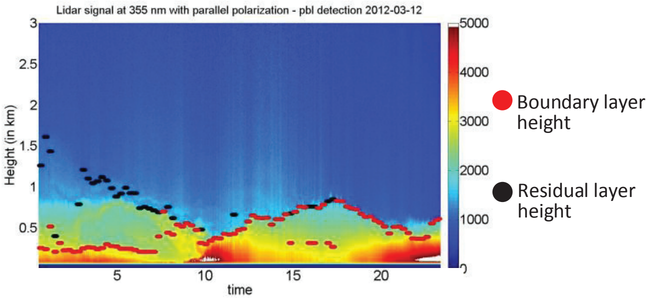

Figure 2: Pbl detection with 2D gradient method: 2012-03-12

The next step is to retrieve base and top of layer detected on elastic channel. The method is based on an automated gradient detection using attenuated backscatter ratio. The ratio of the peak signal to that of the layer base approximates the magnitude of particle backscattering at the altitudes of the peak signal. Because most clouds are considerably denser than aerosols at the same altitude, a preselected value for this ratio can distinguish these layers. Figure 3 shows an example of layer detection.

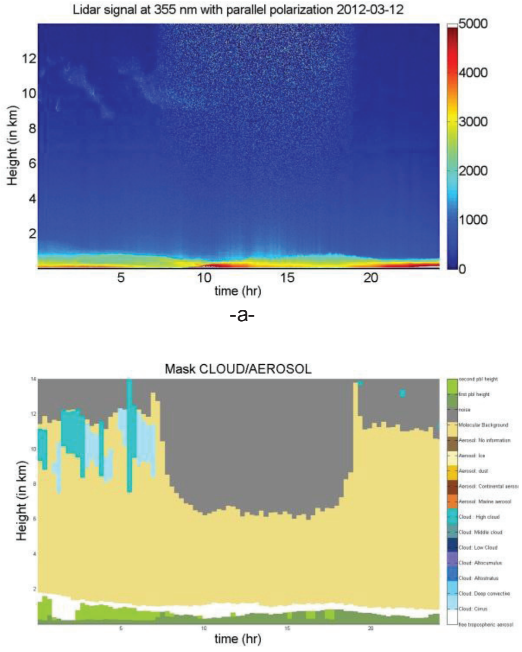

-a-

-b-

Figure 3: (a) parallel polarized channel at 355 nm, (b) Cloud & aerosol mask

In order to retrieve atmospheric parameters in layer detected previously (pbl, aerosol and cloud) and to optimize their classification, a mean value of the aerosol extinction-to-backscatter ratio in each layer detected, hereafter called the lidar ratio (LR), are evaluated using both the elastic and the Raman backscattered signals together. The LR is retrieved as a regularized solution of a first-kind Volterra integral equation. Figure 4 presents a Nitrogen Raman profile with Tikhonov regularization used is the automated algorithm.

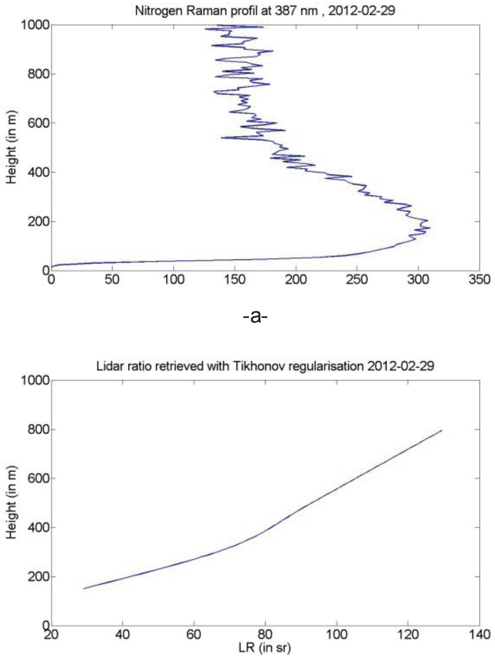

-a-

-b-

Figure 7: -a-: Nitrogen Raman profile and -b-, Lidar ratio retrieved by Tikhonov regularization

If the Raman signal is not available, an alternative approach has been developed to retrieve a mean value of LR. This dichotomous algorithm is based on the inversion of the elastic lidar signal with a klett method using AOD constraint. The layer must be located between two molecular areas. Finally if these two methods are not available, a look up table is used to assume a LR value.

Using elastic channel and LR value (retrieved previously), a profile of extinction and backscatter is determined with a klett inversion. Figure 5 shows a sample of extinction and backscatter images.

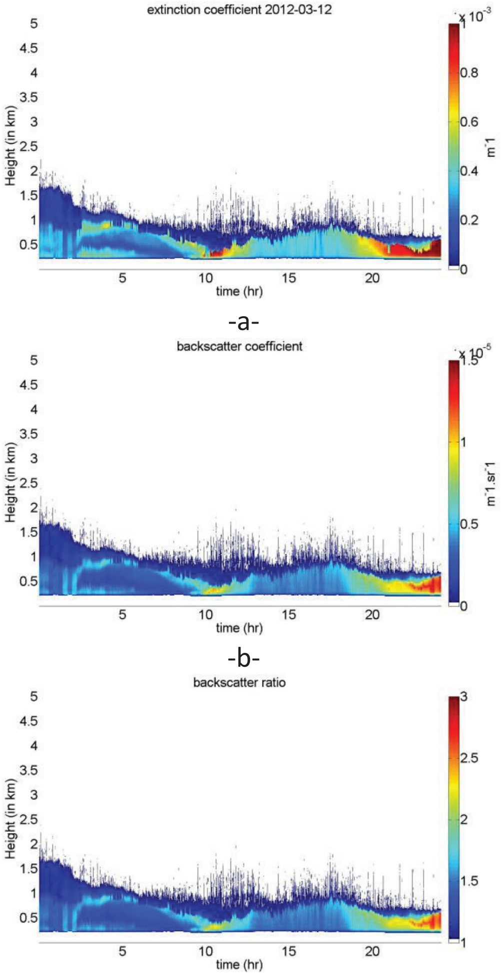

-a-

-b-

-c-

Figure 5: (a) Extinction, (b) backscatter and -c- backscatter ratio profiles in layers detected.

The last step is to determine the linear volume depolarization ratio (δv) and the linear particle depolarization ratio (δp). δv is retrieved using elastic channel (parallel and cross polarization) and calibration constant of the R-MAN510 (figure 6). δp is function of δv and backscatter ratio using the following equation:

$$\delta p = \frac{(1+\delta m).\delta v.R-(1+\delta v).\delta m}{(1+\delta m).R-(1+\delta v)}$$

with

$\delta m : depolarization\ ratio\ in\ molecular$

$R : backscatter\ ratio$

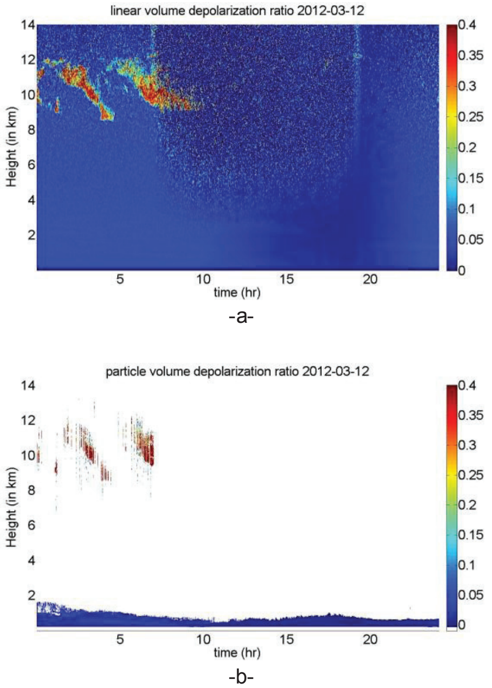

-a-

-b-

Figure 6: linear volume depolarization ratio and (b) linear particle depolarization ratio

LR information and linear depolarization ratio is a dataset to classify automatically the aerosol layer in 4 types (marine aerosol, continental pollution, dust and ice crystals). The cloud are classified in 5 types (deep convective, cirrus, altostratus, altocumulus and low cloud) using altitude of the top layer and optical depth (integrated extinction in cloud layer).

Conclusion:

The example of the eruption of the Eyjafjallajökull volcano that occurred on April-May 2010 has highlighted the interest of atmospheric lidars for the detection and assessment of physics properties in volcanic ashes.

The R-MAN510 contributes to fill in a lack of actual ground based measurements especially in aerosol detection and classification. Nitrogen Raman lidars is a technical that permits to retrieve independently extinction and backscatter coefficients in aerosol layer.

Helicopter downwash measured by continuous-wave Doppler lidars with agile beam steering

Mikael Sjöholm[1], **Nikolas Angelou**[1], **Per Hansen**[1], **Kasper Hjorth Hansen**[1], **Torben Mikkelsen**[1],
Steinar Haga[2], **Jon Arne Silgjerd**[2], **and Neil Starsmore**[3]
[1] *Department of Wind Energy, Section of Test and Measurements, Technical University of Denmark,*
Risø Campus, Frederiksborgvej 399, DK-4000 Roskilde, Denmark, http://www.dtu.dk
[2] *Automasjon og Data AS, Nikkelveien 14, N-4313 Sandnes, Norway, http://www.automasjon.no*
[3] *Starsmore Ltd, Blackwater Hollow, Rookley, P038 NL, United Kingdom, http://www.starsmore.co.uk*

Abstract

A ground-based remote sensing short-range WindScanner with agile beam steering based on a modified ZephIR continuous-wave wind lidar (LIght Detection And Ranging) and a double prism arrangement has recently been developed at the Department of Wind Energy at the DTU Risø campus. The WindScanner measures the line-of-sight component of the wind and by rapid steering of the line-of-sight and the focus position, all locations within a cone with a full top angle of 120° can be reached from about 8 meters out to some hundred meters depending on the range resolution needed. By using three such WindScanners, all three components of the wind can be retrieved.

Here, the first mean 2D turbulent wind fields measured in a horizontal and a vertical plane below a hovering search and rescue helicopter are presented. The line-of-sights of two synchronized WindScanners were scanned within the plane of interest. Since both line-of-sights always were inside the plane scanned, the influence of the wind component perpendicular to the plane was avoided. The results indicate that the flow field below a helicopter can be characterized remotely, which can support helicopter optimization regarding, for example, minimizing the risk to aircraft and personnel when operating in a search and rescue role.

The results from the application of the short-range WindScanner technology to the complex and turbulent helicopter downwash demonstrates the possibilities also within less demanding flows encountered within complex terrain and wind energy related research for which the WindScanner technology primarily has been developed.

1 Introduction

For a long time there has been a vision about rapid 3D measurements of turbulent flows in complex environments [1]. Now, a ground-based remote sensing short-range WindScanner with agile beam steering based on a modified ZephIR (manufactured by Natural Power, UK) coherent continuous-wave wind lidar (LIght Detection And Ranging) and a double prism arrangement has been developed at the Department of Wind Energy at the DTU Risø Campus in Denmark. The WindScanner operating at a wavelength of about 1.5 micrometer measures the line-averaged [2] line-of-sight component of the wind and by rapid steering of the line-of-sight and the focus position, all locations within a cone with a full top angle of 120° can be reached from about 8 meters out to some hundred meters depending on the range resolution needed. By using three such WindScanners, all three components of the wind can be retrieved without taking into account any assumptions about the flow.

In order to challenge the WindScanner by an extremely turbulent and complex flow, a proof-of-principle trial in the downwash flow below a search and rescue helicopter was undertaken. Here, we report about these first mean 2D complex turbulent wind field measurements that also is of interest for the aviation community since knowledge about the helicopter downwash structure under a search and rescue helicopter is crucial for safe rescue operations.

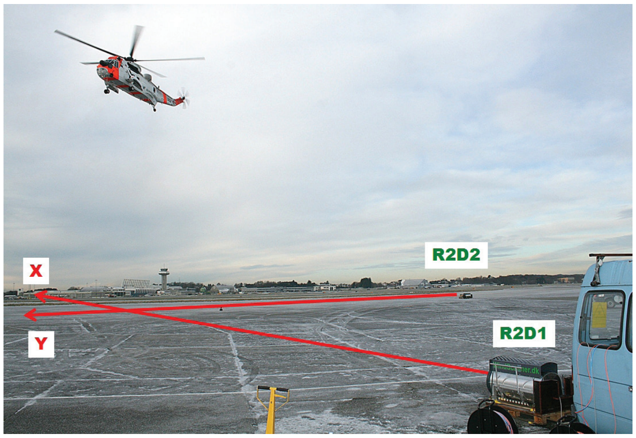

Figure 1: The experimental setup for scanning a horizontal plane below the helicopter.

2 The experimental setup

At the December 2011 helicopter downwash trial, two different configurations were used with the purpose of measuring the flow field in a horizontal plane close to the ground and in a vertical plane below a hovering search and rescue helicopter by two WindScanners. The particular short-range WindScanners used were the units called R2D1 and R2D2. Since only two WindScanners were available, the line-of-sights of the two WindScanners were made sure to be inside the planes scanned such that the influence of the wind component perpendicular to the plane of interest was avoided.

An overview of the setup used during the scanning in the horizontal plane is given in Fig. 1. In order to be able to measure as close to the ground as possible, a special mount with easily adjustable legs as seen in Fig. 1 was designed that allowed for the scanning beam to emanate from a height of about only 32 cm above the EUR-pallet on which it was standing. This means that the scanning horizontal plane was about 46 cm above ground. The EUR-pallet arrangement made the WindScanner easily movable by a lifting fork.

The horizontal scanning pattern was a spiral that spiraled outwards during 10 seconds to a radius of about 30 meters and then back to the center during 2 seconds along a line between the two WindScanners with the helicopter hovering at a height of 90 feet approximately above the origin of the coordinate system used. Almost along the return line in the scanning pattern a sonic anemometer sampling at 100 Hz was traversed while the averaged wind Doppler spectra were acquired at a rate of almost 400 Hz by each WindScanner.

For the scanning of the vertical plane, the location of the two WindScanners were almost the same as for the scanning of the horizontal plane. However, for the vertical plane measurements the scanners were turned such that they were directed towards each other with a distance of 78.8 meters in between and with the helicopter hovering at a height of 70 feet above the center of the line between the two WindScanners.

3 Analysis procedure

The first step in the data analysis is to synchronize the wind Doppler spectra obtained with the correct measurement positions in the atmosphere. Then, the spectra is divided by a noise background spectrum in order to flatten out the spectra such that structures in the spectra that are due to the measurement system itself becomes flat in the normalized spectra. In order to increase the apparent spectral signal-to-noise ratio, several spectra are averaged. In the method used, the spectra are sorted into grid cells with the size of 2 m by 2 m in the horizontal scan and 2 m by 0.5 m in the vertical scan. Subsequently, the median value in each frequency bin is calculated from all the spectra obtained in such a grid cell during a certain time resulting in a so-called median spectrum with less noise.

The wind speed is given by the Doppler shift frequency which is straightforward to calculate in the case of a spectrum corresponding to a constant steady wind speed with low turbulence and good signal-to-noise ratio which means that there is a single narrow peak and the location of that peak corresponds to the velocity that is to be retrieved. However, in a turbulent flow below a helicopter the Doppler peak broadens and it becomes more challenging to find the corresponding mean wind speed during the sampling period and therefore a frequency estimation procedure based on a Gaussian-fit is used.

Based on the two simultaneously measured line-of-sight wind speeds, the combined 2D wind vector can be retrieved as long as the two line-of-sights are not coinciding.

4 The flow field in a horizontal plane close to ground

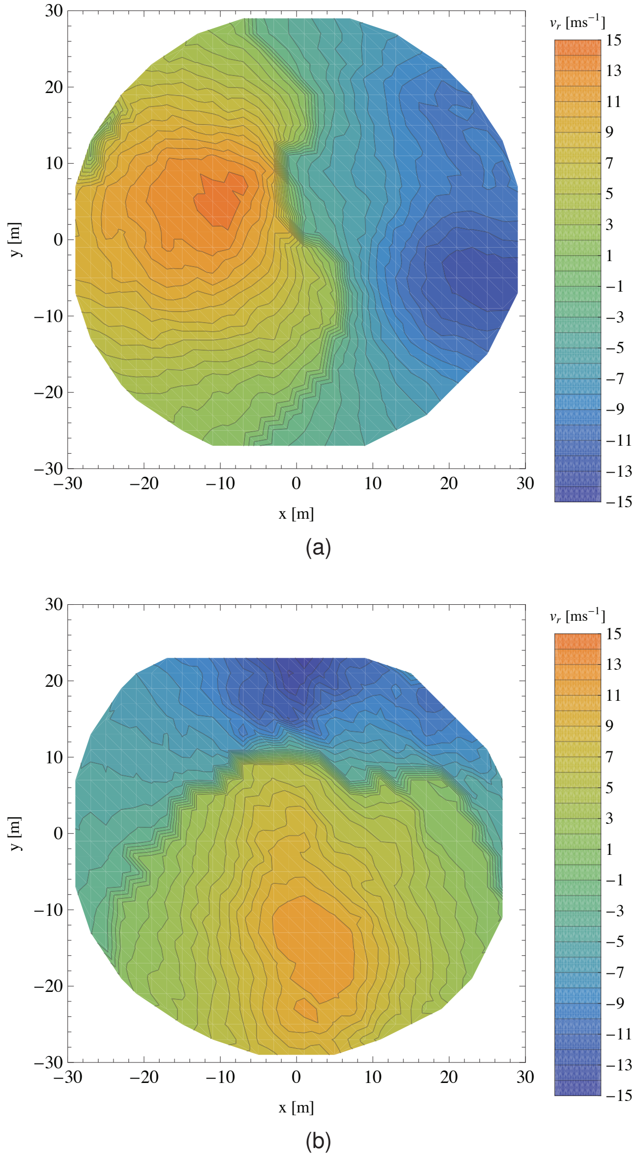

(a)

(b)

Figure 2: The 10-minute average line-of-sight wind component measured by (a) the R2D1 WindScanner and (b) the R2D2 WindScanner in a horizontal plane close to ground.

The 10-minute average line-of-sight wind component measured by the R2D1 WindScanner in a horizontal plane about 46 cm above ground in the time interval 13:01-13:12 on Wednesday 2011-12-07 while the helicopter was hovering at a height of 90 feet is displayed in Fig. 2a. The R2D1 WindScanner was placed at x = -60 m and y = 0 m which explains why the sampled component of the wind vector in the left part of Fig. 2a is positive meaning that the flow away from the helicopter is directed towards the WindScanner and in the right part the flow is away from the WindScanner resulting in a negative wind speed component measured by the R2D1 WindScanner.

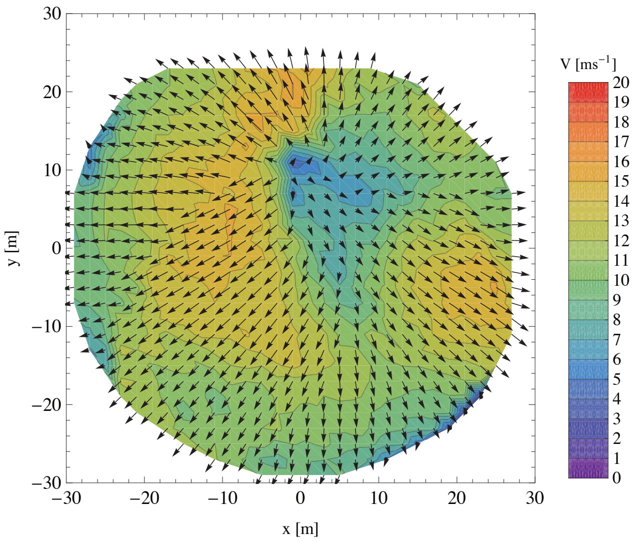

Figure 3: The retrieved 2D wind field in a horizontal plane close to ground.

The corresponding average of the line-of-sight wind component measured by the R2D2 WindScanner placed at x = 0 m and y = -50 m is displayed in Fig. 2b. It is a similar pattern as in Fig. 2a except that it is, as expected, turned 90°

The resulting combined 2D flow field in the horizontal plane is presented in Fig. 3 where it clearly can be seen that it emanates from a location slightly above and to the right of the center of the plot where the helicopter seems to have been located. The measured flow field exhibit, as expected, a shape similar to a doughnut with some complex structures and maximum speeds at about some 15 meters from the center of the calm area below the helicopter.

5 The flow field in a vertical plane below the helicopter

The 9-minute average line-of-sight wind component measured by the R2D1 WindScanner in a vertical plane below the helicopter in the time interval 16:50-17:00 on Wednesday 2011-12-07 while the helicopter was hovering at a height of 70 feet can be

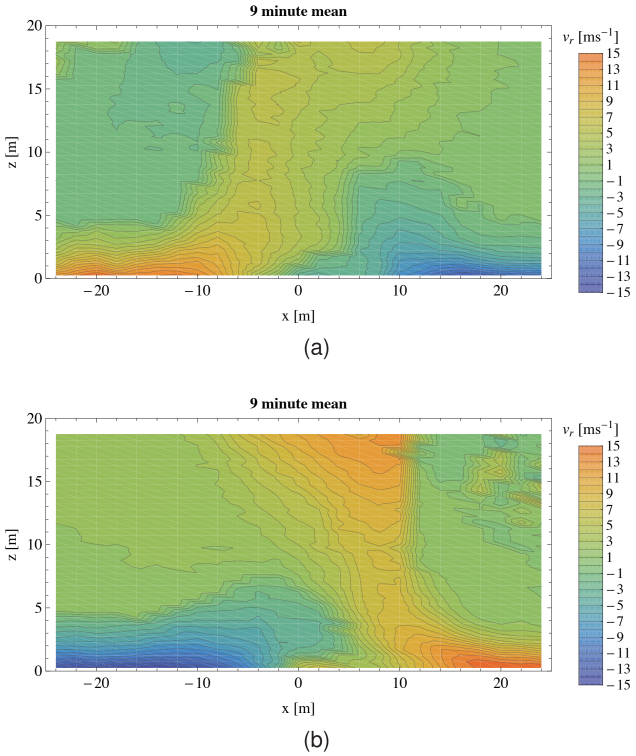

(a)

(b)

Figure 4: The 9-minute average line-of-sight wind component measured (a) by the R2D1 WindScanner and (b) by the R2D2 WindScanner in a vertical plane below the helicopter.

seen in Fig. 4a. The center of the scanner head of the R2D1 Windscanner was placed at x = -39.4 m and z = 0 m which explains why the sampled component of the wind vector in the lower left part of Fig. 4a is positive, since the flow away from the helicopter hovering above approximatively x = 0 m is directed towards the R2D1 WindScanner in that region whereas in the right part the flow is away from the R2D1 WindScanner giving a negative wind speed component measured by the R2D1 WindScanner.

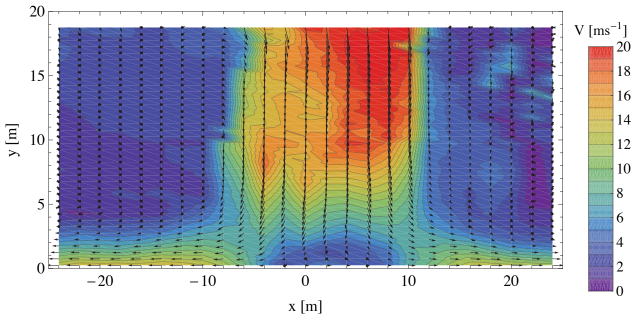

Figure 5: The retrieved 2D wind field in a vertical plane below the helicopter.

The corresponding average of the line-of-sight wind component measured by the R2D2 WindScanner placed at x = 39.4 m and z = 0 m is displayed in Fig. 4b and the resulting combined vertical 2D flow field is presented in Fig. 5. It can clearly be seen that the mean flow below the rotor is directed downwards and confined within a radius of about 10 m and that the flow deflects outwards as it approaches the ground. The helicopter location seems to be slightly off-centered in the positive x-direction.

6 Discussion and Conclusions

The particular results here presented indicate that the complex and turbulent helicopter downwash flow field below a helicopter can be characterized remotely by a short-range WindScanner. This suggests that the WindScanner technology can support helicopter optimization regarding, for example, minimizing the risk to aircraft and personnel when operating in a search and rescue role. Furthermore, it can be concluded that the WindScanner technology advances the possibilities of studying flows encountered within complex terrain and wind energy related research for which the WindScanner technology primarily has been developed.

Acknowledgments

The authors gratefully acknowledge the financial support from the Danish Agency for Science, Technology and Innovation through grant no. 2136-08-0022 for the Danish research infrastructure facility WindScanner.dk (http://www.windscanner.dk).

References

[1] T. Mikkelsen, J. Mann, M. Courtney, and M. Sjöholm. Windscanner: 3-d wind and turbulence measurements from three steerable doppler lidars. In *IOP Conference Series: Earth and Environmental Science*, pages 148–156. ISARS, June 2008.

[2] N. Angelou, J. Mann, M. Sjöholm, and M. Courtney. Direct measurement of the spectral transfer function of a laser based anemometer. *Rev. Sci. Instrum.*, 83(3):033111, 2012.

THE NOISE PART OF SODAR SIGNAL-TO-NOISE

Stuart Bradley[1]

[1]*Physics Department, University of Auckland, Private Bag 92019, Auckland, New Zealand,*
s.bradley@auckland.ac.nz
CIRES Senior Fellow, NOAA and Colorado University, Boulder, Colorado, USA

ABSTRACT

There are really only two basic limitations to the success of a remote sensing method: non-uniqueness of the relationship between sensed variables and required variables; and noise which competes with the signal. For sodars, the relationship between Doppler shift and radial wind component is very direct, and the main limitation is therefore competing background noise. Surprisingly, not a lot is known about the physics of the background noise for sodars. We show that microphone self-noise can be significant. Nevertheless, the fact that any observations with a sodar will show that noise is variable with location and time of day shows that much of the noise is external acoustic noise. Acoustic baffles are quite successful in making the receiver insensitive to local noise generation. The remaining source of noise for sodars is aero-acoustic noise generated by the pressure fluctuations arising from turbulence. Such noise is known to be generated due to wind flow over the rim of the baffles, and is generally the main limitation on sodars measuring in high wind speed conditions. However, aero-acoustic noise is also generated in the free air, although this has not been studied in relation to sodar noise. We develop the theory for background noise, and discuss pathways to improvement of sodar performance through reduction in background noise.

1. SELF-NOISE AND EXTERNAL NOISE

Self-noise refers to random electronic and acoustic noise generated in the receiver. It can be distinguished from external noise either by doing measurements in an anechoic chamber, or by comparing the spectral coherence of two co-located identical receivers. For a phased array system, spectral coherence tests could be completed on the microphone elements in two halves of the array.

A typical sound intensity at a sodar receiver is 10^{-13} W m^{-2} for sound from 100m. The acoustic impedance of air is about Z= 400 N s m^{-3} so the acoustic pressure is about $(400 \times 10^{-13})^{1/2} = 6$ μPa (equivalent to -10dB-SPL). For example, one type of microphone has a sensitivity of 150 mV/Pa, producing an output voltage of 0.9 μV from 100m. The self-noise for this microphone is (dB-SPL A-weighted) 8 dBA, or (20 μPa) $10^{8/20}$ = 50 μPa. The self-noise voltage is (150 mV/Pa)(50 μPa) = 7.5 μVrms, or 8 times the signal level. However, the noise is distributed quite flatly across 10 kHz or more bandwidth. For an analysis bandwidth of, say, 200 Hz, the self-noise will be 0.15 μVrms or less, giving a 100 m SNR of 6 in amplitude, or 15 dB. This signal also needs amplification. A typical preamplifier amplifier and associated input resistors will contribute a similar noise level to that from the microphone. It is difficult to reduce self-noise significantly without a lot of expense. This level also means that multiple microphones or antenna gain needs to be employed as well as, generally, spectral averaging over a number of profiles.

Since the useful range of a sodar varies from day to day, it is clear that much of the background noise is external and broad band. Reduction, to acceptable levels, of locally-generated noise from sources such as traffic and trees is possible through acoustic baffles. The remaining source of noise is aero-acoustic i.e. generated from the air-flow and turbulence. This has two components: that generated from flow over surfaces (the acoustic baffles); and that generated by pressure fluctuations from the turbulence at all heights.

2. SPECTRAL COHERENCE

The coherence between two signals $x(t)$ and $y(t)$ is defined by

$$C_{xy} = \frac{\left|P_{xy}\right|^2}{P_{xx}P_{yy}}, \tag{1}$$

where P_{xy} is the cross-spectral density, and P_{xx} and P_{yy} the auto-spectral density of x and y respectively. The coherence function estimates the extent to which $y(t)$ may be predicted from $x(t)$, or the extent of common input into x and y at each frequency.

Two independent random signals distributed as $N(0,1)$ have the coherence shown in Fig. 1. The coherence is insensitive to the overall amplitude or power of the signals and also to the noise variance. As expected, the coherence of two such signals is spectrally flat. Although the mean of the product of two independent random series tends to zero, the power spectrum is not zero, and the coherence tends to a value of κ=0.174

(established here by simulation, since product-normal distribution does not appear to have analytic moments).

Also shown in Fig. 1 is the average coherence between the outputs of all pairs of rows of a new 16-row phased array receiver, measured in an anechoic chamber (average over 120 pairs). The receiver amplifiers have a band-pass filter around 4 kHz which will reduce reception of external signals below 3 kHz, but shows some correlated external signals from 3 kHz to 5 kHz. There is also low frequency external noise.

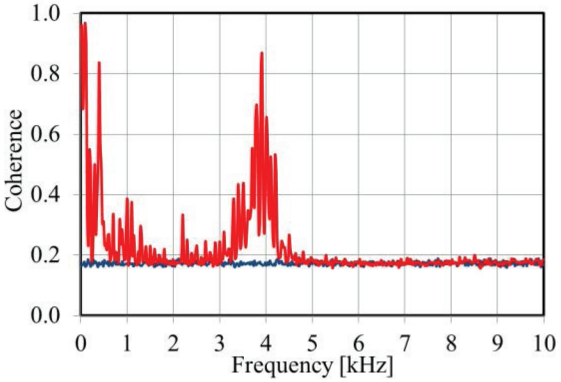

Figure 1. Self-noise of signals in pairs of rows of a phased array receiver (red), compared with the coherence for two independent $N(0,1)$ noise sources (blue).

For similar co-located receivers we can write for the time series

$$\begin{aligned} x(t) &= (1-\alpha)p(t) + \alpha e(t) \\ y(t) &= (1-\alpha)q(t) + \alpha e(t) \end{aligned}, \qquad (2)$$

where p and q are self-noise time series, and e is a common external random noise time series. It is assumed that p and q have the same power and statistical properties. Then

$$\begin{aligned} P_{xx} &= (1-\alpha)^2 P_{pp} + 2\alpha(1-\alpha)P_{pe} + \alpha^2 P_{ee} \\ P_{yy} &= (1-\alpha)^2 P_{qq} + 2\alpha(1-\alpha)P_{qe} + \alpha^2 P_{ee} \\ P_{xy} &= (1-\alpha)^2 P_{pq} + \alpha(1-\alpha)\left(P_{pe} + P_{qe}\right) + \alpha^2 P_{ee} \end{aligned} \qquad (3)$$

and, assuming $P_{pp}=P_{qq}=P_{ee}$ and $P_{pe}=P_{qe}=\kappa^{1/2}P_{ee}$,

$$C_{xy} = \frac{\left[(1-\alpha)^2 \kappa^{1/2} + 2\alpha(1-\alpha)\kappa^{1/2} + \alpha^2\right]^2}{\left[(1-\alpha)^2 + 2\alpha(1-\alpha)\kappa^{1/2} + \alpha^2\right]^2} \qquad (4)$$

or

$$\alpha = \frac{C_{xy}^{1/2} - \left[C_{xy} - \left(2C_{xy}^{1/2} - 1\right)\dfrac{C_{xy}^{1/2} - \kappa^{1/2}}{1-\kappa^{1/2}}\right]^{1/2}}{2C_{xy}^{1/2} - 1} \qquad (5)$$

When $\alpha=1$ (no self-noise), $C_{xy} = 1$, and when $\alpha=0$ (no external-noise), $C_{xy} = \kappa$, as expected. This gives us a scaling from coherence to fraction α of external noise.

In an operational, field, situation, coherence is extremely sensitive to Doppler shift, dropping to 0.4 for two pure sine waves 5 Hz apart when the center frequency is 4500 Hz. However, all rows in a phased array receiver will receive the same audio inputs, so Doppler shift should not affect the degree of coherence. The result, in terms of correlated signal fraction α, of data from a field trial, is shown in Fig. 2. Only three heights, or time delays, are shown. Above 6 kHz self-noise ($\alpha = 0$) dominates. There are a number of obvious non-random external noise sources at frequencies below 6 kHz, with troughs representing more broad-band 'pink' noise. Both types of external noise source are essentially unvarying with time (the same for all heights) and not related to the sodar transmission at 4.5 kHz. However, near the transmitted frequency there is a strong correlated peak at 64-100 m, which decreases at 134-168m, and is smaller still at 202-236 m. This is because the echo signal from the transmission is increasingly a smaller fraction of the common background as time increases since transmission. Around 70% of the recorded signal from 80 m height is coming from echo signals in this case.

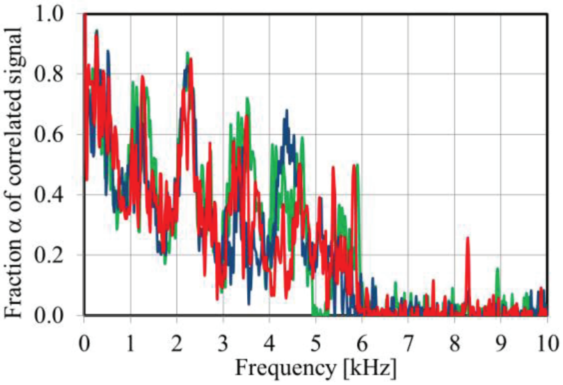

Figure 2. Correlated signal fraction averaged over all pairs of receiver rows with time delays corresponding to 64-100 m (green), 134-168 m (blue), and 202-236 m (red).

The sources of the non-random external signals are not known, mostly because they fall well outside the band of interest for measuring Doppler shift with this sodar receiver, and so have not been considered previously. It is likely they originate from test and sampling equipment such as a PC.

The external signal fraction α is plotted vs height (or time delay) in Fig. 3 for six frequency bands. Except for the band around the transmitted frequency, α is constant (although with a large variance in some cases).

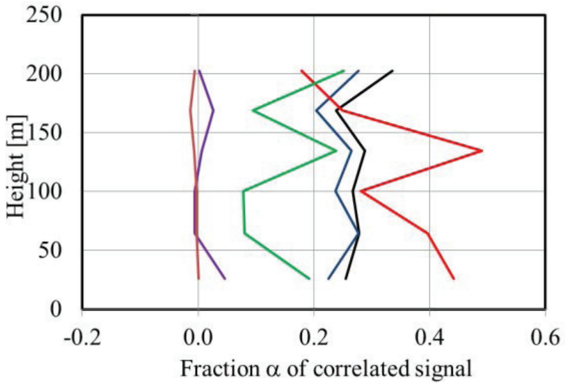

Figure 3. Correlated signal fraction averaged over all pairs of receiver rows vs time delay and for frequency bands centered on 1.8 (black), 2.8 (blue), 4.3 (red), 5.0 (green), 6.4 (purple) and 9.4 kHz (brown).

The mean value of α is shown vs frequency in Fig. 4. This noise appears to depend on 1/*f*.

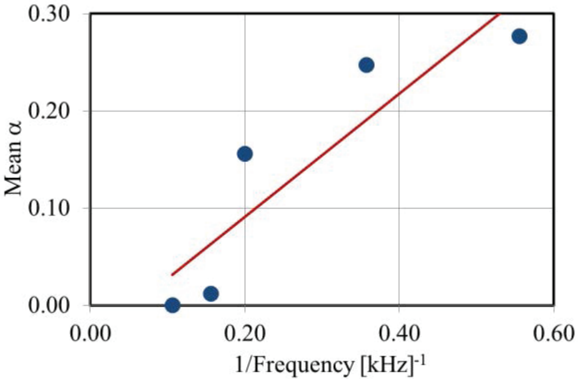

Figure 4. Mean correlated signal fraction vs 1/Frequency, and linear regression.

3. DIRECTIONALITY OF NOISE

It is generally thought that most acoustic background noise for sodars comes from nearby sources close to the ground. This can be checked by considering the directionality of the coherent noise. For this, we combine 2 sets of 8 microphones into two co-located phased arrays. The microphone spacing is 30 mm, giving the beam patterns in Fig. 5 at 4.5 kHz, for the array tilted at 45° and for 5 steering directions. The central half-beam width is about 8°. Spectra are shown in Fig. 6 for elevation angles of 22.5°, 45°, and 67.5°. The reduction in the amplitude of the echo signal with height is clear. But at greater elevation angles the other external noise sources increase in amplitude. This may be partly an effect of the acoustic shielding around the array, and partly due to the fact that we have not included data during the arrival of the direct signal at the array, which means that data from the lowest 26 m is missing. The lowest elevation in Fig. 6 points at 18 m above the transmitter, so only 1/3 of the background noise will appear in spectral plot for the lowest elevation angle.

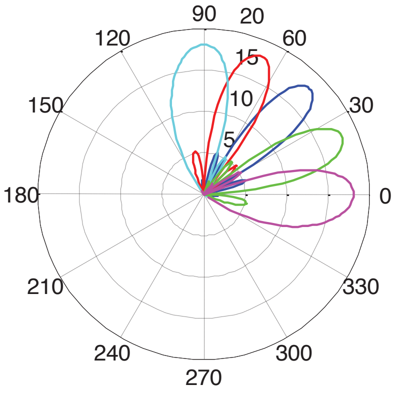

Figure 5. Polar patterns for 5 selected beam steering directions of 8-element arrays. The radial scale is in dB.

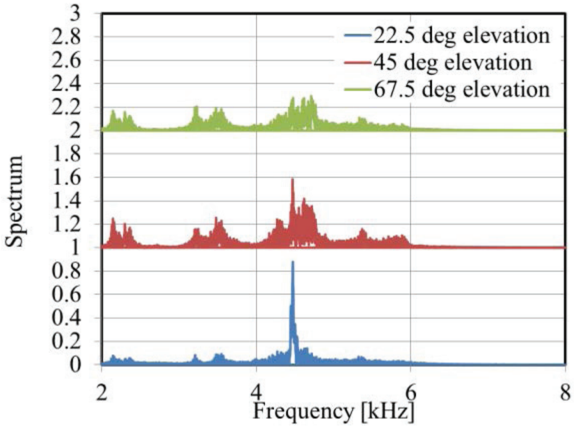

Figure 6. Spectra for the entire profile with beam steering to 22.5°, 45°, and 67.5° elevation. The 45° and 67.5° spectra have been offset for clarity.

The coherences for different beam pointing directions are compared in Fig. 7. There is a large spike at 9 KHz, twice the transmitted frequency, indicating the presence of a second harmonic, most likely through the input preamplifier being driven into a nonlinear region by input overload. There is a lot of detail worthy of interpretation in this plot. The low frequency 0-1 kHz peak and the random noise above 6 kHz are common to all directions. The input just above 1 kHz is dominantly from horizontally and not coming at all from above, and the 1/*f* noise signature has completely gone for noise coming in from above.

It is also possible to compare the array outputs when steered in two different directions. The coherence is then a measure of what common signals come in at both directions. Figure 8 shows a comparison between the 45° and the 67.5° elevations.

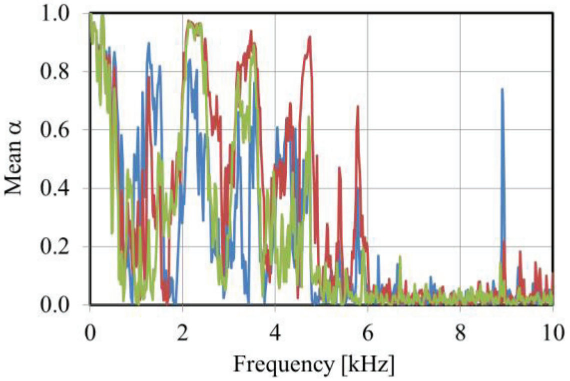

Figure 7. Coherence between two sub-arrays, each of 8 rows of microphones, with beam pointing elevation angles of 22.5° (blue), 45° (red), and 67.5° (green).

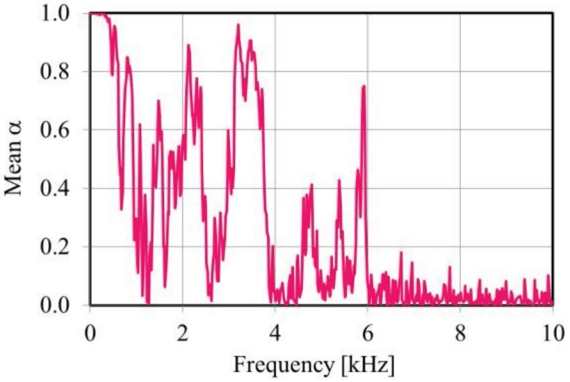

Figure 8. Coherence between two 16-element arrays outputs, steered in two directions (at 45° elevation and at 67.5° elevation).

Apart from the peak around 4.5 kHz, the origin of none of these correlated and persistent signals is known. The peak near 6 kHz is particularly sharp, and warrants further investigation.

4. CONCLUSIONS

Both sodars and lidars are challenged by background noise. This noise is a combination of self-noise and external noise. The external noise can be random or systematic.

In this work we have attempted to identify and separate the self-noise and external sources. This is done by using two or more collocated and identical microphones, which detect the same external noise but contribute independent self-noise. We have developed a methodology for finding the fraction of uncorrelated noise in a multi-microphone system (which includes all sodars).

For the particular system we used in this study, the self-noise was not dominant. Instead, a number of external sources of unknown origin were present. These were generally outside of the frequency band of interest but, being unidentified, could as easily have been close to the transmission frequency and have caused problems. The external noise between these spectral peaks followed a 1/*f* frequency dependence and was not related to the transmitted sodar pulse.

Because we used a 16-row array of microphones, it was also possible to look at the directionality of the external noise. There was a lot of structure in this, most of which has not yet been analyzed. However, it is evident that some of the unidentified large spectral peaks in the external noise come from sources near the ground, whereas other peaks seem ubiquitous. The 1/*f* behavior is not found to be characteristic of external noise originating from above: this is more flat in frequency content.

The suggestion arising from this work is that multiple microphone systems lend themselves to identification of both the nature and the directional properties of the noise which competes with sodar signals. It may be useful for new sodar systems to include the facility for such analysis so that, for example, beam orientation, can be dynamically modified to optimize signal-to-noise ratio.

ACKNOWLEDGMENTS

This work was completed under a CIRES Senior Fellowship at NOAA and Colorado University. The author is grateful for the opportunity and collegiality this has provided.

Session 11 – Oral Presentations

LIDAR MEASUREMENT ACCURACY UNDER COMPLEX WIND FLOW IN USE FOR WIND FARM PROJECTS

Matthieu Boquet[1], Mehdi Machta[1]

[1]*LEOSPHERE, 76 rue Monceau, 75008 Paris, France,mboquet@leosphere.fr*

ABSTRACT

Understanding the wind resource at a prospective project site has long been considered a critical step in the wind farm development process, particularly where high variations in the topography and roughness of the site can lead to uncertain local wind regimes.

The use of remote sensors is one such approach developed by wind experts to reduce project uncertainties related to the wind speed estimation at turbines hub height and over the entire site area.

The application of remote sensor wind data is however conditioned by a detail assessment of error and uncertainty in the instrument measurements, in order to get a quantitative benefit from them.

1. ASSESSING THE WIND RESOURCE

The future production of a wind farm depends on the wind resource across the site and over project life, and on the performance of the turbines array.

Determining the future production (mean value and the uncertainty on this value) drives the financing of the project. Indeed, the better the analysis (i.e. the lower the uncertainty) the more attractive the financial terms bank institutes are able to offer.

In addition to know-how, theories, models and accumulated experiences, the increase of measurements in time and space is one key recommended methodology by wind energy experts and wind farm financing institutes in order to reduce the uncertainty in the assessment of the wind resource.

Remote sensors are gaining attraction to resolve this demand because they can measure up to and above the wind turbine hub height, and because they are portable and can therefore be easily moved to measure at several locations to assess the spatial variation of the wind over the site.

In that sense, they allow a more accurate and secure assessment of the wind resource at the site of interest...

2. REQUIREMENTS ON REMOTE SENSORS

…A remote sensor allows a more accurate and secure assessment of the wind resource only if the remote sensor provides accurate wind data with a high level of confidence, providing at least the same performance than traditional cup anemometry, considered as the reference wind measurement instrument in the wind energy industry.

Measurement campaigns, with inter-comparison between different instrument types, have shown that the estimated uncertainty of most lidars meets these expectations on terrains of relatively simple topography and flow.

Indeed, to enhance the widespread of lidar technology, the previous statement should also be true on terrains where wind regimes are more complicated, especially where topographic variations, roughness, canopy height, high turbulence intensities and high wind shear and veer can affect the remote sensor accuracy.

Sources of measurement bias and uncertainty can be related to the technology itself but also to specific atmospheric conditions. As a matter of fact, the accuracy of a remote sensor technology needs to be assessed according to the environmental parameters in order to ensure that the measurement accuracy will not differ from a validation test site to the application site where is wind resource is prospected.

Therefore a high number of on-site studies and inter-comparisons with IEC-compliant cups in a variety of meteorological and topographical conditions can afford the possibility to make an empirical analysis of the remote sensor technology accuracy and quantify its uncertainties.

3. STATISCAL APPROACH

Knowing the device technology, all potentially influential parameters can be listed (according to knowledge, literature, experience, etc.). For example, wind shear, wind veer, turbulence intensity, atmospheric stability, rain, aerosol concentration, ambient noise… could influence the remote sensor measurement accuracy.

These parameters need to be measured during the accuracy test and the relationship between wind speed deviations (between the remote sensor and the calibrated cup) and the parameters are assessed using a statistical classifier. For example a commonly used classifier for such equivalent studies is the multi-linear regression.

We propose to apply the following methodology:

- One classifier is built per learning data set using a statistical methodology. Here a decision-tree bag has been used:

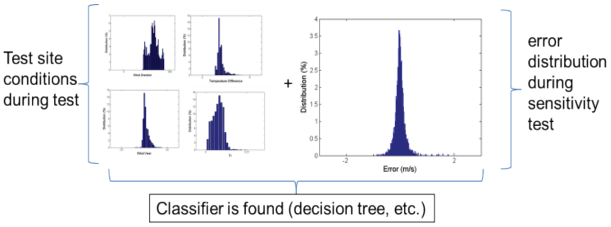

- One data set of variables is built following the probability distributions defined for every variable and thus can be considered representative for most sites of application. This general data set is applied to the classifier, which gives in output the corresponding error distribution of the remote sensor:

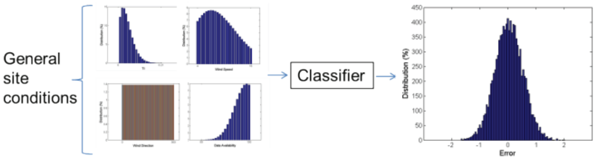

To validate the building method of the classifier, it is required that the classifiers found for various learning data sets give similar remote sensor error distribution with the same general data loaded into theses classifiers. Thus, the obtained error distribution can give an estimation of the remote sensor mean bias and uncertainty.

Some cautions must be taken in applying this methodology:

- The classifier needs to take into account dependency between variables.
- It determines the most influential parameters on the deviations in the data set.
- Attention must be paid to variables known to be influential which are not being measured during the test, or which range of values is not significant enough.
- Parameter variations on site of application could be also loaded as input to the classifier, to give the remote error distribution for the specific conditions of the site of application.

Below is an application on WINDCUBE™ v2 lidar data set, with a classifier being a decision tree bag.

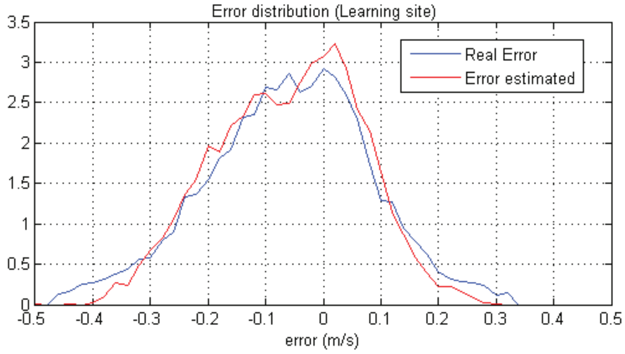

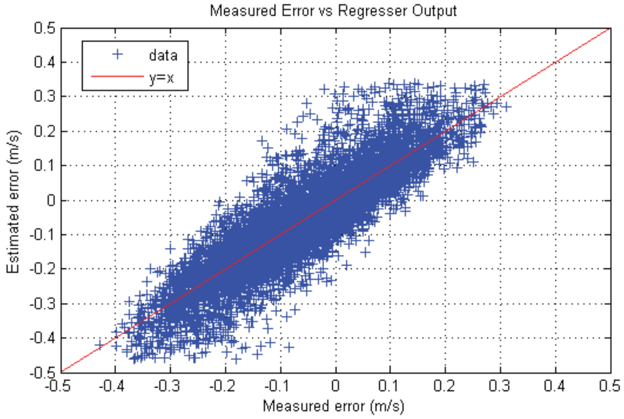

It estimates system error based on atmospheric and instrumental parameters. The classifier predicts the instrument error. Below, classifiers have been found for four learning data sets, and a general data set has been loaded into them:

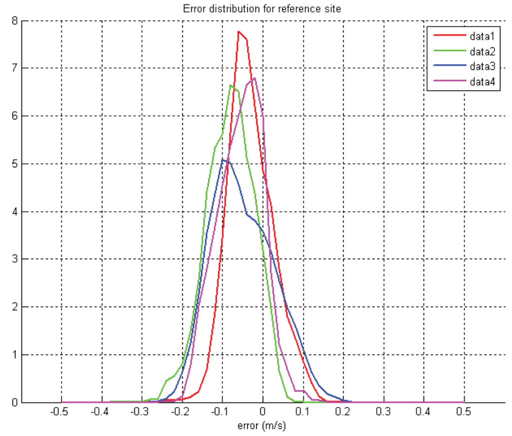

Accuracy is defined as the mean error and is here found to be ~0.05m/s. Uncertainty is defined as the standard deviation of the error and is here found to be lower than 0.2m/s. Results are coherent with the validations against met masts.

4. COMPLEX FLOW CHALLENGE

4.1 Removing the flow homogeneity assumption

Complex flows challenge remote sensors accuracy. Indeed all mono-static remote sensors measure Line of Sight (LoS, or radial) wind velocities along at least 3 beam axis. The LoS wind speeds are then converted to horizontal and vertical wind speeds using the flow homogeneity assumption (same wind speed for all beams at one altitude).

Various studies have shown that the variation of flow inclination cross the remote sensor beams is the main source of bias during the wind speed conversion. Because the WINDCUBE™ lidar provide accurate raw data (LoS velocities) even in complex terrain, the problem resides mainly in the conversion from raw data to horizontal wind speed using the flow homogeneity assumption. Therefore research has been focused on getting rid of the flow homogeneity assumption. It has led to a innovative wind measurement process, using a Flow Complexity Recognition FCR™ algorithm for WINDCUBE™ v2. The FCR™ mode differ from the normal mode in the way it processes the entire vertical profile of wind speed at once using all available LoS wind speeds, including those measured by the vertical beam, and which constraint the wind speed values corresponding to the current flow complexity characteristics:

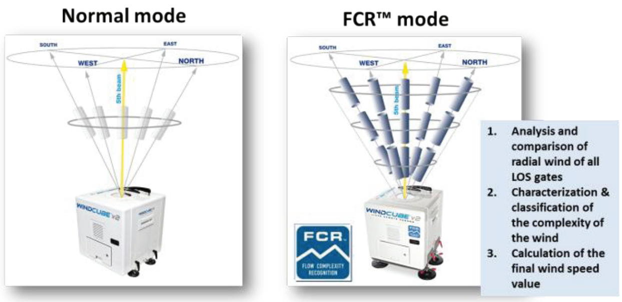

Independent Heights Measurement
Assumption : homogenous wind flow

Entire Profile Direct Measurement
No Assumption on flow homogeneity

4.2 CFD Simulation

In order to study the FCR™ measurement process, CFD calculations have been realized for a variety of flow conditions and topographic complexities. Below an example on a sinusoidal hill of height 100m and width 1000m:

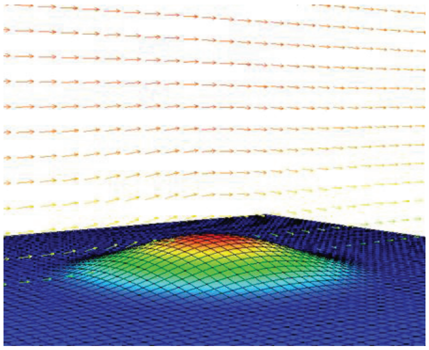

Wind speeds boxes are obtained on these terrains and the remote sensor measurement processes (normal and FCR™) are modeled at several locations of the experimental topographies:

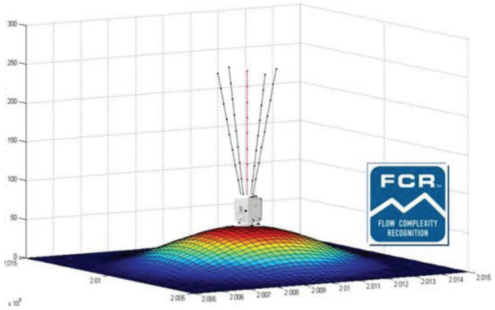

The wind speed values as retrieved by the remote sensor can be compared to the wind speed values directly at the vertical of the instrument, as measured by ideal mast-mounted anemometers. The tables below show respectively the instrument errors in normal mode and in FCR™ mode:

Configuration	RS Error alt. 80m	RS Error alt. 100m	RS Error alt. 120m
Lidar placed at top Mean WS at 10m = 5m/s Shear value = 0.15 Atmo. Stability = Neutre Turbulence = Low	-3.45%	-3.63%	-3.71%
Lidar placed at top Mean WS at 10m = 2m/s Shear value = 0.55 Atmo. Stability = Stable Turbulence = Low	-2.58%	-2.66%	-2.74%
Lidar placed in slope Mean WS at 10m = 5m/s Shear value = 0.15 Atmo. Stability = Neutre Turbulence = Low	-1.46%	-1.63%	-1.78%

Configuration	FCR™ Error alt. 80m	FCR™ Error alt. 100m	FCR™ Error alt. 120m
Lidar placed at top Mean WS at 10m = 5m/s Shear value = 0.15 Atmo. Stability = Neutre Turbulence = Low	0.79%	0.84%	0.78%
Lidar placed at top Mean WS at 10m = 2m/s Shear value = 0.55 Atmo. Stability = Stable Turbulence = Low	0.66%	-0.78%	-0.81%
Lidar placed in slope Mean WS at 10m = 5m/s Shear value = 0.15 Atmo. Stability = Neutre Turbulence = Low	0.44%	0.33%	0.30%

On all cases of this example, the FCR™ measurement process could reduce the theoretical errors ranging from around -3.7% to -1.5% down to errors ranging from around -0.8% to 0.8%.

4.3 On-site measurements

A measurement campaign was held in Greece, on the Center for Renewable Energy Sources (CRES). Three months of wind data were collected by a WINDCUBE™ v1 measuring in normal mode, a WINDCUBE™ v2 equipped with FCT™ and a 100m met mast:

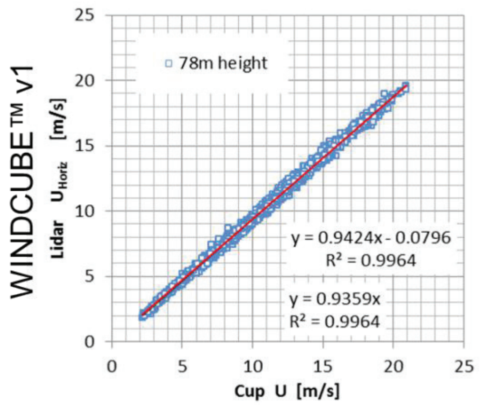

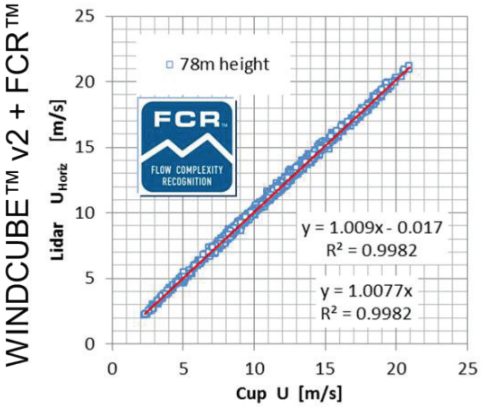

The bias of around -5.8% introduced by the flow homogeneity assumption of the normal mode was here almost entirely cancelled by the FCR™ mode, leading to a residual error against the cup anemometer of around 0.9%.

Dimitri Foussekis, research scientist from CRES, reported: *"At 78m height, wind speed deviations are kept below 1%, with a coefficient of determination R2>0.998. This is an outstanding value approaching results obtained before only in flat terrains."*

5. CONCLUSION

Remote sensors are useful instruments to complement traditional anemometry like mast-mounted cups. This combination of instruments can reduce uncertainties in the wind resource estimation of a site.

However, prior applying remote sensor wind data in a large variety of sites, its accuracy and robustness toward specific environmental variables must be assessed.

A statistical approach has been applied on the WINDCUBE™ lidar and has led to an estimation of measurement uncertainty ranging between 1% and 2%.

Moreover, FCR™ mode allows using the flow homogeneity assumption that defaults remote sensors measurement in complex flow situations.

Therefore the wind speed values measured (and the associated uncertainty) can be quantitatively used for assessment of the wind resource on wind farm sites, resulting in a decrease of the uncertainty in the estimation of the future wind farm production.

ACKNOWLEDGMENTS

The authors would like to thank Dimitri Foussekis from CRES for conducting the lidar measurement campaign.

REFERENCES

1. Breiman L., J. Friedman, R. Olshen, and C. Stone. *Classification and Regression Trees*. Boca Raton, FL: CRC Press, 1984.
2. Albers A. and al., proceedings EWEA2012, *Ground-based remote sensor uncertainty – a case study for a wind lidar*, 2012
3. Bingöl F., PhD Thesis Risoe DTU Wind, *Complex Terrain and Wind Lidars*, 2009

WIND RAMP MEASUREMENT WITH DOPPLER SODAR

Kenneth H. Underwood

[1]*Atmospheric Systems Corporation, 26017 Huntington Ln, Ste F, Valencia, CA 91355 USA), ken@minisodar.com*

ABSTRACT

Wind energy production is slowly transitioning from being a wind farm to power production facility that utilizes wind energy as its source. Increasing wind plant operations are focusing on the forecast of winds for 24 hour and shorter time periods. Forecasting models are ideally suited for the longer period wind field. However critical wind profile measurements are increasingly used to augment the model wind field forecasts and improve the forecast accuracy. A particularly difficult task is to forecast the sudden onset of winds associated with the rapid change in wind direction and wind speed called wind ramp events. These wind ramp events can subject the facility to fines of hundreds of thousands of dollars in some situations.

This paper describes the application of a single station Doppler SoDAR system for the short term forecast of winds. The technique that will be discussed was originally developed in the mid-1990s to support the low level operation of a solar powered UAV. The author believes this experience is also applicable as one of the tools needed for short term wind forecasts associated with the operation of a wind plant and can be extended to the forecast for wind ramp events.

1. SODAR TECHNOLOGY

The SoDAR has been used by meteorologists to study and monitor the atmosphere for 40 years. Its power and challenge is that it operates on the interaction of sound with atmospheric turbulence. This is a fundamental interaction that is independent of mechanical inertia or the suspended particles. The SoDAR has been employed by boundary layer scientists to provide insight into the important turbulent process that we now understand to be important for mixing and transport processes (Singal, 1990).

There are two independent atmospheric quantities measured with a SoDAR. They are (1) the intensity of inertial subrange temperature and humidity fluctuations and (2) the frequency shift associated with the movement of the air volume interrogated by the emitted sound energy (Bradley, 2006).

These principle equations used to interpret the SoDAR are:

Relationship of the acoustic pulse to the acoustic backscattering cross section [Coulter and Underwood, 1980]:

$$P(r) = P_0\,(A\,L_v / r^2)\,e^{-2\alpha r}\,\sigma(r), \qquad (1)$$

Relationship of the Doppler shift ($F_d(r)$) to the local wind field (horizontal and vertical) for uw - reference plane [Underwood, 1981]:

$$F_d(r) = -(2/\lambda)\,(u(r)\sin\varphi + w(r)\cos\varphi), \qquad (2)$$

The data products associated with these relationships when presented in a time – height display format (as seen later in this paper) to emphasize their variation in time and height are most useful for short term wind forecasting.

2. SHORT TERM WIND FORECASTING

In the mid-1990s, the author provided short term wind and turbulence forecasting support for the AeroVironment solar powered UAV at Edwards AFB and on the western shore of Kauai which is part of the Hawaiian island chain. When operating close to the earth's surface, this UAV was subject to low altitude winds and turbulence due to its construction and speed. Pictured below, the pathfinder is shown in flight near the island of Kauai after one of its early AM takeoffs. Erratic low level winds and turbulence could cause the plane to crash. Operations were supported with a high frequency Doppler SoDAR positioned close to the takeoff runway.

Figure1. AeroVironment Pathfinder Plus

3. BOUNDARY LAYER TRANSITIONS

An example of the transition from the stable ABL to an unstable ABL is pictured in figure 2.

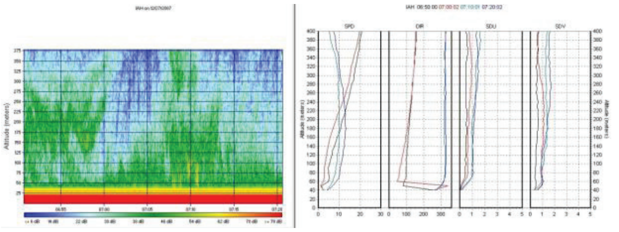

Figure 2. Time evolution of the ABL from a stable to mixed boundary layer as reflected in the facsimile (left) and the wind and turbulence profile (right).

In this example, it is clear that the upper level winds just after the facsimile display showed the transition from a stable atmosphere to an unstable or mixed atmosphere. The downward mixing of the upper level winds accelerated the lower level flow and were coupled with an accompanying change in with direction and increased turbulence levels.

While working with the Pathfinder UAV at Edwards AFB, the author used the facsimile based transition coupled with local measurement of the vertical wind velocity and the downward transport of upper level winds to guide the operations for the solar plane. In effect, a 5 minute notice (at EAFB) was required to bring the UAV to the surface and secure it from increasing winds and turbulence.

4. OBSERVATION OF A WIND RAMP

The following are two consecutive wind tables as measured with an ASC miniSoDAR system at the time of the passage of a wind ramp. The onset of the change in the wind was close to the beginning of the sampling time for the second wind table. It is significant that prior to the wind ramp event the winds were from the ESE at about 5 m/s. The wind speeds changed to about 10 m/s from the WNW. It is a typical shift across a local front.

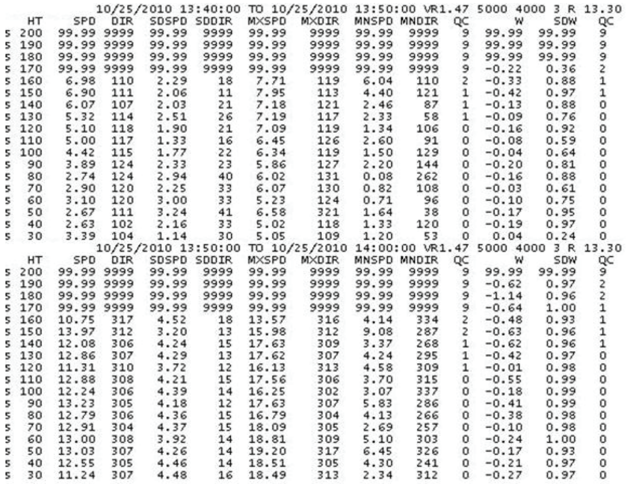

```
            10/25/2010 13:40:00 TO 10/25/2010 13:50:00 VR1.47 5000 4000 3 R 13.30
   HT     SPD  DIR   SDSPD SDDIR  MXSPD  MXDIR  MNSPD MNDIR  QC      W    SDW   QC
 5 200  99.99 9999  99.99  9999  99.99   9999  99.99  9999   9  99.99  99.99   9
 5 190  99.99 9999  99.99  9999  99.99   9999  99.99  9999   9  99.99  99.99   9
 5 180  99.99 9999  99.99  9999  99.99   9999  99.99  9999   9  99.99  99.99   9
 5 170  99.99 9999  99.99  9999  99.99   9999  99.99  9999   9  -0.22   0.36   2
 5 160   6.98  110   2.29    18   7.71    119   6.04   110   2  -0.33   0.88   1
 5 150   6.90  111   2.06    11   7.95    113   4.40   121   1  -0.42   0.97   1
 5 140   6.07  107   2.03    21   7.18    121   2.46    87   1  -0.13   0.88   0
 5 130   5.32  114   2.51    26   7.19    117   2.33    58   1  -0.09   0.76   0
 5 120   5.10  118   1.90    21   7.09    119   1.34   106   0  -0.16   0.92   0
 5 110   5.00  117   1.33    16   6.45    126   2.60    91   0  -0.08   0.59   0
 5 100   4.42  115   1.77    22   6.34    119   1.50   129   0  -0.04   0.64   0
 5  90   3.89  124   2.33    23   5.86    127   2.20   144   0  -0.20   0.81   0
 5  80   2.74  124   2.94    40   6.02    131   0.08   262   0  -0.16   0.88   0
 5  70   2.90  120   2.25    33   6.07    130   0.82   108   0  -0.03   0.61   0
 5  60   3.10  120   3.00    33   5.23    124   0.71    96   0  -0.10   0.75   0
 5  50   2.67  111   3.24    41   6.58    321   1.64    38   0  -0.17   0.95   0
 5  40   2.63  102   2.16    33   5.02    118   1.33   120   0  -0.19   0.97   0
 5  30   3.39  104   1.14    30   5.05    109   1.20    53   0   0.04   0.24   0
            10/25/2010 13:50:00 TO 10/25/2010 14:00:00 VR1.47 5000 4000 3 R 13.30
   HT     SPD  DIR   SDSPD SDDIR  MXSPD  MXDIR  MNSPD MNDIR  QC      W    SDW   QC
 5 200  99.99 9999  99.99  9999  99.99   9999  99.99  9999   9  99.99  99.99   9
 5 190  99.99 9999  99.99  9999  99.99   9999  99.99  9999   9  -0.62   0.97   2
 5 180  99.99 9999  99.99  9999  99.99   9999  99.99  9999   9  -1.14   0.96   2
 5 170  99.99 9999  99.99  9999  99.99   9999  99.99  9999   9  -0.64   1.00   1
 5 160  10.75  317   4.52    18  13.57    316   4.14   334   2  -0.48   0.93   1
 5 150  13.97  312   3.20    13  15.98    312   9.08   287   2  -0.63   0.96   1
 5 140  12.08  306   4.24    15  17.63    309   3.37   268   1  -0.62   0.96   1
 5 130  12.86  307   4.29    13  17.62    307   4.24   295   1  -0.42   0.97   0
 5 120  11.31  310   3.72    12  16.13    313   4.58   309   1  -0.01   0.98   0
 5 110  12.88  308   4.21    15  17.56    306   3.70   315   0  -0.55   0.99   0
 5 100  12.24  306   4.39    14  16.25    302   3.07   337   0  -0.18   0.99   0
 5  90  13.23  305   4.18    12  17.63    307   5.83   286   0  -0.41   0.99   0
 5  80  12.79  306   4.36    15  16.79    304   4.13   266   0  -0.38   0.98   0
 5  70  12.91  304   4.37    15  18.09    305   2.69   257   0  -0.10   0.98   0
 5  60  13.00  308   3.92    14  18.81    309   5.10   303   0  -0.24   1.00   0
 5  50  13.03  307   4.26    14  19.20    317   6.45   326   0  -0.17   0.93   0
 5  40  12.55  305   4.46    14  18.51    305   4.30   241   0  -0.21   0.97   0
 5  30  11.24  307   4.48    16  18.49    313   2.34   312   0  -0.27   0.97   0
```

The associated time series of the 10-minute measurements (speed, direction, vertical velocity and turbulence) surrounding the wind ramp event are plotted in the following four (4) time series graphs.

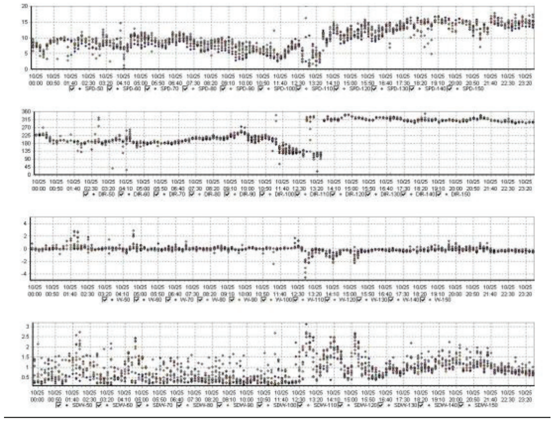

Figure 3. Time series of 10 minute averages of speed (m/s) (top), wind direction, vertical velocity and standard deviation of the vertical velocity (bottom).

While these data capture the local change in the wind field, it has only limited predictive value. But it is suitable for post operational analysis.

5. IMPROVED TIME RESOLUTION

The miniSoDAR system is designed to enable the recording of several data products that are conducive to further study of any particular meteorological event. In particular, it is able to record the moments (intensity, mean frequency shift and signal to noise ratio) associated with each pulse. This section presents the data associated with this ramp event in terms of 1 minute averages for improved temporal resolution.

Prior to the presentation of the moment data, consider whether or not the moment data set is sufficiently robust to capture the wind ramp event.

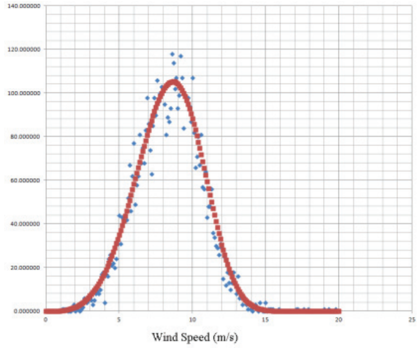

Figure 4. One minute wind speeds and its associated Weibull distribution.

For these data, a statistical hypothesis test to determine if these data satisfy the Weibull distribution is accepted to the 99% percent confidence level.

Plotting the reconstructed time series of one minute data, yields the following results.

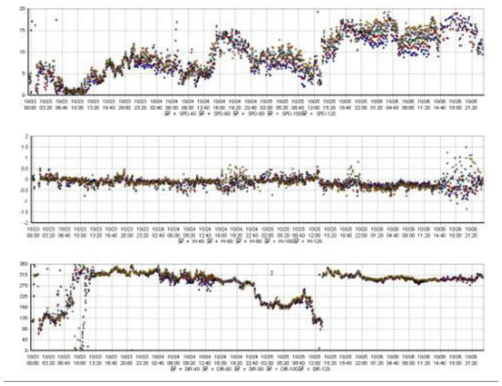

Figure 5. Time series of 1 minute wind speed (top), vertical velocity (middle) and wind direction (bottom).

Examining these time series for significant changes in the wind direction and wind speed, identifies that the ramp event occurred at 13:51. The time series clearly show the change in all time series. So it is clear that the high resolution data is very useful for these events.

6. FACSIMILE DATA

The Doppler data set measures the current wind field above the SoDAR instrument. The measured wind field is the consequence of the turbulent mixing process.

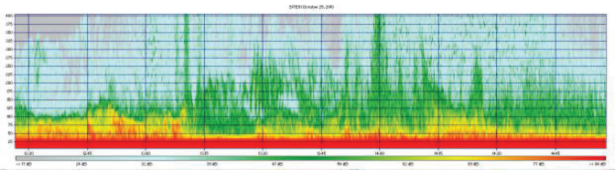

Figure 6. Facsimile presentation of the backscattered intensity associated with the ramp event.

A powerful SoDAR data product is the time height presentation of the backscattered acoustic signal intensity as a function of time. It is called the facsimile presentation. And it is the acoustic data product similar to the radar height range display.

The facsimile data display has been around since the advent of SoDAR technology. A potential signature prior to the wind ramp event is that the ABL is decidedly stable to just prior to the onset of the wind ramp.

7. SUMMARY

These data have demonstrated that a Doppler SoDAR is capable of measuring the short term atmospheric changes associated with the wind ramp events. A strategically placed SoDAR or several SoDAR units would enable wind plant operators sufficient time to adjust their operations thereby reducing lost revenues.

REFERENCES

1. Bradley, Stuart, 2006: Atmospheric Acoustic Remote Sensing. CRC Press, ISBN 978-0-8493-3588-4

2. Coulter, R.L and K. H. Underwood, 1980: Some turbulence and diffusion parameter estimates within cooling tower plumes derived from SoDAR data. *Journal Applied Meteorology*, **19**, pp. 1395-1404.

3. Singal, S.P., 1990: Acoustic Remote Sensing. *Proceedings of the Fifth International Symposium on Acoustic Remote Sensing of the Atmosphere and Oceans, New Delhi, India,* pp 538

3. Underwood, K.H, 1981: SoDAR signal processing methods and the Riso '78 experiment. *Ph.D. Dissertation, Pennsylvania State University, University Park,* pp. **175**.

DOES ASSIMILATION OF SODAR OBSERVATIONS LEAD TO MORE REALISTIC WIND TURBINE INFLOW GENERATION?

Yao Wang[1], Praju KV[1], Sukanta Basu[2]

[1] *2800 Faucette Dr. Raleigh NC, USA 27695, ywang41@ncsu.edu*
[1] *2800 Faucette Dr. Raleigh NC, USA 27695, prajukv@gmail.com*
[2] *2800 Faucette Dr. Raleigh NC, USA 27695, sbasu5@ncsu.edu*

ABSTRACT

Contemporary design standards for wind turbines (e.g., the International Electrotechnical Commission) recommend stochastic models (e.g., the Kaimal spectral model) for turbulence inflow generation. These simple stochastic models are not very representative of atmospheric boundary layer turbulence, as they do not account for the omnipresent atmospheric stability effects. Recently, we proposed two competing multiscale, coupled modeling approaches for the generation of high-resolution, four-dimensional, realistic, inflow turbulence fields. The workhorse behind both modeling approaches is a state-of-the-art, open-source atmospheric model, called the Weather Research and Forecasting (WRF) model. In the first approach, we perform seamless coupled simulations from synoptic-scale (order of ~100 km) down to turbine-scale (order of a few m) flows. In the second approach, we couple the WRF model with a new-generation, tuning-free (dynamic) large-eddy simulation (LES) code in an offline mode. In this approach, the WRF model only simulates atmospheric flows down to the mesoscale (order of ~1 km) and the turbine-scale simulation burden is carried out by the LES code. In this presentation, we will systematically evaluate the impacts of sodar data assimilation on the statistics of simulated inflows (e.g., spectra, coherence). Our primary focus will be on stably stratified flows and associated low-level jets.

1. PRELIMINARY RESULTS

The present study is focused on the West Texas Panhandle region of the US. On July 26-27, 2011, a pronounced low-level jet was observed in this area. During this event, strong winds (~18 m s^{-1}) were observed around 100-200 m above ground level (Fig. 1). Fig. 2 shows the time-height plot of the coupled mesoscale-LES (approach 1) modeled wind speeds. By comparing with observations (i.e., Fig. 1), the coupled run captured the evolution and height of the observed nocturnal LLJs reasonably well.

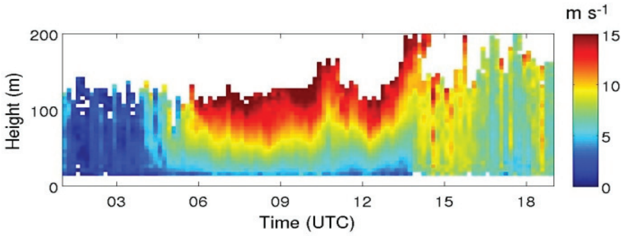

Figure 1. Time-height plots of wind speeds observed by a Scintec SFAS sodar during July 26 and 27, 2011.

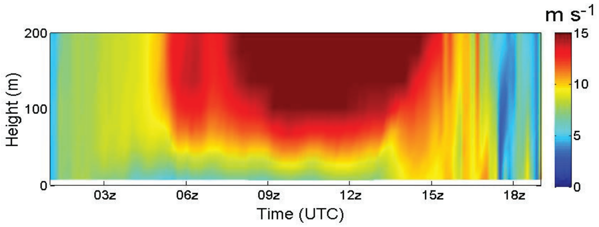

Figure 2. Time-height plot of wind speeds simulated by the coupled mesoscale-LES modeling approach.

ACKNOWLEDGMENTS

This work was partially supported by the National Science Foundation grant CBET-1050806 and AGS-1122315.

REFERENCES

1. International Electrotechnical Commission, 2005: *Wind Turbine Generator System Part 1: Design Requirements*, IEC 61400-1,3rd Ed.

2. Skamarock, W. C., Klemp, J. B., Dudhia, J., Gill, D. O., Barker, D. M., Wang, W., and Powers, J. G., 2005: *Description of the Advanced Research WRF Version 2*, National Center for Atmospheric Research, NCAR/TN-468+STR.

3. Liu Y., Warner, T., Liu Y., Vincent C., Wua W., Mahoney B., Swerdlin S., Parks K., and Boehnert J., 2011: *Simultaneous nested modeling from the synoptic scale to the LES scale for wind energy applications*, J. Wind Engineering and Industrial Aerodynamics, 99, 308–319.

Session 12 – Oral Presentations

Semi-Diurnal Baroclinic Wave Momentum Fluxes at Kaena Ridge, Hawaii

Robert Pinkel

Scripps Institution of Oceanography, La Jolla
CA, 92093-0213

ABSTRACT

Kaena Ridge, Hawaii is a site of energetic conversion of the semi-diurnal barotropic tide. Diffuse baroclinic wave beams emanate from the critical-slope regions near the ridge crest, directed upward and southward from the north flank of the ridge, upward and northward from the south flank. Here we attempt to quantify the momentum fluxes associated with generation at the Ridge. Continuous vertical profiles of density and vertical velocity from 80-800m were obtained from the Research Platform FLIP over the southern edge of the ridge, as an aspect of the Hawaii Ocean Mixing Experiment. Data are used to estimate the Reynolds stress, Eulerian buoyancy flux, and the combined Eliassen-Palm Flux in the semi-diurnal band. An upward-southward stress maximum of ~ 0.5 10^{-4} $m^2 s^{-2}$ appears at depths 300-500m, generally consistent with beam-like behavior. A strong off-ridge buoyancy flux (~ 0.3 10^{-4} m^2 s^{-3}) combines with large along-ridge Reynolds stresses to form an Eliassen Palm flux whose along-ridge and across-ridge magnitudes are comparable. The stress azimuth rotates clockwise with increasing altitude above the ridge crest. The principal upward-southward beam is found to be at depths 100-300 m, shallower than are predicted by an analytic 2-dimensional model and a 3-D numerical simulation. This discrepancy is consistent with previous observations of the baroclinic energy flux. If these observed tidal momentum fluxes were to diverge in a 100m thick near-surface layer, the forcing would be comparable to a moderate wind stress. Pronounced lateral gradients of baroclinic tidal stresses can be expected offshore of Hawaiian topography.

INTRODUCTION

In the ocean, internal waves are ubiquitous and their ability to transport momentum is potentially significant. For example, if an upward propagating plane wave with horizontal velocity u_1~ 0.1 m/s and vertical velocity u_3=0.001 m/s is completely dissipated as it encounters the sea surface, the stress on the surface is roughly 1 N/m^2, comparable to that exerted by a 5-10 m/s wind.

For the atmosphere, it has long been appreciated that gravity wave momentum fluxes play a significant role in the global zonal momentum balance. However, there is no corresponding open-ocean evidence for wave momentum fluxes of significant magnitude. In pioneering field investigations of Ruddick and Joyce 1979, Brown and Owen, 1981, and Plueddemann, 1987, statistically significant wave Reynolds stresses were not observed. The quasi-isotropy of the oceanic wavefield in the horizontal is associated with near-zero correlations between horizontal and vertical velocities, and correspondingly small momentum fluxes.

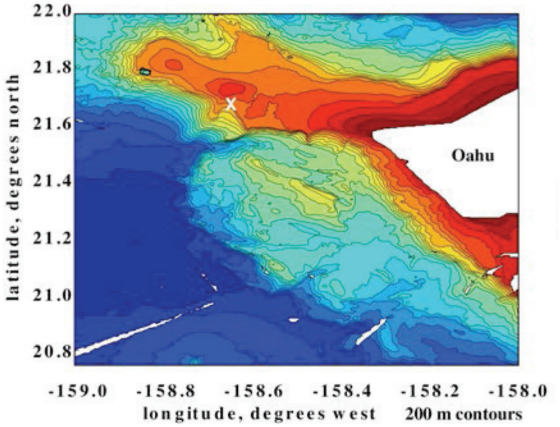

Figure 1. Plan view of Kaena Ridge, left. Darkest colors correspond to 5000 m. depth. Flip was tri-moored on the S. rim, white X. A hill rises ~500 m above the ~1000 m ridge crest, 8 km to the north.

OBSERVATIONS

As an aspect of the Hawaii Ocean Mixing Experiment, HOME, the Research Platform FLIP was moored at the south rim of the Kaena Ridge, collecting a 35-day record of the density and velocity fields in the upper 800 m of the 1100 m water column. The time-continuity of the measurements facilitates the extraction of tidal-frequency signals from the energetic non-tidal signals at the site. In the semi diurnal (D_2) frequency band, the coherence between horizontal and vertical velocity exceeds 0.5, reflecting the extreme anisotropy and quasi-deterministic nature of the generation process. The combination of signal strength and high coherence renders the task of estimating wave momentum transport tractable relative to the early open-ocean studies.

The flanks of the Kaena Ridge are supercritical to semi-diurnal baroclinic tides. The site of most-intense tidal conversion is the Ridge "shoulder", the fringe surrounding the crest with critical slope, $h = |\boldsymbol{k_H}|/|k_3|$. Here, $h(x_1,x_2)$ gives the height of the topography, $k_H=(k_1,k_2,0)$ is the horizontal wavenumber of the baroclinic tide, k_3 the vertical wavenumber. The cross-ridge extent of the critical regions, 5-10 km, is small relative to the overall width of the Ridge, 20-30 km. Models of the generation process indicate that an upward and southward energy flux emanates from the north shoulder of the ridge, while an upward and northward flux is initiated at the southern shoulder. A similar pattern for momentum is anticipated.

At the south-rim measurement site, the D_2 tide appears as a predominantly low-mode phenomenon, with roughly one-quarter vertical wavelength spanning the 1100 m water-column. Tidal crests display downward phase propagation in mid water column, consistent with a ridge-crest generation site. In the upper 250m the phase pattern becomes irregular, possibly a result of the surface reflection of tidal signals generated at distant ridge-top locations.

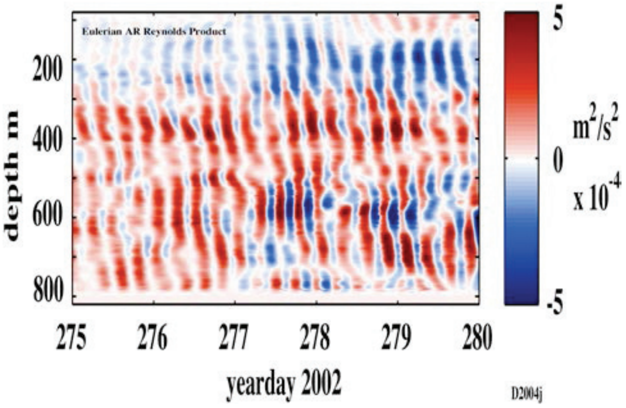

Figure 2. A five-day record of the D_2 Reynolds product, u_1u_3 during the second spring tide of the experiment. When horizontal and vertical velocities are large and in quadrature, alternating red and blue bands are seen at frequency $2D_2$. When they are in-phase or anti-phase, the near zero-frequency signal is the Reynolds stress, seen as the changing "background" color of the image.

To examine the signals comprising the momentum flux, the total velocity field can be band-pass filtered about the semi diurnal frequency. The D_2 along-ridge Reynolds product, u_1u_3, Figure 2, displays the various interacting factors that establish the mean stress. The records consist of a series of vertically coherent stripes at frequency $2D_2$, overlaying a difference-frequency signal that changes rather slowly in time. The vertical scale of the stripes is comparable to that of the D_2 signals. Downward phase propagation is seen at mid-depths. The sense of phase propagation is less consistent near the surface and near the bottom (of the observational window). A time average of $\mathbf{u_H}u_3$ over multiple tidal cycles removes the $2D_2$ variability, leaving the difference-frequency signal as the Reynolds stress. The depth-variability of the stress can be quite rapid (eg., Fig. 2, 300m), in spite of the fact that the dominant motions are of large vertical scale. The time variability of this signal is limited by the bandwidth, 0.8 cpd, of the D_2 bandpass filter.

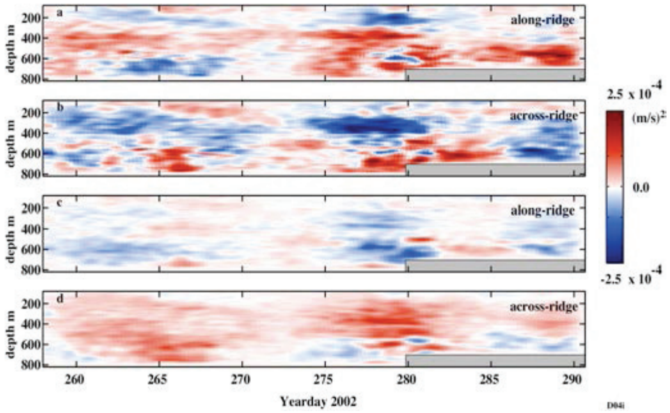

Figure 3. The along-ridge and cross-ridge Reynolds stress (a, b) and mass flux (c, d) for the 35 day Nearfield record. A 24.8-hour running mean filter converts perturbation maps (Fig.2) into these flux maps. The maps are shifted in time to account for the lag of the filter. The grey region at depths below 700m starting at yearday 280 represents data lost due to CTD failure.

The entire Nearfield record of D_2 Reynolds stress and mass flux, $f<\eta\ \mathbf{u_H}>$, is presented in Figure 3. The existence of the fortnightly cycle is apparent in both the stress and mass flux fields. Upward and northward stresses are seen at depths below 600m and upward and southward fluxes above. Flux magnitudes increase at all depths with the onset of spring tides, suggesting a rapid penetration-time from the ridge into the interior. The flux patterns vary slightly from one spring tide to the next, possibly due to low-frequency current variability. Along-ridge stresses are of the same magnitude as the cross-ridge. Strong upward and eastward stresses are seen below 300m during spring tides

The mass flux signals are remarkably regular, with magnitude roughly half that of the stress. The mass flux nearly vanishes during the neap tides, with some hint of an actual reversal in the along-ridge flux.

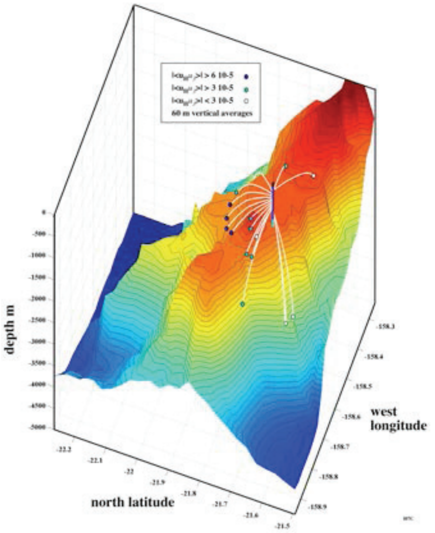

Figure 4. The ridge-crest topography with the D_2 rays arriving at FLIP traced backward to their presumed site of generation. The black dot represents FLIP, to scale, the blue line below is the section of the water column sampled, and the light blue extension gives the water depth at the measurement site. The color of the dots at the point of origin of each ray corresponds to the magnitude of the Reynolds stress along the ray in m^2/s^2.

DISCUSSION

A steady clockwise rotation of the Reynolds stress vector with increasing elevation is one of the surprise findings of the experiment. We feel that the three-dimensionality of the Ridge is the key factor in its creation. The distance between the FLIP site and the westward end of the Ridge, ~40km, is comparable with the horizontal wavelength of a mode-three wave and only slightly greater than the width of the Ridge at the site. One can back-trace the Reynolds stress vectors arriving at FLIP, identifying the point of origin on the Ridge (Figure4). Not surprisingly, the deepest observed arrivals are generated on the south flank of the ridge and are associated with upward and northward propagation. The clockwise upward spiral generally follows the topography of the west end of the Ridge. It’s notable that at many of the sites of origin the rays are locally tangent to the topography. This is particularly true for the strongest sites on the north face of the Ridge. D_2 rays can only reach the upper 150m of FLIP’s observation window if launched from the shallow topography where the Ridge shoals toward Oahu. This is indeed the azimuth of the observed (weak) arrival.

In examining the D_2 horizontal energy fluxes at the FLIP site, Rainville and Pinkel (2006a) find an identical spiral (their Figures 9a and 10a), with along-ridge energy fluxes of magnitude comparable to the cross-ridge fluxes. These results suggest that baroclinic waves are generated along the azimuth of critical topographic gradients, rather than parallel to the barotropic forcing or normal to the large-scale orientation of the ridge.

Even though the wave Reynolds stress is small compared to the surface stress from high winds, the spatial scale of variability is much smaller than in the open ocean. Thus the curl of the stress is large comparable to open ocean values. Can the fortnightly modulation of the stress (divergence) be detected in sub-inertial flows?

ACKNOWLEDGEMENTS

The authors thank Eric Slater, Mike Goldin, Lloyd Green, Tony Aja and Tyler Hughen for the design, construction, and operation of the instruments used in this experiment. Captain Tom Golfinos and the crew of the R.P. FLIP ably deployed the tri-mooring on the edge of Kaena Ridge crest and operated the platform for the duration of the experiment. This work was supported by NSF as an aspect of the Hawaii Ocean Mixing Ex

TWO-COMPONENT HORIZONTAL MOTION VECTORS FROM THE RAMAN-SHIFTED EYE-SAFE AEROSOL LIDAR (REAL)

Shane D. Mayor

Department of Physics, California State University Chico, sdmayor@csuchico.edu

ABSTRACT

Two-component horizontal motion vectors of aerosol features were calculated by applying a cross-correlation algorithm to square image blocks extracted from consecutive pairs of elastic backscatter lidar scans. The resulting vector components were compared with corresponding horizontal wind components from tower-mounted sonic anemometers located at the center of the image blocks. 180 245 pairs of vectors derived from 75 days of field data collected between 19 March and 11 June 2007 were used in the analysis. Examples of time-series comparisons from various boundary layer states and statistical results of the comparisons will be presented. The correlation between the lidar-derived motion components and sonic anemometer wind components tends to be highest during light wind conditions with low TKE. Examples of two-dimensional and two-component vector flow fields will also be presented.

1. INTRODUCTION

This paper is a condensed version of a manuscript recently accepted for publication in the *Journal of Atmospheric and Oceanic Technology* [1]. It describes 2-component horizontal wind measurements made by applying a cross-correlation motion estimation algorithm to scans from the Raman-shifted Eye-safe Aerosol Lidar (REAL) [2] (see Fig. 1) during the 2007 Canopy Horizontal Array Turbulence Study (CHATS) [3]. Previous work on the topic of deriving winds from elastic backscatter lidar data are described in [4-12]. The present work is unique because it employs an *eye-safe* lidar system and the derived vector components are compared with in situ velocity measurements within the scan area. The REAL transmits 6 ns pulses at a pulse rate of 10 Hz and operates at 1.54 microns wavelength.

Figure 1: The Raman-shifted Eye-safe Aerosol Lidar (REAL) at the California State University Chico Farm.

2. EXPERIMENTAL SETUP

CHATS took place in Dixon, California, from mid-March through early-June of 2007. The focus of the experiment was a horizontal array of sonic anemometers located approximately 100 m south of a 30 m tall vertical instrumented tower in a large walnut orchard. The REAL was located 1.61 km directly north of the 30 m tower. PPI scans were directed toward the south as shown in Fig. 2. The lidar scan plane intersected the tower between 18 and 20 m AGL (see Fig. 3). Because of uncertainty in the exact altitude of the lidar beam at the tower and frequent strong vertical wind shear just above the trees, no attempt has been made to compare mean lidar-derived velocities with mean sonic anemometer data. Therefore, in this paper (and in [1]), only the vector components resulting from pairs of lidar scans are compared with anemometer data averaged over the time it took the lidar to collect a pair of scans. A visual depiction of how the lidar-derived vectors were calculated and compared with the sonic anemometer time series data is shown in Fig. 4.

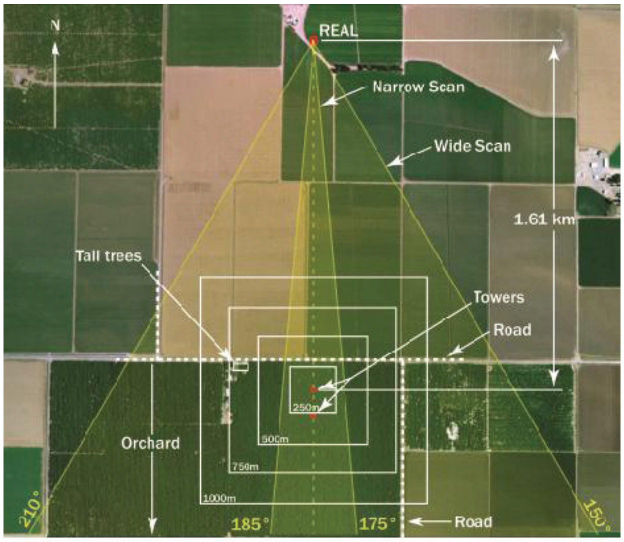

Figure 2. Plan-view of the experimental area. The shaded regions from 150^o – 210^o and 175^o – 185^o azimuth represent the areas covered by "wide" and "narrow" PPI scans, respectively. The vertical tower (VT) was located 1.61 km directly south of the REAL. The white squares centered on the VT represent the image blocks extracted from the gridded PPI scan data that were used to compute motion vectors via the cross-correlation technique.

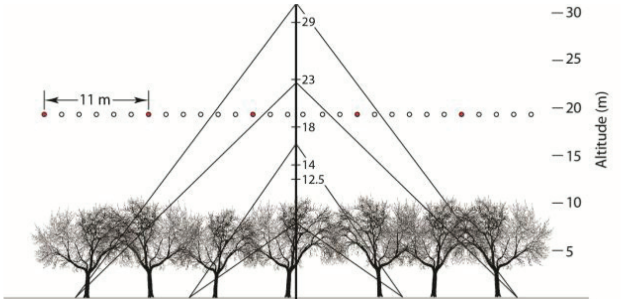

Figure 3. Diagram showing the approximate altitude, spacing, and size of REAL laser pulses with respect to the tree tops and the vertical tower at CHATS. This diagram is an east-west cross section looking either towards (north) or away (south) from the lidar. Shaded circles represent laser pulses from one scan at an azimuthal scan rate of 4^{o} s^{-1}. At this scan rate, the pulses are spaced 11 m apart at 1.61 km range from the lidar.

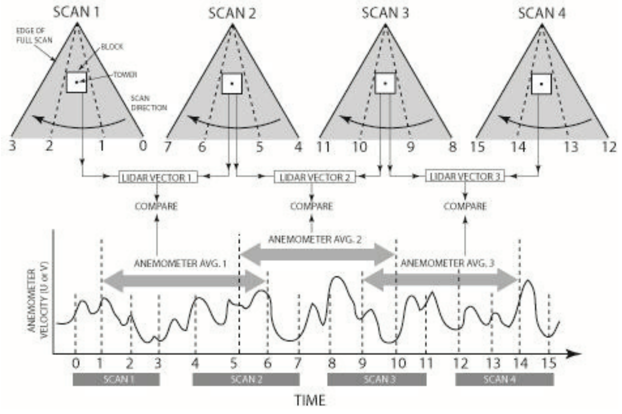

Figure 4. Visual depiction of how anemometer time series data were averaged for comparison with the vectors derived from lidar scans. This example considers a series of four consecutive PPI scans that result in three vectors. The anemometer data are averaged over the periods corresponding to when the lidar's beam enters the block on the first scan (positions 1, 5, and 9 in time) and exits the block on the subsequent scan (positions 6, 10 and 14 in time).

3. TIME-SERIES COMPARISONS

The experiment resulted in over 1000 hours of time series comparisons like those shown in Fig. 5, 6, and 7. In the time-series comparisons, the colored lines are of the slightly averaged sonic anemometer wind components (u is the east-west component; v is the north-south component) and the black points are the result of the cross-correlation algorithm when applied to a square block centered on the tower location. Four block sizes were used (shown as squares on centered on tower in Fig. 2). Larger blocks result in less scatter in the lidar-derived points and better correlations with the sonic anemometer data. In some cases it is possible to achieve good results with the smallest block size (250 m x 250 m) as shown in Fig. 5. However, during more windy and turbulent conditions, it is necessary to use much larger block sizes. The lidar-derived vector components shown in Figs. 6 and 7 used 1 km^2 blocks.

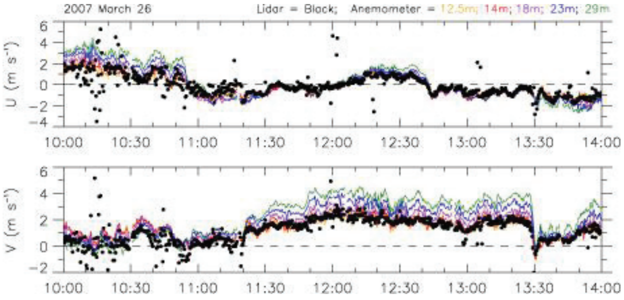

Figure 5. Time series of lidar-derived (black points) and averaged sonic anemometer (color traces) velocity components for a 4-hour period during light wind conditions. A 250 m x 250 m block size was used for the lidar-derived velocity estimates.

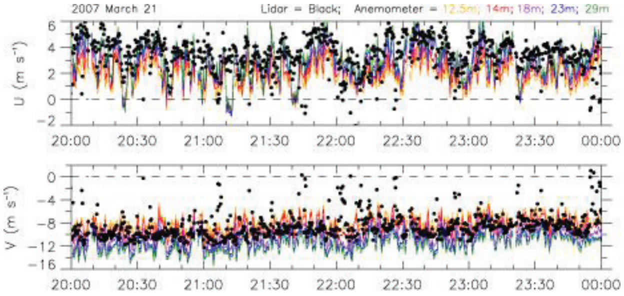

Figure 6. Time series of lidar-derived (black points) and averaged sonic anemometer (color traces) velocity components for a 4-hour period during strong wind conditions. A 1 km^2 block size was used for the lidar-derived velocity estimates.

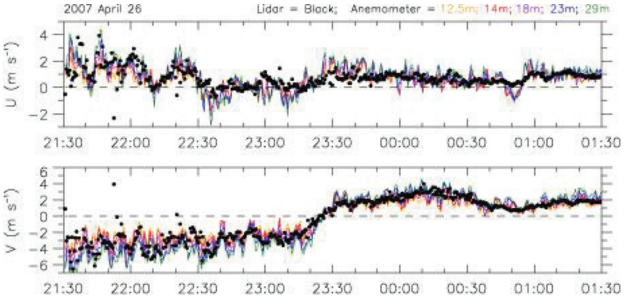

Figure 7. Time series of lidar-derived (black points) and averaged sonic anemometer (color traces) velocity components for a 4-hour period during moderate wind conditions with a frontal passage. A 1 km^2 block size was used for the lidar-derived velocity estimates.

Figure 5 is a good example of the typical performance at night when winds are light and variable and the atmosphere tends toward stability. In general, it was found that the cross-correlation provides the best correlation with the sonic anemometer data at night.

Figure 6 is an example of what can be achieved during a very windy day when the boundary layer is turbulent and near-neutral. During these conditions, the point to point correlation is not that good, but the cross-correlation algorithm is capable of capturing the mean flow. Again, as pointed out in the previous section, means were not computed and compared due to uncertainty of the precise altitude of the laser beam at the tower and the existence of strong vertical wind shear immediately above the trees.

Figure 7 shows a near reversal in flow direction with the passage of a density current front. The details of this case, and 6 others like it, are described in detail in [13]. This case represents a more moderate range of wind speeds than those shown in Figs. 5 and 6.

In all, 180 245 pairs of vectors were compared for a wide variety of weather conditions over the nearly three month field experiment. For each vector computed from the lidar data, several scalar variables were recorded. These include wind speed (from the sonic anemometer data); turbulent kinetic energy (TKE, measured from sonic anemometers); maximum of the cross-correlation function (CCF max, from the lidar data); and mean signal to noise ratio (SNR) of the lidar data in the block area. It was found that the correlation between lidar-derived velocity components and sonic anemometer velocity components became worse as the TKE or wind speed increased and became better as the mean SNR or CCF max increased.

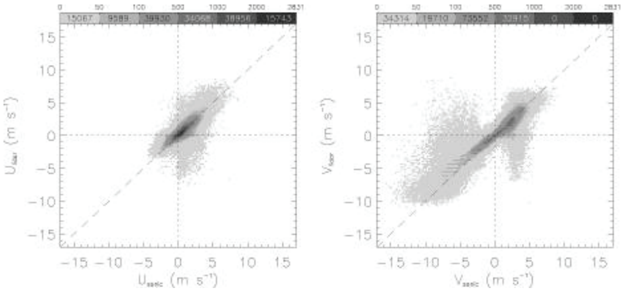

Figure 8. Distribution of 18 m AGL sonic anemometer wind components versus aerosol motion components derived from the lidar data after application of the QC model. The linear correlation coefficient for the u-component comparisons (left panel) is 0.75 and the v-component comparisons (right panel) is 0.90.

A quality control (QC) model was developed and is described in detail in [1]. It uses the sonic anemometer data as a reference to generate equations that can be used to predict the difference based on the mean SNR and CCF max. This is useful for discarding low quality wind estimates---especially when the algorithm is applied to areas on the scan without co-located sonic anemometer data.

Figure 8 is a shaded scatterplot of the comparisons after application of the quality control model. Because of the high density of data points, the number of occurrences of comparisons was accumulated into 0.2 m s^{-1} by 0.2 m s^{-1} bins and shaded according the gray shade scale at the top. We chose to shade bins (even those containing only 1 data point) to reveal the behavior of the algorithm over all conditions including infrequent high wind events. The vast majority of data points lie within the darker shaded region along the dashed identity line. It is important to note that the distribution is also the result of the non-uniform distribution of wind speeds and directions that were experienced during CHATS.

4. TWO-DIMENSIONAL WIND FIELDS

The cross-correlation algorithm can be applied to a grid of locations over the entire scan area. Doing so results in vector flow fields such as those shown in Figs. 9 and 10. The flow field shown in Fig. 9 is the lidar estimate of the two-component horizontal wind field at 00:19:47 UTC on 26 March 2007. It was calculated using 1 km^2 blocks and one pair of scans separated by 17 s. Vectors were calculated every 10 m in the horizontal Cartesian dimensions and streamlines were launched every 100 m. At the time, a vortex was located 2.7 km south and 0.2 km west of the lidar. The flow field also reveals a saddle point 3.5 km south of the lidar and 0.3 km east of the lidar. In situ data show light (< 3 m s^{-1}) and variable winds until approximately 01:30 UTC when a uniform WSW flow swept across the region.

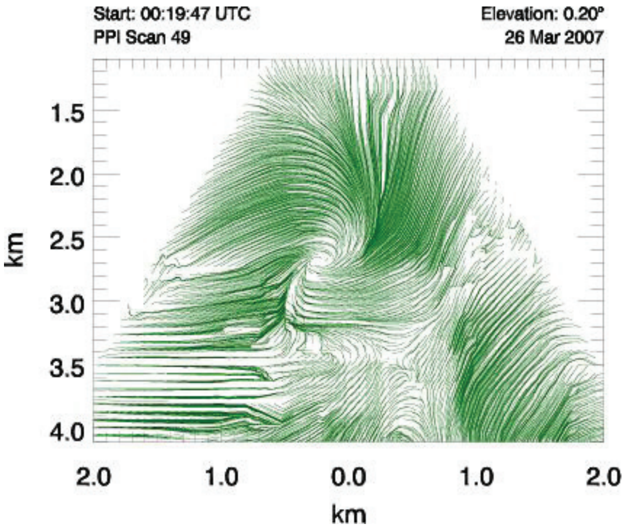

Figure 9. Streamlines from the application of the cross-correlation algorithm to a pair of PPI scans through a convective afternoon atmospheric surface layer when winds were light and variable. Scans were separated in time by 17 s. A block size of 1 km^2 was applied at the grid interval of 10 m. Streamlines were launched every 100 m.

Figure 10 reveals the flow field when a density current front [13] approximately bisected the scans area. Flow north of the front was northerly (indicated by blue streamlines) and flow south of the front was southerly (indicated by red streamlines). However, in addition to the narrow band of convergence at the front, the lidar-derived flow fields reveal eastward transport of air that flows into a vortex centered 3.7 km south and 1.5 km east of the lidar. These observations show that flow may not rise over the front uniformly and rather may be transported significant horizontal distances before being swept up into narrow and rapidly rising currents.

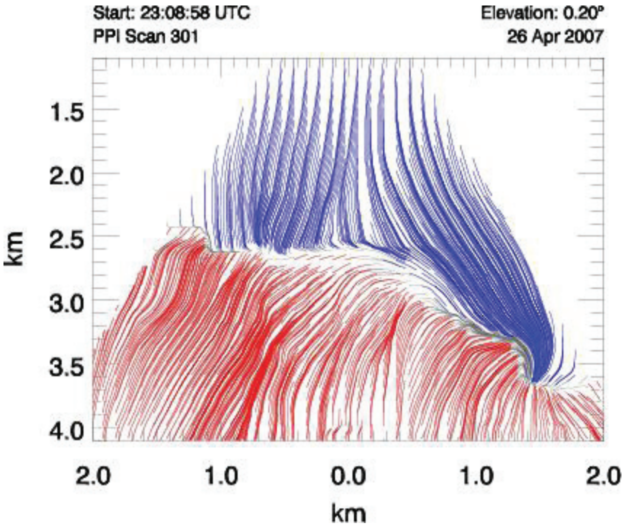

Figure 10. Streamlines from the application of the cross-correlation algorithm to a pair of PPI scans when a density current front was advancing from the south. Streamlines are colored according to the sign of the v component with blue indicating northerly flow north of the front and red indicating southerly flow south of the front. The scans were separated by 30 s and a 1 km^2 block was applied at the grid spacing of 10 m. Streamlines were launched every 100 m.

5. NEXT STEPS

The CSU Chico Atmospheric Lidar Group is currently working on several fronts to improve this capability. One effort involves stabilization and remote control of the lidar system for long-term and unattended operation. Another effort involves real-time calculation of the wind fields using graphical processing units. We are also developing of software to visualize the flow-fields in near-real-time from any web-browser.

ACKNOWLEDGMENTS

This work was supported by NSF AGS 0924407.

REFERENCES

1. Mayor, S. D., J. P. Lowe, and C. F. Mauzey, 2012: Two-component horizontal aerosol motion vectors in the atmospheric surface layer from a cross-correlation algorithm applied to elastic backscatter lidar data, *J. Atmos. Ocean. Technol.* In press.

2. Mayor, S. D., S. M. Spuler, B. M. Morley, and E. Loew, 2012: Polarization lidar at 1.54-microns and observations of plumes from aerosol generators, Opt. Eng., **46**, DOI: 10.1117/12.781902.

3. Patton E. G., et al., 2011: The Canopy Horizontal Array Turbulence Study (CHATS), *Bull. Amer., Meteor. Soc.*, **92**, pp. 593-611.

4. Eloranta, E. W., J. M. King, and J. A. Weinman, 1975: The determination. of wind speeds in the boundary layer by monostatic lidar. *J. Appl. Meteor.*, **14**, pp. 1485–1489.

5. Sroga, J. T., E. W. Eloranta, and T. Barber, 1980: Lidar measurements of wind velocity profiles in the boundary layer. *J. Appl. Meteor.*, **19**, 598–605.

6. Kunkel, K. E., E. W. Eloranta, and J. Weinman, 1980: Remote determination of winds, turbulence spectra and energy dissipation rates in the boundary layer from lidar measurements. *J. Atmos. Sci.*, **37**, 978–985.

7. Sasano, Y., H. Hirohara, T. Yamasaki, H. Shimizu, N. Takeuchi, and T. Kawamura, 1982: Horizontal wind vector determination from the displacement of aerosol distribution patterns observed by a scanning lidar. *J. Appl. Meteor.*, **21**, 1516–1523.

8. Hooper, W. P. and E. W. Eloranta, 1986: Lidar measurements of wind in the planetary boundary layer: the method, accuracy and results from joint measurements with radiosonde and kytoon. *J. Clim. Appl. Meteor.*, **25**, 990–1001.

9. Kolev, I., O. Parvanov, and B. Kaprielov, 1988: Lidar determination of winds by aerosol inhomogeneities: motion velocity in the planetary boundary layer. *Appl. Optics*, **27**, 2524–2531.

10. Schols, J. L. and E. W. Eloranta, 1992: The calculation of area-averaged vertical profiles of the horizontal wind velocity from volume imaging lidar data. *J. Geophys. Res*, **97**, 18 395–18 407.

11. Piironen, A. K. and E. W. Eloranta, 1995: Accuracy analysis of wind profiles calculated from volume imaging lidar data. *J. Geophys. Res*, **100**, 25 559–25 567.

12. Mayor, S. D. and E. W. Eloranta, 2001: Two-dimensional vector wind fields from volume imaging lidar data. *J. Appl. Meteor.*, **40**, 1331–1346.

13. Mayor, S. D., 2011: Observations of seven density current fronts in Dixon, California. *Mon.Wea. Rev*. **139**, 1338-1351.

Wind lidar profile measurements in the coastal boundary layer: comparison with WRF modelling

R. Floors[1]**, A. Peña**[1]**, C.L. Vincent**[1]**, S-E Gryning**[1] **and E. Batchvarova**[2]
[1]*DTU Wind Energy, Risø Campus, Technical University of Denmark,*
Frederiksborgvej 399, 4000 Roskilde, Denmark (rofl@dtu.dk)
[2]*National Institute of Meteorology and Hydrology, Sofia 1784, Bulgaria*

Abstract

We use measurements from a pulsed wind lidar to study the wind speed profile in the planetary boundary layer (PBL) up to 600 m above the surface at a coastal site. Due to the high availability and quality of wind lidar data and the high vertical range of the measurements, it is possible to study the sensitivity of PBL schemes of mesoscale models to both lower and upper boundary conditions. We therefore run the mesoscale weather research and forecasting (WRF) model using two different roughness descriptions, two different synoptic forcings and two different PBL schemes at two vertical resolutions. When WRF is compared to the wind lidar data combined with measurements from a tall meteorological mast, it is found that the model surface layer fluxes are largely overestimated and that the vertical wind speed profile does not have enough shear in the lower part of the PBL, partly as a consequence of the smooth-to-rough transition at the coastline. When using a more representative roughness than the default, the biases in the surface friction velocity and heat flux are reduced and the wind speed is slightly improved. Both PBL schemes show too much mixing during stable conditions and an underestimation in the amount of observed low level jet. The wind speed predicted by WRF does not improve when a higher resolution is used. Therefore, both the inhomogeneous (westerly) and homogeneous (easterly) flow contribute to a large negative bias in the mean wind speed profile at heights between 100 and 200 m.

1 Introduction

The change of wind speed with height and its development in time are key issues for the wind energy industry. As wind turbines get taller, our knowledge of the wind speed above the surface layer has to be improved. Recent studies have shown that WRF often poorly represents turbulent parameters like the friction velocity u_* and heat flux H [1, 7]. For description, modelling and forecasting of the behaviour of winds and turbulence it is essential to have a realistic estimate of the magnitude of the surface layer fluxes. Verification of the vertical structure of the PBL often proves difficult, because of lack of data of sufficient resolution in time and space. One promising new method for measuring the wind profile is the wind lidar. They have been available for some time, but recently they improved in terms of reliability, accuracy and range [5]. Wind speed measurements from a wind lidar up to 600 m, combined with the observations from a meteorological mast at a coastal site in Denmark provide information about both upper air and near surface winds and turbulence. We study the sensitivity of the wind profile modelled by WRF with two PBL parameterizations and two vertical model resolutions to both lower and upper boundary conditions; the surface layer momentum flux (by redefining the landuse properties) and synoptic forcing (by using NCEP final analysis and ERA interim reanalysis data), respectively. We run WRF in prognostic mode on a domain covering Northern Europe for two 15 day periods.

2 Methods

2.1 Observations

A pulsed wind lidar (Windcube70) operates at the National Test Station of Wind Turbines at Høvsøre since April 2010. Wind speeds are measured at a near by meteorological mast together with turbulence parameters. The wind lidar measures wind speed and direction every 50 m starting at 100 m above the ground and reaching up to 2 km height depending on the aerosol content of the atmosphere. The wind lidar is equipped with a rotating silicon prism providing four azimuthal scans 90° from each other at a inclination angle (relative to the zenith) of 15°. One 360 degree full scan (rotation) is performed every 30 s. The data are stored into 10-min average quantities. The reported range of measurements depends on a threshold on the 10-min averaged carrier to noise ratio (CNR). This threshold (here -22 dB) can also be used as an estimate for PBL height: because the lidar needs

Table 1: Observations available at the Høvsøre site

Observations

Data source		Heights [m]
Cup	C	10, 40, 60, 80, 100, 116.5, 160
Sonic	S	10
Lidar	L	100–600 (50 m interval)

aerosols to measure the wind speed it cannot measure above the PBL height and the signal becomes noisy.

The agreement between lidar and cup anemometer wind speed at 100 m height for the two analysed periods is excellent. Using linear regression fitted through origo, gives a correlation coefficient R^2 and slope coefficient of almost 1.00. Due to its high measuring frequency, the lidar gives very robust statistics compared to radio soundings.

At Høvsøre the flow is strongly influenced by the sea-land contrast. The data is classified into two categories based on the wind direction D at 60 m: the westerly sector ranges between 225 and 315 degrees and the easterly sector between 30 and 150 degrees.

2.2 Model

In WRF the vertical diffusion is modelled by the PBL scheme. We use the first order YSU scheme and the 1.5 order MYNN scheme. The YSU scheme prescribes the values of the eddy diffusivity K_m directly, while the MYNN scheme uses an additional prognostic equation for the turbulent kinetic energy. A detailed description of the PBL parameterization for YSU and MYNN can be found in Hong et al. [3] and Nakanishi & Niino [4], respectively. The surface layer scheme calculates the turbulent fluxes u_{*0} and H based on a bulk method using Monin-Obukhov similarity theory (MOST).

3 Results

3.1 Lower boundary conditions

Because u_{*0} and H are the most important parameters governing the shape of the wind profile, they were compared with the model simulation from WRF. The roughness length z_0 and the stability correction ϕ_m were calculated from observations. The roughness length in WRF was too high, $z_0 \approx 0.08$, so the value from the observations, $z_0 = 0.015$, was implemented in WRF (table 2). It is possible that the surface layer scheme calculates a too high u_{*0}, because the observed dimensionless shear in the coastal area can be different from the modelled one. In the internal boundary layer the dimensionless wind shear can be up to 50% larger than unity, because U decreases faster with height than u_* [6]. Although the ϕ_m functions was under predicted in WRF, it was found that this did not contribute significantly to the overestimation in u_{*0}. Also there was no significant difference between the ϕ_m function for the easterly and westerly sector, which shows that MOST was valid at the first model level.

Table 2: Summary of the model runs and observations for the two periods 15–30 Sep. and 15–30 Oct.

Name	PBL scheme	No. vert. levels (in range lidar)	Boundary conditions	z_0 [m]
M_{41}	MYNN	41 (8)	FNL	0.080
Y_{41}	YSU	41 (8)	FNL	0.080
M_{63}	MYNN	63 (22)	FNL	0.080
Y_{63}	YSU	63 (22)	FNL	0.080
MC_{41}	MYNN	41 (8)	FNL	0.015
YC_{41}	YSU	41 (8)	FNL	0.015
ME_{41}	MYNN	41 (8)	ERA	0.080
YE_{41}	YSU	41 (8)	ERA	0.080

- Noah land surface scheme
- Thompson microphysics scheme
- RRTM longwave radiation
- Dudhia shortwave radiation
- New Kain-Fritsch cumulus scheme

Table 3: Results from linear regression through origin for the westerly sector (top, number of samples, $N = 1366$) and easterly sector (bottom, $N = 310$).

Var.	M_{41}	MC_{41}	Y_{41}	YC_{41}
u_{*0}	1.39	1.10	1.36	1.07
H	1.50	1.09	1.14	0.98
U_{10}	1.05	1.11	1.03	1.08
U_{100}	0.95	0.95	0.94	0.95
U_{650}	0.99	0.98	0.95	0.95
u_{*0}	1.10	0.99	1.30	1.14
H	1.38	1.07	1.50	1.34
U_{10}	0.95	1.11	1.10	1.26
U_{100}	0.83	0.87	0.91	0.95
U_{650}	0.97	0.97	0.96	0.96

For both easterly and westerly winds, the model runs M_{41} and Y_{41} overestimate u_{*0} (table 3). Using lower roughness in MC_{41} and YC_{41} reduces u_{*0} to more realistic values and similar results are found for the heat flux. For homogeneous conditions the YSU scheme still has a large positive bias for H, which was also observed in [7]. The MYNN scheme does not show this large overestimation in H. The 10 m winds were overestimated in most conditions, even when the surface layer fluxes showed no bias.

The internal boundary layer that forms at the smooth-to-rough change results in an high friction velocity at Høvsøre, which then decreases further inland (figure 1, right). This is in agreement with experimental and nu-

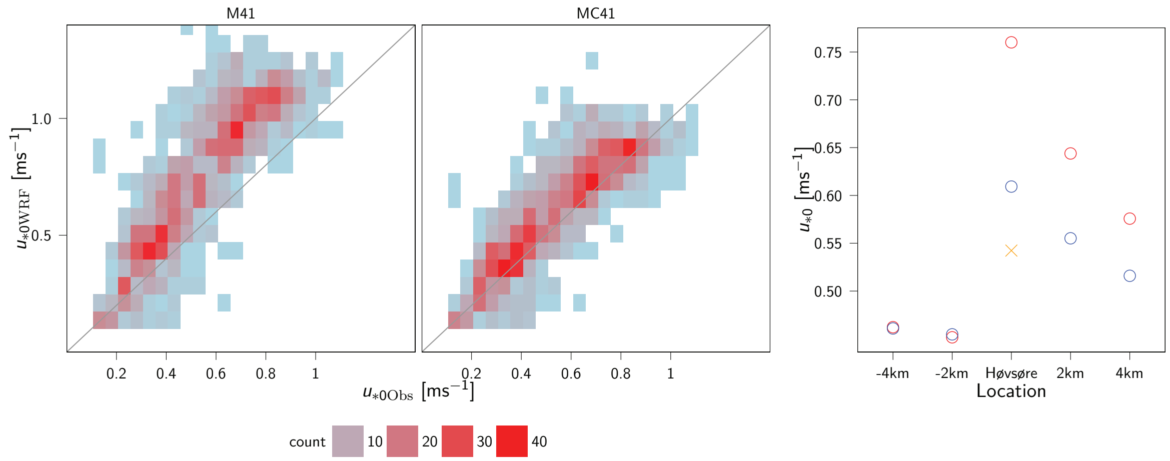

Figure 1: Scatter plot of the observed and modelled u_* with the default (left) and realistic (middle) surface roughness. The right figure shows u_* at 5 grid points (M_{41}=red circles, MC_{41}=blue circles and cross=observed) with westerly flow at Høvsøre

merical studies of the flow in the internal boundary layer, but the effect is found very close to the coastline only [6]. The equilibrium layer of the internal boundary layer, where the fluxes are in equilibrium with the new surface roughness, extents to approximately 16 m at the meteorological mast [2]. Therefore it is unrealistic that for both WRF simulations, the surface layer fluxes have not reached their equilibrium values after more than 2 km.

3.2 The wind profile and PBL schemes

For the westerly sector the wind speed profiles for the vertical cross section are shown in figure 2. Upstream at sea (-4 km), the profiles show a high near surface wind speed which decreases once the wind crosses the shoreline. The realistic surface roughness simulations (right) show a more realistic wind speed at 10 m when an equilibrium with the surface fluxes forms after several kilometers.

The MYNN scheme adapts quicker to the surface conditions and shows a higher decrease in wind speed at 10 m, whereas the YSU scheme shows deviations between upstream and downstream profiles up to larger heights. It is clear that none of the PBL schemes model the high shear in the layer between 0–200 m. Increasing the vertical resolution from 8 tot 22 levels did not have any noticeable effect on the shear in this layer. For the easterly sector there was a large under prediction in stable conditions, because WRF did not model the low level jet (not shown).

3.3 Upper boundary conditions

In figure 2 the observed and modelled wind profiles do not approach the same geostrophic wind near the top of the boundary layer. To investigate the effect the simulations were repeated but using the ERA-interim data. In table 4 the wind speeds at 650 m winds for the two sources of (re)analysis data are shown. The difference between NCEP final analysis data (M_{41} and Y_{41}) versus ERA interim data (ME_{41} and YE_{41}) is generally small. Therefore we discard the data used to initialize the model as the source of under prediction in high level winds.

Table 4: Results from linear regression through origin.

		U_{650}			
		M41	ME41	Y41	YE41
West	slope	0.99	0.96	0.95	0.93
	R^2	0.76	0.78	0.80	0.81
East	slope	0.97	0.98	0.96	0.97
	R^2	0.84	0.83	0.82	0.81

4 Conclusions

The momentum transfer in the coastal boundary layer and the shape of the wind profile was modelled with version 3.3 of the WRF-ARW model for a four week period with flow from the east with homogeneous upwind conditions and flow from the west with inhomogeneous upwind conditions. Simulations were performed with a first and a higher order closure scheme and two vertical resolutions.

The default roughness in WRF was too high, but simulations with a lower roughness still gave a over prediction of the surface layer fluxes. This was partially caused by the large changes in wind profile and surface layer fluxes in grid points near the coast. The flow adjustment in was too slow and the wind profile approach the corrected surface values only after several grid points in land. For flow with homogeneous upwind conditions WRF over estimates the surface layer fluxes with both the realistic and default surface roughness. This results in a slightly too high near surface wind speed in WRF.

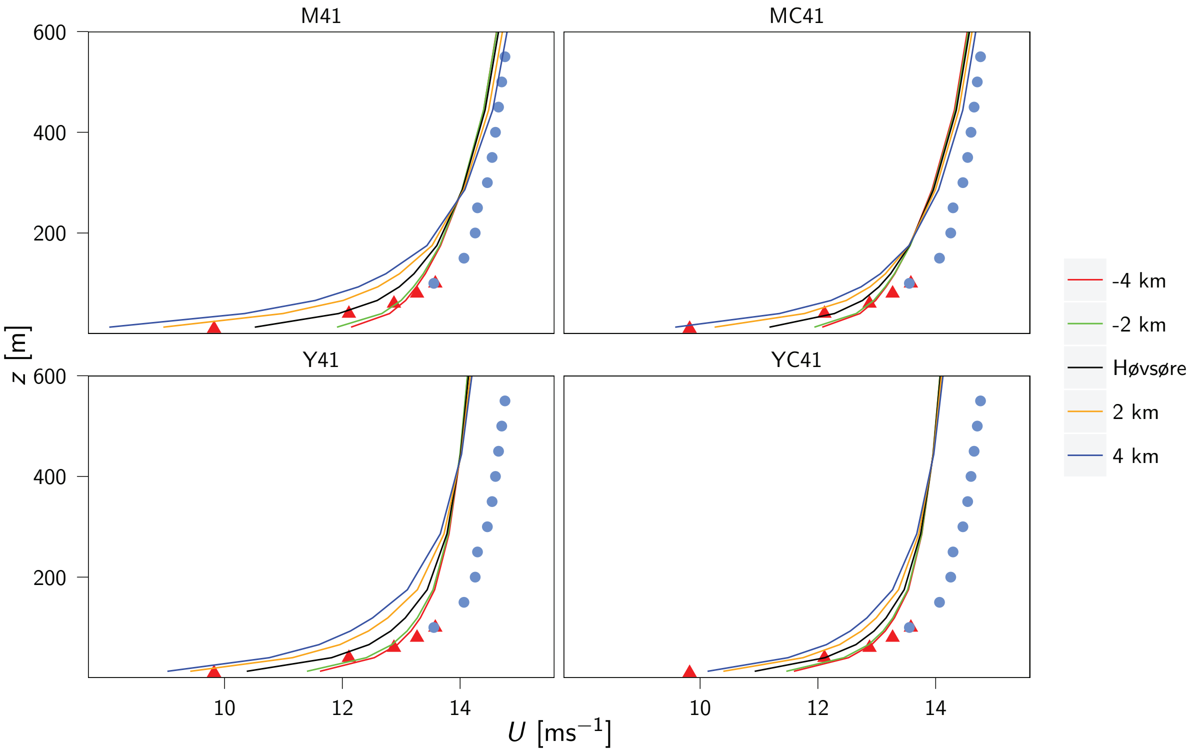

Figure 2: Measured and modelled mean wind speed profiles for westerly winds for different grid points in WRF. For the abbreviations, see table 2

At larger heights there is again an under prediction in wind speed. This is a consequence of the enhanced mixing of PBL schemes in stable conditions and was found for both first and second order schemes. The amount and strength of low level jets was under estimated. Increasing the vertical resolution and using different boundary conditions did not improve the results for both homogeneous and inhomogeneous conditions.

The observed behaviour of the surface layer fluxes and wind profiles suggest that output from mesoscale models should be treated with care near the coastline. The negative wind speed bias in both sectors results in an under estimation of mean wind speed, which is important for wind turbines that are often located near the shoreline and becoming larger in size. The new wind lidar measurements proved to be highly useful for evaluating the performance of the PBL schemes and will be further studied for different locations in the near future.

Acknowledgements

The study is supported by the Danish Research Agency Strategic Research Council (Sagsnr. 2104-08-0025) “Tall wind” project and the EU FP7-People-IEF VSABLA (PIEF-GA-2009-237471). The contribution of C.L. Vincent was supported by the Danish Council for Independent Research - Technology and Production Sciences individual post-doc project (case number 10-093196).

References

[1] Floors, R., Batchvarova, E., Gryning, S.-E., Hahmann, A. N., Peña, A., & Mikkelsen, T. (2011a). Atmospheric boundary layer wind profile at a flat coastal site – wind speed lidar measurements and mesoscale modeling results. *Advances in Science and Research*, 6(April 2010), 155–159.

[2] Floors, R., Gryning, S., Peña, A., & Batchvarova, E. (2011b). Analysis of diabatic flow modification in the internal boundary layer. *Meteorologische Zeitschrift*, 20(6), 649–659.

[3] Hong, S.-Y., Noh, Y., & Dudhia, J. (2006). A new vertical diffusion package with an explicit treatment of entrainment processes. *Monthly Weather Review*, 134(9), 2318–2341.

[4] Nakanishi, M. & Niino, H. (2009). Development of an improved turbulence closure model for the atmospheric boundary layer. *Journal of the Meteorological Society of Japan*, 87(5), 895–912.

[5] Peña, A., Hasager, C. B., Gryning, S.-E., Courtney, M., Antoniou, I., & Mikkelsen, T. (2009). Offshore wind profiling using light detection and ranging measurements. *Wind Energy*, 12(2), 105–124.

[6] Shir, C. C. (1972). A numerical computation of air flow over a sudden change of surface roughness. *Journal of the Atmospheric Sciences*, 29(2), 304–310.

[7] Steeneveld, G. J., Tolk, L. F., Moene, A. F., Hartogensis, O. K., Peters, W., & Holtslag, A. A. M. (2011). Confronting the WRF and RAMS mesoscale models with innovative observations in the Netherlands: Evaluating the boundary layer heat budget. *Journal of Geophysical Research*, 116(D23), D23114.

Alignment of stress, mean wind, and vertical gradient of the velocity vector

J. Berg[1] , **J. Mann**[1] **and E. G. Patton**[2]

[1]Technical University of Denmark, Department of Wind Energy, Frederiksborgvej 399, 4000 Roskilde, Denmark, jbej@dtu.dk.
[2]National Center for Atmospheric Research, MMM Division, Boulder, Colorado, US

Abstract

In many applications in the atmospheric surface layer the *turbulent-viscosity hypothesis* is applied, i.e. the stress vector can be described through the vertical gradient of velocity. In the atmospheric surface layer, where the Coriolis force and baroclinic effects are considered negligible, this is supposedly a good approximation. High resolution large-eddy simulation (LES) data show that it is indeed the case. Through analysis of WindCube lidar measurements accompanied by sonic measurements we show that this is, on the other hand, rarely the case in the real atmosphere. This might indicate that large scale mechanisms play an important role in the misalignment observed in the atmosphere. Baroclinicity is one candidate of a such, instationarity another. In this contribution we will present ongoing work: data from both a WindCube lidar, sonic anemometers and LES and discuss the results in the context of atmospheric boundary layer modeling.

The measurements are from the Danish wind turbine test sites at Høvsøre. With the WindCube lidar we are able to reach heights of 250 meters and hence capture the entire atmospheric surface layer both in terms of wind speed and the direction of the mean stress vector.

1 Introduction

We present experimental evidence of misalignment of the mean stress vector and the vertical gradient of the velocity vector. If perfectly aligned, the angle

$$\beta = \tan^{-1}(\frac{dV}{dz}/\frac{dU}{dz}) - \tan^{-1}(\langle v'w' \rangle / \langle u'w' \rangle) \tag{1}$$

should be zero. In the above equation, U and V are the two components of the mean wind (often $V = 0$ from the definition of coordinate system) and $\langle u'w' \rangle$ and $\langle u'w' \rangle$ are the two components of the mean momentum flux (Reynolds stresses). That any such alignment should exist is not clear at all, it is, however, still the main ansatz behind the *turbulent-viscosity hypothesis* (Pope, 2000), widely used in modeling of the atmospheric boundary layer.

Another interesting and much more studied quantity is the angle between the mean wind direction and the mean stress vector, defined as

$$\alpha = \tan^{-1}(V/U) - \tan^{-1}(\langle v'w' \rangle / \langle u'w' \rangle). \tag{2}$$

In the absent of the Coriolis force, which is considered to be neglected in the atmospheric surface layer, the angle, α should be zero for homogeneous surface conditions. Grachev et al. (2003) discuss the non-zero angle, observed in offshore conditions, as a result of ocean swell. In (Barnardes and Dias, 2010; Weber, 1999) the scatter around zero angle is discussed in terms of averaging and inhomogeneous surface conditions. We show in this paper, that a systematic angle exists, even for homogeneous surface conditions. Due to its fixed coordinate system, the wind lidar seem like the obvious choice of instrument and its usage in the present context is therefore the main focus of this contribution.

2 Sonic anemometer measurements at Bolund

The Bolund measurement campaign in the winter of 2007-2008 in Denmark (Berg et al., 2011) indicated that the surface fluxes (sonic measurements in 5 m and 12 m) were misaligned with the mean wind. Figure 1 shows histograms of α for upstream conditions with fetch lengths of 800 m and 7 km. The measurements (12 m above sea level) are carried out on an offshore platform in a shallow water fjord and should therefore not be influenced by swell as discussed in Grachev et al. (2003). The mean value of α is 15° and 21° for the two fetch classes, respectively. The variance is, however, much larger for the shorter fetch, as expected, due to inhomogeneous conditions and accompanying high turbulence levels onshore. The sign of α is in agreement with an ABL Ekman spiral in the northern hemisphere (the wind vector is to the right of the momentum flux vector), although the value is much

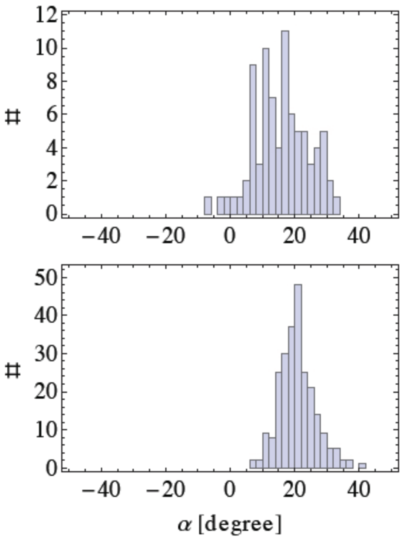

Figure 1: Histogram of α measured at Bolund. *Top:* Short fetch, 800 m. *Bottom:* Long fetch, 7 km. . We have used 30-min averages of momentum flux and wind speed in neutral/near-neutral conditions.

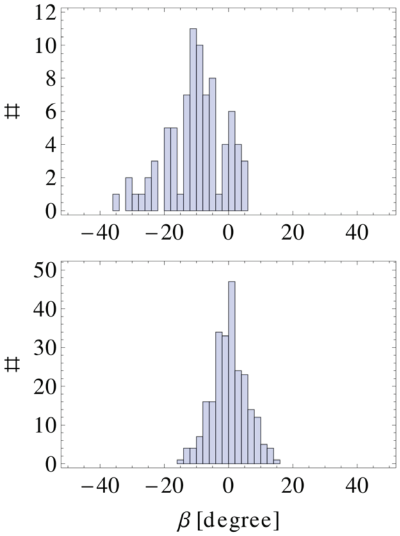

Figure 2: Histogram of the angle, β, measured at Bolund. *Top:* Short fetch, 800 m. *Bottom:* Long fetch, 7 km. . We have used 30-min averages of momentum flux and wind speed in neutral/near-neutral conditions.

higher than we would expect taking the low measurement height (12 m) into account.

We have also calculated the angle, β, where the gradient wind speed vector is calculated as a finite difference between the two heights, 5 m and 12 m. The result is presented in Figure 2. For the short fetch, the mean of β equals $-10°$ while it is zero for the long fetch as assumed by the *turbulent-viscosity hypothesis*. Again the variance is largest in the short fetch case.

3 Lidar measurements at Høvsøre

The Bolund measurements were done with sonic anemometers close to the surface. The ultimate goal would be to monitor the behavior throughout the ABL: for which sonic anemometers seem inadequate due to the tall masts needed and alignment issues. We therefore turn to pulsed lidars, more specifically WindCube from the French company Leosphere, which have shown to successfully measure turbulent fluxes in the streamwise direction by using a two beam technique (Mann et al., 2010): the authors furthermore find from theoretical considerations that for heights above approximately 50 m, the constant systematic error on measuring $\langle u'w' \rangle$ is approximately 20%. In this paper the transverse component, $\langle v'w' \rangle$, is of equally importance, in principle, if the error on $\langle u'w' \rangle$ is of similar size - we might expect the angles, α and β to be unbiased by the filtering of the WindCube measurements. We use the technique described in Mann et al. (2010) for estimation for both the streamwise and the transverse component of momentum flux and apply the same quality criterion.

We now look at simultaneous measurements from a sonic anemometer and the WindCube at the Danish test site for large wind turbines at Høvsøre (see Peña (2009) for a site description of Høvsøre). As shown in Figure 3, where we present measurements of the angle, α, this is unfortunately not fully the case for all three different stability cases: for neutral stratification the slope of the best linear fit is just above 0.7, while it is much lower in the stable and unstable case. We would expect the best correlation in the unstable case, due to more similar turbulent integral length scales in the streamwise and transverse directions. This is, however, not observed. It turns out (not shown) that the transverse component, $\langle v'w' \rangle$, is worse correlated between the sonic anemometer and the lidar than $\langle u'w' \rangle$; even the slightest random error in the sonic measurements, for example due to flow distortion from the mast, can alter the correlation. Further studies should look into this. For the time being we will move on and look at WindCube measurements all the way through the surface layer.

In Figure 4 we present vertical profiles of the angles, α, β and γ, from measurements with a WindCube at Høvsøre. γ is the wind veer angle and is thus an indicator of the atmospheric Ekman spiral. Only wind speeds higher than 7 m s^{-1} are shown. Looking first at the blue curves representing, α, the largest values are observed for the stable case (top panel) in agreement with the low height of the ABL and hence an intensification of the Ekman spiral; the two angles, α and γ also seems to follow the same trend (in all three stability cases). The unsta-

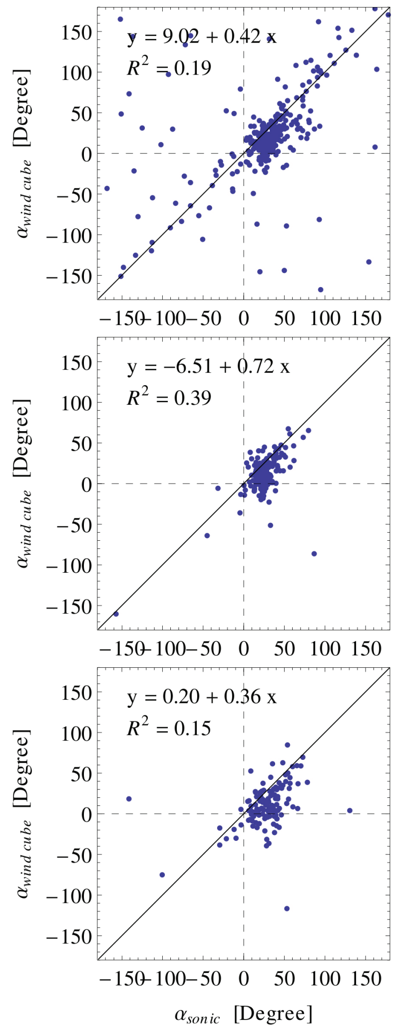

Figure 3: Sonic anemometers vs. WindCube for measurements of the angle, α, at Høvsøre in 100 m in Easterly wind for various stratification: *Top:* Stable. *Middle:* Neutral. *Bottom:* Unstable. We have used 30-min averages of momentum flux and wind speed.

ble profile is rather noisy, but still the trend seems to be consist of positive values of β. The angles in the neutral case are all lower than in the Bolund case, even at 250 m. The wind direction is easterly, which mean that the upstream conditions are fairly homogeneous, even far upstream. We are, however, close (approximately 2 km) to the west coast of Jylland (Danish main peninsula) and large horizontal temperature gradients inducing baroclinicity could potentially add complexity to the larger scales (meso-scales) and hence alter the observations.

The purple curves represent the angle, β. For all three stability classes it is close to zero at 40 m in agreement with the long fetch measurements from Bolund. It then grows close to linearly with height. The growth is largest in the stable case (again the unstable case is very noisy). This is in contrast with the *turbulent-viscosity hypothesis*. In wind energy siting applications the hypothesis is the basis of the state-of-the art numerical models (most often using K-ϵ closure). Whether the misalignment documented here has any practical importance the future will tell.

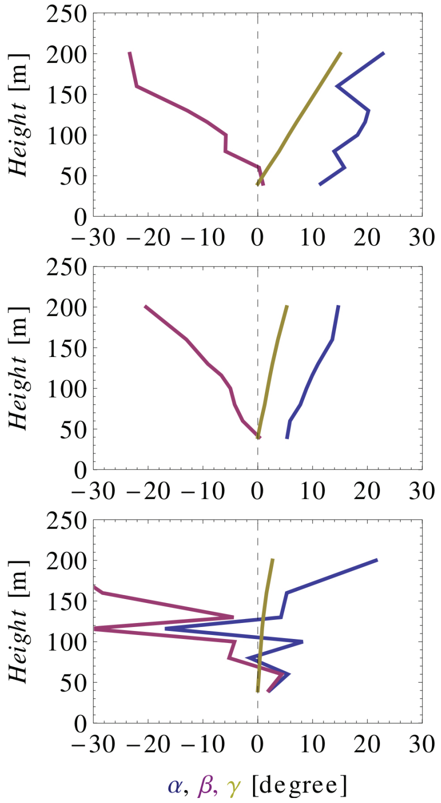

Figure 4: Vertical profiles of the angles, α (blue) and β (purple) and γ (yellow), measured at Høvsøre with WindCube in Easterly wind. *Top:* Stable. *Middle:* Neutral. *Bottom:* Unstable. We have used 30-min averages of momentum flux and wind speed.

For the low wind speed cases (winds smaller than 7 m s^{-1}) the trends observed in the angles, α, β and γ are amplified, i.e. larger angles as we move up in the atmosphere (not shown).

The same results were obtained from pure sonic anemometer measurements at the meteorological mast at Høvsøre, so the non-perfect correlations presented in Figure 3 cannot explain the findings.

4 LES

In order to study the angles, α and β, under more controlled settings, we use high resolution LES. The pseudospectral LES code of Sullivan and Patton (2011) simulates the ABL over flat, homogeneous terrain, with high temporal and spatial resolution. A database containing

LES results from this code has been established, for different ABL states and surface conditions. In Figure 5 we present the LES data. The Figure is constructed in the same way as Figure 4. Besides the exact numbers (the LES stable case is a low wind speed case with a ABL height of 150 m), the main difference from the WindCube data presented in Figure 4 at Høvsøre is the zero angle obtained for β throughout the surface layer. I.e. the momentum flux and the vertical gradient of the velocity vector is aligned.

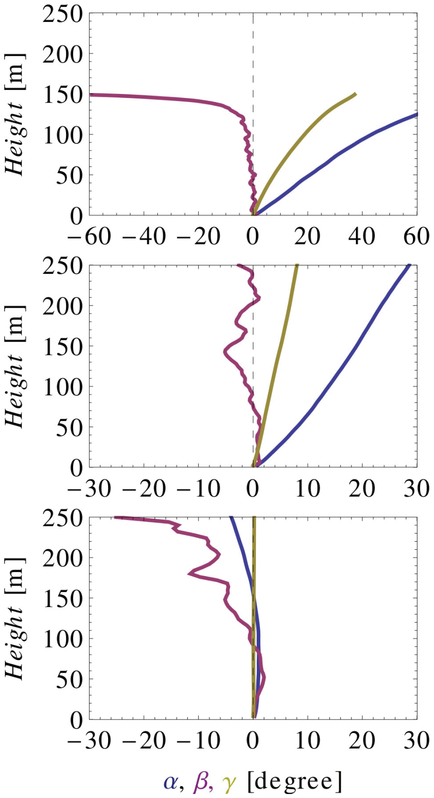

Figure 5: Vertical profiles of the angles, α (blue) and β (purple) and γ (yellow) from LES. *Top:* Stable. *Middle:* Neutral. *Bottom:* Unstable.

5 Final comments

From comparing the measurements from Bolund, Høvsøre and the LES data one thing is certain: we need a theory including more than just the local micro scales. LES is in many ways the logical starting point, since they only include the micro scales. Setting appropriate boundary conditions, for example a horizontal temperature gradient to mimic meso-scale effects, in future LES might seem like a way to go. We should also study other sites with different geography, how does the growth of numerous internal boundary layers affect the transverse momentum flux? The new Danish site of Østerild will be explored in the near future.

Besides sonic anemometers and WindCube lidar we will also try to use the continuous-wave lidar, ZephIR from QinetiQ (Natural Power). Its problem with measuring in the transverse direction should, however, be addressed before any reliable estimate of the momentum flux vector can be obtained.

JB would like to thank fellow colleague Ameya Sathe for helping out a newbie on WindCube issues. The work was partially supported by the `http://www.comwind.mek.dtu.dk` *Center for Computational Wind Turbine Aerodynamics and Atmospheric Turbulence* under the Danish council for strategic research, Grant No. 09-067216.

References

Barnardes, M. and Dias, N. L. (2010). The alignment of the mean wind vector and stress vectors in the unstable surface layer. *Boundary-Layer Meteorol.*, 134:41–59.

Berg, J., Mann, J., Bechmann, A., Courtney, M. S., and Jørgensen, H. E. (2011). The Bolund Experiment, Part I: Flow Over a Steep, Three-Dimensional Hill. *Boundary-Layer Meteorol.*, 141:219.

Grachev, A. A., Fairall, C. W., Hare, J. E., Edson, J. B., and Miller, S. D. (2003). Wind Stress Vector over Ocean Waves. *J. Phys. Ocean.*, 33:2408–2429.

Mann, J., Peña, A., Bingöl, F., Wagner, R., and Courtney, M. S. (2010). Lidar Scanning of Momentum Flux in and above the Atmospheric Surface Layer. *J. Atmos. Ocean. Technol.*, 27:959–976.

Peña, A. (2009). *Sensing the wind profile*. PhD thesis, University of Copenhagen (Risø-PhD-45(EN), www.risoe.dtu.dk).

Pope, S. B. (2000). *Turbulent Flows*. Cambridge University Press, 770 pp.

Sullivan, P. P. and Patton, E. G. (2011). The effect of mesh resolution on convective boundary layer statistics and structures generated by large-eddy simulation. *J. Atmos. Sci.*, 68:2395–2415.

Weber, R. O. (1999). Remarks on the definition and estimation of friction velocity. *Boundary-Layer Meteorol.*, 93:197–209.

Session 13 – Oral Presentations

Turbulence measurements using six lidar beams

Ameya Sathe and Jakob Mann
DTU Wind Energy, Risø campus, Frederiksborgvej 399, 4000 Roskilde, Denmark

Abstract

The use of wind lidars for measuring wind has increased significantly for wind energy purposes. The mean wind speed measurement using the velocity azimuth display (VAD) technique can now be carried out as reliably as the traditional instruments like the cup and sonic anemometers. Using the VAD technique the turbulence measurements are far from being reliable. Two mechanisms contribute to systematic errors in the measurement of turbulence. One is the averaging of small scales of turbulence due to the volume within which lidars measure wind speed. The other is the contamination by the cross components of the Reynolds stress tensor, which arises because, in a VAD scan the lidar beams are combined to obtain different components of the wind field. In this work we demonstrate theoretically, how the contamination by the cross components can be avoided by using the measured variances of the line-of-sight velocities of six lidar beams. Under certain assumptions the volume averaging can then be avoided using the ensemble averaged line-of-sight Doppler velocity spectra. In this way, we can then in principle measure the true turbulence using six lidar beams.

1 Introduction

If say we had a perfect instrument that could measure the wind speed then we could measure all scales of turbulence without having to worry about any flow distortions. We imagine that such a dream instrument would have infinitely small measuring volume and would stably float at different points in space. Unfortunately, we do not live in a 'Harry Potter' world that have magic wands to virtually do anything, simply with a wave of a wand. We then have to deal with real-world instruments that have a finite measuring volume and a certain geometry. At present the best available instruments to measure turbulence are the sonic anemometers. These instruments need to be mounted on a meteorological mast (met-mast), and care has to be taken to avoid flow distortions due to the mast and the instrument itself. Met-masts are expensive structures, particularly as their sizes increase with the increasing height of the wind turbines ($>$ 150 m). With rapid expansion of offshore wind energy the cost of installing a met-mast in water increases manifold. If wind turbines would have been confined to only onshore sites and their sizes would have remained relatively small (say up to 50 m) then the wind energy industry would have been content with traditional met-mast anemometry. With new developments, the motivation to look for alternative ways of measuring wind speed has grown manifold. Fortunately, lidars are being investigated in their ability to measure wind speeds.

For wind energy purposes, lidars have been used only recently (since 2006). For meteorological studies they have been used for quite a long time (since 1960s). For wind energy purposes their utility in measuring the mean wind speed has been verified in several studies [Kindler et al., 2007, Peña et al., 2009, Smith et al., 2006]. In all these studies the velocity azimuth display (VAD) technique was employed in data processing. Turbulence measurements are however subjected to large systematic errors. Sathe and Mann [2012], Sathe et al. [2011] explain in detail these systematic errors. Two sources of systematic errors that render imprecise turbulence measurements are:

1. Averaging due to the large sample volume within which lidars measure wind speed
2. Contamination by the cross components of the Reynolds stress tensor

The first source of systematic error results in reducing the amount of measured turbulence. The second source of systematic error results in increasing the amount of measured turbulence. The combined result of these two contrasting effects depends on the type of the lidar (continuous wave or pulsed), height of the measurement, and atmospheric stability [Sathe et al., 2011]. In this work we demonstrate theoretically, how in principle it is possible to counter these sources of systematic errors.

2 Theoretical Considerations

At first it is useful to see mathematically how the cross components of the Reynolds stress tensor (R_{ij}) contribute in the measurement of turbulence using the VAD scan.

According to Sathe et al. [2011],

$$\langle \mathrm{v}'_m \mathrm{v}'_n \rangle_{\text{lidar}} = \int \Phi_{ij}(\boldsymbol{k}) X_i{}^m(\boldsymbol{k}) X_j^{*n}(\boldsymbol{k})\, d\boldsymbol{k}, \qquad (1)$$

where $\boldsymbol{v} = (u, v, w)$ is the wind field, $\langle \mathrm{v}'_m \mathrm{v}'_n \rangle_{\text{lidar}}$ is the component of the Reynolds stress tensor, $\Phi_{ij}(\boldsymbol{k})$ is the three dimensional spectral tensor, $\boldsymbol{k} = (k_1, k_2, k_3)$ is the wave vector, $\int d\boldsymbol{k} \equiv \int_{-\infty}^{\infty}\int_{-\infty}^{\infty}\int_{-\infty}^{\infty} dk_1 dk_2 dk_3$, $X_i{}^m(\boldsymbol{k})$ is the weighting function for the m^{th} component of the wind field and $*$ denotes complex conjugation. In Eq. (1) the Einstein summation is clearly evident on the right hand side.

2.1 How to get rid of contamination by the cross components of the Reynolds stress tensor?

Instead of using a VAD scan, Eberhard et al. [1989] proposed using variances of the line-of-sight velocities. From simple geometrical considerations we then get,

$$\begin{aligned}\langle {v'_r}^2 \rangle &= \langle {u'}^2 \rangle \sin^2\phi \cos^2\theta + \langle {v'}^2 \rangle \sin^2\phi \sin^2\theta \\ &+ \langle {w'}^2 \rangle \cos^2\phi + 2\langle u'v' \rangle \sin^2\phi \sin\theta \cos\theta \\ &+ 2\langle u'w' \rangle \sin\phi \cos\phi \cos\theta \\ &+ 2\langle v'w' \rangle \sin\phi \cos\phi \sin\theta\end{aligned} \qquad (2)$$

where $\langle {v'_r}^2 \rangle$ is the line-of-sight velocity variance, $\mathrm{v}'_i\mathrm{v}'_j$ are the components of the Reynolds stress tensor for $i, j = 1..3$, θ is the azimuth angle and ϕ is the half-opening angle. Thus, if we orient the lidar beams at certain θ and ϕ then $\langle {v'_r}^2 \rangle$ is only a function of six unknown components of R_{ij}. If we denote $\boldsymbol{\Sigma} = \left(\langle {u'}^2 \rangle, \langle {v'}^2 \rangle, \langle {w'}^2 \rangle, \langle u'v' \rangle, \langle u'w' \rangle, \langle v'w' \rangle\right)$ as a matrix of six unknown components of R_{ij} and $\boldsymbol{S} = \left(\langle {v'_{r_1}}^2 \rangle, \langle {v'_{r_2}}^2 \rangle, ..., \langle {v'_{r_6}}^2 \rangle\right)$ as a matrix of the variances of line-of-sight velocities, then mathematically we can write (from Eq. 2),

$$\boldsymbol{\Sigma} = \boldsymbol{M^{-1}S} \qquad (3)$$

where, $\boldsymbol{M}$ is a 6×6 matrix of the coefficients of $\boldsymbol{\Sigma}$. In principle we then need six lidar beams to measure R_{ij}. However, choosing any random combination of lidar beams would introduce random errors in the measurement of R_{ij}. In order to minimize the random errors in the measurement of R_{ij}, Sathe [2012] derived the objective function,

Minimize $f(\boldsymbol{X}) =$

$$Tr\left(\begin{bmatrix} \frac{7}{8} & \frac{1}{8} & 0 & 0 & 0 & 0 \\ \frac{1}{8} & \frac{7}{8} & 0 & 0 & 0 & 0 \\ 0 & 0 & 1 & 0 & 0 & 0 \\ 0 & 0 & 0 & \frac{3}{2} & 0 & 0 \\ 0 & 0 & 0 & 0 & 1 & 0 \\ 0 & 0 & 0 & 0 & 0 & 1 \end{bmatrix} \boldsymbol{M}^{-1}\boldsymbol{M}^{-1T}\right) \qquad (4)$$

subject to constraints,

$0^\circ \leq \theta_i|_{i=1..6} \leq 360^\circ$

$0^\circ \leq \phi_i|_{i=1..6} \leq 45^\circ$

where $\boldsymbol{X} = (\theta_i, \phi_i)|_{i..6}$. By optimizing Eq. (4), we get the optimum configuration as given in table 1. Substituting the values of θ_i, ϕ_i from table 1 in Eq. (3)

Table 1: Optimum configuration

i	1	2	3	4	5	6
θ_i	0	72	144	216	288	288
ϕ_i	45	45	45	45	45	0

we can then estimate $\boldsymbol{\Sigma}$ from the measurements of $\boldsymbol{S}$. We thus obtain R_{ij} without any contamination by the cross components.

2.2 How to get rid of volume averaging?

To get rid of volume averaging Mann et al. [2010] derived an expression for a continuous wave lidar such that ensemble averaged Doppler spectra is used instead of individual Doppler spectra. Mathematically, it is given as,

$$\langle S(v_r) \rangle = \int_{\infty}^{\infty} \varphi(s) p(v_r(s)) ds, \qquad (5)$$

where $\langle S(v_r) \rangle$ is the ensemble averaged Doppler spectra, $\varphi(s)$ is the weighting function, and $p(v_r(s))$ is the probability density function of v_r at position s. By assuming a reasonable $p(v_r(s))$ (e.g. Gaussian) we obtain $\langle S(v_r) \rangle$ as a function of unfiltered line-of-sight velocity variance σ. Using the measurements we can then fit Eq. (5) and obtain σ.

3 Results

Using the theoretical considerations from section 2, we compare the theoretical calculations of the ratio of variances measured by lidar (continuous wave and pulsed) and that of a point measurement. Owing to lack of measurements we could not get rid of volume averaging. We make the comparisons for three stability conditions, neutral, stable and unstable. The ZephIR manufactured by

Natural Power is used as a continuous wave lidar, and the WindCube manufactured by Leosphere is used as a pulsed lidar. Fig. 1 shows the comparison of the ratio of the variances measured by lidar to that of the point measurement using the VAD scan and the six beam method. We define systematic error as the deviation of the lidar measured turbulence with respect to the true turbulence. Thus, the farther the ratio is from one the more the systematic error. At first it is clearly seen that the variances are attenuated significantly for both lidars, particularly for the w component using the VAD scan. Since the six beam method uses one vertical beam the attenuation is reduced significantly. For the continuous wave lidar the systematic errors increase with height, whereas for the pulsed lidar they decrease with height using both measurement techniques. This is because the measurement volume of the continuous wave lidar increases quadratically with height resulting in greater averaging of turbulence. For a pulsed lidar the measurement volume is constant with height. Furthermore it is interesting to note that using a VAD scan for the pulsed lidar there is hardly any systematic error at greater heights. This is because the averaging of turbulence in the measurement volume is compensated by the contamination by the cross components of R_{ij}. Informally, we can say that the pulsed lidar measures the right turbulence for the wrong reasons. Therefore one should be careful in using the turbulence measurements by the VAD scan-

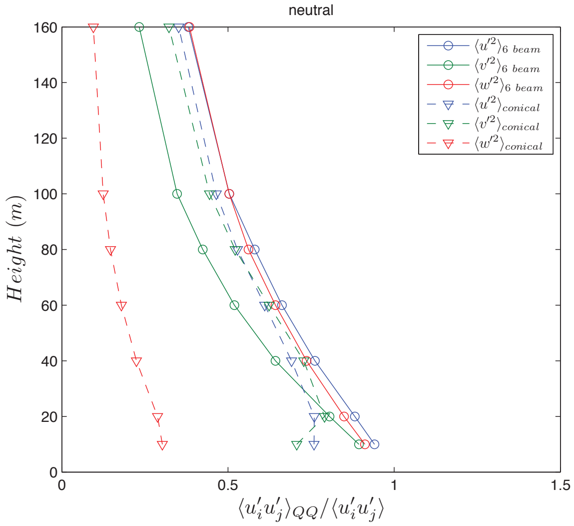

(a) ZephIR

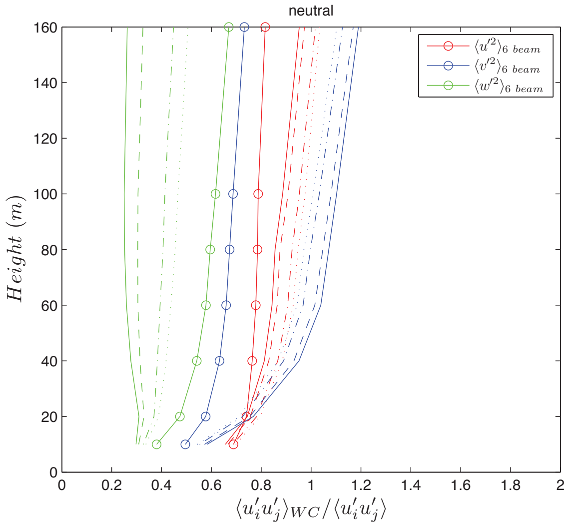

(b) WindCube

Figure 1: Ratio of ZephIR (QQ) and Windcube (WC) variances with respect to the point variances under neutral conditions using the six Beam approach and the VAD (conical) scan

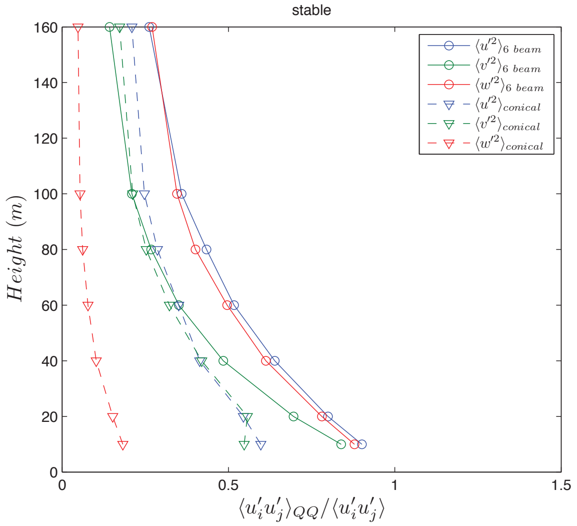

(a) ZephIR

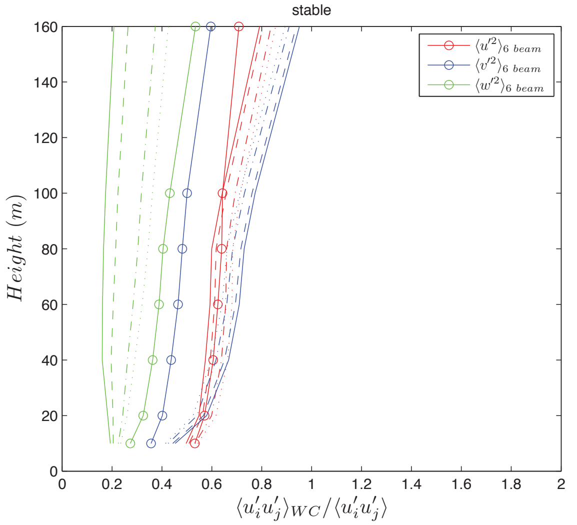

(b) WindCube

Figure 2: Same as Fig. 1 but under stable conditions

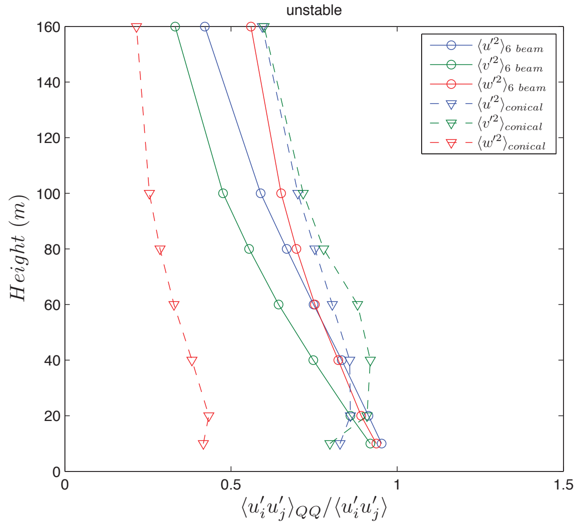

(a) ZephIR

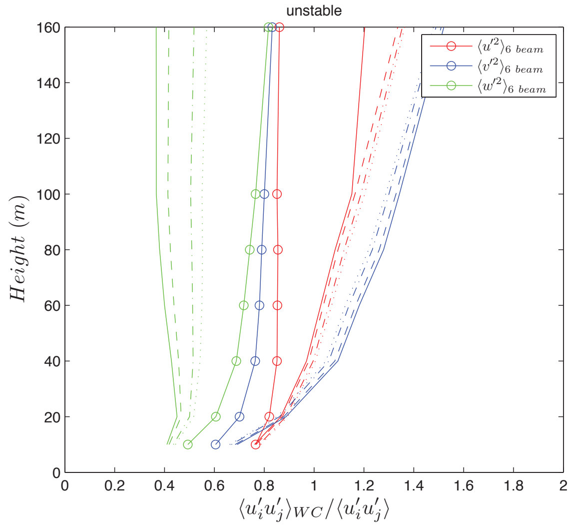

(b) WindCube

Figure 3: Same as Fig. 1 but under unstable conditions

ning technique even if the systematic errors seem negligible. Its implications are clearly seen when we study turbulence spectra [Sathe and Mann, 2012]. For the six beam method the only systematic errors are due to the volume averaging. This is much more evident when we observe Fig. 3 for the pulsed lidar, where we see overestimation of turbulence using the VAD scan. This is because under unstable conditions turbulence scales are large and there is not much averaging in the measurement volume. However, the contamination by the cross components results in measuring more turbulence. For the six beam method we can see that there is no overestimation of turbulence. Under stable conditions (Fig. 2), we observe much more averaging of turbulence due to smaller turbulence scales than under neutral and unstable conditions.

4 Conclusions

The VAD scan should not be used for turbulence measurements since they result in obvious systematic errors; volume averaging and contamination by the cross components. Thus, even if we had a perfect lidar where there was no volume averaging there will always be contamination by the cross components of the Reynolds stress tensor. The six beam method in principle does not suffer from the contamination by the cross components, and has the potential to measure precise turbulence, if and when we get rid of the volume averaging.

References

W L. Eberhard, R E. Cupp, and K R. Healy. Doppler lidar measurements of profiles of turbulence and momentum flux. *Journal of Atmospheric and Oceanic Technology*, 6:809–819, 1989. doi: 10.1175/1520-0426(1989)006⟨0809:DLMOPO⟩2.0.CO;2.

D. Kindler, A. Oldroyd, A. Macaskill, and D. Finch. An eight month test campaign of the QinetiQ ZephIR system: Preliminary results. *Meteorologische Zeitschrift*, 16(5):479–489, 2007. doi: 10.1127/0941-2948/2007/0226.

J. Mann, A. Peña, F. Bingöl, R. Wagner, and M S. Courtney. Lidar scanning of momentum flux in and above the surface layer. *Journal of Atmospheric and Oceanic Technology*, 27(6):792–806, 2010. doi: 10.1175/2010JTECHA1389.1.

A. Peña, C B. Hasager, S-E. Gryning, M. Courtney, I. Antoniou, and T. Mikkelsen. Offshore wind profiling using light detection and ranging measurements. *Wind Energy*, 12(2):105–124, 2009. doi: 10.1002/we.283.

A. Sathe. *Influence of wind conditions on wind turbine loads and measurement of turbulence using lidars*. PhD Thesis, Delft University of Technology, 2012.

A. Sathe and J. Mann. Measurement of turbulence spectra using scanning pulsed wind lidars. *Journal of Geophysical Research*, 117:D01201, 11 PP., 2012. doi: 10.1029/2011JD016786.

A. Sathe, J. Mann, J. Gottschall, and M S. Courtney. Can wind lidars measure turbulence? *Journal of Atmospheric and Oceanic Technology*, 28(7):853–868, 2011. doi: 10.1175/JTECH-D-10-05004.1.

D A. Smith, M. Harris, A S. Coffey, T. Mikkelsen, H E. Jørgensen, J. Mann, and R. Danielian. Wind lidar evaluation at the Danish wind test site in Høvsøre. *Wind Energy*, 9:87–93, 2006. doi: 10.1002/we.193.

A NEW FM-CW RADAR FOR PRECIPITATION AND BOUNDARY-LAYER SCIENCE

Paul E. Johnston[1,2], David A. Carter[1,2], David M. Costa[1,2], James R. Jordan[1,2], Allen B. White[2]

[1]*Cooperative Institute for Research in Environmental Science (CIRES), University of Colorado at Boulder, CIRES, Box 216 UCB, Boulder, CO 80309-0216, USA, paul.e.johnston@noaa.gov*
[2]*NOAA Earth System Research Laboratory(ESRL), 325 Broadway, Boulder, CO 80305, USA, allen.b.white@noaa.gov*

ABSTRACT

Investigators at the Cooperative Institute for Research in Environmental Sciences (CIRES) and the Earth System Research Laboratory (ESRL) have developed a new, award-winning, frequency modulated, continuous wave (FM-CW) S-band radar for precipitation and potentially boundary-layer science. The radar is part of a larger project with the California Department of Water Resources to bring a 21-st century observing system to bear on the state's water resources and flood protection issues. The radar uses vertical profiles of radar reflectivity and Doppler vertical velocity to measure the snow level, the altitude in the atmosphere where falling snow changes into rain. This level is taken to be the altitude of the peak radar reflectivity in the radar bright band resulting from the melting process. The snow level is important to the hydrometeorological prediction, especially in the mountainous areas, because it determines the amount of a basin that is exposed to rain versus snow. The current design is able to detect the snow level during precipitation by transmitting less than 1.0 W of power. Even with this low-powered transmitter, clear-air boundary layer echoes have been detected. A new version of the radar currently being built will use a higher powered transmitter that will enable more robust detection of boundary layer echoes, including the convective boundary layer capping inversion. This paper will describe the network of snow-level detecting radars being deployed in California and will examine the potential application of this instrument to scientific problems involving the planetary boundary layer.

1. INTRODUCTION

In the early 1970s, NOAA's Wave Propagation Laboratory (a predecessor to the current ESRL) developed a FM-CW radar for clear-air studies in the lower atmosphere. This radar operated at S-band frequencies (2800-3000 MHz) and demonstrated observations of clear air turbulence in the boundary layer with 1 meter resolution [1]. The authors in [1] also observed many insects in the data, but were able to discriminate clear-air returns from insect returns. In this radar the first ranges were close enough to the radar that insects could be detected visually and followed through the observations.

During the same period, NOAA's Aeronomy Laboratory (another ESRL predecessor) developed pulse Doppler radars for clear-air studies of the atmosphere. Gage and Balsley [2] reviewed the pulse technique showing wind measurements to 20 km heights. Pulsed systems were eventually developed at several frequencies (50 MHz, 404 MHz, 449 MHz, 915 MHz, and 1290 MHz) becoming useful instruments for wind measurement in a variety of applications and environments.

Both techniques showed promise for probing the atmosphere. Due to the high frequency of the S-Band FM-CW, its clear-air performance was limited to the lowest parts of the troposphere, but provided very high resolution. By utilizing much lower frequencies, the pulsed systems demonstrated the ability to measure winds into the stratosphere, at much coarser vertical resolution.

In the 1990s, interest in the vertical structure of precipitating clouds led the Aeronomy Laboratory researchers to adapt the pulsed Doppler wind-profiler techniques to S-band for the study of precipitation processes [3]. This pulsed S-band became the S-PROF radar system used by ESRL researchers for precipitation and weather research. Five S-PROF radars are currently in use, two of which utilize the original WPL FM-CW antennas.

The S-PROF pulsed radars have exhibited robust operation in many field campaigns. In 2007, a need arose to develop a snow-level sensing radar to support the California Department of Water Resources. A lower cost system was desired, so that more sites could be monitored. Additionally, several minor issues with the pulsed radars needed to be addressed. The three major issues with the S-PROF radars are range resolution, loss of sensitivity with snow, and low altitude performance. This led ESRL/CIRES researchers to develop a new S-band FM-CW radar.

2. SNOW-LEVEL RADAR DESCRIPTION

The Snow Level Radar (SLR) is an FM-CW radar designed for all weather operation. One of the problems encountered with the S-PROF radars is high attenuation when the radar antennas are covered with melting snow. Figure 1 shows the SLR at Colfax,

Figure 1. The SLR located in Colfax, CA with the snow, 8 December 2009. The transmit and receive antennas are located under the slanted plastic covers.

California in December 2009. The transmit and receive antennas are located in the shrouds, with steep covers to let snow slide off. The radar electronics are located in the equipment enclosure located between the two antennas. The entire radar uses a utility trailer as a platform, making these systems easily transportable.

The SLR transmits a 730 mW signal, with a center frequency of 2835 MHz. The SLR uses the Double-FFT processing technique described by Barrick [4] and by Strauch [5]. The first FFT converts the received signal from frequencies to range each sweep. The second FFT converts the sweep to sweep data to velocity spectra at each range. After the first FFT, the data are composed of complex voltages as a function of range, just like the data in a pulsed radar system. This allows the use of ESRL's pulse Doppler analysis software and algorithms to be used with negligible changes. The output data formats are the same as ESRL's pulsed systems so no additional software development was required to analyze and display the data.

Typical operating parameters for the SLR give 252 range gates spaced every 40 m starting at 40 m above the radar, extending to 10 km. The full scale Nyquist velocity is 23 m s^{-1}. Approximately 100 256-point power spectra are averaged together to give 30 second reflectivity and velocity profiles.

The reflectivity and velocity profiles are used as inputs to the automated brightband detection algorithm developed by White [6] to compute snow levels from radar data every 10 minutes. The snow-level data are transmitted from each radar every hour to provide near real-time information about precipitation and snow-level above the radar site.

A variation of the SLR is being constructed. Instead of a ~1 W output, it will have 12 W output. This will increase the sensitivity of the SLR so it can be used for observing some clear-air turbulence in the boundary layer.

3. RADAR DATA

Working with other agencies, ESRL has installed seven SLR radars in the central valley of California; shown in Figure 2. Data from six of these radars is shown in Figure 3, as displayed on the Internet: (www.esrl.noaa.gov/psd/data/obs/). The top panel is the northernmost site, Happy Camp. The panels then proceed the next site south, Shasta Dam, then Oroville Dam, Colfax, New Exchequer Dam, and the southernmost site, Pine Flat Dam.

Figure 2. Map of snow-level radars in central California.

Relative radar reflectivity is shown the contours in Fig. 3. Many features common in the SLR data are shown. When there is stratiform rain, the brightband is very evident. In the Oroville and Colfax systems, there are instrumental artifacts which create lines in the data. When it is not raining, ground clutter, birds, and some clear-air turbulence are evident in the backscattered signals.

The speckled region starting about 0300 UTC on 31 March in the Pine Flat data (lowest panel) is a nocturnal bird migration. This migration is evident in other radars, but is clearest at Pine Flat. The migration starts about an hour after sunset, continuing nearly to sunrise.

There are hints of the top of the daytime convective boundary layer in several of the radars. The clearest boundary layer is in the Colfax data, about 2000 UTC on 30 March, with a height near 2 km.

4. RADAR SENSITIVITY

The data from a SLR has been calibrated to absolute units by comparison with a tipping bucket rain gage.

The radar calibration constant was determined so that the total accumulation of rain observed the SLR matched the amount measured by the rain gage for the same storm. This provides a calibration of the radar so that estimates of the sensitivity of the radar can be computed. White, et al, [7] determined the calibration for the S-Band pulsed system, with 100 m pulses.

Figure 4 shows the minimum detectable reflectivity for precipitation for the FM-CW SLR and the S-PROF radar. The 100-m S-PROF curve shows the calibration of [7]. The curve to farthest to the right shows the calibrated SLR value. The next curve shows the standard 60 m data from S-PROF is 8 dB more sensitive than the SLR. The dashed grey curve is the calibration curve for the S-PROF operating with 100 m resolution described in [7]. The dashed black curve shows the expected performance of a SLR with a 12 W transmitter is close to S-PROF sensitivity.

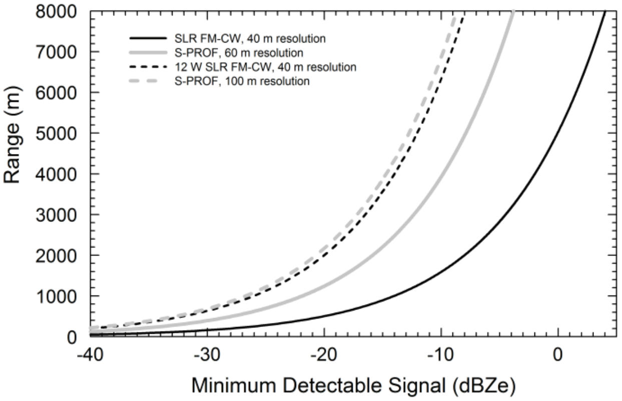

Figure 4. Curves showing the minimum detectable signal for SLR and S-PROF radars for precipitation backscatter.

Once a calibration factor has been determined, it is straightforward to convert from the volume reflectivity for raindrops to a volume reflectivity for clear air based on the structure parameter for the index of refraction, C_n^2. Figure 5 shows the same curves as Figure 4, scaled for the clear air backscatter. The SLR normally operates with a full-scale velocity of 24 m s^{-1}. For operation in clear-air, the full-scale velocity can be changed to 12 m s^{-1}, which will give 3 dB more sensitivity to the radar, as shown in Fig. 5.

5. CONCLUSIONS

ESRL's new FM-CW radar has demonstrated the ability to monitor the brightband and determine snow levels. This new instrument is not as sensitive as the S-PROF radars. The addition of a higher power transmitter will bring the sensitivity close to the S-PROF performance. Even with the high power amplifier, the SLR cost is a small fraction of the S-PROF system.

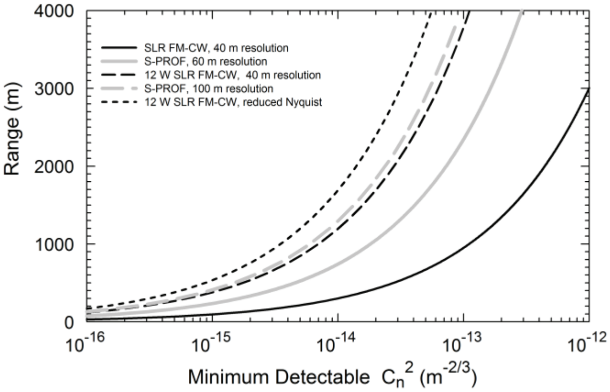

Figure 5. Curves showing the sensitivity of S-PROF and SLR to clear-air turbulence backscatter.

ACKNOWLEDGMENTS

The California Department of Water Resources is acknowledged for the provision of funding. The talented and dedicated engineering team is the Water Cycle Branch of ESRL assisted with the deployment, operation, and maintenance of the SLRs.

REFERENCES

1. Bean, B. R., R. E. McGavin, R. B. Chadwick, and B. D. Warner, 1971: Preliminary results of utilizing the high resolution FM radar as a boundary-layer probe. *Bound-Lay Meteorol*, **1,** 466-473.

2. Gage, K. S., and B. B. Balsley, 1978: Doppler Radar Probing of the Clear Atmosphere. *Bulletin of the American Meteorological Society*, **59,** 1074-1093.

3. Ecklund, W. L., C. R. Williams, P. E. Johnston, and K. S. Gage, 1999: A 3-GHz Profiler for Precipitating Cloud Studies. *Journal of Atmospheric and Oceanic Technology*, **16,** 309-322.

4. Barrick, D. E., 1973: FM/CW Radar Signals and Digital Processing, NOAA Technical Report ERL 283-WPL 26.

5. Strauch, R. G., 1976: Theory and Application of the FM-CW Doppler Radar, Department of Electrical Enginnering, University of Colorado, 97 pp.

6. White, A. B., D. J. Gottas, E. T. Strem, F. M. Ralph, and P. J. Neiman, 2002: An Automated Brightband Height Detection Algorithm for Use with Doppler Radar Spectral Moments. *Journal of Atmospheric and Oceanic Technology*, **19,** 687-697.

7. White, A. B., J. R. Jordan, B. E. Martner, F. Martin Ralph, and B. W. Bartram, 2000: Extending the Dynamic Range of an S-Band Radar for Cloud and Precipitation Studies. *Journal of Atmospheric and Oceanic Technology*, **17,** 1226-1234.

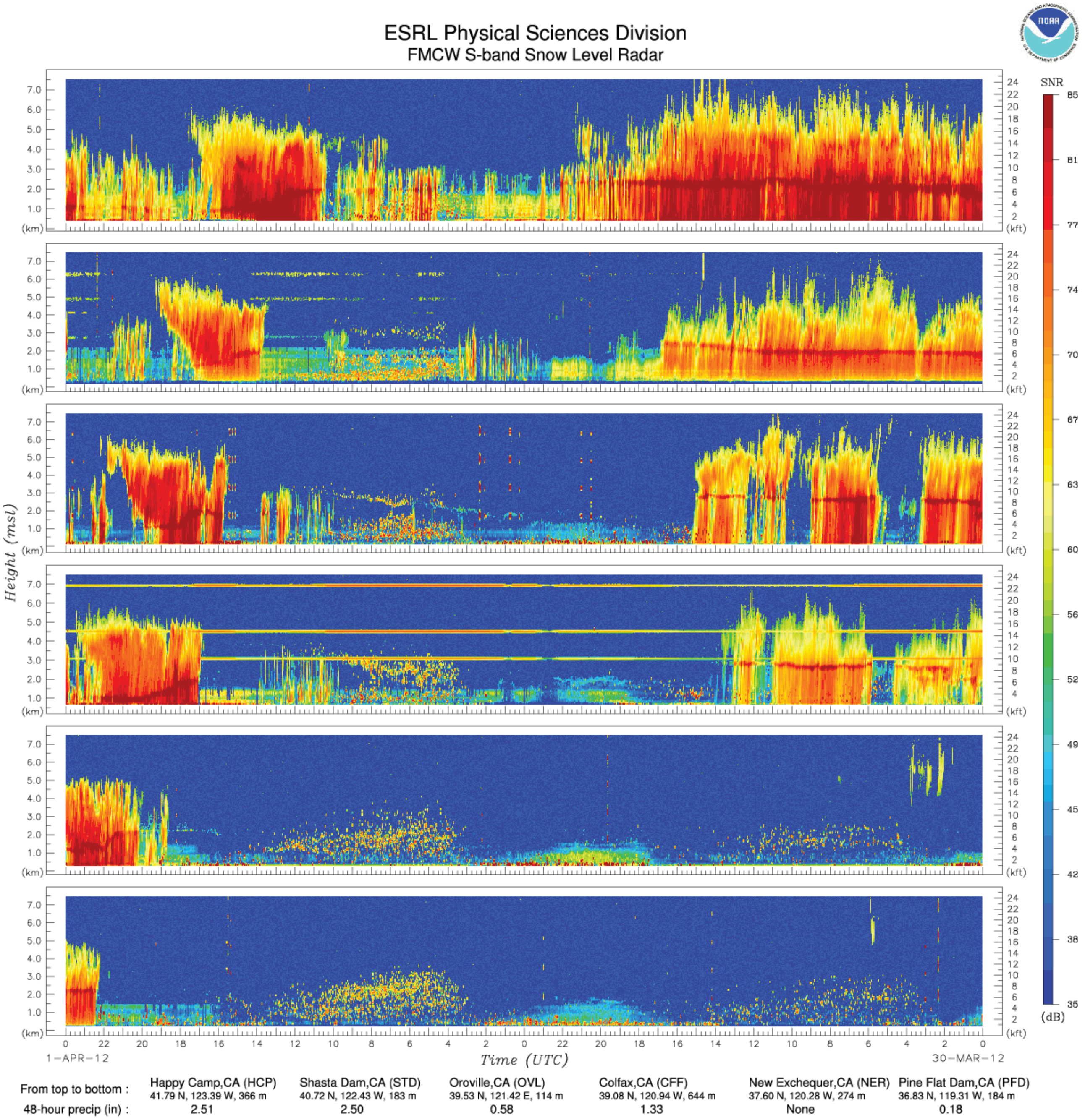

Figure 3. Relative reflectivity for six SLRs for 30-31 March 2012. The radars are displayed in north to south order.